BEILSTEIN JOURNAL OF NANOTECHNOLOGY

Engineered nanomedicines for advanced therapies

Edited by Michael K. Danquah and
Francesca Baldelli Bombelli

Imprint

Beilstein Journal of Nanotechnology
www.bjnano.org
ISSN 2190-4286
Email: journals-support@beilstein-institut.de

The *Beilstein Journal of Nanotechnology* is published by the Beilstein-Institut zur Förderung der Chemischen Wissenschaften.

Beilstein-Institut zur Förderung der Chemischen Wissenschaften
Trakehner Straße 7–9
60487 Frankfurt am Main
Germany
www.beilstein-institut.de

BEILSTEIN JOURNAL OF NANOTECHNOLOGY

Gold-coated plant virus as computed tomography imaging contrast agent

Alaa A. A. Aljabali[*1], Mazhar S. Al Zoubi[2], Khalid M. Al-Batanyeh[3], Ali Al-Radaideh[4], Mohammad A. Obeid[1], Abeer Al Sharabi[5], Walhan Alshaer[6], Bayan AbuFares[3], Tasnim Al-Zanati[1], Murtaza M. Tambuwala[7], Naveed Akbar[8] and David J. Evans[9]

Full Research Paper

Open Access

Address:
[1]Yarmouk University - Faculty of Pharmacy, Department of Pharmaceutical Sciences, Irbid, Jordan, [2]Yarmouk University - Faculty of Medicine, Department of Basic Medical Sciences, Irbid, Jordan, [3]Yarmouk University - Faculty of Science, Department of Biological Sciences, Irbid, Jordan, [4]Hashemite University - Department of Medical Imaging, Zarqa, Jordan, [5]National Agricultural Research Center, Amman, Jordan, [6]University of Jordan - Cell Therapy Center, Amman, Jordan, [7]SAAD Centre for Pharmacy and Diabetes, School of Pharmacy and Pharmaceutical Science Ulster University, Coleraine, UK, [8]University of Oxford - Cardiovascular Medicine, John Radcliffe Hospital, Oxford, UK and [9]John Innes Centre, Norwich Research Park, Norwich, UK

Email:
Alaa A. A. Aljabali[*] - alaaj@yu.edu.jo

* Corresponding author

Keywords:
biomedical imaging; computed tomography (CT); gold; nanotechnology; viruses; targeting

Beilstein J. Nanotechnol. **2019,** *10,* 1983–1993.
doi:10.3762/bjnano.10.195

Received: 31 May 2019
Accepted: 25 September 2019
Published: 07 October 2019

This article is part of the thematic issue "Engineered nanomedicines for advanced therapies".

Guest Editor: M. K. Danquah

Abstract

Chemical modification of the surface of viruses, both the interior and the exterior, imparts new functionalities, that have potential applications in nanomedicine. In this study, we developed novel virus-based nanomaterials as a contrast agent for computed tomography (CT) imaging in vitro. The gold-coated cowpea mosaic virus (Au-CPMV) particles were generated by the electrostatic adsorption of positively charged electrolyte on the virus capsid with the subsequent incubation and reduction of anionic gold complexes. Au-CPMV particles as a CT contrast agent offer a fast scan time (less than 2 min), low cost, and biocompatibility and allow for high-resolution imaging with ca. 150 Hounsfield units (HU). The Au-CPMV surface was further modified allowing for the incorporation of targeting molecules of specific cell types.

Introduction

Numerous types of nanomaterials are currently under investigation in medicine, including dendrimers, polymeric nanoparticles (NPs), liposomes and protein-based NPs. Each system has advantages and disadvantages in terms of its toxicity, biocompatibility, immunogenicity, distribution and the payload being carried.

Modified protein cages are robust systems that combine imaging capabilities and target selectivity on the same platform. One application is the development of magnetic resonance imaging (MRI) contrast agents. Current contrast agents achieve their effect by increasing the relaxation rates (longitudinal relaxation rate (R_1), transverse relaxation rate (R_2), and pseudo-transverse relaxation rate (R_2*)) of water protons in tissues through the catalysis of alignment of nuclear spins [1], thus manipulating the MR image contrast. This effect is known as paramagnetic relaxation enhancement [2] and is common among contrast agents containing gadolinium [3] and iron oxide nanoparticles [4]. CT is a non-invasive, diagnostic imaging tool that allows for 3-D visual reconstruction and tissue segmentation. It relies on the use of X-rays with wavelengths between 0.01 nm and 10 nm [5]. The CT image is generated from the 360° rotation of the X-ray beam source around the object, with a detector positioned opposite to the radiation source. The obtained attenuation profiles are processed mathematically by algorithms to create a 3-D image reconstructed from the dataset of the scanned object and expressed in Hounsfield units (HU) [6]. X-ray attenuation and the image contrast result from the scattering (differential) of the X-rays in the tissue. Tissue and bones absorb X-rays more strongly than air [7].

NPs hold great potential as molecular imaging tools [8]. In general, NPs carry high contrast agent payloads in comparison to smaller moieties [9]. Semiconductor quantum dots (QDs) are nanosized crystals, a photostable fluorophore with a broad excitation spectrum but narrow emission at wavelengths dependent on the size and chemical composition of the core [10]. NPs, such as QDs and magnetic NPs, generate a contrast signal that is unmatched by smaller chemical counterparts [11]. Although iodine-based contrast agents are the most commonly used CT contrast agents nowadays [12], a variety of materials have been used as CT contrast agents including gold nanoparticles (AuNPs) [13], bromine [14], platinum [15], ytterbium [16], gadolinium [4], and tungsten [15]. Many of the systems are made up of a core that is coated with a polymeric material such as liposomes [17], micelles [13], lipoproteins or polymeric nanoparticles [18]. One of the first examples of such NP-based systems was reported by Caride et al. using brominated phospholipids packaged into liposomes and administered to dogs. Contrast enhancement signals of 40 HU were observed in the liver of imaged animals [14]. Two hours after injection, micelles loaded with 17.7 wt % of iodine at a dose of 170 mg of iodine per kilogram were able to show an attenuation of 150 HU in the heart [19], 57 HU in the liver and 90 HU in the spleen [20].

The development of AuNPs as imaging agents was invigorated after Hainfeld reported the formulation of a 1.9 nm contrast X-ray imaging agent after the injection of rats with 2.7 g gold per kilogram with no observable toxic effects [21]. Cai et al. synthesized AuNPs coated with PEG-2000 with a hydrodynamic radius of 38 nm and a 10 nm core [22] that generated a 100 HU signal in the aorta at a dose of 493 mg of gold per kilogram with a mean circulation half-life of 14.6 h. Von Maltzahan et al. developed PEGylated gold nanorods (13 × 47 nm) as CT contrast agents and for photothermal tumor therapy. The study resulted in tumor elimination and mice survival over 50 days [23]. Further, van Schooneveld et al. reported micelle-based AuNPs by generating 66 nm AuNPs coated with an 11 nm layer of silica and showed that for mice injected with these particles a contrast signal was observed [13]. Popovtzer et al. reported successful CT imaging of squamous cell carcinoma using gold nanorods coated with anti-antigen A9 [24].

The low sensitivity of contrast media represents a major challenge in the targeted CT imaging approach [23]. The minimum detectable signal was defined by Krause [25] to be 30 HU [26], with an attenuation rate of gold being 5.1 HU and with a concentration difference of 5.9 mM between the target and the background noise [27]. The accumulation of such concentration of the contrast agent is very difficult [28]. Therefore, the need to develop different forms on nanoparticles that are densely loaded with CT contrast agents for use in clinical settings will be of great value. The work reported here explores the development of a plant virus-based NP as a CT imaging agent.

In this study, the plant cowpea mosaic virus (CPMV) was coated with a gold shell and the use as a CT contrast agent was evaluated. Although a few publications reported the decoration of the surface of virus capsids with preformed AuNPs in specific patterns [29], to the best of our knowledge, this is the first time that modified plant virus particles have been used for CT imaging in vitro; the generated particles have potential for clinical imaging applications.

Results and Discussion

Characterization of Au-CPMV

A colloidal solution of Au-CPMV was synthesized based on the previously described method [30], by the adsorption of positively charged polymer on the CPMV virus capsid followed by subsequent reduction of gold ions onto the virus capsid. The approach allowed for the control of the size and generated a highly monodisperse distribution with limited coalescence. Au-CPMV assemblies were freely suspended; no aggregation was observed by nanoparticle tracking analysis (NTA) or dynamic light scattering (DLS). The successful coating of CPMV particles with gold was confirmed by TEM (Figure 1). Nearly spherical NPs were observed the average diameters of

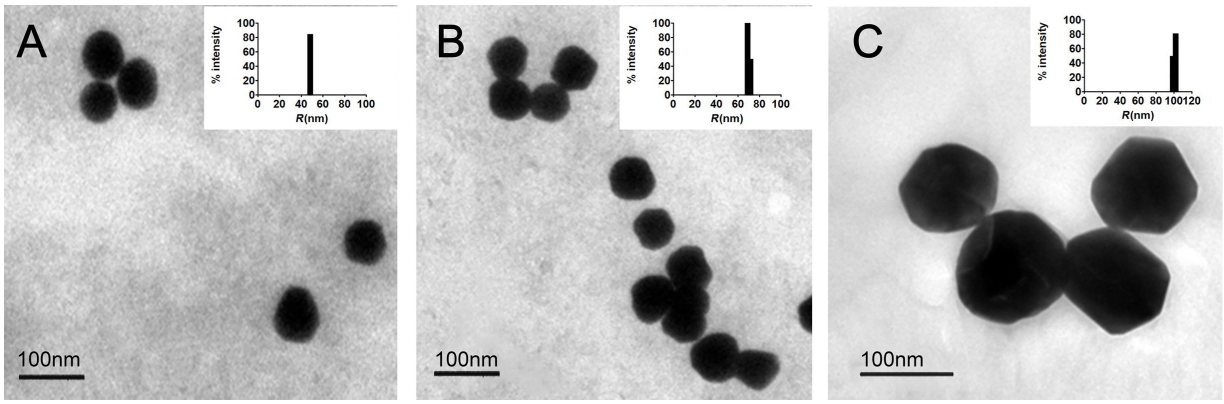

Figure 1: Unstained TEM images of Au-CPMV with the corresponding DLS size distribution histograms (inset). (A) 50 nm Au-CPMV particles; (B) 70 nm Au-CPMV particles; (C) 100 nm Au-CPMV.

which are given in Table 1. Au-CPMV particles imaged by TEM appeared smaller in size than in NTA and DLS measurements, because TEM measures the solid cores of the particles. Three different sizes of NPs were generated (50, 70 and 100 nm) by varying the amount of gold hydroxide. The Au-CPMV particles were dark red in color. Characteristic SPR bands of Au-CPMV were observed in the UV–vis spectrum at λ = 535 nm for particles with a diameter of 50 nm, at λ = 552 nm for particles with a diameter of 70 nm and at λ = 572 nm for particles with a diameter of 100 nm (see below in Figure 3C). This confirms the formation of spherical particles for all three sizes. The surface plasmon resonance depends on the shape and the size of the NPs. For instance, ellipsoid shapes with three different axes have three different dipole modes. When the size of the spherical AuNPs increases, their SPR does not red-shift significantly. However, when the spectrum of rod-shaped particles is recorded the SPR shifts dramatically. The central resonance peak around 520–530 nm represents the transverse SPR, which corresponds to the electron oscillation [31] vertically to the long axis and it coincides spectrophotometrically with the SPR spectrum of spherical nanoparticles [32].

The hydrodynamic diameter and the polydispersity of the Au-CPMV suspended colloidal particles were measured by DLS and NTA. Bare unfunctionalized particles showed a hydrodynamic diameter and polydispersity index (PDI) values of the Au-CPMV particles are listed in Table 1. The values are in accordance with the size observed from the TEM images and further confirms the narrow size distribution of the three types of Au-CPMV particles. The particle size measured by DLS is influenced by the substances adsorbed on the NP surface and by the electrical double layer (solvation shell). Therefore, the size measured in DLS instruments appears to be slightly bigger than that measured by TEM [33]. Particles with PDI values below 0.1 are considered highly monodisperse [33]. Furthermore, to confirm the monodispersity of the particles the Cumulants fit correlogram generated by the DLS instruments, that measures the time at which the correlation starts to significantly decay, gave a slope of 85.3° consistent with a monodisperse distribu-

Table 1: Size, particle count and zeta potential of bare (unfunctionalized) particles, functionalized NPs and CPMV. The concentration of the Au-CPMV particles was 0.5 mg/mL gold for all three particle sizes. Particle count (number of particles per mL) as measured by NTA, n = 6 measurements.

particles	TEM (nm)	DLS		NTA (nm)	particle count (× 10^9/mL)	zeta potential (mV)
		Z-ave (nm)	PDI (nm)			
CPMV	27 ± 2.0	30 ± 1.1	0.05 ± 0.01	28.9 ± 1	3.56	−13
Au-CPMV (50 nm)	44.5 ± 4.2	50.2 ± 3.2	0.04 ± 0.01	51 ± 2	2.32	−45.9 ± 3.1
Au-CPMV (70 nm)	63.5 ± 4.0	68.0 ± 2.0	0.13 ± 0.03	71 ± 3	1.87	−48.2 ± 1.8
Au-CPMV (100 nm)	92.0 ± 3.8	96.0 ± 4.1	0.15 ± 0.08	100 ± 5	1.08	−43.7 ± 2.1
$^{PEG\ 5000}$Au-CPMV	—	50.2 ± 3.2	0.12 ± 0.07	—	—	−30.2 ± 2.1
$^{VCAM1\text{-}PEG5000}$Au-CPMV	—	56.1 ± 2.4	0.16 ± 0.02	—	—	−20.5 ± 1.2

tion. The steeper the line (closer to 90°) the more monodisperse the particles are.

The zeta potential cannot be measured directly, rather it is deduced from the electrophoretic mobility of the charged NPs under an applied electric field. The electrophoretic mobility toward the positive or the negative electrode determines the zeta potential values as negative or positive. The zeta potential values for Au-CPMV particles of different suspensions are summarized in Table 1. The zeta potential is consistent, in each case, with the formation of a similar layer deposited on the surface of the Au-CPMV particles [34]. The zeta potential values of unfunctionalized Au-CPMV agrees with previously reported values [35] ranging between −43.7 ± 2.1 mV and −48.2 ± 1.8 mV [36]. The zeta potential of $^{\text{VCAM1-PEG5000}}$Au-CPMV is −20.5 ± 1.2 mV, that of $^{\text{PEG 5000}}$Au-CPMV is −30.2 ± 2.1 mV. One of the advantages of zeta potential measurements is the possibility to classify NP stability based on the surface charge values. NPs with values in the range of ±30 mV are considered highly stable [37]. The high values of zeta potential observed here confirm the electrostatic repulsion between the NPs that increases their stability and extends their shelf life. The zeta potential of the particles measured after 10 months storage at 4 °C gave similar values.

NTA analysis of the Brownian motion of the Au-CPMV samples on a particle-by-particle basis and the subsequent employment of the Stokes–Einstein equation allows for the derivation of NP size and concentration. Au-CPMV with a concentration of ca. 0.5 mg/mL gold contains roughly 10^9 to 10^{10} Au-CPMV particles per milliliter as determined by NTA. The solution was diluted to obtain ca. 3500 NPs in the quartz cuvette (300 µL) of the instruments under laminar flow. Of these 3500 NPs ca. 100–200 NPs are illuminated at any given time as determined from still images of the recorded video using ImageJ software. The particle size distribution obtained from NTA analysis (Figure 2A) showed a peaks of 51 ± 2 nm, 71 ± 3 nm and 100 ± 5 nm, respectively, with over 90% of the particles being within the measured size thus confirming the narrow size distribution. CPMV (uncoated particles) have an average diameter of 28 nm and a surface charge of ca. 13 mV [38].

Surface functionalization and UV–visible studies

One of the objectives of the present work was the development of a smart cell-specific contrast agent based on the surface modification of Au-CPMV with specific antibodies to target desired cells. Quantification of the amount of antibody attached to the $^{\text{VCAM1-PEG5000}}$Au-CPMV was determined spectrophotometrically at λ = 565 nm using BCA reagent and found to be 1.95 ± 0.18 mg/mL gold. Further, the hydrodynamic radius of the $^{\text{VCAM1-PEG5000}}$Au-CPMV increases from 50.2 ± 3.2 nm to 56.1 ± 2.4 nm after rigorous purification of the antibody-labeled particles suggesting successful modification of their exterior

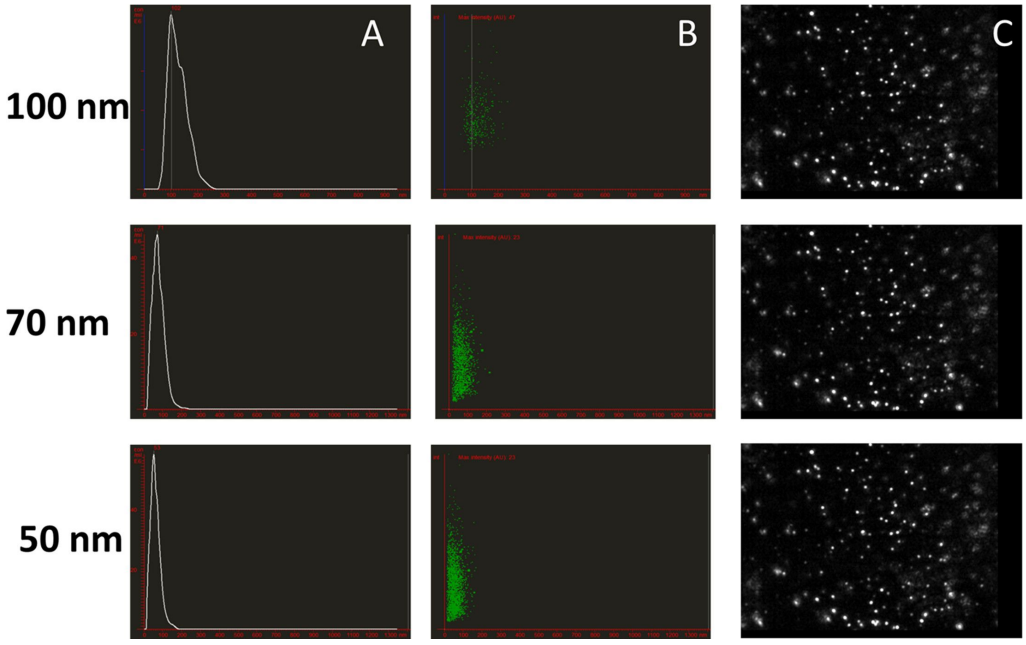

Figure 2: NTA measurement of Au-CPMV at 25 °C recorded from three consecutive runs (60 s) for each sample. (A) particle size (concentration particles/mL as a function of the size); (B) representative NTA scattering distributions of each population (size as a function of intensity) showing compact clustering and indicating highly monodisperse particles with no aggregation, each dot represents a single particle; (C) representative NTA video frame. Data was recorded from six independent experiments.

surface. This observed increase in the hydrodynamic radius is consistent with the previous report of particles coated with proteins [39]. In addition, the UV–vis spectrum was used to evaluate the surface functionalization of Au-CPMV. The localized surface plasmon resonance (LSPR) spectrum shifted by almost 4 nm (Figure 3A). This shift of the extinction maximum from 534 nm to 538 nm is a result of an increase in the local refractive index at the Au-CPMV surface as reported in the literature following surface modification with proteins [40] and indicates that the surface of the Au-CPMV particles is "smooth". The shift would be greater if the surface had an uneven shape. In addition, the 4 nm red-shift of the LSPR peak suggests that the modification of the Au-CPMV surface with antibodies has been successful. This increase in the absorbance shift is expected as the SPR of the AuNPs is sensitive to their interparticle distance and surface state [41]. Furthermore, the LSPR band of Au-CPMV is dependent on the size of the particles. The peak absorbance wavelength increases with the increase of the particle diameter as shown in (Figure 3C). The UV–vis spectrum was used to calculate the concentration of Au-CPMV particles using the Beer–Lambert law with λ = 535 nm and an extinction coefficient $\varepsilon = 1.8 \times 10^{10}$ $M^{-1}{\cdot}cm^{-1}$ for a particle diameter of 50 nm, with λ = 552 nm and $\varepsilon = 6.70 \times 10^{10}$ $M^{-1}{\cdot}cm^{-1}$ for a particle diameter of 70 nm, and with λ = 572 nm using $\varepsilon = 1.57 \times 10^{11}$ $M^{-1}{\cdot}cm^{-1}$ for particles with a diameter of ca. 100 nm. In addition, the EDX spectrum of $^{\text{VCAM1-PEG5000}}$Au-CPMV clearly confirms the presence of gold with a signal at 2.120 keV and 9.712 keV as indicated by the white arrows (Figure 3B) and a strong signal from sulfur (red arrow in Figure 3B) from the linker on the surface of the Au-CPMV particles.

To confirm successful modification of the Au-CPMV with antibodies zeta potential measurements were carried out [39]. The zeta potential of the 50 nm Au-CPMV particles decreased from −45.9 ± 3.1 mV to −53.8 ± 2.4 mV upon antibody coating of the particles. The zeta potential value of $^{\text{VCAM1-PEG5000}}$Au-CPMV becomes more negative [38], which is consistent with the literature [42].

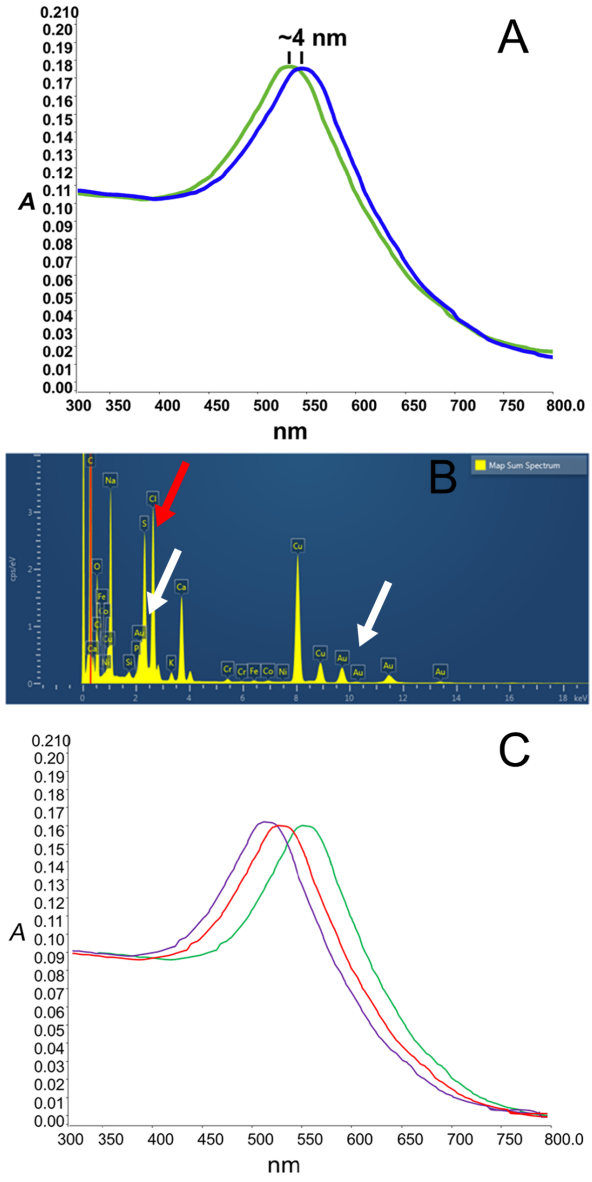

Figure 3: (A) UV–vis spectrum of 50 nm unconjugated Au-CPMV (green) and antibody-labeled Au-CPMV particles (blue). The spectrum shows a red-shift of 4 nm, while preserving the overall shape and intensity of the spectrum, confirming successful coupling of the antibody to the Au-CPMV surface. (B) EDX analysis confirms the presence of gold (white arrows) and sulfur (red arrow), Si and Cr signals are from the sample holder. (C) UV–vis spectrum of the SPR bands of Au-CPMV; λ_{max} = 535 nm for particles with a diameter of 50 nm (purple line), λ_{max} = 552 nm for particles with a diameter of 70 nm (red line) and λ_{max} = 572 nm for particles with a diameter of 100 nm (green line).

In vitro fluorescent cell imaging

Confocal fluorescence microscopy was performed on the cell lines to demonstrate the specificity and the distribution of the labeled NPs. As shown in Figure 4B, green-fluorescent labeled $^{\text{VCAM1-PEG5000}}$Au-CPMV particles incubated with RAW264.7 cells showed significant and specific binding of the fluorescent labeled antibody on the exterior of Au-CPMV to the surface of the RAW264.7 cells. Fluorescence microscopy confirmed that the $^{\text{VCAM1-PEG5000}}$Au-CPMV can selectively bind to their target, whereas, the $^{\text{IgG-PEG5000}}$Au-CPMV control did not show any fluorescence signal, which is indicative that no binding to the surface of the cells occurred (Figure 4A). The merged confocal microscopy image in Figure 4C demonstrates the successful attachment of the $^{\text{VCAM1-PEG5000}}$Au-CPMV to the surface of the RAW264.7 cells: $^{\text{VCAM1-PEG5000}}$Au-CPMV in green, blue and red indicate the cell nucleus and the plasma membrane, respectively, the images represent the overall mor-

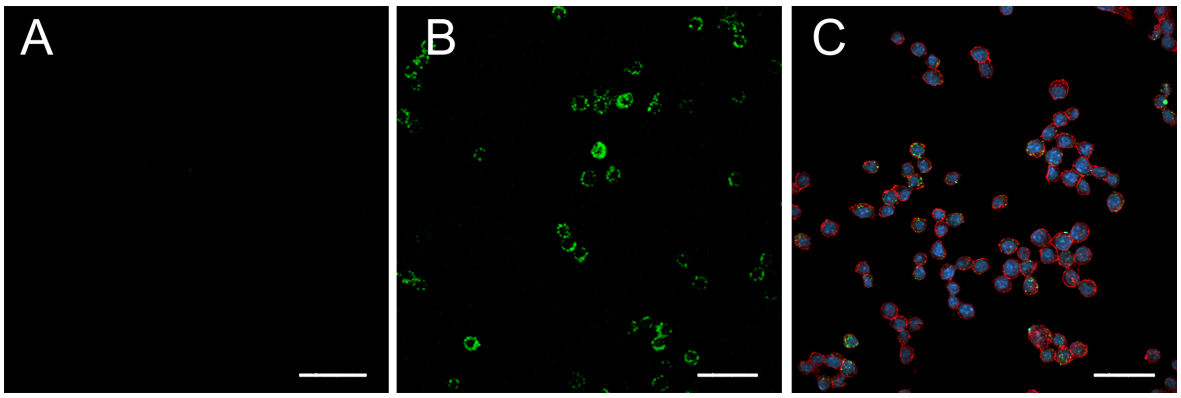

Figure 4: Confocal fluorescence microscopy images of fluorescent labeled $^{VCAM1\text{-}PEG5000Au}$CPMV particles. RAW246.7 actin filaments were labeled with DY-554 phalloidin (red) and DAPI (blue). (A) $^{IgG\text{-}PEG5000}$Au-CPMV (B) $^{VCAM1\text{-}PEG5000}$Au-CPMV showing the binding of the particles to the cells surface and (C) merged image of the cells with $^{VCAM1\text{-}PEG5000}$Au-CPMV showing stained cells and the binding of the particles. Scale bars: 100 μm.

phology of the RAW264.7 cells. Thus, we conclude that the prepared $^{VCAM1\text{-}PEG5000}$Au-CPMV is an acceptable targeting model for further in vivo studies.

STEM–EDX elemental maps

Low-voltage STEM offers a contrast enhancement over conventional TEM analysis due to lower energy (20–30 kV). The higher electron scattering provides better insight into the morphology of materials with low atomic numbers [43]. In the case of imaging Au-CPMV particles in RAW246.7 cells in vitro, the electron-dense particles appeared to be outside the cell and on the cellular surface as shown in (Figure 5A). The images revealed that Au-CPMV particles maintain their original shape and size, indicating that they are resistant to solubilization or oxidation. The dual STEM and EDX spectra from the $^{Antibody\text{-}PEG5000}$Au-CPMV gave useful information about the spatial distribution of gold and sulfur across the cellular surface. The simultaneously acquired EDX spectrum images confirmed that gold and sulfur are at the surface as a consequence of the modification of Au-CPMV with the antibody linker. Furthermore, STEM-EDX analysis provided compositional and topographical 3-D elemental distributions (Figure 5).

CT Imaging

Iodine-containing compounds are routinely used as CT imaging agents [44] due to the high X-ray attenuation of iodine [45]. It

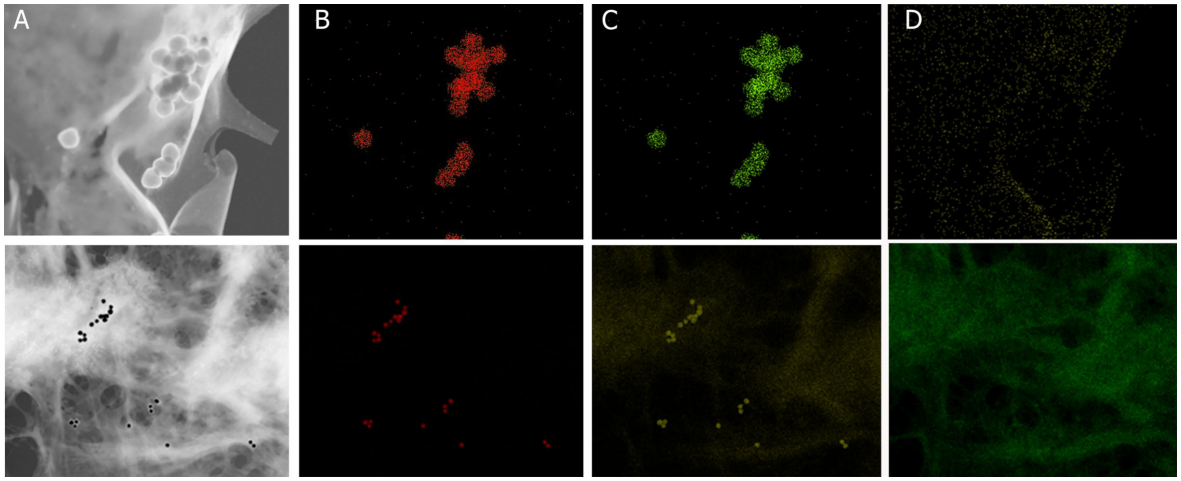

Figure 5: (A) High-resolution TEM image of $^{Antibody\text{-}PEG5000Au}$CPMV; (B) elemental EDX map of gold; the signal is distributed almost uniformly on the same position as the electron-dense particles in (A); (C) sulfur from the linker attachment to the nanoparticles distributed uniformly on the same position as the electron-dense particles in (A); (D) carbon from the biological matrix of the cells. The electron dose is $20e^{-}/Å^{2}$ per frame (200 kV, probe current of 691 pA). Top and lower panels represent different magnifications of two independent experiments.

has been shown that gold provides on average a three times higher X-ray attenuation per unit weight than iodine [46]. This was the rationale to use AuNPs as CT imaging agents. The Au-CPMV particle sizes of 50, 70 and 100 nm were selected to ensure that the particles will bind specifically to their target tissue without being so small as to induce cell toxicity. This occurs at sizes smaller than 50 nm because of diffusion into the cells. We believe that the Au-CPMV particles have suitable sizes for optimal imaging quality and biocompatibility in clinical applications. Herein, we report the size effect of the three Au-CPMV samples on X-ray attenuation as measured by CT. The generated signals are shown in Figure 6. The average CT number from three scans for each sample was 183 HU, 133 HU, and 115 HU for the 50 nm, 70 nm, and 100 nm particles, respectively. This can be attributed to the increase of the total surface area of all NPs with decreasing particle size. In addition, gold has a significantly higher X-ray attenuation coefficient (at 100 keV: gold 5.16 cm^2/g; iodine 1.94 cm^2/g; water 0.171 cm^2/g) [47,48].

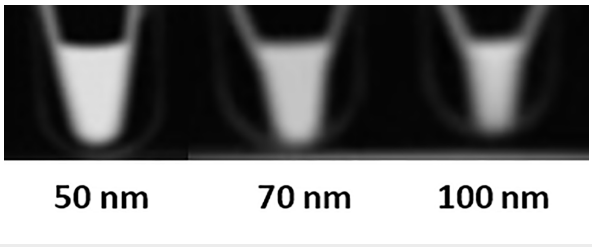

Figure 6: CT images of Au-CPMV particles of different sizes suspended in DD water at, the gold concentration is 200 µg of gold suspended in 200 µl aqueous solution for each sample. The average CT values from three scans for each sample were 183 HU, 133 HU, and 115 HU for the 50 nm, 70 nm, and 100 nm, respectively.

Conclusion

CT has become an extremely useful imaging tool. CT yields non-invasive, three-dimensional high-resolution images. CT contrast agents have evolved from iodinated molecules to complex nanoparticles. Au-CPMV particles are easy to synthesize while having control over the NPs size. In addition, the ability to tune the surface functionalities allows for the use of such particles in biomedical applications. The Au-CPMV particles reported here exhibit excellent stability over at least almost a year. No visible aggregation nor changes in particles size was observed in samples stored at 4 °C. Their surface can be modified with molecules to enhance tissue targeting. Coupling of fluorescent labeled antibodies to the nanoparticles have enabled cell line studies. As a CT agent, Au-CPMV particles generated on average a signal of 150 HU in a size-dependent manner showing contrast enhancement similar to, or better than, other contrast agents. Au-CPMV-labeled cell tracking has great potential for use in clinical studies.

Experimental

Materials

Poly(allylamine hydrochloride) (PAH, $M_W \approx 15{,}000$), hydrogen tetrachloroaurate trihydrate 99.9%+, sodium chloride, 50 and 100 kDa cut-off Millipore filter membranes, potassium carbonate, sucrose, dimethyl sulfoxide (DMSO; 25%), 2-(*N*-morpholino)ethanesulfonic acid (MES) buffer, isopropanol, tetrachloroauric acid, trypsin, ethylenediaminetetraacetic acid (EDTA), HEPES sodium salt, Triton™ X-100, phosphate-buffered saline (PBS) tablets, and bovine serum albumin (BSA) were purchased from Sigma-Aldrich; potassium carbonate was purchased from BDH; hydroxylamine hydrochloride (99%) was purchased from Lancaster Synthesis; carborundum (fine-grade silicon carbide) was purchased from Parchem; carboxyl-PEG 5000-SH, (1-ethyl-3-(3-dimethylaminopropyl)carbodiimide hydrochloride) (EDC), *N*-hydroxysulfosuccinimide (sulfo-NHS), bicinchoninic acid (BCA) protein assay kit, RPMI, foetal calf serum, and T125 mm tissue culture flasks were purchased from ThermoFisher Scientific; EGM-2 medium was purchased from Lonza. Cell culture medium phenol red-free (high-glucose Dulbecco modified eagle medium (DMEM) supplemented with 10% (v/v) fetal bovine serum (FBS); 100 units/M1 penicillin, gentamicin antibiotic (50 µg/mL), fungizone (1.3 µg/mL) and 2 mM L-glutamine), anti-VCAM1 (FITC-labeled, EPR17010-83; Abcam) and macrophage cell line (RAW264.7) were purchased from American Type Culture Collection (ATCC; Manassas, VA).

Methods

CPMV propagation

CPMV propagation followed our previously published method [38]. Black-eyed peas plant (*Vigna unguiculata*) were grown from seeds, obtained locally, in a greenhouse for 10 days. Primary leaves were rubbed with carborundum (fine-grade silicon carbide abrasive) and treated with CPMV (50 µL of 0.1 mg/mL) suspended in 10 mM sodium phosphate buffer pH 7.0. The leaves were sprinkled with tap water to remove the excess carborundum. 14 days after infection, the infected leaves were harvested and stored at −20 °C prior to use.

CPMV isolation

Infected leaves were homogenized to extract CPMV particles following our previously published protocol [34].

CPMV-poly(allylamine) hydrochloride (^{PAH}CPMV)

^{PAH}CPMV particles were prepared as previously reported [30]. CPMV (1 mg/mL) was suspended in double-distilled (DD) water and added dropwise to a freshly prepared aqueous solution of PAH (1 mg/mL; supplemented with 250 mM NaCl) over 5–10 min under continuous stirring at 500–800 rpm at ambient temperature. ^{PAH}CPMV particles were washed four times with

DD water (15 mL each) on 50 kDa cut-off Millipore filter membranes, followed by dialysis with 12,400 molecular weight cut-off (MWCO) against 10 mM sodium phosphate buffer pH 7.0 for 15 h.

Gold hydroxide solution

Gold hydroxide solution was prepared following the published protocol [30]. Hydrogen tetrachloroaurate ($HAuCl_4 \cdot 3H_2O$) (17.4 mL of 25 mM aqueous solution) was diluted with DD water (982.6 mL), and potassium carbonate (249 mg, 1.8 mM) was added. The solution was aged for 1–2 days in dark (foil wrapped) at 4 °C, during which it changed color from yellow to colorless indicative of gold hydroxide formation

Gold-coated CPMV (Au-CPMV)

Particles were prepared following the published protocol [30]. Freshly prepared ^{PAH}CPMV (approximately 1 mg/mL) was incubated with gold hydroxide solution (0.8 mL to generate 50 nm particles, 1.1 mL to generate 70 nm particles and 1.5 mL to generate 90 nm particles). The solution was stirred continuously at 500 rpm for 2 h at ambient temperature. Freshly prepared aqueous solution of hydroxylamine hydrochloride was added to a final concentration of 20 mM. The reaction was left to proceed for further 30 min at ambient temperature. The Au-CPMV particles were centrifuged at 5000*g* for 20 min to remove any large aggregates. The supernatant was layered on sucrose gradients (15 mL, 10–70 % (w/v) dissolved in 10 mM sodium phosphate buffer pH 7.0). Sucrose fractions containing Au-CPMV (light blue color) were collected and dialyzed against 10 mM sodium phosphate buffer pH 7.0 using 50 kDa MWCO.

$^{Carboxyl\text{-}PEG5000}$Au-CPMV

Freshly prepared Au-CPMV (1 mg/mL) suspended in PBS buffer (20 mM sodium phosphate, 150 mM NaCl; pH 7.4) was added to a solution of carboxyl-PEG 5000-SH (spacer arm length 15.8 Å, 10 mg) dissolved in DMSO (1 mL). The reaction was stirred for ca. 12 h at ambient temperature. $^{Carboxyl\text{-}PEG5000}$Au-CPMV particles were dialyzed for 24 h against 100 mM sodium phosphate, 0.15 M NaCl, buffer pH 7.4 using 100 kDa dialysis membranes.

$^{VCAM1\text{-}PEG5000}$Au-CPMV

$^{Carboxyl\text{-}PEG5000}$Au-CPMV were buffer-exchanged using 14000 kDa dialysis bags in 2-(*N*-morpholino)ethanesulfonic acid (MES) buffer, pH 6.0 for 12–14 h. To $^{Carboxyl\text{-}PEG5000}$Au-CPMV (100 µL, ca. 1 mg/mL), aqueous EDC (50 µL, 200 mM) and aqueous (*N*-hydroxysulfosuccinimide)sulfo-NHS (200 µL, 800 mM) was added. The reaction was left to proceed for 1 h at ambient temperature (25 °C) then precipitated with isopropanol (500 µL). Activated $^{Esterfied\text{-}PEG5000}$Au-CPMV was resuspended in anti-VCAM1 (FITC-labeled, 20 µL of 1 mg/mL) antibody solution in PBS, pH 7.4 (EPR17010-83; Abcam) and reacted at 4 °C overnight (ca. 15 h). $^{VCAM1\text{-}PEG5000}$Au-CPMV was centrifuged at 5000*g* and washed four times with DD water to remove unbound antibodies. Particles were purified on PD-10 columns pre-equilibrated with 10 mM sodium phosphate buffer (pH 7.0). $^{IgG\text{-}PEG5000}$Au-CPMV were prepared as a negative control following the same procedure.

Antibody quantification

Bicinchoninic acid (BCA) protein assay kit from ThermoFisher Scientific was used according to the manufacturer's instructions [49]. $^{VCAM1\text{-}PEG5000}$Au-CPMV and $^{IgG\text{-}PEG5000}$Au-CPMV (200 µL of 0.1 mg Au) and BCA reagent (200 µL) were mixed together and incubated at 60 °C for 10 min. The samples were left to cool for 30 min and then centrifuged at 14000*g* for 40 min (Thermo Scientific CL10 Centrifuge) to pellet the particles. The supernatant BCA dye absorbance was measured at λ = 565 nm using a microplate reader. The change in absorbance is a consequence of the reduction of Cu^{2+} to Cu^{+} and, thus, an indicator of the presence of protein.

Murine macrophage (RAW264.7)

Cell culture: A mouse monocyte/macrophage cell line (RAW264.7), was purchased from American Type Culture Collection (ATCC; Manassas, VA). RAW264.7 cells were plated in T125 mm tissue culture flasks at 6000 cells/cm^2 in growth medium phenol red-free following the published protocol [50]. All cells were cultured in a humidified incubator at 95% humidity and 5% CO_2 maintained at 37 °C. For experiments cells were seeded the day prior to the incubation with the NPs at 3.5×10^4 cells/cm^3 of growth surface and were used between passages 2 and 3. Subculture occurred after 60–70% confluence after trypsinization (0.025% trypsin, 0.5 mM EDTA, 10 mM HEPES buffer pH 6.5).

RAW264.7 cell labeling and confocal microscopy: Cells of a murine endothelial line (100 µL of 1×10^6 cells/mL, RAW264.7) were cultured on a glass coverslip, kept in a six-well plate for 10–12 h prior to the NP addition. $^{VCAM1\text{-}PEG5000}$Au-CPMV (100 µg/mL) was incubated with the cells on the coverslip for 2 h at 4 °C. Coverslips were washed three times with 10 mM sodium phosphate buffer pH 7.0 to remove free NPs. Cells were fixed in 4% paraformaldehyde/PBS (pH 7.0) for 15 min at ambient temperature (25 °C). Cells were rinsed three times for 5 min with PBS (10 mL) and incubated in 0.2% Triton X-100 for further 10 min. After three five-minute rinses with PBS and preincubation with 2% BSA to block nonspecific staining, cells were stained with fluorescein phalloidin (red) (5 to 10 µg/mL) for 20 min to stain F-actin. After three additional five-minute washes with PBS (10 mL),

the nuclei were stained with 4′,6-diamidino-2-phenylindole (DAPI) (1 μg/mL in PBS) for 15 min. Samples were washed three times with 10 mL of PBS and analyzed with a fluorescence microscope (Cytation Cell Imager; BioTek Instruments, Inc).

Transmission electron microscopy

TEM images were recorded using a Titan FEI microscope, operating at 300 kV and fitted with a post-column Gatan Tridiem GIF 863 imaging filter. Samples were dispersed in water at a concentration of 0.01–0.05 mg/mL and deposited on 400 mesh carbon grids (SPI supplies), samples were air dried prior to imaging.

Energy-dispersive X-Ray spectroscopy

A FIB Scios system was used combined with a scanning electron microscope (SEM) and a focused ion beam equipped with X-MaxN 50 mm^2 EDS system to measure 0.3–3 μm with a detection limit of ca. 1%. The sample was placed at a 52° tilt angle and at a eucentric height (or WD) of 7–10 mm from the pole piece. The Auger electrons were set to ca. 1 nm, secondary electrons to 100 nm and inelastically backscattered electrons to 1 μm under vacuum.

The EDX data was processed by Aztec software from Oxford Instruments. Images were recorded on CCD camera with mapping resolution of 2048 × 1600. The beam was selected with accelerating voltage for imaging, beam current 100 pA at 30 kV and a spot size of 5–6, fast scan rate of dwell time (0.1–0.3 μs), detector ETD (SE) and a working distance (FWD).

UV–visible spectroscopy

The absorption measurements were recorded on a PerkinElmer Lambda 25 spectrometer. CPMV concentration was determined using the Beer–Lambert equation with a mass extinction coefficient of 8.1 $mL{\cdot}mg^{-1}{\cdot}cm^{-1}$ [51]. Au-CPMV concentration was determined from peak SPR wavelength λ = 535 nm using $\varepsilon = 1.8 \times 10^{10}\ M^{-1}{\cdot}cm^{-1}$ for a particle diameter of 50 nm, SPR wavelength of λ =552 nm using $\varepsilon = 6.70 \times 10^{10}\ M^{-1}{\cdot}cm^{-1}$ for a particle diameter of 70 nm, and from SPR peak wavelength λ = 572 nm using $\varepsilon = 1.57 \times 10^{11}\ M^{-1}{\cdot}cm^{-1}$ for particles with a diameter ca. 100 nm [36]. Spectroscopic analyses were recorded at ambient temperature (21–28 °C) using quartz cuvettes with an optical path length of 1 cm.

Dynamic light scattering

DLS measurements were carried out on a Wyatt DynaPro™ DP-801 system coupled with Dynamics V7.0.0.95 software. Measurements were recorded with the following settings: 20 mW He–Ne laser, λ_0 = 780 nm, scattering angle θ = 90°, molar refractive index of 1.33; viscosity of 0.8872 at 25 °C; the attenuator was set up automatically and ranged between 6 to 9. Corresponding quartz cells were flushed with deionized water followed by a 1% (v/v) aqueous Hellmanex solution (strong alkaline cleaning concentrate made of phosphates and surfactants from Helma Analytics) and air dried prior to being filled with sample solution (500 μL). The outer surface of the cells was wiped gently with a sheet of soft lens cleaning tissue. In total, 10 successive DLS measurements were carried out per sample after 2 min waiting time to allow the solutions to be at rest. The hydrodynamic radius (intensity particle size distribution was used for all measurements) was calculated by the instrument from the translational diffusion coefficient using the Stokes–Einstein equation.

Zeta potential measurements

The zeta potential of the particles was measured on a Zetasizer™ NanoZS-90 (Malvern Instruments) equipped with a 4 mW, λ_0 = 632 nm He–Ne laser operating with a detector angle of θ = 173° degree. The cell voltage of the instrument was fixed to 80 V during measurements. The reference beam had an intensity within 2000 and 3500 kcps. Zeta potential values were reported as an average of three measurements from each sample.

Nanoparticle tracking analysis

Hydrodynamic diameters of the nanoparticles and their concentration (particle numbers) were measured by nanoparticle tracking analysis (NTA) using a NanoSight LM10 with a laser module LM14 set at a wavelength of 532 nm, NTA 2.3 build 0033 analytical software (Malvern Instruments Ltd, Malvern) and a high-sensitivity sCMOS camera. Particles were suspended in PBS buffer pH 7.4. The samples were injected in the sample chamber with sterile syringes until the solution reached the tip of the nozzle. Ten 30 s videos using a camera level of 7 and a detection threshold of 5, were recorded for each sample and the software was used to estimate concentration and NP size. Measurements were recorded at ambient temperature with camera setting of 380 gain and shutter speed of 15 ms with auto particle detection settings. The instrument was calibrated with 100 nm standard polystyrene beads with known concentrations prior to sample recordings.

Scanning transmission electron microscopy

A FEI Titan 80-300 TEM/STEM (spherical aberration corrector $C_s \approx 1.2$ mm) operating at 300 kV and equipped with EDAX detector for X-ray analysis and elemental mapping was used. The microscope objective lens is a FEI Tecnai “Super Twin”. The CCD Gatan Orius SC200D camera located above the viewing chamber is a 4K (2048 × 2048) pixel cooled CCD. The high-angle annular dark field scanning transmission electron microscopy (HAADF-STEM) images further confirmed the

existence of dimeric structures (Figure 5A), composed of a brighter core and a darker attachment. STEM-energy dispersive X-ray (EDX) elemental mapping measurements were conducted to analyze chemical composition.

Fluorescent imaging of labeled cells

Antibody-PEG5000Au-CPMV particles of concentration 50 μg Au/mL were incubated with cells as described above using 20×10^3 cells. Images were recorded on Olympus IX 81 Inverted fluorescence microscope using LUC PLAN 40× objective (numerical aperture 0.6; Olympus). Images were taken using a back-illuminated electron multiplying charge-coupled camera (Andor Technology, Belfast, Northern Ireland)

Computed tomography (CT) scanning

Scanning was performed three times (different days) on a multislice GE CT (Optima CT660) scanner (GE MEDICAL SYSTEMS) using clinical settings for helical brain scanning (80 kVp and 330 mAs) in a coronal plane to the tubes-containing nanoparticles with in-plane resolution of 0.5 × 0.5 mm and slice thickness of 5 mm. Images were retrospectively reconstructed into an isotropic voxel of 0.5 mm^3 and loaded into the ImageJ software (https://imagej.nih.gov/ij/) in analyze format to calculate the average signals (mean CT number) for each sample from the three scans.

Acknowledgments

This work was financially supported by the Deanship of Research and Graduate Studies at Yarmouk University, Irbid, Jordan, Grant Number 18/2017.

ORCID® iDs

Alaa A. A. Aljabali - https://orcid.org/0000-0002-9519-6338
Mazhar S. Al Zoubi - https://orcid.org/0000-0003-0248-4777
Mohammad A. Obeid - https://orcid.org/0000-0001-9698-489X
Walhan Alshaer - https://orcid.org/0000-0003-2946-7328
Tasnim Al-Zanati - https://orcid.org/0000-0002-4224-9555
Murtaza M. Tambuwala - https://orcid.org/0000-0001-8499-9891
David J. Evans - https://orcid.org/0000-0002-6290-2849

References

1. Cole, L. E.; Vargo-Gogola, T.; Roeder, R. K. *ACS Nano* **2015,** *9,* 8923–8932. doi:10.1021/acsnano.5b02749
2. Tu, C.; Osborne, E. A.; Louie, A. Y. *Ann. Biomed. Eng.* **2011,** *39,* 1335–1348. doi:10.1007/s10439-011-0270-0
3. Uchida, M.; Qazi, S.; Edwards, E.; Douglas, T. Use of Protein Cages as a Template for Confined Synthesis of Inorganic and Organic Nanoparticles. In *Protein Cages: Methods and Protocols;* Orner, B. P., Ed.; Humana Press: New York, NY, U.S.A., 2015; Vol. 1252, pp 17–25. doi:10.1007/978-1-4939-2131-7_2
4. Carrascosa, P.; Capunay, C.; Deviggiano, A.; Bettinotti, M.; Goldsmit, A.; Tajer, C.; Carrascosa, J.; Garcia, M. J. *Heart (London, U. K.)* **2010,** *96,* 1543–1549. doi:10.1136/hrt.2009.183699
5. Lusic, H.; Grinstaff, M. W. *Chem. Rev.* **2013,** *113,* 1641–1666. doi:10.1021/cr200358s
6. Kalender, W. A. *Computed tomography: fundamentals, system technology, image quality, applications;* Publicis: Munich, Germany, 2011.
7. Cormode, D. P.; Naha, P. C.; Fayad, Z. A. *Contrast Media Mol. Imaging* **2014,** *9,* 37–52. doi:10.1002/cmmi.1551
8. Cormode, D. P.; Skajaa, T.; Fayad, Z. A.; Mulder, W. J. M. *Arterioscler., Thromb., Vasc. Biol.* **2009,** *29,* 992–1000. doi:10.1161/atvbaha.108.165506
9. Elrod, D. B.; Partha, R.; Danila, D.; Casscells, S. W.; Conyers, J. L. *Nanomedicine (N. Y., NY, U. S.)* **2009,** *5,* 42–45. doi:10.1016/j.nano.2008.06.007
10. Rizvi, S. B.; Ghaderi, S.; Keshtgar, M.; Seifalian, A. M. *Nano Rev.* **2010,** *1,* 5161. doi:10.3402/nano.v1i0.5161
11. Gao, Z.; Ma, T.; Zhao, E.; Docter, D.; Yang, W.; Stauber, R. H.; Gao, M. *Small* **2016,** *12,* 556–576. doi:10.1002/smll.201502309
12. Yordanov, A. T.; Lodder, A. L.; Woller, E. K.; Cloninger, M. J.; Patronas, N.; Milenic, D.; Brechbiel, M. W. *Nano Lett.* **2002,** *2,* 595–599. doi:10.1021/nl020246x
13. van Schooneveld, M. M.; Cormode, D. P.; Koole, R.; van Wijngaarden, J. T.; Calcagno, C.; Skajaa, T.; Hilhorst, J.; Hart, D. C. 't.; Fayad, Z. A.; Mulder, W. J. M.; Meijerink, A. *Contrast Media Mol. Imaging* **2010,** *5,* 231–236. doi:10.1002/cmmi.376
14. Caride, V. J.; Sostman, H. D.; Twickler, J.; Zacharis, H.; Orphanoudakis, S. C.; Jaffe, C. C. *Invest. Radiol.* **1982,** *17,* 381–384. doi:10.1097/00004424-198207000-00014
15. Yu, S.-B.; Watson, A. D. *Chem. Rev.* **1999,** *99,* 2353–2378. doi:10.1021/cr980441p
16. Pan, D.; Schirra, C. O.; Senpan, A.; Schmieder, A. H.; Stacy, A. J.; Roessl, E.; Thran, A.; Wickline, S. A.; Proska, R.; Lanza, G. M. *ACS Nano* **2012,** *6,* 3364–3370. doi:10.1021/nn300392x
17. Torchilin, V. P.; Frank-Kamenetsky, M. D.; Wolf, G. L. *Acad. Radiol.* **1999,** *6,* 61–65. doi:10.1016/s1076-6332(99)80063-4
18. Cormode, D. P.; Skajaa, T.; van Schooneveld, M. M.; Koole, R.; Jarzyna, P.; Lobatto, M. E.; Calcagno, C.; Barazza, A.; Gordon, R. E.; Zanzonico, P.; Fisher, E. A.; Fayad, Z. A.; Mulder, W. J. M. *Nano Lett.* **2008,** *8,* 3715–3723. doi:10.1021/nl801958b
19. Rumberger, J. A. *J. Am. Coll. Cardiol.* **2008,** *52,* 1733–1735. doi:10.1016/j.jacc.2008.08.034
20. Sun, I.-C.; Eun, D.-K.; Na, J. H.; Lee, S.; Kim, I.-J.; Youn, I.-C.; Ko, C.-Y.; Kim, H.-S.; Lim, D.; Choi, K.; Messersmith, P. B.; Park, T. G.; Kim, S. Y.; Kwon, I. C.; Kim, K.; Ahn, C.-H. *Chem. – Eur. J.* **2009,** *15,* 13341–13347. doi:10.1002/chem.200902344
21. Hainfeld, J. F.; Slatkin, D. N.; Focella, T. M.; Smilowitz, H. M. *Br. J. Radiol.* **2006,** *79,* 248–253. doi:10.1259/bjr/13169882
22. Cai, Q.-Y.; Kim, S. H.; Choi, K. S.; Kim, S. Y.; Byun, S. J.; Kim, K. W.; Park, S. H.; Juhng, S. K.; Yoon, K.-H. *Invest. Radiol.* **2007,** *42,* 797–806. doi:10.1097/rli.0b013e31811ecdcd
23. von Maltzahn, G.; Park, J.-H.; Agrawal, A.; Bandaru, N. K.; Das, S. K.; Sailor, M. J.; Bhatia, S. N. *Cancer Res.* **2009,** *69,* 3892–3900. doi:10.1158/0008-5472.can-08-4242
24. Popovtzer, R.; Agrawal, A.; Kotov, N. A.; Popovtzer, A.; Balter, J.; Carey, T. E.; Kopelman, R. *Nano Lett.* **2008,** *8,* 4593–4596. doi:10.1021/nl8029114

25. Krause, W. *Adv. Drug Delivery Rev.* **1999,** *37,* 159–173. doi:10.1016/s0169-409x(98)00105-7
26. Regino, C. A. S.; Walbridge, S.; Bernardo, M.; Wong, K. J.; Johnson, D.; Lonser, R.; Oldfield, E. H.; Choyke, P. L.; Brechbiel, M. W. *Contrast Media Mol. Imaging* **2008,** *3,* 2–8. doi:10.1002/cmmi.223
27. Galper, M. W.; Saung, M. T.; Fuster, V.; Roessl, E.; Thran, A.; Proksa, R.; Fayad, Z. A.; Cormode, D. P. *Invest. Radiol.* **2012,** *47,* 475–481. doi:10.1097/rli.0b013e3182562ab9
28. NIST X-Ray Mass Attenuation Coefficients - Version History | NIST. https://www.nist.gov/pml/x-ray-mass-attenuation-coefficients (accessed April 14, 2019).
29. Blum, A. S.; Soto, C. M.; Wilson, C. D.; Cole, J. D.; Kim, M.; Gnade, B.; Chatterji, A.; Ochoa, W. F.; Lin, T.; Johnson, J. E.; Ratna, B. R. *Nano Lett.* **2004,** *4,* 867–870. doi:10.1021/nl0497474
30. Aljabali, A. A. A.; Lomonossoff, G. P.; Evans, D. J. *Biomacromolecules* **2011,** *12,* 2723–2728. doi:10.1021/bm200499v
31. Lee, K.-S.; El-Sayed, M. A. *J. Phys. Chem. B* **2005,** *109,* 20331–20338. doi:10.1021/jp054385p
32. Tabor, C.; Murali, R.; Mahmoud, M.; El-Sayed, M. A. *J. Phys. Chem. A* **2009,** *113,* 1946–1953. doi:10.1021/jp807904s
33. Bhattacharjee, S. *J. Controlled Release* **2016,** *235,* 337–351. doi:10.1016/j.jconrel.2016.06.017
34. Aljabali, A. A. A.; Barclay, J. E.; Lomonossoff, G. P.; Evans, D. J. *Nanoscale* **2010,** *2,* 2596–2600. doi:10.1039/c0nr00525h
35. Aljabali, A. A. A.; Evans, D. J. *Methods Mol. Biol. (N. Y., NY, U. S.)* **2014,** *1108,* 89–95. doi:10.1007/978-1-62703-751-8_6
36. Aljabali, A. A. A.; Akkam, Y.; Al Zoubi, M.; Al-Batayneh, K.; Al-Trad, B.; Abo Alrob, O.; Alkilany, A.; Benamara, M.; Evans, D. *Nanomaterials* **2018,** *8,* 174. doi:10.3390/nano8030174
37. Patel, V. R.; Agrawal, Y. K. *J. Adv. Pharm. Technol. Res.* **2011,** *2,* 81–87. doi:10.4103/2231-4040.82950
38. Aljabali, A. A. A.; Evans, D. J. *Methods Mol. Biol. (N. Y., NY, U. S.)* **2014,** *1108,* 97–103. doi:10.1007/978-1-62703-751-8_7
39. Aljabali, A. A. A.; Barclay, J. E.; Steinmetz, N. F.; Lomonossoff, G. P.; Evans, D. J. *Nanoscale* **2012,** *4,* 5640–5645. doi:10.1039/c2nr31485a
40. Häfele, V.; Trügler, A.; Hohenester, U.; Hohenau, A.; Leitner, A.; Krenn, J. R. *Opt. Express* **2015,** *23,* 10293–10300. doi:10.1364/oe.23.010293
41. Anfossi, L.; Baggiani, C.; Giovannoli, C.; Giraudi, G. *Anal. Bioanal. Chem.* **2009,** *394,* 507–512. doi:10.1007/s00216-009-2722-z
42. Cui, X.; Liu, M.; Li, B. *Analyst* **2012,** *137,* 3293–3299. doi:10.1039/c2an35328h
43. Guise, O.; Strom, C.; Preschilla, N. *Microsc. Microanal.* **2008,** *14* (Suppl. 2), 678–679. doi:10.1017/s1431927608087035
44. Hainfeld, J. F.; Slatkin, D. N.; Smilowitz, H. M. *Phys. Med. Biol.* **2004,** *49,* N309–N315. doi:10.1088/0031-9155/49/18/n03
45. Mironava, T.; Hadjiargyrou, M.; Simon, M.; Jurukovski, V.; Rafailovich, M. H. *Nanotoxicology* **2010,** *4,* 120–137. doi:10.3109/17435390903471463
46. Jackson, P. A.; Rahman, W. N. W. A.; Wong, C. J.; Ackerly, T.; Geso, M. *Eur. J. Radiol.* **2010,** *75,* 104–109. doi:10.1016/j.ejrad.2009.03.057
47. National Institute of Standards and Technology | NIST. https://www.nist.gov/ (accessed April 14, 2019).
48. Cole, L. E.; Ross, R. D.; Tilley, J. M.; Vargo-Gogola, T.; Roeder, R. K. *Nanomedicine (N. Y., NY, U. S.)* **2015,** *10,* 321–341. doi:10.2217/nnm.14.171
49. Aljabali, A. A. A.; Hussein, E.; Aljumaili, O.; Zoubi, M. A.; Altrad, B.; Albatayneh, K.; Abd Al-razaq, M. A. *IOP Conf. Ser.: Mater. Sci. Eng.* **2018,** *305,* 012005. doi:10.1088/1757-899x/305/1/012005
50. Akbar, N.; Digby, J. E.; Cahill, T. J.; Tavare, A. N.; Corbin, A. L.; Saluja, S.; Dawkins, S.; Edgar, L.; Rawlings, N.; Ziberna, K.; McNeill, E.; Johnson, E.; Aljabali, A. A.; Dragovic, R. A.; Rohling, M.; Belgard, T. G.; Udalova, I. A.; Greaves, D. R.; Channon, K. M.; Riley, P. R.; Anthony, D. C.; Choudhury, R. P. *JCI Insight* **2017,** *2,* No. e93344. doi:10.1172/jci.insight.93344
51. Aljabali, A. A. A.; Sainsbury, F.; Lomonossoff, G. P.; Evans, D. J. *Small* **2010,** *6,* 818–821. doi:10.1002/smll.200902135

License and Terms

BEILSTEIN JOURNAL OF NANOTECHNOLOGY

Mannosylated brush copolymers based on poly(ethylene glycol) and poly(ε-caprolactone) as multivalent lectin-binding nanomaterials

Stefania Ordanini[1], Wanda Celentano[1,2], Anna Bernardi[3] and Francesco Cellesi[*1,§]

Full Research Paper

Open Access

Address:
[1]Department of Chemistry, Materials and Chemical Engineering "G. Natta", Politecnico di Milano, via Mancinelli 7, Milano 20131, Italy, [2]Humanitas Research Hospital, Via Manzoni 56, Rozzano, Milano 20089, Italy and [3]Department of Chemistry, Università degli Studi di Milano, via Golgi 19, Milano 20133, Italy

Email:
Francesco Cellesi[*] - francesco.cellesi@polimi.it

* Corresponding author
§ Tel.: +39-02-23993099

Keywords:
atom transfer radical polymerization (ATRP); glycopolymer; lectin; poly(ethylene glycol); poly(ε-caprolactone); ring-opening polymerization (ROP)

Beilstein J. Nanotechnol. **2019,** *10,* 2192–2206.
doi:10.3762/bjnano.10.212

Received: 30 July 2019
Accepted: 23 October 2019
Published: 07 November 2019

This article is part of the thematic issue "Engineered nanomedicines for advanced therapies".

Guest Editor: F. Baldelli Bombelli

Abstract

A class of linear and four-arm mannosylated brush copolymers based on poly(ethylene glycol) and poly(ε-caprolactone) is presented here. The synthesis through ring-opening and atom transfer radical polymerizations provided high control over molecular weight and functionality. A post-polymerization azide–alkyne cycloaddition allowed for the formation of glycopolymers with different mannose valencies (1, 2, 4, and 8). In aqueous media, these macromolecules formed nanoparticles that were able to bind lectins, as investigated by concanavalin A binding assay. The results indicate that carbohydrate–lectin interactions can be tuned by the macromolecular architecture and functionality, hence the importance of these macromolecular properties in the design of targeted anti-pathogenic nanomaterials.

Introduction

Carbohydrate–protein interactions are involved in many biological processes, including cell recognition and cell–cell adhesion. These interactions drive pathological events, such as cellular infections by viruses (e.g., HIV and Ebola [1,2]) and toxins (e.g., Shiga and Cholera toxins [3]). Carbohydrate–protein interactions in biological systems are mostly multivalent, which allows one to enhance their strength with respect to the weak single saccharide–protein connections. Carbohydrate-binding proteins are known as lectins. A way to interfere with pathological carbohydrate–protein interactions is the use of artificial ligands able to antagonize lectins, possibly with higher affinity than the natural ligands. Multivalent glycoconjugates have been recently synthesized with the aim of producing powerful anti-pathogenic agents [4]. The so called "cluster glycoside effect" is the enhanced activity of a multivalent glycoderivative with respect to the monovalent saccharide [5].

Glycopolymers, i.e., polymers presenting pendant saccharides, are an important and well-studied class of synthetic glycoclusters [6]. They have the advantage of being easy to synthesize and present larger valencies with respect to other multivalent compounds, thus exhibiting an amplified binding potency towards lectins. In some cases, glycopolymers have shown affinities for lectins that are comparable to those of antigens and antibodies [7]. Nevertheless, polymers often lack homogeneity; they can be highly polydisperse and poorly characterized, and this represents a clear limitation for therapeutic applications, since different molecular weight, architecture and functionality can influence the macromolecule bioactivity [8]. Controlled radical polymerization (CRP) techniques, such as atom transfer radical polymerization (ATRP), reversible addition fragmentation chain transfer (RAFT) polymerization, single-electron transfer living radical polymerization (SET-LRP) and nitroxide-mediated radical polymerization (NMP), are often used to produce well-defined glycopolymers with controlled molecular weight and narrow molecular weight distribution [9,10]. In particular, ATRP is a living radical polymerization catalyzed by a transition metal, normally copper or ruthenium, and initiated by halogenated compounds, typically alkyl halides. ATRP is tolerant of a large range of functional groups; the use of multifunctional initiators allows for the synthesis of materials with different topologies, e.g., comb-like and star polymers [11].

ATRP of an unprotected carbohydrate-functionalized monomer, starting from a four-arm initiator based on poly(ε-caprolactone), led to a library of glucose-functionalized aggregates able to bind the glucose- and mannose-binding lectin Concanavalin A (Con A) [12]. The combination of ATRP of protected alkyne monomers and a copper-catalyzed azide–alkyne click cycloaddition (CuAAC) with azide-bearing sugars was reported as an effective strategy to prepare multivalent mannose- and galactose-pendant polymers. Their interaction with Con A strictly depended on the mannose epitope density: fully mannosylated polymers were more active than the corresponding partially galactose-functionalized molecules [13]. Analogous copolymers were tested as ligands for DC-SIGN, a tetravalent lectin involved in the early stage of HIV infection [1]. Also in this case, molecules presenting the highest mannose density had the highest activity towards the lectin [14]. A class of five-arm and eight-arm glycopolymers bound to DC-SIGN with picomolar affinities, one order of magnitude more than the corresponding linear molecules. The authors speculated that this may occur because of the ability of star-shaped polymers to bind simultaneously the four lectin carbohydrate-recognition domains [15]. DC-SIGN was efficiently targeted also by mannose-decorated polymers synthesized through SET-LRP of glycomonomers [16]. When amphiphilic glycopolymers were produced, they formed nanoparticles in aqueous solution, and their binding activities were also affected by shape and size [17]. In addition, the high surface area of spherical self-assembled structures can confer glycopolymers a high affinity towards lectins [18].

Among different synthetic macromolecules used in biomedical applications, copolymers based on poly(ethylene glycol) (PEG) and poly(ε-caprolactone) (PCL) are found in many FDA-approved products [19]. PCL repeating units are constituted by five non-polar methylene groups and one labile ester group. It was reported that biodegradability and performance of PCL in cell culture studies are enhanced when it is modified with PEG [20]. PEG is a hydrophilic nontoxic polymer that does not promote immune responses. Pegylation reduces the nonspecific binding of nanoparticles to blood proteins and macrophages, making them non-immunogenic and non-antigenic [21].

PEG-PCL copolymers are amphihilic materials that can spontaneously assemble in aqueous media, forming colloidal aggregates (e.g., micelles and vesicles) above their critical aggregation concentration (CAC). The resulting self-assembled nanoparticles can act as drug carriers and delivery systems, being able to accommodate a hydrophobic drug within their hydrophobic core [22], or chemically bind bioactive agents [23,24].

In this work, we used ATRP to produce a library of brush copolymers, which were synthesized via random copolymerisation of PEG- and PCL-based macromonomers. Their polymeric backbones were then mannosylated through a post-polymerization CuAAC, in order to obtain potential lectin ligands. Copolymers of different shapes were synthesized, i.e., linear or four-arm, according to the initiator used for the ATRP. The percentage of PCL blocks bearing a triple bond with respect to the PEG blocks was varied. Different clickable polymeric backbones were produced and finally mannosylated, obtaining different overall mannose valencies (1, 2, 4, and 8). The structures, acronyms and valencies of the synthesized comb-like-glycopolymers are reported in Figure 1. The final glycopolymers have a flexible structure that should confer them the possibility to freely adjust the position of the mannose residues, matching the one of the lectin binding sites. Their capability to effectively expose mannose and behave as lectin ligands was investigated using Concanavalin A as a model lectin. Moreover, the glycopolymers are amphiphilic materials, and their ability to spontaneously self-assemble in nano-sized-aggregates was also examined.

Results and Discussion

Synthesis of the PCL-based macromonomer

Propargyl-poly(ε-caprolactone)-methacrylate (**Pg-PCL-MA**) was prepared in two steps starting from ε-caprolactone, through

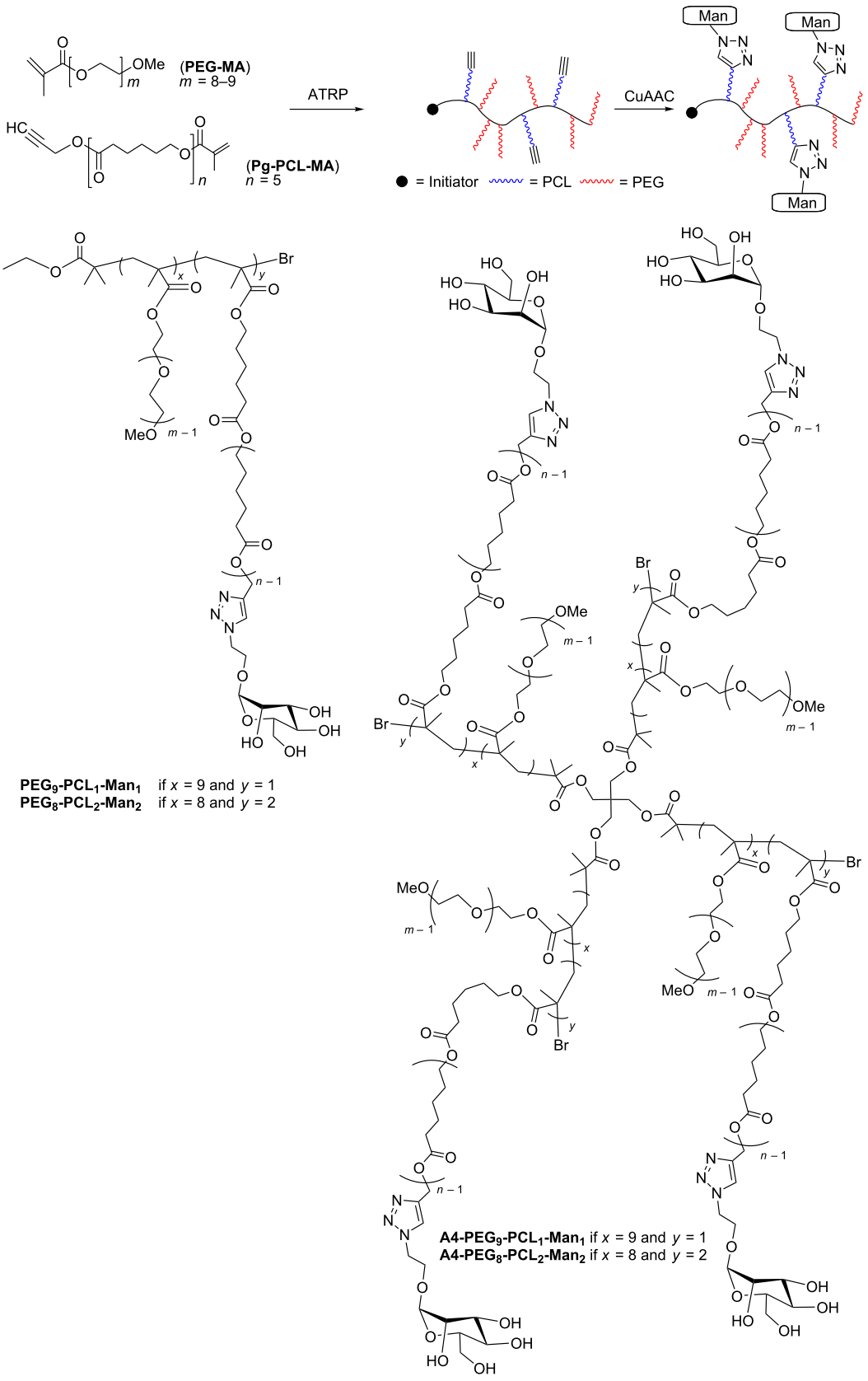

Figure 1: Synthetic approach (upper panel), final structure and nomenclature (lower panels) of the mannose-functionalized PEG-PCL copolymers.

a bulk ROP initiated by propargyl alcohol and catalyzed by tin(II) 2-ethylhexanoate [25] (Scheme 1, step a), targeting a degree of polymerization (DP) equal to 5. Reaction conversions were monitored by means of ^{1}H NMR analysis; almost full monomer conversion (99%) was obtained after 6 h. The dispersity of the purified polymer was 1.19. Subsequent methacrylation of the terminal hydroxy group was accomplished in high conversions (≥95%) using freshly distilled methacryloyl chloride, in order to remove cyclic reactive impurities [26] (Scheme 1, step b).

Synthesis of the clickable alkyne polymers (A4-)PEG$_x$-PCL$_y$

Polymeric backbones with the general formula **(A4-)PEG$_x$-PCL$_y$** were synthesized through ATRP, randomly copolymerizing different percentages of commercially available poly(ethylene glycol)methyl ether methacrylate (**PEG-MA**, average M_n = 500 Da, with 8 or 9 ethylene oxide repeating units) and propargyl-poly(ε-caprolactone)-methacrylate (**Pg-PCL-MA**) in the presence of Cu(I)Br/1,1,4,7,10,10-hexamethyltriethylenetetramine (HMTETA) catalyst [27]. Ethyl α-bromoisobutyrate (**1**)

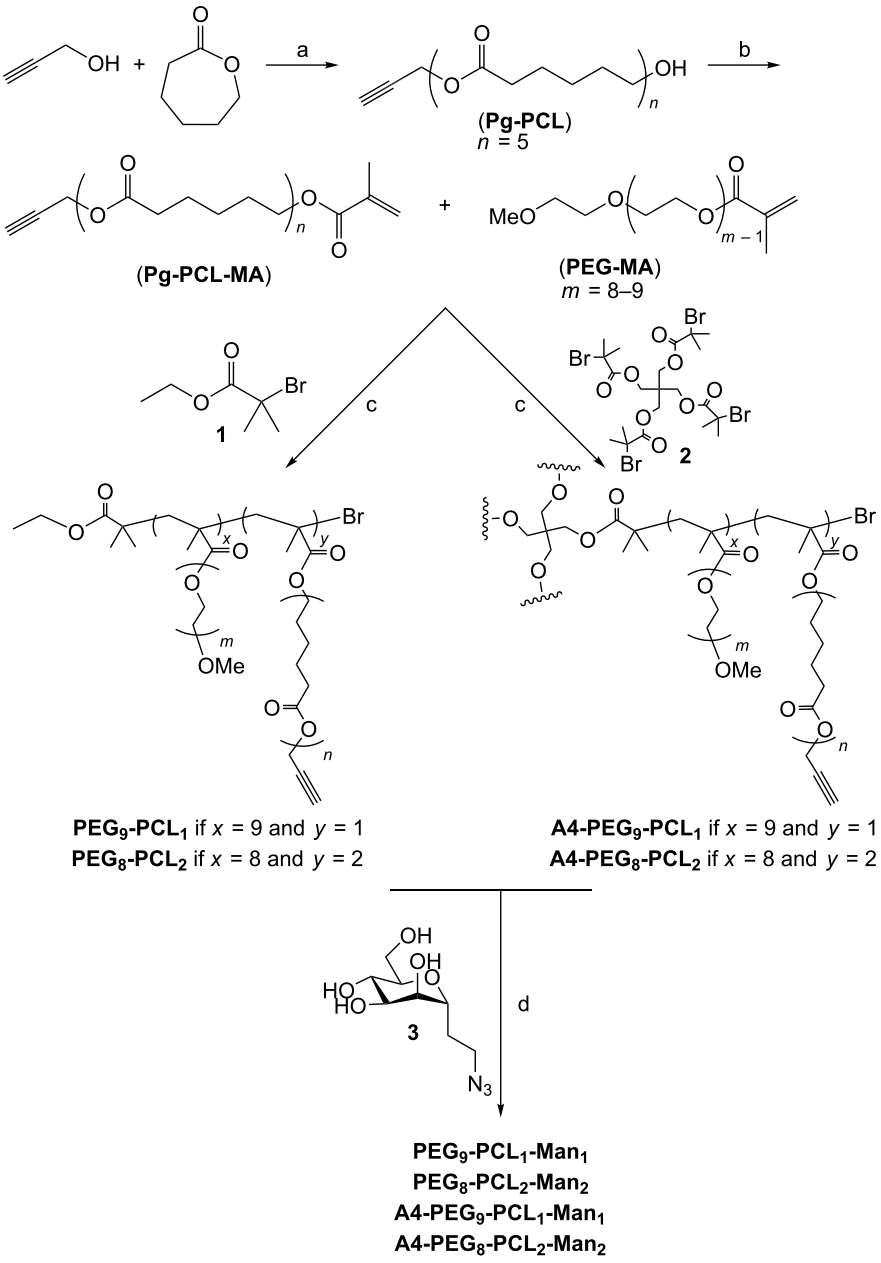

Scheme 1: Synthetic pathway to obtain linear and four-arm mannosylated copolymers.

and pentaerythritol tetrakis(2-bromoisobutyrate) (**2**) were chosen as the initiators for linear and four-arm polymers, respectively (Scheme 1, step c).

A DP value of 10 (for the linear polymers and for each branch of the four-arm ones) was targeted, in order to obtain macromolecules of different valencies, while maintaining relatively short and flexible polymer chains, which minimize steric hindrance during lectin binding. Different percentages of PEG and PCL macromonomers were used, since the number of PCL side chains defined the final number of pendant mannose, as well as the self-assembly behavior in water. Remarkably, when the ratios PEG/PCL were 9:1 or 8:2, the polymerizations achieved high conversions (≥87% after 6 h), as calculated from ^{1}H NMR spectroscopy results (see Figure S2, Supporting Information File 1). The semilogarithmic kinetic plots revealed first-order kinetics (Figure 2A), demonstrating a good reaction control over the polymer molecular weight and the molecular weight distribution, which was also confirmed by dispersity Đ values lower than 1.24 (Figure 2B, Table 1). The deviation of the number average molecular weight calculated by ^{1}H NMR from the value obtained by GPC (which was substantial for the four-arm polymers) was likely to be caused by the polystyrene calibration and by the intrinsic limitation of the GPC to determine the exact molecular weight of comb-like and hyperbranched polymers, as observed in numerous earlier publications [28].

Increasing the percentage of PCL to PEG/PCL = 7:3, the reactions stopped at a conversion of around 58% (Table 1 and Figure S3, Supporting Information File 1). It is known that copper-catalyzed ATRP can be complicated by the presence of monomers bearing triple bonds, which can indeed coordinate the copper species. Moreover, also the acetylene group can be subjected to radical addition and subsequent polymerization and cross-linking [29]. For this reason, polymerizations using PCL monomers bearing protected triple bonds were also performed [30]. However, no improvements were obtained even by using trimethylsilyl-protected-Pg-PCL-MA, the homopolymerization of which achieved a conversion of 55% (see Supporting Information File 1), comparable to the homopolymerization of Pg-PCL-MA (43%). The use of a more active catalytic system

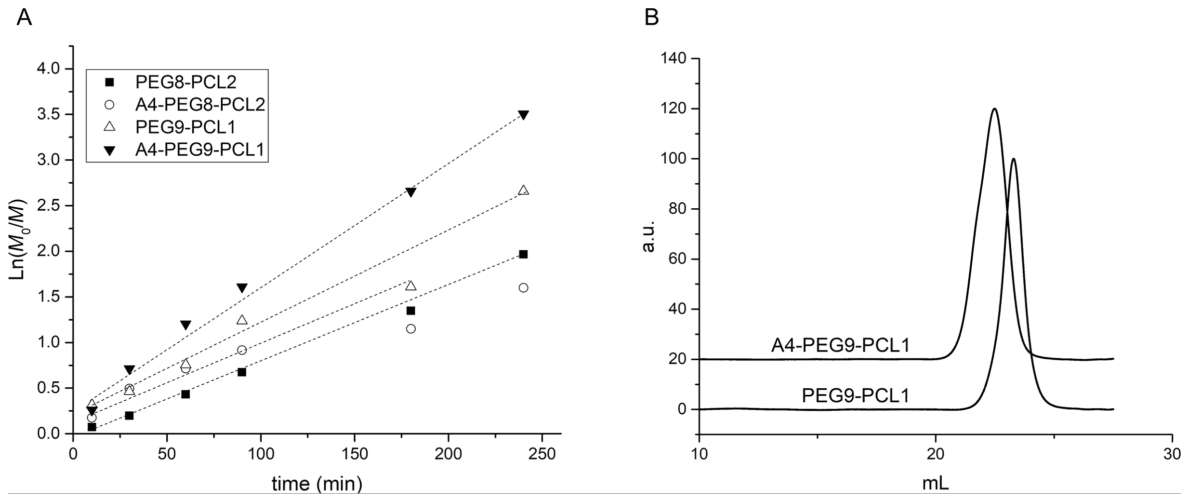

Figure 2: A) Kinetic profiles obtained for the synthesis of **(A4-)PEG$_9$-PCL$_1$** and **(A4-)PEG$_8$-PCL$_2$** copolymers. Reactions were conducted using CuBr/HMTETA as catalytic system, at 50 °C under nitrogen atmosphere. B) GPC chromatograms of **PEG$_9$-PCL$_1$** and **A4-PEG$_9$-PCL$_1$**.

Table 1: Summary of properties of the copolymers obtained by ATRP. PEG/PCL macromonomers molar ratio, conversion, number average molecular weight obtained by ^{1}H NMR ($M_{n,NMR}$) and GPC ($M_{n,GPC}$), and dispersity Đ (by GPC) are listed in the table.

polymer	PEG/PCL [mol/mol]	conversion (%)	$M_{n,NMR}$ [g/mol]	$M_{n,GPC}$ [g/mol]	Đ
PEG$_9$-PCL$_1$	9/1	95	5040	6090	1.24
PEG$_8$-PCL$_2$	8/2	91	4990	6301	1.06
PEG$_7$-PCL$_3$	7/3	58	3425	—	—
A4-PEG$_9$-PCL$_1$	9/1	98	20780	9640	1.11
A4-PEG$_8$-PCL$_2$	8/2	87	18760	11340	1.06

such as *N*,*N*,*N*′,*N*′′,*N*′′-pentamethyldiethylenetriamine (PMDETA) [31] did not improve the outcome of the reaction. The characterisation of the copolymer with a PEG/PCL ratio of 7:3 was therefore abandoned, and further study was focused on the copolymers with higher PEG/PCL ratios. The copolymerization of **PEG-MA** and **TMS-Pg-PCL-MA** in an 8:2 ratio catalyzed by CuBr/PMDETA achieved almost full conversions, but the kinetic was not linear (Figure S10, Supporting Information File 1), whilst the analogous reaction with a **PEG-MA**/**Pg-PCL-MA** ratio of 8:2 stopped at a conversion value of 65%.

Final products were purified through filtration over a neutral alumina pad to remove the copper catalyst, followed by precipitation in diethyl ether.

Synthesis of the mannosylated polymers

The sugar functionalization of the polymeric backbone was performed through CuAAC click reaction (Scheme 1, step d), by combining the triple bonds with 2-azidoethyl α-D-mannopyranoside (**3**), synthesized as already reported [32] (see Supporting Information File 1, Figure S1).The reaction conditions for the CuAAC were chosen according to [33]. In particular, the catalytic copper species was produced in situ by reducing copper(II) sulfate pentahydrate with sodium ascorbate, in the presence of tris[(1-benzyl-1*H*-1,2,3-triazol-4-yl)methyl]amine (TBTA) as copper(I)-stabilizing ligand. Both the actual PCL percentage and the molecular weight of the reacting polymers were calculated according to ^{1}H NMR analysis. An excess of 1.5 equiv of azide-bearing mannose **3** with respect to each triple bond was used. 2-azidoethyl α-D-mannopyranoside consumption was assessed through thin layer chromatography (TLC), whilst the triple bond conversion was monitored by means of ^{1}H NMR analysis. The disappearance of the alkyne proton peak (3.0 ppm) and the appearance of a signal for the C=C–H proton of triazole (8.1 ppm) were observed (Figure 3). The shift of the peak corresponding to the methylene group near the triple bond (4.5 ppm) and the appearance of the signal of mannose anomeric protons (Man-H1, 4.7 ppm) in the product spectrum also confirmed the functionalization.

Reactions were completed after three days. The crudes were purified by dialysis against water, and the final products **(A4-)PEG$_x$-PCL$_y$-Man$_y$** were lyophilized, achieving moderate to high yields.

Nanoparticle formation and size characterization

Dynamic light scattering (DLS) was used to determine the hydrodynamic diameter (D_h) of the polymers and their glycoderivatives, once dispersed in aqueous solution. Firstly, the non-mannosylated polymers were tested in three different media (H_2O, 10 mM PBS, 0.9% w/v NaCl) and at three different temperatures (10, 25 and 37 °C; concentration of 1 mg/mL, see Supporting Information File 1, Figures S11–S22, Tables S1–S4). In any medium, polymers formed nanoparticles with D_h varying from 7.5 to 11.3 nm, a size range which corresponds to 99–100% of the volume distribution. The remaining 0–1% was due to the presence of aggregates with a size of hundreds of nanometers as revealed by the scattering intensity distributions (Supporting Information File 1). Because of the limitation of the CONTIN algorithm used by this DLS analysis to determine a bimodal distribution of particle sizes [34], the predominance of small nanoparticles was confirmed by transmission electron microscopy (TEM) imaging (Figure 4), where dehydrated flattened particles of small size (10–20 nm) are shown together with few larger particles (50–100 nm).

Comparing the results obtained at the three different temperatures, it was observed that these polymers were not thermoresponsive, although PEG-copolymers may generally present a lower critical solubility temperature (Tables S1–S4) [35]. For our purposes, this could be an advantage, since they maintain the same size under different operation conditions: storage, room and body temperature.

Also the DLS distributions of the mannosylated **(A4-)PEG$_x$-PCL$_y$-Man$_y$** glycopolymers in aqueous media (water and HBS buffer) were characterized by two populations. The volume distribution was still dominated by small-size nanomaterials ($D_h \approx 10$ nm, Figure 5), although their intensity generally decreased with respect to larger colloids (Table 2 and Supporting Information File 1, Figures S23 and S24). This tendency may be due to the presence of the mannose residues that, being connected to the hydrophobic PCL chains, could affect the self-assembly of the macromolecules and generate some aggregates. Remarkably, four-arm species had a slightly lower D_h than the corresponding linear species.

Turbidity assay

The ability of glycopolymers to bind lectins was assessed using Concanavalin A (Con A), a model lectin able to recognize α-D-mannosyl and β-D-glucosyl residues. At physiological pH values, Con A is a tetramer, composed by four 26 kDa monomeric units, each of them possessing one coordination site [36,37]. When multivalent carbohydrate compounds bridge multiple Con A tetramers, insoluble clusters are formed, turning the originally transparent solution turbid (Figure 6B). Each single macromolecule may interact with many Con A receptors, although steric effects prevent binding of every mannose residue [38] (Figure 6A). Glycopolymers were tested in the presence of Con A in HBS buffer at pH 7.4. A fixed mannose

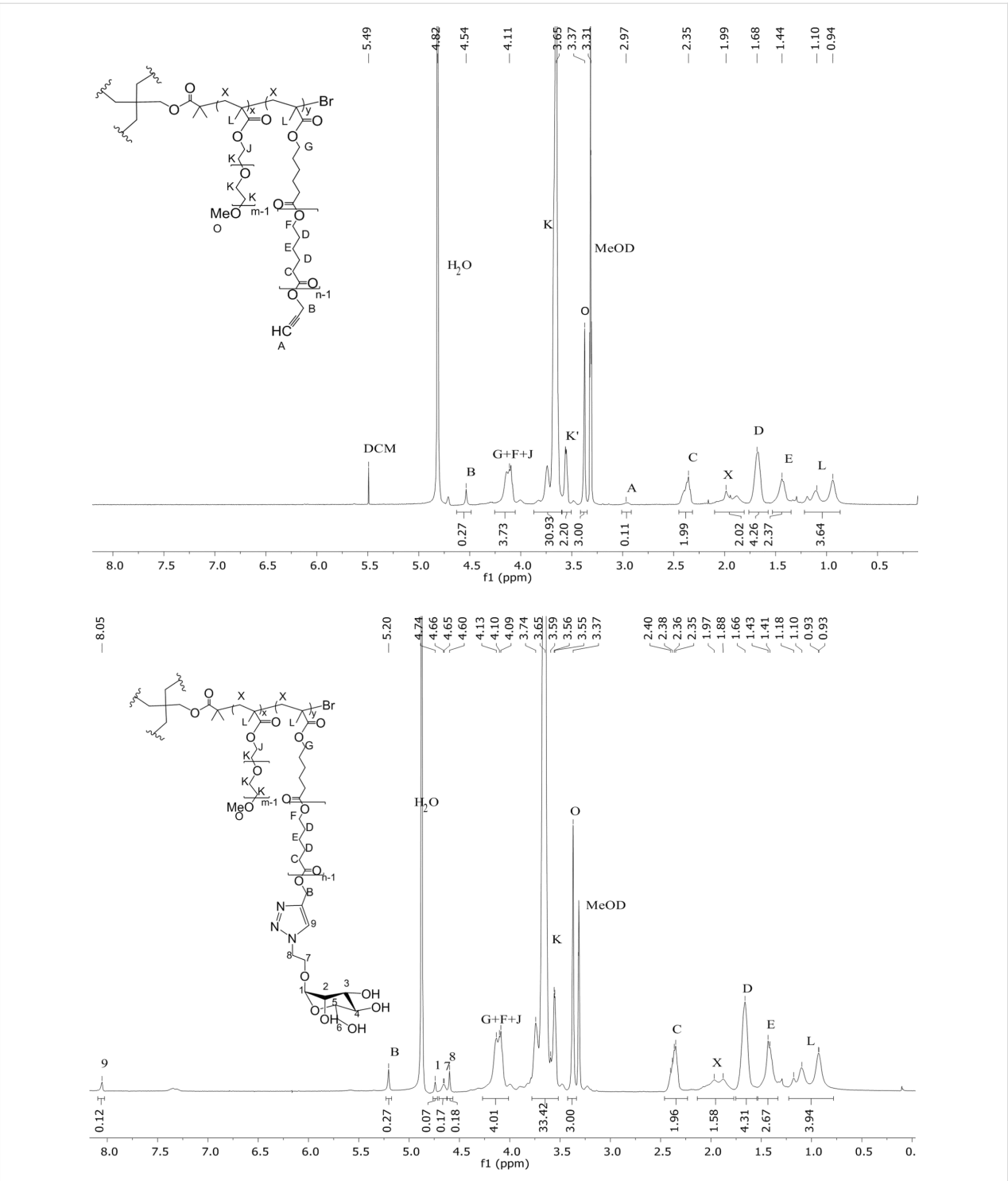

Figure 3: Comparison of the ^{1}H NMR spectrum of one selected polymer (**A4-PEG$_8$-PCL$_2$**, MeOD) before (upper panel) and after (lower panel) the mannosylation reaction. The disappearance of the peak of the alkyne proton (A, upper) and the appearance of the peak of the triazole (9, lower), together with the presence of the Man-H1 proton (1, lower) in the product demonstrate the formation of the mannosylated polymer (**A4-PEG$_8$-PCL$_2$-Man$_2$**).

concentration 2.5 times higher than the Con A binding site concentration was used, and turbidity was measured using an UV–vis spectrometer (Figure 7). The kinetics of glycopolymer-induced clustering were also investigated. In particular, the initial rates of Con A clustering, expressed as arbitrary units per minute (k, AU/min), were derived from the initial slope

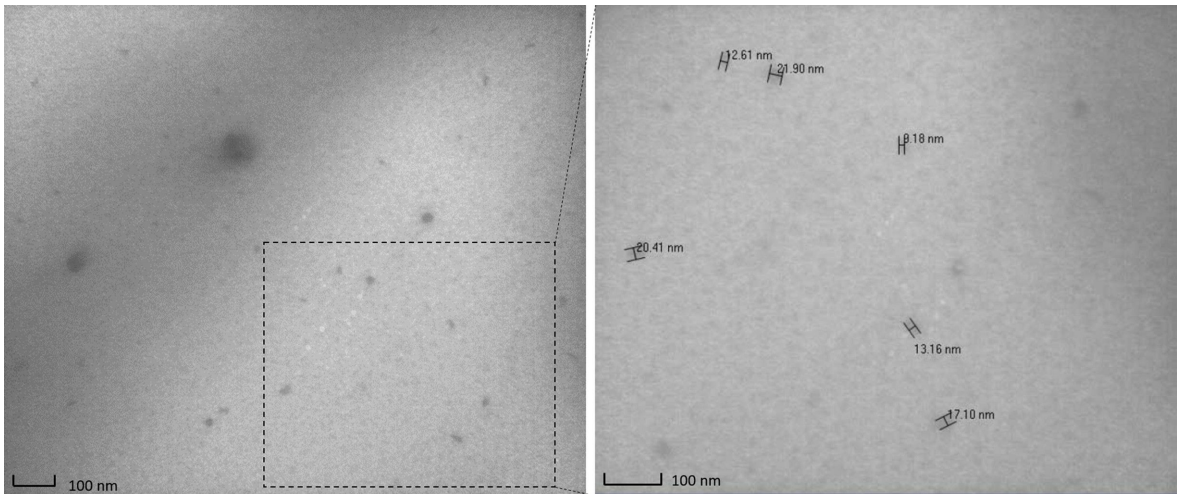

Figure 4: TEM images of **A4-PEG$_8$-PCL$_2$** 10 mg/mL in water; size distribution is dominated by small nanoparticles (diameter ≤ 20 nm).

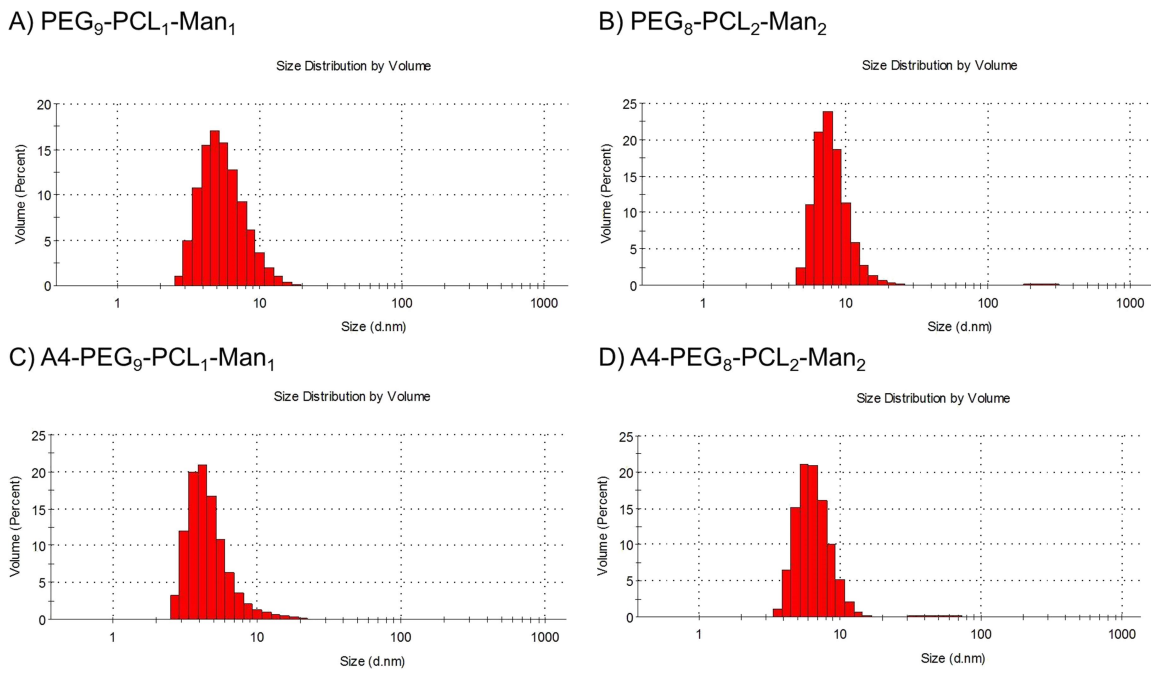

Figure 5: DLS size distribution (vol %) of the glycopolymers **PEG$_9$-PCL$_1$-Man$_1$** (A), **PEG$_8$-PCL$_2$-Man$_2$** (B), **A4-PEG$_9$-PCL$_1$-Man$_1$** (C), **A4-PEG$_8$-PCL$_2$-Man$_2$** (D), tested in water (1 mg/mL) at 25 °C.

Table 2: DLS analyses of polymers and corresponding glycopolymers in water (1 mg/mL) at 25 °C.

general formula	valency	hydrodynamic radius (nm) (intensity (%))	
		polymer	glyco derivative
PEG$_9$-PCL$_1$-(Man$_1$)	1	8.5 (73)	8.6 (83)
PEG$_8$-PCL$_2$-(Man$_2$)	2	10.2 (73)	10.8 (6)
A4-PEG$_1$-PCL$_1$-(Man$_1$)	4	8.1 (79)	5.8 (12)
A4-PEG$_8$-PCL$_2$-(Man$_2$)	8	9.6 (63)	8.0 (10)

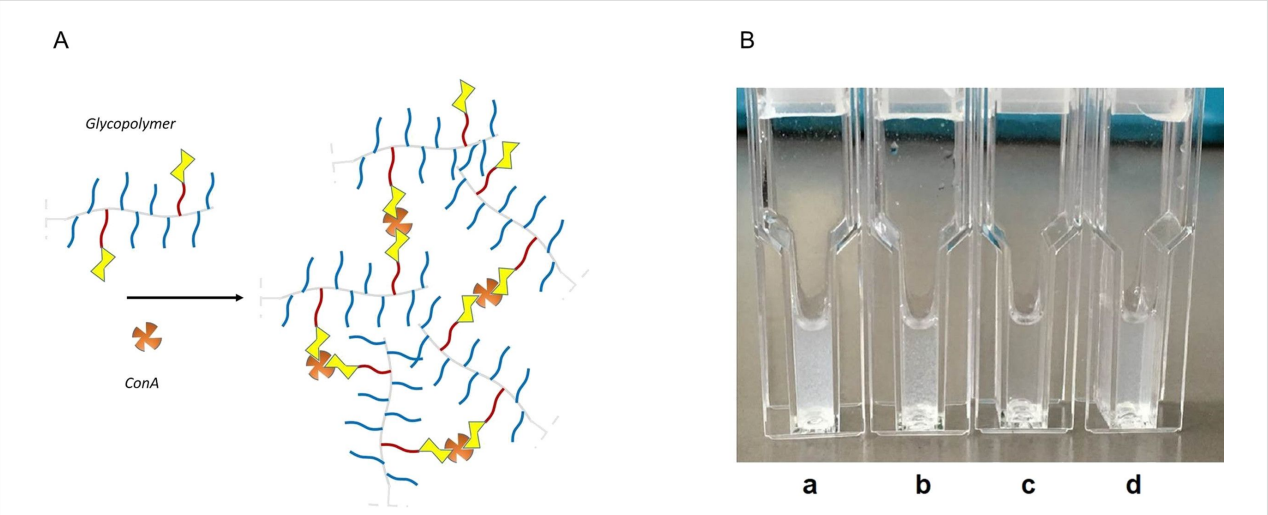

Figure 6: A) Schematic representation of Con A clustering by multivalent ligands. B) Con A suspensions after interaction with (a) **PEG$_8$-PCL$_2$-Man$_2$** (turbid), (b) **A4-PEG$_8$-PCL$_2$-Man$_2$** (turbid), (c) **PEG$_9$-PCL$_1$-Man$_1$** (transparent) and (d) **A4-PEG$_9$-PCL$_1$-Man$_1$** (turbid).

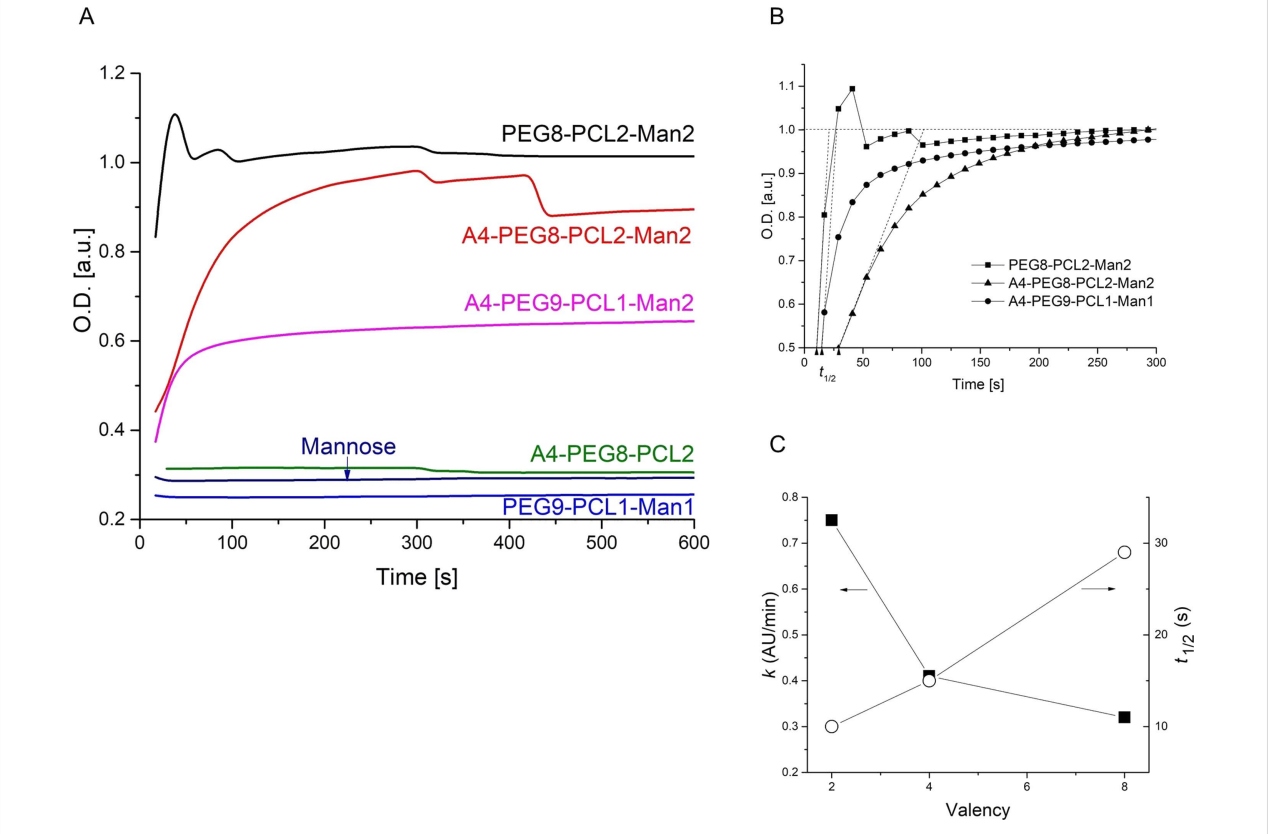

Figure 7: Turbidimetric assay results. A) Optical density (OD) data were recorded at 420 nm every 12 s for 10 min. B) $t_{1/2}$ was calculated as the time to reach half (OD= 0.5 a.u.) of the maximum optical density in normalized OD curve. The initial slope of the OD curve was used to determine the initial aggregation rate *k*. C) *k* (AU/min) and $t_{1/2}$ plotted as function of mannose valency.

of the curves; the time to reach half of the maximum turbidity ($t_{1/2}$) was determined from the endpoint of precipitation (Table 3).

The curves of the optical density (OD) measured as a function of the time (Figure 7) confirmed that polymers without mannose residues (**A4-PEG$_8$-PCL$_2$**) and mannose itself were

Table 3: Initial rates of Con A precipitation (k, AU/min) and time to reach half of the maximum turbidity ($t_{1/2}$, s) in turbidity assays.

Glycopolymer	Valency	k (AU/min)	$t_{1/2}$ (s)
PEG_9-PCL_1-Man_1	1	—	—
PEG_8-PCL_2-Man_2	2	0.75	10
A4-PEG_9-PCL_1-Man_1	4	0.41	15
A4-PEG_8-PCL_2-Man_2	8	0.32	29

not able to induce Con A clustering. In contrast, **PEG_8-PCL_2-Man_2**, **A4-PEG_8-PCL_2-Man_2** and **A4-PEG_9-PCL_1-Man_1** were able to bind Con A in a multivalent fashion, leading to an increase of turbidity. Interestingly, turbidity was not observed with the monovalent compound **PEG_9-PCL_1-Man_1**, suggesting that the polymer and the resulting nanosized colloid in water do not have a suitable valency for the formation of Con A clusters. We assumed that the mannose residues were not hidden within the polymer colloids but were exposed for binding, since all the other glycopolymers did precipitate the lectin. The divalent compound **PEG_8-PCL_2-Man_2** was the most efficient agglutinating agent of the series, even more potent than the octa- and tetra-valent polymers. In the case of the divalent compound **PEG_8-PCL_2-Man_2**, the absorbance quickly reached a plateau and then remained almost constant, although a stepwise variation of the OD indicated a partial precipitation of the aggregates, as shown in Figure 6B. The same happened for the octavalent glycopolymer **A4-PEG_8-PCL_2-Man_2**, but with a much lower initial rate. This behavior was already reported in the literature and it was ascribed to the slower Con A precipitation and the formation of cross-linked complexes over time [12,38,39]. Regarding the four-arm macromolecules, the tetravalent **A4-PEG_9-PCL_1-Man_1** showed a similar behavior as **A4-PEG_8-PCL_2-Man_2**, but it reached a much lower plateau, which indicated the formation of smaller colloidal clusters when the valency was reduced from 8 to 4. Moreover, the octavalent compound seemed to bound Con A more slowly (k-octa = 0.32 AU/min vs k-tetra = 0.41 AU/min, Table 3). This result may be ascribed to an effect of the different polymer composition on the aggregation kinetics. As general trend, the rate constant k of Con A clustering decreased as the valency increased, and consequently the time to reach half of the maximum turbidity $t_{1/2}$ increased as the valency increased (Table 3 and Figure 7C).

According to these results, it seemed that the Con A clustering activity of these macromolecules depended not only on their valency, but also on their molecular weight and architecture [40]. For example, the best result obtained for the divalent polymer, which has a lower mannose density, may depend on its lower steric hindrance, which results in a more efficient Con A binding.

Conclusion

A series of amphiphilic polymers, with linear or four-arm structure and consisting of a random sequence of PEG and PCL blocks, was successfully synthesized via a combination of ROP and ATRP. Polymers were subsequently mannosylated through a CuAAC click reaction, obtaining final glycopolymers with a mannose valency of 1, 2, 4 or 8. This synthetic strategy was exploited to produce well-defined nanomaterials that self-assemble in aqueous media forming ultrasmall nanoparticles. The ability of these glyco-functionalized nanoparticles to efficiently expose mannose to lectins was investigated with the model Concanavalin A, through turbidity assays. While the monovalent macromolecule was not able to induce Con A clustering, the linear divalent glycopolymer had a binding kinetics faster than the other four-arm compounds, and tetravalent one was even more active than the octavalent. These results indicated that besides mannose valency, macromolecular architecture can deeply influence the capability to bind lectins. According to their tunable characteristics, these glycopolymers can be potentially utilized as targeted anti-pathogenic nanomaterials and as well as for cell-targeted drug delivery.

Experimental

General procedures

Chemicals were purchased by commercial sources and used without further purification, unless otherwise indicated. Polyethylene glycol methyl ether (M_n = 500 Da) was purchased from Sigma-Aldrich. 2-Azidoethyl α-D-mannopyranoside (**3**) was synthesized as already described [32]. When anhydrous and oxygen-free conditions were required, the reactions were performed under nitrogen atmosphere. Inhibitor-free THF used for ATRP reactions was degassed prior use; THF used for click reaction was dried over Na/benzophenone and freshly distilled. Thin-layer chromatography (TLC) was performed on Silica Gel 60 F254 plates (Merck) with UV detection (254 and 365 nm) or using appropriate developing solutions. Flash column chromatography was performed on silica gel 230–400 mesh (Merck). Automated flash chromatography was performed on a Biotage® Isolera™ Prime system. NMR experiments were recorded on a Bruker AVANCE 400 MHz instrument at 298 K. Chemical shifts (δ) are reported in ppm downfield from the deuterated solvent as internal standard, coupling constants (J) in Hz. The

^{1}H NMR resonances of compounds were assigned with the assistance of COSY and HSQC experiments. HSQC experiments were also used to assign the chemical shift of protons overlapping with the solvent signals. Signals were abbreviated as s, singlet; bs, broad singlet; d, doublet; t, triplet; q, quartet; m, multiplet. Sugar protons were numbered as customary. GPC analyses were carried out with Jasco instrument and following set up: 2055i auto sampler; RI-2031 refractive index detector; CO-2060 plus oven column; PU-2080 pump; three PLgel 300 mm·7.5 mm (5 µm particle size) (10E4, 10E5, 500 A) and a PLgel 50 mm·7.5 mm (5 µm particle size) guard, using THF as eluent at 35 °C. The system was controlled using polystyrene calibration kits (by RESTEK and Sigma-Fluka); samples were dissolved in THF at a concentration of 4 mg/mL and filtered (PTFE filters, 0.45 µm).

Synthesis of propargyl-poly(ε-caprolactone) (Pg-PCL). **Pg-PCL** was synthesized as reported in a previous work [25]. Briefly, ε-caprolactone (20 g, 0.175 mol, 5 equiv) was added in a round flask and heated up to 130 °C. A second yellowish solution containing propargyl alcohol (2.04 mL, 0.035 mol, 1 equiv) and tin(II) 2-ethylhexanoate ($Sn(Oct)_2$, 0.0709 g, 0.175 mmol, 0.005 equiv) was prepared, stirred under a nitrogen flow for 20 min, and then added to the ε-caprolactone. The reaction mixture was stirred for 6 h at 130 °C, then stopped by cooling the flask to room temperature. Purification was carried out by dissolving the crude in 22 mL of methanol and dropping it in 1320 mL of vigorously stirred water. The resulting precipitate was isolated by removing the supernatant, dissolved in CH_2Cl_2 and anhydrified with anhydrous sodium sulphate. Subsequently it was filtered, and the filtrate was dried under reduced pressure, obtaining 20 g of final product **Pg-PCL** as a colorless viscous oil. $Conversion_{\varepsilon\text{-CL}}$ = 99%; $conversion_{propargyl\ alcohol}$ = 96%; yield = 92%; $M_{n,NMR}$ = 716 g·mol^{-1}; $M_{n,GPC}$ = 1345 g·mol^{-1}; PDI = 1.19 (relative to linear polystyrene). ^{1}H NMR (400 MHz, $CDCl_3$) δ 4.65 (d, J = 2.4 Hz, 2H, -CH_2-CCH), 4.03 (t, J = 6.6 Hz, 2H·(n − 1), -CH_2-OC(O)-), 3.61 (t, J = 6.5 Hz, 2H, -CH_2-OH), 2.45 (t, J = 2.4 Hz, 1H, -CH_2-CCH), 2.38 – 2.19 (m, 2H·n, -OC(O)-CH_2-), 1.70–1.52 (m, 4H·n, -OC(O)-CH_2CH_2-, -C$H_2$$CH_2$-OC(O)-), 1.45–1.24 (m, 2H·n, -CH_2C$H_2$$CH_2$-).

Synthesis of propargyl-poly(ε-caprolactone)-methacrylate (Pg-PCL-MA). **Pg-PCL-MA** was synthesized as reported in a previous work [25]. Briefly, **Pg-PCL** (5 g, 0.007 mol, 1 equiv) was added in a round flask and three cycles of vacuum–nitrogen were performed. 167 mL of dry toluene were added under nitrogen flow and the flask was cooled to 0 °C for 30 min. Triethylamine (1.46 mL, 0.01 mol, 1.5 equiv) and freshly distilled methacryloyl chloride (1.10 mL, 0.01 mol, 1.5 equiv) were sequentially added to the reaction mixture. The reaction mixture was stirred at room temperature under dynamic nitrogen atmosphere for 15 min and under static nitrogen atmosphere overnight. The crude was filtered through a celite pad (h = 6 cm, Φ = 2 cm), washing with toluene, and then the filtrate was evaporated under reduced pressure. The residue was taken up in 112.5 mL of CH_2Cl_2, washed with brine (3 × 45 mL) and dried over anhydrous sodium sulfate. The solvent was evaporated under vacuum, obtaining 4.14 g of final product **Pg-PCL-MA** as a pale yellow viscous oil. $Conversion_{OH->OMA}$ = 95%; yield = 75%; $M_{n,NMR}$ = 740 g·mol^{-1}; $M_{n,GPC}$ = 1380 g·mol^{-1}; PDI = 1.05 (relative to linear polystyrene). ^{1}H NMR (400 MHz, $CDCl_3$) δ 6.04 (s, 1H, H_2C-C(CH_3)-), 5.50 (s, 1H, H_2C-C(CH_3)-), 4.63 (d, J = 2.4 Hz, 2H, -CH_2-CCH), 4.10 (t, J = 13.1 Hz, 2H, -CH_2-O-MA), 4.02 (t, J = 6.7 Hz, 2H·(n − 1), -CH_2-OC(O)-), 2.44 (t, J = 2.4 Hz, 1H, -CH_2-CCH), 2.38–2.19 (m, 2H·n, -OC(O)-CH_2-), 1.89 (s, 3H, H_2C-C(CH_3)-), 1.75–1.50 (m, 4H·n, -OC(O)-CH_2CH_2-, -C$H_2$$CH_2$-OC(O)-), 1.50–1.25 (m, 2H·n, -CH_2C$H_2$$CH_2$-).

General procedure (1) for the synthesis of PEG_x-PCL_y. THF (inhibitor-free) was degassed under nitrogen for 10 min. **Pg-PCL-MA** (y equiv) and poly(ethylene glycol) methyl ether methacrylate (M_n = 500 Da, x equiv) were added in a Schlenk tube and three cycles of vacuum–nitrogen were performed. The catalyst solution was prepared as follows: Copper(I)bromide (500 mg) was inserted in a Schlenk tube and three cycles of vacuum–nitrogen were performed. THF (6 mL) and the ligand 1,1,4,7,10,10-hexamethyltriethylenetetramine (HMTETA, 0.95 mL) were added, obtaining a light green mixture that was stirred at room temperature under N_2 for 10 min. Finally, THF, the catalyst solution (containing CuBr/HMTETA 1 equiv with respect to the initiator) and the initiator (1 equiv, ethyl 2-bromo-2-methylpropionate (**1**)) were added to the monomers. The reaction mixture was stirred for 6 h at 50 °C under nitrogen atmosphere. The purification was performed by filtering the reaction mixture through a neutral alumina pad (h = 1.5 cm/m_{crude} (g), Φ = 2 cm), washing with CH_2Cl_2. Then the filtrate was dried under reduced pressure and the resulting crude was dissolved in the minimum amount of CH_2Cl_2 (ca. 1 mg/mL) and dripped in cold diethyl ether (CH_2Cl_2/Et_2O = 1:60). The mixture was stored at −20 °C for 3 h and then the resulting precipitate was isolated by removing the supernatant.

General procedure (2) for the synthesis of A4-PEG_x-PCL_y. THF (inhibitor-free) was degassed under nitrogen for 10 min. **Pg-PCL-MA** (4y equiv) and poly(ethylene glycol) methyl ether methacrylate (M_n = 500 Da, 4x equiv) were added in a Schlenk tube and three cycles of vacuum–nitrogen were performed. The catalyst solution was prepared as follows: Copper(I)bromide (500 mg) was inserted in a Schlenk tube and three cycles of vacuum–nitrogen were performed. THF (6 mL) and the ligand 1,1,4,7,10,10-hexamethyltriethylenetetramine (HMTETA,

0.95 mL) were added, obtaining a light green mixture that was stirred at room temperature under N_2 for 10 min. Finally, THF, the catalyst solution (containing CuBr/HMTETA 4 equiv with respect to the initiator) and the initiator (1 equiv, pentaerythritol tetrakis(2-bromo-isobutyrate, **2**) 80 mg/mL in THF) were added to the monomers. The reaction mixture was stirred for 6 h at 50 °C under nitrogen atmosphere. The purification was performed by filtering the reaction mixture through a neutral alumina pad (h = 1.5 cm/m_{crude} (g), Φ = 2 cm), washing with CH_2Cl_2. Then the filtrate was dried under reduced pressure and the resulting crude was dissolved in the minimum amount of CH_2Cl_2 (ca. 1 mg/mL) and dripped in cold diethyl ether (CH_2Cl_2/Et_2O = 1:60). The mixture was stored at −20 °C for 3 h and then the resulting precipitate was isolated by removing the supernatant.

Synthesis of PEG$_9$-PCL$_1$. The reaction between **Pg-PCL-MA** (245 mg, 0.306 mmol, 1 equiv) and poly(ethylene glycol) methyl ether methacrylate (1.38 g, 2.751 mmol, 9 equiv) was performed according to general procedure (1) in THF ([initiator] = 0.068 M), in the presence of CuBr (44 mg, 0.306 mmol, 1 equiv) and HMTETA (0.083 mL, 0.306 mmol, 1 equiv). Ethyl 2-bromo-2-methylpropionate **1** (45 µL, 0,348 mmol, 1 equiv) was the initiator. 713 mg of final product **PEG$_9$-PCL$_1$** were obtained. Conversion = 95%; real PEG = 92%; yield = 62%; $M_{n,NMR}$ = 5040 g·mol^{-1}; $M_{n,GPC}$ = 6090 g·mol^{-1}; PDI = 1.24 (relative to linear polystyrene). ^{1}H NMR (400 MHz, $CDCl_3$) δ 4.67 (d, J = 2.4 Hz, 2H·y, -CH_2-CCH), 4.19–3.82 (m, 2H·n·y + 2H·x, PCL: -C$H_{2,PCL}$-OC(O)-backbone, -CH_2-OC(O)-, PEG: -C$H_{2,PEG}$-OC(O)-backbone), 3.75–3.50 (m, (4H·(m − 1) + 2H)·x, PEG: -CH_2CH_2-), 3.37 (s, 3H·x, -OCH_3), 2.47 (bs, 1H·y, -CH$_2$-CCH), 2.40–2.25 (m, (2H·n)·y, PCL: -OC(O)-CH_2-), 2.08–1.72 (m, 2H·(y + x), -C$H_{2,backbone}$-), 1.73–1.53 (m, (4H·n)·y, PCL: -OC(O)-CH$_2$CH_2-, -CH_2CH$_2$-OC(O)-), 1.43–1.27 (m, (2H·n)·y, PCL: -CH$_2$CH_2CH$_2$-), 1.17–0.69 (m, 3H·(y + x), -C$H_{3,backbone}$).

Synthesis of PEG$_8$-PCL$_2$. The reaction between **Pg-PCL-MA** (517 mg, 0.696 mmol, 2 equiv) and poly(ethylene glycol) methyl ether methacrylate (1.39 g, 2.784 mmol, 8 equiv) was performed according to general procedure (1) in THF ([initiator] = 0.068 M), in the presence of CuBr (50 mg, 0.348 mmol, 1 equiv) and HMTETA (0.095 mL, 0.348 mmol, 1 equiv). Ethyl 2-bromo-2-methylpropionate (**1**, 51 µL, 0.348 mmol, 1 equiv) was the initiator. 1.48 g of final product **PEG$_8$-PCL$_2$** were obtained. Conversion = 91%; real PEG = 82%; yield = 92%; $M_{n,NMR}$ = 4990 g·mol^{-1}; $M_{n,GPC}$ = 6301 g·mol^{-1}; PDI = 1.06 (relative to linear polystyrene). ^{1}H NMR (400 MHz, $CDCl_3$) δ 4.67 (d, J = 2.4 Hz, 2H·y, -CH_2-CCH), 4.15–4.0 (m, (2H·n)·y + 2H·x, PCL: -C$H_{2,PCL}$-OC(O)-backbone, -CH_2-OC(O)-, PEG: -C$H_{2,PEG}$-OC(O)-backbone), 3.75–3.51 (m, (4H·(m − 1) + 2H)·x, PEG: -CH_2CH_2-), 3.36 (s, 3H·x, -OCH_3), 2.47 (bs, 1H·y, -CH$_2$-CCH), 2.48–2.28 (m, (2H·n)·y, PCL: -OC(O)-CH_2-), 1.95–1.70 (m, 2H·(x + y), -C$H_{2,backbone}$-), 1.75–1.55 (m, (4H·n)·y, PCL: -OC(O)-CH$_2$CH_2-, -CH_2CH$_2$-OC(O)-), 1.45–1.30 (m, (2H·n)·y, PCL: -CH$_2$CH_2CH$_2$-), 1.16–0.66 (m, 3H·(x + y), -C$H_{3,backbone}$).

Synthesis of A4-PEG$_9$-PCL$_1$. The reaction between **Pg-PCL-MA** (240 mg, 0.3 mmol, 4 equiv) and poly(ethylene glycol) methyl ether methacrylate (1.35 g, 2.695 mmol, 36 equiv) was performed according to general procedure (2) in THF ([initiator] = 0.02 M), in the presence of CuBr (43 mg, 0.3 mmol, 4 equiv) and HMTETA (0.082 mL, 0.3 mmol, 4 equiv). Pentaerythritol tetrakis(2-bromo-isobutyrate) (**2**, 55 mg, 0.075 mmol, 1 equiv) was the initiator. 1.24 g of final product **A4-PEG$_9$-PCL$_1$** were obtained. Conversion = 98%; real PEG = 94%; yield = 85%; $M_{n,NMR}$ = 20780 g·mol^{-1}; $M_{n,GPC}$ = 9640 g·mol^{-1}; PDI = 1.11 (relative to linear polystyrene). ^{1}H NMR (400 MHz, $CDCl_3$) δ 4.66 (d, J = 2.5 Hz, 2H·y, -CH_2-CCH), 4.20–3.95 (m, (2H·n)·y + 2H·x, PCL: -C$H_{2,PCL}$-OC(O)-backbone, -CH_2-OC(O)-, PEG: -C$H_{2,PEG}$-OC(O)-backbone), 3.75–3.48 (m, (4H·(m − 1) + 2H)·x, PEG: -CH_2CH_2-),), 3.36 (s, 3H·x, -OCH_3), 2.47 (bs, 1H·y, -CH$_2$-CCH), 2.45–2.20 (m, (2H·n)·y, PCL: -OC(O)-CH_2-), 2.05–1.80 (m, 2H·(y + x), -C$H_{2,backbone}$-), 1.73–1.53 (m, (4H·n)·y, PCL: -OC(O)-CH$_2$CH_2-, -CH_2CH$_2$-OC(O)-), 1.48–1.30 (m, (2H·n)·y, PCL: -CH$_2$CH_2CH$_2$-), 1.16–0.73 (m, 3H·(y + x), -C$H_{3,backbone}$).

Synthesis of A4-PEG$_8$-PCL$_2$. The reaction between **Pg-PCL-MA** (660 mg, 0.89 mmol, 8 equiv) and poly(ethylene glycol) methyl ether methacrylate (1.78 g, 3.55 mmol, 32 equiv) was performed according to general procedure (2) in THF ([initiator] = 0.02 M), in the presence of CuBr (64 mg, 0.44 mmol, 4 equiv) and HMTETA (0.121 mL, 0.44 mmol, 4 equiv). Pentaerythritol tetrakis(2-bromo-isobutyrate) (**2**, 81 mg, 0.11 mmol, 1 equiv) was the initiator. 1.5 g of final product **A4-PEG$_8$-PCL$_2$** were obtained. Conversion = 87%; real PEG = 84%; yield = 74% $M_{n,NMR}$ = 18760 g·mol^{-1}; $M_{n,GPC}$ = 11340 g·mol^{-1}; PDI = 1.06 (relative to linear polystyrene). ^{1}H NMR (400 MHz, $CDCl_3$) δ 4.67 (d, J = 2.4 Hz, 2H·y, -CH_2-CCH), 4.15–3.95 (m, (2H·n)·y + 2H·x, PCL: -C$H_{2,PCL}$-OC(O)-backbone, -CH_2-OC(O)-, PEG: -C$H_{2,PEG}$-OC(O)-backbone), 3.75–3.51 (m, (4H·(m − 1) + 2H)·x, PEG: -CH_2CH_2-), 3.36 (s, 3H·x, -OCH_3), 2.47 (bs, 1H·y, -CH$_2$-CCH), 2.49–2.25 (m, (2H·n)·y, PCL: -OC(O)-CH_2-), 2.0–1.75 (m, 2H·(y + x), -C$H_{2,backbone}$-), 1.74–1.55 (m, (4H·n)·y, PCL: -OC(O)-CH$_2$CH_2-, -CH_2CH$_2$-OC(O)-), 1.45–1.30 (m, (2H·n)·y, PCL: -CH$_2$CH_2CH$_2$-), 1.16–0.66 (m, 3H·(y + x), -C$H_{3,backbone}$).

General procedure for the CuAAC reaction. In the optimized copper(I)-catalyzed azide–alkyne cycloaddition

(CuAAC) procedure, starting materials and reagents were added to the reaction mixture as solids or as solutions in water or THF. Water was degassed by bubbling with nitrogen, and THF was freshly distilled. The reagents were added to the reaction vessel in the following order: polymer (1 equiv, solid), TBTA (0.2 equiv, 27 mg/mL in THF), $CuSO_4{\cdot}5H_2O$ (0.1 equiv, 21 mg/mL in H_2O), sodium ascorbate (0.4 equiv, 67 mg/mL in H_2O) and, after 10 min, 2-azidoethyl α-D-mannopyranoside **3** (1.5 equiv per each triple bond, 32 mg/mL in H_2O). The final concentration of the alkyne groups was 30 mM in a 1:1 THF/H_2O mixture. The reaction mixture was stirred at room temperature for 3 days, under nitrogen atmosphere and protected from light, adding 0.25 equiv of sodium ascorbate after 2, 29 and 47 h. The sugar consumption was monitored by TLC (eluent: $CHCl_3$/MeOH 7:3) and the product formation by ^{1}H NMR. When intermediates were observed but the azide monovalent ligand **3** was totally consumed, the latter was added (0.75 equiv) together with additional 0.25 equiv of sodium ascorbate. The solvent was evaporated and the crude redissolved in water (9 mg/mL) and dialyzed against an excess (60 times) of water (regenerated cellulose membrane with MWCO = 3500 Da) for 1 day, changing the water three times. Final glycopolymers were lyophilized. Final ^{1}H NMR spectra are reported in Figures S6–S9 (Supporting Information File 1).

Synthesis of monovalent glycopolymer PEG$_9$-PCL$_1$-Man$_1$. The reaction between **PEG$_9$-PCL$_1$** (150 mg, 0.022 mmol$_{PCL}$, 1 equiv$_{PCL}$) and (2-azidoethyl)-α-D-mannopyranoside (**3**, 8.4 mg, 0.034 mmol, 1.5 equiv) was performed in 1:1 THF/H_2O ([alkyne] = 30 mM) according to the general procedure. 124.1 mg of final product PEG$_9$-PCL$_1$-Man$_1$ were obtained. Conversion = 100%; yield = 80%. ^{1}H NMR (400 MHz, CD_3OD) δ 8.04 (s, 1H·y, $H_{triazole}$), 5.20 (s, 2H·y, -O-CH_2-triazole), 4.74 (bs, 1H·y, H_1^{Man}), 4.72–4.62 (m, 4H·y, -N-CH_2CH_2-O$_{linker}$), 4.23–4.02 (m, (2H·n)·y + 2H·x, PCL: -C$H_{2,PCL}$-OC(O)-backbone, -CH_2-OC(O)-, PEG: -C$H_{2,PEG}$-OC(O)-backbone), 3.74–3.52 (m, (2H + 4H·(m − 1))·x, PEG: -CH_2CH_2-), 3.37 (s, 3H·x, -OCH$_3$), 2.45–2.30 (m, (2H·n)·y, PCL: -OC(O)-CH_2-), 2.10–1.75 (m, 2H·(y + x), -C$H_{2,backbone}$-), 1.74–1.55 (m, (4H·n)·y, PCL: -OC(O)-CH$_2$CH_2-, -CH_2CH$_2$-OC(O)-), 1.56–1.32 (m, (2H·n)·y, PCL: -CH$_2$CH_2CH$_2$-), 1.23–0.76 (m, 3H·(y + x), -C$H_{3,backbone}$).

Synthesis of divalent glycopolymer PEG$_8$-PCL$_2$-Man$_2$. The reaction between **PEG$_8$-PCL$_2$** (150 mg, 0.05 mmol$_{PCL}$, 1 equiv$_{PCL}$) and (2-azidoethyl)-α-D-mannopyranoside (**3**, 19 mg, 0.075 mmol, 1.5 equiv) was performed in 1:1 THF/H_2O ([alkyne] = 30 mM) according to the general procedure. 105 mg of final product **PEG$_8$-PCL$_2$-Man$_2$** were obtained. Conversion = 100%; yield = 65%; ^{1}H NMR (400 MHz, CD_3OD) δ 8.05 (s, 1H·y, $H_{triazole}$), 5.20 (s, 2H·y, -O-CH_2-triazole), 4.74 (bs, 1H·y, H_1^{Man}), 4.69–4.52 (m, 4H·y, -N-CH_2CH_2-O$_{linker}$), 4.26–4.03 (m, (2H·n)·y + 2H·x, PCL: -C$H_{2,PCL}$-OC(O)-backbone, -CH_2-OC(O)-, PEG: -C$H_{2,PEG}$-OC(O)-backbone), 3.80–3.50 (m, (2H + 4H·(m − 1))·x, PEG: -CH_2CH_2-), 3.37 (s, 3H·x, -OCH$_3$), 2.48–2.28 (m, (2H·n)·y, PCL: -OC(O)-CH_2-), 2.00–1.75 (m, 2H·(x + y), -C$H_{2,backbone}$-), 1.75–1.50 (m, (4H·n)·y, PCL: -OC(O)-CH$_2$CH_2-, -CH_2CH$_2$-OC(O)-), 1.50–1.30 (m, (2H·n)·y, PCL: -CH$_2$CH_2CH$_2$-), 1.24–0.80 (m, 3H·(x + y), -C$H_{3,backbone}$).

Synthesis of tetravalent glycopolymer A4-PEG$_9$-PCL$_1$-Man$_1$. The reaction between **A4-PEG$_9$-PCL$_1$** (150 mg, 0.017 mmol$_{PCL}$, 1 equiv$_{PCL}$) and (2-azidoethyl)-α-D-mannopyranoside (**3**, 6.3 mg, 0.025 mmol, 1.5 equiv) was performed in 1:1 THF/H_2O ([alkyne] = 30 mM) according to the general procedure. 117.9 mg of final product **A4-PEG$_9$-PCL$_1$-Man$_1$** were obtained. Conversion = 100%; yield = 76%. ^{1}H NMR (400 MHz, CD_3OD) δ 8.04 (s, 1H·y, $H_{triazole}$), 5.20 (s, 2H·y, -O-CH_2-triazole), 4.73 (bs, 1H·y, H_1^{Man}), 4.67–4.52 (m, 4H·y, -N-CH_2CH_2-O$_{linker}$), 4.22–4.05 (m, (2H·n)·y + 2H·x, PCL: -C$H_{2,PCL}$-OC(O)-backbone, -CH_2-OC(O)-, PEG: -C$H_{2,PEG}$-OC(O)-backbone), 3.70–3.55 (m, (2H + 4H·(m − 1))·x, PEG: -CH_2CH_2-), 3.37 (s, 3H·x, -OCH$_3$), 2.48–2.25 (m, (2H·n)·y, PCL: -OC(O)-CH_2-), 2.05–1.80 (m, 2H·(y + x), -C$H_{2,backbone}$-), 1.75–1.55 (m, (4H·n)·y, PCL: -OC(O)-CH$_2$CH_2-, -CH_2CH$_2$-OC(O)-), 1.50–1.30 (m, (2H·n)·y, PCL: -CH$_2$CH_2CH$_2$-), 1.20–0.82 (m, 3H·(y + x), -C$H_{3,backbone}$).

Synthesis of octavalent glycopolymer A4-PEG$_8$-PCL$_2$-Man$_2$. The reaction between **A4-PEG$_8$-PCL$_2$** (150 mg, 0.044 mmol$_{PCL}$, 1 equiv$_{PCL}$) and (2-azidoethyl)-α-D-mannopyranoside (**3**, 16.6 mg, 0.067 mmol, 1.5 equiv) was performed in 1:1 THF/H_2O ([alkyne] = 30 mM) according to the general procedure. 145.2 mg of final product **A4-PEG$_8$-PCL$_2$-Man$_2$** were obtained. Conversion = 100%; yield = 90%. ^{1}H NMR (400 MHz, CD_3OD) δ 8.05 (s, 1H·y, $H_{Triazole}$), 5.20 (s, 2H·y, -O-CH_2-triazole), 4.74 (bs, 1H·y, H_1^{Man}), 4.70–4.58 (m, 4H·y, -N-CH_2CH_2-O$_{linker}$), 4.28–4.03 (m, (2H·n)·y + 2H·x, PCL: -C$H_{2,PCL}$-OC(O)-backbone, -CH_2-OC(O)-, PEG: -C$H_{2,PEG}$-OC(O)-backbone), 3.74–3.55 (m, (2H + 4H·(m − 1))·x, PEG: -CH_2CH_2-), 3.37 (s, 3H·x, -OCH$_3$), 2.48–2.30 (m, (2H·n)·y, PCL: -OC(O)-CH_2-), 2.20–1.75 (m, 2H·(y + x), -C$H_{2,backbone}$-), 1.73–1.60 (m, (4H·n)·y, PCL: -OC(O)-CH$_2$CH_2-, -CH_2CH$_2$-OC(O)-), 1.52–1.31 (m, (2H·n)·y, PCL: -CH$_2$CH_2CH$_2$-), 1.25–0.77 (m, 3H·(y + x), -C$H_{3,backbone}$).

Particle size measurements by DLS

DLS analyses of polymers (1 mg/mL, filtered solutions with PTFE 0.45 μm filters) were performed using a Malvern Instrument Zetasizer Nano ZS instrument equipped with a 4 mW He–Ne laser operating at λ = 634 nm. Particle size distribution

by scattering intensity (%) was determined by the CONTIN algorithm, as provided by the Zetasizer software (Malvern, UK). Particle size distribution by volume (%) was calculated from the scattering intensity distributions by the Zetasizer software, by setting the refractive index of the material R.I. = 1.465, which corresponds nearly to the refractive indices of poly(ethylene glycol) methacrylate M_n = 500 Da (R.I. = 1.467) as well as of the ε-caprolactone repeating units (R.I. = 1.463), as reported by the supplier (Sigma Aldrich).

Transmission electron microscopy

TEM images were acquired with a DeLong America LVEM5 microscope, equipped with a field-emission gun and operating at 5 kV. TEM samples were prepared by dropping 10 μL of sample (10 mg/mL in water) on a copper grid (400 mesh) placed on filter paper. The grid was left to dry overnight for evaporating the solvent.

Turbidimetric assay

This assay was performed in filtered (PTFE, 0.2 μm) HEPES-buffered saline (HBS), containing 10 mM HEPES, 150 mM NaCl and 1 mM $CaCl_2$ at pH 7.4, according to a procedure already reported in the literature [38]. The stock solution of Con A (6 μM with respect to the tetramer, M_W = 104000 Da) was freshly prepared. Turbidity measurements were performed by adding 100 μL of the glycopolymer solution in HBS buffer to 500 μL of stock Con A solution. Final concentrations were 50 μM per mannose residue and 20 μM per Con A binding site, corresponding to a ratio Con A binding site/mannose = 1:2.5. The Con A-glycopolymer solution was vigorously stirred for 11 s using a micropipette and then placed in a Jasco V-630 UV–vis spectrometer at 30 °C, using semi-micro disposable cuvettes (optical PS, 2.5 mL volume, 1 cm path length). Optical Density (OD) data were recorded at 420 nm every 12 s for 10 min. $t_{1/2}$ was calculated as the time to reach half of the maximum optical density in the OD curve. The first three points of the curve was fit with a straight line and its slope was used to determine the initial rate of Con A aggregation k.

Supporting Information

Supporting Information File 1

Additional experimental data.
[https://www.beilstein-journals.org/bjnano/content/supplementary/2190-4286-10-212-S1.pdf]

Acknowledgements

This study was supported by Regione Lombardia (POR FESR 2014–2020) within the framework of the NeOn project (ID 239047).

ORCID® iDs

Francesco Cellesi - https://orcid.org/0000-0001-6106-9317

References

1. Geijtenbeek, T. B. H.; Torensma, R.; van Vliet, S. J.; van Duijnhoven, G. C. F.; Adema, G. J.; van Kooyk, Y.; Figdor, C. G. *Cell* **2000,** *100,* 575–585. doi:10.1016/s0092-8674(00)80693-5
2. Alvarez, C. P.; Lasala, F.; Carrillo, J.; Muñiz, O.; Corbí, A. L.; Delgado, R. *J. Virol.* **2002,** *76,* 6841–6844. doi:10.1128/jvi.76.13.6841-6844.2002
3. Merritt, E. A.; Hol, W. G. *Curr. Opin. Struct. Biol.* **1995,** *5,* 165–171. doi:10.1016/0959-440x(95)80071-9
4. Bernardi, A.; Jiménez-Barbero, J.; Casnati, A.; De Castro, C.; Darbre, T.; Fieschi, F.; Finne, J.; Funken, H.; Jaeger, K.-E.; Lahmann, M.; Lindhorst, T. K.; Marradi, M.; Messner, P.; Molinaro, A.; Murphy, P. V.; Nativi, C.; Oscarson, S.; Penadés, S.; Peri, F.; Pieters, R. J.; Renaudet, O.; Reymond, J.-L.; Richichi, B.; Rojo, J.; Sansone, F.; Schäffer, C.; Turnbull, W. B.; Velasco-Torrijos, T.; Vidal, S.; Vincent, S.; Wennekes, T.; Zuilhof, H.; Imberty, A. *Chem. Soc. Rev.* **2013,** *42,* 4709–4727. doi:10.1039/c2cs35408j
5. Lundquist, J. J.; Toone, E. J. *Chem. Rev.* **2002,** *102,* 555–578. doi:10.1021/cr000418f
6. Gerke, C.; Ebbesen, M. F.; Jansen, D.; Boden, S.; Freichel, T.; Hartmann, L. *Biomacromolecules* **2017,** *18,* 787–796. doi:10.1021/acs.biomac.6b01657
7. Miura, Y.; Hoshino, Y.; Seto, H. *Chem. Rev.* **2016,** *116,* 1673–1692. doi:10.1021/acs.chemrev.5b00247
8. Kochendoerfer, G. G.; Chen, S.-Y.; Mao, F.; Cressman, S.; Traviglia, S.; Shao, H.; Hunter, C. L.; Low, D. W.; Cagle, E. N.; Carnevali, M.; Gueriguian, V.; Keogh, P. J.; Porter, H.; Stratton, S. M.; Wiedeke, M. C.; Wilken, J.; Tang, J.; Levy, J. J.; Miranda, L. P.; Crnogorac, M. M.; Kalbag, S.; Botti, P.; Schindler-Horvat, J.; Savatski, L.; Adamson, J. W.; Kung, A.; Kent, S. B. H.; Bradburne, J. A. *Science* **2003,** *299,* 884–887. doi:10.1126/science.1079085
9. Vázquez-Dorbatt, V.; Lee, J.; Lin, E.-W.; Maynard, H. D. *ChemBioChem* **2012,** *13,* 2478–2487. doi:10.1002/cbic.201200480
10. Ragupathy, L.; Millar, D. G.; Tirelli, N.; Cellesi, F. *Macromol. Biosci.* **2014,** *14,* 1528–1538. doi:10.1002/mabi.201400146
11. Matyjaszewski, K.; Xia, J. *Chem. Rev.* **2001,** *101,* 2921–2990. doi:10.1021/cr940534g
12. Dai, X.-H.; Dong, C.-M. *J. Polym. Sci., Part A: Polym. Chem.* **2008,** *46,* 817–829. doi:10.1002/pola.22426
13. Ladmiral, V.; Mantovani, G.; Clarkson, G. J.; Cauet, S.; Irwin, J. L.; Haddleton, D. M. *J. Am. Chem. Soc.* **2006,** *128,* 4823–4830. doi:10.1021/ja058364k
14. Becer, C. R.; Gibson, M. I.; Geng, J.; Ilyas, R.; Wallis, R.; Mitchell, D. A.; Haddleton, D. M. *J. Am. Chem. Soc.* **2010,** *132,* 15130–15132. doi:10.1021/ja1056714
15. Mitchell, D. A.; Zhang, Q.; Voorhaar, L.; Haddleton, D. M.; Herath, S.; Gleinich, A. S.; Randeva, H. S.; Crispin, M.; Lehnert, H.; Wallis, R.; Patterson, S.; Becer, C. R. *Chem. Sci.* **2017,** *8,* 6974–6980. doi:10.1039/c7sc01515a
16. Zhang, Q.; Collins, J.; Anastasaki, A.; Wallis, R.; Mitchell, D. A.; Becer, C. R.; Haddleton, D. M. *Angew. Chem., Int. Ed.* **2013,** *52,* 4435–4439. doi:10.1002/anie.201300068
17. Yilmaz, G.; Messager, L.; Gleinich, A. S.; Mitchell, D. A.; Battaglia, G.; Becer, C. R. *Polym. Chem.* **2016,** *7,* 6293–6296. doi:10.1039/c6py01523a

18. Ting, S. R. S.; Chen, G.; Stenzel, M. H. *Polym. Chem.* **2010,** *1,* 1392–1412. doi:10.1039/c0py00141d
19. Grossen, P.; Witzigmann, D.; Sieber, S.; Huwyler, J. *J. Controlled Release* **2017,** *260,* 46–60. doi:10.1016/j.jconrel.2017.05.028
20. Wei, X.; Gong, C.; Gou, M.; Fu, S.; Guo, Q.; Shi, S.; Luo, F.; Guo, G.; Qiu, L.; Qian, Z. *Int. J. Pharm.* **2009,** *381,* 1–18. doi:10.1016/j.ijpharm.2009.07.033
21. Pasut, G. *Polymers (Basel, Switz.)* **2014,** *6,* 160–178. doi:10.3390/polym6010160
22. Ordanini, S.; Cellesi, F. *Pharmaceutics* **2018,** *10,* 209. doi:10.3390/pharmaceutics10040209
23. Mikhail, A. S.; Allen, C. *Biomacromolecules* **2010,** *11,* 1273–1280. doi:10.1021/bm100073s
24. Danafar, H.; Rostamizadeh, K.; Davaran, S.; Hamidi, M. *Drug Dev. Ind. Pharm.* **2017,** *43,* 1908–1918. doi:10.1080/03639045.2017.1355922
25. Celentano, W.; Battistella, J.; Silvestri, I. P.; Bruni, R.; Huang, X.; Li, M.; Messa, P.; Ordanini, S.; Cellesi, F. *React. Funct. Polym.* **2018,** *131,* 164–173. doi:10.1016/j.reactfunctpolym.2018.07.011
26. Warneke, J.; Wang, Z.; Zeller, M.; Leibfritz, D.; Plaumann, M.; Azov, V. A. *Tetrahedron* **2014,** *70,* 6515–6521. doi:10.1016/j.tet.2014.07.019
27. Bruni, R.; Possenti, P.; Bordignon, C.; Li, M.; Ordanini, S.; Messa, P.; Rastaldi, M. P.; Cellesi, F. *J. Controlled Release* **2017,** *255,* 94–107. doi:10.1016/j.jconrel.2017.04.005
28. Chen, Y.; Lord, M. S.; Piloni, A.; Stenzel, M. H. *Macromolecules* **2015,** *48,* 346–357. doi:10.1021/ma501742v
29. Sumerlin, B. S.; Tsarevsky, N. V.; Louche, G.; Lee, R. Y.; Matyjaszewski, K. *Macromolecules* **2005,** *38,* 7540–7545. doi:10.1021/ma0511245
30. Opsteen, J. A.; van Hest, J. C. M. *Chem. Commun.* **2005,** 57–59. doi:10.1039/b412930j
31. Tang, W.; Kwak, Y.; Braunecker, W.; Tsarevsky, N. V.; Coote, M. L.; Matyjaszewski, K. *J. Am. Chem. Soc.* **2008,** *130,* 10702–10713. doi:10.1021/ja802290a
32. Gu, L.; Luo, P. G.; Wang, H.; Meziani, M. J.; Lin, Y.; Veca, L. M.; Cao, L.; Lu, F.; Wang, X.; Quinn, R. A.; Wang, W.; Zhang, P.; Lacher, S.; Sun, Y.-P. *Biomacromolecules* **2008,** *9,* 2408–2418. doi:10.1021/bm800395e
33. Ordanini, S.; Varga, N.; Porkolab, V.; Thépaut, M.; Belvisi, L.; Bertaglia, A.; Palmioli, A.; Berzi, A.; Trabattoni, D.; Clerici, M.; Fieschi, F.; Bernardi, A. *Chem. Commun.* **2015,** *51,* 3816–3819. doi:10.1039/c4cc09709b
34. Rasteiro, M. G.; Lemos, C. C.; Vasquez, A. *Part. Sci. Technol.* **2008,** *26,* 413–437. doi:10.1080/02726350802367399
35. Ward, M. A.; Georgiou, T. K. *Polymers (Basel, Switz.)* **2011,** *3,* 1215–1242. doi:10.3390/polym3031215
36. Senear, D. F.; Teller, D. C. *Biochemistry* **1981,** *20,* 3076–3083. doi:10.1021/bi00514a014
37. Wu, Q.; Wang, L.; Yu, H.; Wang, J.; Chen, Z. *Chem. Rev.* **2011,** *111,* 7855–7875. doi:10.1021/cr200027j
38. Cairo, C. W.; Gestwicki, J. E.; Kanai, M.; Kiessling, L. L. *J. Am. Chem. Soc.* **2002,** *124,* 1615–1619. doi:10.1021/ja016727k
39. Gestwicki, J. E.; Cairo, C. W.; Strong, L. E.; Oetjen, K. A.; Kiessling, L. L. *J. Am. Chem. Soc.* **2002,** *124,* 14922–14933. doi:10.1021/ja027184x
40. Chen, Y.; Chen, G.; Stenzel, M. H. *Macromolecules* **2010,** *43,* 8109–8114. doi:10.1021/ma100919x

License and Terms

BEILSTEIN JOURNAL OF NANOTECHNOLOGY

Bombesin receptor-targeted liposomes for enhanced delivery to lung cancer cells

Mohammad J. Akbar, Pâmela C. Lukasewicz Ferreira, Melania Giorgetti, Leanne Stokes and Christopher J. Morris*

Full Research Paper

Open Access

Address:
School of Pharmacy, University of East Anglia, Norwich, UK

Email:
Christopher J. Morris* - Christopher.J.Morris@uea.ac.uk

* Corresponding author

Keywords:
bombesin; GRPR; liposome; lung cancer; targeting

Beilstein J. Nanotechnol. **2019,** *10,* 2553–2562.
doi:10.3762/bjnano.10.246

Received: 30 September 2019
Accepted: 03 December 2019
Published: 19 December 2019

This article is part of the thematic issue "Engineered nanomedicines for advanced therapies".

Guest Editor: F. Baldelli Bombelli

Abstract

Background: Gastrin-releasing peptide is a member of the bombesin family of peptides. Its cognate receptor, gastrin releasing peptide receptor (GRPR), is widely expressed in cancers of the lung, pancreas and ovaries. Gastrin releasing peptide (GRP) is an autocrine growth factor in small cell lung cancer, which has very poor patient outcomes. High affinity antagonist peptides have been developed for in vivo cancer imaging. In this report we decorated pegylated liposomes with a GRPR antagonist peptide and studied its interaction with, and accumulation within, lung cancer cells.

Results: An N-terminally cysteine modified GRPR antagonist (termed cystabn) was synthesised and shown to inhibit cell growth in vitro. Cystabn was used to prepare a targeted 1,2-distearoyl-*sn*-glycero-3-phosphoethanolamine-*N*-[amino(polyethylene glycol)-2000] (DSPE-PEG2000) lipid conjugate that was formulated into liposomes. The liposomes displayed desirable colloidal properties and good stability under storage conditions. Flow cytometric and microscopic studies showed that fluorescently labelled cystabn-decorated liposomes accumulated more extensively in GRPR over-expressing cells than matched liposomes that contained no cystabn targeting motif.

Conclusion: The use of GRPR antagonistic peptides for nanoparticle targeting has potential for enhancing drug accumulation in resistant cancer cells.

Introduction

Small-cell lung cancer (SCLC) accounts for approximately one in five lung cancer diagnoses. In spite of global efforts to reduce tobacco smoking in recent decades, the incidence of smoking-associated cancers such as SCLC remains high with more than 142,000 deaths from lung cancer estimated in the United States for 2019 [1]. Approximately 80% of the world's 1.1 billion smokers live in low- and middle-income countries, where access to state of the art healthcare and diagnostic technologies is limited [2]. Alarmingly, the average life expectancy of an untreated SCLC patient is less than four months due to the high likelihood of diagnosis at the metastatic stage. With intensive chemo- and radiotherapy the median survival extends to only 14–18 months meaning new therapeutic approaches for targeted drug delivery to SCLC are desperately needed.

SCLC belongs to a class known as neuroendocrine tumours in which malignant cells secrete hormones and growth factors – a trait inherited from the neuroendocrine cells of the bronchial epithelium that are transformed and give rise to the early SCLC tumours. Of the hormones known to be secreted by SCLC cells, gastrin-releasing peptide (GRP), is the most widely studied. GRP is the human homologue of the amphibian peptide, bombesin, and plays a role in embryonic development and adult repair of bronchial epithelia [3]. The GRP receptor, hereafter termed GRPR, is a G-protein-coupled receptor and member of the bombesin (BB) receptor family: BB1 receptor is activated by neuromedin B (NMB); BB2 (also called GRPR) is activated by GRP; the BB3 receptor shares only 50% homology with BB1 and BB2 and is an orphan receptor with an unidentified endogenous ligand.

The expression of bombesin-related peptides and the BB receptors by SCLC cell lines and primary tumours have been widely studied for the past three decades [3-6]. GRP and NMB secretion by SCLC is known to cause an autocrine growth loop that drives tumour growth. Therefore, a number of experimental therapeutics or imaging agents targeted at the GRP-GRPR interaction, including anti-GRP antibodies and GRPR peptide antagonists have been developed. These agents have demonstrated antitumour responses in a number of preclinical models of pancreatic cancer [7] and imaging of breast [8], pancreatic [9] and glioma [10] tumours.

The use of GRPR antagonists is motivated by their inability to cause downstream cell growth effects, but is counter-balanced by a greatly reduced rate of receptor internalisation. Nonetheless, a number of reports have illustrated that GRP/bombesin-based antagonists display superior in vivo targeting capacity cf. agonist peptides [11]. It is therefore reasonable to exploit the enhanced targeting capacity of the antagonist peptides for enhanced targeting of SCLC. Indeed, we postulate that high-affinity binding of antagonist peptides to SCLC cell surface GRPR would be expected to increase the local accumulation of the liposomes in the cell surface, thus increasing the probability of drug accumulation in the target cells, without activating GRPR signalling. For example, by increasing the fraction of liposomes that are membrane-bound through GRPR binding cf. non-targeted liposomes, which exchange rapidly between the free and cell surface-bound state, would indirectly increase the relative intracellular accumulation. Access to the intracellular compartment would be achieved by constitutive plasma membrane endocytosis (e.g., pinocytosis), resulting in membrane internalisation, endosome formation and trafficking through the endo-lysosomal system.

Nanomedicines to improve cancer therapy have been widely studied and have resulted in a number of approved therapies such as Doxil® in the 1990s and the recent approval of Onivyde® [12]. In the lung cancer field, cisplatin formulated as a pegylated liposomal formulation (Lipoplatin®) has delivered comparable antitumour response against non-small cell lung cancer tumours with reduced side effects when delivered in combination with paclitaxel compared to when cisplatin and paclitaxel solutions are used in combination [13]. In preclinical studies, improved therapeutic responses have been achieved by adopting an active targeting approach. Typically, this involves the incorporation of a surface-bound moiety that selectively binds to a cognate receptor/protein on the tumour cell surface, leading to accumulation of nanocarriers in the tumour. A diversity of targeting ligands has been explored, including antibodies, proteins, peptides and aptamers. Targeted nanoparticles such as HER2-targeted MM-302 [14], transferrin receptor-targeted CALAA-01 [15], and prostate-specific membrane antigen (PSMA)-targeted BIND-014 [16] have reached the clinic but detailed information about the clinical advantage of using targeted platforms is still forthcoming. In this study we explored whether surface engraftment of a GRPR antagonist peptide could be used to target GRPR expressing lung cancer cells for the purposes of enhanced liposome delivery to lung cancer.

Results and Discussion

GRPR as a target in lung cancer

The functionality of GRPR in SCLC cells was confirmed by Fura-2 studies in which NCI-H345 or NCI-H82 SCLC cell models were exposed to a dose-range of the canonical GRPR agonist peptide, Tyr^4-Bn. A dose-dependent increase in intracellular calcium release was observed for NCI-H345 but not the GRPR deficient SCLC line, NCI-H82 (Figure 1a,b), as previ-

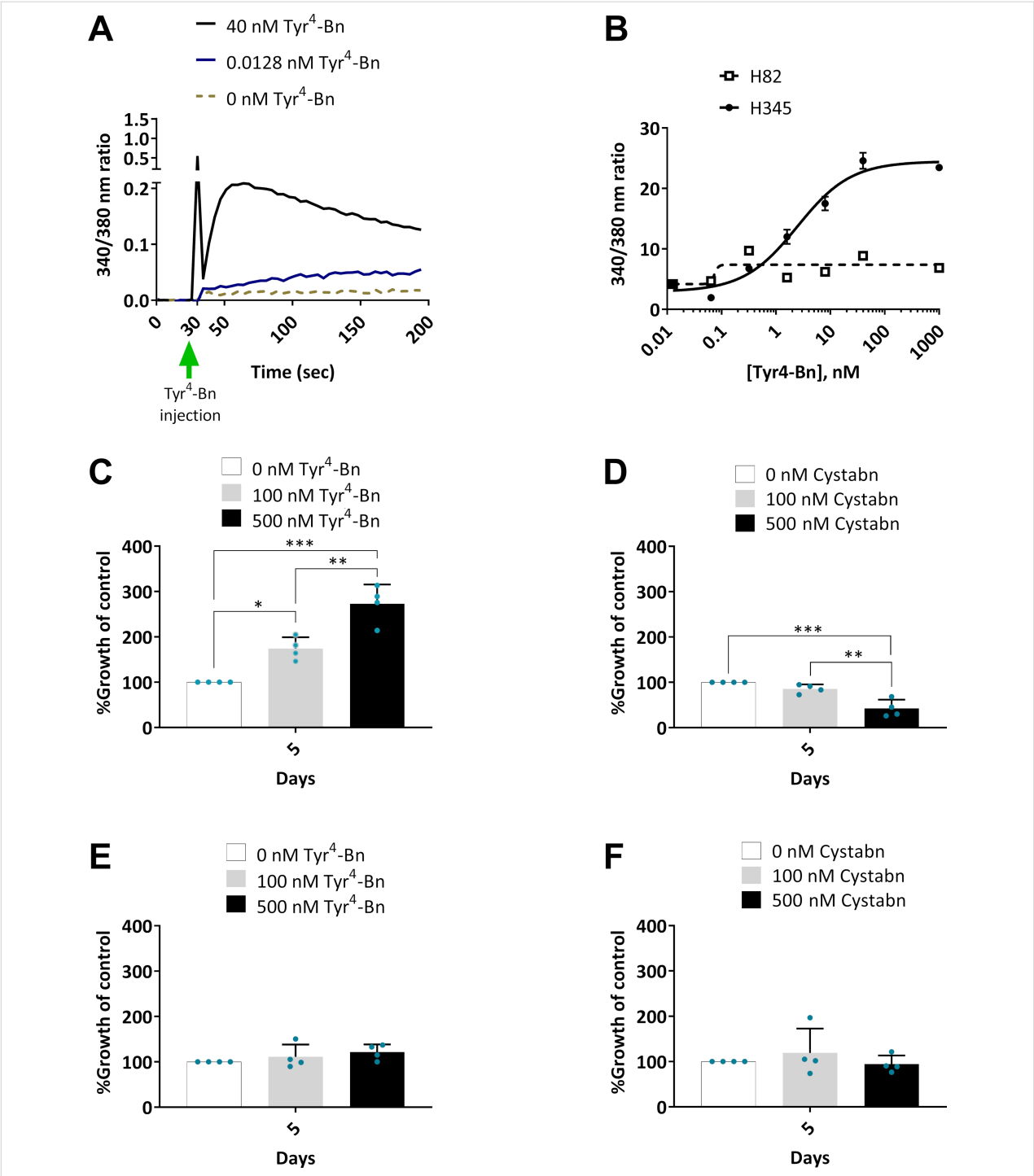

Figure 1: GRPR functionality in lung cancer cells. (A) Exemplar fluorescence trace from H345 cells loaded with Ca^{2+} reporter dye, Fura-2 AM before injection of GRPR agonist, Tyr^4-Bn. Baseline fluorescence was monitored for 30 s before peptide injection. (B) Escalating concentrations of Tyr^4-Bn were injected into H345 or H82 cells and the Fura-2 AM fluorescence emission monitored over 200 s. Peak Fura-2 ratios at 340/380 nm were plotted against agonist concentration. Data are mean ± SD. H345 cells were cultured over 5 days in selenite-insulin-transferrin (SIT) serum-free medium in the presence of escalating concentrations of Tyr^4-Bn (C) or cystabn (D) before cell growth quantification by MTS assay. Similarly, (E, F) show MTS growth data for H82 cells in the presence of Tyr^4-Bn (E) or cystabn (F). Error bars are SD.

ously reported [17,18]. The physiological role of GRPR includes the stimulation of a mitogenic response after receptor internalisation [19]. SCLC growth as a result of stimulation by nanoparticle targeting ligands is highly undesirable. We therefore sought to explore the use of GRPR antagonist peptides on the liposomal carriers. Here, we exploited a peptide derived

from the work of Mansi et al. who showed that the radiolabelled antagonist peptide, ^{111}In-DO3A-CH_2CO-G-aminobenzoyl-D-Phe-Q-W-A-V-G-H-Sta-Leu-NH_2 increased by 3.5-fold the relative tumour accumulation of radiolabel compared to the agonist peptide, ^{111}In-DO3A-CH_2CO-G-aminobenzoyl-Q-W-A-V-G-H-L-M-NH_2 [20,21]. This report reinforced the concept that the use of GRPR antagonist peptides was strongly preferable to the use of agonist peptides which have the potential to fuel tumour growth. The use of antagonists in preference to agonists is not, however, accepted by all. Different groups, using different agonist/antagonist peptide pairs as well as different imaging probes and visualisation approaches, have reached different conclusions about which approach should be used [22,23]. Based upon preferable in vitro and in vivo properties reported by others we based our work on the statine (Sta)-based antagonist peptide, D-Phe-Gln-Trp-Ala-Val-Gly-His-Sta-Leu-NH_2.

The published peptide structure was modified to bear an N terminal L-cysteine residue, which enables subsequent attachment to a functionalised lipid carrier. The peptide, hereafter termed cystabn, was prepared by fluorenylmethoxycarbonyl (Fmoc) solid-phase peptide synthesis and characterised by HPLC and mass spectrometry (data not shown). To confirm the persistent functionality of the peptide after cysteine addition, NCI-H345 cells were exposed to escalating concentration of Tyr^4-Bn and cystabn in serum-free conditions. As expected, Tyr^4-Bn resulted in a scalable increase ($p < 0.05$) in cell number as judged by MTS assay (Figure 1c). In contrast, exposure to cystabn, reduced cell proliferation over a 5 day period (Figure 1d), thus confirming that the addition of an N terminal cysteine did not interfere with GRPR binding. Exposure of NCI-H82 cells to the Tyr^4-Bn agonist (Figure 1e) and cystabn antagonist peptide (Figure 1f) caused no change in cell growth.

These cell proliferation studies were performed in serum-free conditions in line with previous studies [24,25] for two principle reasons. Firstly, the removal of serum from the culture medium depletes bovine bombesin-like peptides that could otherwise stimulate cell growth. Secondly, the presence of serum proteases could rapidly reduce the integrity of the peptides, as demonstrated for other bombesin-related peptides that displayed mouse and human serum half-lives measured in the tens of hours [26]. The specificity of Tyr^4-Bn and cystabn activity was confirmed in GRPR depleted NCI-H82 cells. In contrast to results from NCI-H345 cells, the addition of Tyr^4-Bn to NCI-H82 caused no noticeable increase in cell proliferation and cystabn effected no reduction in proliferation. This demonstrated that cystabn functionally targeted GRPR expressing cells in a specific manner – a key feature of a targeting ligand to enable high tumour localisation.

Formulation of a GRP-targeted liposomal carrier

Having validated GRPR as a functional target on the surface of SCLC cells we next prepared a targeted liposomal carrier. The presence of a single thiol group in the cystabn peptide affords facile functionalisation of DSPE-PEG_{2000}-maleimide thorough thiol coupling chemistry. Successful conjugation of the peptide was confirmed by MALDI–TOF mass spectrometry (Figure 2a,b). The most abundant mass peak of DSPE-PEG_{2000}-cystabn (calculated mass: 4137.41 Da, assuming perfect monodispersity of the PEG_{2000} group) was observed at 4188 Da (Figure 2a) and was separated from surrounding peaks by 44 Da, which represents the mass of a single ethylene glycol unit (Figure 2b).

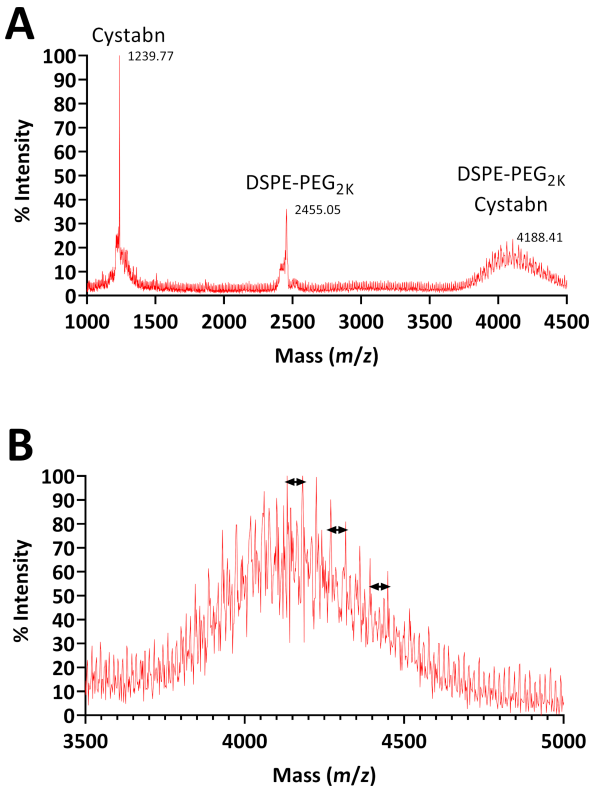

Figure 2: Mass spectrometry characterisation of cystabn-lipid conjugate. MALDI–TOF mass spectra of crude DSPE-PEG_{2000}-cystabn conjugate (A) and purified, post-dialysis, DSPE-PEG_{2000}-cystabn conjugate (B).

Liposomal formulations were developed to incorporate DSPE-PEG_{2000}-cystabn or control DOPE-PEG_{2000} (see below Table 2, in section Materials). Liposomes without targeting cystabn peptide (control-lipo) contained 5 mol % DOPE-PEG_{2000}, whereas targeted formulations (target-lipo) were loaded with 3 mol % of targeting DSPE-PEG_{2000}-cystabn conjugate with the total mass of PEG-lipid made up to 5% with

DOPE-PEG$_{2000}$. The formulations were prepared using the thin-film technique to yield small and monodisperse vesicles as judged by dynamic light scattering (DLS) analysis (Table 1).

Table 1: Colloidal properties of control- and target-lipo formulations.[a]

	control-lipo	target-lipo (3 mol % cystabn conjugate)
Z-Ave (d.nm)	101 ± 2.1	90 ± 0.6
PDI	0.058 ± 0.007	0.050 ± 0.020
zeta potential (mV)	−1.64 ± 2.13	−2.15 ± 0.2

[a]Data shown are mean ± SD, n = 3 independent experiments.

The colloidal properties of both liposomal formulations were highly similar in terms of size, polydispersity and zeta potential and consistent with those reported for other pegylated liposomes by others [27]. The vesicles were colloidally stable in PBS over 72 h at temperatures of 4, 25 and 37 °C with no significant changes in size, PDI or zeta potential observed (Figure 3a,b). It was noted that the diameter of both liposome formulations was larger than the 50 nm pore diameter of the terminal extrusion membrane. This is likely due to the deformation of the vesicles under pressure during extrusion and subsequent expansion after emergence from the pore.

Commercial realisation of targeted nanomedicines is contingent upon the development of platforms that are sufficiently resistant to aggregation in body fluids such as blood. The stability of control and targeted liposomes was examined after exposure to 10% heat-inactivated FBS for 24 or 72 h at different temperatures (Figure 3c,d). There were noticeable increased in liposome size and PDI as a function of both incubation time and temperature. For example, the control-lipo vesicles increased to 125 nm diameter after 24 or 72 h incubation at 37 °C. We noted a transition from a unimodal size distribution of liposomes in PBS buffer to a multimodal size distribution after extended incubation with 10% FBS. This caused sharp increases in the PDI of both formulations with increases in size and polydispersity (PDI) being greater for the target-lipo vesicles.

The emergence of particle populations with different sizes is not unexpected considering that FBS represents a complex, concentrated cocktail of polydisperse proteins of different sizes [27]. Indeed, the surface properties of various nanoparticles have been shown to change dramatically in the presence of plasma or serum [28] with the establishment of an adsorbed protein corona around the nanoparticle. It is now widely accepted that the particle protein corona presents a new biomolecular interface that underpins the dynamic interactions of nanosystems and their biological targets. The presentation of a high affinity GRPR antagonist peptide on the liposomal surface is expected to maintain liposomal cell-binding affinity by virtue of its high affinity for the receptor. Although, steric blockade of the targeting motif is possible due to the dynamic exchange events association with the evolution of the hard and soft corona, even on pegylated liposomes.

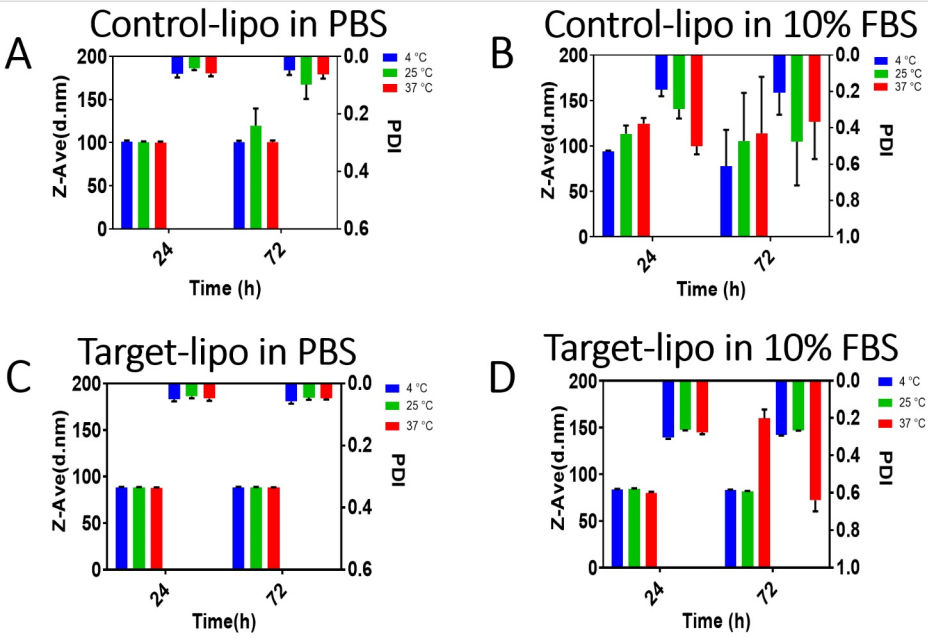

Figure 3: Colloidal stability of liposomes. Control and target liposomes were exposed to PBS (A,C) or 10% FBS in PBS (B,D) at three temperatures for 24/72 h then analysed by DLS. Data shown are mean ± SD, n = 3.

Cell binding and uptake of GRPR-targeted liposomes

The targeting capacity of cystabn-decorated liposomes was examined using two different approaches. To examine this, we exploited a GRPR overexpression construct transfected into the widely used, adherent non-SCLC cell line A549. This model grows more rapidly than SCLC cells and its adherent phenotype allows for easier manipulation. First, quantification of cell-uptake was judged by flow cytometry analysis of A549-GRPR cells exposed to fluorescently tagged target-lipo (FL-Target-lipo) or tagged control-lipo (FL-Control-lipo) formulations. Preliminary studies using FL-Target-lipo including 1 mol % targeting lipid showed marginal increases in relative cellular accumulation (data not shown). To overcome this, the density of targeting lipid was increased to 3 mol %. To examine for active internalisation and intracellular accumulation of liposomes at the endocytosis permissive temperature of 37 °C, we subtracted the median fluorescence intensity (MFI) attributable to cell-surface adsorption of liposomes at 4 °C, to yield a "normalised cell MFI" at each time point and for each formulation.

For non-targeted FL-Control-lipo, there was a modest increase in normalised fluorescence over time (blue bars, Figure 4a). In contrast, the fluorescence of FL-Target-lipo increased over time (red bars, Figure 4a). Drawing comparison between the control and targeted liposome groups, it was clear to see that at 15 min, fluorescence was no greater in cells treated with FL-Target-lipo compared to FL-Control-lipo. However, at 60 min and beyond cell fluorescence was greater ($p < 0.05$) in cells treated with target-lipo.

We next confirmed the flow cytometric results using fluorescence microscopy. Following 5 min exposure to either control (Figure 4b) or target-liposomes (Figure 4c), A549-GRPR cells displayed greater cellular fluorescence signals in the FL-Target-lipo group. Cells exposed to FL-Control-lipo displayed a diffuse cell membrane-like staining with few green fluorescent puncta. Whereas, the target-lipo exposed cells displayed many more fluorescent puncta as well as a widespread increase in cellular fluorescence. Our observations here indicate that GRPR targeting with cystabn peptide increases cell uptake of liposomes, most likely through receptor-mediated uptake.

Taken together the flow cytometry and microscopy data demonstrate that, using a fluorescently labelled model liposomal carrier, the relative increase in cell uptake afforded by cystabn functionalisation is modest but significant. To put our data into context, approximately two-fold enhanced delivery of an oligonucleotide-bombesin [3,7-14] conjugate was observed by Ming et al. [29]. Using a similar approach to ours, Accardo et al.

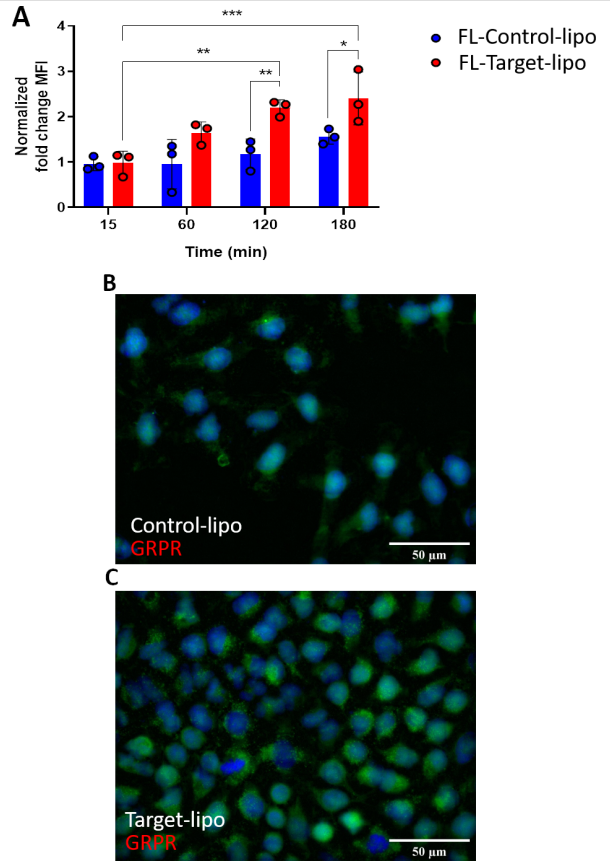

Figure 4: GRPR targeting with cystabn increases cell accumulation of liposomes. (A) A549-GRPR cells were exposed to 1 µg/mL of control or target liposomes for 15–180 min before washing and analysis of liposomal 1,2-dihexadecanoyl-*sn*-glycero-3-phosphoethanolamine (DHPE)-fluorescein intensity by flow cytometry. Fold-change median fluorescence intensity (MFI) was determined by correcting for the background MFI from cells exposed for matched time periods on ice. Data shown are mean ± SD, $n = 3$. A549-GRPR cells were exposed to 1 µg/mL of control (B) or target (C) liposomes (green) for 5 min, washed, fixed and nuclei labelled with Hoechst (blue).

studied liposomal delivery of doxorubicin into PC-3 prostate cells using a modified bombesin targeting peptide [30]. The authors showed a reduction in mouse PC-3 xenograft size compared to non-targeted doxorubicin liposomes and saline control, consistent with tumour accumulation of the delivery system. In summary, an increase in SCLC cellular accumulation of a liposomal drug cargo would be beneficial for therapy, especially considering the chemotherapeutic resistance profile that is often displayed by clinical SCLC [31].

Future studies on cystabn-targeted liposomal carriers will examine the uptake and trafficking of these nanocarriers, particularly with regards to their efficiency of carrying chemotherapeutic agents into the cell. Poor intracellular accumulation of nanocarriers can be improved through targeted and triggered drug release, for example through the incorporation of temperature-sensitive [32] or light-sensitive lipids [33]. These approaches

have shown promise in enhancing the cellular/tumoural accumulation of chemotherapeutic agents in various models [34,35].

In spite of the enhanced cellular delivery shown here, the application of GRPR targeting nanosized delivery systems to different cancers should be considered carefully due to variability in GRPR expression across malignant diseases. Published reports, using techniques such as reverse-transcriptase polymerase chain reaction (RT-PCR) and immunostaining, have shown that between 63–100% of prostate tumours are GRPR positive, while SCLC tumours are more heterogeneous, with 29–85% of tumours expressing GRPR [36]. This demonstrates that GRPR expression is not a universal marker of SCLC or any other tumour and that future development of GRPR-targeted therapeutics would require patient stratification according to the expression status.

Conclusion

This report demonstrates that the functionalisation of liposomes with a GRPR antagonist peptide is sufficient to promote the accumulation of liposomes within GRPR expressing cells such as SCLC. Increased internalisation of drug-loaded GRPR targeted liposomes in treatment-resistant tumours such as SCLC could offer improved therapeutic outcomes.

Experimental

Materials

Fmoc-protected amino acids, piperazine, HCTU, HOBt, DMF were all from AGTC (Hessle, UK). Rink Amide MBHA resin was from Novabiochem (UK). HPLC solvents and all cell culture media were from Sigma-Aldrich (Poole, UK). Lipids were from Avanti Polar Lipids (USA). Sources of other exceptional items are mentioned in the text.

Calcium release assay

NCI-H345 and NCI-H82 cells were loaded with 2 μM Fura-2AM (Thermo Fisher, UK) in Hank's Balanced Salt Solution (HBSS) loading buffer containing sulfinpyrazone at 37 °C for 40–60 minutes. Following loading, the buffer was replaced with HBSS and allowed to warm to 37 °C in a Flexstation 3 microplate reader (Molecular Devices). Fluorescence of Fura-2 was recorded using dual excitation (340 and 380 nm) and emission 520 nm. Agonist was automatically injected using the Flexstation compound plate and tips at a specific time point. PMT settings were medium and 3 reads performed per well. Data is represented as 340/380 ratio using zero baseline for normalisation.

Cell proliferation assay

The proliferation of NCI-H345 and NCI-H82 cells in the presence or absence of Tyr^4-Bn and cystabn was studied in selenium–insulin–transferrin (SIT) medium comprising 30 nM sodium selenite, 5 μg/mL human insulin, 10 μg/mL human transferrin and 2 mM L-glutamine in RPMI-1640 media. The cells were seeded in 96 well plates overnight at a density of 30,000 cells per well. The cells were then treated with 100 or 500 nM Tyr^4-Bn or cystabn and for 5 days with peptide replenishment at day 3. Cell proliferation was determined using the CellTiter 96® AQueous One assay (Promega).

Peptide synthesis

Cystabn (Cys-D-Phe-Gln-Trp-Ala-Val-Gly-His-Sta-Leu-NH_2) was synthesized on the Rink Amide MBHA resin using Fmoc chemistry. After initial deprotection of the resin with 2 × 5 min 5% piperazine in DMF, each coupling step involved addition to 1 equiv of resin, Fmoc-protected amino acid, HCTU, HOBt and DIPEA (4:4:4:8 equiv) in 1.5 mL DMF. The mixture was incubated for 30 min at RT with occasional gentle agitation then washed with DMF (×3). This process was repeated to increase the peptide yield. Successful Fmoc removal and coupling of amino acids was confirmed with the Kaiser test. After successful coupling and Fmoc deprotection of the N-terminal amino acid, the resin was washed with DMF (3 × 5 mL, 1 min), then DCM (3 × 5 mL, 5 min) and the resin dried under nitrogen then stored in vacuo for 3–5 h. Simultaneous side chain deprotection and peptide cleavage from the resin was achieved using TFA/TIPS/EDT/H_2O (94:2:2:2), performed at RT for 4 h. The peptide was precipitated in diethyl ether overnight at −20 °C. Precipitated peptide was harvested by centrifugation (3000 rpm, 10 min, 4 °C). Peptide precipitate was washed (×3 cold diethyl ether) then dissolved in 10% aqueous acetic acid and lyophilised to yield a white powder.

Peptide-PEG-lipid conjugate synthesis

One equivalent of DSPE-PEG_{2000}-maleimide (6.8 μmol in 4 mL chloroform) was added to two equivalents of cystabn (13.3 μmol in 2 mL methanol) and stirred for 24 h at RT under nitrogen gas. After confirmation of successful conjugation by MALDI–TOF mass spectrometry analysis the solvent was evaporated and the reaction mixture re-dissolved in milli-Q water. Unreacted peptide was removed by dialysis against milli-Q water at RT for three days (the water changed every 2 h then left overnight) using 2 kDa cut-off benzoylated dialysis tubing (SpectroPor, Spectrum Labs, New Brunswick, USA). The purified conjugate was lyophilised to a dry white powder.

Characterisation of peptides and conjugates

HPLC

Samples were analysed using a gradient elution method using mobile phase A (H_2O + 0.1% TFA) and B solution (acetonitrile + 0.1% TFA) on a Perkin Elmer HPLC system comprising of binary solvent pump, autosampler, UV–vis detector and Peltier

column oven. Mobile phases were membrane degassed using Millipore vacuum filtration with a 0.2 μm filter. The gradient profile was 0–5 min 5% B, 5–25 min 5–95% B and 5 min 5% B. Peptide samples (≈1 mg/mL in milli-Q water) were eluted on a Phenomenex Luna® C18 (2) LC Column (5 μm, 100 Å, 150 × 4.6 mm, Phenomenex, UK). Conjugate analysis was performed on a Hypersil™ BDS C8 LC Column (3 μm, 130 Å, 150 × 4.6 m, Thermo Scientific, UK). Samples of 10 μL were injected and elution monitored at 280 nm.

MALDI–TOF

Peptide samples (2 mg/mL in 1:1 acetonitrile: milli-Q water + 0.1% TFA) were mixed with an equal volume of a saturated solution of α-cyanohydroxycinnamic acid (Sigma) and 1 μL spotted twice onto the same well of a clean MALDI sample plate. Peptide-PEG_{2000}-lipid conjugates were dissolved in chloroform at 2 mg/mL and a 1:1 mixture prepared with saturated methanolic solution of universal MALDI matrix (Sigma-Aldrich, UK). Samples were analysed using linear ion detection mode on a SHIMADZU Axima-CFR MALDI–TOF.

Liposomal formulation

Lipids for each liposomal formulation were dissolved in chloroform and mixed in a round-bottomed flask (see Table 2, below). The concentration of lipid-PEG-peptide conjugate solutions in chloroform were determined by UV spectroscopy using the molar extinction coefficient for the peptide tryptophan residue (5560 AU/mmol/mL). A thin film was produced by slow evaporation of the solvent under vacuum followed by one hour under high vacuum to remove solvent traces. The film was hydrated with PBS to a final lipid concentration of 10 mg/mL then heated to 55 °C and vortexed extensively to produce MLVs. Five cycles of freeze-thawing (dry ice-acetone followed by heating to 55 °C) were performed to produce reduce the lamellarity of the vesicles. Finally, lipid suspensions were extruded (21×) through polycarbonate membranes of 200 nm, 100 nm and 50 nm pore sizes to produce a narrow size distribution of LUVs.

Characterization of liposomal formulations

Liposomes were characterized for size and zeta potential using Zetasizer Nano ZS. For size measurements the liposomal suspension was diluted 1:10 with PBS. For zeta potential measurements, the liposomal suspension was diluted 1:10 with PBS and transferred to a clean folded capillary cell (Malvern, DTS1070).

Liposomal stability in PBS and 10% serum

An aliquot of the liposomal suspension was diluted 1:10 with either PBS or 10% FBS in PBS and transferred to individual microcentrifuge tubes. Samples were incubated at 4, 25 or 37 °C. After 0, 24 and 72 hours the samples were transferred to cuvettes and measured for size and PDI as described above.

Table 2: Formulation components of liposomes reported in this study.

formulation name	components
control-lipo	DOPC/cholesterol/DOPE-PEG2000 (57:38:5 mol %)
target-lipo	DOPC/cholesterol/DOPE-PEG2000/DSPE-PEG2000-cystabn (57:38:2:3 mol %)
FL-Control-lipo	DOPC/cholesterol/DOPE-PEG2000/DHPE-fluorescein (56:38:5:1 mol %)
FL-Target-lipo	DOPC/cholesterol/DOPE-PEG2000/DSPE-PEG2000-cystabn/DHPE-fluorescein (56:38:2:3:1 mol %)

Cell culture and transfection

The adherent, non-small cell cancer cell line A549 was stably transfected with a plasmid encoding HA epitope-tagged human GRP receptor (3xHA-GRPR pcDNA3.1+ plasmid #GRPR00TN00, UMR cDNA Resource Center, USA) using FuGene 6 and selected using 750 μg/mL G418 over three weeks. Cells were subsequently maintained in 100 μg/mL G418.

Flow cytometry

A549-GRPR cells were washed with warm PBS and blocked for 5 h in 0.2% BSA in RPMI-1640 medium. The cells were dissociated using Versene and aliquoted at a concentration of 10^6 cells per mL in phenol-red free SFM. The samples were incubated at 37 or 4 °C for 5 min before treating with Control-lipo or Target-lipo (1 μg/mL total lipids concentration) for 15–180 min. After incubation at 37 °C, cells were transferred onto ice and washed using 500 μL phenol red-free SFM. Samples were analysed on a Beckman Coulter CytoFlex flow cytometer using exited using 488 nm laser and the emitted wavelength acquired using 585/42 bandpass filter. After doublet exclusion, 10^4 events/sample were acquired in the gated population, and analysed using CytExpert software (v2.3, Beckman Coulter, USA).

Fluorescence microscopy

Cells were seeded onto 16 mm coverslips, and incubated for 24 h. Cells were washed (×3) with PBS for 5 min at RT and treated with 1 μg/mL (total lipid) of fluorescein-labelled control or target liposomes for 5 min at 37 °C. Coverslips were washed (×3) with PBS, fixed with 4% PFA (10 min at RT) and residual PFA quenched by 50 mM NH_4Cl (15 min, RT). The cells washed with PBS (×3) for 5 min, permeabilised with 0.2% Triton X-100 (10 min). Nuclei were stained with Hoechst

33258, 1 µg/mL in PBST) then mounted on glass slides using Prolong Gold mounting medium (Invitrogen). The cells were viewed under a widefield microscope (Zeiss AxioPlan 2ie) and images taken using Axiovision software and analysed using Fiji software.

Acknowledgements

We are grateful to Prof Francesca Baldelli for valuable advice during the project.

Funding

We are also grateful for Imam Abdulrahman bin Faisal University for its financial sponsorship of this work represented by Saudi Arabian Cultural Bureau in London.

ORCID® iDs

Pâmela C. Lukasewicz Ferreira - https://orcid.org/0000-0003-2134-9829
Christopher J. Morris - https://orcid.org/0000-0002-7703-4474

References

1. American Cancer Society. Key Statistics for Lung Cancer. 2019; https://www.cancer.org/cancer/lung-cancer/about/key-statistics.html.
2. Action on Smoking and Health. ASH Fact sheet: Tobacco and the Developing World. 2019; https://ash.org.uk/wp-content/uploads/2019/07/ASH-Factsheet_Developing-World_v3.pdf (accessed Dec 11, 2019).
3. Moody, T. W.; Korman, L. Y. *Ann. N. Y. Acad. Sci.* **1988,** *547,* 351–359. doi:10.1111/j.1749-6632.1988.tb23902.x
4. Moody, T. W.; Carney, D. N.; Cuttitta, F.; Quattrocchi, K.; Minna, J. D. *Life Sci.* **1985,** *37,* 105–113. doi:10.1016/0024-3205(85)90413-8
5. Moody, T. W.; Murphy, A.; Mahmoud, S.; Fiskum, G. *Biochem. Biophys. Res. Commun.* **1987,** *147,* 189–195. doi:10.1016/s0006-291x(87)80105-5
6. Bepler, G.; Zeymer, U.; Mahmoud, S.; Fiskum, G.; Palaszynski, E.; Rotsch, M.; Willey, J.; Koros, A.; Cuttitta, F.; Moody, T. W. *Peptides* **1988,** *9,* 1367–1372. doi:10.1016/0196-9781(88)90204-5
7. Chanda, N.; Kattumuri, V.; Shukla, R.; Zambre, A.; Katti, K.; Upendran, A.; Kulkarni, R. R.; Kan, P.; Fent, G. M.; Casteel, S. W.; Smith, C. J.; Boote, E.; Robertson, J. D.; Cutler, C.; Lever, J. R.; Katti, K. V.; Kannan, R. *Proc. Natl. Acad. Sci. U. S. A.* **2010,** *107,* 8760–8765. doi:10.1073/pnas.1002143107
8. Santos-Cuevas, C. L.; Ferro-Flores, G.; Arteaga de Murphy, C.; Pichardo-Romero, P. A. *Nucl. Med. Commun.* **2008,** *29,* 741–747. doi:10.1097/mnm.0b013e3282ffb45c
9. Mansi, R.; Minamimoto, R.; Macke, H.; Iagaru, A. H. *J. Nucl. Med.* **2016,** *57* (Suppl. 3), 67S–72S. doi:10.2967/jnumed.115.170977
10. Zhang, J.; Li, D.; Lang, L.; Zhu, Z.; Wang, L.; Wu, P.; Niu, G.; Li, F.; Chen, X. *J. Nucl. Med.* **2016,** *57,* 9–14. doi:10.2967/jnumed.115.165316
11. Cescato, R.; Maina, T.; Nock, B.; Nikolopoulou, A.; Charalambidis, D.; Piccand, V.; Reubi, J. C. *J. Nucl. Med.* **2008,** *49,* 318–326. doi:10.2967/jnumed.107.045054
12. Shi, J.; Kantoff, P. W.; Wooster, R.; Farokhzad, O. C. *Nat. Rev. Cancer* **2017,** *17,* 20–37. doi:10.1038/nrc.2016.108
13. Stathopoulos, G. P.; Antoniou, D.; Dimitroulis, J.; Michalopoulou, P.; Bastas, A.; Marosis, K.; Stathopoulos, J.; Provata, A.; Yiamboudakis, P.; Veldekis, D.; Lolis, N.; Georgatou, N.; Toubis, M.; Pappas, C.; Tsoukalas, G. *Ann. Oncol.* **2010,** *21,* 2227–2232. doi:10.1093/annonc/mdq234
14. MM-302 Plus Trastuzumab vs. Chemotherapy of Physician's Choice Plus Trastuzumab in HER2-Positive Locally Advanced/Metastatic Breast Cancer Patients (HERMIONE). Merrimack Pharmaceuticals, 2014; https://ClinicalTrials.gov/show/NCT02213744.
15. Safety Study of CALAA-01 to Treat Solid Tumor Cancers. Calando Pharmaceuticals, 2008; https://ClinicalTrials.gov/show/NCT00689065.
16. A Phase 2 Study to Determine the Safety and Efficacy of BIND-014 (Docetaxel Nanoparticles for Injectable Suspension) as Second-line Therapy to Patients With Non-Small Cell Lung Cancer. BIND Therapeutics, 2013; https://ClinicalTrials.gov/show/NCT01792479.
17. Yang, H.-K.; Scott, F. M.; Trepel, J. B.; Battey, J. F.; Johnson, B. E.; Kelley, M. J. *Lung Cancer* **1998,** *21,* 165–175. doi:10.1016/s0169-5002(98)00054-3
18. Moreno, P.; Mantey, S. A.; Lee, S. H.; Ramos-Álvarez, I.; Moody, T. W.; Jensen, R. T. *Peptides* **2018,** *101,* 213–226. doi:10.1016/j.peptides.2018.01.016
19. Jensen, R. T.; Battey, J. F.; Spindel, E. R.; Benya, R. V. *Pharmacol. Rev.* **2008,** *60,* 1–42. doi:10.1124/pr.107.07108
20. Mansi, R.; Wang, X.; Forrer, F.; Kneifel, S.; Tamma, M.-L.; Waser, B.; Cescato, R.; Reubi, J. C.; Maecke, H. R. *Clin. Cancer Res.* **2009,** *15,* 5240–5249. doi:10.1158/1078-0432.ccr-08-3145
21. Mansi, R.; Abiraj, K.; Wang, X.; Tamma, M. L.; Gourni, E.; Cescato, R.; Berndt, S.; Reubi, J. C.; Maecke, H. R. *J. Med. Chem.* **2015,** *58,* 682–691. doi:10.1021/jm5012066
22. Nanda, P. K.; Wienhoff, B. E.; Rold, T. L.; Sieckman, G. L.; Szczodroski, A. F.; Hoffman, T. J.; Rogers, B. E.; Smith, C. J. *In Vivo* **2012,** *26,* 583–592.
23. Yang, M.; Gao, H.; Zhou, Y.; Ma, Y.; Quan, Q.; Lang, L.; Chen, K.; Niu, G.; Yan, Y.; Chen, X. *Theranostics* **2011,** *1,* 220–229. doi:10.7150/thno/v01p0220
24. Moody, T. W.; Berna, M. J.; Mantey, S.; Sancho, V.; Ridnour, L.; Wink, D. A.; Chan, D.; Giaccone, G.; Jensen, R. T. *Eur. J. Pharmacol.* **2010,** *637,* 38–45. doi:10.1016/j.ejphar.2010.03.057
25. Moody, T. W.; Tashakkori, N.; Mantey, S. A.; Moreno, P.; Ramos-Alvarez, I.; Leopoldo, M.; Jensen, R. T. *Front. Endocrinol.* **2017,** *8,* 176. doi:10.3389/fendo.2017.00176
26. Lantry, L. E.; Cappelletti, E.; Maddalena, M. E.; Fox, J. S.; Feng, W.; Chen, J.; Thomas, R.; Eaton, S. M.; Bogdan, N. J.; Arunachalam, T.; Reubi, J. C.; Raju, N.; Metcalfe, E. C.; Lattuada, L.; Linder, K. E.; Swenson, R. E.; Tweedle, M. F.; Nunn, A. D. *J. Nucl. Med.* **2006,** *47,* 1144–1152.
27. Palchetti, S.; Colapicchioni, V.; Digiacomo, L.; Caracciolo, G.; Pozzi, D.; Capriotti, A. L.; La Barbera, G.; Laganà, A. *Biochim. Biophys. Acta, Biomembr.* **2016,** *1858,* 189–196. doi:10.1016/j.bbamem.2015.11.012
28. Monopoli, M. P.; Åberg, C.; Salvati, A.; Dawson, K. A. *Nat. Nanotechnol.* **2012,** *7,* 779–786. doi:10.1038/nnano.2012.207
29. Ming, X.; Alam, M. R.; Fisher, M.; Yan, Y.; Chen, X.; Juliano, R. L. *Nucleic Acids Res.* **2010,** *38,* 6567–6576. doi:10.1093/nar/gkq534
30. Accardo, A.; Mansi, R.; Salzano, G.; Morisco, A.; Aurilio, M.; Parisi, A.; Maione, F.; Cicala, C.; Ziaco, B.; Tesauro, D.; Aloj, L.; De Rosa, G.; Morelli, G. *J. Drug Targeting* **2013,** *21,* 240–249. doi:10.3109/1061186x.2012.741138

31. Sabari, J. K.; Lok, B. H.; Laird, J. H.; Poirier, J. T.; Rudin, C. M. *Nat. Rev. Clin. Oncol.* **2017,** *14,* 549–561. doi:10.1038/nrclinonc.2017.71
32. Dou, Y.; Hynynen, K.; Allen, C. *J. Controlled Release* **2017,** *249,* 63–73. doi:10.1016/j.jconrel.2017.01.025
33. Lou, J.; Zhang, X.; Best, M. D. *Chem. – Eur. J.* **2019,** *25,* 20–25. doi:10.1002/chem.201803389
34. Weinstein, J.; Magin, R.; Yatvin, M.; Zaharko, D. *Science* **1979,** *204,* 188–191. doi:10.1126/science.432641
35. Allen, T. M.; Cullis, P. R. *Adv. Drug Delivery Rev.* **2013,** *65,* 36–48. doi:10.1016/j.addr.2012.09.037
36. Patel, O.; Shulkes, A.; Baldwin, G. S. *Biochim. Biophys. Acta, Rev. Cancer* **2006,** *1766,* 23–41. doi:10.1016/j.bbcan.2006.01.003

License and Terms

BEILSTEIN JOURNAL OF NANOTECHNOLOGY

Fully amino acid-based hydrogel as potential scaffold for cell culturing and drug delivery

Dávid Juriga[1], Evelin Sipos[1], Orsolya Hegedűs[2], Gábor Varga[2], Miklós Zrínyi[1], Krisztina S. Nagy[*1,2] and Angéla Jedlovszky-Hajdú[*1]

Full Research Paper

Open Access

Address:
[1]Laboratory of Nanochemistry, Department of Biophysics and Radiation Biology, Semmelweis University, Nagyvarad square 4, Budapest, Hungary and [2]Department of Oral Biology, Semmelweis University, Nagyvarad square 4, Budapest, Hungary

Email:
Krisztina S. Nagy[*] - s.nagykriszti@gmail.com;
Angéla Jedlovszky-Hajdú[*] - hajdu.angela@med.semmelweis-univ.hu

* Corresponding author

Keywords:
biocompatibility; cystamine; hydrogel; lysine; poly(amino acid); poly(aspartic acid); polymer

Beilstein J. Nanotechnol. **2019,** *10,* 2579–2593.
doi:10.3762/bjnano.10.249

Received: 30 August 2019
Accepted: 10 December 2019
Published: 27 December 2019

This article is part of the thematic issue "Engineered nanomedicines for advanced therapies".

Guest Editor: F. Baldelli Bombelli

Abstract

Polymer hydrogels are ideal scaffolds for both tissue engineering and drug delivery. A great advantage of poly(amino acid)-based hydrogels is their high similarity to natural proteins. However, their expensive and complicated synthesis often limits their application. The use of poly(aspartic acid) (PASP) seems an appropriate solution for this problem due to the relatively cheap and simple synthesis of PASP. Using amino acids not only as building blocks in the polymer backbone but also as cross-linkers can improve the biocompatibility and the biodegradability of the hydrogel. In this paper, PASP cross-linked with cystamine (CYS) and lysine-methylester (LYS) was introduced as fully amino acid-based polymer hydrogel. Gels were synthesized employing six different ratios of CYS and LYS. The pH dependent swelling degree and the concentration of the elastically active chain were determined. After reduction of the disulfide bonds of CYS, the presence of thiol side groups was also detected. To determine the concentration of the reactive cross-linkers in the hydrogels, a new method based on the examination of the swelling behavior was established. Using metoprolol as a model drug, cell proliferation and drug release kinetics were studied at different LYS contents and in the presence of thiol groups. The optimal ratio of cross-linkers for the proliferation of periodontal ligament cells was found to be 60−80% LYS and 20−40% CYS. The reductive conditions resulted in an increased drug release due to the cleavage of disulfide bridges in the hydrogels. Consequently, these hydrogels provide new possibilities in the fields of both tissue engineering and controlled drug delivery.

Introduction

The number of medical applications of polymer hydrogels increased substantially during the last decades due to their similarity to soft tissues [1-3]. Polymer hydrogels possess properties of solid materials such as deformability and rigidity, but at the same time they are permeable for small molecules. One of the most beneficial properties of polymer hydrogels is that they are sensitive to alterations of the local environmental conditions, such as the pH value or temperature. Polymer hydrogels can change their swelling degree depending on the changing environmental conditions. Therefore, hydrogels can be used as drug delivery systems [4], implants [5,6], coatings [7,8] or scaffolds for tissue engineering [2,3,9,10]. Besides these stimuli-responsive properties, the chemical and physical structure, the mechanical properties [10] as well as biocompatibility and biodegradability are also fundamental features of polymers developed for numerous medical applications [11,12].

Polymer hydrogels are capable of releasing physically entrapped drug molecules. The release kinetics of the loaded drug molecules depend significantly on the swelling degree of the polymer matrix [13-16]. Recently, smart hydrogels showing strong and abrupt responses (changes in their swelling degree) to small changes of the environmental conditions have been the subject of extensive research [17-22].

The composition of the polymer backbone determines almost all of the properties of the hydrogels. For biological applications, in general, the polymer backbone and its degradation products have to be biodegradable and biocompatible [11,23]. In contrast to many synthetic polymers, the degradation products of poly(amino acid)s, which are mainly built from only one or two types of amino acids, are biocompatible nutrients. In addition, poly(amino acid)s have enormous structural diversity and they supposedly lack immunogenicity [24,25]. In summary, the use of poly(amino acid)s has practically only one disadvantage: their synthesis is usually complicated and expensive [3].

Recently, various types of polymer-based hydrogels have been developed for purposes of tissue engineering and regenerative medicine [26]. Most of these polymers try to mimic or recreate the natural environment of the cells, namely the extracellular matrix (ECM) [27]. Among them, synthetic, amino acid-based polymers attract particular attention due to their tunable properties and the structural similarity to the native ECM [26]. The poly(amino acid)s being tested for biomedical applicability can be classified into three groups: anionic, cationic and neutral poly(amino acid)s [28,29]. The effect of poly-L-lysine, which has a cationic character, on the cell behavior has been widely studied in the field of tissue engineering [30,31], while among the anionic poly(amino acid)s, poly(glutamic acid) is typically used for the development of hydrogel scaffolds [32]. Moreover, our research group demonstrated previously that hydrogels based on the anionic poly(aspartic acid) (PASP) are also well-suited for tissue engineering purposes [25].

Another field of potential biomedical applications of poly(amino acid)s is drug delivery. Poly(amino acid)-based microcarriers can improve the pharmacological and therapeutic properties of various drugs [28]. By applying such microcarriers, the drug release kinetics can be controlled. Among the anionic amino acids, glutamic acid was previously used for the preparation of polymer-based microcarriers [33]. However, there are only sporadic data available regarding PASP-based drug delivery systems [34-37].

Although the preparation of most types of poly(amino acid)s is expensive, the synthesis of PASP can be relatively cost-efficient, and it does not require extreme conditions, as we described previously [25,37-40]. In the last decades, the interest of scientists in PASP-based hydrogels increased significantly due to their potential applications in medical, pharmaceutical and environmental fields [25,34,41-44]. Several publications can be found concerning different types of cross-linkers to prepare PASP-based hydrogels [22,34,45]. However, the number of studies describing the use of pure amino acids or amino acid derivatives as cross-linkers is limited [22,46]. For hydrogels made of fully amino acid-based polymers, biodegradability as well as biocompatibility could be improved due to their specific chemical composition. In our previous publications, we presented the synthesis of PASP and several preparation methods of PASP-based hydrogels based on cross-linking with diaminobutane (DAB) and CYS in two-step reactions [21,22,25]. The chemical [22], swelling [13], mechanical and responsive properties [21] of these gels as well as their applicability as scaffolds for osteosarcoma cells (MG-63) [25] have been investigated. We showed that MG-63 cells can proliferate on PASP-based hydrogels [25], which led to the idea that similar fully amino acid-based gels may also support the growth of untransformed cells.

In the present study, derivatives based exclusively on amino acids, namely, on lysine-methylester (LYS) and CYS, were used as cross-linkers for preparing PASP-based hydrogels. CYS is biologically active and can provide free thiol groups under reductive conditions, while the advantage of LYS is that it can partially decrease the anionic character of aspartic acid. In addition, LYS also facilitates the electrostatic interaction between anionic plasma membrane sites and cationic polymer sites. Therefore, it supports cell adhesion and proliferation [47]. The swelling, mechanical and degradation properties of the gels

containing LYS and CYS at different ratios were investigated since these attributes are crucial for biomedical applications. The swelling degree was determined at different pH values and under redox conditions. For biocompatibility studies, cell viability tests were carried out using primary cultures of human periodontal ligament-derived cells (PDLCs) instead of the previously used tumor cell line. Periodontal ligament as a source of stem-like cells is easily accessible during surgical removal of wisdom teeth [48]. PDLCs hold great promise for application in the field of tissue engineering [49]. Cell viability was assessed using the WST-1 reagent [2-(4-iodophenyl)-3-(4-nitrophenyl)-5-(2,4-disulfophenyl)-2*H*-tetrazolium] (Roche, Switzerland), while the cell morphology was observed under a two-photon microscope. Moreover, the release kinetics of the model drug metoprolol were also examined under various environmental conditions.

Experimental

Materials

Following materials have been used in this study: L-aspartic acid (CAS: 56-84-8, Aldrich, ≥98%), orthophosphoric acid (CAS: 7664-38-2, Aldrich, ≥99%), dimethylformamide (CAS: 68-12-2, VWR, ≥99.9%) cystamine dihydrochloride (CAS: 56-17-7, Fluka, ≥98%), lysine methyl ester dihydrochloride (CAS: 26348-70-9, Bachem, 97%), dimethyl sulfoxide (CAS: 67-68-5, VWR, ≥99%), dibutylamine (CAS: 111-92-2, Aldrich, ≥99.5%), citric acid monohydrate (CAS: 5949-29-1, VWR, 100%, normapur), imidazole (CAS.288-32-4, Sigma-Aldrich, ≥99.5%, puriss), sodium chloride (CAS: 7647-14-5, Sigma-Aldrich, puriss), sodium hydroxide (CAS: 1310-73-2, Reanal, puriss), borax (CAS: 1303-96-4, Hungaropharma, ≥99.5%), disodium hydrogen phosphate (CAS: 7558-79-4, Sigma-Aldrich, ≥98%), trisodium phosphate (CAS: 10101-89-0, Sigma-Aldrich, ≥98%), phosphate-buffered saline (PBS) tablet (Sigma), DL-dithiothreitol (CAS: 3483-12-3, Sigma, ≥99%).

Synthesis of poly(succinimide)

Poly(succinimide) (PSI) was synthesized by thermal polycondensation of the mixture of L-aspartic acid and orthophosphoric acid. The mixture was loaded into a 1 L flask and inserted into a rotary evaporator (IKA). The temperature was increased to 180 °C while the pressure was decreased to 5 mbar. After 7 h, brown foam was gained, which was dissolved in dimethylformamide (DMF). Subsequently, the solution was precipitated, washed with distilled water and finally dried at 40 °C. Details of this method were published previously [25,37,38].

Simultaneous cross-linking of PSI by CYS and LYS

PSI was dissolved in dimethyl sulfoxide (DMSO) at a concentration of 25 wt % and mixed with the cross-linker solution, which contained cystamine dihydrochloride (CYS·2HCl) and lysine methyl ester dihydrochloride (LYS·2HCl) at different ratios in DMSO (Table 1). During cross-linking, the free primary amino groups of the cross-linkers react with the imide groups of the succinimide rings in a nucleophilic addition reaction (Figure 1, step 1). Dibutylamine (DBA) was added to the reaction mixture in order to adjust the pH value.

The mixture was loaded into glass frames in order to prepare gel films. After 24 h, the gelation occurred and every sample had a PSI content of 15 wt % at a theoretical degree of 20 cross-links. The degree of cross-links is defined as the molar ratio of monomers and cross-linking agents. The reaction of the gel formation is shown in Figure 1, step 1.

Six gel types were prepared with different ratio of the cross-linking agents (Table 1). The number in the name of the samples indicates the molar percentage of CYS of the total amount of cross-linking agents. For example, PSI-100CYS-LYS contains only CYS while in the case of PSI-0CYS-LYS, only LYS was used as cross-linking agent.

Preparation of PASP-based hydrogels

PASP-based hydrogels were formed by mild alkaline hydrolysis of the PSI gels. The gels were immersed into an imidazole-based buffer (pH 8, concentration c = 0.1 M, ionic strength I = 0.25 M). The buffer was changed daily for four days. The reaction is depicted in Figure 1, step 2.

Table 1: The applied amounts of the various components during the gel synthesis.

Gel sample	PSI solution (mg)	CYS·2HCl (mg)	LYS·2HCl (mg)	DMSO (µL)	DBA (µL)
PSI-100CYS-LYS	600	17.4	0.0	325.5	26.1
PSI-80CYS-LYS	600	13.9	3.6	325.4	26.1
PSI-60CYS-LYS	600	10.4	7.2	325.3	26.1
PSI-40CYS-LYS	600	7.0	10.8	325.1	26.1
PSI-20CYS-LYS	600	3.5	14.4	325.0	26.1
PSI-0CYS-LYS	600	0.0	18.0	324.9	26.1

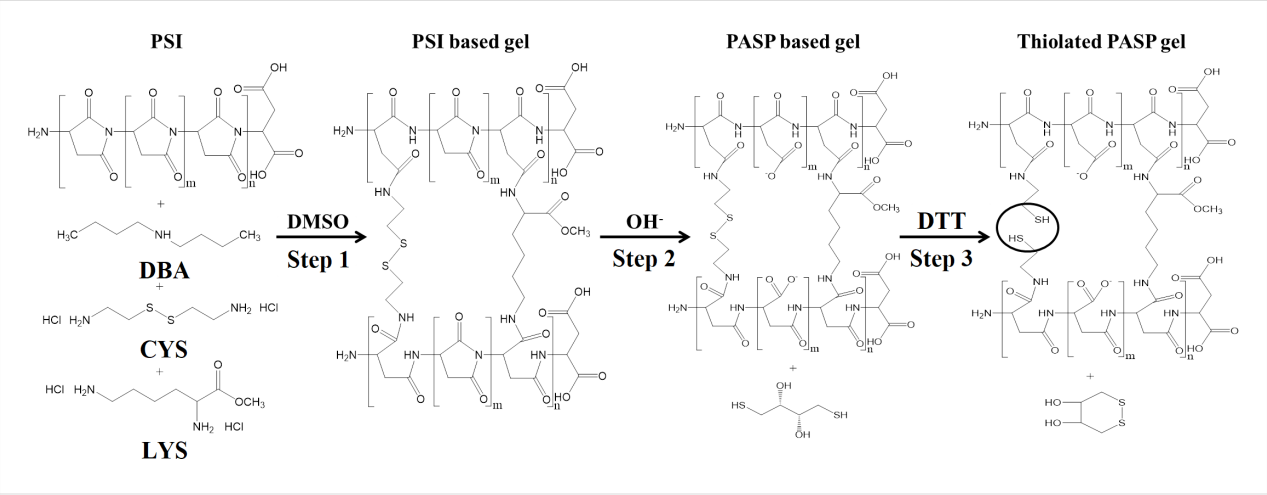

Figure 1: Synthesis of the simultaneously cross-linked and thiolated PSI and PASP gels.

To prepare thiolated PASP-based hydrogels, 0.1 M dithiothreitol (DTT) solution was used, prepared with the same imidazole buffer that was mentioned previously. The cleavage of the disulfide bonds leads to the formation of cysteamine molecules in the polymer matrix, which is indicated by CYSE instead of CYS in the nomenclature. The reaction is shown in Figure 1, step 3.

Effect of the pH value on the equilibrium degree of swelling

To determine the pH value-dependent degree of swelling of both the PSI- and the PASP-based gels, gel disks of three different diameters (6, 10 and 14 mm) were prepared. The weight of the disks was measured after reaching the equilibrium swelling degree in DMSO (for the PSI-based gels) or in an imidazole buffer of pH 8 (for the PASP-based gels). After that, the gel disks were immersed in buffers with different pH values (2.3–13.8) but the same ionic strength (c = 0.1 M, I = 0.25 M) for two days. Then, the buffers were changed, and the weight of the disks was measured two days later, following that the liquid had been carefully sponged up from the outer surface of the gels. Finally, the gels were dried at 40 °C, and the degree of swelling was calculated as the quotient of the weight of the swelled and the dried gel (m_{dried}). Three parallel measurements were carried out for each gel diameter.

Determination of the concentration of the elastically active chains by mechanical measurements

To measure the elastic modulus (G), gel cylinders of 1 cm in diameter and height were prepared with the same constitution as described above. G was assessed by vertical stress–strain measurements using an Instron 5942 (Intest kft., Hungary) mechanical tester, and its exact value was calculated by determining the stress–strain behavior during unidirectional compression. The temperature and the volume of the gels were constant during deformation, therefore, the Neo–Hooken law could be used to describe the deformation of the gels [21]:

$$\sigma_N = -G(\lambda - \lambda^{(-2)}) \quad (1)$$

where σ_N is the nominal stress and λ is the deformation ratio, which can be calculated as the ratio of the actual height and the initial height of the cylinder. G can be expressed as:

$$G = RTA \cdot v^* \cdot q_0^{-2/3} \cdot \Phi^{1/3} \quad (2)$$

where R is the gas constant, T is the temperature, Φ represents the polymer volume fraction of the gel, v^* is the concentration of the elastically active chains in the dry network (expressed in moles), and q_0 denotes the so-called memory term, by which the network "remembers" its initial state. The molecular interpretation of q_0 is controversial for networks prepared in solution. A is a model-dependent parameter. According to the Flory theory A = 1, while in the James–Guth and Staverman theories A = 0.5 [50,51]. For the present experiments, the parameter of the Flory theory was used. The value of v^* was calculated using Equation 2.

Swelling of the PASP hydrogels in DTT solution

Different PASP-XCYS-LYS gel disks of 6 mm in diameter were prepared and immersed in a 0.1 M DTT solution at pH 8. Changes of the concentration were avoided during the measurements by using a large amount of the solution in relation to the

gel disks. The swelling kinetics were monitored under an Alpha ScopeTek STO-3 light microscope. Pictures were taken every 5 min during one day and the ScopePhoto program was used to measure the diameter of the gel disks. In each case, three parallel measurements were carried out. The relative degree of swelling (Q_{rel}) was calculated as a ratio of the volume of the gels (Q_V) after and before the DTT treatment.

$$Q_{rel} = \frac{Q_{V,\text{ after DTT}}}{Q_{V,\text{ before DTT}}} \quad (3)$$

To study the effect of the DTT concentration on the swelling degree of the gels, PASP-20CYS-LYS gels were immersed in DTT solutions of pH 8 at different DTT concentrations (0.001−1.6 mmol/mL). In order to avoid the oxidation of DTT, the samples were rinsed with nitrogen gas. The weight of the gel disks was measured before and after being treated with DTT over five days. For all samples, two parallel measurements were carried out. The kinetic evaluation is based on the Tanaka–Fillmore–Peters–Candau (TFPC) theory [13].

Isolation and culturing of tooth-derived cells

The PDLCs originated from human wisdom teeth, which were surgically removed from healthy young adults at the Department of Dentoalveolar Surgery, Semmelweis University (according to the ethical guidelines set by the Ethical Committee of the Hungarian Medical Research Council). This study was approved by the Semmelweis University Regional and Institutional Committee of Science and Research Ethics. The number of the ethical permission is: 17458/2012/EKU. After extraction, the teeth were immediately placed into a sterile cell culture medium. The viable periodontal fibers were removed from the tooth surface, put into a sterile box with a sterile blade and digested in 1 mL collagenase I solution (1 mg/mL, Sigma-Aldrich, St. Louis, Missouri) for 1 h at 37 °C. The samples were vortexed every 10 min. After digestion, the fibers were mechanically loosened with needles (21G and 18G) and were centrifuged for 5 min at 250*g*.

The PDLCs were maintained in a humidified incubator (Nuaire, USA) in 100 mm tissue culture dishes (Orange Scientific, Belgium) under standard culture conditions (37 °C, 5% CO_2, 100% humidity). The growth medium of the PDLCs was the following. Eagle's Minimal Essential Medium Alfa (αMEM) (Gibco, USA) was supplemented with 10% fetal bovine serum (FBS, Gibco, USA), 2 mM L-glutamine (Gibco, USA), 100 units/mL penicillin and 100 mg/mL streptomycin (Gibco, USA). When the cell culture became subconfluent, it was passaged at a ratio of 1:20 using a 0.05% trypsin/EDTA solution.

Cell viability assay

Before performing the cell viability assay, the PASP-based gel disks of different constitutions were incubated in the above-mentioned growth medium for 3 h with a medium change after 1.5 h. After incubation, the gel disks were placed into low cell-binding plates (96-well plates, Nunc™ Dishes, St.Louis, Missouri) and sterilized by UV radiation for 1 h. Subsequently, 20,000 PDLCs were seeded on each gel disk in 200 µL medium and cultured for one or three days. Afterwards, each well was washed with PBS (37 °C) to remove swimming or loosely attached cells. To measure the cell viability, a colorimetric assay was performed using the cell proliferation reagent WST-1. The reagent was diluted (1:20) with αMEM containing no phenol red (Gibco, USA). Then, 200 µL solution was applied in each well. After incubation for 2 h at 37 °C, 150 µL of the supernatant solution was transferred from each well into an empty 96-well plate. The absorbance was measured at 450 nm using a microplate reader (Model 3550, Bio-Rad Laboratories, Japan) with a reference wavelength of 655 nm. Gel disks without cells were used as background controls.

Microscopic study of the cells

To visualize the PDLCs, the cells were labelled with a vital dye called Vybrant DiD (Molecular Probes, USA) before seeding. Gel disks of 5 mm diameter were placed into 48-well plates, and 40,000 cells per well were seeded in 400 µL medium. After 1 or 3 days, the wells were washed with PBS (37 °C) and fixed in 4% paraformaldehyde (in PBS) at room temperature for 2 h. The fixed samples were washed twice and then stored in PBS at 4 °C. The examination was carried out under a two-photon microscope (Femto2d, Femtonics, Hungary). A SpectraPhysics DeepSee laser was used at a wavelength of 800 nm to excite the photoactive dye. Images were taken with a 10x objective by the MES4.4v program. The cells can be seen in red color, while green indicates the autofluorescence of the PASP-based gels.

Statistical analysis

To assess the cell viability, PDLC cultures derived from five different patients were used, and five parallel measurements were carried out for each culture. The arithmetic mean and the standard error of the mean (SEM) are indicated in the diagrams. The statistical evaluation of the data was performed by the STATISTICA 10 software applying the Kruskal−Wallis nonparametric ANOVA test followed by a median test. A derived difference was regarded as statistically significant if the probability value is smaller than 0.05 ($p < 0.05$).

Drug release measurement

For the drug release measurement metoprolol was used as a model drug. Gel disks with a thickness of 0.75 mm and a diameter of 6 mm were swelled in physiological saline solution to

reach the equilibrium swelling degree. After that, they were immersed in 100 mg/mL metoprolol tartrate (Sigma-Aldrich) solution for three days, and then the solution was carefully sponged up from the gel surface prior to the measurement. The release of the metoprolol was measured in 20 mL physiological saline solution (c_{NaCl} = 9 g/L, pH 5.5) and in 20 mL 0.1 M DTT (in physiological saline solution). The drug release was followed by a JASCO V-650 spectrophotometer at 274 nm with an optical fiber probe. The concentration of the released metoprolol was calculated using the calibration line (Supporting Information File 1, Figure S1). The mass of the gel disks was measured before the experiment. The concentration was divided by the corresponding mass of the gel to compensate for variations of the gel mass during the parallel measurements.

Results and Discussion

Influence of the pH value on the equilibrium degree of swelling of PSI and the PASP-XCYS-LYS hydrogels

For applications in the field of tissue engineering, the swelling behavior of the amino acid-based hydrogels needs to be determined. Ideally, the swelling properties of the hydrogel scaffold should not change during the application. However, different cell types require scaffolds with different swelling properties (and also different stiffness). The PSI-based gels show a low swelling degree at pH 8 due to the hydrophobic character of the PSI backbone (Figure 2a). Since PSI is insoluble in water, the Huggins interaction parameter increases in an aqueous medium, hence, the gels shrink. Between pH 6 and 8, the swelling degrees abruptly rise as the polymer networks are hydrolyzed. The successful hydrolysis was proved by FTIR spectroscopy (Supporting Information File 1, Figure S2). This kind of abrupt change was described in previous articles, where other molecules or only LYS were applied as cross-linkers [21,22,34]. Between pH 8 and 11, the swelling degrees remain approximately constant, as has been observed for other types of PASP-based hydrogels [21,22,34]. However, for pH values larger than 11, a further increase in the swelling degree is observed (Figure 2a). This increase is due to the cleavage of the disulfide bonds in CYS, as we described in our previous article for DAB and CYS cross-linked hydrogels [21]. Another reason for the swelling can be the hydrolysis of the ester bond in LYS, which increases the concentration of negatively charged groups in the polymer matrix. The PSI-0CYS-LYS gel shows a significantly higher swelling degree at every pH value due to the smaller reactivity of the amine groups in LYS, which leads to a lower amount of cross-links [21].

Regarding the mass swelling degree of the PASP-based hydrogels, two groups can be observed which differ in the ratio of the LYS and the CYS cross-linkers (Figure 2b). The gels with a lower ratio of LYS cross-links (100, 80 and 60CYS-LYS) have a lower swelling degree than the gels with higher LYS concentration (40, 20 and 0CYS-LYS) at every pH value, which also proves the lower reactivity of LYS. The highest swelling degree was measured around pH 6, except for PASP-100CYS-LYS, in which every carboxyl group on the side chains of the aspartic acid monomers is deprotonated. By simultaneously using DAB or DAB/CYS as cross-linking agents, the degree of swelling is increasingly sharp in the range of pH 3–5 [22]. However, the use of LYS causes a monotonic increase of the swelling degree in the acidic pH range due to the free amine groups in the LYS side chain. Protonation of the free amine groups in CYS and LYS results in a decrease of the swelling degree between pH 6 and 10. However, for the DAB cross-linker, the degree of

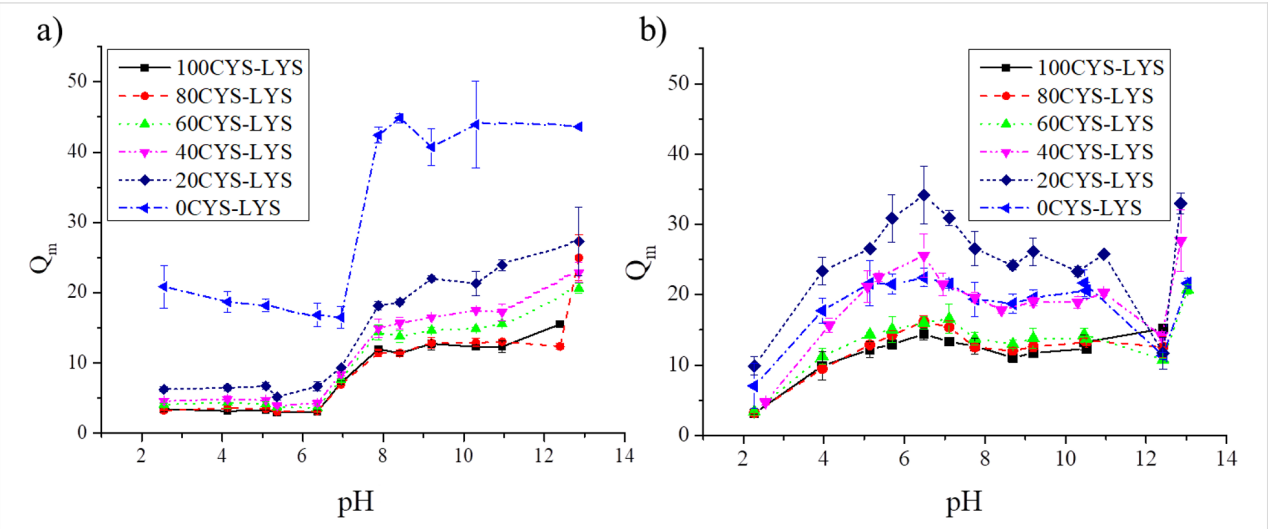

Figure 2: The dependence of the mass swelling degree of (a) the PSI- and (b) the PASP-based gels on the pH value.

swelling remained constant at alkaline pH values as we published in our previous paper [21,22,45]. The further increase of the swelling degree at pH values larger than 12 is the consequence of the cleavage of the disulfide bond of CYS and the hydrolysis of the ester group in the LYS cross-linkers. These findings are in a good agreement with our previous study. Yet, the LYS cross-linker shows a rather different dependence on the pH value than the DAB cross-linker, which could enhance the applicability of these hydrogels as scaffolds for cell culturing [25].

Swelling kinetics of PASP gels in the presence of DTT

The disulfide bonds in the PASP-based hydrogels are sensitive to the redox potential of the local environment [21,34,45]. Therefore, in the presence of a reductive agent such as DTT, the disulfide bonds can be cleaved and the gel can swell in the same way as it can happen under physiological conditions or in vitro. In this section, we demonstrate the results of the swelling kinetics in the presence of DTT (Figure 3).

Figure 3a and Figure 3b show the changes of the relative volume degree of the swelling (Q_{rel}) of the gels dissolved in 0.1 M DTT at pH 8. The 0CYS-LYS gel is not sensitive to the DTT solvent because it does not contain any disulfide bonds. Due to the polyelectrolyte character of PASP, the small but fast increase of Q_{rel} for PASP-0CYS-LYS is most likely caused by the small change of the ionic concentration of the solution (Figure 3a and Figure 3d) [52]. The swelling degree of the 20CYS-LYS gel increases significantly (73%) in the presence of DTT within 2 h, which proves the cleavage of the disulfide bonds in the CYS cross-linkers. Due to the higher cross-linking ability of CYS compared to LYS, Q_{rel} increases almost by a factor of two in these gels although CYS represents only 20%

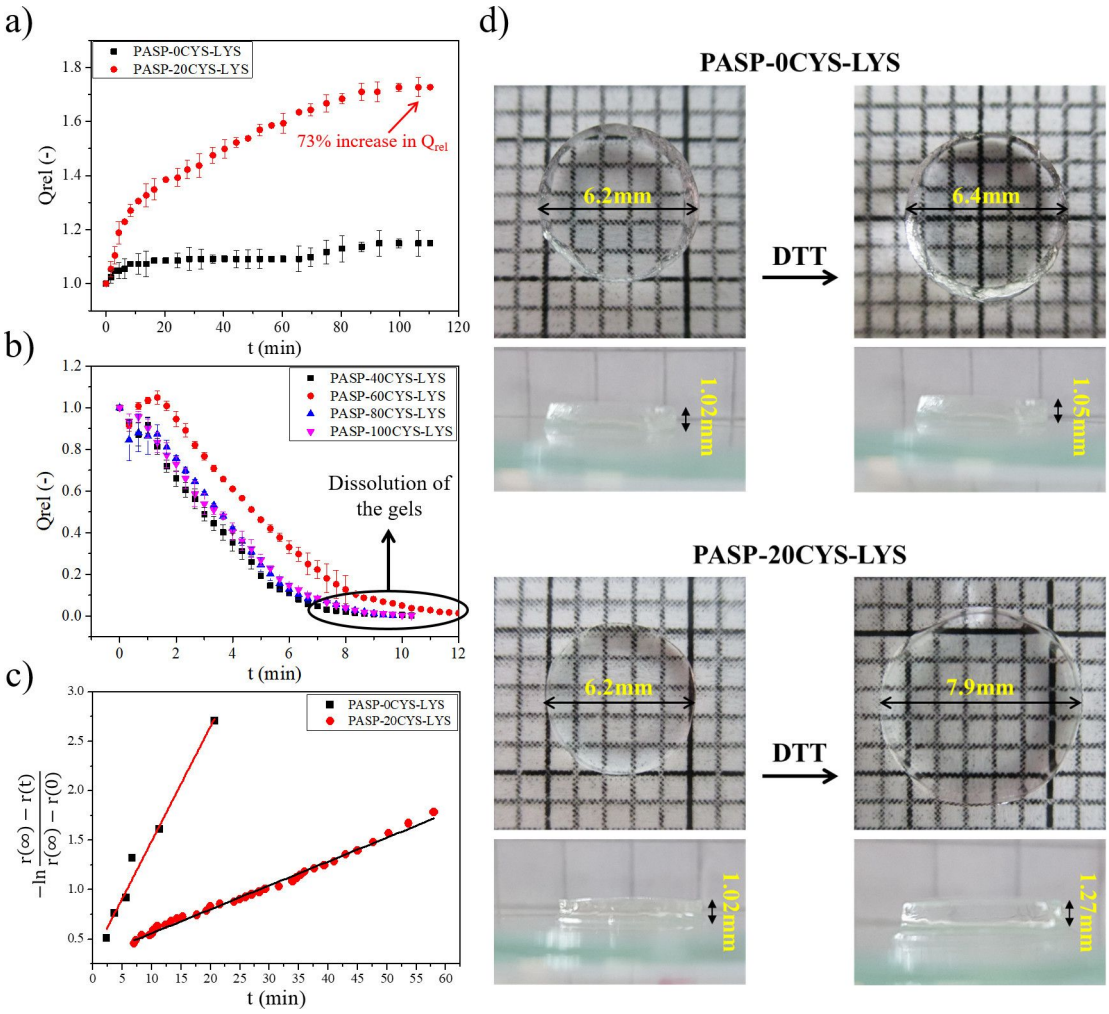

Figure 3: (a) Swelling and (b) dissolution kinetics of different PASP-XCYS-LYS gels in 0.1 M DTT solution at pH 8. (c) Description of the swelling kinetics by THB theory [12] and (d) images of the gels before and after swelling.

of the total cross-linker molecules. For other permanent cross-linkers, such as DAB [21] or poly(ethylene glycol) diglycidyl ether [34], the reduction of the disulfide bonds leads to a lower swelling degree, which also proves the previously mentioned theory. Upon increasing the density of the CYS molecules further, the gels abruptly degrade and dissolve after a few minutes (8–10 min), since the cross-linking density reaches the critical value at which the osmotic pressure bursts the polymer matrix [53].

To describe the swelling kinetics of the 0CYS-LYS and 20CYS-LYS samples, the TFPC theory was used as has been shown in our previous article [13] (Table 2).

Table 2: Swelling kinetics data of the different gels.

Sample	Final Q_{rel}	$r(0)$ (mm)	$r(\infty)$ (mm)	τ (min)
0CYS-LYS	1.09	5.95	6.24	8.69 ± 0.7
20CYS-LYS	1.72	5.95	7.15	41.67 ± 2.1

The swelling of the two hydrogels is based on different processes. The swelling of the 0CYS-LYS hydrogel occurs due to changes of the ionic strength, while the swelling of the 20CYS-LYS hydrogel is induced by the cleavage of the disulfide bonds. The change of the ionic strength is a faster process, therefore, the relaxation time determined for the 0CYS-LYS hydrogel is smaller than that of the 20CYS-LYS hydrogel.

Dependence of the swelling degree of the PASP-20CYS-LYS gels on the amount of DTT in the environment

In order to investigate whether every disulfide bond in the gel disks has been cleaved in the previous experiment and to get a better view of the fate of the scaffold during possible future therapeutic applications, the changes of the swelling degree were measured in the presence of different amounts of DTT. The amount of disulfide bonds was determined in the PASP-20CYS-LYS gels (Figure 4).

The relative swelling degree (Q_{rel}) shows a monotonic increase with the increasing amount of DTT up to about 0.03 mmol (Figure 4). Elevating the amount of DTT, no further changes in Q_{rel} can be seen. In order to determine the amount of disulfide bridges in the gel, a linear regression line was fitted to the first part of the measurement points (0−0.03 mmol DTT) and the constant part (0.03−1.6 mmol DTT) (Figure 4b). The x-coordinate of the intersection point of the two lines gives the minimum amount of DTT (0.025 mmol) that can cleave the total amount of the disulfide bridges. Hence, this amount it is equal to the molar amount of the disulfide bonds in the gel matrix. According to these data, the amount of disulfide bonds in the cross-linkers of the PASP-20CYS-LYS hydrogels is around 0.025 mmol, which is equal to the amount of CYS cross-linkers applied in the synthesis (see above). These results prove that each disulfide bond in the PASP-20CYS-LYS hydrogels has been cleaved by DTT in the described experiments (Figure 3). Due to the dissolution of the hydrogels containing higher amounts of CYS cross-linkers, this method cannot be used to determine the amount of disulfide bonds in these gels.

It is a challenging task to determine the cross-linking density in a polymer matrix. Usually, stress–strain measurements are used for this purpose. However, their results are influenced not only by the density of the chemical cross-links but also by the physical interactions between the polymer matrix and the swelling agent as well as other thermodynamic parameters [21,50,51,54-56]. Consequently, the swelling behavior of different hydrogels

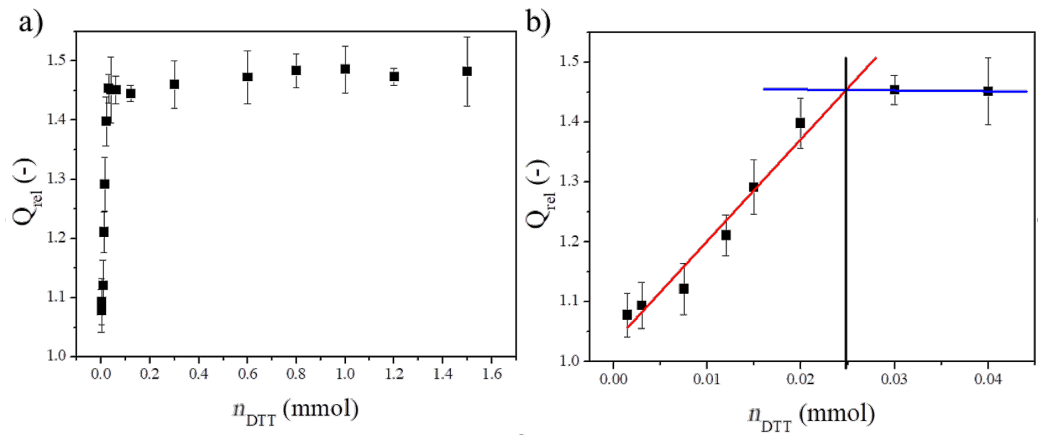

Figure 4: Dependence of the relative swelling degree of the PASP-20CYS-LYS gel on the amount of DTT a) between 0 and 1.6 mmol DDT and b) between 0 and 0.04 mmol DTT.

needs to be investigated in depth, and the relation between the swelling and other thermodynamic parameters is still to be determined. However, such measurements are difficult and require expensive equipment. By the presented method, the number of chemical cross-links can be determined by cleaving the sensitive bonds in the cross-linkers. The changes of the swelling degree as a function of the concentration of the reactant reveal the density of the sensitive bonds. This method is not reported in the literature about polymer gels. Thus, it can be regarded as a novel protocol for the determination of the amount of the sensitive cross-linkers in hydrogels.

Relationship between the mechanical properties and the chemical constitution of the gels

The stiffness of the hydrogel scaffold is a key parameter in the field of tissue engineering. It was described previously that different cell types prefer gels of different stiffness for proliferation [57]. In this section, the mechanical properties of the amino acid-based hydrogels of different chemical constitutions will be explained in detail.

As shown in Figure 3, the swelling properties of the PASP-based gels significantly depend on the chemical constitution of the gels. Consequently, the mechanical properties presumably depend on it as well. The relationship between the molar ratio of the two cross-linking agents (n_{CYS}/n_{LYS}) and the mechanical properties such as the elastic modulus (G) and the concentration of the elastically active chains ($\nu^* q_0^{-2/3}$) can be seen in Figure 5.

Upon increasing the CYS/LYS molar ratio, both G and ν^* monotonically increase in every solvent (Figure 5). This linear increase provides evidence that CYS has a higher cross-linking ability than LYS during the gel synthesis. Namely, larger amounts of cross-links in the polymer matrix lead to higher values of G and ν^* [21]. This indicates that a larger amount of CYS molecules reacts with two amine groups cross-linking the polymer chains. The strong electron withdrawing character of the carboxyl group of the amino-acid group decreases the electron density of the alpha amine group, resulting in a weaker reactivity of LYS. Supposedly, most LYS molecules react only with their side chain amine groups, and the gelation time is longer if the ratio of LYS cross-linkers is higher. This behavior can also contribute to the characteristic dependence of the gel swelling on the pH value (see above). The cross-linking ability of LYS can be improved by phosphoric acid catalysis as was shown by Gyenes and co-workers [22]. However, this method

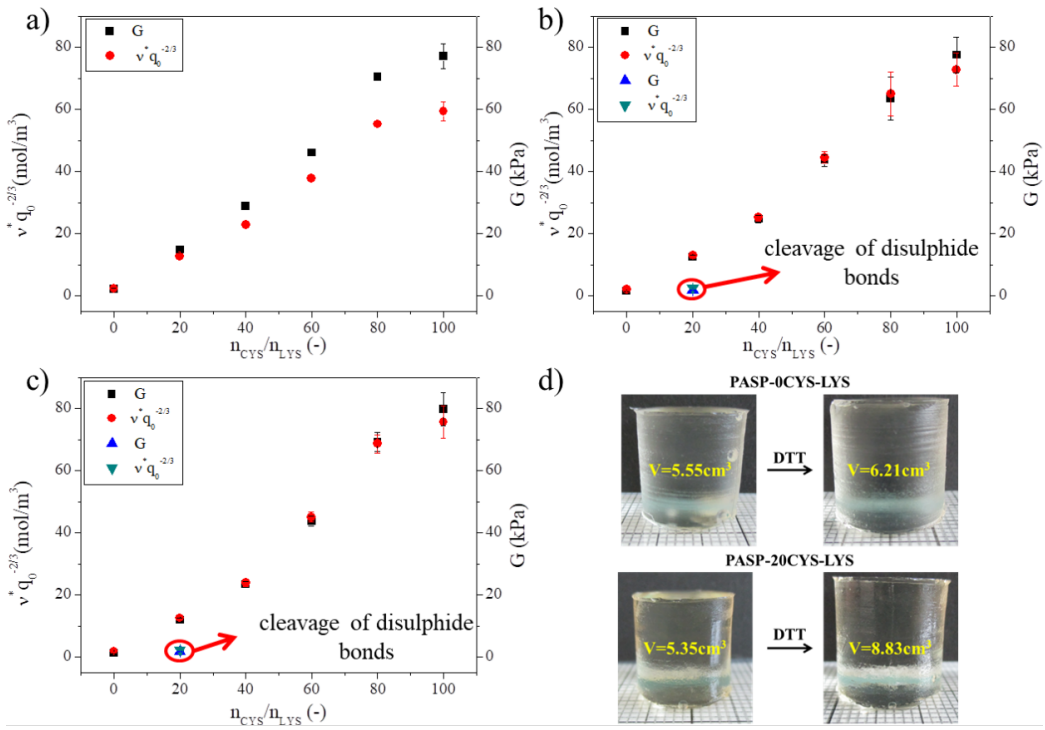

Figure 5: Dependence of the elastic modulus G (black squares, blue triangles) and the concentration of the elastically active chains $\nu^* q_0^{-2/3}$ (red dots, green triangles) on the CYS/LYS molar ratio in a) DMSO, b) imidazole buffer (pH 8, c = 0.1 M, I = 0.25 M) and c) PBS (pH 7.4, I = 0.15 M). d) Gel cylinders before and after DTT treatment.

cannot be used in our case because phosphoric acid precipitates CYS immediately.

Upon hydrolysis, the v^* values increase only very slightly, while the G values decrease (Figure 5a and Figure 5b). Neither of these two parameters changes when replacing the imidazole buffer (pH 8) with PBS (Figure 5b and Figure 5c). The v^* values depend on the swelling degree of the gels (Equation 2), which is changing during hydrolysis (Supporting Information File 1, Table S1). Yet, the swelling degree is not influenced by the change of the buffer from imidazole to PBS since the concentration of ions remains the same in both buffer solutions. This may explain the different values of G and v^* in DMSO (Figure 5a) but both values are similar after hydrolysis. These findings are in accordance with our previous findings [21].

When cleaving the disulfide bonds using DTT, all gels except for the 20CYS-LYS gel turned very soft or dissolved completely (Supporting Information File 1, Figure S2). However, the 20CYS-LYS gel did not dissolve (Figure 5d) but only swelled and turned moderately softer after the DTT treatment. The values of G and v^* decreased significantly (blue and green triangles in Figure 5b and Figure 5c). A similar decrease has been observed for other PASP-based CYS containing hydrogels in which another type of nonsensitive cross-linker was applied simultaneously with CYS [21,34,45].

Application of the PASP-XCYS(E)-LYS gels for cell cultivation

In addition to the elaborate characterization of the swelling and the mechanical properties as well as the thiol content, our aim was to study the applicability of the amino acid-based hydrogels as scaffolds for cell cultivation.

At first, the viability of the growth of PDLCs on the different hydrogels was tested (Figure 6a). After one day of cell growth, the highest cell viability index (referring to the highest cell adhesion) was measured on the 100CYS-LYS gel, which does not contain any LYS at all, only the redox sensitive cross-linker CYS. On day one, the cell viability index was lower for the 20CYS-LYS gel and the 40CYS-LYS gel than for the 100CYS-LYS gel. Still, for both gels, it had doubled after three days of cell growth suggesting that a lower CYS concentration favors cell proliferation. This result is presumably related to the en-

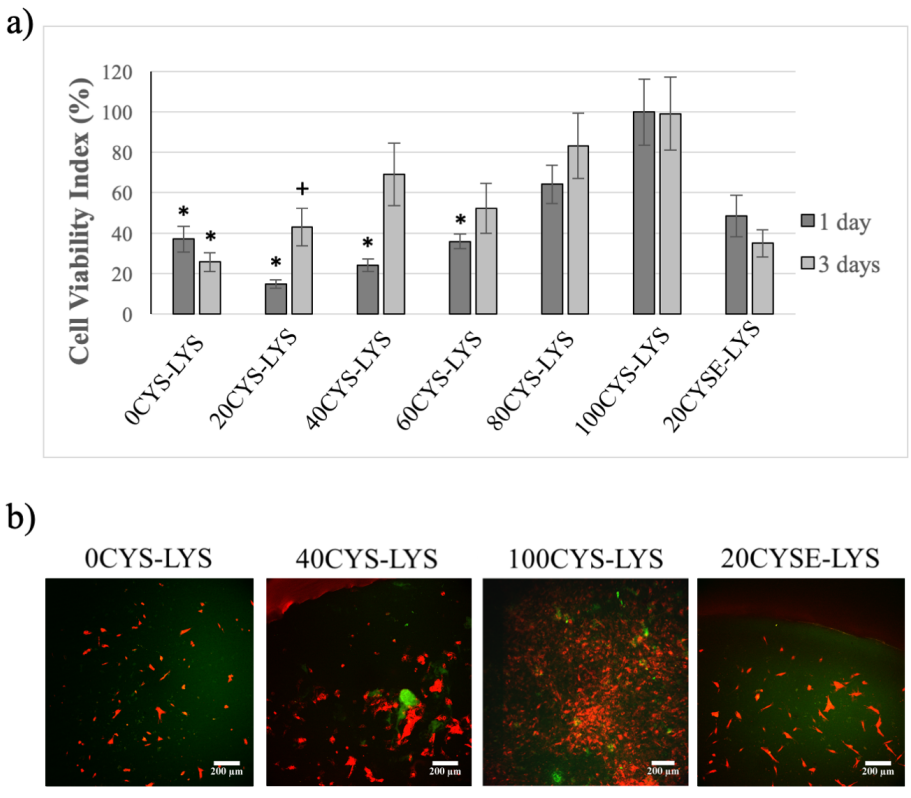

Figure 6: a) Viability of the PDLCs measured one and three days after seeding. The average viability value measured on the 100CYS-LYS gel on day one was considered as 100%. The cell viability indices are given as arithmetic mean ± SEM. * indicates $p < 0.05$ compared to the value of 100CYS-LYS at the corresponding time. + indicates $p < 0.05$ compared to the value of 100CYS-LYS on day one. b) Two-photon microscopic images of the PDLCs on the different hydrogels after three days. The scale bar indicates 200 µm. Each photomicrograph was taken at the same magnification.

hanced elastic modulus of the hydrogels (see above) as well as the relatively low LYS concentration. These results are in accordance with our previous work where we demonstrated that exchanging half of the CYS cross-linkers by DAB improved the proliferation of osteosarcoma cells [25]. However, the aim of the present study is to prepare gels composed of amino acids exclusively and test their biocompatibility on healthy cells. The disulfide bonds in the polymer matrix were supposedly cleaved in the cell medium during the three days of incubation which results in the formation of thiol groups in the hydrogel. The presence of thiol groups supports cell adhesion and proliferation as we showed previously. Therefore, the higher the density of CYS in the polymer matrix, the higher is the viability of the cells [25]. In the literature, several articles can be found about the effect of poly-L-lysine on cell adhesion and proliferation [30,58,59]. It was elucidated that this advantageous feature of poly-L-lysine is concentration-dependent, and the amount of poly-L-lysine should be optimized to reach the highest cell viability [30]. In our hydrogels, LYS is not polymerized but present as a monomer and plays a role as a cross-linker. This function of LYS in scaffolds, which is related to cell proliferation, has not been investigated before. Nevertheless, the positive effect of LYS is highly concentration-dependent. According to the literature, a high amount of LYS has a cytotoxic effect, while a lower amount supports cell adhesion and proliferation. Moreover, the effect of LYS can be diverse depending on whether poly-L-lysine is applied in water-soluble form [58] or as a built-in element in scaffolds [30]. On the other hand, LYS is a permanent cross-linker which is important to maintain the stability of the hydrogel during the cell experiments. Based on our results (Figure 6), the highest viability increase from day one to day three was found for the 20CYS-LYS and 40CYS-LYS gels, suggesting that cross-linker ratios of 60−80% LYS and 20−40% CYS yield the highest proliferation rate of PDLCs. The viability of cells on the 0CYS-LYS gel as well as on the 20CYSE-LYS gel, for which the disulfide bonds were previously created using the reductive agent DTT, decreased slightly from day one to day three. The similar behavior of the cells on these two hydrogels can be explained by the similar gel structure. Neither of these two gels contains CYS as a cross-linker, but only LYS cross-links the polymer chains. As given in Table 1, the initial concentration of LYS in our gels was between 0 and 1.8 wt %. A significant increase of the cell viability from day one to day three was measured for the 40CYS-LYS gels (LYS concentration around 1.5 wt %) which correlates with the findings of Datta et al., who found that the addition of 1.5 wt % of LYS significantly increases the cell viability [30].

The two-photon microscopic images (Figure 6b) confirm the results of our viability assays. Since the cells show a red fluorescence due to the vital stain applied, while the PASP-based hydrogels show a green autofluorescence [25], the gel matrix and the cells are easily distinguished. On day three, only few PDLCs showed a healthy fibroblast morphology on the 0CYS-LYS hydrogel, while the other cells had a rounded shape suggesting that they were unable to adhere to these gels. By increasing the ratio of the CYS cross-linking agents in the gel matrix, the proportion of the viable cells became elevated. The highest amount of PDLCs with fibroblast morphology can be observed on the 100CYS-LYS gel, which correlates well with the viability results.

According to the literature, various forms of lysine-containing scaffolds are able to enhance both the adhesion and the proliferation of stem cells. The most commonly used scaffolds are based on poly-L-lysine [30,59,60] and poly-D-lysine [61]. However, LYS was applied as a cross-linker only in a few cases. The corresponding gels are not fully composed of amino acids or have other disadvantages compared to our gels, for example, expensive preparation methods [62,63].

Drug release kinetics in isotonic and reductive medium

In addition to the possible applications in tissue engineering, the applicability of the amino acid-based hydrogels in drug delivery is very important. Therefore, the second aim of our work was to investigate the potential of the scaffolds as drug carriers. To get a better understanding of the fate of the drug in the living system, the release kinetics were determined not only in an isotonic but also in a reductive medium. Metoprolol was chosen as a model drug because it does not chemically interact with the polymer backbone, but ionic interactions can occur between the polymer matrix and the metoprolol molecules. Hence, theoretically, the only limiting factor of the release of metoprolol is diffusion. Moreover, metoprolol can be measured easily beside DTT by UV–vis spectroscopy.

The kinetics of the metoprolol release from the different PASP-XCYS-LYS gels was studied in both physiological saline (NaCl) and DTT solution (Figure 7). The graph depicts the released concentration of metoprolol normalized to the initial mass of the gel disk (c_{met}) as a function of release time.

The drug release kinetics show a similar behavior for all gel samples in the physiological saline solution (Figure 7, black squares). The released metoprolol reaches the saturation concentration after ca. 50 min in every measurement. The saturation concentration is highest for the PASP-100CYS-LYS sample reaching a concentration of 11 $g/L \cdot g_{gel}$ in physiological NaCl. Upon decreasing the density of CYS cross-links in the hydrogels, the saturation concentration is reduced to around

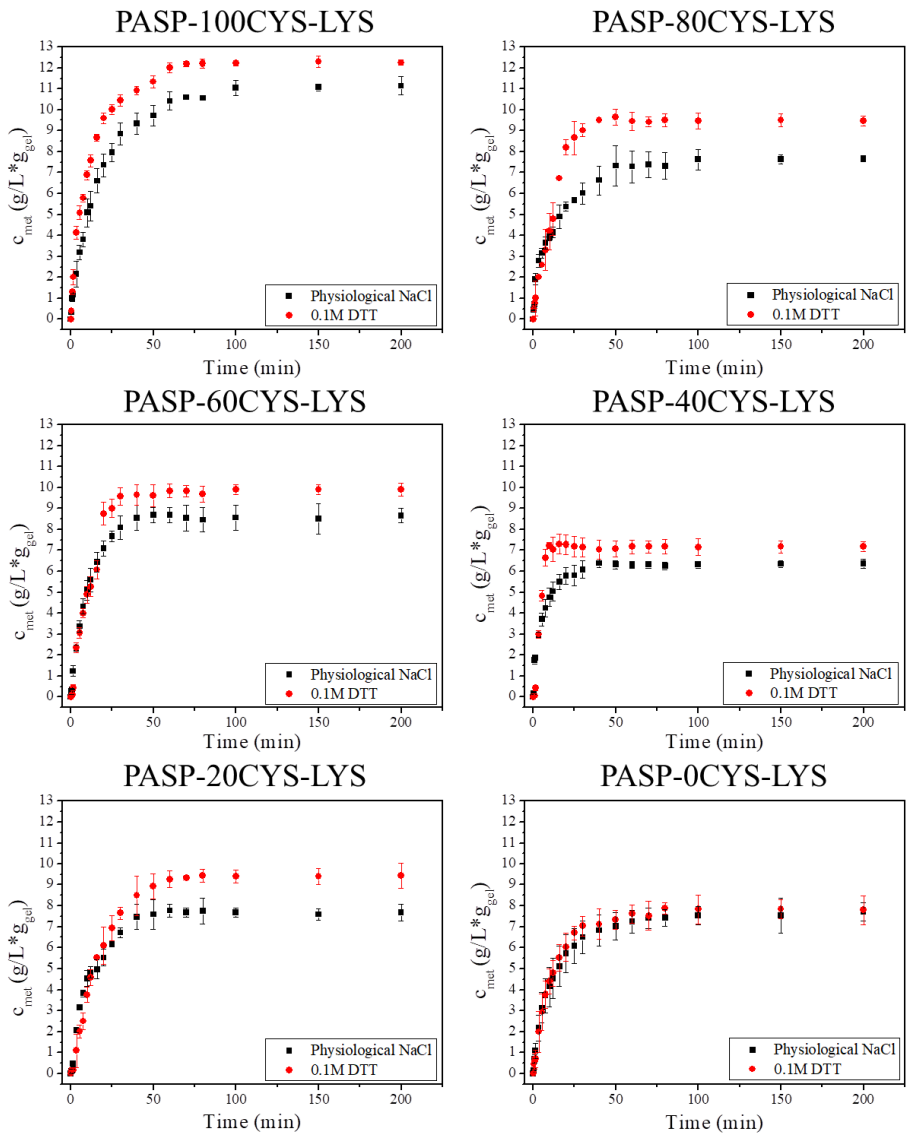

Figure 7: Metoprolol release from the different PASP-XCYS-LYS gels (c_{met}) in physiological saline solution (black squares) and in 0.1 M DTT/physiological saline solution (red circles).

7.5 g/L·g_{gel} for the 20CYS-LYS and the 0CYS-LYS hydrogel. A possible explanation of this phenomenon is the following. Metoprolol has a secondary amino group, which is protonated under these conditions leading to a weak interaction with the negatively charged PASP. As we demonstrated in previous experiments, hydrogels with increasing density of CYS crosslinkers have a higher polymer content (higher elastic modulus). Therefore, gels of higher CYS content can take up more metoprolol molecules from the solution. Consequently, a higher amount of CYS in the gel can result in a higher saturation concentration of metoprolol in the liquid. The kinetics curves are very similar to normal kinetics curves of drug release indicating a burst effect [15].

The presence of DTT leads to a higher saturation concentration of metoprolol presumably due to the cleavage of the disulfide bonds. The dissolution of the PASP-100CYS-LYS gel in the reductive medium is a continuous process. Therefore, the concentration of the released metoprolol in the DTT solution was higher than in the physiological salt solution at each measurement point. For the 40CYS-LYS, the 60CYS-LYS and the 80CYS-LYS gels, the metoprolol concentration increases faster compared to the 0CYS-LYS and the 20CYS-LYS gels in the first 20 min of the metoprolol release, which is presumably caused by the dissolution of the gels (Figure 3b). Although the dissolution of the 40CYS-LYS, the 60CYS-LYS, the 80CYS-LYS and the 100CYS-LYS gels occurs already after 10 min in

DTT solution (Figure 3b), the concentration of metoprolol reaches the saturation concentration only after 20 min. The ionic interaction between the polymer backbone and metoprolol could slow down the dissolution of the gels, which can cause such a difference. A higher degree of swelling leads to a higher diffusion coefficient in the gel matrix and consequently to a faster drug release. A similar observation was described in the case of another PASP-based gel and different other types of hydrogels [34]. For the PASP-20CYS-LYS gel, the drug release kinetics do not differ significantly for the reductive medium and the physiological solution during the first 20 min of release. Thus, the cleavage of the disulfide bonds in PASP-20CYS-LYS seems to be slower. After 20 min, this gel already swelled significantly and the metoprolol concentration increased in DTT solution. The saturated concentration reached a higher value in the DTT solution than in the physiological saline solution by the end of the measurement. The observation that DTT had no influence on the drug release in the case of 0CYS-LYS (Figure 7) is in line with the findings of our study of the swelling kinetics, i.e., that this gel type lacks disulfide bonds making it insensitive to the reductive environment (Figure 3a).

Conclusion

In this work, we tested the suitability of different fully amino acid-based hydrogels for tissue engineering and drug delivery applications. The influence of the chemical constitution of these hydrogels on the swelling and the mechanical properties was studied under different conditions. To prepare PASP-based hydrogels, LYS and CYS were used as cross-linkers at different molar ratios. Whereas LYS acts as a permanent cross-linker in the polymer matrix, CYS is sensitive to changes of the redox potential in the environment. Thus, the redox response of the hydrogels significantly depends on the ratio of the two cross-linkers. By increasing the CYS content, the swelling of the hydrogels becomes faster in different media. According to the mechanical tests, LYS has a lower cross-linking ability than CYS due to the ester group in LYS (lysine methylester). Therefore, a higher LYS content results in a lower elastic modulus and a lower concentration of elastically active chains in the hydrogels. The cleavage of the disulfide bonds leads to a significant decrease of the concentration of the elastically active chains for the 20CYS-LYS gel, which highly influences the release of metoprolol from the gel. Using different amounts of DTT as a reducing agent, the amount of CYS as the reactive cross-linker could be determined precisely. Human PDLCs were used to assess the biocompatibility of the hydrogels. Their viability also proved to depend on the ratio of the two cross-linkers. In summary, PASP-based hydrogels are promising materials for both medical and pharmaceutical applications which can be designed by tailoring the chemical structure of the hydrogels.

Supporting Information

Supporting Information File 1

Additional experimental information.
[https://www.beilstein-journals.org/bjnano/content/supplementary/2190-4286-10-249-S1.pdf]

Funding

This study was supported by the Hungarian Human Resources Development Operational Program (EFOP-3.6.2-16-2017-00006). Additional support was received from the Excellence Program of the Ministry for Innovation and Technology in Hungary within the framework of the therapy thematic program of the Semmelweis University. This work was funded by the National Research, Development and Innovation Office – NKFIH FK 124147, the OTKA 115259, the János Bolyai Research Scholarship of the Hungarian Academy of Sciences and by the ÚNKP-19-4-SE-04 new national excellence program of the Ministry for Innovation and Technology.

ORCID® iDs

Dávid Juriga - https://orcid.org/0000-0003-2655-5584
Gábor Varga - https://orcid.org/0000-0002-5506-8198
Krisztina S. Nagy - https://orcid.org/0000-0002-4942-2947
Angéla Jedlovszky-Hajdú - https://orcid.org/0000-0003-2720-783X

References

1. Drury, J. L.; Mooney, D. J. *Biomaterials* **2003,** *24,* 4337–4351. doi:10.1016/s0142-9612(03)00340-5
2. Fedorovich, N. E.; Alblas, J.; de Wijn, J. R.; Hennink, W. E.; Verbout, A. J.; Dhert, W. J. A. *Tissue Eng.* **2007,** *13,* 1905–1925. doi:10.1089/ten.2006.0175
3. Lee, K. Y.; Mooney, D. J. *Chem. Rev.* **2001,** *101,* 1869–1880. doi:10.1021/cr000108x
4. Li, J.; Mooney, D. J. *Nat. Rev. Mater.* **2016,** *1,* 16071. doi:10.1038/natrevmats.2016.71
5. Brunner, C. A.; Groner, R. W. *Can. J. Plast. Surg.* **2006,** *14,* 151–154. doi:10.1177/229255030601400302
6. Al-Kinani, A. A.; Zidan, G.; Elsaid, N.; Seyfoddin, A.; Alani, A. W. G.; Alany, R. G. *Adv. Drug Delivery Rev.* **2018,** *126,* 113–126. doi:10.1016/j.addr.2017.12.017
7. Annabi, N.; Selimović, Š.; Acevedo Cox, J. P.; Ribas, J.; Afshar Bakooshli, M.; Heintze, D.; Weiss, A. S.; Cropek, D.; Khademhosseini, A. *Lab Chip* **2013,** *13,* 3569–3577. doi:10.1039/c3lc50252j
8. Lu, Y.; Wang, D.; Li, T.; Zhao, X.; Cao, Y.; Yang, H.; Duan, Y. Y. *Biomaterials* **2009,** *30,* 4143–4151. doi:10.1016/j.biomaterials.2009.04.030
9. Cavalcanti, B. N.; Zeitlin, B. D.; Nör, J. E. *Dent. Mater.* **2013,** *29,* 97–102. doi:10.1016/j.dental.2012.08.002
10. Abdallah, M.; Martin, M.; El Tahchi, M. R.; Balme, S.; Faour, W. H.; Varga, B.; Cloitre, T.; Páll, O.; Cuisinier, F. J. G.; Gergely, C.; Bassil, M. J.; Bechelany, M. *ACS Appl. Mater. Interfaces* **2019,** *11,* 32623–32632. doi:10.1021/acsami.9b09337

11. Nair, L. S.; Laurencin, C. T. *Prog. Polym. Sci.* **2007,** *32,* 762–798. doi:10.1016/j.progpolymsci.2007.05.017
12. Duncan, R.; Vicent, M. J. *Adv. Drug Delivery Rev.* **2013,** *65,* 60–70. doi:10.1016/j.addr.2012.08.012
13. Varga, Z.; Molnár, K.; Torma, V.; Zrínyi, M. *Phys. Chem. Chem. Phys.* **2010,** *12,* 12670–12675. doi:10.1039/c0cp00527d
14. Park, K. *J. Controlled Release* **2014,** *190,* 3–8. doi:10.1016/j.jconrel.2014.03.054
15. Lee, P. I. *J. Controlled Release* **1985,** *2,* 277–288. doi:10.1016/0168-3659(85)90051-3
16. Brandl, F.; Kastner, F.; Gschwind, R. M.; Blunk, T.; Teßmar, J.; Göpferich, A. *J. Controlled Release* **2010,** *142,* 221–228. doi:10.1016/j.jconrel.2009.10.030
17. Gyarmati, B.; Némethy, Á.; Szilágyi, A. *Eur. Polym. J.* **2013,** *49,* 1268–1286. doi:10.1016/j.eurpolymj.2013.03.001
18. Kurland, N. E.; Ragland, R. B.; Zhang, A.; Moustafa, M. E.; Kundu, S. C.; Yadavalli, V. K. *Int. J. Biol. Macromol.* **2014,** *70,* 565–571. doi:10.1016/j.ijbiomac.2014.07.036
19. Ahn, S.-k.; Kasi, R. M.; Kim, S.-C.; Sharma, N.; Zhou, Y. *Soft Matter* **2008,** *4,* 1151. doi:10.1039/b714376a
20. Gupta, P.; Vermani, K.; Garg, S. *Drug Discovery Today* **2002,** *7,* 569–579. doi:10.1016/s1359-6446(02)02255-9
21. Zrinyi, M.; Gyenes, T.; Juriga, D.; Kim, J.-H. *Acta Biomater.* **2013,** *9,* 5122–5131. doi:10.1016/j.actbio.2012.08.046
22. Gyenes, T.; Torma, V.; Gyarmati, B.; Zrínyi, M. *Acta Biomater.* **2008,** *4,* 733–744. doi:10.1016/j.actbio.2007.12.004
23. Ulery, B. D.; Nair, L. S.; Laurencin, C. T. *J. Polym. Sci., Part B: Polym. Phys.* **2011,** *49,* 832–864. doi:10.1002/polb.22259
24. Pitarresi, G.; Saiano, F.; Cavallaro, G.; Mandracchia, D.; Palumbo, F. S. *Int. J. Pharm.* **2007,** *335,* 130–137. doi:10.1016/j.ijpharm.2006.11.012
25. Juriga, D.; Nagy, K.; Jedlovszky-Hajdú, A.; Perczel-Kovách, K.; Chen, Y. M.; Varga, G.; Zrínyi, M. *ACS Appl. Mater. Interfaces* **2016,** *8,* 23463–23476. doi:10.1021/acsami.6b06489
26. Park, K. M.; Shin, Y. M.; Kim, K.; Shin, H. *Tissue Eng., Part B* **2018,** *24,* 327–344. doi:10.1089/ten.teb.2018.0027
27. Naahidi, S.; Jafari, M.; Logan, M.; Wang, Y.; Yuan, Y.; Bae, H.; Dixon, B.; Chen, P. *Biotechnol. Adv.* **2017,** *35,* 530–544. doi:10.1016/j.biotechadv.2017.05.006
28. Hu, W.; Ying, M.; Zhang, S.; Wang, J. *J. Biomed. Nanotechnol.* **2018,** *14,* 1359–1374. doi:10.1166/jbn.2018.2590
29. Zhang, X.; Peng, X.; Zhang, S. W. Biodegradable medical polymers. *Science and Principles of Biodegradable and Bioresorbable Medical Polymers;* Woodhead Publishing, 2017; pp 1–33. doi:10.1016/b978-0-08-100372-5.00001-5
30. Datta, S.; Barua, R.; Sarkar, R.; Barui, A.; Chowdhury, A. R.; Datta, P. *IOP Conf. Ser.: Mater. Sci. Eng.* **2018,** *402,* 012113. doi:10.1088/1757-899x/402/1/012113
31. Crompton, K. E.; Goud, J. D.; Bellamkonda, R. V.; Gengenbach, T. R.; Finkelstein, D. I.; Horne, M. K.; Forsythe, J. S. *Biomaterials* **2007,** *28,* 441–449. doi:10.1016/j.biomaterials.2006.08.044
32. Matsusaki, M.; Yoshida, H.; Akashi, M. *Biomaterials* **2007,** *28,* 2729–2737. doi:10.1016/j.biomaterials.2007.02.015
33. Manocha, B.; Margaritis, A. *Crit. Rev. Biotechnol.* **2008,** *28,* 83–99. doi:10.1080/07388550802107483
34. Krisch, E.; Gyarmati, B.; Barczikai, D.; Lapeyre, V.; Szilágyi, B. Á.; Ravaine, V.; Szilágyi, A. *Eur. Polym. J.* **2018,** *105,* 459–468. doi:10.1016/j.eurpolymj.2018.06.011
35. Aderibigbe, B. A.; Ray, S. S. *J. Drug Delivery Sci. Technol.* **2016,** *36,* 34–45. doi:10.1016/j.jddst.2016.09.006
36. Kamaly, N.; Yameen, B.; Wu, J.; Farokhzad, O. C. *Chem. Rev.* **2016,** *116,* 2602–2663. doi:10.1021/acs.chemrev.5b00346
37. Juriga, D.; Laszlo, I.; Ludanyi, K.; Klebovich, I.; Chae, C. H.; Zrinyi, M. *Acta Biomater.* **2018,** *76,* 225–238. doi:10.1016/j.actbio.2018.06.030
38. Molnar, K.; Juriga, D.; Nagy, P. M.; Sinko, K.; Jedlovszky-Hajdu, A.; Zrinyi, M. *Polym. Int.* **2014,** *63,* 1608–1615. doi:10.1002/pi.4720
39. Molnar, K.; Jedlovszky-Hajdu, A.; Zrinyi, M.; Jiang, S.; Agarwal, S. *Macromol. Rapid Commun.* **2017,** *38,* 1700147. doi:10.1002/marc.201700147
40. Jedlovszky-Hajdu, A.; Molnar, K.; Nagy, P. M.; Sinko, K.; Zrinyi, M. *Colloids Surf., A* **2016,** *503,* 79–87. doi:10.1016/j.colsurfa.2016.05.036
41. Kim, M.; Shin, S. W.; Lim, C. W.; Kim, J.; Um, S. H.; Kim, D. *Biomater. Sci.* **2017,** *5,* 305–312. doi:10.1039/c6bm00763e
42. Németh, C.; Gyarmati, B.; Abdullin, T.; László, K.; Szilágyi, A. *Acta Biomater.* **2017,** *49,* 486–494. doi:10.1016/j.actbio.2016.11.065
43. Gong, C.; Lu, C.; Li, B.; Shan, M.; Wu, G. *J. Mater. Sci.* **2017,** *52,* 955–967. doi:10.1007/s10853-016-0391-9
44. Yavvari, P. S.; Awasthi, A. K.; Sharma, A.; Bajaj, A.; Srivastava, A. *J. Mater. Chem. B* **2019,** *7,* 2102–2122. doi:10.1039/c8tb02962h
45. Krisch, E.; Messager, L.; Gyarmati, B.; Ravaine, V.; Szilágyi, A. *Macromol. Mater. Eng.* **2016,** *301,* 260–266. doi:10.1002/mame.201500119
46. Szilágyi, B. Á.; Némethy, Á.; Magyar, A.; Szabó, I.; Bősze, S.; Gyarmati, B.; Szilágyi, A. *React. Funct. Polym.* **2018,** *133,* 21–28. doi:10.1016/j.reactfunctpolym.2018.09.015
47. Samal, S. K.; Dash, M.; Van Vlierberghe, S.; Kaplan, D. L.; Chiellini, E.; van Blitterswijk, C.; Moroni, L.; Dubruel, P. *Chem. Soc. Rev.* **2012,** 7147–7194. doi:10.1039/c2cs35094g
48. Seo, B.-M.; Miura, M.; Gronthos, S.; Mark Bartold, P.; Batouli, S.; Brahim, J.; Young, M.; Gehron Robey, P.; Wang, C. Y.; Shi, S. *Lancet* **2004,** *364,* 149–155. doi:10.1016/s0140-6736(04)16627-0
49. Kadar, K.; Kiraly, M.; Porcsalmy, B.; Molnar, B.; Racz, G. Z.; Blazsek, J.; Kallo, K.; Szabo, E. L.; Gera, I.; Gerber, G.; Varga, G. *J. Physiol. Pharmacol.* **2009,** *60* (Suppl. 7), 167–175.
50. Flory, P. J.; Rehner, J., Jr. *J. Chem. Phys.* **1943,** *11,* 512–520. doi:10.1063/1.1723791
51. Dušek, K.; Prins, W. Structure and elasticity of non-crystalline polymer networks. *Fortschritte Der Hochpolymeren-Forschung;* Springer: Berlin, Germany, 1969; pp 1–102. doi:10.1007/bfb0051042
52. Osada, Y.; Gong, J. *Prog. Polym. Sci.* **1993,** *18,* 187–226. doi:10.1016/0079-6700(93)90025-8
53. Ricka, J.; Tanaka, T. *Macromolecules* **1984,** *17,* 2916–2921. doi:10.1021/ma00142a081
54. Brannon-Peppas, L.; Peppas, N. A. *Chem. Eng. Sci.* **1991,** *46,* 715–722. doi:10.1016/0009-2509(91)80177-z
55. Menzel, C.; Olsson, E.; Plivelic, T. S.; Andersson, R.; Johansson, C.; Kuktaite, R.; Järnström, L.; Koch, K. *Carbohydr. Polym.* **2013,** *96,* 270–276. doi:10.1016/j.carbpol.2013.03.044
56. Moe, S. T.; Elgsaeter, A.; Skjåk-Bræk, G.; Smidsrød, O. *Carbohydr. Polym.* **1993,** *20,* 263–268. doi:10.1016/0144-8617(93)90098-o
57. Santos, E.; Hernández, R. M.; Pedraz, J. L.; Orive, G. *Trends Biotechnol.* **2012,** *30,* 331–341. doi:10.1016/j.tibtech.2012.03.005
58. Lu, H.; Guo, L.; Kawazoe, N.; Tateishi, T.; Chen, G. *J. Biomater. Sci., Polym. Ed.* **2009,** *20,* 577–589. doi:10.1163/156856209x426402

59. Zheng, S.; Guan, Y.; Yu, H.; Huang, G.; Zheng, C. *New J. Chem.* **2019,** *43,* 9989–10002. doi:10.1039/c9nj01675a
60. Shih, I. L.; Van, Y. T.; Shen, M. H. *Mini-Rev. Med. Chem.* **2004,** *4,* 179–188. doi:10.2174/1389557043487420
61. Tian, W. M.; Hou, S. P.; Ma, J.; Zhang, C. L.; Xu, Q. Y.; Lee, I. S.; Li, H. D.; Spector, M.; Cui, F. Z. *Tissue Eng.* **2005,** *11,* 513–525. doi:10.1089/ten.2005.11.513
62. Ma, L.; Gao, C.; Mao, Z.; Zhou, J.; Shen, J. *J. Biomed. Mater. Res., Part A* **2004,** *71,* 334–342. doi:10.1002/jbm.a.30170
63. Liu, S.; Xie, R.; Cai, J.; Wang, L.; Shi, X.; Ren, L.; Wang, Y. *RSC Adv.* **2015,** *5,* 46088–46094. doi:10.1039/c5ra07036h

License and Terms

BEILSTEIN JOURNAL OF NANOTECHNOLOGY

The different ways to chitosan/hyaluronic acid nanoparticles: templated vs direct complexation. Influence of particle preparation on morphology, cell uptake and silencing efficiency

Arianna Gennari‡[1], Julio M. Rios de la Rosa‡[2,3,4], Erwin Hohn[3,5], Maria Pelliccia[2,6], Enrique Lallana[2,3], Roberto Donno[1], Annalisa Tirella[2,3] and Nicola Tirelli*[1,2]

Full Research Paper

Open Access

Address:
[1]Laboratory of Polymers and Biomaterials, Fondazione Istituto Italiano di Tecnologia, 16163 Genova, Italy, [2]NorthWest Centre for Advanced Drug Delivery (NoWCADD), School of Health Sciences, University of Manchester, Oxford Road, Manchester, M13 9PT, United Kingdom, [3]Division of Pharmacy and Optometry, Faculty of Biology, Medicine and Health, Stopford Building, University of Manchester and Manchester Academic Health Science Centre, Manchester, M13 9PT, United Kingdom, [4]current address: Cambridge Enterprise Limited, University of Cambridge, Hauser Forum, 3 Charles Babbage Rd, Cambridge, CB3 0GT, United Kingdom, [5]current address: Novartis EBEWE Pharma Ges.m.b.H. Nfg.KG, Lehenau 10a, 5325 Plainfield, Austria and [6]current address: Orchard Therapeutics plc., 108 Cannon Street, EC4N 6EU London, United Kingdom

Email:
Nicola Tirelli* - Nicola.tirelli@iit.it

* Corresponding author ‡ Equal contributors

Keywords:
aggregation; chitosan; field flow fractionation; light scattering; targeted drug delivery

Beilstein J. Nanotechnol. **2019,** *10,* 2594–2608.
doi:10.3762/bjnano.10.250

Received: 12 September 2019
Accepted: 02 December 2019
Published: 30 December 2019

This article is part of the thematic issue "Engineered nanomedicines for advanced therapies".

Guest Editor: F. Baldelli Bombelli

Abstract

This study is about linking preparative processes of nanoparticles with the morphology of the nanoparticles and with their efficiency in delivering payloads intracellularly. The nanoparticles are composed of hyaluronic acid (HA) and chitosan; the former can address a nanoparticle to cell surface receptors such as CD44, the second allows both for entrapment of nucleic acids and for an endosomolytic activity that facilitates their liberation in the cytoplasm. Here, we have systematically compared nanoparticles prepared either A) through a two-step process based on intermediate (template) particles produced via ionotropic gelation of chitosan with triphosphate (TPP), which are then incubated with HA, or B) through direct polyelectrolyte complexation of chitosan and HA. Here we demonstrate that HA is capable to quantitatively replace TPP in the template process and significant aggregation takes place during the TPP–HA exchange. The templated chitosan/HA nanoparticles therefore have a mildly larger size (measured by dynamic light scattering alone or by field flow fractionation coupled to static or dynamic light scattering), and above all a higher aspect ratio (R_g/R_H) and a lower fractal dimension. We then compared the kinetics of uptake and the (antiluciferase) siRNA

delivery performance in murine RAW 264.7 macrophages and in human HCT-116 colorectal tumor cells. The preparative method (and therefore the internal particle morphology) had little effect on the uptake kinetics and no statistically relevant influence on silencing (templated particles often showing a lower silencing). Cell-specific factors, on the contrary, overwhelmingly determined the efficacy of the carriers, with, e.g., those containing low-MW chitosan performing better in macrophages and those with high-MW chitosan in HCT-116.

Introduction

Chitosan is a linear copolymer of β-1,4-D-glucose-2-amine and *N*-acetyl-D-glucose-2-amine, and is commonly employed as the cationic component in polyplexes and other drug delivery vehicles [1-3]. In comparison to other polycations, its main advantages are the low toxicity and its biodegradability. Biodegradation can occur both enzymatically and oxidatively [4]. A number of methods can be employed to prepare chitosan-based nanoparticles [5-8], the most popular being ionotropic gelation and polyelectrolyte complexation. The distinction between the two is subtle, since they are based on a common driving force, i.e., the electrostatic attraction between protonated amines on chitosan and multiply charged anions, which effectively act as cross-linkers. Electrostatic complexation allows for very mild preparative processes, carried out in water under mild and almost physiological conditions and without the use of chemical reactions. Additionally, electrostatic interactions may not only be used to hold together a particle, but also to encapsulate and retain payloads such as nucleic acids (either in combination with other anionic components [9], or as the only negatively charged molecule [10]).

Ionotropic gelation and polyelectrolyte complexation use anionic components of different size, In the former, typically an inorganic anion of low molecular weight, such as triphosphate (TPP) is used, while in the latter negatively charged polymers, e.g., hyaluronic acid (HA) [11,12] or alginate [13], are commonly used. HA is a particularly interesting component, since its presence allows for a reduced serum protein adsorption on chitosan-containing nanoparticles [14] and a receptor-mediated mechanism of internalization [15]. A larger size of the anionic component corresponds to a higher avidity toward chitosan, thus polyelectrolyte complexes are more stable but also difficult to reverse; this irreversibility makes polyelectrolyte complexation largely a kinetically controlled process, the details of which are in principle more difficult to reproduce. Roughly half way between the two processes, in several cases a low-MW polyanion is used together with a macromolecular anion, attempting to combine stability and reversibility; this is the case with TPP and HA, which have been used together in one-pot preparations [11], or in sequence, i.e., first producing chitosan/TPP nanoparticles, and then adding HA [16,17]. In the latter process, we noticed that molecular weight of chitosan influenced the presentation of HA [18], which affected the nanoparticle internalization in both RAW 264.7 macrophages [19,20] and XS106 dendritic cells [21]. In both cases, nanoparticles based on chitosan of low molecular weight appeared to be surrounded by a corona of loosely bound HA, which on one hand lowered the maximum amount of internalizable particles, but on the other hand made it more sensitive to the presence of additional biofunctional groups on HA [21].

There are, however, several yet unanswered questions regarding the use of TPP in the preparation of nanoparticles, when they also contain HA. These questions are, in particular:

1. whether and how much TPP is retained in the particles, since chitosan–TPP interactions are more easily reversed than chitosan–HA interactions (lower avidity);
2. whether the initial presence of TPP makes the final particles morphologically different; in previous reports, we have referred to the product of the two-step complexation (first between chitosan and TPP, then addition of HA) as HA-coated nanoparticles. Actually, HA is used as a last step and in excess, thus it ought to be the dominant component on the surface of the polyelectrolyte complex. However, the definition of HA-coated particles implies a yet-to-be-proven core–shell structure, as opposed to homogeneous particles obtained via direct chitosan/HA complexation;
3. whether the different process, and the possibly associated differences in composition and morphology may result in a biologically different performance in the cellular delivery of a payload.

Here, we have compared the physico-chemical and carrier properties of the product of chitosan/HA polyelectrolyte complexation ("direct process" in Scheme 1) and that of the process where chitosan–TPP nanoparticles are produced first and act as a kind of template for the final material ("templated process" in Scheme 1). For the latter process, we also aimed to elucidate whether the HA is incorporated in the particles either via surface adsorption or bulk reorganization as showed in Scheme 1.

We then assessed how the possible morphological differences introduced by the different preparative processes may affect nanoparticle uptake and the release of encapsulated payloads

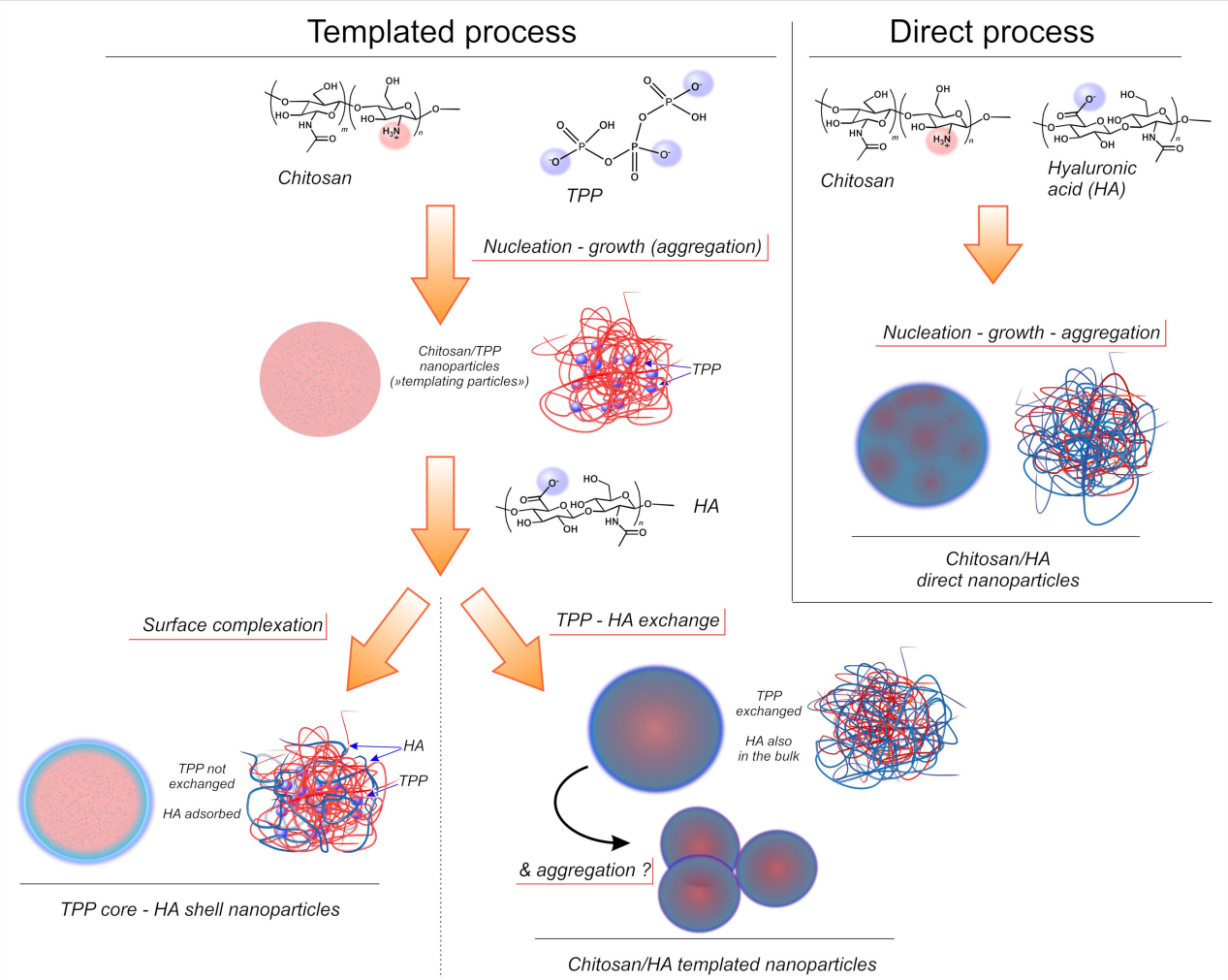

Scheme 1: In the templated process (left), in a lightly acidic aqueous solution the protonated chitosan amines (cationic species in red) are cross-linked by TPP (anionic species in blue). The complexation leads to the nucleation of the particles that increase in size likely more through the adsorption of additional chitosan and TPP species (growth) than through aggregation of smaller intermediate particles, as the ζ-potential of the nanoparticles supposedly always remains positive, and therefore repulsive. When exposed to the polyanionic HA, the two limiting conditions are that the templating nanoparticles either A) adsorb it on their cationic surface, inverting their ζ-potential and therefore yielding HA-coated, core–shell nanoparticles (bottom left), or B) allow HA to replace TPP in their bulk. The latter process likely is morphologically templated, since it occurs within the nanoparticles. In a process based on the direct complexation between chitosan and HA (right), nanoparticles nucleate and then increase in size via either adsorption of individual components (growth) or via aggregation due the presence of patches of different charge on their surface. The possibility of aggregation may lead to a more heterogeneous bulk structure than in the templated process.

using a murine macrophagic (RAW 264.7) and a human colorectal tumor (HCT-116) cell line, both popular in vitro models for the study of cellular interactions of HA-based materials [20,22].

Experimental

Materials and methods

The list of chemicals used is provided in Supporting Information File 1, Section SI1.1. Chitosan of viscosity average molecular weight $\left(\overline{M_v}\right)$ 656 kDa and a degree of deacetylation (DD) of 85% (from ^{1}H NMR; hereafter referred to as $Chit_{650}$ or high-MW chitosan) was purchased from Sigma-Aldrich (Gillingham, UK) and purified prior to use as previously described (boiling in 2% acetic acid, filtration, precipitation with NaOH, ultrafiltration and freeze drying) [16]. Chitosan with $\overline{M_v}$ = 36 kDa and a DD = 85% (hereafter referred to as $Chit_{35}$ or low-MW chitosan) was obtained by oxidative degradation of the above high-MW chitosan (1 wt % in 0.1 M HCl/3 mM sodium nitrite, room temperature, 12 h) [21]. Hyaluronic acid (HA) with weight average molecular weight $\left(\overline{M_w}\right)$ = 180 kDa was kindly donated by Kyowa Hakko Bio Italia Srl (Milan, Italy).

Preparation of chitosan/HA nanoparticles

In all cases, the nanoparticles were prepared under sterile conditions (Cat. II cabinet) with surfaces previously treated with RNaseZap® solution (Thermo Scientific, UK) for the handling

of nucleic acids. All the steps were performed under vigorous magnetic stirring (1,000 rpm) and at 25 °C in 2 mL round bottom Eppendorf tubes.

A) Template-based (TPP) method. In a typical experiment, nanoparticles were prepared by the addition of 72 μL of a 0.1 wt % solution of TPP in deionized water (pH 5 adjusted with 0.1 M HCl) to 928 μL of a 0.069 wt % solution of $Chit_{35}$ or $Chit_{650}$ in 4.6 mM HCl (pH 5 adjusted with 0.1 M NaOH), always at a 1:9 TPP/chitosan weight ratio. In the case of siRNA-loaded nanoparticles, TPP was dissolved in deionized nuclease-free water containing siRNA. The chitosan–TPP nanoparticle (template) dispersion was stirred for 30 min and then mixed with 1 mL of acetate buffer (200 mM, pH 5). After 5 min, 1 mL of the nanoparticle suspension was added to an equal volume of a 1.5 mg/mL HA in acetate buffer (100 mM, pH 5) and kept under stirring for 30 min, always at 25 °C. The resulting nanoparticle (chitosan–TPP/HA) suspension was then dialyzed against deionized water (MWCO = 1,000 kDa) for 5 h, changing the water every 20 min.

B) Direct complexation. 500 μL of a 0.069 wt % chitosan solution prepared as described above was mixed with an equal volume of deionized and nuclease-free water containing siRNA or simply with deionized water for 10 min at 25 °C. The resulting dispersion (with or without siRNA) was added to 1 mL of a 1.5 mg/mL HA solution in water (previously adjusted to pH 5) and stirred for 30 min.

Fluorescently labelled particles were produced using chitosan and HA, which were appropriately labelled as described in Supporting Information File 1, Section SI1.2.

Nanoparticle characterization

Elemental analysis. 5 mL of nanoparticle suspension were dialyzed against deionized water (MWCO = 1,000 kDa) for 5 h, changing the water every 20 min. The composition of freeze-dried nanoparticles was then analysed using a Thermo Flash 2000 Organic Elemental Analyser for carbon (C) and nitrogen (N), and a Thermo Scientific iCAP 6300 DUO ICP Spectrometer for phosphorus (P). Theoretical compositions were calculated under assumption that: i) all glucosamine units in chitosan are protonated complexed to either TPP or HA; ii) TPP has an average of three negative charges (at pH 5.0, which means that two oxygens are still protonated); iii) HA is completely deprotonated and all its carboxylates are either complexed with chitosan or present as sodium salt.

Hydrodynamic size and ζ-potential. Z-average hydrodynamic size, polydispersity index (PDI), and ζ-potential were measured on three independent samples at 25 °C using a Zetasizer Nano ZS instrument (Model ZEN3600, Malvern Instruments Ltd., UK) equipped with a solid state HeNe laser (λ = 633 nm) at a scattering angle of 173°. Size measurement data were obtained by using the General Purpose algorithm. The electrophoretic mobility of nanoparticles was converted into ζ-potential values by means of the Smoluchowski equation using Malvern Zetasizer software (v7.11).

Capillary electrophoresis. Electrophoresis measurements were performed at 25 °C on a P/ACE MDQ Plus (SCIEX, Warrington, UK) equipped with a 50 cm effective length (70 cm total length) capillary with 75 μm internal diameter (Beckam Coulter, Brea, USA) and a photodiode array detector operating at 214 nm. The capillary was first conditioned by successive rinsing steps (all performed at 20 psi): 5 min with 1 M HCl, 2 min with deionized water, 10 min with 0.1 M NaOH, 2 min with deionized water, 5 min with 20 mM phosphate buffer at pH 7.4 (running buffer), 1 min with 0.1 M NaOH, 1 min with deionized water, and finally 1.5 min with the running buffer. Each sample was then injected at 0.5 psi for 10 s, applying 15 kV between the anode and the injection site (normal polarity) for 60 min. At the end of each measurement, the capillary was rinsed with water for 1 min at 20 psi. Data acquisition and analysis were performed respectively with software packages 32 Karat (SCIEX) and OriginPro 8.5.1 (OriginLab Corporation, US). A calibration curve was obtained by injecting HA at known concentration (47, 188 and 750 g/mL), thus allowing to quantify the amount of unbound HA from the area of its peak at 22 min.

Asymmetric-flow field flow fractionation (AF4). An AF2000 TM (Postnova Analytics, Landsberg, Germany) featuring an A4F channel an equipped with a 350 μm spacer and a regenerated cellulose 10 kDa MWCO membrane as accumulation wall was employed in connection with a UV–vis detector operating at 220 nm (S3210, Laserchrom, Rochester, UK), a MALS detector (Viscotek SEC-MALS20, Malvern Instruments, Worcestershire, UK), a refractive index detector (Optilab T-rEX, Wyatt Technology, Dernbach, Germany) and a DLS (Zetasizer Nano SZ, Malvern) in the given order. A 0.02% (w/v) NaN_3 solution filtered through a 0.1 μm pore size filter was used as the eluent. Prior to injection, the nanoparticle suspensions were concentrated to 3 mg/mL via ultrafiltration by using a membrane with MWCO of 10 kDa and DLS was performed to check that no aggregation occurred during this step. In a typical experiment, parameters were set as: 1) the detector flow rate 0.5 mL/min, 2) 100 μL of samples injected over 10 min at 0.3 mL/min, 3) cross flow rate 2.0 mL/min, and 4) focusing flow rate 2.70 mL/min (focusing step). During the elution step, the cross flow was kept constant at 2.0 mL/min for 0.5 min and then exponentially decreased (exponent = 0.40) to

0.09 mL/min over 30 min, and further exponentially decreased (exponent = 0.90) to 0.07 mL/min over 7 min, and kept constant at this value (0.07 mL/min) for 20 min. A rinse step was finally performed for 2 min, i.e., setting cross flow at 0 mL/min and purge valve on. UV–vis, MALS and refractive index data were analysed using AF2000 software (Postnova Analytics GmbH, Germany) and fitted with a Sphere model to obtain the MW and radius of gyration (R_g) distributions. DLS data were analysed using the Zetasizer Nano software (Malvern). The data were also used to calculate:

1. $\rho = R_g/R_h$ (shape factor). This parameter defines key geometrical characteristics of a colloid. ρ values are given in literature [23] for a variety of particle morphologies. For example, ρ = 0.775 for a hard, uniform sphere, 1.0 for vesicles with thin walls (hollow spheres), close to 1.5 for random polymer coil conformations [23,24].
2. Fractal dimension (D). When applied to particulates, the fractal geometry analysis is another important morphological indicator. For example, aggregation of colloidal suspensions typically produces objects for which the mass can be expressed as fractal power of the size (mass fractals [25,26]), i.e., $M\left(R_g\right) \approx {R_g}^{D_m}$, where D_m (≤3) is the so-called mass fractal dimension of the particle aggregate system [27]. For instance, this parameter takes values greater than 2.5 for densely packed particle aggregates, whereas lower D_m values have been ascribed to more branched structures. Mass fractal dimensions of selected topologies have been calculated and can be found elsewhere [23]. In static light scattering, the expression is often approximated with the angular dependency of scattered intensity $I\left(q\right) \propto q^{-D_m}$ expressed as a function of the scattering vector $q = (4\pi n/\lambda)\cdot\sin(\Theta/2)$ but here it was directly obtained as the slope of the nanoparticle mass vs R_g log–log plot.

siRNA loading. Encapsulation efficiency (EE) values (%) were calculated as EE $(A - B)/A\cdot 100\%$ where A is the amount of siRNA in the feed and B is the amount of non-complexed siRNA. The latter was quantified by separating as-prepared nanoparticles from the supernatant through centrifugation at 13,000 rpm for 60 min, and detecting siRNA in the supernatant with RiboGreen® following the manufacturer's instructions and using a Synergy2 Biotek plate reader.

Atomic force microscopy (AFM). Drops (ca. 35 µL) of the chitosan/HA nanoparticle suspensions were deposited on a clean mica surface and left to dry overnight in Petri dishes at room temperature. A molecular force probe 3D AFM (MFP-3D, Asylum Research, Oxford Instruments, Abingdon, UK) equipped with an OTESPA-R3 cantilever (Bruker, Camarillo, CA, USA) was used to acquire AFM images in air at room temperature in tapping mode. Igor-Pro AFM software (Oxford Instrument, UK) was used to analyse the images.

Nuclease protection assay. The protection effect against nuclease degradation of low-M_W and high-M_W chitosan nanoparticles prepared by ionotropic gelation or direct polyelectrolyte complexation was assayed by gel electrophoresis after nuclease and chitosanase/heparin treatment, as already described in [9]. Briefly, 44 µL of siRNA either loaded in the nanoparticles (25 wt % loading with respect to chitosan, a high siRNA loading for precise gel analysis) or dissolved in water at the same concentration (40 µg/mL) were incubated with 22 µL of a solution of RNAse I (15 mM Tris buffer, 0.3 M NaCl, pH 7.0) at a concentration of 0, 0.33 and 3.33 U (corresponding to 0, 0.5, and 5 U of enzymes per 100 µL of final reaction volume, respectively) at 37 °C for 30 min. The nuclease reaction was then quenched with the addition of 7.6 µL of 1.0% SDS (aq). Afterwards, 3 µL of a 0.084 units/µL solution of chitosanase in 50 mM acetate buffer (pH 5.0) were added to the mixture, and the enzymatic reaction was allowed to occur for 3 h. Finally, 4.7 µL of a solution of heparin (200 mg/mL in nuclease-free water; corresponding approximately to a z-Hep/z-siRNA ratio of 250) were added. The resulting mixture was incubated overnight at 25 °C. After centrifugation (13,000 rpm, 30 min), the nucleic acid released in solution was quantified using polyacrylamide gel electrophoresis (PAGE, 18-well/30 µL, 15% Criterion TM TBE-Urea Gel, Biorad; 70 min, 120 V). Gels were imaged with a UV trans-illuminator (ChemiDoc™ MP System #170-8280) adjusting the exposure time to avoid saturation, and the acquired images were analysed using ImageJ software (v1.49p, http://rsb.info.nih.gov/ij).

Cell studies

HCT-116 and RAW 264.7 cell lines were cultured in complete media (McCoy's 5A or high glucose DMEM, respectively) under standard conditions for cell culture (5% v/v CO_2 in air, 37 °C). Further details of the materials used is provided in Supporting Information File 1, Section SI1.1.2.

Preparation of double-concentrated cell culture growth media. 5.95 g McCoy's 5A powder or 6.75 g of DMEM powder, respectively, were dissolved in 175 mL of distilled water followed by addition of 3 g of HEPES. The pH value was then adjusted to 7.4 by adding 1 M HCl and the volume brought to 195 mL with distilled water. The resulting medium was filtered using disposable sterile filter systems (0.22 µm) and supplemented accordingly (20% v/v FBS, 2% v/v Penicilin-Streptomycin), referred to a final volume of 250 mL. Nanoparticle solutions for cellular experiments were prepared by the addition of a given volume of double-concentrated full growth

medium to an equal volume of double-concentrated nanoparticle dispersion (water).

Cytotoxicity experiments. HCT-116 (20,000 cells/cm^2) and RAW 264.7 (30,000 cells/cm^2) were seeded in 48-well plates and left to adhere overnight (5% v/v CO_2 in air, 37 °C). Cells were then exposed to 0.25 mL of nanoparticle suspensions in full medium (concentration: 0.01–0.5 mg/mL) for 24 h, then determining viability using the CellTiter 96® AQueous One Solution Cell Proliferation Assay (MTS assay). Briefly, cells were washed with PBS and incubated for 1 h at 37 °C in medium containing 5% (v/v) of MTS solution. Cell viability was measured by reading the absorbance values at 490 nm (Synergy2 Biotek plate reader using Gen5 software) and normalized against the total protein content in each well (BCA assay). Please note that any influence of phenol-red was ruled out by using medium as blank and subtracting its absorbance to all wells before calculating metabolic activity.

Quantification of cell uptake. HCT-116 (20,000 cells/cm^2) and RAW 264.7 (30,000 cells/cm^2) were seeded in 12-well plates and left to adhere overnight (5% v/v CO_2 in air, 37 °C). Cells were then incubated with 1 mL of fluorescently-labelled nanoparticles (particles produced with either RITC-labelled chitosan or rhodamine-labelled HA; for their synthesis see Supporting Information File 1, Section SI1.2) diluted to 125 μg/mL at 37 °C for specified incubation times, i.e., 0, 2, 4, 8, 16, and 24 h. Afterwards, cells were washed three times with pre-warmed PBS and lysed in 100 μL RIPA Buffer. The total uptake (combined membrane-bound and internalized materials) was calculated from fluorescence measurements of the cell lysates using a calibration curve from nanoparticle aqueous suspensions diluted in cell lysates (range 0.12–125 μg/mL). Measurements were obtained by using a Synergy2 Biotek plate reader (Ex 540/25, Em 620/40 nm), Gen5 software; top 50% optical position. Uptake results were normalized against the total protein content per well (BCA assay).

Silencing experiments. HCT-116 (20,000 cells/cm^2) and RAW 264.7 (30,000 cells/cm^2) were seeded in 48-well plates and left to adhere overnight (5% v/v CO_2 in air, 37 °C). Cells were pre-transfected for 4 h with 0.25 μg of pGL3 vector encapsulated in Lipofectamine™ LTX according to manufacturer's instructions. After subsequent removal of medium and gentle washing with warmed PBS, 0.25 mL of complete medium containing 0.67 μg of anti-Luc siRNA (200 nM) encapsulated in nanoparticles (125 μg/mL) were added to each well, with anti-Luc siRNA/LTX complex used as a positive control for transfection. Cells were incubated for 4 h with the nanoparticles, then medium was discarded and cells were washed with PBS, and further incubated with 0.25 mL of complete medium for 24 h. Finally, cells were washed with PBS and lysed with Glo-lysis buffer (10 min, 25 °C). The luciferase activity was measured after cell lysate centrifugation (4,500 rpm, 2 min) using the ONE Glo luciferase assay following manufacturer's instructions. The relative luminescence units (RLU) were measured using a Synergy2 Biotek plate reader (Gen5 data acquisition software), and normalized against the total protein content (BCA assay) for each well.

Statistical analysis

Stability and silencing data were analysed using a two-sample *t*-test using the Welch correction (i.e., without assuming equal variance). If $p > 0.05$, no statistical difference was assumed; in the figures * means $p < 0.05$, ** means $p < 0.01$, *** means $p < 0.001$, **** means $p < 0.0001$.

Results and Discussion

Template vs direct complexation: physico-chemical comparison

Similarities

The two preparative methods yielded broadly similar nanoparticles (Table 1). Firstly, no significant difference can be seen in their ζ-potential values (strongly negative). $Chit_{650}$ yielded particles marginally larger than $Chit_{35}$, and the width of the particle size distribution – as assessed with DLS as a stand-alone instrument – was also similar (Figure 1, compare dashed and solid lines). Further, both methods allowed for quantitative siRNA entrapment, and the encapsulation did not significantly affect the nanoparticle size (up to a loading of 25 wt % in relation to chitosan; Figure 1 and Table 1). Last, also the stability of the nanoparticles was similar: the behaviour of the nanoparticles prepared by the direct method upon dialysis, storage and dispersion in different media (Supporting Information File 1, Section SI2 and Figure S1) was comparable to that previously reported by our group for the templated method [18].

Very interestingly, the two preparative methods provided particles with a very similar composition. Here, we have normalized the carbon and phosphorous content to that of nitrogen (last two columns in Table 1). TPP has no carbon or nitrogen, therefore the C/N ratio is a reporter of the chitosan/HA composition (see, e.g., how different this indicator is for chitosan alone and for chitosan/HA), and the P/N ratio is a reporter of the TPP content. Please note that the presence of water in the samples does not affect either of these indicators. Independent of the preparative method, the final particles have the same chitosan/HA ratio (the C/N ratio is indistinguishable) and are devoid of TPP (non-detectable phosphorous, differently from chitosan/TPP particles). The latter point indicates a quantitative displacement of TPP by HA, the driving force of which is the higher avidity of the polysaccharide. For example, the individual phosphate groups of siRNA have most likely the same

Table 1: Physico-chemical characterization of the nanoparticles[a].

	Z-average size (nm)	PDI[b]	ζ-potential (mV)	siRNA loading		C/N[e]	P/N[e]
				Size incr.[c]	EE[d]		
$Chit_{35}$-TPP	166 ± 5	0.17 ± 0.05	+37 ± 1		>99%	6.16 (5.72)	0.48 (0.36)
$Chit_{35}/HA_{templ}$	310 ± 50	0.17 ± 0.06	−38 ± 5	3%	>99%	11.56 (9.71)	nd (0.11)
$Chit_{35}/HA_{dir}$	220 ± 30	0.19 ± 0.07	−39 ± 2	0%	>99%	10.08 (9.28)	nd (0)
$Chit_{650}$-TPP	368 ± 15	0.28 ± 0.01	+50 ± 2		>99%	6.49 (5.72)	0.31 (0.36)
$Chit_{650}/HA_{templ}$	320 ± 30	0.17 ± 0.06	−38 ± 4	6%	>99%	11.91 (9.71)	nd (0.11)
$Chit_{650}/HA_{dir}$	260 ± 40	0.20 ± 0.05	−40 ± 2	0%	>99%	9.7 (9.28)	nd (0)

[a]In deionized water, room temperature, concentration of 1 mg/mL. Data are averages ± standard deviation from three separate preparations. [b]PDI: polydispersity index. [c]% of increase in the nanoparticle Z-average size with a 25 wt % (in comparison to chitosan) siRNA loading. The ζ-potential did not appreciably vary upon siRNA loading (−39 to −41 mV for all chitosan/HA nanoparticles). [d]EE: the encapsulation efficiency of siRNA (expressed in wt % in reference to siRNA feed) refers to a loading of 25 wt % in relation to the amount of chitosan. [e]In brackets the theoretical values, which are obtained assuming that all components are quantitatively entrapped in the particles. Please note that our detection limit for P/N is around 0.07.

affinity for chitosan as those of TPP, but siRNA has surely a larger avidity due to its polymeric structure and therefore it is not displaced by HA. We cannot, however, exclude the siRNA/chitosan interactions to be somehow weakened by the presence of HA. The TPP–HA exchange may also be facilitated by the rather low degree of protonation of chitosan, which make its electrostatic interactions more easily reversible.

Finally, the two processes were similar in terms of the presence of unbound HA. CD44, the HA main biological target, is a saturable receptor [28,29], and the initial binding of HA species with molecular weights greater than 30 kDa to CD44 is described as essentially irreversible [29]. It is therefore important to assess whether in the same formulation HA nanoparticles are present together with unbound HA, which could potentially reduce binding and efficacy of the payload-carrying nanoparticles. Using AFM, we have shown that dialysis through membranes with a large MWCO (1,000 kDa) completely removes soluble HA (Figure 1B, right). When analysing the particles before and after dialysis, we saw no significant difference in HA nanoparticle incorporation (always at least 80 wt % of the feed) between the two chitosan polymers of different MW or the two preparative methods (Figure 1B, left).

Differences

The most important difference between the two methods is that the template process yielded larger nanoparticles, either with or without siRNA. We are inclined to ascribe the larger size to aggregation occurring during the TPP–HA exchange, since the ζ-potential inversion (from the positively charged chitosan/TPP to the negatively charged chitosan/HA nanoparticles) implies intermediate stages with negligible electrostatic repulsion.

We have previously shown that in the template process, and only with low-MW chitosan, the particles show a sort of HA corona [18,19]; this does not occur in the direct complexation (Figure 2).

In our original interpretation, we ascribed the HA corona formation to a difficult penetration of HA into the $Chit_{35}$/TPP matrix, which is more densely cross-linked than $Chit_{650}$/TPP (lower entropic penalty to pay for un-coiling lower-MW macromolecules). In the light of the TPP–HA exchange, this interpretation must be revised: the same factor (better packing of $Chit_{35}$) increases the chitosan concentration in the bulk of the templating particles, potentially leading to a tighter HA complexation in the bulk, but also to a reduced surface charge and to a lighter surface complexation. This should also cause a larger extent of aggregation. Conversely, in the absence of a dense chitosan pre-packing (high-MW chitosan, or direct complexation), no corona would form but the particles would be expected to be less aggregated and more compact. In order to shed further light on the nanoparticle morphology we have employed field flow fractionation, using both static (AF4-SLS) and dynamic (AF4-DLS) light scattering detectors. In addition to more accurate size distributions due to the fractionation prior to the in-line analysis, this combination provides also information about the colloid compactness through parameters such as their average radius of gyration R_g (it depends on the mass distribution), the shape factor ρ defined as the R_g/R_H ratio, and the mass fractal dimension D_m defined as the exponent in the relation between mass of a colloidal object M and its R_g, $M \propto (R_g)^{D_m}$. The last two parameters are particularly important: A) ρ = 0.77 for a perfect sphere, ρ = 1.15–1.2 for random coils under θ-conditions and increasing with increasing solvation [30], i.e., it typically increases with decreasing compaction and statistical fluctuations. B) D_m expresses the scaling between the mass of a colloid and its dimension, therefore is a direct measure of its compactness; for example, for a “dense solid” colloid, its value will approach 3, while its values decrease for aggregates, and

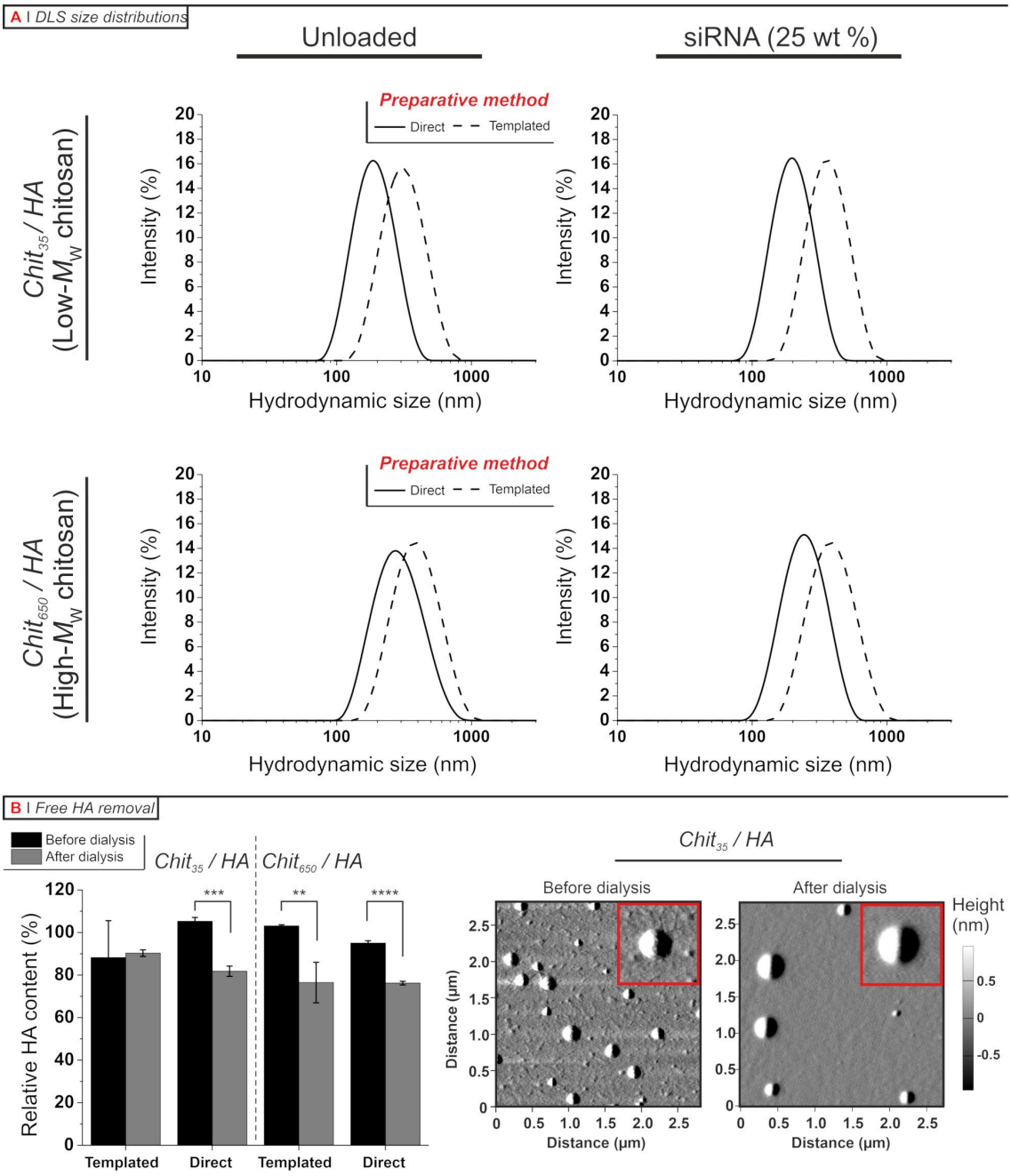

Figure 1: A) Size distribution of chitosan/HA nanoparticles (1 mg/mL, deionized water) prepared from 35 (top) and 650 (bottom) kDa chitosan using a templated (dashed lines) or direct (solid lines) complexation in the absence (left) or presence (right) of siRNA (25 wt % in relation to chitosan). In this and later figures $Chit_{35}$ and $Chit_{650}$ are, respectively, referred to as low-M_W and high-M_W chitosan to avoid the use of subscripts for a better readability. B) Quantification of free HA after nanoparticle preparation. Left: The HA content of the different nanoparticle formulations (1 mg/mL, deionized water) was measured by capillary electrophoresis before and after dialysis (MWCO = 1,000 kDa). Results are expressed as the relative amount of complexed HA (incorporated in the nanoparticle) relative to the total amount of HA in the nanoparticle feed (n = 3). Right: AFM amplitude images of (low-M_W chitosan) nanoparticles after dialysis showing the complete removal of unbound HA (absence of "debris" material on the mica surface).

therefore this parameter has been used for aggregation studies of, e.g., liposomes [26], amphiphilic polymers [31], and gold nanoparticles [32]. We refer the reader to the excellent review of Bushell in 2002 for an extensive physico-mathematical explanation of D_m [25].

Firstly, the AF4-DLS curves (Figure 3A, left) largely overlapped. Thus, it appears that DLS alone (Figure 1) overestimated the difference in hydrodynamic size between the two preparative methods (and overestimated the size itself, possibly due to the disproportionate weight of the scattering from large

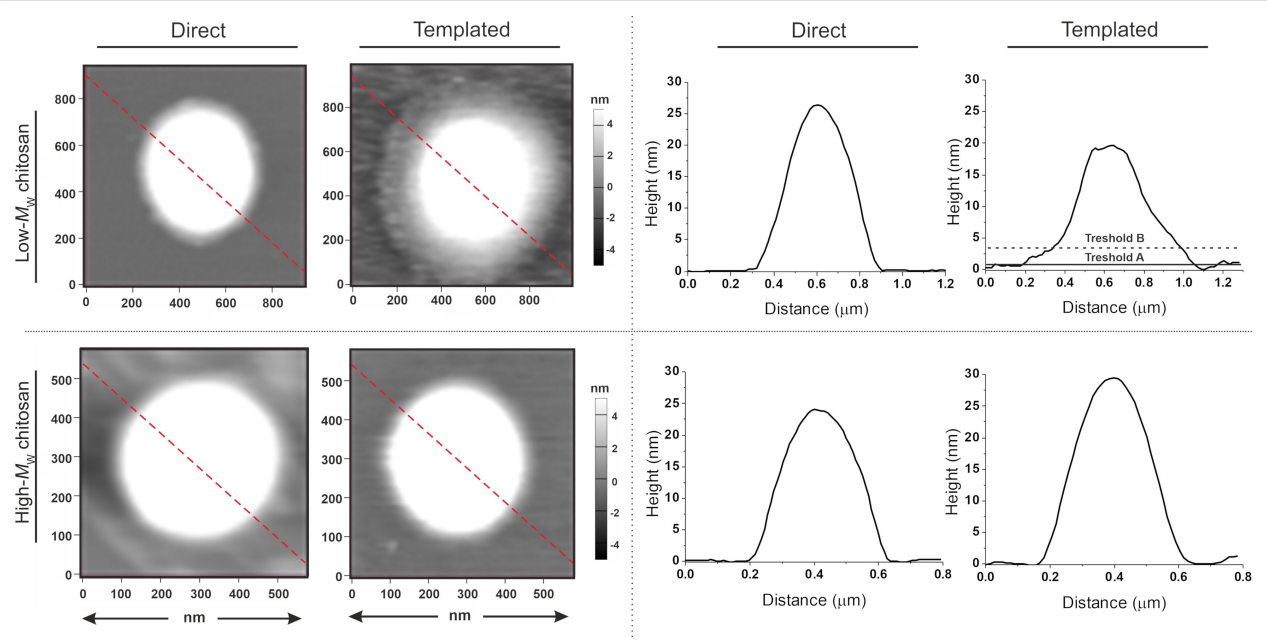

Figure 2: Tapping-mode AFM height images of chitosan/HA dried on mica (left) and height profiles corresponding to the red dashed lines in the images (right). For the templated $Chit_{35}$/HA nanoparticles two thresholds were used to calculate separately the volume distributions of the nanoparticle corona and core. Please note that the HA corona is even more visible in amplitude images, see Supporting Information File 1, Figure S2.

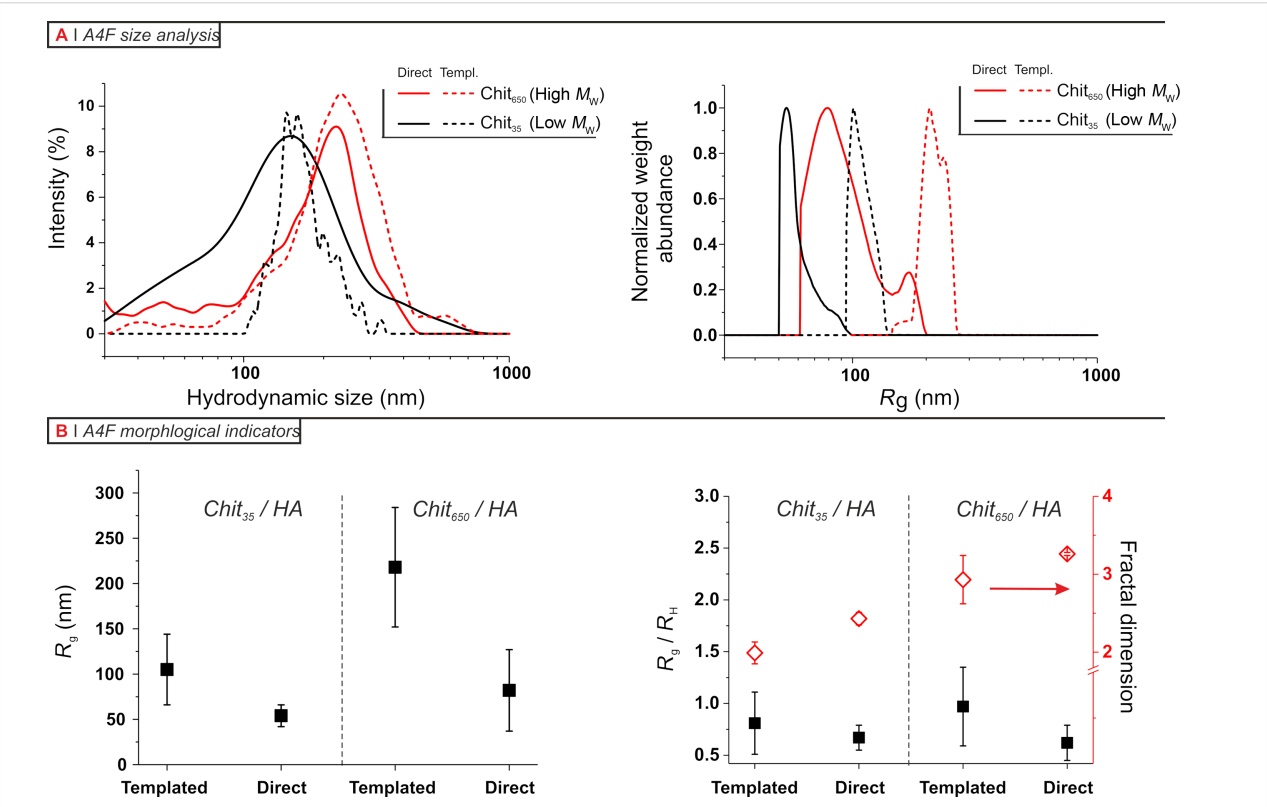

Figure 3: A) Asymmetric-flow field flow fractionation (AF4) characterization of nanoparticles (see also Supporting Information File 1, Figure S3 for examples of AF4 elugrams). Left: hydrodynamic size distributions from in-line DLS. Right: R_g distributions from in-line SLS. B) Morphological indicators obtained from AF4 analysis. Left: Weight-average R_g values and Right: mass fractal dimension and R_g/R_h ratio for the four kinds of chitosan/HA nanoparticles. Please note that the error bars in the first graph are the widths at half maximum of the log-normal fit of the differential R_g distributions, in the second graph are the errors of the fitting.

nanoparticles). Yet, small differences in this sense can still be seen and indeed this effect is confirmed by the distributions obtained through AF4-SLS (Figure 3A, right).

Secondly, there is a clear indication for a less compact structure of the templated particles, which have larger R_g values (Figure 3B, left) but a hydrodynamic size still relatively comparable to that of the particles obtained through direct complexation. This is summed up by the aspect ratio values (black squares in Figure 3B, right): ρ ranges from 0.6–0.8 for nanoparticles from direct complexation (essentially compact spheres), to 0.8–1 for the products of the template process; the latter are compatible with particles having a spherical shape but a relatively looser internal structure.

An even clearer result is provided by the D_m values (red diamonds in Figure 3B, right). D_m is always ≥2, indicating a spherical shape (in agreement with ρ values), but is considerably smaller for the template process. Interestingly, chitosan/HA and chitosan/TPP nanoparticles from direct complexation have almost identical D_m values (both around 3.1–3.2 for $Chit_{650}$ and 2.4–2.5 for $Chit_{35}$), indicating a similarly compact nature. On the contrary, the template chitosan/HA particles had significantly lower D_m values, in particular $Chit_{35}$. This means that the particles displaying an HA corona are also the least compact, which corroborates the above hypothesis for the corona formation (small compact particles connected by loosely bound HA).

Evaluation of CD44-targeted delivery of siRNA

One of the most fundamental aspects to a successful intracellular siRNA delivery is the ability of the carrier to protect the cargo from enzymatic degradation to allow its release in the cytoplasm, where the RNA machinery is located. Hence, as a first step we ruled out any differences in the protective behaviour of our nanoparticles between preparative methods (Figure 4). Specifically, siRNA-loaded nanoparticles were incubated in the presence of RNAse I at concentrations sufficiently high to degrade partially (at 0.5 U) or completely (at 5 U) the same amount of non-encapsulated nucleic acid (labelled as "free" in Figure 4). RNA was then decomplexed by enzymatically digesting chitosan and further displacing its fragments with heparin (more strongly anionic than HA and RNA), and finally analysed by gel electrophoresis. The central point is that all nanoparticles protected their payload from RNAse.

Secondly, we evaluated the biocompatibility of these nanoparticles using two cellular models. These models were murine RAW 264.7 macrophages (already used in our previous studies with chitosan-TPP/HA nanoparticles [19,20]) due to their relatively high CD44 expression [33], and the human colorectal HCT-116, a CD44-overexpressing colorectal line the suitability of which for HA-based targeting therapies has already been reported [22,34,35]. It is worth mentioning that HCT-116 apparently shows a lower CD44 expression (see Supporting Information File 1, Section SI5), but this does not imply a lower CD44 endocytic activity.

The cytotoxicity of the nanoparticles was assessed using the MTS assay, a colourimetric method that measures mitochondrial metabolic activity (data normalized against the protein content, assumed roughly proportional to the cell number). Independently of the preparative method and the MW of chitosan, all formulations had a negligible effect on the cell viability up to 0.5 mg/mL in both models (Figure 5A). Despite the fragile nature of macrophages, the low toxicity seen for HA-coated chitosan nanoparticles is in accordance with what reported in

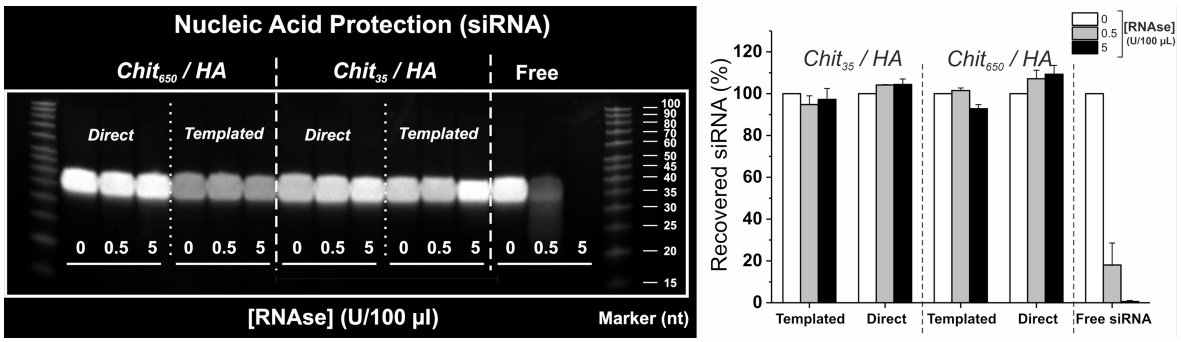

Figure 4: Protection of siRNA payload from enzymatic degradation. Left: PAGE analysis of entrapped siRNA after nanoparticle incubation with increasing concentrations of RNAse I, followed by quenching of nucleases, chitosanase and heparin treatment. Free, non-encapsulated siRNA was used as a control. The siRNA content in the particles was 25 wt % in relation to chitosan. Right: Plot of the band intensities relative to the signal of the negative control (no RNAse I treatment) for each formulation. Error bars represent standard deviation (n = 3). Please note that results are normalized against the amount of siRNA released from formulations incubated with no RNase I (non-degraded) to account for any dilution factor or lose of material, e.g., note the fainter bands detected for templated high-M_W chitosan nanoparticles.

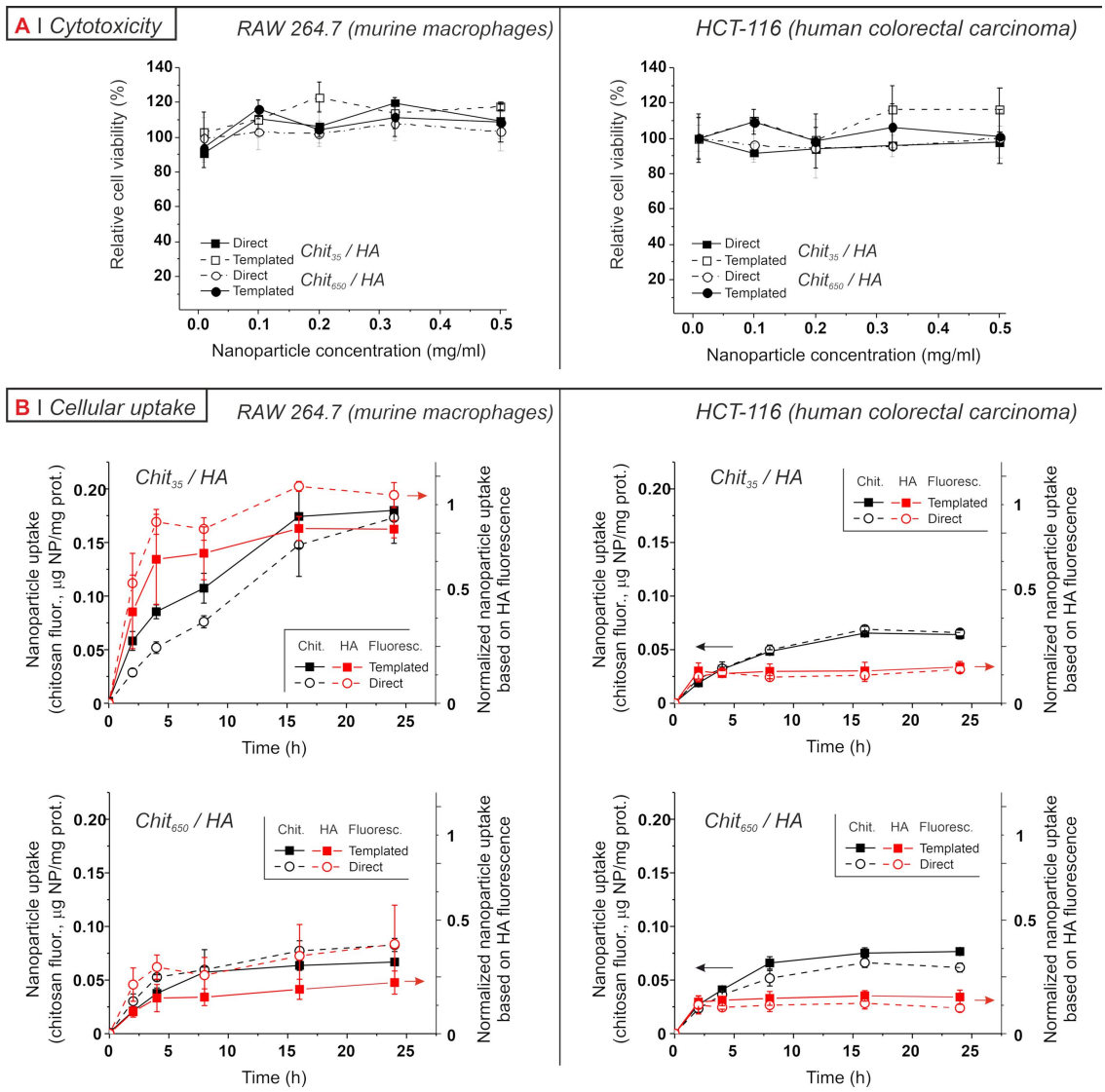

Figure 5: A) Relative cell viability of RAW 264.7 (left) and HCT-116 (right) cell lines as a function of nanoparticle concentrations (0.01–0.5 mg/mL, 24 h incubation). Percentages are relative to the normalized mitochondrial activity of untreated cells. The differences between preparative methods are not statistically significant. B) The cellular uptake of nanoparticles was followed by measuring the fluorescence of lysates after cells were incubated with particles containing RITC-labelled chitosan or rhodamine-labelled HA. The lysate fluorescence is a quantitative measure of the nanoparticle uptake (bound and internalized particles), and the data are first calibrated with nanoparticles dispersed in cell lysates to obtain quantities of nanoparticles and then normalized against the cell protein content to finally obtain values of the amount of nanoparticles uptaken "per cell". It is noteworthy that for any given data point the uptake measured from HA-associated fluorescence was consistently lower than that obtained via chitosan fluorescence. Since the fluorophores are essentially the same, this may be due to a detachment of the two components upon uptake, because the quantum yield of the fluorophores in isolated chitosan or HA and in nanoparticles may be significantly different. For comparison, we have therefore further normalized the data from HA fluorescence to the average value of $Chit_{35}$/HA nanoparticles in RAW macrophages after 24 h. In all graphs, error bars represent standard deviation (n = 3).

RAW 264.7 macrophages for other HA-based nanomaterials, such as HA-coated liposomes [36] and a library of lipid nanoparticles with surface-anchored HA [37], or chitosan-based carriers, such as mannosylated chitosan nanoparticles [38] or siRNA-entrapped chitosan nanoparticles (with or without TPP) [39]. The innocuous character of HA-coated chitosan nanoparticles in HCT-116 is also consistent with previous studies on HA-based cationic nanocarriers [40,41].

Next, we analysed the nanoparticle uptake in the two cell lines for up to 24 h; we tracked the fluorescence associated to nanoparticles in cell lysates, which accounts for both membrane-bound and internalized materials [10]. We used fluorescently labelled chitosan and HA, producing nanoparticles selectively containing one labelled polymer. Following either chitosan- or HA-associated fluorescence (respectively black and red symbols in Figure 5), we observed qualitatively similar uptake

kinetics, which is a sign that the two components are mostly internalized together and therefore indicates a reasonable stability of the particles until binding to cells. However, it is also clear that nature and extent of particle–cell interactions are cell type-dependent, see for example the different kinetics of $Chit_{650}$/HA in macrophages and in HCT-116.

It is immediately apparent (Figure 5B) that the uptake kinetics was not influenced by the preparative method. With both cell lines and both chitosan MW, the particle uptake kinetics showed evidence of saturation and was not affected by the preparative method. We have previously reported that RAW 264.7 macrophages take up differently nanoparticles prepared from chitosan with low and high molecular weight, with the former reaching considerably lower saturation levels than the latter, although more rapidly [14]. We then ascribed this effect to a higher avidity of HA for its receptors provided by the corona arrangement, summarized as "stronger interactions – more receptors clustered around each particle – fewer particles internalized". Here, we confirmed this behaviour in macrophages. However, A) it was recorded also for directly complexed particles (= it is a general feature of $Chit_{35}$/HA complexes), and B) the uptake of all particles in HCT-116 was essentially identical. These two observations seem to discount both the hypothesis of the HA corona as a controlling factor and the possibility that particle compactness plays any major role.

In order to have a more complete overview of the nanoparticle behaviour, we have evaluated their silencing efficiency when loaded with a functional anti-luciferase (anti-Luc) siRNA. To this end, cells were first pre-transfected with a luciferase-encoding plasmid (pGL3) using low-toxicity Lipofectamine (LTX) as a vector, and then treated with anti-Luc siRNA vectored either in nanoparticles or LTX complexes in order to silence luciferase expression. For comparison purposes, we reproduced the experimental conditions previously reported by our group for templated chitosan/HA particles (i.e., delivery of 200 nM anti-Luc per well) on RAW 264.7 macrophages, which are difficult to transfect [15].

Under these conditions, we observed a distinct cell-specific behaviour: A) in macrophages (Figure 6, left), templated $Chit_{35}$/HA particles were internalized less but silenced more than templated $Chit_{650}$/HA, as previously reported [14,15]. The directly complexed $Chit_{35}$/HA particles were again internalized less than $Chit_{650}$/HA, but the increase in silencing was marginal. B) In HCT-116 (Figure 6, right), the preparative method played little role. Very differently from macrophages, $Chit_{35}$/HA particles were internalized similarly $Chit_{650}$/HA, but silenced less.

Besides the obvious conclusion that $Chit_{650}$/HA particles are suitable for HCT-116 and $Chit_{35}$/HA particles are suitable for macrophages, the overall behaviour seems rather erratic, but there are directions for a logical explanation.

First, the two cell lines surely differ in CD44 expression, clustering and endocytic role. For example, HCT-116 cells massively express CD44, both in its standard and variant forms [42]. Their "HA receptor cocktail" may trigger internalization processes with conditions that favour the endosomolytic properties of high-MW chitosan. High-MW polycations should, in principle, be better at membrane disruption. RAW macrophages, on the contrary, may bind and internalize HA through a

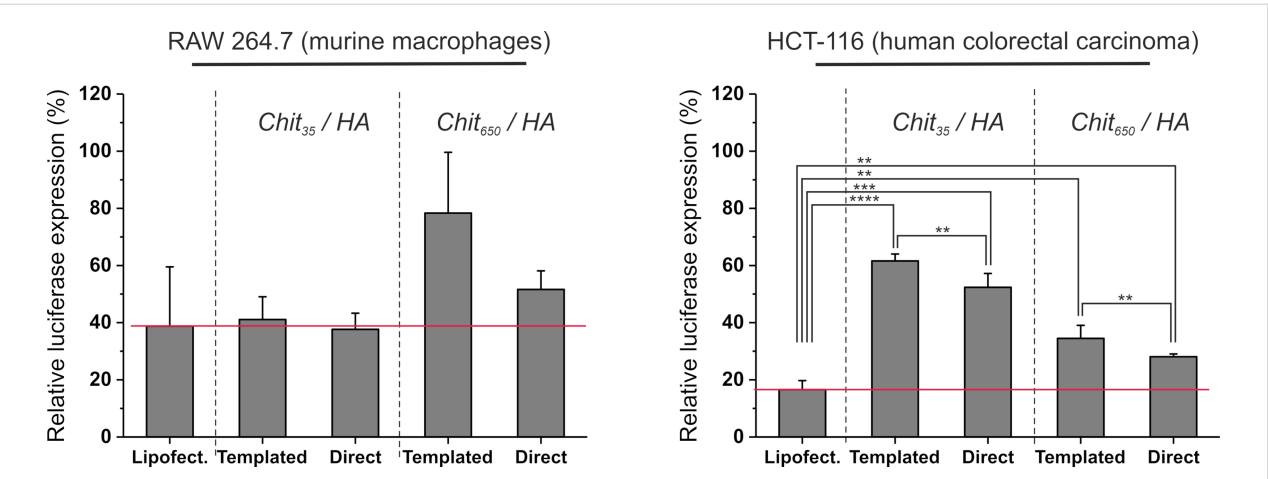

Figure 6: siRNA-mediated luciferase silencing using nanoparticles obtained via a templated or direct complexation method. The results are expressed as the percentage of luciferase expression relative to the average RLUs of the negative control (i.e., cells pre-transfected with the pGL3 plasmid DNA, without anti-Luc siRNA treatment) (n = 3). Statistical analysis (T-test, two-tailed) showed no significant differences between preparative methods in RAW macrophages, but a somehow better silencing efficiency of direct complexation (and of high-M_W chitosan) in HCT-116.

different "receptor cocktail". For example, these macrophages are commonly used as a toll-like receptor 4 (TLR4)-positive model in inflammation, and HCT-116 as a model for limited TLR4 signalling [43]. Further, TLR4 is involved in the modulation of lipid raft-associated interactions between HA and CD44 [44,45]. Therefore, a receptor such as TLR4 might be involved in HA internalization in RAW macrophages and not in HCT-116. In RAW 264.7 macrophages CD44 has been described not only as an endocytic receptor, but also as a fully competent phagocytic receptor for the digestion of large particles [46].

It is therefore not unlikely that the macrophagic "HA receptor cocktail" triggers intracellular processes different from those in HCT-116; for example, in macrophages siRNA liberation from its complex with chitosan may be the controlling step, instead of endolysosome disruption. Under this hypothesis, $Chit_{35}$ has a lower avidity for siRNA [4], and this may be the reason for its better performance. Following this hypothetical train of thoughts, the very low silencing efficiency of templated $Chit_{650}$/HA would be ascribed to the template process yielding aggregates of smaller and possibly more compact particles that may be particularly resistant to siRNA liberation. Indeed, templated particles in general showed a poorer silencing performance, albeit in some cases only slightly. In short, a different controlling factor (e.g., membrane disruption for HCT-116, siRNA release for RAW macrophages) may explain most of the differences seen in the silencing activities.

Conclusion

We have evaluated the effects of the preparative method of nanoparticles (template vs direct, with two chitosan polymers of different MW) on the morphology of the nanoparticles and on their in vitro performance as carriers.

Although both processes are characterized by a simple add–mix procedure of aqueous solutions, the absence of purification (dialysis) steps in the direct complexation method is particularly appealing. Besides the shorter time of preparation, this allows for an easier implementation of aseptic manufacturing conditions.

Moreover, on one hand, the two production processes provided broadly similar nanoparticles with sizes always well below 500 nm, HA on their surface, negligible toxicity, and effective encapsulation and protection of RNA. On the other hand, these particles differed in their dimensions and, above all, in their internal compactness. The template process implied significant aggregation, which we ascribed to the step of TPP–HA exchange. Confirming our previous observations, templated particles based on low-MW chitosan showed an HA corona, which was not present in the directly complexed particles with the same composition.

The in vitro performance was assessed by monitoring uptake and silencing efficiency of both nanoparticle components (HA and chitosan) in two cell lines, leading to the following observations: A) a better silencing performance for low-MW chitosan in RAW macrophages, and for high-MW chitosan in HCT-116; B) a higher uptake of high-MW chitosan-based particles in RAW macrophages, which – together with the poor silencing efficacy – may suggest the involvement of a different internalization machinery; C) the irrelevance of the HA corona for the nanoparticle uptake, and the slightly poorer performance of templated particles in silencing. However, one should extrapolate the irrelevance of HA corona for cell–nanoparticle interactions: in a previous study we have demonstrated that it does allow for a better exposure of HA-bound ligands [16].

The more general conclusion, however, is the strongly cell-dependent nature of the effects that nanoparticle morphology may have on nanoparticle internalization and silencing performance (see point A in the previous paragraph). This highlights the need of a better understanding of the cell-specific binding and trafficking event for a prediction of the therapeutic efficacy of a nanocarrier.

Supporting Information

Supporting Information File 1

Additional experimental description and data.
[https://www.beilstein-journals.org/bjnano/content/supplementary/2190-4286-10-250-S1.pdf]

Acknowledgements

Kyowa Hakko Bio Italia S.r.l. (Milan, Italy) is gratefully acknowledged for the provision of hyaluronic acid. AFM images were acquired at the BioAFM Facility of the University of Manchester.

Funding

This study was supported by EPSRC (PhD studentship for Mr. Rios de la Rosa as part of the North-West Nanoscience (NoWNano) Doctoral Training Centre, EPSRC grant EP/G03737X/1). The Bioimaging Facility of the Faculty of Life Sciences (University of Manchester) is maintained with grants from BBSRC, Wellcome Trust, and the University of Manchester Strategic Fund. The research leading to these results has received funding from the European Community's Seventh Framework Programme (FP7/) under grant agreements nos. 251420 (Replixcel) and 60173 (Univax).

ORCID® iDs

Julio M. Rios de la Rosa - https://orcid.org/0000-0001-9363-1458
Maria Pelliccia - https://orcid.org/0000-0002-8541-520X
Roberto Donno - https://orcid.org/0000-0003-3175-2742
Annalisa Tirella - https://orcid.org/0000-0002-3743-3593
Nicola Tirelli - https://orcid.org/0000-0002-4879-3949

References

1. Bernkop-Schnürch, A.; Dünnhaupt, S. *Eur. J. Pharm. Biopharm.* **2012,** *81,* 463–469. doi:10.1016/j.ejpb.2012.04.007
2. Ragelle, H.; Vandermeulen, G.; Préat, V. *J. Controlled Release* **2013,** *172,* 207–218. doi:10.1016/j.jconrel.2013.08.005
3. Lai, W.-F.; Lin, M. C.-M. *J. Controlled Release* **2009,** *134,* 158–168. doi:10.1016/j.jconrel.2008.11.021
4. Nordtveit, R. J.; Vårum, K. M.; Smidsrød, O. *Carbohydr. Polym.* **1994,** *23,* 253–260. doi:10.1016/0144-8617(94)90187-2
5. Prabaharan, M.; Mano, J. F. *Drug Delivery* **2004,** *12,* 41–57. doi:10.1080/10717540590889781
6. Grenha, A. *J. Drug Targeting* **2012,** *20,* 291–300. doi:10.3109/1061186x.2011.654121
7. Desai, K. G. *Crit. Rev. Ther. Drug Carrier Syst.* **2016,** *33,* 107–158. doi:10.1615/critrevtherdrugcarriersyst.2016014850
8. Garcia-Fuentes, M.; Alonso, M. J. *J. Controlled Release* **2012,** *161,* 496–504. doi:10.1016/j.jconrel.2012.03.017
9. Lallana, E.; Rios de la Rosa, J. M.; Tirella, A.; Pelliccia, M.; Gennari, A.; Stratford, I. J.; Puri, S.; Ashford, M.; Tirelli, N. *Mol. Pharmaceutics* **2017,** *14,* 2422–2436. doi:10.1021/acs.molpharmaceut.7b00320
10. Liu, X.; Howard, K. A.; Dong, M.; Andersen, M. Ø.; Rahbek, U. L.; Johnsen, M. G.; Hansen, O. C.; Besenbacher, F.; Kjems, J. *Biomaterials* **2007,** *28,* 1280–1288. doi:10.1016/j.biomaterials.2006.11.004
11. de la Fuente, M.; Seijo, B.; Alonso, M. J. *Invest. Ophthalmol. Visual Sci.* **2008,** *49,* 2016–2024. doi:10.1167/iovs.07-1077
12. Deng, X.; Cao, M.; Zhang, J.; Hu, K.; Yin, Z.; Zhou, Z.; Xiao, X.; Yang, Y.; Sheng, W.; Wu, Y.; Zeng, Y. *Biomaterials* **2014,** *35,* 4333–4344. doi:10.1016/j.biomaterials.2014.02.006
13. Sarmento, B.; Ribeiro, A.; Veiga, F.; Sampaio, P.; Neufeld, R.; Ferreira, D. *Pharm. Res.* **2007,** *24,* 2198–2206. doi:10.1007/s11095-007-9367-4
14. Almalik, A.; Benabdelkamel, H.; Masood, A.; Alanazi, I. O.; Alradwan, I.; Majrashi, M. A.; Alfadda, A. A.; Alghamdi, W. M.; Alrabiah, H.; Tirelli, N.; Alhasan, A. H. *Sci. Rep.* **2017,** *7,* 10542. doi:10.1038/s41598-017-10836-7
15. Rios de la Rosa, J. M.; Tirella, A.; Gennari, A.; Stratford, I. J.; Tirelli, N. *Adv. Healthcare Mater.* **2017,** *6,* 1601012. doi:10.1002/adhm.201601012
16. Nasti, A.; Zaki, N. M.; de Leonardis, P.; Ungphaiboon, S.; Sansongsak, P.; Rimoli, M. G.; Tirelli, N. *Pharm. Res.* **2009,** *26,* 1918–1930. doi:10.1007/s11095-009-9908-0
17. Zaki, N. M.; Nasti, A.; Tirelli, N. *Macromol. Biosci.* **2011,** *11,* 1747–1760. doi:10.1002/mabi.201100156
18. Almalik, A.; Donno, R.; Cadman, C. J.; Cellesi, F.; Day, P. J.; Tirelli, N. *J. Controlled Release* **2013,** *172,* 1142–1150. doi:10.1016/j.jconrel.2013.09.032
19. Almalik, A.; Karimi, S.; Ouasti, S.; Donno, R.; Wandrey, C.; Day, P. J.; Tirelli, N. *Biomaterials* **2013,** *34,* 5369–5380. doi:10.1016/j.biomaterials.2013.03.065
20. Almalik, A.; Day, P. J.; Tirelli, N. *Macromol. Biosci.* **2013,** *13,* 1671–1680. doi:10.1002/mabi.201300302
21. Gennari, A.; Pelliccia, M.; Donno, R.; Kimber, I.; Tirelli, N. *Adv. Healthcare Mater.* **2016,** *5,* 966–976. doi:10.1002/adhm.201500941
22. Yamada, Y.; Hashida, M.; Harashima, H. *Biomaterials* **2015,** *52,* 189–198. doi:10.1016/j.biomaterials.2015.02.027
23. Schärtl, W. *Light Scattering from Polymer Solutions and Nanoparticle Dispersions;* Springer-Verlag: Berlin, Germany, 2007. doi:10.1007/978-3-540-71951-9
24. Burchard, W. *Adv. Polym. Sci.* **1983,** *48,* 1–124. doi:10.1007/3-540-12030-0_1
25. Bushell, G. C.; Yan, Y. D.; Woodfield, D.; Raper, J.; Amal, R. *Adv. Colloid Interface Sci.* **2002,** *95,* 1–50. doi:10.1016/s0001-8686(00)00078-6
26. Roldán-Vargas, S.; Barnadas-Rodríguez, R.; Quesada-Pérez, M.; Estelrich, J.; Callejas-Fernández, J. *Phys. Rev. E* **2009,** *79,* 011905. doi:10.1103/physreve.79.011905
27. Weitz, D. A.; Huang, J. S.; Lin, M. Y.; Sung, J. *Phys. Rev. Lett.* **1985,** *54,* 1416–1419. doi:10.1103/physrevlett.54.1416
28. Ouasti, S.; Kingham, P. J.; Terenghi, G.; Tirelli, N. *Biomaterials* **2012,** *33,* 1120–1134. doi:10.1016/j.biomaterials.2011.10.009
29. Wolny, P. M.; Banerji, S.; Gounou, C.; Brisson, A. R.; Day, A. J.; Jackson, D. G.; Richter, R. P. *J. Biol. Chem.* **2010,** *285,* 30170–30180. doi:10.1074/jbc.m110.137562
30. Tande, B. M.; Wagner, N. J.; Mackay, M. E.; Hawker, C. J.; Jeong, M. *Macromolecules* **2001,** *34,* 8580–8585. doi:10.1021/ma011265g
31. Pippa, N.; Mariaki, M.; Pispas, S.; Demetzos, C. *Int. J. Pharm.* **2014,** *473,* 80–86. doi:10.1016/j.ijpharm.2014.07.001
32. Kim, T.; Lee, C.-H.; Joo, S.-W.; Lee, K. *J. Colloid Interface Sci.* **2008,** *318,* 238–243. doi:10.1016/j.jcis.2007.10.029
33. Vachon, E.; Martin, R.; Plumb, J.; Kwok, V.; Vandivier, R. W.; Glogauer, M.; Kapus, A.; Wang, X. M.; Chow, C. W.; Grinstein, S.; Downey, G. P. *Blood* **2006,** *107,* 4149–4158. doi:10.1182/blood-2005-09-3808
34. Liang, K.; Bae, K. H.; Lee, F.; Xu, K.; Chung, J. E.; Gao, S. J.; Kurisawa, M. *J. Controlled Release* **2016,** *226,* 205–216. doi:10.1016/j.jconrel.2016.02.004
35. Oommen, O. P.; Duehrkop, C.; Nilsson, B.; Hilborn, J.; Varghese, O. P. *ACS Appl. Mater. Interfaces* **2016,** *8,* 20614–20624. doi:10.1021/acsami.6b06823
36. Glucksam-Galnoy, Y.; Zor, T.; Margalit, R. *J. Controlled Release* **2012,** *160,* 388–393. doi:10.1016/j.jconrel.2011.10.008
37. Mizrahy, S.; Raz, S. R.; Hasgaard, M.; Liu, H.; Soffer-Tsur, N.; Cohen, K.; Dvash, R.; Landsman-Milo, D.; Bremer, M. G. E. G.; Moghimi, S. M.; Peer, D. *J. Controlled Release* **2011,** *156,* 231–238. doi:10.1016/j.jconrel.2011.06.031
38. Shilakari Asthana, G.; Asthana, A.; Kohli, D. V.; Vyas, S. P. *BioMed Res. Int.* **2014,** 1–17. doi:10.1155/2014/526391
39. Xiao, B.; Ma, P.; Ma, L.; Chen, Q.; Si, X.; Walter, L.; Merlin, D. *J. Colloid Interface Sci.* **2017,** *490,* 520–528. doi:10.1016/j.jcis.2016.11.088
40. Jiang, B.-P.; Zhang, L.; Zhu, Y.; Shen, X.-C.; Ji, S.-C.; Tan, X.-Y.; Cheng, L.; Liang, H. *J. Mater. Chem. B* **2015,** *3,* 3767–3776. doi:10.1039/c4tb01738b
41. Liang, G.; Zhu, Y.; Jing, A.; Wang, J.; Hu, F.; Feng, W.; Xiao, Z.; Chen, B. *Gene Ther.* **2016,** *23,* 829–838. doi:10.1038/gt.2016.60

42. Tirella, A.; Kloc-Muniak, K.; Good, L.; Ridden, J.; Ashford, M.; Puri, S.; Tirelli, N. *Int. J. Pharm.* **2019,** *561,* 114–123. doi:10.1016/j.ijpharm.2019.02.032
43. Rutkowsky, J. M.; Knotts, T. A.; Ono-Moore, K. D.; McCoin, C. S.; Huang, S.; Schneider, D.; Singh, S.; Adams, S. H.; Hwang, D. H. *Am. J. Physiol. Endocrinol. Metab.* **2014,** *306,* E1378–E1387. doi:10.1152/ajpendo.00656.2013
44. Yamawaki, H.; Hirohata, S.; Miyoshi, T.; Takahashi, K.; Ogawa, H.; Shinohata, R.; Demircan, K.; Kusachi, S.; Yamamoto, K.; Ninomiya, Y. *Glycobiology* **2008,** *19,* 83–92. doi:10.1093/glycob/cwn109
45. Higashi, A.; Dohi, Y.; Uraoka, N.; Sentani, K.; Uga, S.; Kinoshita, H.; Sada, Y.; Kitagawa, T.; Hidaka, T.; Kurisu, S.; Yamamoto, H.; Yasui, W.; Kihara, Y. *Intern. Med.* **2015,** *54,* 2877–2880. doi:10.2169/internalmedicine.54.4749
46. Vachon, E.; Martin, R.; Kwok, V.; Cherepanov, V.; Chow, C.-W.; Doerschuk, C. M.; Plumb, J.; Grinstein, S.; Downey, G. P. *Blood* **2007,** *110,* 4492–4502. doi:10.1182/blood-2007-02-076539

License and Terms

The definitive version of this article is the electronic one which can be found at:
doi:10.3762/bjnano.10.250

BEILSTEIN JOURNAL OF NANOTECHNOLOGY

Rational design of block copolymer self-assemblies in photodynamic therapy

Maxime Demazeau, Laure Gibot, Anne-Françoise Mingotaud, Patricia Vicendo, Clément Roux* and Barbara Lonetti*

Review

Open Access

Address:
Laboratoire des IMRCP, Université de Toulouse, CNRS UMR 5623, Université Toulouse III - Paul Sabatier, 118 route de Narbonne, 31062, Toulouse, France

Email:
Clément Roux* - c.roux@chimie.ups-tlse.fr;
Barbara Lonetti* - lonetti@chimie.ups-tlse.fr

* Corresponding author

Keywords:
intracellular targeting; micelles; photodynamic therapy (PDT); photochemistry; polymer; self-assembly

Beilstein J. Nanotechnol. **2020,** *11,* 180–212.
doi:10.3762/bjnano.11.15

Received: 29 July 2019
Accepted: 04 December 2019
Published: 15 January 2020

This article is part of the thematic issue "Engineered nanomedicines for advanced therapies".

Guest Editor: F. Baldelli Bombelli

Abstract

Photodynamic therapy is a technique already used in ophthalmology or oncology. It is based on the local production of reactive oxygen species through an energy transfer from an excited photosensitizer to oxygen present in the biological tissue. This review first presents an update, mainly covering the last five years, regarding the block copolymers used as nanovectors for the delivery of the photosensitizer. In particular, we describe the chemical nature and structure of the block copolymers showing a very large range of existing systems, spanning from natural polymers such as proteins or polysaccharides to synthetic ones such as polyesters or polyacrylates. A second part focuses on important parameters for their design and the improvement of their efficiency. Finally, particular attention has been paid to the question of nanocarrier internalization and interaction with membranes (both biomimetic and cellular), and the importance of intracellular targeting has been addressed.

Review

Introduction

After Paul Ehrlich, in 1900, had the very first notion of a drug being delivered at will to a specific site [1], researchers have been elaborating different strategies to achieve this goal. The discovery made by Matsumura and Maeda in the late 1990's that some macromolecular therapeutics spontaneously accumulate in inflamed or cancerous tissues, the so-called enhanced permeability and retention (EPR) effect [2,3], constituted the triggering factor for the development of a whole new part of medicine, namely nanomedicine. Indeed, the observed spontaneous accumulation was explained by the existence of disjunctions between endothelial cells in the proximity of inflamed and cancerous tissues, which enable entities smaller than these gaps

to leave the bloodstream. Secondly, defects of the lymphatic system in tumors prevent these macromolecular therapeutics to be cleared from the tumor, giving them additional time to release their active cargo. This was the first example of targeting tumor tissues, exploiting only the size of the therapeutics, and is usually referred to as passive targeting. At that time, researchers got on the lead to develop intravenous nanocarriers of appropriate size (typically 20–200 nm) to benefit from this EPR effect without being cleared too rapidly through kidneys [4]. This implied a required blood circulation time of at least 24–48 h, which is the time necessary for the EPR effect to occur [5]. However, the first nanocarriers were observed to be rapidly cleared from the body or accumulated in the liver or the spleen [4]. The reason was that they were detected as foreign bodies and taken care of by opsonins, leading to their handling by the mononuclear phagocyte system. Carriers avoiding detection by opsonins had then to be developed and very common polymers, namely poly(ethylene glycol) (PEG) or poly(ethylene oxide) (PEO), were found to fulfil this requirement [6]. In parallel to this development of stealth nanocarriers, polymer chemistry had progressed strongly with the emergence of controlled polymerization. After the discovery of so-called living polymerization (polymerization without any transfer nor any termination reaction) in the 1950's, the development of controlled radical polymerization in the 1990's provided polymer scientists with a range of chemical tools to synthesize polymers and copolymers exhibiting various architectures, from block and gradient to grafted polymers [7]. Designing new nanocarriers exhibiting an external shell based on PEG and a core that could be either hydrophobic or a polyelectrolyte enabled the creation of numerous systems [8]. Depending on their structure, copolymers may also form self-assemblies. This is typically the case for amphiphilic block copolymers, which can form in aqueous solution polymer nanoobjects such as micelles or vesicles. The driving forces of this assembly are a loss of entropy during the self-assembly and different interactions acting on the monomer units of the polymer. Whereas polymer/polymer interactions are favored for the hydrophobic block, interactions between the hydrophobic block and water are strongly disfavored, leading to the isolation of the hydrophobic block into core or membranes [9]. In the last twenty years, thousands of papers have been published on this topic and the reader is referred to recent reviews [10-14]. Basically, the desired properties of an ideal intravenous polymer nanocarrier are biocompatibility, stealthiness, optimal size (20–200 nm), polymer/drug affinity compatible with good encapsulation and release, and a design compatible with the targeted organ [4] (this includes the possible crossing of biological barriers).

The aim of this review is to focus on the benefits provided by block copolymers in photodynamic therapy (PDT), as described schematically in Figure 1 [15]. Its concept lies in the use of photosensitizing molecules that have the ability to transfer their energy to oxygen upon irradiation, leading to the in situ formation of reactive oxygen species (ROS) and the subsequent killing of the surrounding biological tissue. Photosensitizers are chosen to absorb efficiently in the 600–800 nm range in the so-called phototherapeutic window, where biological components have minimal absorption [16]. Photosensitizers are either small molecules exhibiting polycyclic structures such

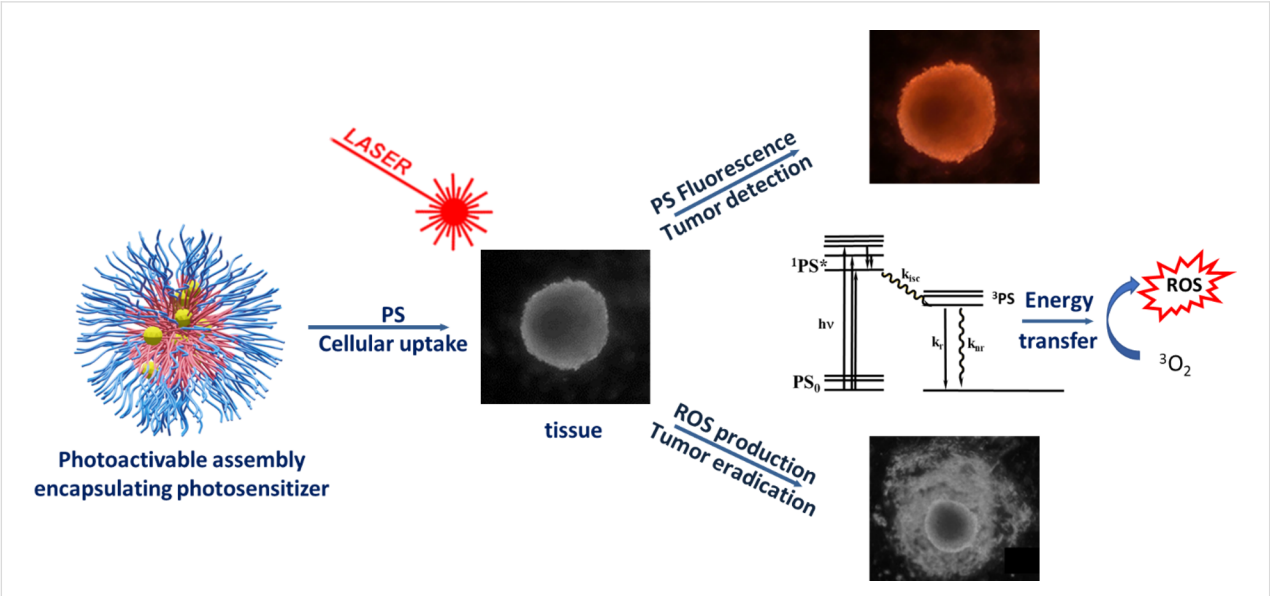

Figure 1: Schematic description of in vitro PDT processes using photosensitizer (PS) encapsulated in a block copolymer self-assembly. ROS: reactive oxygen species.

as porphyrins (Figure 2), inorganic particles such as gold, or so-called upconverting nanoparticles. Developed in its modern form by Dougherty in the 1970's [17], PDT is currently clinically employed in dermatology (e.g., for actinic keratinosis), ophthalmology (e.g., for age-related macular degeneration) or oncology (e.g., for skin, retina, bladder, gastronintestinal, prostate, lung, head and neck cancers). However, as reported by Zhang et al. in a recent review [18], clinical development of PDT remains somewhat limited because of various challenges, ranging from photosensitizer formulation, light dosimetry, to planning and monitoring the treatment [15,18-22]. Some of these points have been recently reviewed: ideal photosensitizers [23], challenges in formulating photosensitizers, and choosing the right light dosimetry [24], as well as monitoring the treatment response [25]. Among all these, the adaptation of light source and dosimetry is currently a very active field. Indeed, protocols adapting the irradiation are tested based on daylight or continuous [26] low irradiation, or using special devices such as fabrics [27] or catheters. The light sources are also diversified from lasers (range of 1–7 W) to diode lasers (2–2.5 W) or LEDs enabling the use of much lower energies. Another point raising much interest in nanomedicine is linked to an optimized biological model that enables to limit in vivo experiments in accordance with the "3 R's" rule of animal testing ethics (the "3 R's" stand for replacement, reduction and refinement aiming at limiting the number of in vivo experiments requiring the sacrifice of animals). 3D systems such as spheroids or cell-derived matrices and using microfluidics have thus been suggested for PDT [28,29].

Based on this existing literature, this review will first present the state-of-the-art (typically since 2014) of block copolymers used for PDT. However, our aim is also to provide an analysis of the methods already used or applicable to improve the efficiency of the nanocarriers. This will be the subject of the second part. A third part will focus on the interactions between the vectors with the cell membrane, either in its native form or in biomimetic models. Finally, cellular entrance processes and intracellular targeting will also be described, showing possible intracellular targeting methods as well as the use of irradiation to promote drug delivery (photochemical internalization).

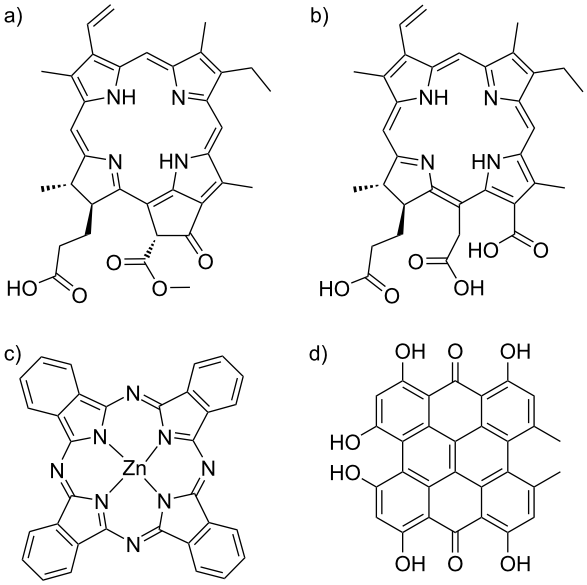

Figure 2: Chemical structures of four molecular photosensitizers commonly used: a) pheophorbide a; b) chlorin-e6; c) zinc phthalocyanine; d) hypericin.

Block copolymers used for vectorization of photosensitizers

Most of the used photosensitizers are highly hydrophobic and have the tendency to aggregate in aqueous environments, which is detrimental for their effectiveness in PDT. Block copolymer nanoassemblies offer the unique possibility to protect the photosensitizer in a hydrophobic environment (as described in Figure 3) and to prevent the aggregation. At the same time, they improve the biodistribution, pharmacokinetics and photochemi-

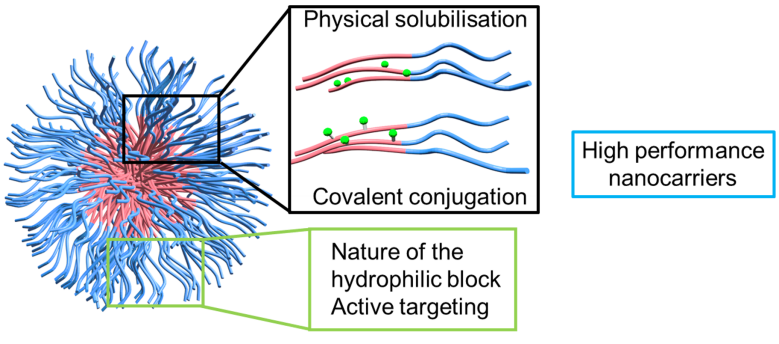

Figure 3: Schematic representation of the strategies used for delivery of photosensitizers using block copolymer self-assemblies.

cal reactivity of the photosensitizer. Thus, typical PDT side effects, i.e., patient skin photosensitivity, can be avoided.

The hydrophilic block of the copolymers will influence the interactions with the surrounding biological media and, in particular, will play a role in the distribution in the body and in cells. The properties of the hydrophobic block can be tailored in order to guarantee a good insertion of the photosensitizer in the nanoobjects and confer the nanovectors with specific functionalities.

The development of polymer engineering has allowed for the design of sophisticated structures that can be varied at will. In the following section we will discuss the block copolymer structures that have been proposed in the literature for PDT in the last years. The chemical structures of some key blocks used for self-assemblies are described in Figure 4. We will first present the structures for the hydrophobic block and then the ones for the hydrophilic block. In the former case, the photosensitizer can be simply solubilized in the interior of the self-assemblies or covalently linked to the copolymer backbone.

Physical solubilization of the photosensitizer

The structures, features and applications of block copolymers used for the physical solubilization of photosensitizers are described in this section and summarized below in Table 1. Most commonly applied are biocompatible, nontoxic and FDA-approved copolymers, such as pluronics [30-35] or biodegradable

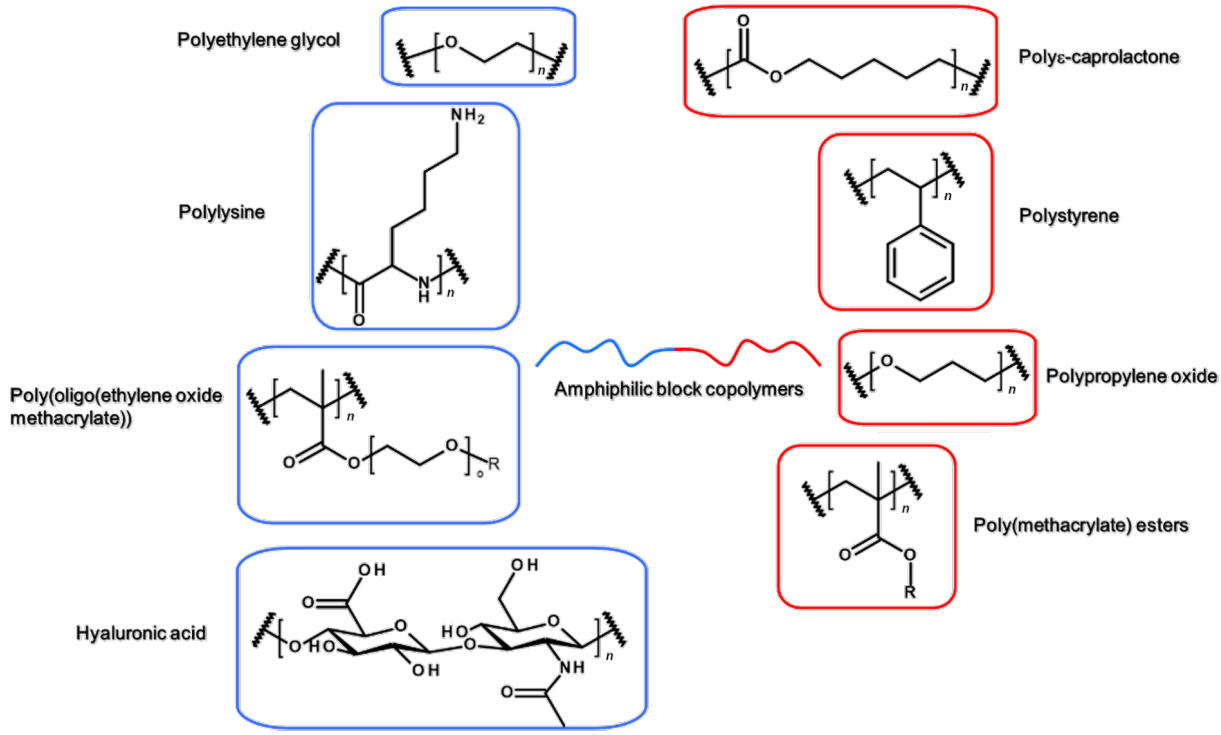

Figure 4: Chemical structures of the main blocks commonly described in recent literature.

Table 1: Passive targeting and photosensitizers solubilized in the hydrophobic core. PIC: poly ion complex; PS: photosensitizer, FI: fluorescence imaging; PCI: photochemical internalization; PA: photoacoustic imaging; PTT: photothermal therapy.

block copolymer	specific feature	comments	ref
poly(ethylene oxide)-*block*-poly(propylene oxide)-*block*-poly(ethylene oxide)	–	in vitro (cancer lines, bacteria) and in vivo	[30,32-35, 57]
poly(ethylene oxide)-*block*-poly[2-(methylacryloyl)ethylnicotinate]	–	osteosarcoma in vitro and in vivo	[43]
poly(styrene)-*block*-poly(acrylic acid)	–	adenocarcinoma in vitro	[58]

Table 1: Passive targeting and photosensitizers solubilized in the hydrophobic core. PIC: poly ion complex; PS: photosensitizer, FI: fluorescence imaging; PCI: photochemical internalization; PA: photoacoustic imaging; PTT: photothermal therapy. (continued)

poly(butadiene)-*block*-poly(1-methyl-2-vinylpyridiniummethyl sulfate)-*block*-poly(methacrylic acid) and poly(ethylene glycol)-block-poly(L-lysine)	PIC	lung carcinoma, in vitro and in vivo	[59]
poly(ethylene oxide)-*block*-poly(L-lysine), poly(L-lysine)-*block*-poly(ethylene oxide)-*block*-poly(L-lysine)	PIC with PS	HUVEC and lung carcinoma, in vitro	[46,47]
poly(ethylene oxide)-*block*-poly(α,β-aspartic acid)/poly([5-aminopentyl]-α,β-aspartamide)	–	lung carcinoma, in vitro	[48]
poly(ethylene oxide)-*block*-poly(α,β-aspartic acid)	PIC with PS	lung carcinoma, in vitro	[49]
poly(*N*-methyl-2-vinylpyridinium iodide)-*block*-poly(ethylene oxide)	PIC with PS	–	[50,51]
branched polyethylene imine modified with perfluorooctanoic acid	O_2 shuttle	cervix carcinoma, in vitro and in vivo	[60]
haemoglobin-conjugated poly(ethylene oxide)-*block*-poly(acrylic acid)-*block*-poly(styrene)	O_2 shuttle	cervix carcinoma, in vitro	[61]
human serum albumin	O_2 shuttle	adenocarcinoma and colon carcinoma, in vitro and in vivo	[62]
poly(oligo(ethylene oxide)methacrylate)-*block*-poly(β-benzyl-L-aspartate)heptafluorobutylamine substituted	O_2 shuttle	image-guided (FI), liver cancer, in vitro and in vivo	[63]
poly((ethylene oxide)methacrylate-*co*-poly(1*H*,1*H*,2*H*,2*H*-perfluorodecyl methacrylate))	O_2 shuttle	lung carcinoma, in vitro	[64]
poly(oligo(ethylene oxide)methyl ether methacrylate)-*block*-poly(L-lysine)	O_2 production	image-guided (FI), liver and breast cancer, in vitro	[65]
methoxy-poly(ethylene oxide)-*block*-poly(ε-caprolactone)-benzyl	degradation	macrophages and endothelial cells, in vitro	[40]
poly(ethylene oxide)-*block*-poly(ε-caprolactone)	degradation	colon cancer and carcinoma, in vitro	[37,66,67]
poly(ethylene glycol)-*block*-poly(lactic acid)	degradation		[38]
poly(ethylene glycol)-*block*-poly(D,L-lactide-*co*-benzyl glycidyl ether)	degradation	macrophage and kidney cells, in vitro	[45]
poly(ethylene glycol)-*block*-poly(ε-caprolactone)-*block*-poly[(2-(piperidin-1-yl)ethyl methacrylate]	O_2 independent, pH-responsive	breast cancer, in vitro and in vivo	[36]
catalase/chitosan	O_2 production, pH-responsive	carcinoma, in vitro and in vivo	[68]
BSA/poly(allylamine hydrochloride)	O_2 production, pH-responsive	breast cancer, in vitro	[69]
poly(ethylene oxide)-*block*-[poly(4,5-dimethoxy-2-nitrobenzyl((5-methyl-2-oxo-1,3-dioxan-5-yl)methyl)carbamate)-*co*-poly(trimethylene carbonate)]	light-responsive	colon cancer, in vitro	[70,71]
poly(ethylene oxide)-*block*-poly(nitrobenzene-containing acetal)	pH- and light-responsive	PCI, cervix carcinoma, in vitro	[72]
arylboronic ester modified amphiphilic copolymer	ROS-responsive	chemo, breast cancer, in vitro and in vivo	[73]
poly(ethylene oxide)-*block*-poly(thioketal-containing 8,8-dimethyl-4,12-dioxo-3,13-dioxa-7,9-dithiapentadecane-1,15-diyldiacrylate)-*block*-poly(ethylene oxide)	O_2 production, ROS-responsive	pancreatic cancer, in vitro and in vivo	[74]
methoxy PEG-Azo-poly(aspartic acid)-imidazole	responsive to ROS and hypoxia	lung cancer, in vitro and in vivo	[75]

Table 1: Passive targeting and photosensitizers solubilized in the hydrophobic core. PIC: poly ion complex; PS: photosensitizer, FI: fluorescence imaging; PCI: photochemical internalization; PA: photoacoustic imaging; PTT: photothermal therapy. (continued)

methoxy poly[(ethylene oxide)-*co*-(aspartic acid)-imidazole]	ROS-responsive	breast cancer, in vitro and in vivo	[76]
adamantane-terminated 6-(5′-(4′-phenoxyl)-10′,15′,20′-triphenylporphyrin) and PEGylated cyclodextrin	redox responsive	breast cancer, in vitro	[77]
human serum albumin (intermolecular disulfide conjugation)	redox responsive	image-guided (FI, PA), PTT, kidney cells, breast cancer, in vitro and in vivo	[78]

aliphatic polyesters, based for instance on ε-caprolactone or lactic acid [36-41]. In particular, the degradation of polyesters in vivo, a combination of both hydrolytic and enzymatic processes, makes them a first choice for the controlled delivery of drugs [42].

Polymers with an acrylate backbone have been also used. The lateral chains can be functionalized in order to introduce functional groups for increasing the affinity to the photosensitizers and the loading efficiency, leading to a 100-fold phototoxicity improvement (in the case of the nicotinate group) [43]. Although not biodegradable, the poly(meth)acrylate backbone is known to be biocompatible, as demonstrated by its long use in opthalmology [44]. Counterintuitively, as it will be detailed in the next section, the introduction of aromatic units is not always an advantage [45].

In order to improve the solubilization of the photosensitizer, other interactions different from hydrophobic interactions have been proposed. For example, electrostatic interactions can improve the photosensitizer loading. Mostly amino acid-based polymers with poly(L-lysine) [46,47] or poly(aspartic acid) [48,49] charged blocks have been employed for poly ion complex assemblies (PICs). This strategy also revealed not to be always appropriate for ROS production and in the case of vinylpyridinium-based block copolymers (with both the pH-insensitive 4-vinilpyridinium and the positively charged *N*-methyl-2-vinylpyridinium iodide), the PIC micelles are even proposed as antioxidants due to the formation of H aggregates between photosensitizer molecules, which hampers the production of singlet oxygen [50,51]. Hence, a careful choice of the hydrophobic block of the copolymer–photosensitizer couple for electrostatic interactions is needed. Interestingly, host–guest complexation of porphyrins in the cavities of cyclodextrin was also proposed as driving force of amphiphilic self-assemblies [52-54].

A main drawback of this kind of nanosystems in which the photosensitizer is simply dissolved in the hydrophobic environment is the possible premature leakage during body circulation (enhanced by degradation) with a consequent lower drug concentration at the target site or other side effects. To tackle this problem, systems responsive to biological signals or containing a covalently linked photosensitizer have been proposed as a solution. The latter strategy will be described below in a dedicated section. In the following, we will focus on responsive photosensitizer-loaded nanosystems.

In such nanosystems, characteristic properties of the tumor microenvironment (endogenous trigger) or an external trigger can act as a stimulus and bring a structural modification of the block copolymer influencing the self-assembly behavior and, consequently, the photosensitizer loading ability. Typical endogenous triggers for pH- and redox-responsive drug delivery are i) acidic tumor tissues (pH 6.0–7.0), endosomes (pH 5.0–6.0) and lysosomes (pH 4.0–5.0) microenvironments, ii) high intracellular glutathione concentration (ca. 10 mM), and iii) very recently, tumor hypoxia (i.e., low oxygen concentrations due to rapid use of blood supply for cancer cell growth) [55]. A typical exogenous trigger is light that can induce the cleavage of covalently linked groups and the solubilization and degradation of the self-assemblies, followed by cargo release [56]. These well-known concepts in nanomedicine have been applied to photodynamic therapy applications.

A responsiveness to the pH value can be induced by inserting ionisable groups (such as amines and carboxylic acids for example) in the polymer backbone in order to induce a change in the nanostructure as a consequence of a change of pH value.

Piperidine groups for example possess a pK_a value close to the acidity of tumor tissues and exhibit a transition from hydrophobic at pH 7.4 to hydrophilic at pH 6.8. As a consequence, micelles increase their diameter and ζ-potential values switch from negative to positive thus accelerating cellular internalization [36]. Poly ion complexes formed thanks to electrostatic interactions between positively charged weak bases and negatively charged weak acids are ideal pH-responsive nanocarriers.

PICs formed by catalase and chitosan showed a stability change in response to the pH value. Between 7.4 in phosphate buffer (comparable to the cytoplasm environment) and pH 5.5 in acetate buffer (comparable to the lysosome environment) the diameter of nanoparticles decreased dramatically in the first 60 min [68].

The reducing power of glutathione (GSH) was exploited in a supramolecular micellar system formed through the host–guest interaction between a PEGylated cyclodextrin and adamantane moieties conjugated to a porphyrin photosensitizer through a disulfide bond. Once the disulfide link was cleaved by glutathione, the porphyrin photosensitizer was released and the size of the nanoobjects in solution increased (Figure 5d) [77]. For a combined photodynamic therapy/photothermal therapy (PDT/PTT) approach, indocyanine green (ICG) has been encapsulated in a protein, namely human serum albumin. First human serum albumin (HSA) is reduced and encapsulates ICG thanks to electrostatic interactions, then the disulfide links are reconstructed for carrier stabilization. This carrier is then glutathione-sensitive and its reduction under in vivo conditions enhanced the PDT efficiency [78].

The cleavage of ROS-responsive groups, such as arylboronic ester lateral groups [73] or thioketal moieties connecting the hydrophilic and hydrophobic blocks [74], were used to alter the hydrophilic/hydrophobic balance and cause the disassembly of the nanoobjects. In another work, amphiphilic block copolymers were obtained by introducing an imidazole functionality on a poly[(ethylene glycol)-*co*-(aspartic acid)] backbone. The imidazole group can act as a singlet oxygen scavenger, which will transform it into a urea moiety. Upon light excitation, the encapsulated chlorin-e6 produces ROS species and the urea formation induces a size expansion of the self-assemblies and a rapid release of the photosensitizer (Figure 5b) [76].

In an original approach, light-responsive self-immolative polymers [70,71] (Figure 5a) based on a polycarbonate backbone have been proposed. Here a photolabile *o*-nitrobenzyl group can be removed through a redox photoisomerization process, leading to the release of a functional amine group inducing intramolecular cyclization. The biological safety of the degradation products has been evaluated.

A quite new concept consists in exploiting hypoxia exacerbated by oxygen consumption during PDT to make nanoobjects work. By combining both hypoxia- and ROS-sensitive groups, a methoxy poly(ethylene oxide)-*block*-poly(aspartic acid) copolymer functionalized with imidazole side chains formed so-called multi-compound micelles. Their internalization could be improved thanks to the deshielding of poly(ethylene oxide) induced by hypoxia which acted on the azobenzene link between the hydrophobic and hydrophilic blocks. Imidazole groups are ROS-sensitive and can be oxidized into urea thus guaranteeing photosensitizer release in intracellular environment (Figure 5b) [75].

Covalent conjugation of photosensitizers

As mentioned above, the physical solubilization of the photosensitizer suffers from the risks of leakage from the nanocarrier before the target is reached. Leakage can be prevented when the photosensitizers are covalently linked to the polymer backbone. However, the photosensitizers are mostly inactive in the self-assemblies when covalently linked and a precise stimulus is needed at the target site in order to activate the photosensitizers and produce ROS under illumination. Recent developments are summarized below in Table 2.

Different strategies have been applied in order to produce singlet oxygen on demand [81]. Among them self-quenching and Förster resonance energy transfer (FRET) quenching are the most frequently used in self-assembled nanocarriers. An alternative possibility to avoid quenching is to mix the photosensitizer-conjugated polymer with a polymer without photosensitizers [82]. Interestingly, the effect of the position of the photosensitizer in the polymer backbone is not trivial and it is an element one can play with in order to maximize the phototoxicity with minimal amounts of photosensitizer as will be discussed in the next section [82].

Self-quenching, also known as aggregation-induced quenching, is typical in nanosystems where the presence of the photosensitizer is the main driving force of the self-assembly. The photosensitizer is then concentrated in the hydrophobic core in a dormant state, due to the formation of π–π-stacked aggregates, that is not phototoxic under illumination. In order to make these systems work, the monomeric state of the photosensitizer has to be restored by a trigger. The first examples of this approach are enzymatically activated copolymers, mostly based on polylysine [83,84]. In these examples chlorin-e6 could be conjugated to the backbone thanks to reactive amine bonds. Not all of the lysine units should be modified to guarantee water solubility and enzymatic activation [83]. PEGylation could also improve solubility, but it was also proved to be detrimental regarding quenching [84]. More recently, polysaccharides based on chitosan or heparin have also been considered [85,86].

Another stimulus for activation used in self-quenched self-assemblies is the reduction of the disufide bond by gluthathione. This approach has been used to chemically link the photosensitizer molecule pheophorbide a via a disulfide

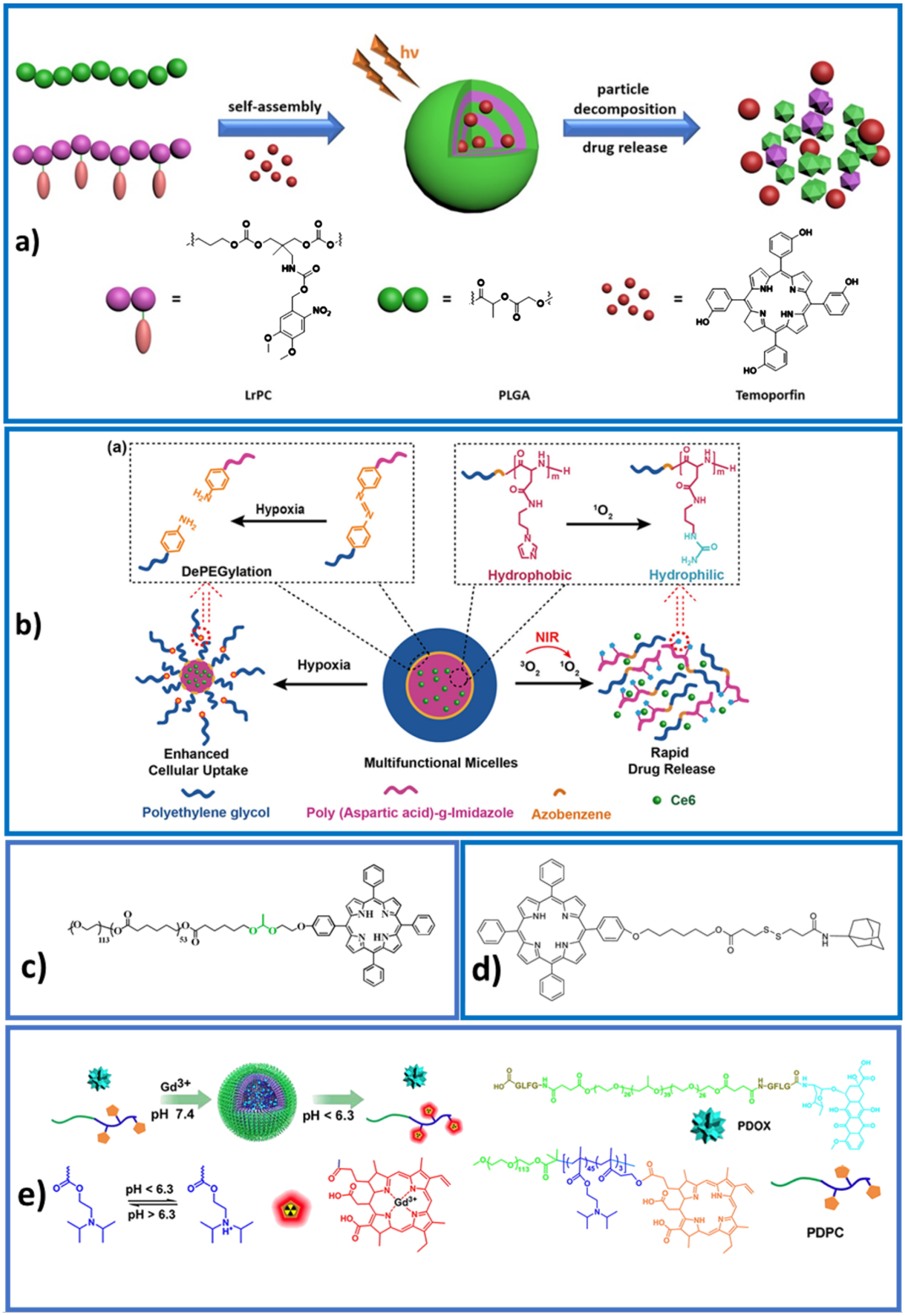

Figure 5: a) Light-responsive self-immolative polymers. Adapted with permission from [70], copyright 2018 American Chemical Society. b) Hypoxia- and ROS-sensitive polymers. Adapted with permission from [75], copyright 2018 American Chemical Society. c) An acetal-containing copolymer that can be hydrolyzed at low pH values. Adapted with permission from [79], copyright 2017 American Chemical Society. d) A disulfide link sensitive to redox conditions and to GSH concentration. Reproduced with permission from [77], copyright 2015 The Royal Society of Chemistry. e) A pH-sensitive polymer. Adapted with permission from [80], copyright 2016 American Chemical Society.

Table 2: Passive targeting and photosensitizers covalently linked to the hydrophobic block. PET: positron emission tomography; FI: fluorescence imaging; MRI: magnetic resonance imaging; NIRFI: near-infrared fluorescence imaging; PTT: photothermal therapy; FRET: Förster resonance energy transfer; PA: photoacoustic imaging; ROS: reactive oxygen species; AIE: aggregation-induced emission; PIC: poly ion complex; PS: photosensitizer.

polymer	specific feature	comments	ref
hybrid telodendrimers comprising linear polyethylene glycol and dendritic oligomers of pyropheophorbide a and cholic acid	redox (self-quenched)	chemo, PET, image-guided (FI), MRI, ovarian and lung cancers, in vitro and in vivo	[87]
poly(ethylene glycol)-*block*-poly(disulfide ester 5-(4-(6-hydroxyhexyl)phenyl)-10,15,20-triphenylporphyrin)-*block*-poly(ethylene glycol)	redox (self-quenched)	lung cancer, in vitro	[88]
biarmed poly(ethylene oxide)-(pheophorbide a)$_2$	redox (self-quenched)	adenocarcinoma, in vitro	[89]
doxorubicin and Zn phthalocyanine conjugated to methoxy polyethylene glycol-*block*-poly(β-benzyl-L-aspartate)	pH value and redox (self-quenched)	chemo, liver cancer, in vitro and in vivo	[90]
poly(ethylene glycol)-*block*-poly(ε-caprolactone)-*alt*-porphyrin	pH value (self-quenched)	chemo, lung cancer, in vitro	[79]
poly(ethylene glycol)-*block*-poly(γ-benzyl-L-glutamate)	(self-quenched)	adenocarcinoma and melanoma, in vitro	[82]
Ce6-poly(ethylene glycol)-*block*(azo)-poly(ε-caprolactone)	hypoxia (self-quenched)	chemo, adenocarcinoma, in vitro	[91]
poly(hydroxypropyl methacrylamide) conjugated pyropheophorbide a	(self-quenched)	NIRFI, colon cancer and melanoma, in vitro and in vivo	[92]
Ce6-conjugated poly(ethylene glycol)-*block*-poly[(diisopropylamino ethyl methacrylate-*co*-hydroxyl methacrylate)]	pH value	chemo, PTT, MRI, PA, NIRFI, breast cancer, in vitro and in vivo	[80]
camptothecin and protoporphyrin IX conjugated to dextran	pH value, redox	chemo, pancreatic cancer and endothelial cells, in vitro and in vivo	[93]
poly(*N*-isopropylacrylamide)-*block*-poly(6-(5′-(4′-phenoxyl)-10′,15′,20′-triphenyl-porphyrin) methacrylate)	temperature	breast cancer, in vitro	[94]
hyperbranched conjugated polymer core and thermoresponsive hyperbranched polyether shell	FRET, temperature	PTT, adenocarcinoma, in vitro and in vivo	[95]
tetraphenylethenethiophene-thioketal-poly(ethylene oxide)	ROS	image-guided (AIE), chemo, breast cancer, in vitro	[96]
Zn porphyrin conjugated to poly(oligo(ethylene oxide)methyl ether methacrylate)-*co*-poly(trifluoroethyl methacrylate)	antihypoxia	carcinoma and melanoma, in vitro	[97]
salicylaldazine hexadecane-*block*-poly(ethylene oxide)	–	image-guided (AIE), adenocarcinoma, in vitro	[98]
modified poly(oligoethylene oxide)-alt-octadecene	–	image-guided (FI), PET, breast cancer and glioblastoma, in vitro and in vivo	[99]
poly(triphenylphosphonium-(2-hydroxypropyl)methacrylamide)-*co*-poly(*N*-(2-hydroxypropyl)methacrylamide)-*co*-poly((2*Z*,2'*Z*)-3,3'-(2,5-bis((4-methylacrylate)(phenyl)amino)-1,4-phenylene)bis(2-(3,5-bis(trifluoromethyl)phenyl)acrylonitrile))	–	image-guided (AIE), lung and neck cancer, in vitro	[100]
poly[(poly(ethylene glycol)methyl ether methacrylate)-*co*-(3-aminopropyl methacrylate)]-*block*-poly(methyl methacrylate)	–	image-guided (FI, PA), MRI, breast cancer, in vitro and in vivo	[101]
poly(styrene-*co*-5,10,15,20-tetrakis(pentafluorophenyl)porphyrin)-*block*-poly(ethylene oxide monomethyl ether acrylate)	–	glioblastoma, in vitro	[102]

Table 2: Passive targeting and photosensitizers covalently linked to the hydrophobic block. PET: positron emission tomography; FI: fluorescence imaging; MRI: magnetic resonance imaging; NIRFI: near-infrared fluorescence imaging; PTT: photothermal therapy; FRET: Förster resonance energy transfer; PA: photoacoustic imaging; ROS: reactive oxygen species; AIE: aggregation-induced emission; PIC: poly ion complex; PS: photosensitizer. (continued)

poly(ethylenimine)-beta-carotene conjugate and pheophorbide a modified heparine (PIC)	scavenger "quenched"	breast cancer, in vitro	[103]
porphyrin conjugated poly(ethylene oxide)-*block*-poly(pentafluorophenyl methacrylate)	antihypoxia	liver cancer, in vitro	[104]
catalase-meso-tetra(*p*-hydroxyphenyl)-poly(ethylene oxide)	O_2 production	breast cancer, in vitro and in vivo	[105]
poly[oligo(ethylene oxide) methyl ether methacrylate]-*block*-poly(ortho-substituted 9,10-diphenylanthracene methacrylate-*co*-*n*-hexyl methacrylate tetraphenyl porphyrin-*co*-*n*-butyl methacrylate)	singlet oxygen production without PS	PTT, liver cancer, in vitro and in vivo	[106]

bond to the two arms of a methoxy poly(ethylene oxide) [89], or to the aspartate backbone of a poly(ethylene oxide)-*block*-poly(β-benzyl-L-aspartate) [90]. The latter example is proposed for chemotherapy as doxorubicin is also chemically linked through an acid-labile hydrazone linker to the aspartate backbone. In another recent example the hydrophobic central block was made of porphyrin molecules linked by disulfide groups; in the intracellular microenvironment the reduction by glutathione could activate the porphyrin molecules for PDT [88].

For self-assembled nanoparticles that are too labile and easily disassemble in vivo, cross-linking with disulfide bonds has been proposed for stabilization. Li et al. [87] proposed telodendrimers formed by linear polyethylene oxide and pheophorbide a and cholic acid at the ends of dendritic polylysine. The insertion of four cysteine mioeties in the oligolysine backbone allowed for a stabilization of the nanoparticles through disulfide bonds and conferred a sensitiveness to GSH at intracellular level. The authors showed that the intact micelles generated heat upon irradiation, thus allowing PTT, while fluorescence and ROS generation were the main deactivation processes in the case of disassembled micelles. This is an example of "all in one" nanomedicine used for chemotherapy combining loading with doxorubicin, PDT and PTT. This is possible thanks to the activation of the photosensitizer and multimodal imaging using the fluorescence of the photosensitizer (near-infrared fluorescence imaging, NIRFI) and the addition of Gd^{3+} ions (magnetic resonance imaging, MRI) or $^{64}Cu^{2+}$ (positron emission tomography, PET).

A pH-sensitive acetal bond between poly(ε-caprolactone) and porphyrin was used to release porphyrin at pH 5 (Figure 5c) [79]. In a poly(ethylene glycol)-*block*-poly(ε-caprolactone) polymer conjugated with chlorin-e6, an azobenzene group that can be cleaved at very low oxygen concentrations links the hydrophobic and the hydrophilic block. Upon irradiation and depletion of oxygen due to the PDT activity of chlorin-e6, the block copolymer nanovector disassembled and the anticancer drug, doxorubicin, was released [91].

The photoactivity of the photosensitizer can also be modulated by conjugation with a quencher molecule different from the photosensitizer itself. IR780 could be used as a quencher of chlorin-e6 fluorescence in albumin-based nanosystems [107]. Upon NIR excitation and IR780 degradation chlorin-e6 is activated.

In an original way, Huang et al. exploited FRET activation in a reverse manner [95]. The photosensitizer is covalently linked to a thermo-responsive hyperbranched polyether shell, which keeps it far away from the hyperbranched conjugated core. Upon NIR excitation of the core block, because of the photothermal effect, the shell shrinks thus bringing the photosensitizer closer to the core allowing for fluorescence resonance energy transfer and singlet oxygen production. In other proposed polymers, fluorescence quenching is not discussed, but in vitro studies prove the higher phototoxicity of the covalently linked photosensitizer [94,102].

An original way of preventing ROS production before reaching the target site is the use of a scavenger. In the work from Li et al. [103], a PIC is formed between a negatively charged heparine modified with pheophorbide a and a positively charged polyethyleneimine coupled to β-carotene. After disassembly of the nanoparticles, the mean distance between pheophorbide a and β-carotene increases thus activating PDT.

In an alternative strategy, aggregation-induced emission (AIE) fluorophores have been proposed as a solution to aggregation-induced quenching. These luminogens are characterized by high emission and efficient ROS production in the aggregated state under light irradiation, which is why they can be used for

image-guided PDT [96,98,100]. As an example, tetraphenylethenethiophene (TPETP) conjugated to PEG through an ROS-sensitive thioketal link was proposed to overcome the drug resistance of cancer cells. Indeed, it induced membrane permeability of the endo-lysosome and particle disassembly after white-light irradiation thus triggering the release of doxorubicin in the cytosol [96]. In the study by Zheng et al. [100] the AIE fluorophore is used as cross-linker and increases the aggregates stability.

The hydrophilic blocks

Chemical compositions. For many years, polyethylene oxide (PEO) also referred to as poly(ethylene glycol) (PEG) has been the favorite hydrophilic component in copolymers whenever a biological application was sought. Indeed, one of the key features of PEO is to provide (steric) stabilization by excluding other macromolecules and particles due to the high flexibility and large exclusion volume of PEO strands in water. This imparts biocompatibility and prolonged circulation time to the objects by minimizing the adsorption of proteins and adhesion to cells [108,109]. A hydrophobic cargo, well within the hydrophobic core is thus protected from hydrolysis and enzymatic degradation. Besides, PEO prevents the recognition from the mononuclear phagocyte system and preliminary clearance from the bloodstream is reduced. Although PEO has been widely available to chemists around the world, its actual synthesis remains a task for specialists. Most often, as in the work described by Ibrahimova et al. [82], PEG is assembled as a presynthesized block. Astute chemists have managed to assemble complex architectures, such as the multicompartment nanovectors described by Synatschke et al. [59], where the combination of polyionic complexes and amphiphilic polymers lead to bottlebrush-on-sphere assemblies.

Numerous examples can be found for nanovectors for PDT sensitizers having a PEO hydrophilic block. Pluronics, for example, are ABA triblock copolymers where block A is PEO and block B is poly(propylene oxide) PPO. Pluronics-based structures have been explored extensively in PDT applications and continue to garner attention, as in the study by Py-Daniel and co-workers [57].

In a recent study, Vilsinki et al. [58] used polyacrylate as a hydrophilic block, effectively rendering the self-assemblies highly negatively charged at physiological pH values. Indeed, negatively charged nanoparticles are known to be capable of evading the mononuclear phagocyte system and enjoy prolonged blood circulation [58,110].

Active targeting through hydrophilic block. Recent efforts in targeting through the hydrophilic block are summarized in Table 3. Carbohydrates have been used in order to confer targeting properties and they are often modified by grafting the hydrophobic photosensitizers in order to yield the amphiphilic properties necessary for self-assembly [93,111,112]. Among the targeting molecules, hyaluronic acid [111,112] is known to interact with CD44 over-expressed by some tumor cells. Mannitol [113] or galactose [114] have been used for their inherent biocompatibility and bioadhesive/targeting properties. Interestingly mannitol derivatives could be obtained with an environmentally friendly strategy using a lipase for sugar transesterification.

Liu et al. have described a tri-block polymer system functionalized with galactose (PMAGP-POEGMA-Plys-Bodipy) [114]. Poly(oligo(ethylene glycol) methyl ether methacrylate) (POEGMA) plays the role of a hydrophilic shell for micelle

Table 3: Polymers used for active targeting. FI: fluorescence imaging; PA: photoacoustic imaging.

polymer	specific feature	comments	ref
poly(ethylene glycol)-*block*-poly(lactic acid)-folate	–	ovarian cancer, in vitro and in vivo	[39]
hyaluronic acid-*block*-poly(D,L-lactide-*co*-glycolide)	–	lung cancer, in vitro	[111]
chlorin-e6 conjugated hyaluronic acid	image-guided (FI, PA), stimulus by oxygen shuttle, redox (self-quenched)	breast cancer, in vitro and in vivo	[112]
poly(D-galactose methyl methacrylate)-*block*-poly[oligo(ethylene glycol) methyl ether methacrylate]-*block*-poly(carbobenzoxy-L-lysine)	image-guided (FI)	liver cancer and carcinoma, in vitro	[114]
poly(2,5-anhydro-3,4-di-*O*-benzyl-D-mannitol-*block*-poly(ethylene oxide); poly(2,5-anhydro-3,4-di-*O*-decanoyl-D-mannitol-*block*-poly(ethylene oxide); poly(2,5-anhydro-3,4-di-*O*-myristoyl-D-mannitol-*block*-poly(ethylene oxide)	–	lung cancer, in vitro	[113]
disulfide-containing poly(ε-caprolactone)-*block*-poly(ethylene oxide) mixed with biotinylated poly(ethylene oxide)-cypate	redox-responsive	liver cancer, in vitro and in vivo	[115]

stabilization, and the derivatized polylysin (Plys) acts as a hydrophobic core to load the photosensitizer (BODIPY), while PMAGP mainly serves to direct the target delivery to hepatoma cancer cells.

Folate (FA) has been extensively studied as a targeting moiety [116] due to the overexpression of folate receptors in a number of tumor types including ovarian [117] or breast cancers [118]. One of the most recent examples of FA use in PDT applications is by Li et al., where the authors have designed a FA-PEO-PLA construct to deliver hypocrellin B, a sensitizer extracted from fungi, to intraperitoneal tumors [39]. It was shown that the sensitizer concentration reached a maximum after 2 h in the targeted organs, as opposed to after at least 6–12 hours in other peritoneal organs, thereby creating a large window of opportunity for treatment with reduced side effects.

When targeting cell surface receptors, two strategies can be distinguished using antibodies directed against a chosen receptor, or using the ligand of the receptor itself. The group of Torchilin pioneered the use of antibody-based active targeting by copolymer self-assemblies [119], and applied it to the delivery of PDT sensitizers [120]. Many groups have explored this strategy since. More recently, one of the most often targeted cell-surface entities has been EGFR (epidermal growth factor receptor, overexpressed in a variety of solid tumors such as non-small cell lung cancer, head and neck carcinoma, ovarian, kidney, and pancreatic cancer). Chang et al. have explored the potential of PLA-PEG-AntiEGFR self-assemblies loaded with chlorin-e6 as a photosensitizer and found that this construct led to the increased internalization of the micelles through receptor-mediated endocytosis, which in turn led to increased cytotoxicity upon light activation [121]. Very recently, Zhang et al. have exploited the highly selective interaction between avidin and biotin to specifically target cells overexpressing the biotin receptor [115].

High-performance nanoassemblies

The current trends for polymer vector design point to the development of versatile and "all in one" nanocarriers embedding different functions in order to both visualize the tumor and kill it. For this purpose, PDT has been associated with multimodal imaging and other treatments such as chemotherapy or photothermal therapy (PTT). Doxorubicin or camptotecin, the most frequently used chemotherapeutic molecules, can be encapsulated [73,87,96,115] or chemically linked [80,90,93] to the polymer backbone and released under a precise stimulus. Chlorin-e6 [80], ICG [78], IR825 [80], IR 780 [106] or cypate [36,115] or pheophorbide [87] have been employed for the photothermal effect.

Regarding imaging, the tendency is to couple different techniques such as fluorescence, photoacoustic and magnetic resonant imaging. The photosensitizer itself can act both as a fluorescent probe and as a photoacoustic agent, for example chlorine-e6 [80,99,112] covalently bonded to the polymer backbone. Otherwise, IR825 [101] has been used in the interior of the polymer micelles for photoacoustic (PA) imaging. Other photosensitizers proposed for image-guided PDT are ICG [78], TCPP [101] and pheophorbide a-conjugated poly(*N*-(2-hydroxypropyl)methacrylamide) when irradiated at 680 nm [92]. Besides, the chelating properties of porphyrins towards ions such as Mn^{2+} [101] or Gd^{3+} [80] or ^{64}Cu [99] can be used for magnetic resonant imaging (MRI).

Oxygen self-compensation. Local tumor hypoxia is one of the issues of PDT as the inefficient oxygen supply hampers the therapy efficiency based on the energy transfer to surrounding oxygen [122]. Moreover, oxygen consumption during the treatment exacerbates hypoxia conditions provoking PDT hypoxia resistance due to increase in tumor invasiveness and metastasis [123].

In terms of the design of nanocarriers, different solutions have been recently proposed (see below in Figure 6) in order to (i) deliver oxygen in tumor tissues by using oxygen "shuttles"; (ii) produce oxygen in situ using chemical or photothermal reactions or (iii) circumvent the use of oxygen. Details of these solutions are as follows:

1. Taking inspiration from red blood cells, which transport oxygen via haemoglobin, the poly(acrylic acid) block in poly(ethylene glycol)-*block*-poly(acrylic acid)-*block*-polystyrene self-assemblies was conjugated to haemoglobin via carbodiimide chemistry [61]. The resultant carrier loaded with zinc phthalocyanine (ZnPc) was able to generate more singlet oxygen than the one without haemoglobin. Perfluorocarbon (PFC) is recognized for its biocompatibility, its ability to dissolve significant amounts of oxygen and to increase singlet oxygen lifetime [124]. A proposed solution is to stabilize a perfluorinated solvent by an hydrophilic shell, using lipids [125], albumin [62] or hyaluronic acid conjugated with chlorin-e6 conjugated [112]. In this way oxygen molecules can be absorbed in the core and the photosensitizer IR780 in the shell. A main drawback of this approach is extravasation from the nanoobjects, which can be avoided with perfluorinated block copolymers, which can simultaneously guarantee a high local concentration of PFC. Perfluorinated block copolymers are poorly soluble in water, thus a low total amount of fluorine was measured in the first reported examples (polymer con-

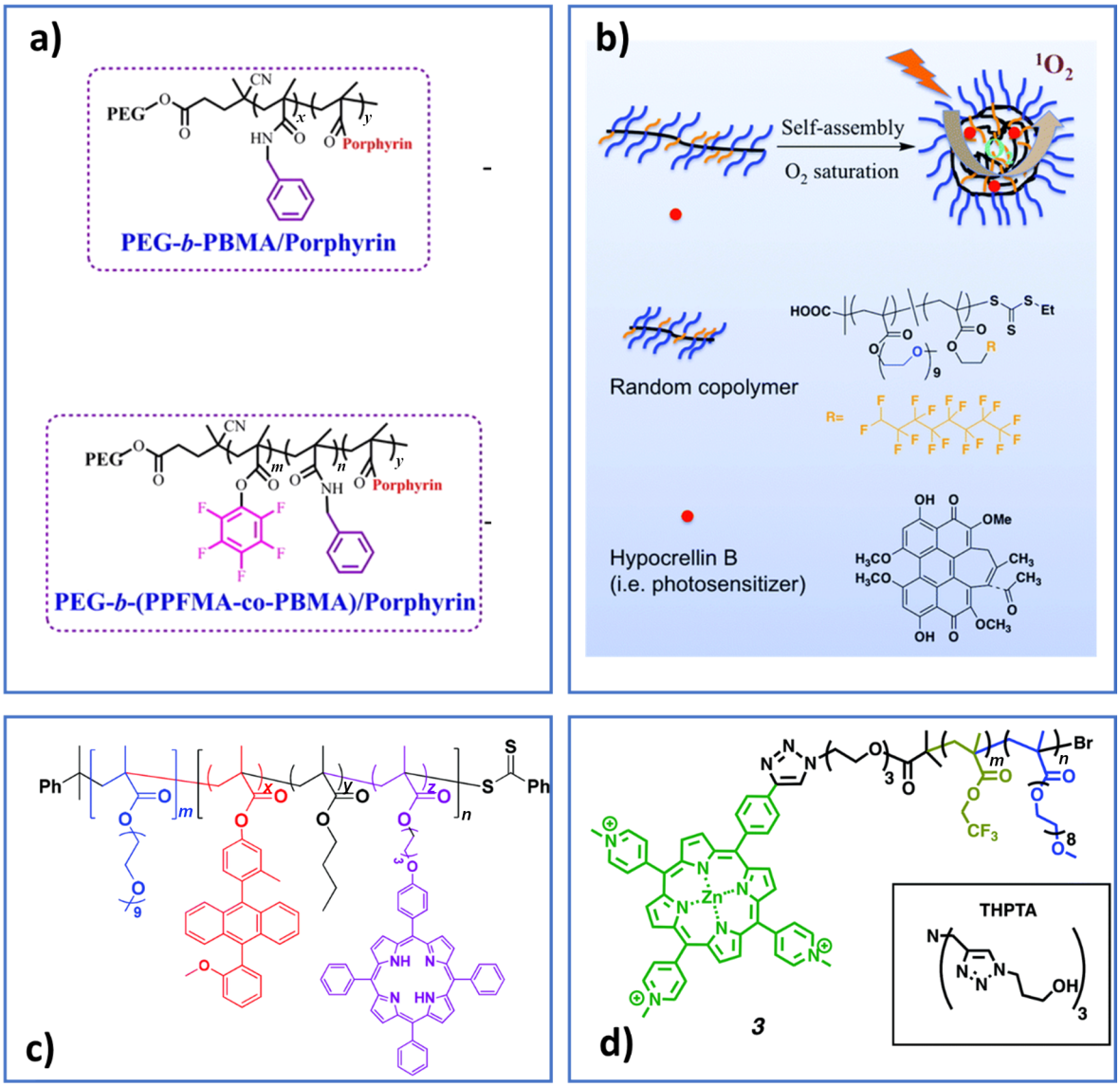

Figure 6: Block copolymers used as nanocarriers for overcoming hypoxia; a) adapted with permission from [104], copyright 2016 American Chemical Society, b) reproduced with permission from [64], copyright 2019 The Royal Society of Chemistry, c) reproduced with permission from [106], copyright 2018 The Royal Society of Chemistry, and d) reproduced with permission from [97], copyright 2017 The Royal Society of Chemistry.

centration 0.1 mg·mL^{-1} in [104]). Efforts have been made in order to increase the solubility of fluorinated polymers by using charged poly(ethylene imine) stars (around 2 mg·mL^{-1} in [60]), for example. Another approach is to use random copolymers allowing for higher polymer concentrations (3 mg·mL^{-1} and up to 10 mg·mL^{-1} in [97] and [64] (Figure 6b), respectively). In [97] (Figure 6d) and [104] (Figure 6a) the photosensitizer was covalently linked to the polymer backbone; in both cases face-to-face H-type aggregation took place to some extent, nevertheless the higher oxygen concentration compensated it and singlet oxygen production efficiency was improved.

2. Polymer self-assemblies containing catalase [68] or MnO_2 nanoparticles [65,69] have been developed as they can catalytically decompose endogenous H_2O_2 present in the tumor environment thus increasing the oxygen level in cancer cells. The electrostatic interactions between negatively charged catalase or bovine serum albumin and positively charged chitosan or poly(allylamine)-coated MnO_2 have been exploited to obtain pH-sensitive nanovectors [68,69]. The low concentration of endogenous H_2O_2 together with the instability of catalase in physiological environments containing proteases, as well as the potential toxicity of Mn can be a limit. A nanocapsule where the catalase is protected by a brush-like PEO

protective shell covalently linked to the photosensitizer meso-tetra(phydroxyphenyl) used as cross-linker was reported [105].

In another elegant approach, polymer nanovesicles have been recently proposed as H_2O_2 reservoir [74]. In the aqueous pool of the nanovesicles, poly(amidoamine) (PAMAM) dendrimers conjugating chlorin-e6 and cypate were loaded together with H_2O_2. Upon NIR irradiation the cypate increased the temperature inducing the decomposition of H_2O_2 into oxygen.

3. An emerging strategy is to design nanocarriers able to transport reactive oxygen species in an inert form that can be activated once the vector reaches the tumors. Endoperoxides can be selected as a chemical source of singlet oxygen produced via thermal cycloreversion in an oxygen-independent manner [36,106]. This was possible thanks to the co-encapsulated cypate [36] or IR780 [106], which could induce hyperthermia through NIR irradiation. In [36], a 9,10-diphenylanthracene derivative is loaded while in [106] it is covalently linked to the methacrylate backbone together with the photosensitizer.

It might seem surprising that there is no special paragraph in this review to fully describe the observed PDT efficiency both in vitro and in vivo for each system presented here. Generally speaking, all polymeric vectors described in this review led to an improvement of the PDT efficiency. However, an overall comparison is meaningless, because for each research group the experimental parameters might be very different. To already many parameters in nanomedicine (including vector, cell line, 2D vs 3D, and in vitro vs in vivo conditions), the PDT conditions need to be added: irradiation source, wavelength of irradiation, irradiation power, total irradiance of the biological tissue. We therefore decide to let the reader examine each result depending on his standpoint and preferred to focus on the vector development philosophy. Nevertheless, the biological tests performed and the type of cancer examined are reported in Tables 1, 2 and 3 for the examples described in this section.

Formulation optimization

As mentioned in the introduction of this review, there are many requirements an optimized nanovector needs to fulfil, i.e., biocompatibility, a controlled size between 20 and 200 nm, the highest possible loading, no release of the photosensitizer before the delivery site and an efficient ROS formation upon irradiation. To achieve this, the inherent properties of the photosensitizer itself are essential, but this is beyond the scope of this review, and the literature is rich on this point [23,37,126-130]. Our aim in this part is to focus on the vector and examine the different methodologies that can be used to optimize the final PDT efficiency. When using noncovalent encapsulation, the essential point is the relative interaction between the PS and its vector, compared to all competitive interactions in the biological medium. The proteins, lipids, extracellular matrix components are all ingredients that can transform or dissociate the vector, leading to the release of the PS. Increasing the stability of the vector can therefore be important, but some commercialized systems such as Abraxane® use endogenous proteins such as human serum albumin (HSA) to take care of the drug traffic. In the case of PS and PDT, a first example has been described after a structural optimization of the PS (modified indocyanine) [131]. It is also noteworthy that human serum albumin has also been used in another study to deliver ICG, but a covalent disulfide bond was used to link HSA to the PS [78]. If a stable vector will have more chance to deliver its cargo to the appropriate site, a poor affinity between PS and the vector would be detrimental to the application, since this would lead to early release of the PS. Therefore, optimizing the PS/vector affinity is also of importance. But here again, a too stable vector might be problematic if the ROS produced upon irradiation are unable to reach the cellular components. This limitation is also the central one for PS covalently linked to the vector, as already mentioned before, and the disassembly of the nanovector is necessary. This short introduction clearly shows the very high complexity of vector development for PDT. In the subsequent paragraphs, we will thus examine each strategy for optimizing the vector formulation.

Figure 7 presents the different parameters that can be modified on the polymer itself, the links between them, and the specifications needed for the application.

The two central parameters that can be adjusted are the chemical structure of the polymer (including its chain morphology, either block, gradient or random and the comonomer ratios for copolymers) and the chain length, i.e., the molecular weight. The chemical structure will govern the prerequisite not mentioned in Figure 7, which is the biocompatibility. Obviously, a polymer that is not biocompatible will be rejected very early in the process of selection. Having said this, part 1 of this review showed the large variety of polymers used for PDT, going from aliphatic polyesters, polyacrylates to peptides or polysaccharides. The chemical structure will influence the crystallinity of the vector, its morphology (micelles, vesicles, or worm-like micelles), its stability ((bio)degradation or dissociation), the affinity to the PS and its loading and positioning inside the vector, and the possibility to introduce stimuli-responsive groups (enabling appropriate release). Similarly, the molecular weight of the polymer will have an impact on the crystallinity, the vector morphology, its stability and the PS loading. Most often, block copolymers are used but some points are noteworthy. For instance, Peng's team has described the

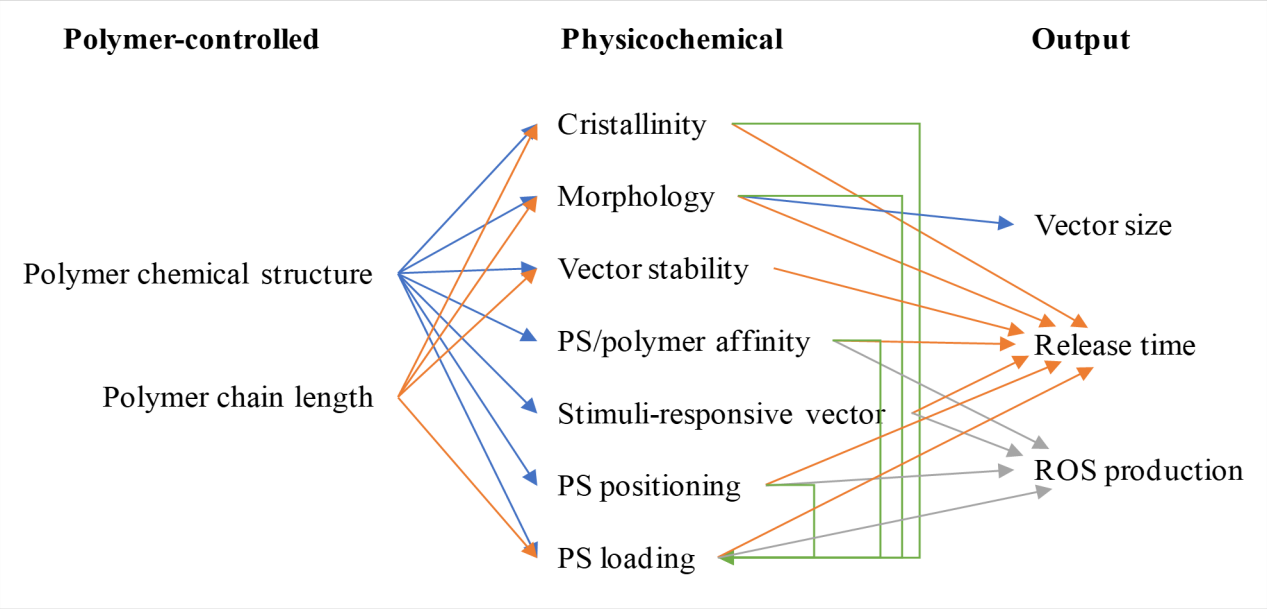

Figure 7: Schematic representation of the interplay between polymer structure, physicochemical characteristics, and their impact on PDT key parameters. PS: photosensitizer.

comparison between diblock and triblock copolymers based on polylysine (Plys) and PEO for PIC formation and they showed that Plys-PEO-Plys triblock was better than the diblock for PDT [46]. Regarding the ratios between the different comonomers, a thorough study assessed the encapsulation of chlorin-e6 in vectors based on pluronics exhibiting a large range of hydrophilic–lipophilic balance (HLB) and showed that an optimal HLB existed for a high PDT efficiency [35].

Cristallinity

Albertsson's team published a study comparing semi-crystalline to amorphous vectors based on ε-caprolactone (CL), L-lactide (LA) or ε-decalactone (DL) copolymers. All polymers formed micelles ranging from 25 to 60 nm but only those incorporating DL were amorphous. The study showed that the critical aggregation concentration was higher for amorphous systems and that the loading of aniline pentamer was better in the amorphous vector [132,133]. A similar loading improvement in amorphous vectors for indomethacin was described by Alexander and co-workers [134].

Morphology/size

Morphology includes both the assessment of the shape and the difference between micelles and vesicles, both being spherical but, respectively, hydrophobic or hydrophilic at their core. This is very rapidly linked to the vector size, since micelles will exhibit a typical size of 10–30 nm, vesicles will be typically larger than 60 nm. It is furthermore important to point out that the morphology of polymer self-assemblies is far from clear. Whereas the morphology of lipidic assembled systems is quite simple, the unambiguous determination of the morphology of polymeric systems is complicated. Small objects based on amphiphilic polymers with a size typically smaller than 30 nm can be described as micelles (hydrophobic core, hydrophilic corona) and this is confirmed by TEM and radiation scattering experiments (either light or X-rays or neutrons). For polymer vesicles, cryo-TEM images yield often doubtless morphology information. However, there are numerous systems that cannot be described as micelles or vesicles. Such cases are for instance large compound micelles constituted of small micelles [135,136]. The definite morphology assessment of the assembly needs the use of cryo-TEM or scattering techniques and is time-consuming. This explains why the literature is full of examples where authors might indicate micelles as a generic term or just nanoparticles without giving technical proof of the actual morphology.

Regarding the shape, a fundamental study was that of Discher on PEO-PCL vectors, which pointed at a higher efficiency using elongated vectors compared to spherical ones [137-139]. Simulations [139-141] showed that from a thermodynamic standpoint it is always more favorable to encapsulate spherocylindrical particles instead of spheres with the same radius and that endocytosis of spherocylinders occurs with parallel alignment to the membrane surface (Figure 8). Recent reviews have shown the importance of controlling the shape of the vectors, both for cell penetration but also for the behavior in the blood stream [142]. Regarding PDT more specifically, Till et al. examined the PDT efficiency of pheophorbide a when incorporated in micellar, vesicular or worm-like PEO-PCL vectors in two

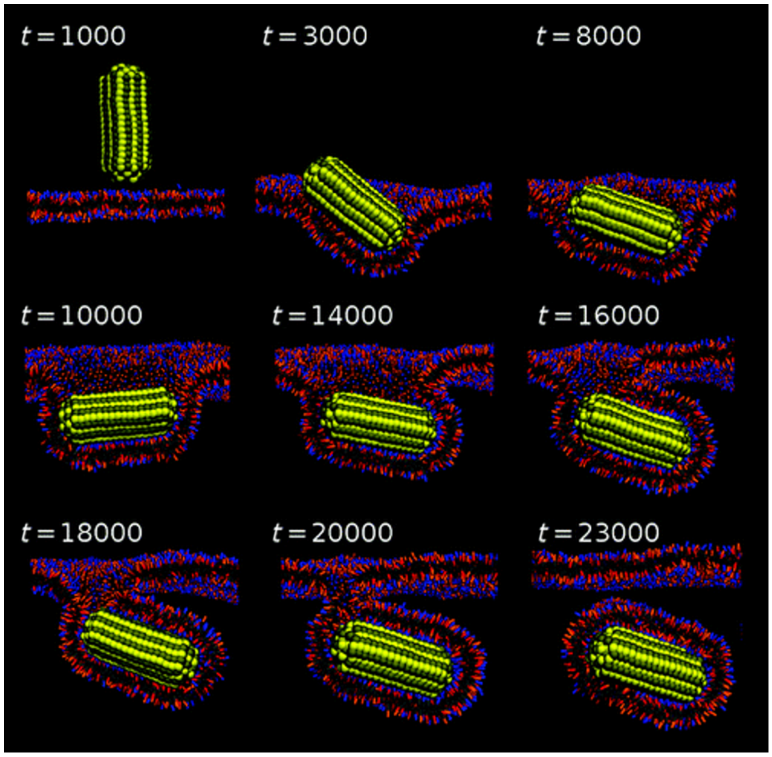

Figure 8: Representative snapshots describing the endocytosis pathway for spherocylindrical nanoparticles. Reprinted with permission from [141], copyright 2011 American Chemical Society.

cell lines (FaDu or HCT 116) [66,67]. No strong improvement was observed for elongated systems working on 3D spheroids and, interestingly, a micelle/vesicle mixture led to synergistic effects on HCT 116 cells but antagonistic effects for FaDu cells [67].

Vector stability

The stability has to be assessed from two standpoints: the degradation of the polymer itself and the possible dissociation of the vector in the biological medium. Regarding degradation, the polymer should be stable enough for the application period, which is typically from a few hours to two days, corresponding to the usual time to benefit from the EPR effect. This stability specification is therefore not very demanding and most recent polymers fulfill it. In contrast, the possible dissociation upon confrontation to biological media is an essential point that has been examined from the very beginning of nanomedicine [11]. The major concern based in the case of lipidic vectors was that polymeric vectors might dissociate upon sudden dilution following injection. While this might be true for systems at thermodynamical equilibrium, it is not any more for kinetically frozen vectors, which is very often the case for polymeric self-assemblies. Thus, for polymeric self-assemblies, we cannot talk anymore of critical micelle concentration (cmc) but only of critical aggregation concentration (cac) as the threshold for which their formation is observed. A typical cac range for amphiphilic block copolymers used in nanomedicine is a few milligrams per liter, which represents roughly the micromolar range. This has to be compared to cmc values of small surfactants, which are typically closer to the millimolar range. Furthermore, an important point is that dissociation of the self-assembly will not necessarily occur as soon as the concentration drops below the cac, owing to a kinetic lag linked to the low mobility of the polymer chains, as demonstrated in an early study of Kataoka et al. who showed that dissociation took place over several days [143]. The most frequently suggested solution to avoid any dissociation upon dilution is cross-linking of the vector. For PDT and other therapeutic cases this has been also described [66], showing a strong improvement of the treatment. The PS can be used both as ROS generator and also as cross-linker [101].

Regarding the stability in biological media, different conditions have been described, going from exposure to single proteins to the harshest one being fetal bovine serum (FBS). FRET follow-up has been often performed to examine the stability of polymeric self-assemblies and this review will only cite a few recent examples based on various techniques, which examined the stability of polymeric vectors using field flow fractionation, enabling therefore an efficient separation between the proteins of the medium and the vectors [45,144]. As exemplified in

Figure 9, field flow fractionation allows for a confirmation of the integrity of the self-assembled objects, since it is often coupled to orthogonal detection techniques, such as refractive index (RI) or light scattering measurements and absorption spectroscopy. Even if the application is PDT, this step is general and is performed without the PS inside the vector [29]. This enables a classification of the ability of the vectors to resist FBS with time. The comparison of PEO-PCL, PEO-PLA and PEO-PStyrene exhibiting similar sizes showed that PEO-PStyrene was the most stable. The advantage of PS for PDT is that their fluorescence will depend on their environment. This has been used to track existing transfer from the vector to albumin [145].

PS/vector affinity and loading

The encapsulation of the PS by non-covalent binding implies that the choice of PS/vector pair is essential for the application. A comparison of the affinity between different PSs and pluronics polymers has been recently published and indicated differences in aggregation among all systems [32]. Going further, the PS might be specifically modified to optimize its affinity towards the desired vector. This has been performed on indocyanine in order to have good transport properties by HAS [131]. Once the PS has been chosen, the PS/vector affinity can be tuned by adjusting the polymer structure, introducing additional functional groups that are able to interact with the PS. This approach by itself is not new and Kataoka et al. used this

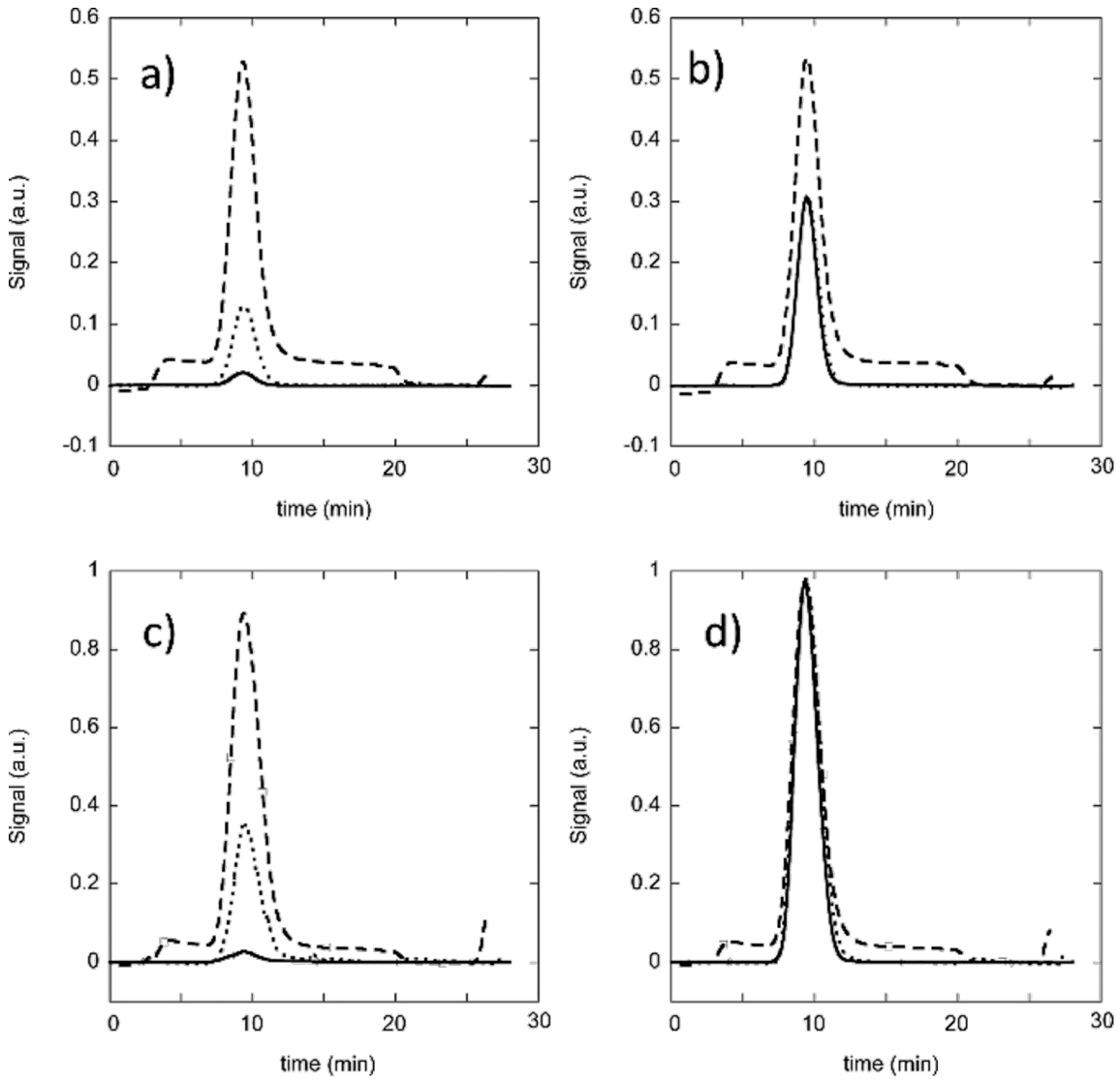

Figure 9: Field flow fractograms of PEO(2400)-*b*-PDLLA(2000) and PEO(3100)-*b*-PS(2300) micelles. The multi-angle light scattering (MALS) signal is represented by the dotted line, the RI signal by the dashed line, and the absorption at 412 nm by the full line. (a) Empty PEO(2400)-*b*-PDLLA(2000), (b) PEO(2400)-*b*-PDLLA(2000)/Pheo, (c) empty PEO(3100)-*b*-PS(2300), and (d) PEO(3100)-*b*-PS(2300)/Pheo. Reprinted with permission from [29], copyright 2014 American Chemical Society.

strategy in 2005 to improve the loading of paclitaxel in PEO-PAsp micelles [146]. A typical recent example describes the introduction of benzylglycidyl ether groups on the hydrophobic backbone of polylactide, in order to improve the loading of aluminium phthalocyanine AlClPc [45]. Using a peptide backbone is another elegant and powerful means to optimize the affinity by adapting the amino acid sequence [145], as shown in Figure 10. Porphyrins have also been used in the polymer backbone to increase subsequent PS encapsulation [94]. Another approach to modulate the PS/vector affinity is the use of supramolecular complexes, particularly based on cyclodextrins. Several recent examples have been published [52-54,147] as well as a recent review [21].

The PDT efficiency strongly depends on the PS loading but a too high encapsulation might lead to aggregation of the PS inside the vector. This would decrease the interest of using the polymeric vectors. Therefore, the optimal loading has to be determined for each system. Ping et al. described a simple UV–visible spectroscopy method to assess the degree of aggregation inside the vector, thanks to the evolution of the PS spectrum (zinc phthalocyanine in their case) [148]. Shi et al. described the modification of the PS by introducing bulky aromatic ligands which inhibited the formation of H-aggregates [37] (Figure 11).

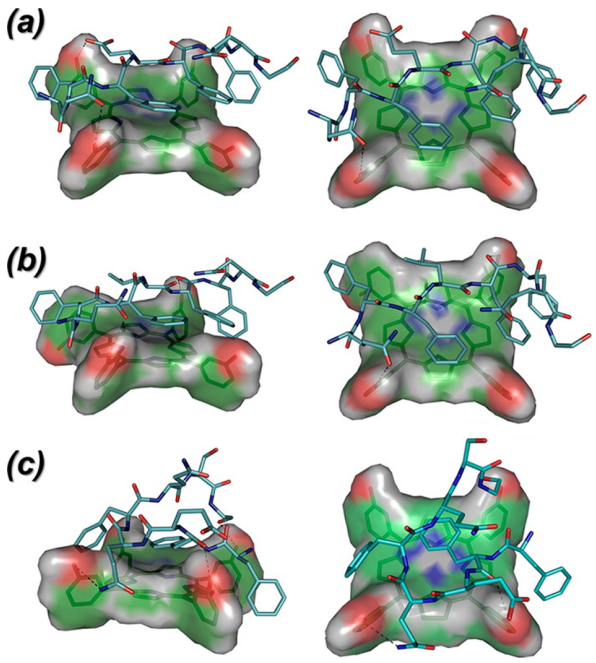

Figure 10: Idealized docking of 5,10,15,20-tetrakis(3-hydroxyphenyl)chlorin (*m*-THPC, shown as van der Waals surface) binding to peptide host sequences. Reprinted with permission from [145], copyright 2013 American Chemical Society.

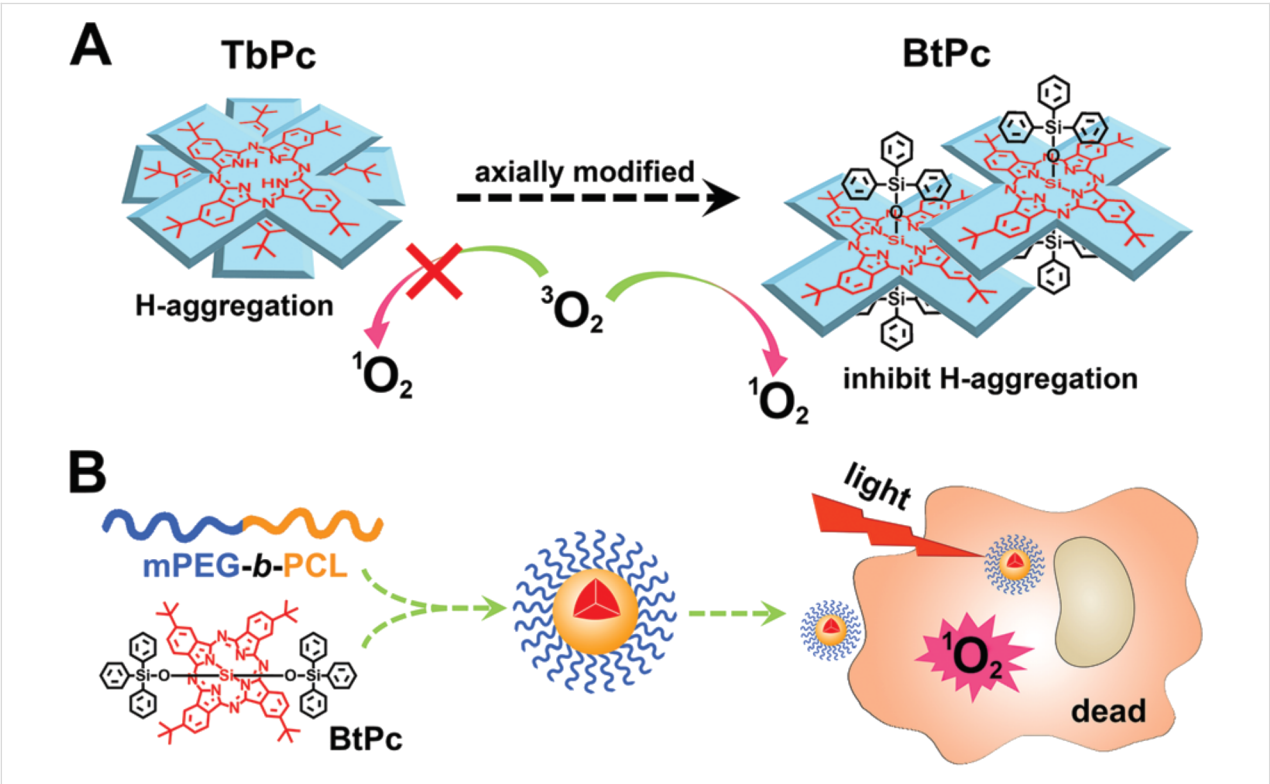

Figure 11: Modulation of PDT efficiency through introduction of bulky substituents on the PS, which inhibit aggregation. Reproduced with permission from [37], copyright 2018 The Royal Society of Chemistry.

A special case is that of PICs, which are based on electrostatic interactions between a charged PS and an oppositely charged copolymer. This approach was first described for PDT by Kataoka et al. in 2005 [47] and has been examined from time to time since then. Recent examples [46,103] described the formation of PICs based on polylysine/tetrasulfonate phthalocyanine or heparin/polyethylene imine interaction. The approach proposed by Huh et al. is original since the polyelectrolyte complex is formed by association of a pheophorbide-modified heparin to polyethylene imine-β-carotene, the carotene moiety acting as a ROS scavenger as long as the PIC is formed [103]. The principle is that, once internalized, heparin will be degraded enzymatically and the PIC thus dissociates, enabling the production of ROS upon irradiation.

Stimuli-responsive vectors

This strategy has been examined a lot during the last years, in a general manner for nanomedicine but also for PDT. As already explained above, the principle is to benefit from the biological medium environment to trigger the drug release (the PS for PDT). The decrease in pH value in cancer tissues has been regularly used in nanomedicine to break a pH-sensitive bond leading to the dissociation of the vector and the subsequent release of the drug [80]. Recently, several studies focused on hypoxia, which might be considered as a strong drawback for PDT but could be reversed towards an asset if the vector can be rendered sensitive to this. The study published by Zhao from 2018 is a typical example [75]. The vector consisted of PEO and PAsp (modified with imidazole moieties) blocks linked via an azobenzene group. Because this group was shown to be cleaved by azoreductase under hypoxic conditions [149], the observed stronger cellular penetration [75] was explained by a de-PEGylation of the vector upon contact with the hypoxic tissues.

PS positioning

Since PDT relies on the local production of ROS to kill the diseased cells and since the lifetime of these ROS can vary from 0.01 to 0.18 μs [150,151] depending on their structure and environment, the location of ROS production is essential. For instance, singlet oxygen is known to travel only a few nanometers in aqueous solution [151]. It has been shown to be able to exit 20 nm polymeric micelles before being scavenged in a model solution [152]. However, the situation clearly changes if the vector is larger or if the PS has been released from its vector by the biological environment. That is why several studies focused on this point, examining either covalent or non-covalent systems. An elegant study [82] synthesized PEO-poly(benzylglutamate) PBLG copolymers, introducing an aza-BodiPy PS either at the end of PBLG (in the center of the vector) or at the PEO–PBLG junction (therefore at the border between hydrophilic and hydrophobic areas). In both cases, 90 nm vesicles were formed, but the PDT effect was increased in the latter case, when the PS was located at the PEG and PBLG junction.

For non-covalent systems, the problem of PS positioning has also been evaluated by several teams. Wilk's team published an elegant characterization of PEO-PLA micelles encapsulating three different phthalocyanines, i.e., ZnPc, ZnPcF and tetrasulfonate-ZnPc [38]. They characterized PS positioning in solution by ^{1}H NMR NOE and in the dried state by XPS coupled with ion sputtering, which enabled them to obtain depth profiles of the Zn atom. They corroborated a decreased ROS production of ZnPc to its location in the core of the vector, contrary to the two other PS, which were preferably distributed in the PEO corona. This means that, for cases where there is no PS release before PDT activation, the optimized positioning of the PS should be ideally near the hydrophilic/hydrophobic junction to limit the distance to be travelled by ROS and the possible early PS release.

The preceding paragraphs have examined each parameter in an independent manner. As already shown in Figure 7, interdependency clearly exists and the obtained therapeutic efficiency is a global result of all these parameters. In order to optimize a vector formulation, more systematic methods exist, namely the multivariate design of experiments (DOE) and the approach using Hansen solubility parameters (HSP).

DOE, in contrast to the usual one-variable-at-a-time (OVAT) method, generates experiments with multiple variables changing simultaneously. The subsequent mathematical treatment enables the optimization of experimental conditions to get the desired result and also indicates which parameters lead to synergistic or antagonist effects. This approach has been regularly used for the formulation of lipidic vectors [153] and is also increasingly assessed for polymeric systems [154-157]. To our knowledge, only two examples have performed DOE for PDT vectors. Both of them dealt with pluronic-based nanocarriers formulated with aluminium chloride phthalocyanine [34] or with hypericin for oncology and antimicrobial applications [33].

Whereas DOE does not make any assumption on the quality of the drug–vector affinity, the HSP method is based on the comparison of solubility parameters for both components. The principle, described in Figure 12, is that products exhibiting similar solubility will be more easily mixed. Recent examples for the formulation of polymeric vectors can be found in [134,158].

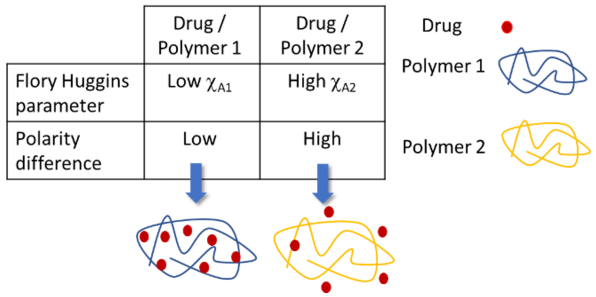

Figure 12: Use of Hansen solubility parameters to optimize polymeric nanovectors.

Processes of interaction with membranes

When looking at the efficiency of a block copolymer-based nanocarrier, it is crucial to understand how it can interact with the cell membrane. The plasma membrane of eukaryotic cells is a highly selective barrier that protects all living cells from the surrounding microenvironment and efficiently limits the entry and exit of biomolecules and ions. Thus, nanovectors developed in the field of drug delivery have to overcome this physical barrier to penetrate within the cells. Understanding how nanoobjects and cell membranes interact is crucial but is clearly not trivial given the wide variety of nanoparticles properties (such as size, charge, shape, surface modification) and the complexity of biological systems. Interestingly, interactions of carbon-based and metallic nanoparticles with membranes and cellular uptake have been widely described [159,160], offering lines of thought in the case of cellular uptake of polymeric nanovectors that have been only little studied until now.

In the following paragraphs we will describe some recent efforts to understand the mechanisms involved in the internalization of self-assemblies into cells. We will first describe the use of model membranes, lipid self-assemblies the size, shape and composition of which can be controlled. Even if almost all the reported examples in this section deal with copolymers without the presence of a photosensitizer, the experimental methods and the results obtained are valid in the case of PDT when the photosensitizer is inside a nanocarrier. Besides, the photosensitizer could have non-negligible effects on the final physicochemical properties of the nanocarriers and the membranes. The examples reported here could inspire research in this sense in the field of PDT and we will describe some works on cells.

Interactions with model membranes

Lipid monolayers are a very simple but powerful tool to probe the interactions between a membrane and external compounds such as polymers. Using a monolayer made of 1,2-dipalmitoyl-*sn*-glycero-3-phosphocholine (DPPC) and cholesterol, Sandez-Macho et al. [161] have been able to show how different PEO-PPO-PEO copolymers with different sizes of the PEO blocks interacted with the membrane. They showed that the shorter the PEO blocks, the more the polymer expanded the surface area per lipid and increased the membrane permeability. These effects have been confirmed by haemolysis assays. Yaroslavov et al. [162] used DPPC/DOPG (1,2-dioleyl-*sn*-glycero-3-phosphoglycerol) monolayers to characterize the effect of various polybetaines on the membrane. They showed that upon complexation with the anionic monolayer, the polybetaine generated an expansion of the monolayer depending on the length of the spacer between the positive and negative charges of the betaine. The polybetaine generating the smaller expansion of the monolayer was also the one showing the least cytotoxicity on human breast carcinoma cell MCF7. Schwieger et al. [163] used monolayers made of different types of lipids, changing the nature of the polar heads or of the chains, to investigate the interactions between the lipids and two types of PGMA-PPO-PGMA triblock copolymers, one presenting fluorinated end chains. They showed that the fluorinated polymer incorporated more strongly in the monolayer than the non-fluorinated one. They noted that the strength of the interaction between the hydrophilic PGMA and the polar head depended on its nature and that it was stronger for phosphatidyl ethanolamine (PE) polar heads than for phosphatidyl choline (PC) polar heads. This effect was more apparent for the fluorinated polymer. Their experiments also suggested a partial miscibility of polymer in the lipid bilayer, forming some hybrid polymer–lipid monolayers.

Supported lipid bilayers are a type of planar model membrane where a complete bilayer is deposited on a substrate. This geometry allows for the use of classical techniques of surface analysis, such as microscopy or spectroscopy. Ramadurai et al. [164] used a 1,2-dioleyl-*sn*-glycero-3-phosphocholine (DOPC) bilayer deposited on a PDMS surface presenting microcavities to investigate the interactions between the membrane and different types of amphiphilic invertible polymers (AIP) micelles, a class of stimuli-responsive polymers that form micellar structures in polar solvents that can invert in non-polar solvents. Through fluorescence lifetime correlation spectroscopy, they showed that the most hydrophobic polymer they studied led to an increase of the membrane viscosity, attributed to the adsorption of the micelles on the bilayer. They also used electrochemical impedance spectroscopy and noted that the same polymer led to a strong decrease of the membrane resistance, linked to an increase of its permeability.

Liposomes are vesicles composed of a lipid bilayer. They have a close resemblance to cell membranes and can be used as

substitute to investigate the interactions between cell membranes and nanocarriers. Liposomes can be produced in ways that allow for the control of the composition of the bilayer and of the internal aqueous phase. It is possible to prepare liposomes containing a self-quenching fluorescent dye in its internal aqueous phase and to follow the release of this dye under different types of stimuli. Because the dye release rate is related to the permeability of the liposome, this type of experiments is used to monitor the effects of polymers or nanoparticles on the integrity of membranes. Wilkosz et al. [165] used calcein-loaded 1-palmitoyl-2-oleoyl-*sn*-glycero-3-phosphocholine (POPC) liposomes to investigate the effect of cationic polymers and copolymers on the membrane. They showed that the densely substituted polycations generated a quick release of the calcein. They assumed that this was due to the formation of pores in the membrane. This theory was confirmed using molecular dynamics (MD) simulations. Palominos et al. [166] have prepared calcein-loaded DPPC liposomes mixed with two types of PCL-PEO-PCL copolymers of different block sizes. They showed that, in the concentration range that they studied, both polymers reduced the permeability of the membrane with the longer one having a greater effect. These results come as a confirmation of what they measured using two fluorescent dyes, laurdan and 1,6-diphenyl-1,3,5-hexatriene (DPH). By measuring the fluorescence polarisation of laurdan and the fluorescence anisotropy of DPH, it is possible to determine the physicochemical properties of the bilayer. Laurdan and DPH can "sense" their environment and insert themselves, respectively, at the interface of the bilayer and in the midst of the hydrophobic chains. Using this, they showed that the shorter copolymer had an effect only on the inner part of the bilayer while the longer one had an effect on both the interface and the inner part of the bilayer. By mixing POPC unilamellar liposomes with PEO-PPO copolymers of different block sizes and analyzing these mixtures with pulsed-field-gradient NMR, Zhang et al. [167] quantified polymer diffusion in the absence and presence of liposomes. From their results, they could assess the binding of the polymers to the liposomes. They showed that larger molecular weight and higher hydrophobicity of the polymer resulted in a higher binding percentage and liposomes surface coverage. They also noted that the binding percentage was independent of the incubation time, meaning that the polymer–membrane interactions occur immediately after mixing and reach an equilibrium state quickly. A recent example on pheophorbide a-loaded micelles interacting with giant vesicles shows a synergy between the photosensitizer and the polymer. An extended production of internal vesicles, resembling endosomes, is observed in the synthetic giant unilamellar vesicles, after interaction of pheophorbide a-loaded copolymer nanocarriers [168]. This does not happen when the photosensitizer is not loaded in the nanocarriers. All the performed experiments indicate that intimate interactions of the nanocarriers with the model bilayer are key for successful delivery and lipid oxidation is necessary for this pathway.

Computer-simulated interactions

Computer simulations enable one to model lipid bilayers and to examine how they behave in presence of polymer molecules or self-assemblies. Zaki and Carbone [169] used MD simulations to assess the effects of PEO-PPO-PEO triblock copolymers on DPPC bilayers under mechanical stress. They showed that the copolymer inserted itself in the membrane, leading to the formation of hybrid membrane with better mechanical properties. Houang et al. [170] compared the results obtained with MD simulations and with physiological studies. They used PEO-PPO copolymers with different PPO end groups and tested them as membrane stabilizer both in silico and in vitro. Using a POPC bilayer model under mechanical stress for their MD simulations, they showed that copolymers with a more hydrophobic end group could insert themselves deeper in the membrane bilayer while the more hydrophilic copolymers stayed close to the polar interface. These results validated the ones obtained from the animal model where the copolymer with the most hydrophobic end group was the one that helped muscle cells the most to resist mechanical stress. Raman et al. [171] used MD simulations to model a DOPC bilayer and to observe how PEO-PCL copolymers of different block sizes and their micelles could mix with the membrane. They showed that micelles with higher hydrophilic-to-hydrophobic ratio did not interact with the bilayer whereas those with lower hydrophilic-to-hydrophobic ratio were internalized over the course of their simulation. During this internalization, they saw a change in the structure of the micelles, going from a core–shell conformation to a Janus conformation with the PEO chains located at the interface close to the polar head groups and the PCL chains in the hydrophobic core of the bilayer. No effect on the area per lipid, average thickness and order parameter was measured. Guan et al. [172] explored different pathways of block copolymer micelles and membrane interactions by using a model of a lipid bilayer containing a proportion of lipid that could bind to the micelles. Figure 13 describes the results of their coarse-grained molecular simulations, where, by changing the binding strength, they isolated four types of pathways, i.e., attachment, semi-endocytosis, endocytosis, and fusion, linked to the wrapping parameter of the bilayer around the micelle. They showed that endocytosis was the most efficient pathway for the uptake of micelles and that fusion could result in membrane damage. They looked at the effects of the aggregation number of the micelles, length of the polymer and stiffness of the hydrophobic chains on the uptake of the micelles. Their results indicated that smaller aggregation number and polymer length led to a weaker uptake but higher

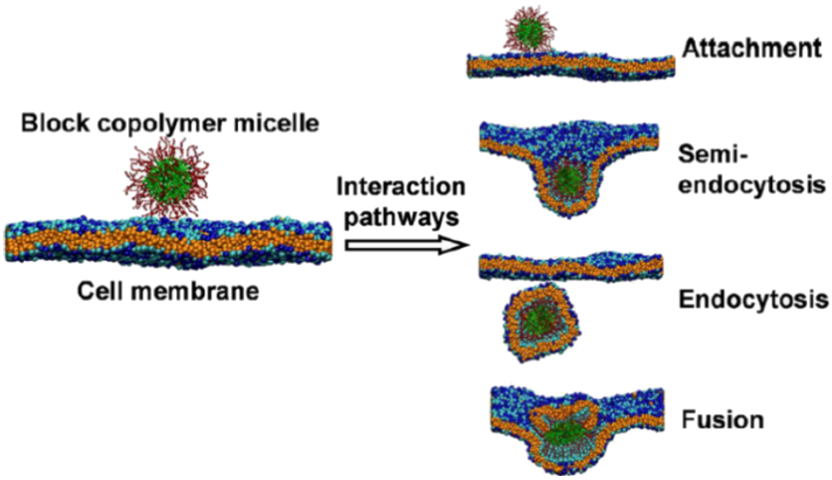

Figure 13: Types of pathways of block copolymer micelle–cell membrane interactions. Reprinted with permission from [172], copyright 2017 American Chemical Society.

values of these parameters generated more damage. They noted that lower hydrophobic chains stiffness could lead to micelles with a higher internalization efficiency and a lower toxicity.

Interactions with cells

Classical strategies to decipher cellular uptake mechanisms are based on selective chemical inhibition of the various endocytic processes or incubation at 4 °C instead of 37 °C to decrease cellular processes. Special attention should be paid to the use of fluorescent probes encapsulated within nanovectors to determine the fate of photosensitizers. Indeed, uncontrolled release of the fluorophore from the carrier may produce unreliable results. Conventional tools used to visualize/quantify cellular uptake are flow cytometry and confocal microscopy, which has been punctually combined with surface-enhanced infrared absorption spectroscopy (SEIRAS) [173] or FRET imaging [174]. In the context of PDT with polymeric nanoparticles, we identified some experimental qualitative/quantitative studies of interactions between nanoparticles and cell membranes, cellular uptake and drug release. Kerdous et al. proposed an original way to study the mechanisms of release of pheophorbide a-loaded in PEO-PCL, when exposed to human breast cancer cells MCF-7 [175]. Using a fluorescent confocal microscope setup that enabled concomitant spectroscopic and excited state lifetime measurements of the fluorescence emission signal of the photosensitizer, they demonstrated that pheophorbide delivery in a very minor way involved the internalization of nanoparticles. The major drug delivery mechanisms came from a direct transfer of the amphiphilic drug from the nanoparticle to the cell membrane by collision. Similarly, using PEO-PCL micelles loaded with fluorescent photosensitizer pheophorbide a or fluorescent copolymers, Till et al. demonstrated that pheophorbide a directly migrates from the micelles to the cell membrane without disruption of the vector or partial drug release in the vicinity of the cell [176]. At a different scale, Xue et al. observed by flow cytometry experiments after 4 h and 24 h of incubation with PEO-terminated ZnTPPC6-based poly disulfide ester (PEO-*b*-PTPPDS-*b*-PEO) micelles (134 nm) with A549 tumor cells, that the intracellular uptake of these polymeric micelles was a time-dependent process and proposed that cellular uptake came from endocytosis rather than the simple passive diffusion of free porphyrin with prolonged incubation time [88]. Wan et al. performed a detailed study about uptake mechanisms of 45 nm micelles of poly(aspartic acid)-*graft*-poly(ethylene oxide-indocyanine green) loaded with the antitumor drug paclitaxel, written PTX@PAsp-*g*-(PEO-ICG) [177]. Human ovarian cancer cells SK-OV-3 were pre-treated for 30 min with PBS at 37 °C as control and different inhibitory solutions, i.e., PBS at 4 °C for low-temperature incubation with slowed cellular processes, 2-deoxy-D-glucose (50 mM)/NaN_3 (10 mM) to deplete the cells from energy (ATP) essential for endocytosis, or sucrose at 0.45 M as hypertonic solution to inhibit of clathrin-mediated endocytosis. After these pre-treatments, cells were incubated with polymeric micelles for 2 h at 37 °C before analysis by flow cytometry. While ATP depletion and hypertonic treatment failed to inhibit the cellular uptake of PTX@PAsp-*g*-(PEO-ICG), incubation at 4 °C reduced it by 66%. These results indicate that the cell uptake mechanism of PTX@PAsp-*g*-(PEO-ICG) was not through endocytosis (ATP required), but largely attributed to passive transportation. In conclusion, it has to be underlined that nanoparticles entering the cell via endocytic pathways will be directed to endosomal/lysosomal compart-

ments, trapped within vesicles, while those entered through passive diffusion freely access the cytoplasm. In the latter case, depending on the photosensitizer (or drug)/polymer couple, distinct drug release mechanisms can be considered. These are photosensitizer release in the vicinity of cell membrane, direct transfer of the photosensitizer upon contact of the vector with the cell membrane, or penetration of the photosensitizer together with its carrier. Strategies developed to target specific subcellular organelles in the context of PDT will be discussed below. Finally, it has to be kept in mind that in silico and in vitro experiments on human cells represent a first step in understanding the interactions between membranes and polymeric nanovectors, meaning that in vivo experiments will be further needed to confirm cellular uptake efficacy.

Subcellular organelle-targeted photodynamic therapy with polymeric nanovectors

The presence of photosensitizer and O_2 under light irradiation during PDT generates reactive oxygen species (ROS) such as singlet oxygen ($^1O_2$), which is highly reactive and irreversibly oxidizes adjacent biological substrates such as signaling proteins or nucleic acids. Cell and tissue exposure to $^1O_2$ results in the breakdown of cellular microstructures and cell death. The $^1O_2$ lifetime was measured in vivo in rats after irradiation of aluminium tetrasulfonated phthalocyanine and appears to be 0.03–0.17 μs in liver and 0.04–0.18 μs in skin [150]. In vitro, the intracellular radius of action of $^1O_2$ was estimated between 10 to 20 nm, corresponding to a lifetime of 0.01–0.04 μs [151]. Because of the fast decay and degradation of $^1O_2$, photosensitizers have to be localized as close as possible to the targeted cellular organelles, mainly mitochondria, lysosome, or nucleus.

Challenges are to develop smart release approaches with precise spatiotemporal control for cancer therapy. Strategies adopted for intracellular targeting can be divided into passive, active and activable, in the latter case nanovectors remain photodynamically inactive until they reach the tumor site and more precisely the targeted intracellular compartment [178]. As already discussed in the section on stimuli-responsive polymers, providing nanovectors responding to an endogenous stimulus in addition to an external trigger can clearly improve the spatiotemporal control of their functions while limiting side effects from their inherent distribution in both normal and tumor tissues. Subcellular localization of the photosensitizer is largely governed by its concentration and its physicochemical properties (molecular weight, lipophilicity, amphiphilicity, ionic charge, and protein binding characteristics) [179]. On the one hand, lipophilic, anionic dyes generally localize in membrane structures (including plasma, mitochondrial, endoplasmic reticulum and nuclear membranes), while hydrophilic materials seem to accumulate in lysosomes [180]. On the other hand, cationic sensitizers such as rhodamines and cyanines preferentially accumulate in mitochondria [181] due to electrical potential gradients across the mitochondrial membrane, allowing a targeted approach for PDT [182,183]. Even if beyond the scope of this review, the physicochemical properties of the chosen photosensitizer also help to passively target intracellular compartments.

Until today, several strategies for targeting subcellular organelles, including cell nucleus [184,185], lysosome [186], mitochondria, endoplasmic reticulum, and even plasma membrane, have been proposed to maximize the antitumor effects of PDT [187]. These strategies are schematized in Figure 14, listed in Table 4 and presented below.

Endosome/lysosome-targeted PDT and photochemical internalization

An approach described to target lysosomes was to synthetize positively charged ruthenium(II) polypyridyl complexes that selectively localize in lysosomes through endocytosis and induce serious phototoxicity in human 3D tumor spheroids after two-photon photodynamic therapy [186]. Another promising way to develop lysosome-targeted PDT relies on photochemical internalization (PCI) strategies based on polymeric nanovectors. PCI is a concept designed by Berg et al. based on photodynamic therapy [188,189]. This technique results from the activation of a photosensitizer at a specific wavelength after its cellular internalization in endosomes. The photosensitizer in the excited state induces the formation of reactive oxygen species such as singlet oxygen that will disrupt the endosomal membrane. This technique allows for a spatiotemporal control of the release of the endosomal content into the cytosol [190]. PCI is applied for the codelivery of a photosensitizer with an active agent such as nucleic acids [191], proteins [192], anticancer agents [193-195], or nanoparticles [48,196]. In the area of nanomedicine, this concept may be a powerful tool when associated with nanovectors such as copolymer micelles to increase the efficacy of the drug delivery [168]. This strategy was particularly successful in the case of drug delivery of camptothecin using dual degradable and pH-sensitive nanoparticles of PEO-acetal [72] and hematoporphyrin as a photosensitizer or of doxorubicin encapsulated in block copolymer micelles of porphyrin-modified PEO-PCL [79].

Plasma membrane-targeted PDT

Usually, PDT efficacy requires the adequate cellular uptake of polymeric vectors loaded with photosensitizer. Since the cell plasma membrane plays the fundamental role of a selective barrier leading frequently to an inadequate internalization of nanovectors, some authors proposed to target the plasma membrane integrity through the peroxidation of lipids via ROS produced during PDT in order to eradicate tumor cells [197]. Inter-

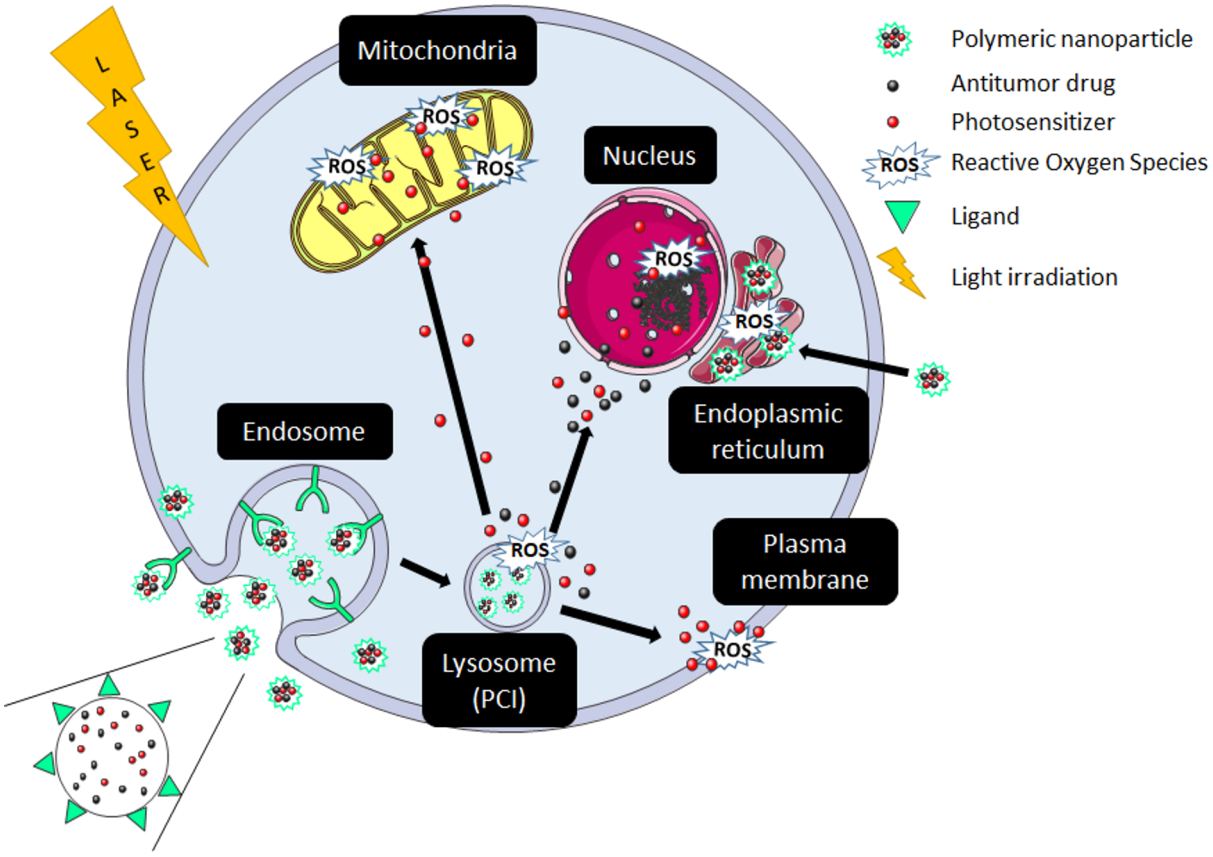

Figure 14: Schematic view of photodynamic therapy (PDT) strategies with polymeric nanovectors targeting subcellular organelles. PCI: photochemical internalization. ROS: reactive oxygen species.

estingly, the loss of plasma membrane integrity because of PDT leads to cell necrosis rather than apoptosis [198] further eliciting antitumor immune responses. Distinct strategies were proposed to target the plasma membrane. Among them, Kim et al. developed ZnPc-loaded membrane fusogenic liposomes, engineered to fuse with the plasma membrane and deliver ZnPc within it [199]. They confirmed that membrane localization of ZnPc molecules led to rapid membrane disruption upon irradiation and to a subsequent necrosis-like cell death. Recently, Jia et al. developed self-assembled polymeric nanoparticles (80 nm diameter) composed of PEO and glycol chitosan (GC) and loaded with protoporphyrin IX (GC-PEO-PpIX) [200]. Interestingly, the PpIX moieties exhibit a high affinity for plasma membrane. Indeed, when the nanoparticles encountered the plasma membrane, the nanoparticles dissassembled and PpIX photosensitizer remained anchored to the lipid bilayer through multisite anchoring. It was observed in vitro on A549 human pulmonary cancer cells that plasma membrane targeted-PDT acted in two synergistic ways: plasma membrane integrity was first lost, leading secondly to a massive entry of nanovectors within the cell, causing the destruction of intracellular organelles. PpIX presented in vitro a remarkable PDT efficacy when encapsulated within GC-PEO-PpIX micelles compared to free PpIX (i.e., after laser irradiation at 635 nm at 14 $mW{\cdot}cm^{-2}$ for 1 min, cell viability was respectively 50% and more than 95%). In vivo results on nude mice bearing U14 subcutaneous tumors demonstrated that GC-PEO-PpIX micelles achieved a good tumor accumulation and retention, paving the way to use them as theranostic agent for image-guided PDT. Mice treated with GC-PEO-PpIX had the tumors eliminated without regrowth within 22 days of observation, while free PpIX exhibited little therapeutic efficacy. In conclusion, the authors demonstrated that plasma membrane-targeted PDT efficiently induced plasma membrane permeability upon laser irradiation, allowing for a massive penetration of nanovectors loaded with photosensitizer within the cytoplasm. These synergic processes promise to bypass improper cellular uptake or lysosomal escape issues faced by therapeutic strategies based on nanovectors. It could be a promising solution to avoid/limit cancer cell resistance to drugs observed with conventional antitumor therapies.

Table 4: Overview of the subcellular organelle-targeted photodynamic therapy with polymeric nanovectors strategies. PS: photosensitizer. PM: plasma membrane.

targeted cellular compartment	targeting	stimuli	polymer	PS and associated drug	biological tests	ref
mitochondria	1: folic acid targeting endo/lysosomes 2: ammonium-functionalized cations (porphyrin) targeting mitochondria	1: low-pH-triggered lysosomal escape 2: redox-induced disassembly (cytoplasm) and subsequent drug release 3: light irradiation (mitochondria)	PEG-PDBO-BPT	5-(3-hydroxy-*p*-(4-trimethylammonium)butoxyphenyl)-10,15,20-triphenylporphyrin chlorin (MTPP) + camptothecin	in vitro + in vivo	[219]
	carboxybutyltriphenylphosphonium	light irradiation	folate-cholesteryl albumin (FA-chol-BSA)	carboxybutyltriphenylphosphonium-pheophorbide a (TPP-Pheo a)	in vitro + in vivo	[203]
endosomes	folic acid	pH-sensitive	PEG-poly (β-benzyl-L-aspartate)	pheophorbide a (hydrophobic)	in vitro	[220]
cytoplasm	folic acid targeting endo/lysosomes	light-triggered drug release through ROS production	mPEG-*b*-PPADT poly(1,4-phenylene-acetone dimethylene thioketal) (PPADT)-PEG	*meso*-tetraphenylporphyrin + paclitaxel	in vitro + in vivo	[221]
	biotin targeting endo/lysosomes	light-triggered drug release through ROS production	mPEG-*b*-PPADT poly(1,4-phenylene-acetone dimethylene thioketal) (PPADT)-PEG	silicon 2,3-naphthalocyanine bis(trihexylsilyloxide) (SiNc) + paclitaxel	in vitro + in vivo	[222]
plasma membrane	protoporphyrin IX moieties	light irradiation	glycol chitosan (GC) and polyethylene glycol (PEG)	protoporphyrin IX	in vitro + in vivo	[200]
endoplasmic reticulum	coordination affinity of the Ca^{2+} ion to the multi-carboxyl group of the polymer	light irradiation	poly(aspartic acid) and polyethylene glycol (PEG)	indocyanine green + paclitaxel	in vitro + in vivo	[177]

Mitochondria-targeted PDT

Mitochondria are a target of choice because they are numerous in cells, widely distributed in the cytoplasm, and play a pivotal role in metabolism and cell apoptosis [201]. Furthermore, molecular oxygen, which is a pre-requisite for PDT efficacy, is present in mitochondria because it is required as a terminal electron acceptor for ATP production [202]. Some authors chose to chemically modify known photosensitizers such as pheophorbide a with carboxybutyltriphenylphosphonium to specially target mitochondria [203]. TPP-based lipophilic cations have the ability to cross the mitochondrial membrane. By combining this therapeutic agent with folate-cholesteryl albumin (FA-chol-BSA), they obtained nanoparticles of 161.4 ± 14.3 nm of diameter which were readily taken up by murine and human tumor cells in vitro. Interestingly, the modified photosensitizer specifically accumulated within the mitochondria, leading to mitochondrial dysfunction and cell apoptosis after light irradiation. Nanoparticles loaded with TPP-Pheo a were quicker to induce an antitumor effect in vivo in mice model than non-modified Pheo a, which did not target mitochondria. Another strategy proposed was to add the lipophilic TPP cation directly on polymers used to produce nanoparticles, instead of modifying a photosensitizer [204,205]. This approach was followed with FDA-approved and biodegradable poly(lactic-*co*-glycolic acid) PLGA nanoparticles loaded with the antitumor drugs lonidamine and α-tocopheryl succinate. A higher mitochondrial uptake of the chemotherapeutics was demonstrated when nanoparticles were targeting mitochondria thanks to TPP. Nanoparticles are classically taken up by the endosomal pathway, which represents a physical barrier for mitochondria-targeted nanoparticles. But interestingly, these PLGA-*block*-PEO-TPP nanoparticles displayed amazing endosomal and lysosomal escape properties. The authors proposed that positively charged PEG exhibits a buffering capacity preventing endosomes acidification. This increases ATPase activity and counter ions accumulation in endosomal vesicles leading to osmotic swelling, membrane disruption and nanoparticle release within the cytoplasm, in a similar mechanism as

observed with the strongly buffering polyamines poly(ethylene imine) (PEI) or PAMAM [206]. Self-assembled PEG-PCL-TPP bromide micelles (40 nm diameter) efficiently deliver coenzyme Q10 antioxidant within mitochondria to restore cellular functions [207]. Other mitochondrial targeting strategies have been developed for PDT. Among these are hollow silica nanoparticles loaded with catalase enzyme to produce the O_2/chlorin-e6 photosensitizer/pH-responsive anionic polymer PEG/2,3-dimethylmaleic anhydride-*co*-poly(allylamine hydrochloride)/(3-carboxypropyl)TPP bromide to target mitochondria [208], pyropheophorbide a loaded onto nanographene oxide (NGO) particles [209] because single-walled carbon nanotubes previously showed a tropism for mitochondria [210], and an iridium(III) complex (Ir-P(ph)$_3$) [211]. Although they do not rely on polymeric nanoobjects, these approaches are important to note for a better overview over possibilities to target mitochondria.

Nucleus-targeted PDT

Passive diffusion through the nuclear pore complexes is a way to enter a cell nucleus. Gaus et al. demonstrated that passive nuclear targeting can be achieved by adapting polymeric nanoparticle shapes to the architecture of nuclear pore complexes [212]. Working with poly(oligoethylene glycol methacrylate)-*block*-poly(styrene-*co*-vinylbenzaldehyde) nanoparticles, they demonstrated that rod-like (5–10 nm × 100–300 nm) and worm-like nanoparticles (5–10 nm × 400–700 nm) were more suitable than micelles and vesicles to penetrate the cell nucleus and deliver the associated doxorubicin. Even if this work was not led in the context of PDT, it demonstrated that the shape of polymeric nanoparticles appears to be a relevant criterion to design nanovectors capable of passively diffuse across the nuclear membrane. An original work was realized by El-Akra et al. in order to target the nucleus of estrogen-dependent cancer and vascular endothelial cells to eliminate both tumor and blood vessel cells using PDT [213]. For this purpose, estradiol and pheophorbide a (E-Pheo a) were linked by two amide bonds via oxoethylene or oxopropylene spacers. Efficient cellular uptake and intranuclear localization was confirmed in vitro in human MCF-7 breast cancer cells known to highly express estrogen receptors (EsR). E-Pheo a was shown to be seven times more phototoxic than a control compound in EsR-positive MCF-7 cell lines and human EA.hy926 vascular endothelial cells. In EsR-negative SKBR3 cells the same phototoxicity was observed for both compounds. Some PDT strategies, although not using polymeric nanovectors, were designed to target the nucleus using a cyclometalated iridium(III) complex [214]. However, it must be kept in mind that nucleus-targeted PDT agents caused great damage to the DNA of cancer cells, which also generates a high risk of genetic mutation in surrounding healthy cells.

Endoplasmic reticulum-targeted PDT

The endoplasmic reticulum (ER) is a dynamic organelle dedicated to protein synthesis and folding, calcium storage and lipid/carbohydrate metabolism [215]. Some authors proposed as therapeutic strategy to interfere with ER functions by generating stress through ER-targeted PDT. In vitro cellular assay was developed to screen ER-targeting photosensitizers with ideal photoactivity [216]. Wan et al. designed ER-targeted micelles for PDT that can be efficiently loaded with the antitumor drug paclitaxel [177]. It is a new type of biodegradable comb-like polymer, namely poly(aspartic acid)-*graft*-(PEG-ICG). ICG, in addition to being an imaging agent, exhibits PDT and photothermal therapy effects under near-infrared irradiation. The authors hypothesized that the carboxy-containing polymers are able to target the ER through the strong coordination affinity of Ca^{2+} ions to the carboxy groups of the polymer owing to the extremely high concentration of Ca^{2+} ions within the ER compared to the cytosol (Figure 15).

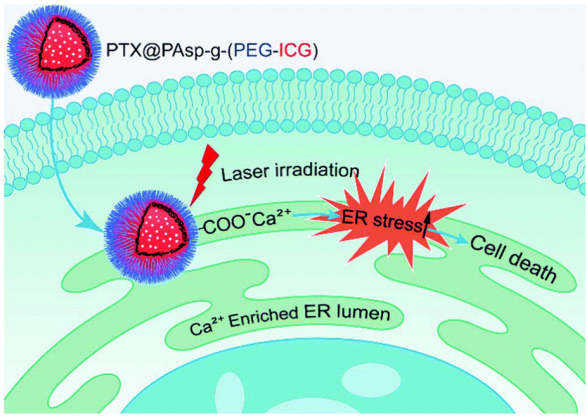

Figure 15: Illustration of the PTX@PAsp-*g*-(PEG-ICG) ER-targeting process and mechanism of cell death. PTX@PAsp-*g*-(PEG-ICG) micelles accumulate in the ER lumen through the coordination affinity of the Ca^{2+} ions to the carboxy groups of PAsp. Upon laser irradiation of the photosensitizer ICG, the generated ROS would lead to elevated stress and induce cancer cell death. ER: endoplasmic reticulum. ICG: indocyanine green. ROS: reactive oxygen species. Reproduced with permission from [177], copyright 2018 The Royal Society of Chemistry.

Using SK-OV-3 human ovary tumor cells, they demonstrated that micelles uptake mechanism was largely attributed to passive diffusion and not to endocytosis. Under laser irradiation (0.2 W cm^{-2}, 785 nm, 30 s), PTX@PAsp-*g*-(PEG-ICG) micelles induced a ten-fold ROS production in SK-OV-3 cells, compared to the non-irradiated cells, underlining the high potential of these micelles for PDT. Cell death through apoptosis was measured in vitro in glioma cancer cells U-87 MG. While PTX@PAsp-*g*-(PEG-ICG) micelles without irradiation induced only 10.6% of cell apoptosis, cell apoptosis jumped to 73.2% after irradiation (0.2 W·cm^{-2}, 785 nm, 5 min). The

viability of U-87 MG cells was assessed in vitro after incubation for 24 h with PTX@PAsp-*g*-(PEG-ICG). Free paclitaxel at a concentration of 2.5 μg·mL^{-1} decreased cell viability by 40% while PTX@PAsp-*g*-(PEG-ICG) with laser irradiation (2 W·cm^{-2}, 785 nm, 30 s) reduced the cell viability by 100%, indicating that PDT and drug vectorization remarkably enhanced chemotherapeutic effects. In vivo experiments on nude mice bearing U-87 MG tumor indicated that PTX@PAsp-*g*-(PEG-ICG) micelles preferentially accumulate in the tumor site. The mouse group "PTX@PAsp-*g*-(PEG-ICG) micelles treated with laser irradiation" displayed a more effective tumor inhibition, with complete tumor remission in two mice at day 21, than other groups (PBS control, taxol-treated, non-irradiated PTX@PAsp-*g*-(PEG-ICG) micelles). In this example, authors aimed and achieved to induce tumor cell death by causing stress through ER-targeted PDT. However, biologists are increasingly exploring the causes and consequences of ER stress in malignancy. Accumulation of misfolded proteins in the endoplasmic reticulum causes ER stress and activation of the unfolded protein response, which in turn promotes cancer development and progression through active modulation of immune cell functions [217]. Thus, nowadays, clinical antitumor therapeutic strategies aim to control ER stress responses in cancer cells to enhance the efficacy of standard chemotherapies instead of creating new ER stress [218].

Conclusion

In this review, we have described the developments of the last five years regarding block copolymer nanocarriers used in PDT. The main concerns have been the control of the copolymer structure, which must be designed in order to optimize the nanocarrier performance in term of photosensitizer loading and release at the tumor tissue. Sophisticated stimuli-responsive systems have been conceived to allow for drug release according to the environmental conditions. Some effort has also been addressed to overcome hypoxia, a hallmark of tumor tissues, and a main drawback for PDT. Interestingly, the main trend of the last three years (about 35% of the cited work published during this period) is aimed at developing intelligent "all in one" nanocarriers in which different drugs are loaded in the same nanocarrier. Combined treatments are more and more proposed and PDT is often associated with chemotherapy or photothermal therapy. Theranostic nanotechnologies, where diagnostic is combined with therapy, enable multimodal imaging (fluorescence or near-infrared fluorescence imaging, MRI, PET) thanks to the addition of fluorescent molecules, contrast agents or radioactive species. These unique, multifunctional nanocarriers are complex by nature and their mechanism of action is not well understood, as we stressed in the section on processes of interaction with membranes. Besides, another often overlooked aspect is the fate of polymer nanocarriers in biological fluids and in particular the possible influence of other macromolecules such as proteins on their stability and structure. This has been assessed in the field of inorganic nanomaterials, where more and more attention has been addressed towards the nano–bio interface in order to understand the interactions between engineered nanomaterials and biological systems. This established approach for inorganic nanoparticles is also essential in the case of soft self-assembled nanocarriers and should be more often examined. Indeed, the nanovector should not be considered by itself but characterized with its associated protein corona. This new assembly vector/corona should be defined as the real nanocarrier of the drug or the PS.

Some efforts have been also made in terms of cell targeting in order to improve the nanocarrier accumulation in the tumor tissues. Another aspect of targeting that is less taken into account in the nanocarrier community is the possibility to bring the photosensitizer to the organelles inside the cell.

We are convinced that the essential directions of future research should be the following:

1. It would be important to decipher the mechanism of nanovectors with a physicochemical perspective, i.e., to understand the main parameters in terms of copolymer nature and structure that favor photosensitizer cell internalization. To date, only theoretical works and some physicochemical studies address it mostly using biomimetic membranes. This aspect is essential to guide design choices to improve therapy efficiency.
2. The scientific community should make some efforts to establish standard PDT protocols so that the different proposed nanocarriers could be compared. The necessity for a "minimum information standard" [223] has been already proposed for inorganic nanomaterials. It consists in a standardization of material characterization, biological characterization and experimental details. This process would allow one to select the best nanocarrier properties thus sensibly helping the development of polymer nanocarriers and possibly resulting in more chances to go to clinical trials.
3. Finally, the design of nanocarrier targeting properties remains a challenge, going largely beyond the PDT application. Increasing knowledge about the protein corona will undoubtedly shed a new light on this topic.

List of Abbreviations

AIE: aggregation induced emission; AIP: amphiphilic invertible polymers; DOE: design of experiments; DOPC: 1,2-dioleyl-*sn*-glycero-3-phosphocholine; DOPG: 1,2-dioleyl-*sn*-glycero-3-phosphoglycerol; DPPC: 1,2-dipalmitoyl-*sn*-glycero-

3-phosphocholine; DPH: 1,6-diphenyl-1,3,5-hexatriene; EPR: enhanced permeation and retention effect; ER: endoplasmic reticulum; FA: folate; FBS: foetal bovine serum; FDA: Food and Drug Administration; FI: fluorescence imaging; FRET: Förster resonance energy transfer; GC: glycol chitosan; GSH: glutathione; HLB: hydrophilic–lipophilic balance; HSP: Hansen solubility parameter; HSA: human serum albumin; ICG: indocyanin green; MD: molecular dynamics; MRI: magnetic resonance imaging; NIR: near infra red; NIRFI: near infra red fluorescence imaging; NOE: nuclear Overhauser effect; OVAT: one-variable-at-a-time; PA: photoacoustic imaging; PAMAM: poly(amidoamine); PAsp: poly(aspartate); PBLG: poly(γ-benzyl-L-glutamate); PBS: phosphate buffered saline; PCI: photochemical internalization; PCL: poly(ε-caprolactone); PIC: poly ion complexes; PDMS: poly(dimethyl siloxane); PDT: photodynamic therapy; PEG: poly(ethylene glycol); PEI: poly(ethylene imine); PEO: poly(ethylene oxide); PET: positron emission tomography; PFC: perfluorocarbon; PGMA: poly(glycidyl methacrylate); PLA: poly(lactic acid); PLGA: poly(lactic-*co*-glycolic acid); Plys: poly(lysine); PMAGP: poly(6-*O*-methacryloyl-D-galactopyranose); POEGMA: poly[oligo(ethylene glycol) methyl ether methacrylate]; POPC: 1-palmitoyl-2-oleoyl-*sn*-glycero-3-phosphocholine; PpIX: protoporphyrin IX; PPO: poly(propylene oxide); PTT: photothermal therapy; PTX: paclitaxel; PS: photosensitizer; ROS: reactive oxygen species; TCPP: 5,10,15,20-tetrakis(4-carboxyphenyl)porphyrin; TEM: transmission electron microscopy; TPETP: tetraphenylethenethiophene; TPP: triphenylphosphonium; ^{1}H NMR: proton nuclear magnetic resonance; XPS: X-ray photoelectron spectroscopy; ZnPc: zinc phthalocyanine

ORCID® iDs

Maxime Demazeau - https://orcid.org/0000-0002-2347-4167
Laure Gibot - https://orcid.org/0000-0001-7255-4123
Anne-Françoise Mingotaud - https://orcid.org/0000-0001-7873-845X
Patricia Vicendo - https://orcid.org/0000-0001-5874-1547
Clément Roux - https://orcid.org/0000-0001-5707-4471
Barbara Lonetti - https://orcid.org/0000-0003-4291-6861

References

1. Schwartz, R. S. *N. Engl. J. Med.* **2004,** *350,* 1079–1080. doi:10.1056/nejmp048021
2. Matsumura, Y.; Maeda, H. *Cancer Res.* **1986,** *46,* 6387–6392.
3. Maeda, H. *Bioconjugate Chem.* **2010,** *21,* 797–802. doi:10.1021/bc100070g
4. Bertrand, N.; Leroux, J.-C. *J. Controlled Release* **2012,** *161,* 152–163. doi:10.1016/j.jconrel.2011.09.098
5. Fang, J.; Nakamura, H.; Maeda, H. *Adv. Drug Delivery Rev.* **2011,** *63,* 136–151. doi:10.1016/j.addr.2010.04.009
6. Knop, K.; Hoogenboom, R.; Fischer, D.; Schubert, U. S. *Angew. Chem., Int. Ed.* **2010,** *49,* 6288–6308. doi:10.1002/anie.200902672
7. Matyjaszewski, K.; Spanswick, J. *Mater. Today* **2005,** *8,* 26–33. doi:10.1016/s1369-7021(05)00745-5
8. Riehemann, K.; Schneider, S. W.; Luger, T. A.; Godin, B.; Ferrari, M.; Fuchs, H. *Angew. Chem., Int. Ed.* **2009,** *48,* 872–897. doi:10.1002/anie.200802585
9. Dionzou, M.; Morère, A.; Roux, C.; Lonetti, B.; Marty, J.-D.; Mingotaud, C.; Joseph, P.; Goudounèche, D.; Payré, B.; Léonetti, M.; Mingotaud, A.-F. *Soft Matter* **2016,** *12,* 2166–2176. doi:10.1039/c5sm01863c
10. Crucho, C. I. C. *ChemMedChem* **2015,** *10,* 24–38. doi:10.1002/cmdc.201402290
11. Eetezadi, S.; Ekdawi, S. N.; Allen, C. *Adv. Drug Delivery Rev.* **2015,** *91,* 7–22. doi:10.1016/j.addr.2014.10.001
12. Bobo, D.; Robinson, K. J.; Islam, J.; Thurecht, K. J.; Corrie, S. R. *Pharm. Res.* **2016,** *33,* 2373–2387. doi:10.1007/s11095-016-1958-5
13. Weissig, V.; Pettinger, T. K.; Murdock, N. *Int. J. Nanomed.* **2014,** *9,* 4357–4373. doi:10.2147/ijn.s46900
14. Weissig, V.; Guzman-Villanueva, D. *Int. J. Nanomed.* **2015,** *10,* 1245–1257. doi:10.2147/ijn.s65526
15. Obaid, G.; Broekgaarden, M.; Bulin, A.-L.; Huang, H.-C.; Kuriakose, J.; Liu, J.; Hasan, T. *Nanoscale* **2016,** *8,* 12471–12503. doi:10.1039/c5nr08691d
16. Bashkatov, A. N.; Genina, E. A.; Kochubey, V. I.; Tuchin, V. V. *J. Phys. D: Appl. Phys.* **2005,** *38,* 2543–2555. doi:10.1088/0022-3727/38/15/004
17. Dougherty, T. J.; Grindey, G. B.; Fiel, R.; Weishaupt, K. R.; Boyle, D. G. *J. Natl. Cancer Inst.* **1975,** *55,* 115–121. doi:10.1093/jnci/55.1.115
18. Lucky, S. S.; Soo, K. C.; Zhang, Y. *Chem. Rev.* **2015,** *115,* 1990–2042. doi:10.1021/cr5004198
19. Li, T.; Yan, L. *Pharmaceuticals* **2018,** *11,* 133. doi:10.3390/ph11040133
20. Master, A.; Livingston, M.; Sen Gupta, A. *J. Controlled Release* **2013,** *168,* 88–102. doi:10.1016/j.jconrel.2013.02.020
21. Ben Mihoub, A.; Larue, L.; Moussaron, A.; Youssef, Z.; Colombeau, L.; Baros, F.; Frochot, C.; Vanderesse, R.; Acherar, S. *Molecules* **2018,** *23,* 1936. doi:10.3390/molecules23081936
22. Debele, T. A.; Peng, S.; Tsai, H.-C. *Int. J. Mol. Sci.* **2015,** *16,* 22094–22136. doi:10.3390/ijms160922094
23. Sun, W.; Zhao, X.; Fan, J.; Du, J.; Peng, X. *Small* **2019,** *15,* 1804927. doi:10.1002/smll.201804927
24. Protti, S.; Albini, A.; Viswanathan, R.; Greer, A. *Photochem. Photobiol.* **2017,** *93,* 1139–1153. doi:10.1111/php.12766
25. Lamch, Ł.; Pucek, A.; Kulbacka, J.; Chudy, M.; Jastrzębska, E.; Tokarska, K.; Bułka, M.; Brzózka, Z.; Wilk, K. A. *Adv. Colloid Interface Sci.* **2018,** *261,* 62–81. doi:10.1016/j.cis.2018.09.002
26. Shi, X.; Zhang, H.; Jin, W.; Liu, W.; Yin, H.; Li, Y.; Dong, H. *J. Photochem. Photobiol., B* **2019,** *198,* 111586. doi:10.1016/j.jphotobiol.2019.111586
27. Mordon, S.; Cochrane, C.; Tylcz, J. B.; Betrouni, N.; Mortier, L.; Koncar, V. *Photodiagn. Photodyn. Ther.* **2015,** *12,* 1–8. doi:10.1016/j.pdpdt.2014.11.002
28. Mohammad-Hadi, L.; MacRobert, A. J.; Loizidou, M.; Yaghini, E. *Nanoscale* **2018,** *10,* 1570–1581. doi:10.1039/c7nr07739d
29. Gibot, L.; Lemelle, A.; Till, U.; Moukarzel, B.; Mingotaud, A.-F.; Pimienta, V.; Saint-Aguet, P.; Rols, M.-P.; Gaucher, M.; Violleau, F.; Chassenieux, C.; Vicendo, P. *Biomacromolecules* **2014,** *15,* 1443–1455. doi:10.1021/bm5000407

30. Berwin Singh, S. V.; Kim, J.; Park, H.; Khang, G.; Lee, D. *Macromol. Res.* **2017,** *25,* 749–755. doi:10.1007/s13233-017-5078-9
31. Chu, M.; Li, H.; Wu, Q.; Wo, F.; Shi, D. *Biomaterials* **2014,** *35,* 8357–8373. doi:10.1016/j.biomaterials.2014.05.049
32. Gjuroski, I.; Furrer, J.; Vermathen, M. *ChemPhysChem* **2018,** *19,* 1089–1102. doi:10.1002/cphc.201701318
33. Montanha, M. C.; Silva, L. L.; Pangoni, F. B. B.; Cesar, G. B.; Gonçalves, R. S.; Caetano, W.; Hioka, N.; Tominaga, T. T.; Consolaro, M. E. L.; Diniz, A.; Kimura, E. *J. Photochem. Photobiol., B* **2017,** *170,* 247–255. doi:10.1016/j.jphotobiol.2017.04.008
34. Vilsinski, B. H.; Gerola, A. P.; Enumo, J. A.; Campanholi, K. da S. S.; Pereira, P. C. de S.; Braga, G.; Hioka, N.; Kimura, E.; Tessaro, A. L.; Caetano, W. *Photochem. Photobiol.* **2015,** *91,* 518–525. doi:10.1111/php.12421
35. Zhiyentayev, T. M.; Boltaev, U. T.; Solov'eva, A. B.; Aksenova, N. A.; Glagolev, N. N.; Chernjak, A. V.; Melik-Nubarov, N. S. *Photochem. Photobiol.* **2014,** *90,* 171–182. doi:10.1111/php.12181
36. Han, Y.; Chen, Z.; Zhao, H.; Zha, Z.; Ke, W.; Wang, Y.; Ge, Z. *J. Controlled Release* **2018,** *284,* 15–25. doi:10.1016/j.jconrel.2018.06.012
37. Jing, C.; Wang, R.; Ou, H.; Li, A.; An, Y.; Guo, S.; Shi, L. *Chem. Commun.* **2018,** *54,* 3985–3988. doi:10.1039/c7cc09954a
38. Lamch, Ł.; Tylus, W.; Jewgiński, M.; Latajka, R.; Wilk, K. A. *J. Phys. Chem. B* **2016,** *120,* 12768–12780. doi:10.1021/acs.jpcb.6b10267
39. Li, J.; Yao, S.; Wang, K.; Lu, Z.; Su, X.; Li, L.; Yuan, C.; Feng, J.; Yan, S.; Kong, B.; Song, K. *Cancer Sci.* **2018,** *109,* 1958–1969. doi:10.1111/cas.13605
40. Wennink, J. W. H.; Liu, Y.; Mäkinen, P. I.; Setaro, F.; de la Escosura, A.; Bourajjaj, M.; Lappalainen, J. P.; Holappa, L. P.; van den Dikkenberg, J. B.; al Fartousi, M.; Trohopoulos, P. N.; Ylä-Herttuala, S.; Torres, T.; Hennink, W. E.; van Nostrum, C. F. *Eur. J. Pharm. Sci.* **2017,** *107,* 112–125. doi:10.1016/j.ejps.2017.06.038
41. Yang, T.; Liu, L.; Deng, Y.; Guo, Z.; Zhang, G.; Ge, Z.; Ke, H.; Chen, H. *Adv. Mater. (Weinheim, Ger.)* **2017,** *29,* 1700487. doi:10.1002/adma.201700487
42. Grossen, P.; Witzigmann, D.; Sieber, S.; Huwyler, J. *J. Controlled Release* **2017,** *260,* 46–60. doi:10.1016/j.jconrel.2017.05.028
43. Yu, W.; Ye, M.; Zhu, J.; Wang, Y.; Liang, C.; Tang, J.; Tao, H.; Shen, Y. *Nanomedicine (N. Y., NY, U. S.)* **2018,** *14,* 1099–1110. doi:10.1016/j.nano.2018.02.005
44. Calles, J. A.; Bermúdez, J.; Vallés, E.; Allemandi, D.; Palma, S. Polymers in Ophthalmology. In *Advanced Polymers in Medicine;* Puoci, F., Ed.; Springer: Cham, 2015; pp 147–176. doi:10.1007/978-3-319-12478-0_6
45. Pound-Lana, G. E. N.; Garcia, G. M.; Trindade, I. C.; Capelari-Oliveira, P.; Pontifice, T. G.; Vilela, J. M. C.; Andrade, M. S.; Nottelet, B.; Postacchini, B. B.; Mosqueira, V. C. F. *Mater. Sci. Eng., C* **2019,** *94,* 220–233. doi:10.1016/j.msec.2018.09.022
46. Huang, Y.; Ma, D.; Pan, S.; Lin, P.; Lin, Y.; Yang, H.; Peng, Y. *J. Nanopart. Res.* **2015,** *17,* 41. doi:10.1007/s11051-014-2819-y
47. Jang, W.-D.; Nishiyama, N.; Zhang, G.-D.; Harada, A.; Jiang, D.-L.; Kawauchi, S.; Morimoto, Y.; Kikuchi, M.; Koyama, H.; Aida, T.; Kataoka, K. *Angew. Chem., Int. Ed.* **2005,** *44,* 419–423. doi:10.1002/anie.200461603
48. Chen, H.; Xiao, L.; Anraku, Y.; Mi, P.; Liu, X.; Cabral, H.; Inoue, A.; Nomoto, T.; Kishimura, A.; Nishiyama, N.; Kataoka, K. *J. Am. Chem. Soc.* **2014,** *136,* 157–163. doi:10.1021/ja406992w
49. Zhang, G.-D.; Harada, A.; Nishiyama, N.; Jiang, D.-L.; Koyama, H.; Aida, T.; Kataoka, K. *J. Controlled Release* **2003,** *93,* 141–150. doi:10.1016/j.jconrel.2003.05.002
50. Zhao, L.; Ma, R.; Li, J.; Li, Y.; An, Y.; Shi, L. *Biomacromolecules* **2008,** *9,* 2601–2608. doi:10.1021/bm8004808
51. Zheng, R.; Wu, Z.; Yan, Y.; Wang, J.; Huang, J. *RSC Adv.* **2015,** *5,* 17253–17256. doi:10.1039/c4ra16259e
52. Castriciano, M. A.; Zagami, R.; Casaletto, M. P.; Martel, B.; Trapani, M.; Romeo, A.; Villari, V.; Sciortino, M. T.; Grasso, L.; Guglielmino, S.; Scolaro, L. M.; Mazzaglia, A. *Biomacromolecules* **2017,** *18,* 1134–1144. doi:10.1021/acs.biomac.6b01752
53. Conte, C.; Scala, A.; Siracusano, G.; Sortino, G.; Pennisi, R.; Piperno, A.; Miro, A.; Ungaro, F.; Sciortino, M. T.; Quaglia, F.; Mazzaglia, A. *Colloids Surf., B* **2016,** *146,* 590–597. doi:10.1016/j.colsurfb.2016.06.047
54. Xiong, H.; Zhou, D.; Zheng, X.; Qi, Y.; Wang, Y.; Jing, X.; Huang, Y. *Chem. Commun.* **2017,** *53,* 3422–3425. doi:10.1039/c6cc10059g
55. Fleige, E.; Quadir, M. A.; Haag, R. *Adv. Drug Delivery Rev.* **2012,** *64,* 866–884. doi:10.1016/j.addr.2012.01.020
56. Saravanakumar, G.; Kim, J.; Kim, W. J. *Adv. Sci.* **2017,** *4,* 1600124. doi:10.1002/advs.201600124
57. Py-Daniel, K. R.; Namban, J. S.; de Andrade, L. R.; de Souza, P. E. N.; Paterno, L. G.; Azevedo, R. B.; Soler, M. A. G. *Eur. J. Pharm. Biopharm.* **2016,** *103,* 23–31. doi:10.1016/j.ejpb.2016.03.028
58. Vilsinski, B. H.; Witt, M. A.; Barbosa, P. M.; Montanha, M. C.; Nunes, C. S.; Bellettini, I. C.; de Castro, L. V.; Sato, F.; Baesso, M. L.; Muniz, E. C.; Caetano, W. *J. Mol. Liq.* **2018,** *271,* 949–958. doi:10.1016/j.molliq.2018.09.034
59. Synatschke, C. V.; Nomoto, T.; Cabral, H.; Förtsch, M.; Toh, K.; Matsumoto, Y.; Miyazaki, K.; Hanisch, A.; Schacher, F. H.; Kishimura, A.; Nishiyama, N.; Müller, A. H. E.; Kataoka, K. *ACS Nano* **2014,** *8,* 1161–1172. doi:10.1021/nn4028294
60. Wang, Q.; Li, J.-M.; Yu, H.; Deng, K.; Zhou, W.; Wang, C.-X.; Zhang, Y.; Li, K.-H.; Zhuo, R.-X.; Huang, S.-W. *Biomater. Sci.* **2018,** *6,* 3096–3107. doi:10.1039/c8bm00852c
61. Wang, S.; Yuan, F.; Chen, K.; Chen, G.; Tu, K.; Wang, H.; Wang, L.-Q. *Biomacromolecules* **2015,** *16,* 2693–2700. doi:10.1021/acs.biomac.5b00571
62. Ren, H.; Liu, J.; Su, F.; Ge, S.; Yuan, A.; Dai, W.; Wu, J.; Hu, Y. *ACS Appl. Mater. Interfaces* **2017,** *9,* 3463–3473. doi:10.1021/acsami.6b14885
63. Yuan, P.; Ruan, Z.; Jiang, W.; Liu, L.; Dou, J.; Li, T.; Yan, L. *J. Mater. Chem. B* **2018,** *6,* 2323–2331. doi:10.1039/c8tb00493e
64. Hu, H.; Yan, X.; Wang, H.; Tanaka, J.; Wang, M.; You, W.; Li, Z. *J. Mater. Chem. B* **2019,** *7,* 1116–1123. doi:10.1039/c8tb01844h
65. Liu, L.; Ruan, Z.; Yuan, P.; Li, T.; Yan, L. *Nanotheranostics* **2018,** *2,* 59–69. doi:10.7150/ntno.22754
66. Till, U.; Gibot, L.; Vicendo, P.; Rols, M.-P.; Gaucher, M.; Violleau, F.; Mingotaud, A.-F. *RSC Adv.* **2016,** *6,* 69984–69998. doi:10.1039/c6ra09013c
67. Till, U.; Gibot, L.; Mingotaud, C.; Vicendo, P.; Rols, M.-P.; Gaucher, M.; Violleau, F.; Mingotaud, A.-F. *Nanotechnology* **2016,** *27,* 315102. doi:10.1088/0957-4484/27/31/315102
68. Shen, L.; Huang, Y.; Chen, D.; Qiu, F.; Ma, C.; Jin, X.; Zhu, X.; Zhou, G.; Zhang, Z. *Theranostics* **2017,** *7,* 4537–4550. doi:10.7150/thno.19546

69. Prasad, P.; Gordijo, C. R.; Abbasi, A. Z.; Maeda, A.; Ip, A.; Rauth, A. M.; DaCosta, R. S.; Wu, X. Y. *ACS Nano* **2014,** *8,* 3202–3212. doi:10.1021/nn405773r
70. Sun, J.; Birnbaum, W.; Anderski, J.; Picker, M.-T.; Mulac, D.; Langer, K.; Kuckling, D. *Biomacromolecules* **2018,** *19,* 4677–4690. doi:10.1021/acs.biomac.8b01446
71. Anderski, J.; Mahlert, L.; Sun, J.; Birnbaum, W.; Mulac, D.; Schreiber, S.; Herrmann, F.; Kuckling, D.; Langer, K. *Int. J. Pharm.* **2019,** *557,* 182–191. doi:10.1016/j.ijpharm.2018.12.040
72. Pasparakis, G.; Manouras, T.; Vamvakaki, M.; Argitis, P. *Nat. Commun.* **2014,** *5,* 3623. doi:10.1038/ncomms4623
73. Li, Y.; Lv, S.; Song, Z.; Dang, J.; Li, X.; He, H.; Xu, X.; Zhou, Z.; Yin, L. *Nanoscale* **2018,** *10,* 14554–14562. doi:10.1039/c8nr03611j
74. Li, J.; Wei, K.; Zuo, S.; Xu, Y.; Zha, Z.; Ke, W.; Chen, H.; Ge, Z. *Adv. Funct. Mater.* **2017,** *27,* 1702108. doi:10.1002/adfm.201702108
75. Li, J.; Meng, X.; Deng, J.; Lu, D.; Zhang, X.; Chen, Y.; Zhu, J.; Fan, A.; Ding, D.; Kong, D.; Wang, Z.; Zhao, Y. *ACS Appl. Mater. Interfaces* **2018,** *10,* 17117–17128. doi:10.1021/acsami.8b06299
76. Li, X.; Gao, M.; Xin, K.; Zhang, L.; Ding, D.; Kong, D.; Wang, Z.; Shi, Y.; Kiessling, F.; Lammers, T.; Cheng, J.; Zhao, Y. *J. Controlled Release* **2017,** *260,* 12–21. doi:10.1016/j.jconrel.2017.05.025
77. Liu, F.; Ma, Y.; Xu, L.; Liu, L.; Zhang, W. *Biomater. Sci.* **2015,** *3,* 1218–1227. doi:10.1039/c5bm00045a
78. Sheng, Z.; Hu, D.; Zheng, M.; Zhao, P.; Liu, H.; Gao, D.; Gong, P.; Gao, G.; Zhang, P.; Ma, Y.; Cai, L. *ACS Nano* **2014,** *8,* 12310–12322. doi:10.1021/nn5062386
79. Tian, J.; Xu, L.; Xue, Y.; Jiang, X.; Zhang, W. *Biomacromolecules* **2017,** *18,* 3992–4001. doi:10.1021/acs.biomac.7b01037
80. Wang, T.; Wang, D.; Yu, H.; Wang, M.; Liu, J.; Feng, B.; Zhou, F.; Yin, Q.; Zhang, Z.; Huang, Y.; Li, Y. *ACS Nano* **2016,** *10,* 3496–3508. doi:10.1021/acsnano.5b07706
81. Lovell, J. F.; Liu, T. W. B.; Chen, J.; Zheng, G. *Chem. Rev.* **2010,** *110,* 2839–2857. doi:10.1021/cr900236h
82. Ibrahimova, V.; Denisov, S. A.; Vanvarenberg, K.; Verwilst, P.; Préat, V.; Guigner, J.-M.; McClenaghan, N. D.; Lecommandoux, S.; Fustin, C.-A. *Nanoscale* **2017,** *9,* 11180–11186. doi:10.1039/c7nr04403h
83. Choi, Y.; Weissleder, R.; Tung, C.-H. *ChemMedChem* **2006,** *1,* 698–701. doi:10.1002/cmdc.200600053
84. Campo, M. A.; Gabriel, D.; Kucera, P.; Gurny, R.; Lange, N. *Photochem. Photobiol.* **2007,** *83,* 958–965. doi:10.1111/j.1751-1097.2007.00090.x
85. Lee, S. J.; Park, K.; Oh, Y.-K.; Kwon, S.-H.; Her, S.; Kim, I.-S.; Choi, K.; Lee, S. J.; Kim, H.; Lee, S. G. *Biomaterials* **2009,** *30,* 2929–2939. doi:10.1016/j.biomaterials.2009.01.058
86. Li, L.; Bae, B.-c.; Tran, T. H.; Yoon, K. H.; Na, K.; Huh, K. M. *Carbohydr. Polym.* **2011,** *86,* 708–715. doi:10.1016/j.carbpol.2011.05.011
87. Li, Y.; Lin, T.-y.; Luo, Y.; Liu, Q.; Xiao, W.; Guo, W.; Lac, D.; Zhang, H.; Feng, C.; Wachsmann-Hogiu, S.; Walton, J. H.; Cherry, S. R.; Rowland, D. J.; Kukis, D.; Pan, C.; Lam, K. S. *Nat. Commun.* **2014,** *5,* 4712. doi:10.1038/ncomms5712
88. Xue, Y.; Tian, J.; Xu, L.; Liu, Z.; Shen, Y.; Zhang, W. *Eur. Polym. J.* **2019,** *110,* 344–354. doi:10.1016/j.eurpolymj.2018.11.033
89. Kim, W. L.; Cho, H.; Li, L.; Kang, H. C.; Huh, K. M. *Biomacromolecules* **2014,** *15,* 2224–2234. doi:10.1021/bm5003619
90. Gao, D.; Lo, P.-C. *J. Controlled Release* **2018,** *282,* 46–61. doi:10.1016/j.jconrel.2018.04.030
91. Wang, W.; Lin, L.; Ma, X.; Wang, B.; Liu, S.; Yan, X.; Li, S.; Tian, H.; Yu, X. *ACS Appl. Mater. Interfaces* **2018,** *10,* 19398–19407. doi:10.1021/acsami.8b03506
92. Fang, J.; Šubr, V.; Islam, W.; Hackbarth, S.; Islam, R.; Etrych, T.; Ulbrich, K.; Maeda, H. *Eur. J. Pharm. Biopharm.* **2018,** *130,* 165–176. doi:10.1016/j.ejpb.2018.06.005
93. Wang, Y.; Wei, G.; Zhang, X.; Xu, F.; Xiong, X.; Zhou, S. *Adv. Mater. (Weinheim, Ger.)* **2017,** *29,* 1605357. doi:10.1002/adma.201605357
94. Xu, L.; Liu, L.; Liu, F.; Cai, H.; Zhang, W. *Polym. Chem.* **2015,** *6,* 2945–2954. doi:10.1039/c5py00039d
95. Huang, Y.; Qiu, F.; Shen, L.; Chen, D.; Su, Y.; Yang, C.; Li, B.; Yan, D.; Zhu, X. *ACS Nano* **2016,** *10,* 10489–10499. doi:10.1021/acsnano.6b06450
96. Yuan, Y.; Xu, S.; Zhang, C.-J.; Liu, B. *Polym. Chem.* **2016,** *7,* 3530–3539. doi:10.1039/c6py00449k
97. Wallat, J. D.; Wek, K. S.; Chariou, P. L.; Carpenter, B. L.; Ghiladi, R. A.; Steinmetz, N. F.; Pokorski, J. K. *Polym. Chem.* **2017,** *8,* 3195–3202. doi:10.1039/c7py00522a
98. Zhang, Y.; Wang, C.-X.; Huang, S.-W. *Nanomaterials* **2018,** *8,* 921. doi:10.3390/nano8110921
99. Cheng, L.; Kamkaew, A.; Sun, H.; Jiang, D.; Valdovinos, H. F.; Gong, H.; England, C. G.; Goel, S.; Barnhart, T. E.; Cai, W. *ACS Nano* **2016,** *10,* 7721–7730. doi:10.1021/acsnano.6b03074
100. Zheng, Y.; Lu, H.; Jiang, Z.; Guan, Y.; Zou, J.; Wang, X.; Cheng, R.; Gao, H. *J. Mater. Chem. B* **2017,** *5,* 6277–6281. doi:10.1039/c7tb01443k
101. Liu, X.; Yang, G.; Zhang, L.; Liu, Z.; Cheng, Z.; Zhu, X. *Nanoscale* **2016,** *8,* 15323–15339. doi:10.1039/c6nr04835h
102. Obata, M.; Tanaka, S.; Mizukoshi, H.; Ishihara, E.; Takahashi, M.; Hirohara, S. *J. Polym. Sci., Part A: Polym. Chem.* **2017,** *55,* 3395–3403. doi:10.1002/pola.28716
103. Li, L.; Cho, H.; Kim, S.; Kang, H. C.; Huh, K. M. *Carbohydr. Polym.* **2015,** *121,* 122–131. doi:10.1016/j.carbpol.2014.12.035
104. Que, Y.; Liu, Y.; Tan, W.; Feng, C.; Shi, P.; Li, Y.; Xiaoyu, H. *ACS Macro Lett.* **2016,** *5,* 168–173. doi:10.1021/acsmacrolett.5b00935
105. Wang, H.; Chao, Y.; Liu, J.; Zhu, W.; Wang, G.; Xu, L.; Liu, Z. *Biomaterials* **2018,** *181,* 310–317. doi:10.1016/j.biomaterials.2018.08.011
106. Yuan, Z.; Yu, S.; Cao, F.; Mao, Z.; Gao, C.; Ling, J. *Polym. Chem.* **2018,** *9,* 2124–2133. doi:10.1039/c8py00289d
107. Zhang, Y.; He, L.; Wu, J.; Wang, K.; Wang, J.; Dai, W.; Yuan, A.; Wu, J.; Hu, Y. *Biomaterials* **2016,** *107,* 23–32. doi:10.1016/j.biomaterials.2016.08.037
108. Pelaz, B.; del Pino, P.; Maffre, P.; Hartmann, R.; Gallego, M.; Rivera-Fernandez, S.; de la Fuente, J. M.; Nienhaus, G. U.; Parak, W. J. *ACS Nano* **2015,** *9,* 6996–7008. doi:10.1021/acsnano.5b01326
109. D'souza, A. A.; Shegokar, R. *Expert Opin. Drug Delivery* **2016,** *13,* 1257–1275. doi:10.1080/17425247.2016.1182485
110. Wolfram, J.; Yang, Y.; Shen, J.; Moten, A.; Chen, C.; Shen, H.; Ferrari, M.; Zhao, Y. *Colloids Surf., B* **2014,** *124,* 17–24. doi:10.1016/j.colsurfb.2014.02.035
111. Wang, X.; Wang, J.; Li, J.; Huang, H.; Sun, X.; Lv, Y. *J. Drug Delivery Sci. Technol.* **2018,** *48,* 414–421. doi:10.1016/j.jddst.2018.10.018
112. Hu, D.; Zhong, L.; Wang, M.; Li, H.; Qu, Y.; Liu, Q.; Han, R.; Yuan, L.; Shi, K.; Peng, J.; Qian, Z. *Adv. Funct. Mater.* **2019,** *29,* 1806199. doi:10.1002/adfm.201806199

113. Khatri, V.; Bhatia, S.; Achazi, K.; Deep, S.; Kohli, E.; Sharma, S. K.; Haag, R.; Prasad, A. K. *RSC Adv.* **2017,** *7,* 37534–37541. doi:10.1039/c7ra04994c
114. Liu, L.; Ruan, Z.; Li, T.; Yuan, P.; Yan, L. *Biomater. Sci.* **2016,** *4,* 1638–1645. doi:10.1039/c6bm00581k
115. Zhang, C.; Wang, Y.; Zhao, Y.; Liu, H.; Zhao, Y.; Li, X.; Lin, Q. *Nanomaterials* **2019,** *9,* 91. doi:10.3390/nano9010091
116. Sudimack, J.; Lee, R. J. *Adv. Drug Delivery Rev.* **2000,** *41,* 147–162. doi:10.1016/s0169-409x(99)00062-9
117. Walters, C. L.; Arend, R. C.; Armstrong, D. K.; Naumann, R. W.; Alvarez, R. D. *Gynecol. Oncol.* **2013,** *131,* 493–498. doi:10.1016/j.ygyno.2013.07.080
118. Leone, J. P.; Bhargava, R.; Theisen, B. K.; Hamilton, R. L.; Lee, A. V.; Brufsky, A. M. *Oncotarget* **2015,** *6,* 30327–30333. doi:10.18632/oncotarget.4639
119. Torchilin, V. P.; Lukyanov, A. N.; Gao, Z.; Papahadjopoulos-Sternberg, B. *Proc. Natl. Acad. Sci. U. S. A.* **2003,** *100,* 6039–6044. doi:10.1073/pnas.0931428100
120. Roby, A.; Erdogan, S.; Torchilin, V. P. *Eur. J. Pharm. Biopharm.* **2006,** *62,* 235–240. doi:10.1016/j.ejpb.2005.09.010
121. Chang, M.-H.; Pai, C.-L.; Chen, Y.-C.; Yu, H.-P.; Hsu, C.-Y.; Lai, P.-S. *Nanomaterials* **2018,** *8,* 121. doi:10.3390/nano8020121
122. Henderson, B. W.; Dougherty, T. J. *Photochem. Photobiol.* **1992,** *55,* 145–157. doi:10.1111/j.1751-1097.1992.tb04222.x
123. Dang, J.; He, H.; Chen, D.; Yin, L. *Biomater. Sci.* **2017,** *5,* 1500–1511. doi:10.1039/c7bm00392g
124. Sen Gupta, A. *Wiley Interdiscip. Rev.: Nanomed. Nanobiotechnol.* **2017,** *9,* e1464. doi:10.1002/wnan.1464
125. Cheng, Y.; Cheng, H.; Jiang, C.; Qiu, X.; Wang, K.; Huan, W.; Yuan, A.; Wu, J.; Hu, Y. *Nat. Commun.* **2015,** *6,* 8785. doi:10.1038/ncomms9785
126. Liu, Y.; Meng, X.; Bu, W. *Coord. Chem. Rev.* **2019,** *379,* 82–98. doi:10.1016/j.ccr.2017.09.006
127. Li, X.; Zheng, B.-D.; Peng, X.-H.; Li, S.-Z.; Ying, J.-W.; Zhao, Y.; Huang, J.-D.; Yoon, J. *Coord. Chem. Rev.* **2019,** *379,* 147–160. doi:10.1016/j.ccr.2017.08.003
128. Luby, B. M.; Walsh, C. D.; Zheng, G. *Angew. Chem., Int. Ed.* **2019,** *58,* 2558–2569. doi:10.1002/anie.201805246
129. Shum, J.; Leung, P. K.-K.; Lo, K. K.-W. *Inorg. Chem.* **2019,** *58,* 2231–2247. doi:10.1021/acs.inorgchem.8b02979
130. Pucelik, B.; Gürol, I.; Ahsen, V.; Dumoulin, F.; Dąbrowski, J. M. *Eur. J. Med. Chem.* **2016,** *124,* 284–298. doi:10.1016/j.ejmech.2016.08.035
131. Tan, X.; Luo, S.; Long, L.; Wang, Y.; Wang, D.; Fang, S.; Ouyang, Q.; Su, Y.; Cheng, T.; Shi, C. *Adv. Mater. (Weinheim, Ger.)* **2017,** *29,* 1704196. doi:10.1002/adma.201704196
132. Glavas, L.; Olsén, P.; Odelius, K.; Albertsson, A.-C. *Biomacromolecules* **2013,** *14,* 4150–4156. doi:10.1021/bm401312j
133. Glavas, L.; Odelius, K.; Albertsson, A.-C. *Polym. Adv. Technol.* **2015,** *26,* 880–888. doi:10.1002/pat.3524
134. Kakde, D.; Taresco, V.; Bansal, K. K.; Magennis, E. P.; Howdle, S. M.; Mantovani, G.; Irvine, D. J.; Alexander, C. *J. Mater. Chem. B* **2016,** *4,* 7119–7129. doi:10.1039/c6tb01839d
135. Zhang, L.; Eisenberg, A. *Polym. Adv. Technol.* **1998,** *9,* 677–699. doi:10.1002/(sici)1099-1581(1998100)9:10/11<677::aid-pat845>3.3.co;2-r
136. Bacinello, D.; Garanger, E.; Taton, D.; Tam, K. C.; Lecommandoux, S. *Biomacromolecules* **2014,** *15,* 1882–1888. doi:10.1021/bm500296n
137. Geng, Y.; Dalhaimer, P.; Cai, S.; Tsai, R.; Tewari, M.; Minko, T.; Discher, D. E. *Nat. Nanotechnol.* **2007,** *2,* 249–255. doi:10.1038/nnano.2007.70
138. Cai, S.; Vijayan, K.; Cheng, D.; Lima, E. M.; Discher, D. E. *Pharm. Res.* **2007,** *24,* 2099–2109. doi:10.1007/s11095-007-9335-z
139. Geng, Y.; Discher, D. E. *Polymer* **2006,** *47,* 2519–2525. doi:10.1016/j.polymer.2005.11.093
140. Yue, T.; Xu, Y.; Sun, M.; Zhang, X.; Huang, F. *Phys. Chem. Chem. Phys.* **2015,** *18,* 1082–1091. doi:10.1039/c5cp06511a
141. Vácha, R.; Martinez-Veracoechea, F. J.; Frenkel, D. *Nano Lett.* **2011,** *11,* 5391–5395. doi:10.1021/nl2030213
142. Williford, J.-M.; Santos, J. L.; Shyam, R.; Mao, H.-Q. *Biomater. Sci.* **2015,** *3,* 894–907. doi:10.1039/c5bm00006h
143. Yokoyama, M.; Sugiyama, T.; Okano, T.; Sakurai, Y.; Naito, M.; Kataoka, K. *Pharm. Res.* **1993,** *10,* 895–899. doi:10.1023/a:1018921513605
144. Miller, T.; Rachel, R.; Besheer, A.; Uezguen, S.; Weigandt, M.; Goepferich, A. *Pharm. Res.* **2012,** *29,* 448–459. doi:10.1007/s11095-011-0555-x
145. Wieczorek, S.; Krause, E.; Hackbarth, S.; Röder, B.; Hirsch, A. K. H.; Börner, H. G. *J. Am. Chem. Soc.* **2013,** *135,* 1711–1714. doi:10.1021/ja311895z
146. Hamaguchi, T.; Matsumura, Y.; Suzuki, M.; Shimizu, K.; Goda, R.; Nakamura, I.; Nakatomi, I.; Yokoyama, M.; Kataoka, K.; Kakizoe, T. *Br. J. Cancer* **2005,** *92,* 1240–1246. doi:10.1038/sj.bjc.6602479
147. Zuo, C.; Peng, J.; Cong, Y.; Dai, X.; Zhang, X.; Zhao, S.; Zhang, X.; Ma, L.; Wang, B.; Wei, H. *J. Colloid Interface Sci.* **2018,** *514,* 122–131. doi:10.1016/j.jcis.2017.12.022
148. Ping, J.-t.; Peng, H.-s.; Duan, W.-b.; You, F.-t.; Song, M.; Wang, Y.-q. *J. Mater. Chem. B* **2016,** *4,* 4482–4489. doi:10.1039/c6tb00307a
149. Rao, J.; Khan, A. *J. Am. Chem. Soc.* **2013,** *135,* 14056–14059. doi:10.1021/ja407514z
150. Niedre, M.; Patterson, M. S.; Wilson, B. C. *Photochem. Photobiol.* **2002,** *75,* 382–391. doi:10.1562/0031-8655(2002)0750382dnildo2.0.co2
151. Moan, J.; Berg, K. *Photochem. Photobiol.* **1991,** *53,* 549–553. doi:10.1111/j.1751-1097.1991.tb03669.x
152. Knop, K.; Mingotaud, A.-F.; El-Akra, N.; Violleau, F.; Souchard, J.-P. *Photochem. Photobiol. Sci.* **2009,** *8,* 396–404. doi:10.1039/b811248g
153. Ferreira, M.; Chaves, L. L.; Lima, S. A. C.; Reis, S. *Int. J. Pharm.* **2015,** *492,* 65–72. doi:10.1016/j.ijpharm.2015.07.013
154. Feng, C.; Yuan, X.; Chu, K.; Zhang, H.; Ji, W.; Rui, M. *Int. J. Biol. Macromol.* **2019,** *125,* 700–710. doi:10.1016/j.ijbiomac.2018.12.003
155. Liu, Y.; Wang, Y.; Zhao, J. *Int. J. Biol. Macromol.* **2019,** *124,* 667–680. doi:10.1016/j.ijbiomac.2018.11.258
156. Izadiyan, Z.; Basri, M.; Fard Masoumi, H. R.; Abedi Karjiban, R.; Salim, N.; Kalantari, K. *Mater. Sci. Eng., C* **2019,** *94,* 841–849. doi:10.1016/j.msec.2018.10.015
157. Eskandari, Z.; Kazdal, F.; Bahadori, F.; Ebrahimi, N. *J. Drug Delivery Sci. Technol.* **2018,** *48,* 393–402. doi:10.1016/j.jddst.2018.10.009
158. Shi, C.; Sun, Y.; Wu, H.; Zhu, C.; Wei, G.; Li, J.; Chan, T.; Ouyang, D.; Mao, S. *Int. J. Pharm.* **2016,** *512,* 282–291. doi:10.1016/j.ijpharm.2016.08.054
159. Zhao, F.; Zhao, Y.; Liu, Y.; Chang, X.; Chen, C.; Zhao, Y. *Small* **2011,** *7,* 1322–1337. doi:10.1002/smll.201100001
160. Cheng, L.-C.; Jiang, X.; Wang, J.; Chen, C.; Liu, R.-S. *Nanoscale* **2013,** *5,* 3547–3569. doi:10.1039/c3nr34276j

161. Sandez-Macho, I.; Casas, M.; Lage, E. V.; Rial-Hermida, M. I.; Concheiro, A.; Alvarez-Lorenzo, C. *Colloids Surf., B* **2015,** *133,* 270–277. doi:10.1016/j.colsurfb.2015.06.019
162. Yaroslavov, A. A.; Sitnikova, T. A.; Rakhnyanskaya, A. A.; Yaroslavova, E. G.; Sybachin, A. V.; Melik-Nubarov, N. S.; Khomutov, G. B. *Colloid Polym. Sci.* **2017,** *295,* 1405–1417. doi:10.1007/s00396-017-4054-4
163. Schwieger, C.; Blaffert, J.; Li, Z.; Kressler, J.; Blume, A. *Langmuir* **2016,** *32,* 8102–8115. doi:10.1021/acs.langmuir.6b01574
164. Ramadurai, S.; Kohut, A.; Sarangi, N. K.; Zholobko, O.; Baulin, V. A.; Voronov, A.; Keyes, T. E. *J. Colloid Interface Sci.* **2019,** *542,* 483–494. doi:10.1016/j.jcis.2019.01.093
165. Wilkosz, N.; Jamróz, D.; Kopeć, W.; Nakai, K.; Yusa, S.-i.; Wytrwal-Sarna, M.; Bednar, J.; Nowakowska, M.; Kepczynski, M. *J. Phys. Chem. B* **2017,** *121,* 7318–7326. doi:10.1021/acs.jpcb.7b05248
166. Palominos, M. A.; Vilches, D.; Bossel, E.; Soto-Arriaza, M. A. *Colloids Surf., B* **2016,** *148,* 30–40. doi:10.1016/j.colsurfb.2016.08.038
167. Zhang, W.; Haman, K. J.; Metzger, J. M.; Hackel, B. J.; Bates, F. S.; Lodge, T. P. *Langmuir* **2017,** *33,* 12624–12634. doi:10.1021/acs.langmuir.7b02279
168. Montis, C.; Till, U.; Vicendo, P.; Roux, C.; Mingotaud, A. F.; Violleau, F.; Demazeau, M.; Berti, D.; Lonetti, B. *Nanoscale* **2018,** *10,* 15442–15446. doi:10.1039/c8nr04355h
169. Zaki, A. M.; Carbone, P. *Langmuir* **2017,** *33,* 13284–13294. doi:10.1021/acs.langmuir.7b02244
170. Houang, E. M.; Haman, K. J.; Kim, M.; Zhang, W.; Lowe, D. A.; Sham, Y. Y.; Lodge, T. P.; Hackel, B. J.; Bates, F. S.; Metzger, J. M. *Mol. Pharmaceutics* **2017,** *14,* 2333–2339. doi:10.1021/acs.molpharmaceut.7b00197
171. Raman, A. S.; Pajak, J.; Chiew, Y. C. *Chem. Phys. Lett.* **2018,** *712,* 1–6. doi:10.1016/j.cplett.2018.09.049
172. Guan, Z.; Wang, L.; Lin, J. *Biomacromolecules* **2017,** *18,* 797–807. doi:10.1021/acs.biomac.6b01674
173. Wang, T.; Bai, J.; Jiang, X.; Nienhaus, G. U. *ACS Nano* **2012,** *6,* 1251–1259. doi:10.1021/nn203892h
174. Chen, H.; Kim, S.; Li, L.; Wang, S.; Park, K.; Cheng, J.-X. *Proc. Natl. Acad. Sci. U. S. A.* **2008,** *105,* 6596–6601. doi:10.1073/pnas.0707046105
175. Kerdous, R.; Sureau, F.; Bour, A.; Bonneau, S. *Int. J. Pharm.* **2015,** *495,* 750–760. doi:10.1016/j.ijpharm.2015.09.032
176. Till, U.; Gibot, L.; Mingotaud, A.-F.; Ehrhart, J.; Wasungu, L.; Mingotaud, C.; Souchard, J.-P.; Poinso, A.; Rols, M.-P.; Violleau, F.; Vicendo, P. *Molecules* **2016,** *21,* 1643. doi:10.3390/molecules21121643
177. Wan, J.; Sun, L.; Wu, P.; Wang, F.; Guo, J.; Cheng, J.; Wang, C. *Polym. Chem.* **2018,** *9,* 1206–1215. doi:10.1039/c7py01994g
178. Bugaj, A. M. *Photochem. Photobiol. Sci.* **2011,** *10,* 1097–1109. doi:10.1039/c0pp00147c
179. Castano, A. P.; Demidova, T. N.; Hamblin, M. R. *Photodiagn. Photodyn. Ther.* **2004,** *1,* 279–293. doi:10.1016/s1572-1000(05)00007-4
180. Moan, J.; Berg, K.; Kvam, E.; Western, A.; Malik, Z.; Rück, A.; Schneckenburger, H. Intracellular Localization of Photosensitizers. In *Ciba Foundation Symposium 146 - Photosensitizing Compounds: Their Chemistry, Biology and Clinical Use;* Bock, G.; Harnett, S., Eds.; John Wiley & Sons, Ltd: Chichester, United Kingdom, 1989; pp 95–111. doi:10.1002/9780470513842.ch7
181. Ehrenberg, B.; Montana, V.; Wei, M. D.; Wuskell, J. P.; Loew, L. M. *Biophys. J.* **1988,** *53,* 785–794. doi:10.1016/s0006-3495(88)83158-8
182. Oseroff, A. R.; Ohuoha, D.; Ara, G.; McAuliffe, D.; Foley, J.; Cincotta, L. *Proc. Natl. Acad. Sci. U. S. A.* **1986,** *83,* 9729–9733. doi:10.1073/pnas.83.24.9729
183. Castro, D. J.; Saxton, R. E.; Fetterman, H. R.; Castro, D. J.; Ward, P. H. *Otolaryngol.–Head Neck Surg.* **1988,** *98,* 581–588. doi:10.1177/019459988809800608
184. Yu, Z.; Pan, W.; Li, N.; Tang, B. *Chem. Sci.* **2016,** *7,* 4237–4244. doi:10.1039/c6sc00737f
185. Han, K.; Zhang, W.-Y.; Zhang, J.; Lei, Q.; Wang, S.-B.; Liu, J.-W.; Zhang, X.-Z.; Han, H.-Y. *Adv. Funct. Mater.* **2016,** *26,* 4351–4361. doi:10.1002/adfm.201600170
186. Huang, H.; Yu, B.; Zhang, P.; Huang, J.; Chen, Y.; Gasser, G.; Ji, L.; Chao, H. *Angew. Chem., Int. Ed.* **2015,** *54,* 14049–14052. doi:10.1002/anie.201507800
187. Liu, L.-H.; Qiu, W.-X.; Zhang, Y.-H.; Li, B.; Zhang, C.; Gao, F.; Zhang, L.; Zhang, X.-Z. *Adv. Funct. Mater.* **2017,** *27,* 1700220. doi:10.1002/adfm.201700220
188. Berg, K.; Selbo, P. K.; Prasmickaite, L.; Tjelle, T. E.; Sandvig, K.; Moan, J.; Gaudernack, G.; Fodstad, Ø.; Kjølsrud, S.; Anholt, H. *Cancer Res.* **1999,** *59,* 1180–1183.
189. Weyergang, A.; Berstad, M. E. B.; Bull-Hansen, B.; Olsen, C. E.; Selbo, P. K.; Berg, K. *Photochem. Photobiol. Sci.* **2015,** *14,* 1465–1475. doi:10.1039/c5pp00029g
190. Ohtsuki, T.; Miki, S.; Kobayashi, S.; Haraguchi, T.; Nakata, E.; Hirakawa, K.; Sumita, K.; Watanabe, K.; Okazaki, S. *Sci. Rep.* **2015,** *5,* 18577. doi:10.1038/srep18577
191. Bøe, S. L.; Hovig, E. *Ther. Delivery* **2013,** *4,* 1125–1140. doi:10.4155/tde.13.78
192. Jin, H.; Lovell, J. F.; Chen, J.; Ng, K.; Cao, W.; Ding, L.; Zhang, Z.; Zheng, G. *Photochem. Photobiol. Sci.* **2011,** *10,* 810–816. doi:10.1039/c0pp00350f
193. Liu, C.; Chen, Z.; Wang, Z.; Li, W.; Ju, E.; Yan, Z.; Liu, Z.; Ren, J.; Qu, X. *Nanoscale* **2016,** *8,* 12570–12578. doi:10.1039/c5nr07719b
194. Lee, C.-S.; Na, K. *Biomacromolecules* **2014,** *15,* 4228–4238. doi:10.1021/bm501258s
195. Liu, G.; Hu, J.; Zhang, G.; Liu, S. *Bioconjugate Chem.* **2015,** *26,* 1328–1338. doi:10.1021/bc500548r
196. Shieh, M.-J.; Hsu, C.-Y.; Huang, L.-Y.; Chen, H.-Y.; Huang, F.-H.; Lai, P.-S. *J. Controlled Release* **2011,** *152,* 418–425. doi:10.1016/j.jconrel.2011.03.017
197. Li, S.-Y.; Qiu, W.-X.; Cheng, H.; Gao, F.; Cao, F.-Y.; Zhang, X.-Z. *Adv. Funct. Mater.* **2017,** *27,* 1604916. doi:10.1002/adfm.201604916
198. Ahn, W. S.; Bae, S. M.; Huh, S. W.; Lee, J. M.; Namkoong, S. E.; Han, S.-J.; Kim, C. K.; Kim, J.-K.; Kim, Y.-W. *Int. J. Gynecol. Cancer* **2004,** *14,* 475–482. doi:10.1111/j.1048-891x.2004.14308.x
199. Kim, J.; Santos, O. A.; Park, J.-H. *J. Controlled Release* **2014,** *191,* 98–104. doi:10.1016/j.jconrel.2014.05.049
200. Jia, H.-R.; Jiang, Y.-W.; Zhu, Y.-X.; Li, Y.-H.; Wang, H.-Y.; Han, X.; Yu, Z.-W.; Gu, N.; Liu, P.; Chen, Z.; Wu, F.-G. *J. Controlled Release* **2017,** *255,* 231–241. doi:10.1016/j.jconrel.2017.04.030
201. Fulda, S.; Galluzzi, L.; Kroemer, G. *Nat. Rev. Drug Discovery* **2010,** *9,* 447–464. doi:10.1038/nrd3137
202. Semenza, G. L. *Science* **2007,** *318,* 62–64. doi:10.1126/science.1147949
203. Battogtokh, G.; Ko, Y. T. *Nanomedicine (N. Y., NY, U. S.)* **2017,** *13,* 733–743. doi:10.1016/j.nano.2016.10.014
204. Marrache, S.; Dhar, S. *Proc. Natl. Acad. Sci. U. S. A.* **2012,** *109,* 16288–16293. doi:10.1073/pnas.1210096109

205. Marrache, S.; Pathak, R. K.; Dhar, S. Mitochondrial Medicine. In *Manipulating Mitochondrial Function;* Weissig, V.; Edeas, M., Eds.; Methods in Molecular Biology, Vol. 2; Humana Press: New York, NY, 2015; pp 103–112. doi:10.1007/978-1-4939-2288-8
206. Sonawane, N. D.; Szoka, F. C.; Verkman, A. S. *J. Biol. Chem.* **2003,** *278,* 44826–44831. doi:10.1074/jbc.m308643200
207. Sharma, A.; Soliman, G. M.; Al-Hajaj, N.; Sharma, R.; Maysinger, D.; Kakkar, A. *Biomacromolecules* **2012,** *13,* 239–252. doi:10.1021/bm201538j
208. Yang, G.; Xu, L.; Xu, J.; Zhang, R.; Song, G.; Chao, Y.; Feng, L.; Han, F.; Dong, Z.; Li, B.; Liu, Z. *Nano Lett.* **2018,** *18,* 2475–2484. doi:10.1021/acs.nanolett.8b00040
209. Wei, Y.; Zhou, F.; Zhang, D.; Chen, Q.; Xing, D. *Nanoscale* **2016,** *8,* 3530–3538. doi:10.1039/c5nr07785k
210. Zhou, F.; Xing, D.; Wu, B.; Wu, S.; Ou, Z.; Chen, W. R. *Nano Lett.* **2010,** *10,* 1677–1681. doi:10.1021/nl100004m
211. Lv, W.; Zhang, Z.; Zhang, K. Y.; Yang, H.; Liu, S.; Xu, A.; Guo, S.; Zhao, Q.; Huang, W. *Angew. Chem., Int. Ed.* **2016,** *55,* 9947–9951. doi:10.1002/anie.201604130
212. Hinde, E.; Thammasiraphop, K.; Duong, H. T. T.; Yeow, J.; Karagoz, B.; Boyer, C.; Gooding, J. J.; Gaus, K. *Nat. Nanotechnol.* **2017,** *12,* 81–89. doi:10.1038/nnano.2016.160
213. El-Akra, N.; Noirot, A.; Faye, J.-C.; Souchard, J.-P. *Photochem. Photobiol. Sci.* **2006,** *5,* 996–999. doi:10.1039/b606117f
214. Tian, X.; Zhu, Y.; Zhang, M.; Luo, L.; Wu, J.; Zhou, H.; Guan, L.; Battaglia, G.; Tian, Y. *Chem. Commun.* **2017,** *53,* 3303–3306. doi:10.1039/c6cc09470h
215. Schwarz, D. S.; Blower, M. D. *Cell. Mol. Life Sci.* **2016,** *73,* 79–94. doi:10.1007/s00018-015-2052-6
216. Lin, S.; Zhang, L.; Lei, K.; Zhang, A.; Liu, P.; Liu, J. *Cell Stress Chaperones* **2014,** *19,* 927–937. doi:10.1007/s12192-014-0517-4
217. Wang, M.; Kaufman, R. J. *Nat. Rev. Cancer* **2014,** *14,* 581–597. doi:10.1038/nrc3800
218. Cubillos-Ruiz, J. R.; Bettigole, S. E.; Glimcher, L. H. *Cell* **2017,** *168,* 692–706. doi:10.1016/j.cell.2016.12.004
219. Dai, L.; Cai, R.; Li, M.; Luo, Z.; Yu, Y.; Chen, W.; Shen, X.; Pei, Y.; Zhao, X.; Cai, K. *Chem. Mater.* **2017,** *29,* 6976–6992. doi:10.1021/acs.chemmater.7b02513
220. Zhao, L.; Kim, T.-H.; Kim, H.-W.; Kim, S. Y. *Int. J. Polym. Mater. Polym. Biomater.* **2015,** *64,* 733–744. doi:10.1080/00914037.2014.1002131
221. Seah, G. L.; Yu, J. H.; Yang, M. Y.; Kim, W. J.; Kim, J.-H.; Park, K.; Cho, J.-W.; Kim, J. S.; Nam, Y. S. *J. Controlled Release* **2018,** *286,* 240–253. doi:10.1016/j.jconrel.2018.07.046
222. Seah, G. L.; Yu, J. H.; Koo, B. I.; Lee, D. J.; Nam, Y. S. *J. Mater. Chem. B* **2018,** *6,* 7737–7749. doi:10.1039/c8tb02323a
223. Faria, M.; Björnmalm, M.; Thurecht, K. J.; Kent, S. J.; Parton, R. G.; Kavallaris, M.; Johnston, A. P. R.; Gooding, J. J.; Corrie, S. R.; Boyd, B. J.; Thordarson, P.; Whittaker, A. K.; Stevens, M. M.; Prestidge, C. A.; Porter, C. J. H.; Parak, W. J.; Davis, T. P.; Crampin, E. J.; Caruso, F. *Nat. Nanotechnol.* **2018,** *13,* 777–785. doi:10.1038/s41565-018-0246-4

License and Terms

The definitive version of this article is the electronic one which can be found at:
doi:10.3762/bjnano.11.15

BEILSTEIN JOURNAL OF NANOTECHNOLOGY

Using gold nanoparticles to detect single-nucleotide polymorphisms: toward liquid biopsy

María Sanromán Iglesias[1] and Marek Grzelczak[*2]

Review

Open Access

Address:
[1]Centro de Física de Materiales CSIC-UPV/EHU and Donostia International Physics Center (DIPC), Paseo Manuel de Lardizabal 5, 20018 Donostia-Sebastián, Spain and [2]Ikerbasque, Basque Foundation for Science, 48013 Bilbao, Spain

Email:
Marek Grzelczak* - marek.grzelczak@dipc.org

* Corresponding author

Keywords:
amplification reactions; biomarkers; colorimetric biosensing; gold nanoparticles; plasmonics; single-point mutation

Beilstein J. Nanotechnol. **2020,** *11,* 263–284.
doi:10.3762/bjnano.11.20

Received: 12 September 2019
Accepted: 21 January 2020
Published: 31 January 2020

This article is part of the thematic issue "Engineered nanomedicines for advanced therapies".

Guest Editor: F. Baldelli Bombelli

Abstract

The possibility of detecting genetic mutations rapidly in physiological media through liquid biopsy has attracted the attention within the materials science community. The physical properties of nanoparticles combined with robust transduction methods ensure an improved sensitivity and specificity of a given assay and its implementation into point-of-care devices for common use. Covering the last twenty years, this review gives an overview of the state-of-the-art of the research on the use of gold nanoparticles in the development of colorimetric biosensors for the detection of single-nucleotide polymorphism as cancer biomarker. We discuss the main mechanisms of the assays that either are assisted by DNA-based molecular machines or by enzymatic reactions, summarize their performance and provide an outlook towards future developments.

Introduction

Cancer is a leading cause of death accounting for about 8.8 million deaths in 2015 [1]. The list of tumor-linked substances, i.e., biomarkers for diagnosis and prognosis purposes is continuously increasing. Cancer biomarkers are present in tumor tissues or serum and encompass a wide variety of molecules, including DNA, mRNA, enzymes, metabolites, transcription factors, and cell surface receptors. The first report on cell-free DNA in body fluids by Mandel and Metais in 1948 [2], opened the possibility to screen the presence of a disease through a simple blood test, setting thus a milestone of "liquid biopsy". Liquid biopsy has the potential to accelerate the early cancer diagnosis by the detection of biomolecules such as cell-fee DNA directly in blood samples.

Currently, the development of liquid biopsies is directly linked to the state-of-the-art of advanced techniques in the field of genomics such as digital PCR, next generation sequencing (NGS), fluorescence in situ hybridization (FISH) and BEAMing. These facilitate the fast design of mutational profiles of tumor DNA, helping the prioritization of anti-cancer therapy.

Although these techniques are without parallel in the analysis of genetic material and the detection of mutations, they require an operation by specialized personnel in large infrastructures such as hospitals or research centers. The democratization of liquid biopsy and therefore the advancement of personal medicine needs efficient point-of-care devices that are simple to use (preferentially colorimetric), disposable and cost-efficient, making them available to a wide range of users. It has been shown that progress in the development of such devices requires improved strategies for signal transduction, which might rely on the use of emergent nanomaterials.

Over the last decade, a number of novel and optically active nanomaterials involving semiconductor or metal nanocrystals enabled the development of sensing devices with rather simple transduction mechanisms [3]. For example, the aggregation-induced color change of a solution containing plasmonic nanoparticles (from red to blue) in the presence of molecules offers an excellent tool for colorimetric sensing without the need of using advanced techniques. Similarly, selective fluorescence quenching of organic dyes or semiconducting nanoparticles by plasmonic nanoparticles offers an unprecedented sensitivity in native physiological media. Coupling these nanomaterial-based systems with enzymatic reactions can further increase the sensitivity and selectivity of a given sensor, leading to a scenario in which a tiny structural alteration of a biomolecule can be detected within seconds even at sub-picomolar concentration.

Here, we review recent advancements in the development of sensors based on metallic nanoparticles for the detection of mutations in circulating tumor DNA molecules. By introducing the importance of DNA molecules as biomarkers in the field of liquid biopsy and by discussing current technologies in clinics, we review the performance of recent sensors for single-point mutation in which gold nanoparticles act as signal transducers. We classify the discussed sensors according to whether the underlying mechanisms of detection involve enzymatic reactions or not.

Review

Liquid biopsy

Tissue biopsy is the state-of-the-art protocol in clinics for the evaluation of tumor progression. This procedure, however, constitutes a significant barrier for monitoring oncogenic mutations since it can introduce clinical risks for the patient [4], heterogeneity of tumor cells [5], and difficulties in the sampling of tumor cells that in turn can lead to inadequate amounts of tissue for genetic testing. Thus, the possibility of extracting valuable biochemical information on tumor progression directly from physiological media became a straightforward solution to the issues of conventional biopsy. Table 1 summarizes the main benefits of liquid biopsy concerning cancer diagnosis, prediction and prognosis emphasizing that it is a promising tool in monitoring tumor-specific changes during the entire course of the disease. It can be used for the early-stage detection of cancer, the identification of indicators for disease recurrence and progression and the evaluation of a given treatment in nearly real-time. In the context of the present review, the early-stage diagnosis of cancer by novel sensing devices is prioritized in the subsequent discussion.

Table 1: Benefits of liquid biopsy in diagnosis, prediction and prognosis of cancer.

stage	information/benefits	ref.
diagnosis	early detection	[6-11]
	monitoring of minimal residual disease	[12-15]
prediction	assessment of molecular heterogeneity of overall disease	[16,17]
	monitoring of tumor dynamics	[18-20]
	identification of genetic determinants for targeted therapy	[21,22]
	evaluation of early treatment response	[23,24]
	assessment of evolution of resistance in real time	[25,26]
prognosis	identification of high risk of recurrence	[27]
	correlation with changes in tumor burden	[28,29]

Circulating tumor DNA and single-nucleotide polymorphism

The list of biomarkers that are present in blood and that exhibit potential for cancer diagnosis experiences continuously grows. These biomarkers include circulating tumor cells (CTCs) [30], circulating membranous structures [31], circulating cell-free nucleic acids (cfDNA) [4], microRNA, RNA [32] and proteins [33] (Figure 1). For the discussion here, the detection of circulating cell-free DNA is relevant. While all types of cells (tumor and nonmalignant) release cfDNA into the extracellular system [34], the circulating tumor DNA (ctDNA) is released uniquely by tumor cells. Several release mechanisms have been identified. 1) Secretion after cell death through apoptosis and necrosis, 2) secretion from tumor cells in the form of free or encapsulated DNA fragments, and 3) secretion from phagocytized tumor cells [35-38]. It has been observed that with the increase of tumor load, the local fraction of ctDNA increases compared to the overall amount of cfDNA in the sample [39]. However, this tendency is patient-dependent. The average length of ctDNA fragments generated from cell apoptosis ranges from 145 to 180 bp. Longer fragments of up to 10 kbp are secreted by cell necrosis [40-44].

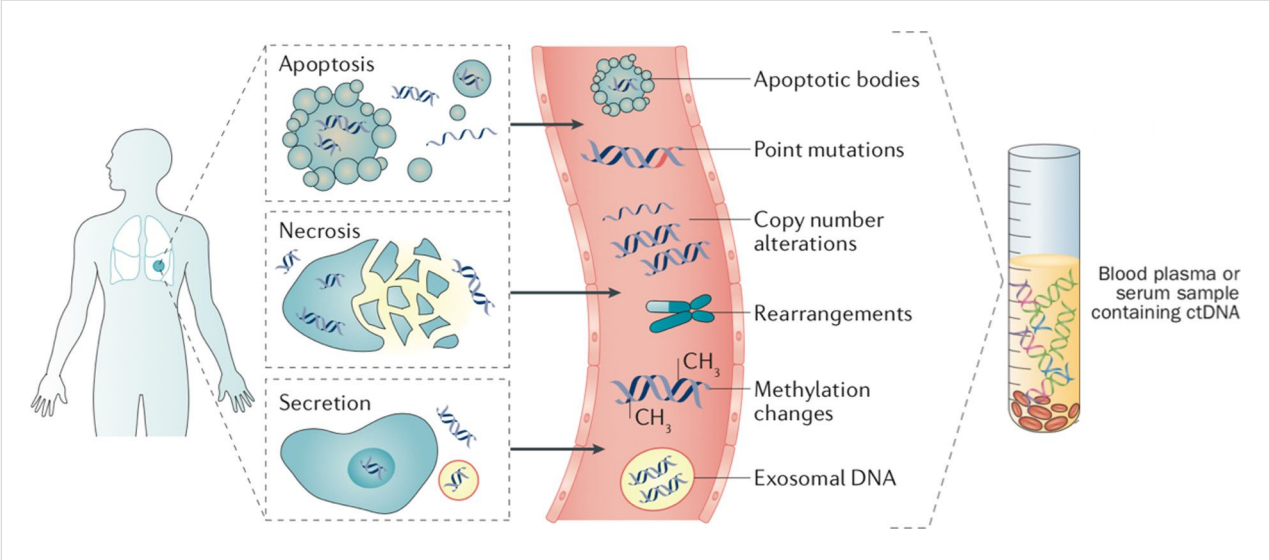

Figure 1: Alterations in cell-free DNA. Cell-free DNA can be released from both cancerous and normal cells located in the tumor environment through apoptosis, necrosis or secretion. Once in the bloodstream, cfDNA may exist either free or associated with extracellular entities such as exosomes. cfDNA can carry multiple classes of tumor-derived genetic alterations including point mutations, copy-number fluctuations and structural rearrangements. Reprinted with permission from [45], copyright 2017 Springer Nature.

Moreover, in solid malignancies, circulating tumor DNA differs from cell-free DNA by somatic mutations [18,46,47]. In leukemia, for example, the increased amount of cfDNA originates from cancer cells. Nonetheless, four main types of gene alterations occurring in cfDNA are classified:

1. **Single-point mutations or single-nucleotide polymorphism (SNP).** A base substitution at one nucleotide that may result in a change of the amino acid sequence of the encoded protein or premature truncation of the protein (Figure 2).
2. **Copy-number alteration.** Duplications, insertions or deletions of one or a few nucleotides leading to the addition or subtraction of amino acids in the protein.
3. **Exon or gene copy-number changes.** Large duplications or deletions encompassing entire exons (protein-encoding regions in a gene) and affecting the functional domains of the protein.
4. **Structural modifications.** Translocations or inversions within a gene that result in fusion genes and associated fusion proteins.

Among these four gene alterations, the SNPs in ctDNA are known as the major contributors to the genetic variations, representing more than 80% of all known polymorphisms at a frequency of around 1 every 1000 bases [48]. To date, around 1.42 million single-base variations have been identified. These small variations may occur in noncoding or coding regions of the genes. SNPs in coding regions can be either synonymous (without altering the encoded amino acid) or nonsynonymous (altering the encoded amino acid), hence, possibly altering the function of the corresponding protein (Figure 2) [49,50].

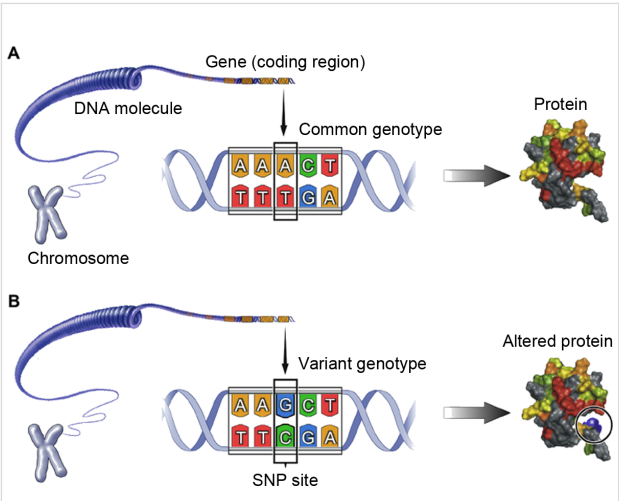

Figure 2: Single-nucleotide polymorphisms (SNPs) are genetic mutations that alter single base in DNA, causing sequence modification in amino acids and malfunction of a corresponding protein. Reprinted with permission from [51], copyright 2014 Elsevier.

Approximately, 50% of all SNPs occur in noncoding regions, 25% are silent mutations with no effect on gene function and phenotype, and the remaining 25% lead to mutations of the gene function [52,53]. These SNPs can influence the promoter activity (gene expression), the activity of messenger RNA (mRNA), gene conformation (stability) and the translational efficiency. Keeping in mind the importance of these modifica-

tions, SNPs can be proposed as biomarkers in the clinical diagnosis of diseases, personalized medicine and drug treatment.

Genotyping is an essential process in determining which genetic variants alter the encoded amino acid sequence and thus the function of a given protein. Based on the molecular mechanism, the majority of SNP genotyping assays fall in one of four groups [54,55]. These include (1) allele-specific hybridization (mutation-dependent hybridization of short nucleotides with variable target DNA), (2) primer extension (DNA polymerase-based incorporation of specific desoxyribonucleotides complementary to the DNA template, (3) allele-specific ligation (ligase-based covalent linking of two oligonucleotides upon hybridization on a DNA template), and (4) invasive cleavage (nuclease-based cleavage of the 3D structure formed when two overlapping oligonucleotides hybridize perfectly to a target DNA). The genotyping method should meet several requirements, namely, facile development from sequence information, cost-efficiency, robustness of the reaction, scalability, high-throughput discrimination and the possibility for automatization with minimal hands-on operation. We will demonstrate in the following sections that the advancement of laboratory-based sensors for SNP discrimination benefits from the current state-of-the-art in genotyping techniques in SNP determination, especially in the context of conceptual novelty.

Tumor-specific aberrations containing SNP

Because the fraction of circulating DNA that is derived from the tumor can range between 0.01% and 93% [41], analytical techniques of high sensitivity are currently implemented to obtain reliable information on tumor-associated genetic modifications and to follow tumor dynamics [4,16,46,56]. These techniques are mainly modifications of the well-known polymerase chain reaction (PCR), establishing thus the state-of-the-art in clinics in the discrimination of SNP. The most relevant types of cancer including colorectal, breast, ovarian, pancreatic and lung cancer comprise several common tumor-specific aberrations of single-point mutations, which are frequently selected as targets in the development of novel biosensors based on nanoparticles. Further below, we describe the working principles of biosensors that were designed for the detection of the primary tumor-specific aberrations listed in Table 2.

Table 2: Tumor-associated genetic modifications in circulating cell-free DNA.[a]

tumor type	tumor-specific aberration
colorectal cancer [18]	APC, KRAS, PIK3CA, TP53
breast cancer [19]	PIK3CA, TP53, BRCA1
ovarian cancer [56]	TP53, PTEN, EGFR, BRAF, KRAS
pancreatic cancer [57]	KRAS
non-small-cell lung cancer [58]	KRAS

[a]KRAS = Kirsten rat sarcoma; APC = adenomatosis polyposis soli; PIK3CA = phosphatidylnositol-4,5-bisphosphate 3-kinase catalytic subunit alpha; TP53 = tumor protein p53, BRCA1 = breast cancer gene 1, PTEN = phosphatase and tensin homolog, EGFR = epidermal growth factor receptor, BRAF = B-Raf proto-oncogene, serine/threonine kinase.

Colloidal gold as a signal transducer in SNP detection

With the increased diversity of available optically active nanomaterials, optical assays have attracted wide interest. Particularly attractive is the colorimetric detection of analytes in a liquid phase, which represents a direct way to evaluate the presence of an analyte by the naked eye. This facilitates its implementation as a transduction system in point-of-care devices. Therefore, noble metal nanoparticles (metallic gold) are widely applied in the development of biological sensing devices. Gold is an inert metal that exhibits exceptional chemical stability in physiological media and the readiness for surface functionalization with desired biomolecules through stable Au–S bonds. The key properties of gold nanoparticles are their optical properties, which yield an exceptional light absorbance in the visible spectral range. This is explained by the fact that in the metallic core, the conductive electrons experience coherent oscillations in the presence of incoming electromagnetic radiation, thereby giving rise to the so-called localized surface plasmon resonance (LSPR). The position and the bandwidth of the LSPR can be modulated by the shape of the nanocrystals and can vary between 400 and 2000 nm. The high absorption cross section (plasmonic nanoparticles absorb photons over a region about ten times larger than their physical diameters) [59], and the lack of photobleaching (unlike organic fluorescent dyes and semiconductor nanocrystals) are additional parameters making plasmonic nanocrystals attractive materials for biosensing. Importantly, the position of the plasmon band and its bandwidth are also strictly related to the local environment. The collation of a nanoparticle at a nanometric distance from the surface of another nanoparticle induces a redshift of the maximum of the surface plasmon band because of plasmon coupling, causing a color change of the solution. Thus, the control over aggregation or redispersion processes is of paramount importance in the design of devices for the naked-eye detection of molecular events on the surface of nanoparticles.

The early experiments by Mirkin and co-workers [60,61] on the aggregation of gold nanoparticles stabilized with radially distributed single-stranded DNA (Au@DNA) through selective hybridization of complementary DNA opened up new possibilities in the development of colorimetric sensors capable of

discriminating single-point mutations. This methodology comprised the selective aggregation of two types of noncomplementary DNA-stabilized gold nanoparticles of 13 nm in diameter (Figure 3a). A target oligonucleotide (24–30 bases) that was complementary to the single-stranded DNA (ssDNA) of both types of nanoparticles induced an aggregation through hybridization. The main advantage of this method is the low risk of false positives.

Maeda et al. have proposed the so-called noncross-linking method for SNP detection, which is based on the nonselective aggregation of one single type of DNA-coated gold nanoparticles (Figure 3b) [62]. The target DNA (15 bases) containes a single-point mutation at the 5′ terminus, which provides steric stability to the nanoparticles, thus ensuring colloidal stability at a higher salt concentrations. On the contrary, the perfect match sequence (mutation-free 5′ terminus) formed a rigid double-stranded DNA (dsDNA) on the particle surface, decreasing steric and electrostatic repulsions, thereby causing gradual aggregation. This method allows for a sensitivity of 500 nM in the discrimination of single-base mutation.

Rothberg and Li proposed the use of citrate-stabilized gold nanoparticles instead of DNA-coated nanoparticles, which are prone to aggregate at a high salt concentration [63]. The working principle of this system rests on the fact that ssDNA exhibits a higher affinity to the surface of metallic gold as dsDNA. This is because ssDNA molecules contain a large number of functional groups facilitating electrostatic interactions with the gold surface (Figure 3c). Therefore, at a high salt concentration, adsorbed ssDNA stabilizes the nanoparticles against aggregation. In contrast, the preferential hybridization of target

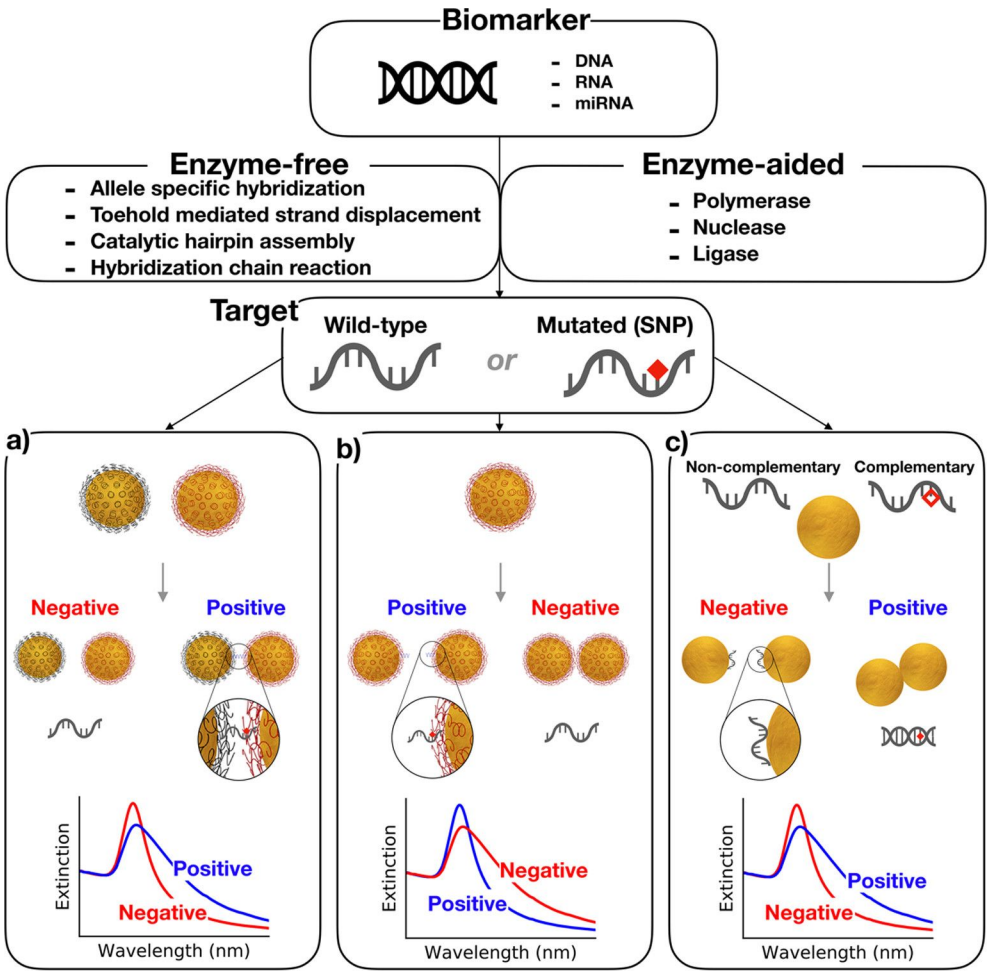

Figure 3: Gold nanoparticle-based colorimetric assays in the colloidal phase. a) Cross-linking hybridization assay: Through the specific hybridization of DNA, the distance between the particles decreases leading to a color change. b) Noncross-linking hybridization assay: An increase in the ionic strength causes an aggregation of nanoparticles (blue solution), which is prevented by the presence of the complementary target. c) Colorimetric assay based on unmodified nanoparticles: Single-stranded DNA (ssDNA) stabilizes gold nanoparticles against salt-induced aggregation, while in the presence of double-stranded DNA (dsDNA) particles undergo aggregation.

Table 3: Summary of particle-based optical assays for the detection of biomarkers.

nanoparticles (NPs)	target length/biomarker	procedure	limit of detection [Ref.]
absorbance/enzyme-free			
AuNPs (13 nm)	30 nt/—	hybridization assay	10 fmol [60]
AuNPs (13 nm)	24 nt/—	colloidal stability of NPS in the presence of ssDNA or dsDNA	100 fmol [63]
AuNPs (13 nm)	24 nt/—	hybridization assay	10 pmol [61]
AuNPs (13 nm)	14 nt/—	salt-induced aggregation of unmodified AuNPs	0.25 μM [65]
AuNPs (18 nm)	20 nt/EGFR	salt-induced aggregation of unmodified AuNPs	80 μM [66]
AuNPs (13 nm)	41 nt/JAK2	salt-induced aggregation of unmodified AuNPs	0.2 μM [67]
AuNPs (13 nm)	22 nt/—	a logic gate using two distinct target DNA molecules as input to discriminate SNPs using unmodified gold nanoparticles as indicators	100 pmol [68]
AuNPs (10 nm)	34 nt/—	the product of the catalytic strand displacement cascade disassembly AuNPs	0.1 μM [69]
AuNPs (13 nm)	14 nt/—	hybridization assay based on Au@LNA/DNA chimeras	0.1 μM [70]
AuNPs (15 nm)	15 nt/—	noncross-linking hybridization assay	0.5 μM [62]
AuNPs (14 nm)	395 nt/M. tuberculosis	noncross-linking aggregation of Au@DNA within rpoB locus	30 μg/mL [71]
AuNPs (14 nm)	16 nt/—	aggregation of unmodified AuNPs induced by CHA	0.1 pM [72]
AuNPs (40 nm), microbeads (MBs, 2.8 μm)	101 nt/KRAS	MBs@streptavidine hybridizes with the biotinylated target that is complementary to Au@DNA	20 pM [73]
AuNPs (13 nm)	22 nt/—	hybridization of peptide nucleic acid (PNA) and DNA prevents aggregation of nanoparticles	1 μM [74]
AuNPs (13 nm)	24 nt/CFTR	hybridization assay using a miniaturized optical monitoring system	10 nM [75]
AuNPs (15 nm)	22 nt/—	sequential hybridization to the target by allele-specific surface-immobilized capture probes and gene-specific Au@DNA	500 ng genomic DNA [76]
AuNPs (15 nm)	24 nt/—	hairpin-based amplification assay combined with lateral flow test	10 pM [77]
AuNPs (13, 20, 40 nm)	24 nt/—	aggregation of AuNPs by target-induced DNA circuits	200 pM (HCR), 14 pM (CHA) [78]
AuNPs (30 nm), MBs (2–3 μm)	27 nt/—	MBs@DNA, Au@DNA and target hybridization followed by magnetic separation and scanometric detection based on silver reduction for signal amplification	500 zM (10 copies) [79]
AuNPs (13 nm)	27 nt/—	sandwich assay between target, Au@DNA and a flatbed scanner; signal amplification by Ag reduction	50 fM [80]
AuNPs (20 nm)	84 nt/EGFR	hairpin assembly produces short DNA catalyst, which induces aggregation of unmodified AuNPs	7.7 fM [81]
AuNRs	24 nt/—	combination of HCR and unmodified gold nanorods for signal transduction	1.47 nM [82]
AuNPs (13 nm)	19 nt/BRCA1	DNA-fueled molecular machine modulates the kinetics of Au@DNA aggregation	0.26 nM [83]
AuNPs (15 nm)	38 nt/—	target DNA hybridizes with Au@DNA, triggering a HCR that inhibits aggregation of AuNPs	0.5 nM [84]
AuNPs (43 nm)	22 nt/—	oriented aggregation of nanoparticles on Y-shaped DNA duplex	10 pM [85]

Table 3: Summary of particle-based optical assays for the detection of biomarkers. (continued)

AuNPs (40 nm), MBs (1.5 µm)	30 nt/—	MBs@DNA, Au@DNA, target hybridization followed by magnetic separation and scanometric detection based on silver reduction for signal amplification	100 amol [86]
AuNPs (15 nm)	265 nt/hepatitis C	release and adsorption of free primers on the nanoparticle ensuring stability	50 copies [87]
AuNPs (75 nm)	22 nt/—	hybridization assay	3 nM [88]
AuNPs (5, 10, 12, 20 nm)	60 nt/KRAS	target-stabilized nanoparticles interacting with matching or mismatching probe lines in a microfluidic channel	5 fmol [89]
AuNPs (13 nm), growth (40 nm)	20 nt/—	DNA hybridization-mediated autocatalytic overgrowth of gold nanoparticles	60 nM [90]
AgNPs (13 nm)	22 nt/—	PNAs induce aggregation of citrate-stabilized AuNPs, which is prevented by DNA targets that complex selectively to PNA	1 µM [91]
AuNPs (18 nm)	12, 21, 42 nt/c-KIT	selective aggregation of PNA-stabilized AuNPs by target DNA and positively charged AuNPs through electrostatic interactions	0.1 µM [92]
AuNPs (15 nm)	30 nt/hepatitis A	combination of “click chemical” ligation chain reactions on gold nanoparticles and a magnetic separation to detect DNA and RNA	50 zM [93]
AuNPs (13, 46, 63 nm)	19 nt/BRCA1	colorimetric detection based on sandwich assay	10.85 fmol [94]
AuNPs (63 nm)	70, 140 nt/EGFR	colorimetric detection based on sandwich assay combined with a preincubation step	100 pM [95]
AuNPs (25, 53 nm)	70, 140 nt/EGFR	chemical modifications of capture probes for a selective aggregation of nanoparticles	5 nM [96]
SiO_2 microparticles (MPs) and AuNPs	22 nt/miR-21	DNA I located on SiO_2MPs captures miRNA, DNA II labeled with EDTA·2Na chelates Au^{3+} ions and regulates the growth of AuNPs	8.9 fM [97]
absorbance/enzyme-aided			
AuNPs (56, 13 nm)	30 nt/—	modulation of the enzyme activity of thrombin on the surface of AuNPs relative to fibrinogen	12 pM [98]
AuNPs (13 nm)	112, 230, 316 nt/BRCA1	allele-specific PCR with thiol-labeled primers for the specific stabilization of unmodified AuNPs	20 ng genomic DNA [99]
AuNPs (13 nm)	40 nt/KRAS	selective ligation of two adjacent Au@DNA probes in the presence of a mutation	74 pM [100]
AuNPs (14 nm)	36, 48, 80 nt/—	nanoparticle amplification assisted by nicking endonuclease (NEase) for the detection of target DNA	10 pM [101]
AuNPs (15 nm)	24 nt/keratin 10	isothermal strand displacement polymerase reaction to produce biotin–digoxin-labeled dsDNA in combination with a lateral flow strip	0.08 pM [102]
AuNPs (20 nm)	40 nt/—	aggregation of Au@DNA in the presence of single-strand-specific nuclease	100 nM [103]
AuNPs (13 nm)	22 nt/miR-122	miRNA–probe heteroduplex as substrate of double strand nuclease, releasing a probe to aggregate the nanoparticles	16 pM [104]
AuNPs (13 nm)	43 nt/EGFR	coupling of invasive reactions with NEase-assisted nanoparticle amplification to produce linkers that prevent aggregation	1 pM [105]
AuNPs (12 nm)	33 nt/—	exonuclease III (Exo III)-induced cleavage of dangling ends on Au@dsDNA causing specific aggregation	2 nM [106]
AuNPs (13 nm)	23 nt/—	coupling of polymerase and NEase through an isothermal exponential amplification reaction to selectively detach DNA from Au@DNA	46 fM [107]
AuNPs (13 nm)	30 nt/KRAS	cyclic enzymatic cleavage based on Exo III in the presence of the target and a linker to induce aggregation of Au@DNA	15 pM [108]
AuNPs (15 nm), MBs (1 µm)	46 nt/BRCA1	Au@DNA complexed with magnetic beads using horseradish peroxidase (HRP, enzymatic catalysis) and bovine serum albumin (BSA, nonspecific blocker)	25 pM [109]
AuNPs (13 nm)	34 nt/—	combination of padlock probe for rolling-circle amplification and NEase-assisted nanoparticle amplification	1 pM [110]

Table 3: Summary of particle-based optical assays for the detection of biomarkers. (continued)

AuNPs (42 nm)	1130 nt/ chlamydia trachomatis	isothermal target and probe amplification for the hybridization of target amplicons and Au@DNA followed by RNA cleavage	10^2 copies [111]
AuNPs (15 nm)	16, 32 nt/ cytochromes P450	single-base primer extension in combination with noncrosslinking assay	1 μM [112]
AuNPs (13 nm)	16–80 nt/rtM204V	selective stabilization of unmodified AuNPs with nucleoside monophosphates after nuclease cleavage	5 nM [113]
AuNPs (20 nm)	—/hepatitis B	ligation chain reaction to induce aggregation of Au@DNA	20 aM [114]
fluorescence/enzyme-free			
AuNPs (13 nm)	26 nt/—	combination of AuNP fluorescence anisotropy and toehold-mediated strand-displacement reaction	0.95 nM [115]
PS NPs (40 nm)	57 nt/PKD1	fluorescence-enhancement from nanoparticle-hybridized DNA complexes by nanostructured photonic crystals due to phase matching of excitation and emission	50 aM [116]
Ag nanoclusters	22 nt/miR-141	target-triggered CHA and fluorescence enhancement of DNA–silver nanoclusters to detect miRNA	0.3 nM [117]
AuNPs (5 nm)	24 nt/—	distance-dependent modulation of electrochemiluminescence from CdS:Mn nanocrystals by gold nanoparticles.	2.9 fM [118]
quantum dots (QDs, 10 nm)	19 nt/miR-21	p19-QDs with multiplex antenna capture miRNA-21/antimiRNA-21-Cy3 duplex to form a Förster resonance energy transfer (FRET) detection system between QDs and Cy3	0.6 fM [119]
MBs (1 μm)	21 nt/miR-27a	dual toehold-mediated circular strand displacement amplification-based DNA circuit as fluorescent strategy for the detection of miRNA-27a	0.8 pM [120]
fluorescence/enzyme-aided			
AuNPs (5 nm)	25 nt/—	enhancement of the electrochemiluminescence of a CdS film by a combination of an isothermal circular amplification reaction of polymerase, NEase and Au@DNA	5 aM [121]
QDs (15 nm)	21 nt/miR-196a2T	miRNA detection by coupling rolling circle amplification and NEase with streptavidin-coated QDs	51 aM [122]
carbon dots (CDs, 8 nm)	52 nt/H7N9 virus	carbon nanodot-based fluorescent sensing strategy for H7N9 utilizing isothermal strand displacement amplification	3.4 fM [123]
graphene QDs (5 nm)	22 nt/miR-141	pentaethylenehexamine- and histidine-functionalized graphene QD for a microRNA fluorescence biosensing nanoplatform coupled with molecular beacon double-cycle amplification	0.43 aM [124]
QDs (5 nm)	—/miR-148, miR-21	QD-assisted FRET signal generation	42 fM [125]
optical microscopy			
AuNPs (5 nm)	22 nt/LET7	differential interference contrast microscopy with a microarray platform comprising hairpins as capture probes and Au@DNA as signaling probe	10 fM [126]
AuNPs (40 nm)	45 nt/p53	aggregation of oligonucleotide-modified organic nanospheres coded with fluorescent dyes (red/green/blue)	200 fmol [127]
AuNPs (15 nm)	15 nt/—	surface plasmon resonance imaging of Au@DNA in a PDMS–gold–glass hybrid microchip	32 nM [128]
AuNPs (50 nm)	28, 60, 90 nt/—	dark-field microscopy for the detection of head-to-tail Au@DNA hybridization	4 pM (28 nt)/40 pM (60 nt) [129]
AuNPs (50 nm)	46 nt/HeLa cells	dark-field microscopy combined with Rayleigh scattering spectrophotometry for single-particle detection	10 HeLa cells [130]

DNA with complementary strands left the nanoparticles uncovered, facilitating aggregation. The authors were able to detect single-base mismatches at the level of 43 nM using gold nanoparticles of 13 nm. This method, however, had a rather low selectivity and could only differentiate DNA strands containing three or more mismatched bases.

These examples are characterized by their simplicity requiring no expensive equipment or reagents. The detection of SNPs was achieved by mixing a DNA target with a probe followed by the direct naked-eye readout. The need for further improvements motivated the researchers to increases the complexity of the assays. Today, the methods for SNP detection can be classified as enzymatic and nonenzymatic. In enzyme-free strategies, the signal amplification is achieved by a cascade of hybridization reactions prior to the optical signal transduction. One of the mechanisms that are discussed in the following section benefits from free energy driving cascades of toehold-mediated strand-displacement reactions. Other heavily exploited mechanisms are based on the formation of DNA circuits and include hybridization chain reaction (HCR), catalytic hairpin assembly (CHA) and entropy-driven catalysis [64]. These mechanisms have shown a great potential for developing biosensors of high sensitivity and high selectivity since the target DNA itself is used as a catalyst to cyclically amplify the process of DNA self-assembly. The strategies based on enzymatic tools, on the other hand, are characterized by an extraordinary potential for signal amplification. The main advantages of using enzymes involve: a) the capability of modifying oligonucleotides (e.g., polymerases, nucleases, helicases, ligases), b) an extraordinary catalytic activity and c) biocompatibility. Table 3 summarizes the examples for the detection of DNA targets with single-point mutations using gold nanoparticles as signal transducers. We classified the assays by the used enzymatic reactions for signal amplification.

Enzyme-free SNP discrimination using gold nanoparticles

Although the first works on the selective aggregation of Au@DNA by complementary ssDNA offered a conceptual novelty in the field of biosensing, the simple aggregation of nanoparticles via complementary target DNA suffered from low detection sensitivity and selectivity. To overcome these limitations, new amplification methods were proposed using diverse molecular mechanisms. Mirkin and co-workers have implemented a bio-bar-code method to detect single-point mutations in target DNA associated with the anthrax factor [79]. The assay comprised magnetic beads coated with a sequence of oligonucleotides and Au@DNA modified with two types of oligonucleotides (1:100 ratio), one that was complementary to the target sequence and the other complementary to a bar-code sequence. The magnetic beads and the Au@DNA formed a sandwich structure linked by the target sequence, which was magnetically separated from the wild-type DNA. This process was followed by the release of bar-code sequences, which were then captured on a chip-based scanometric system and amplified via the autocatalytic reduction of silver(I) by hydroquinone. The authors demonstrated a sensitivity of 500 zM, which translates to about ten copies in 30 μL of the sample.

To improve the sensitivity of the colorimetric sensors, several groups have proposed to use modified nucleic acids. The most common modified nucleic acids are peptide nucleic acids (PNAs) and locked nucleic acids (LNAs), which are obtained by intercalating natural and artificial nucleobases or by modifying internucleoside linkages. Lee and co-workers have proposed the colorimetric detection of a point mutation in codon 559 of c-Kit using targets of different lengths (12-, 21- or 42-mer) [92]. PNA-coated AuNPs (18 nm) were complementary to the wild-type target sequence that hybridized with the PNA probes on the AuNPs. This hybridization made the particles negatively charged because of the phosphate backbone in the target DNA sequences preventing their aggregation. Uncharged particles underwent aggregation. The detection limit was 100 fmol/μL for a target with 21 bases. Chakrabarti and Klibanov built an assay based on the difference in the thermal stability of PNA–DNA and DNA–DNA duplexes [131]. The authors observed that the PNA-modified AuNPs aggregated due to the neutralization of the charges of the PNAs. Upon the addition of complementary DNA, the colloidal stability was recovered because of the hybridization of the negatively-charged DNA with the neutral PNA-modified AuNPs. The group of Graham has reported the functionalization of AuNPs (13 nm) with LNAs, revealing a remarkable binding affinity and selectivity towards DNA targets with 22 bases [70]. The use of LNA/DNA chimeras enhanced the stability of duplexes formed with AuNP conjugates, which could discriminate between mismatching DNA and complementary target DNA at a detection limit of 100 nM.

The use of unmodified gold nanoparticles as signal transductors is another strategy for the selective detection of SNPs. Zhou and co-workers have proposed the use of binary DNA probes that were split in the middle and complementary to the target DNA [67]. Upon the addition of target DNA to the solution of binary DNA probes and citrate-protected AuNPs of 13 nm in diameter, the hybridization between the target DNA and the binary DNA probes enhanced the salt-induced aggregation. However, the presence of DNA molecules with single-base mismatches prevented the aggregation of AuNPs and the solution remained stable. This approach yielded a detection limit of 5 nM. Lee and co-workers have reported the detection of mutations in exon 19 and exon 21 of the epidermal growth factor receptor (EGFR) isolated from both the lung cancer cell lines and the cancer tissues of patients with non-small-cell lung cancer [66]. The citrate-stabilized gold nanoparticles underwent selective aggregation upon the addition of mutated DNA that hybridized with the complementary probe of 20 bases. Yet,

the gold nanoparticles remained stable in the presence of wild-type DNA complementary to the probe sequence. In the eight specimens of non-small-cell lung cancer patients, the deletion of the mutant form of exon 19 and the L858R point mutation in exon 21 were detected at a concentration of 10 ng/μL.

Another strategy to improve the sensitivity of colorimetric biosensors based on plasmonic nanoparticles is the use of a molecular tool known as toehold-mediated strand displacement [132], in which one strand of DNA (output) is exchanged spontaneously with another strand (input). In such a process, an original ssDNA strand, which is complexed with a protector ssDNA, has a region – the toehold – that is complementary to the third strand of an ssDNA – the invading strand. The displacement starts with the selective hybridization of the invading strand with original strands, followed by a progressive branch migration of the invading domain to finally displace the protector ssDNA. The process is energetically favored since the reverse reaction is slower by several orders of magnitude. When the protector strand possesses a toehold region, it can turn into an invading strand itself, giving rise to a strand-displacement cascade. Duan et al. have proposed the use of a toehold-mediated strand-displacement cascade, in which the product of the strand displacement (length of 34 bases) was consumed by the disassembly of AuNPs [69]. The assay allowed for an SNP discrimination at a detection limit of 1 nM in a complex physiological medium such as fetal bovine serum.

Liang and co-workers [83] built on the previous results and developed a strategy to discriminate single-base mutations through the assembly of AuNPs driven by a DNA-fueled molecular machine (Figure 4). In their design, the initial mixture contained two different types of nanoparticles: first, AuNPs functionalized with multi-stranded DNA molecules (S), and second, Au@DNA acting as the fuel. The key in the design of S were two open-terminal domains, named α and γ. A reaction was initialized by a catalyst (X) binding to the γ domain of S. Thus, releasing a by-product, an intermediate species was produced, which had a single-stranded region complementary to the DNA sequence of the fuel. In the next step, the fuel displaced the catalyst X, resulting in the cross-linking aggregation of the two DNA–AuNP complexes. The catalyst was released back into the solution. The authors observed that the aggregation of nanoparticles was slower by a factor of 10 when the sequence of the catalyst contained single-base mismatches (spurious catalyst). This colorimetric bioassay could detect single-base changes associated with the breast cancer gene BRCA1. The detection limit was 0.26 nM, corresponding to 31.2 fmol of a target.

Recently, advances in the development of DNA circuits based on hybridization and strand-exchange reactions have attracted much attention. Two examples of DNA circuits are commonly exploited, HCR [133] and CHA [134], both introduced by the Pierce group. These are based on the storage of potential energy in two hairpin species. In HCR, a single-stranded DNA initiator interacts with the first hairpin, exposing a new single-stranded region, which in turn opens the second hairpin species. Then, the chain reaction proceeds. Namely, single-stranded regions that are identical to the original single-stranded DNA

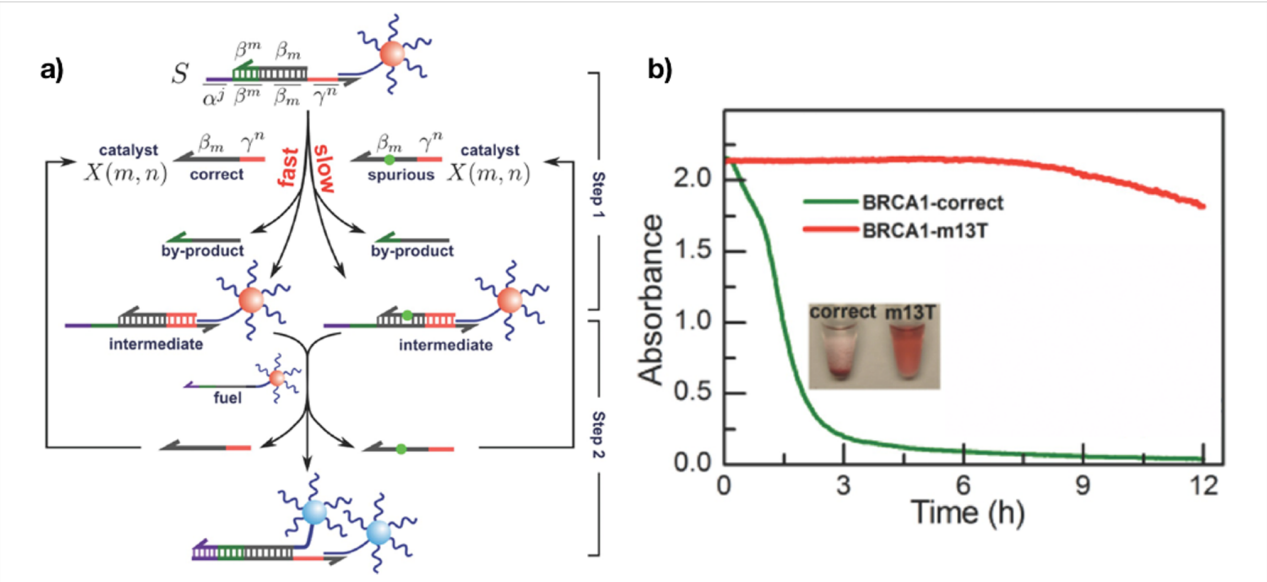

Figure 4: Discrimination of SNPs by means of the kinetics of particle aggregation. a) The spurious catalyst decelerates the toehold-exchange reaction and thus the formation of aggregates. (b) Time-dependent change of the color of the assay using spurious and correct targets. Reprinted with permission from [83], copyright 2014 John Wiley and Sons.

initiator get exposed and finally open other hairpins. As a result, double helices are formed until all hairpins are consumed. On the other hand, CHA relies on the exponential amplification of a target sequence. In the presence of a target, the so-called hairpin detection probe (HDP) is unfolded to form a duplex and expose its concealed domain. The corresponding hairpin assistant probe (HAP) replaces the target to form specific HDP/HAP complexes. The target is released based on a thermodynamically driven entropy gain process. The released target then triggers the next cycle to produce numerous HDP/HAP complexes [135].

In their work, Sang and co-workers [72] have proposed a method called target-catalyzed hairpin assembly amplification. Aggregation of nanoparticles at an elevated salt concentration was prevented by three kinetically frozen hairpin structures, which exhibited an affinity toward metallic gold. The addition of a DNA target activated a cascade of assembly steps to form stiff branched junctions, thus consuming all three hairpin structures. The electrostatic repulsion between the junctions and the negatively charged AuNPs made negligible their binding to the gold surface, leading to the aggregation at high salt concentrations. By this method, a detection limit of 0.1 pM for a single-point mutation in sequences of 16 nucleotides was achieved.

Chanho Park et al. [81] have extended this strategy by using catalyst DNA (c-DNA) to discriminate single-base mutations in long (84 molecules) EGFR mutated DNA. The catalyst c-DNA was complementary to the so-called c-c DNA, a longer DNA sequence (Figure 5). The introduction of target DNA to a solution containing c-DNA and c-c DNA led to the formation of duplexes between c-c DNA and target DNA molecules. As a result, c-DNA was released again and initiated the assembly of branched junctions with three metastable hairpin DNA molecules. Two of these hairpins were attached to the surface of AuNPs, such that the formation of the branched junctions altered the colloidal stability of the nanoparticles, leading to a gradual aggregation. The detection limit of this method was 7.7 fM.

With the aim of improving the sensitivity of the plasmon-based colorimetric sensor, Ying and co-workers [82] have used gold nanorods as a signal transducers. Due to their intense longitudinal surface plasmon band, gold nanorods exhibit a higher sensitivity to changes of the colloidal stability as compared to spherical nanoparticles. Thus, by using gold nanorods one can lower the detection limit. The authors used unmodified gold nanorods for an HCR process as illustrated in Figure 6. The presence of a target DNA induced the hybridization of a hairpin DNA, producing a nicked double helix. Through electrostatic repulsion, this double helix prevented the aggregation of the gold nanorods at high salt concentrations. However, in the absence of a target DNA, the gold nanorods easily aggregated because of weak protection by hairpin DNA. Following this approach, the authors were able to detect target DNA in a range of 0–60 nM at a detection limit of 1.47 nM. The method is highly selective in distinguishing matching and single-base mismatching DNA.

Enzyme-aided SNP discrimination

Owing to their high selectivity and strong catalytic properties, enzymes are molecular tools capable of improving sensitivity and selectivity of colorimetric sensors by several orders of magnitude. The most commonly exploited enzymes are nucleases,

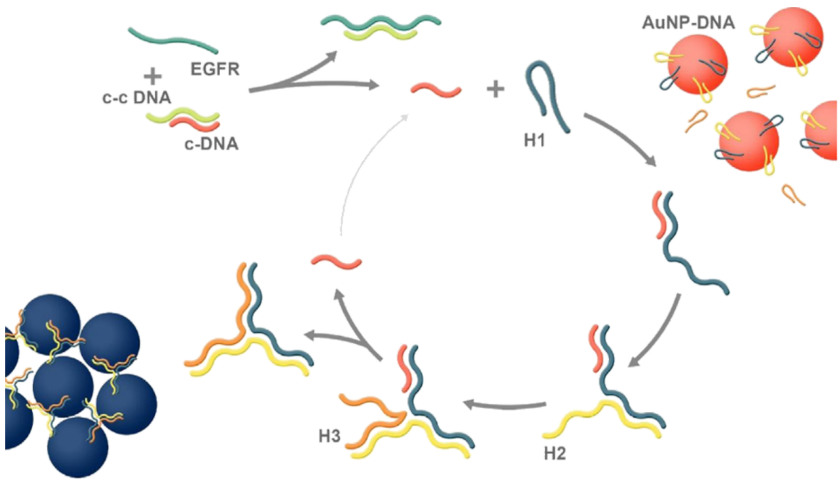

Figure 5: Working principle of the colorimetric assay for the detection of EGFR mutants in long DNA sequences. The presence of a target releases the catalyst oligonucleotide initiating CHA, which in turn progressively aggregate gold nanoparticles. Reprinted with permission from [81], copyright 2018 John Wiley and Sons.

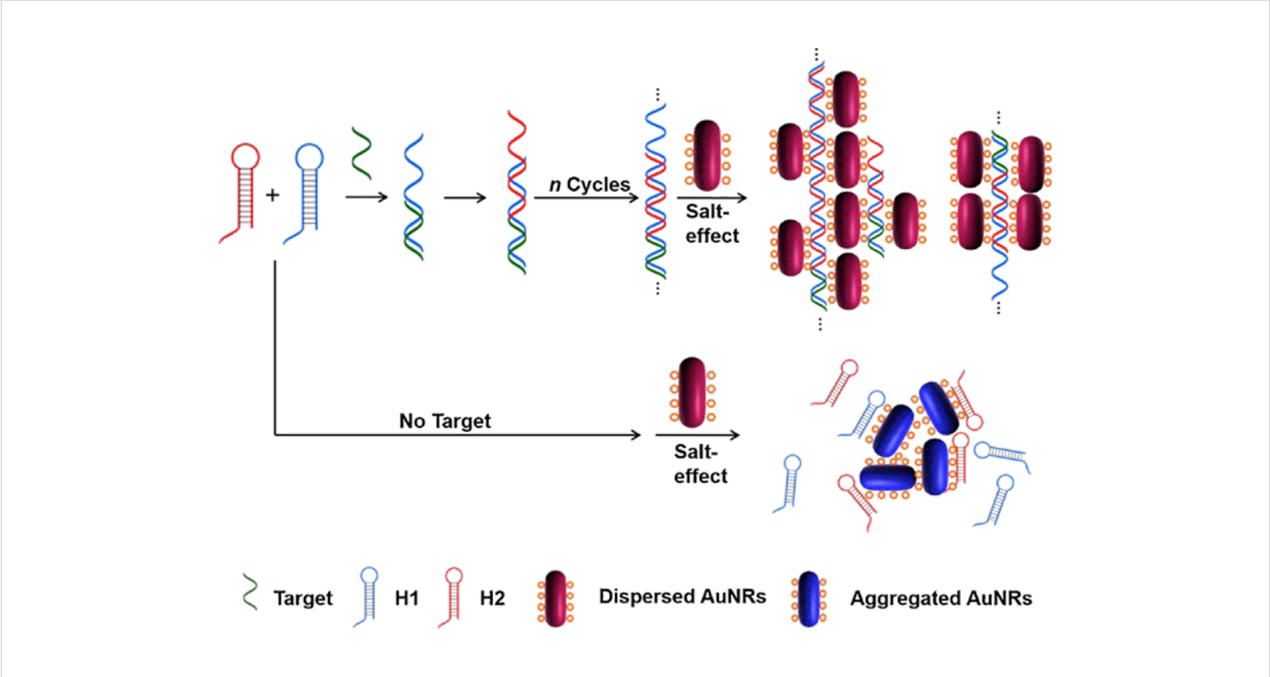

Figure 6: The combination of unmodified gold nanorods as signal transducers in an HCR amplification process for the colorimetric detection of single-base mutations. Reprinted with permission from [82], copyright 2018 Elsevier.

polymerases and ligases. Another advantage of using enzymes is their capability to sustain catalytic cycles, thus amplifying the number of available oligonucleotide sequences, which after reaching a concentration threshold induce the aggregation of nanoparticles. Therefore, a relatively low concentration of enzymes is required (1 U/μL) to maintain cyclic reactions and amplify the concentration of the DNA strands. However, the time required to reach the concentration threshold of a given strand is relatively long (hours), slowing down the operation of an assay. An additional drawback is that enzymatic reactions require a precisely controlled temperature range to ensure proper functioning, affecting the robustness of an assay under real-world conditions. Nonetheless, as shown over the last decade, the integration of enzymes into nanoparticle-based colorimetric assays is a conceptual innovation in the discrimination of DNA mutations in complex physiological media.

To implement enzymes into assays for single-nucleotide discrimination using gold nanoparticles as signal transducers, exonuclease-assisted signal amplification (EASA) is commonly used. By coupling cyclic enzymatic cleavage and signal amplification by gold nanoparticles, Yang and co-workers were able to reach a detection limit of 15 pM [108]. Their system consisted of exonuclease III (Exo III), a linker strand and two batches of spherical Au@DNA (Figure 7). The linker was hybridized with a target DNA forming a duplex that could be digested by Exo III, which in turn led to the release of the target for other binding/cleavage events. The linker sequence was complementary to Au@DNA. When digested by Exo III, the linker could not couple with the Au@DNA particles, thus preventing particle aggregation. However, in the absence of a target, no linker DNA was digested, allowing for the progressive hybridization to Au@DNA and therefore aggregation. The activity of Exo III strictly depends on the type of 3′ terminus affecting the selectivity of the assay. More precisely, a fully complementary target led to recessed 3′ termini, while a mismatch yielded protruding 3′ termini. Hence, the method allowed for the discrimination of single and triple-base mismatches.

Ye and co-workers explored the duplex-specific nuclease (DSN) [104] for the detection of microRNA (Figure 8). The system consisted of a probe complex, DSN and two sets of different ssDNA-modified gold nanoparticles. The probe complex is formed by two strands with a loop in the middle and hybridization regions at the termini. Target miRNA invaded the probe complex forming a substrate (probe B) that was hydrolyzed by the enzyme, leading to the release of probe A and target miRNA. This cyclic invasion/digestion process caused a gradual increase of the concentration of probe A, triggering the aggregation of nanoparticles. Without a miRNA target, the probe complex remained undigested and the colloidal stability of the nanoparticles was conserved. DSN is capable of discriminating single-nucleotide mismatches in short DNA–RNA duplexes. The method reached a detection limit of 5 nM for mismatched miRNA (G-miR-122).

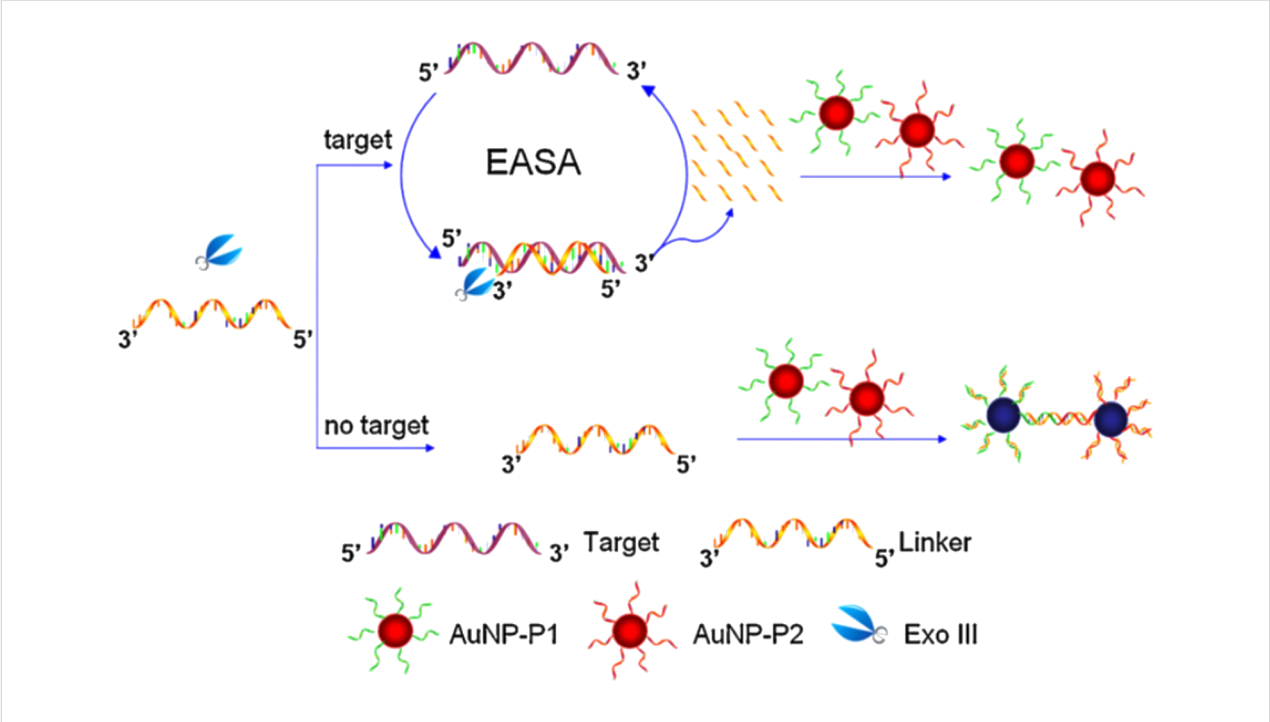

Figure 7: Working principle of EASA for the colorimetric detection of DNA mismatches. The consumption of a large amount of linker DNA strands by a few initial target molecules leads to the preservation of the colloidal stability of gold nanoparticles. In the absence of a target, the intact linker DNA hybridizes with Au@DNA leading to a gradual color change. Reprinted with permission from [108], copyright 2011 Elsevier.

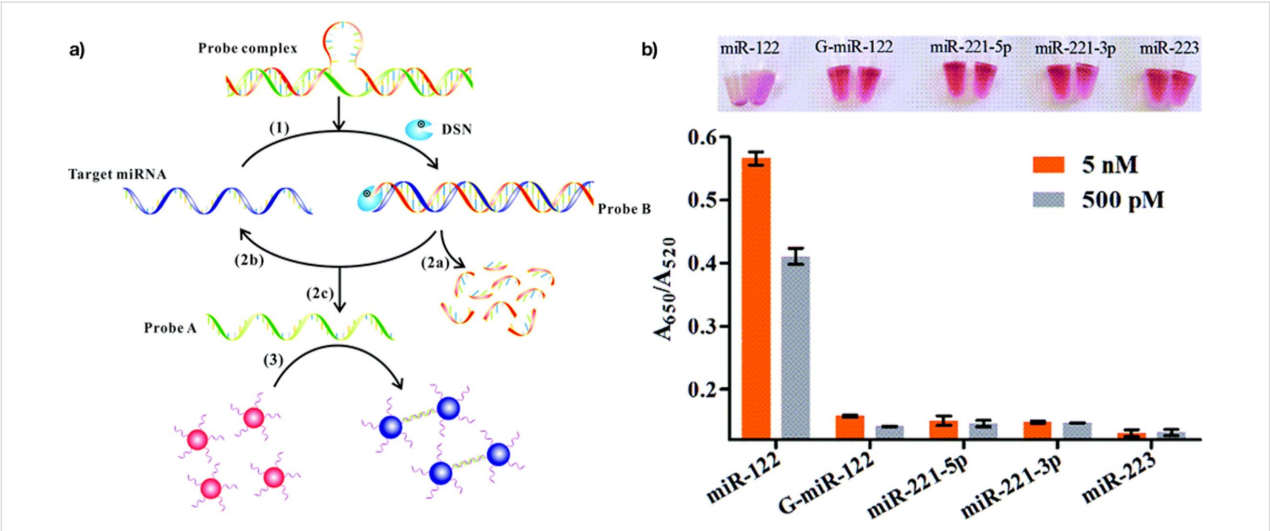

Figure 8: Schematic illustration of the colorimetric method for the detection of specific miRNA based on the amplification of DSN-assisted nanoparticles using AuNPs as the signal output. Reprinted with permission from [104], copyright 2015 Royal Society of Chemistry.

Another enzyme-assisted approach used in the discrimination of single-base mutations involves the combination of nicking endonuclease (NEase) and DNA polymerase giving rise to the so-called isothermal exponential amplification reaction (EXPAR). The EXPAR technique uses a DNA template, deoxynucleotide triphosphates (dNTPs) and two enzymes to achieve the exponential amplification of a target sequence. DNA polymerase and NEase are used in the same reaction mixture. Once connected to the template, the trigger DNA is extended along the template by the DNA polymerase. After the extension, the dsDNA contains the NEase recognition sequence, and the NEase cleaves the extended trigger DNA strand. The displaced strand and another template molecule then hybridize, initiating a new amplification cycle [136,137].

The group of Ye has used EXPAR with a sensing probe immobilized on the surface of gold nanoparticles (Figure 9) [107]. The key point here was the design of the sensing probe, which had three domains: a polyadenine block with a phosphorothioate modification in the backbone, two sequences complementary to the target miRNA and a recognition site of the NEase. When the target miRNA connected to the sensing probe, the EXPAR process commenced. The DNA polymerase extended the double-stranded fragment with a recognition site for an endonuclease that nicked the fragment enabling its release. This new fragment by being equal to the target miRNA, initiated a new EXPAR cycle, leading to the release of the sensing probe from the nanoparticles and as a consequence, their aggregation. This method yielded a detection limit of the specific miRNA of roughly 46 fM. In addition, the authors tested the selectivity of this assay using G-miR-221-3p. This test revealed a relatively good specificity, demonstrating that single-nucleotide differences between similar miRNAs members could be identified.

To improve visual detection of single-point mutation on device conditions, Liu and co-workers developed an approach that combined isothermal strand-displacement polymerase reactions (ISDPR) and lateral flow strip (LFS) [102]. The mixture for ISDPR comprised biotin-modified hairpin, digoxin-modified primer, polymerase, and deoxynucleotide mixture (Figure 10a). A mutant DNA hybridized with the hairpin probe, leading to a conformational change, and stem separation (step 1), followed by polymerization reaction by the polymerase (step 2), forming biotin- and digoxin-attached duplex DNA (step 3). The process was further amplified through the next cycle (step 4). Overall, by the cyclic process, a large number of biotin- and digoxin-attached duplex DNA were produced using a little amount of the initial mutant DNA. The duplex DNA was later detected visually on the LFS through dual immunoreactions, using two batches of gold nanoparticles functionalized either with anti-digoxin and anti-biotin antibodies to obtain color signal at test and control zones, respectively. With this test, authors were able to detect visually the presence of R156H-mutant gene at the concentration down to 1 fM.

Another interesting approach of using gold nanoparticles for SNP detection is based on the fact that gold nanoparticles are capable of quenching fluorescence through Förster resonance energy transfer. By involving an isothermal circular amplification reaction of polymerase and NEase, the group of Chen [121] used gold nanoparticles to either quench or enhance the electrochemiluminescence of CdS films through the modulation of the distance between metallic and semiconductor components by a DNA machine (Figure 11). Their system consisted of a CdS film, a composite of AuNPs (5 nm) and hairpin DNA, a primer, and polymerase and NEase. In the presence of AuNPs–hairpin DNA, the luminescence of CdS was quenched (Figure 11A). The luminescence was recovered after adding target DNA, causing a conformational transition from hairpin to linear DNA. This opening initiated polymerization of DNA (Figure 11C), which in turn displaced previously hybridized target DNA (Figure 11D). In such a design, one target DNA strand could open many hairpin DNA strands, increasing the fluoresce signal. An additional increase of the fluorescence signal was achieved by the action of NEase that nicked an extended double

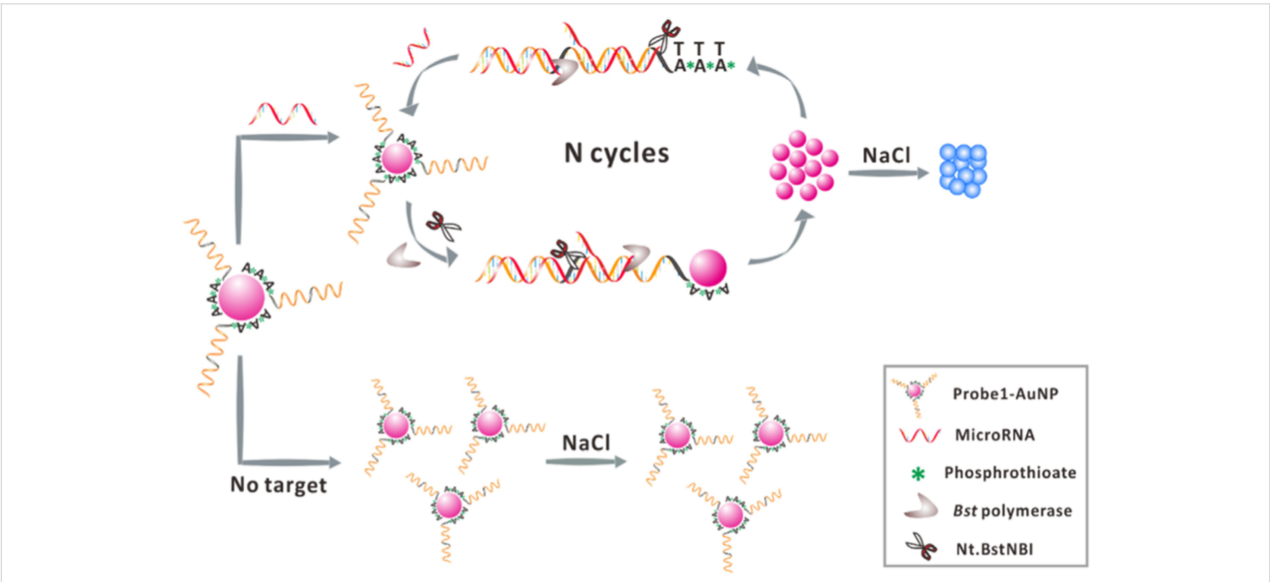

Figure 9: Colorimetric method for the detection of specific miRNA based on the combination of enzyme-assisted exponential amplification and AuNP-based colorimetric detection. The sensing probe attached to the gold nanoparticles can be easily disrupted by the enzymes, ensuring thus an improved performance. Reprinted with permission from [107], copyright 2016 Elsevier.

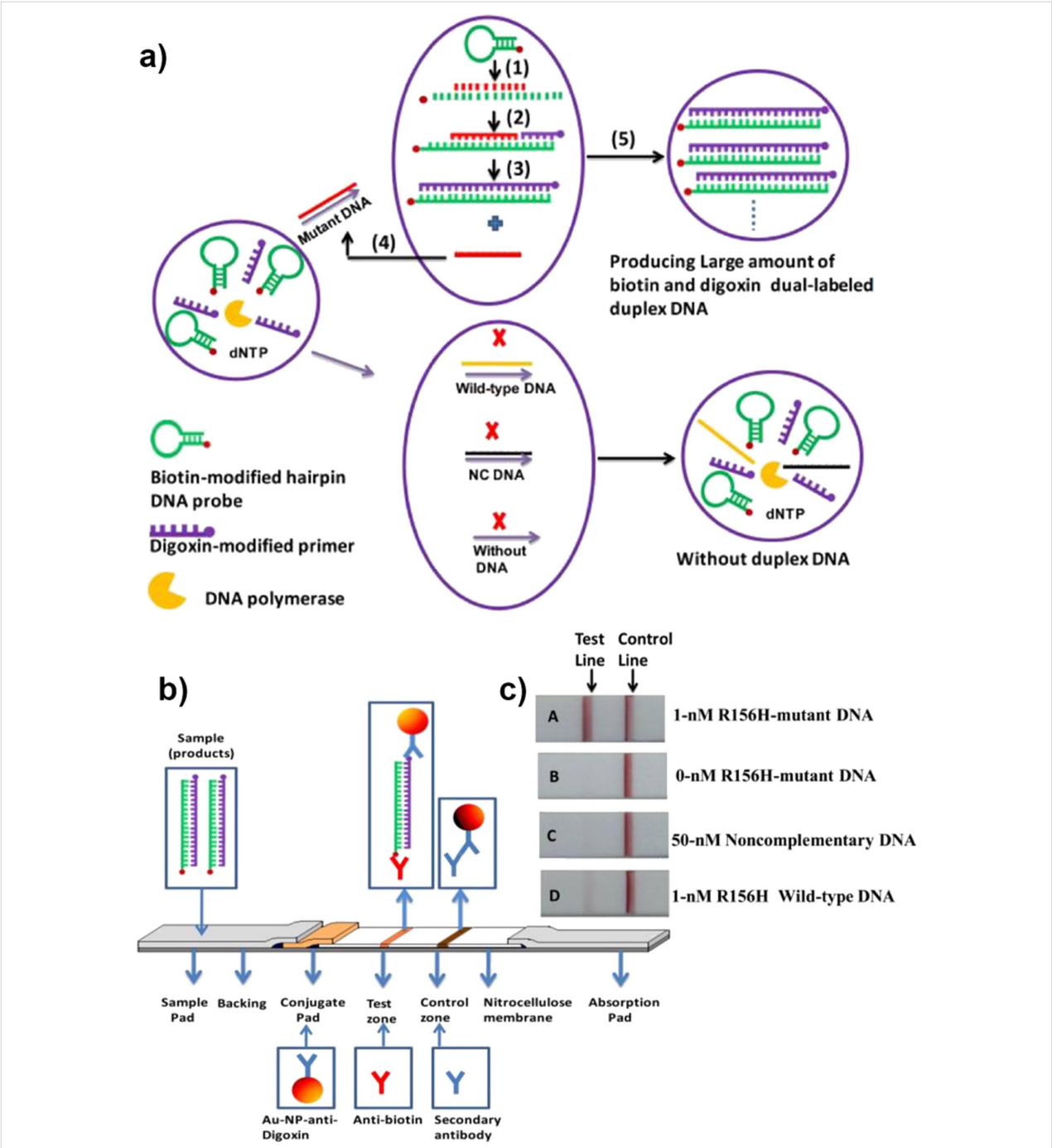

Figure 10: The combination of isothermal strand-displacement polymerase reactions and lateral flow strip for visual detection of gene mutations. a) Schematic illustration of isothermal strand-displacement polymerase reactions and the formation of digoxin- and biotin- attached duplex DNA complexes b) The mechanism of detection on lateral flow strip and c) visualization of the presence of mutation. Reprinted with permission from [102], copyright 2012 Elsevier.

helix strand, allowing for a subsequent polymerization process and displacement of the DNA trigger. The authors estimated that the presence of one polymerase molecule and one NEase molecule was enough to complete 22 cycles over a period of 40 min. The use of a target DNA with single-point mutation led to a decrease of the relative fluorescence by 87%.

DNA ligase is an enzyme capable of repairing nicks, i.e., missing phosphodiester bonds, in a DNA sequence. Assays based on such enzyme rely on the ability to covalently join two oligonucleotides when they hybridize next to each other on a given template. In an inverted scenario, one can use the so-called padlock probe, a linear oligonucleotide with two ter-

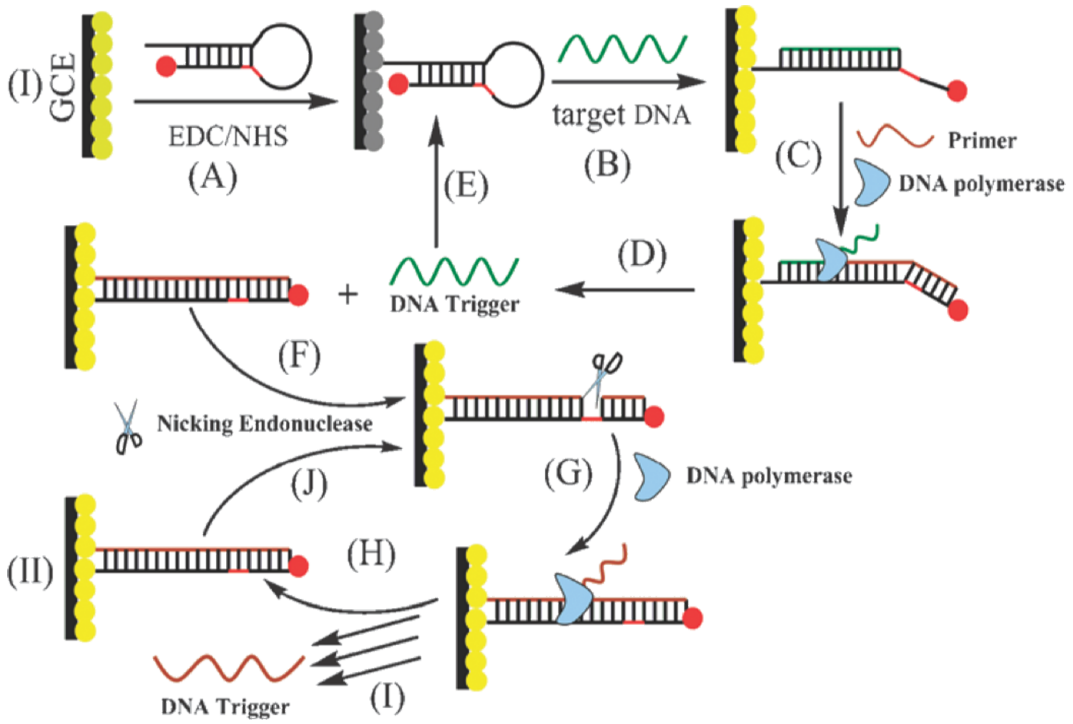

Figure 11: The use of gold nanoparticles as fluorescence quencher in the discrimination of SNP through cyclic enzyme-aided polymerization and nicking of oligonucleotides. The presence of a mutation decreases the fluorescence of the CdS films by nearly 90%. Reprinted with permission from [121], copyright 2011 Royal Society of Chemistry.

minal segments complementary to a short target sequence. Upon hybridization to a target DNA, the two ends become juxtaposed and can be joined by a DNA ligase if there is a perfect match. Liu and co-workers [110] have proposed the use of a padlock probe that contained a segment with the sequence identical to a linker probe *a′–b′* and target-complementary segments at both termini of the molecule (Figure 12a). The ends were brought in contact to form a circular oligonucleotide upon hybridization to the target DNA in the presence of a DNA ligase, serving as a template for a rolling circle amplification reaction. The produced prolonged DNA containing copies of the complementary sequence of the padlock template underwent selective scission in the presence of endonuclease. As a result, if the target DNA was complementary to the padlock probe, the nicked linker block would bind to the complementary DNA attached to gold nanoparticles without aggregation. If there was a mismatch, however, the linker probe would remain intact, facilitating the gradual aggregation of nanoparticles through hybridization. The authors demonstrated a colorimetric discrimination of single-point mutation, which decreases when the mismatch position is shifted away from the ligation site (Figure 12b).

In another study, Zhou and co-workers have proposed a colorimetric detection of DNA by coupling an invasive reaction (strand displacement) with NEase-assisted nanoparticle amplification [105]. In the proposed method, the target sequence was first hybridized to two probes (up- and down-stream) followed by enzymatic cleavage using flap endonuclease, producing many flaps from a target DNA (Figure 13a). Then, in another enzymatic reaction, the flaps were ligated with a P-oligo sequence, allowing for a nicking of the complementary strand (Linker) by NEase. The amplified linker strands bound to Au@DNA gold nanoparticles preventing their aggregation. In contrast, in the absence of the target, the consecutive enzymatic reactions were inhibited, leading to the preservation of the linker strands, and its subsequent hybridization with gold nanoparticles, causing aggregation. The specificity of the method was demonstrated by the discrimination of mutated strands (1%) in the presence of a large amount of wild-type DNA backgrounds (Figure 13b,c).

Conclusion

The last two decades of extensive studies have proven that plasmonic nanoparticles (especially gold) exhibit properties that facilitate their implementation in molecular assays the for detection of genetic mutations in biological samples. Recent results also show that further complexification and coupling of the nanoparticles with DNA-based molecular amplification tools is a way to provide tests of binary readout and of rational

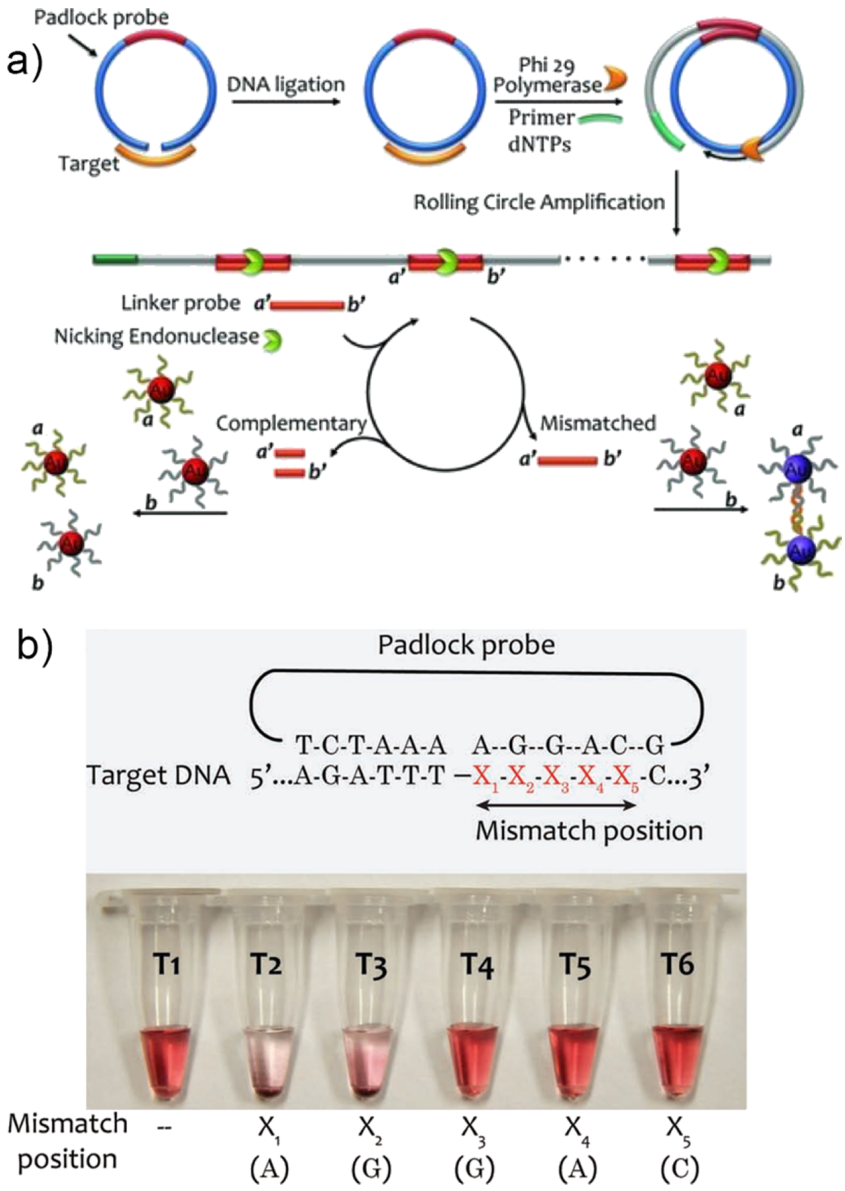

Figure 12: Colorimetric DNA detection through rolling circle amplification (RCA) and NEase-assisted nanoparticle amplification (NEANA). a) Working principle of the assay. b) Colorimetric detection of single-point mutation located in the proximity of ligation point. Reprinted with permission from [110], copyright 2012 John Wiley and Sons.

sensitivity, with limits of detection reaching real-world requirements. It is, however, noteworthy that recent advancements, as discussed above, have been made mostly in the context of the (bio)molecular components of given assays. That is, while the amplification methods, based on DNA molecular machines or enzyme-assisted processes, were the subject of constant improvements, the plasmonic component remains barely explored. However, a vast number of plasmonic nanomaterials with different shapes, sizes and compositions is commonly available, offering a broad range of optical properties not only in the visible but also in the near-infrared spectral range. Shape anisotropy (rods) and regiospecific surface functionalization (tip versus lateral parts) enable the fabrication of colloidal systems with limited degrees of freedom. In such systems, the possible orientations of particles relative to each other are restricted, which imposes a colorimetric transition, i.e., a blueshift or redshift of the localized surface plasmon resonance [138]. It is reasonable to assume that development of biosensors for liquid biopsy will benefit from growing research on dynamic self-assembly of nanoparticles, in which interparticle forces [139], mutual orientation and interparticle distances are well controlled by chemical stimuli. Finally, we foresee that the detection of genetic mutations by plasmonic nanoparticles will be strongly enhanced by a complementary detection of disease-

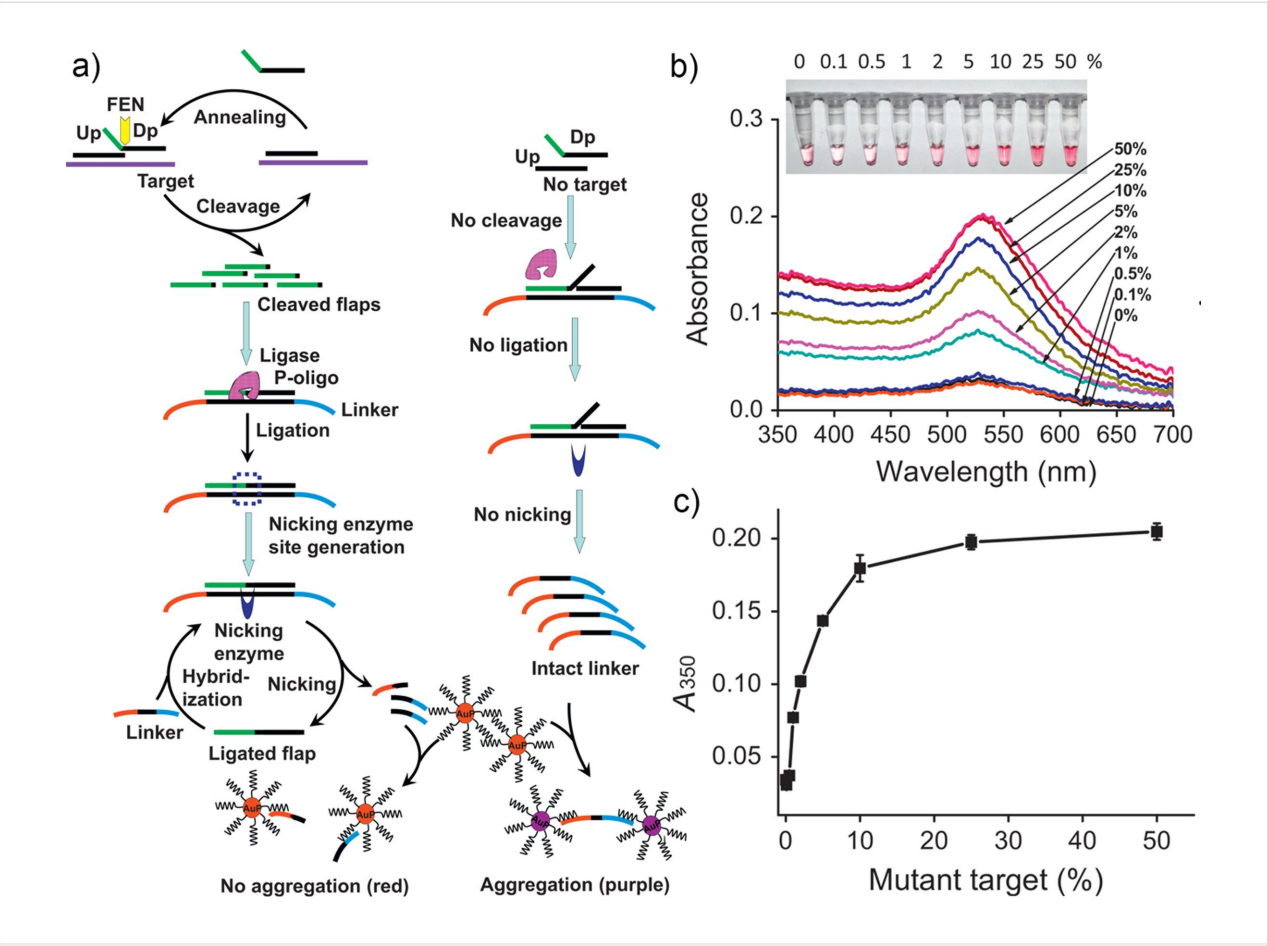

Figure 13: a) The working principle of DNA target detection through an invasive reaction coupled with NEase-assisted nanoparticle amplification. b) Optical characterization of the assay solution spiked with different amounts of c.2573 T>G mutant EGFR gene in the presence of a background wild-type EGFR sequence, showing a specificity down to 1%. c) The relation of increased absorbance with increasing the relative concentration of mutated sequence in assay mixture. Reprinted with permission from [105], copyright 2015 Elsevier.

related proteins. Specifically, the recently proposed protein corona sensor arrays in which the composition of protein corona reflects the presence of a given cancer enabled new venues in detecting diseases directly from a blood sample [140]. Moreover, the simultaneous detection of genetic mutations and disease-specific proteins, as shown recently [141], brings great promises to liquid biopsy.

With the aim of reaching real-world applications, the current assays, which have demonstrated functionality under laboratory conditions, require optimization to be incorporated into point-of-care diagnostic tools. Lateral flow tests are especially attractive since they exhibit numerous advantages including minimal operator-dependent interpretation of the test (binary output), small value, low cost, relatively short detection time (minutes), and the possibility for integration with personalized electronic devices [142-145]. Still, the integration of different stages such as sample preparation, molecular amplification, and transduction zones requires new design of lateral flow devices to become fully operative. Recent works, as the one by Liu et al. discussed above, suggests the feasibility of such an approach [102].

Several limitations need to be addressed as well. One of the known issues in colloidal biosensing is the spontaneous formation of a protein corona on the surface of the particles in physiological media [146], inhibiting the interaction of the biomarkers with the colloid, thereby altering the sensitivity and selectivity of an assay. The inhibition of binding events by the corona layer may lead to false negatives, while corona-mediated unspecific binding leads to false positives. To minimize the protein adsorption, one can tailor the chemical composition of ligands by the use of zwitterionic compounds or the use of antifouling polymers such as polyethylene glycol.

Finally, the availability of whole-genome sequencing as offered by recently established private companies (e.g., Veritas Genetics and Novogene) allows for the determination of

hundreds of mutations from a single sample at relatively low cost (200 US dollars). However, the time required to complete such an analysis exceeds several weeks, making it unfeasible for the fast monitoring of tumor dynamics. Therefore, point-of-care diagnostic tools that offer rapid (hours) discrimination of an individual mutation remain an aim to be pursued in the further development of personalized medicine.

ORCID® iDs

María Sanromán Iglesias - https://orcid.org/0000-0003-0619-6879
Marek Grzelczak - https://orcid.org/0000-0002-3458-8450

References

1. Ferlay, J.; Soerjomataram, I.; Dikshit, R.; Eser, S.; Mathers, C.; Rebelo, M.; Parkin, D. M.; Forman, D.; Bray, F. *Int. J. Cancer* **2015,** *136,* E359–E386. doi:10.1002/ijc.29210
2. Mandel, P.; Metais, P. *C. R. Seances Soc. Biol. Ses Fil.* **1948,** *142,* 241–243.
3. Li, W.; Wang, H.; Zhao, Z.; Gao, H.; Liu, C.; Zhu, L.; Wang, C.; Yang, Y. *Adv. Mater. (Weinheim, Ger.)* **2019,** *31,* 1805344. doi:10.1002/adma.201805344
4. Crowley, E.; Di Nicolantonio, F.; Loupakis, F.; Bardelli, A. *Nat. Rev. Clin. Oncol.* **2013,** *10,* 472–484. doi:10.1038/nrclinonc.2013.110
5. Bedard, P. L.; Hansen, A. R.; Ratain, M. J.; Siu, L. L. *Nature* **2013,** *501,* 355–364. doi:10.1038/nature12627
6. Sozzi, G.; Conte, D.; Leon, M.; Cirincione, R.; Roz, L.; Ratcliffe, C.; Roz, E.; Cirenei, N.; Bellomi, M.; Pelosi, G.; Pierotti, M. A.; Pastorino, U. *J. Clin. Oncol.* **2003,** *21,* 3902–3908. doi:10.1200/jco.2003.02.006
7. Kim, K.; Shin, D. G.; Park, M. K.; Baik, S. H.; Kim, T. H.; Kim, S.; Lee, S. *Ann. Surg. Treat. Res.* **2014,** *86,* 136–142. doi:10.4174/astr.2014.86.3.136
8. Chen, X.; Bonnefoi, H.; Diebold-Berger, S.; Lyautey, J.; Lederrey, C.; Faltin-Traub, E.; Stroun, M.; Anker, P. *Clin. Cancer Res.* **1999,** *5,* 2297–2303.
9. Sozzi, G.; Conte, D.; Mariani, L.; Vullo, S. L.; Roz, L.; Lombardo, C.; Pierotti, M. A.; Tavecchio, L. *Cancer Res.* **2001,** *61,* 4675–4678.
10. Madhavan, D.; Wallwiener, M.; Bents, K.; Zucknick, M.; Nees, J.; Schott, S.; Cuk, K.; Riethdorf, S.; Trumpp, A.; Pantel, K.; Sohn, C.; Schneeweiss, A.; Surowy, H.; Burwinkel, B. *Breast Cancer Res. Treat.* **2014,** *146,* 163–174. doi:10.1007/s10549-014-2946-2
11. Frattini, M.; Gallino, G.; Signoroni, S.; Balestra, D.; Lusa, L.; Battaglia, L.; Sozzi, G.; Bertario, L.; Leo, E.; Pilotti, S.; Pierotti, M. A. *Cancer Lett.* **2008,** *263,* 170–181. doi:10.1016/j.canlet.2008.03.021
12. Chan, K. A.; Jiang, P.; Zheng, Y. W.; Liao, G. J.; Sun, H.; Wong, J.; Siu, S. S. N.; Chan, W. C.; Chan, S. L.; Chan, A. T.; Lai, P. B.; Chiu, R. W.; Lo, Y. *Clin. Chem.* **2013,** *59,* 211–224. doi:10.1373/clinchem.2012.196014
13. Flohr, T.; Schrauder, A.; Cazzaniga, G.; Panzer-Grümayer, R.; van der Velden, V.; Fischer, S.; Stanulla, M.; Basso, G.; Niggli, F. K.; Schäfer, B. W.; Sutton, R.; Koehler, R.; Zimmermann, M.; Valsecchi, M. G.; Gadner, H.; Masera, G.; Schrappe, M.; van Dongen, J. J. M.; Biondi, A.; Bartram, C. R. *Leukemia* **2008,** *22,* 771–782. doi:10.1038/leu.2008.5
14. McBride, D. J.; Orpana, A. K.; Sotiriou, C.; Joensuu, H.; Stephens, P. J.; Mudie, L. J.; Hämäläinen, E.; Stebbings, L. A.; Andersson, L. C.; Flanagan, A. M.; Durbecq, V.; Ignatiadis, M.; Kallioniemi, O.; Heckman, C. A.; Alitalo, K.; Edgren, H.; Futreal, P. A.; Stratton, M. R.; Campbell, P. J. *Genes, Chromosomes Cancer* **2010,** *49,* 1062–1069. doi:10.1002/gcc.20815
15. Shaw, J. A.; Page, K.; Blighe, K.; Hava, N.; Guttery, D.; Ward, B.; Brown, J.; Ruangpratheep, C.; Stebbing, J.; Payne, R.; Palmieri, C.; Cleator, S.; Walker, R. A.; Coombes, R. C. *Genome Res.* **2012,** *22,* 220–231. doi:10.1101/gr.123497.111
16. Leary, R. J.; Sausen, M.; Kinde, I.; Papadopoulos, N.; Carpten, J. D.; Craig, D.; O'Shaughnessy, J.; Kinzler, K. W.; Parmigiani, G.; Vogelstein, B.; Diaz, L. A.; Velculescu, V. E. *Sci. Transl. Med.* **2012,** *4,* 162ra154. doi:10.1126/scitranslmed.3004742
17. Chan, K. C. A.; Jiang, P.; Chan, C. W. M.; Sun, K.; Wong, J.; Hui, E. P.; Chan, S. L.; Chan, W. C.; Hui, D. S. C.; Ng, S. S. M.; Chan, H. L. Y.; Wong, C. S. C.; Ma, B. B. Y.; Chan, A. T. C.; Lai, P. B. S.; Sun, H.; Chiu, R. W. K.; Lo, Y. M. D. *Proc. Natl. Acad. Sci. U. S. A.* **2013,** *110,* 18761–18768. doi:10.1073/pnas.1313995110
18. Diehl, F.; Schmidt, K.; Choti, M. A.; Romans, K.; Goodman, S.; Li, M.; Thornton, K.; Agrawal, N.; Sokoll, L.; Szabo, S. A.; Kinzler, K. W.; Vogelstein, B.; Diaz Jr, L. A. *Nat. Med.* **2008,** *14,* 985–990. doi:10.1038/nm.1789
19. Dawson, S.-J.; Tsui, D. W. Y.; Murtaza, M.; Biggs, H.; Rueda, O. M.; Chin, S.-F.; Dunning, M. J.; Gale, D.; Forshew, T.; Mahler-Araujo, B.; Rajan, S.; Humphray, S.; Becq, J.; Halsall, D.; Wallis, M.; Bentley, D.; Caldas, C.; Rosenfeld, N. *N. Engl. J. Med.* **2013,** *368,* 1199–1209. doi:10.1056/nejmoa1213261
20. Heitzer, E.; Ulz, P.; Belic, J.; Gutschi, S.; Quehenberger, F.; Fischereder, K.; Benezeder, T.; Auer, M.; Pischler, C.; Mannweiler, S.; Pichler, M.; Eisner, F.; Haeusler, M.; Riethdorf, S.; Pantel, K.; Samonigg, H.; Hoefler, G.; Augustin, H.; Geigl, J. B.; Speicher, M. R. *Genome Med.* **2013,** *5,* 30. doi:10.1186/gm434
21. Karapetis, C. S.; Khambata-Ford, S.; Jonker, D. J.; O'Callaghan, C. J.; Tu, D.; Tebbutt, N. C.; Simes, R. J.; Chalchal, H.; Shapiro, J. D.; Robitaille, S.; Price, T. J.; Shepherd, L.; Au, H.-J.; Langer, C.; Moore, M. J.; Zalcberg, J. R. *N. Engl. J. Med.* **2008,** *359,* 1757–1765. doi:10.1056/nejmoa0804385
22. Kuo, Y.-B.; Chen, J.-S.; Fan, C.-W.; Li, Y.-S.; Chan, E.-C. *Clin. Chim. Acta* **2014,** *433,* 284–289. doi:10.1016/j.cca.2014.03.024
23. Valtorta, E.; Misale, S.; Sartore-Bianchi, A.; Nagtegaal, I. D.; Paraf, F.; Lauricella, C.; Dimartino, V.; Hobor, S.; Jacobs, B.; Ercolani, C.; Lamba, S.; Scala, E.; Veronese, S.; Laurent-Puig, P.; Siena, S.; Tejpar, S.; Mottolese, M.; Punt, C. J. A.; Gambacorta, M.; Bardelli, A.; Di Nicolantonio, F. *Int. J. Cancer* **2013,** *133,* 1259–1265. doi:10.1002/ijc.28106
24. Thierry, A. R.; Mouliere, F.; El Messaoudi, S.; Mollevi, C.; Lopez-Crapez, E.; Rolet, F.; Gillet, B.; Gongora, C.; Dechelotte, P.; Robert, B.; Del Rio, M.; Lamy, P.-J.; Bibeau, F.; Nouaille, M.; Loriot, V.; Jarrousse, A.-S.; Molina, F.; Mathonnet, M.; Pezet, D.; Ychou, M. *Nat. Med.* **2014,** *20,* 430–435. doi:10.1038/nm.3511
25. Mohan, S.; Heitzer, E.; Ulz, P.; Lafer, I.; Lax, S.; Auer, M.; Pichler, M.; Gerger, A.; Eisner, F.; Hoefler, G.; Bauernhofer, T.; Geigl, J. B.; Speicher, M. R. *PLoS Genet.* **2014,** *10,* e1004271. doi:10.1371/journal.pgen.1004271

26. Misale, S.; Yaeger, R.; Hobor, S.; Scala, E.; Janakiraman, M.; Liska, D.; Valtorta, E.; Schiavo, R.; Buscarino, M.; Siravegna, G.; Bencardino, K.; Cercek, A.; Chen, C.-T.; Veronese, S.; Zanon, C.; Sartore-Bianchi, A.; Gambacorta, M.; Gallicchio, M.; Vakiani, E.; Boscaro, V.; Medico, E.; Weiser, M.; Siena, S.; Di Nicolantonio, F.; Solit, D.; Bardelli, A. *Nature* **2012,** *486,* 532–536. doi:10.1038/nature11156
27. Lecomte, T.; Berger, A.; Zinzindohoué, F.; Micard, S.; Landi, B.; Blons, H.; Beaune, P.; Cugnenc, P.-H.; Laurent-Puig, P. *Int. J. Cancer* **2002,** *100,* 542–548. doi:10.1002/ijc.10526
28. Spindler, K.-L. G.; Pallisgaard, N.; Vogelius, I.; Jakobsen, A. *Clin. Cancer Res.* **2012,** *18,* 1177–1185. doi:10.1158/1078-0432.ccr-11-0564
29. Schmitt, M. W.; Kennedy, S. R.; Salk, J. J.; Fox, E. J.; Hiatt, J. B.; Loeb, L. A. *Proc. Natl. Acad. Sci. U. S. A.* **2012,** *109,* 14508–14513. doi:10.1073/pnas.1208715109
30. Alix-Panabières, C.; Pantel, K. *Nat. Rev. Cancer* **2014,** *14,* 623–631. doi:10.1038/nrc3820
31. Taylor, D. D.; Gercel-Taylor, C. *Semin. Immunopathol.* **2011,** *33,* 441–454. doi:10.1007/s00281-010-0234-8
32. Kosaka, N.; Iguchi, H.; Ochiya, T. *Cancer Sci.* **2010,** *101,* 2087–2092. doi:10.1111/j.1349-7006.2010.01650.x
33. Luna Coronell, J. A.; Syed, P.; Sergelen, K.; Gyurján, I.; Weinhäusel, A. *J. Proteomics* **2012,** *76,* 102–115. doi:10.1016/j.jprot.2012.07.022
34. Diaz, L. A., Jr.; Bardelli, A. *J. Clin. Oncol.* **2014,** *32,* 579–586. doi:10.1200/jco.2012.45.2011
35. Aarthy, R.; Mani, S.; Velusami, S.; Sundarsingh, S.; Rajkumar, T. *Mol. Diagn. Ther.* **2015,** *19,* 339–350. doi:10.1007/s40291-015-0167-y
36. Chaudhuri, A. A.; Binkley, M. S.; Osmundson, E. C.; Alizadeh, A. A.; Diehn, M. *Semin. Radiat. Oncol.* **2015,** *25,* 305–312. doi:10.1016/j.semradonc.2015.05.001
37. Ignatiadis, M.; Lee, M.; Jeffrey, S. S. *Clin. Cancer Res.* **2015,** *21,* 4786–4800. doi:10.1158/1078-0432.ccr-14-1190
38. Polivka, J., Jr.; Pesta, M.; Janku, F. *Expert Rev. Mol. Diagn.* **2015,** *15,* 1631–1644. doi:10.1586/14737159.2015.1110021
39. Newman, A. M.; Bratman, S. V.; To, J.; Wynne, J. F.; Eclov, N. C. W.; Modlin, L. A.; Liu, C. L.; Neal, J. W.; Wakelee, H. A.; Merritt, R. E.; Shrager, J. B.; Loo, B. W.; Alizadeh, A. A.; Diehn, M. *Nat. Med.* **2014,** *20,* 548–554. doi:10.1038/nm.3519
40. Fan, X.; White, I. M.; Shopova, S. I.; Zhu, H.; Suter, J. D.; Sun, Y. *Anal. Chim. Acta* **2008,** *620,* 8–26. doi:10.1016/j.aca.2008.05.022
41. Jahr, S.; Hentze, H.; Englisch, S.; Hardt, D.; Fackelmayer, F. O.; Hesch, R. D.; Knippers, R. *Cancer Res.* **2001,** *61,* 1659–1665.
42. Mouliere, F.; Robert, B.; Arnau Peyrotte, E.; Del Rio, M.; Ychou, M.; Molina, F.; Gongora, C.; Thierry, A. R. *PLoS One* **2011,** *6,* e23418. doi:10.1371/journal.pone.0023418
43. Siravegna, G.; Bardelli, A. *Mol. Oncol.* **2016,** *10,* 475–480. doi:10.1016/j.molonc.2015.12.005
44. Schwarzenbach, H.; Hoon, D. S. B.; Pantel, K. *Nat. Rev. Cancer* **2011,** *11,* 426–437. doi:10.1038/nrc3066
45. Wan, J. C. M.; Massie, C.; Garcia-Corbacho, J.; Mouliere, F.; Brenton, J. D.; Caldas, C.; Pacey, S.; Baird, R.; Rosenfeld, N. *Nat. Rev. Cancer* **2017,** *17,* 223–238. doi:10.1038/nrc.2017.7
46. Diehl, F.; Li, M.; Dressman, D.; He, Y.; Shen, D.; Szabo, S.; Diaz, L. A.; Goodman, S. N.; David, K. A.; Juhl, H.; Kinzler, K. W.; Vogelstein, B. *Proc. Natl. Acad. Sci. U. S. A.* **2005,** *102,* 16368–16373. doi:10.1073/pnas.0507904102
47. Holdhoff, M.; Schmidt, K.; Donehower, R.; Diaz, L. A. *J. Natl. Cancer Inst.* **2009,** *101,* 1284–1285. doi:10.1093/jnci/djp240
48. Brookes, A. J. *Gene* **1999,** *234,* 177–186. doi:10.1016/s0378-1119(99)00219-x
49. Kim, S.; Misra, A. *Annu. Rev. Biomed. Eng.* **2007,** *9,* 289–320. doi:10.1146/annurev.bioeng.9.060906.152037
50. Collins, F. S.; Guyer, M. S.; Chakravarti, A. *Science* **1997,** *278,* 1580–1581. doi:10.1126/science.278.5343.1580
51. Camp, K. M.; Trujillo, E. *J. Acad. Nutr. Diet.* **2014,** *114,* 299–312. doi:10.1016/j.jand.2013.12.001
52. Halushka, M. K.; Fan, J.-B.; Bentley, K.; Hsie, L.; Shen, N.; Weder, A.; Cooper, R.; Lipshutz, R.; Chakravarti, A. *Nat. Genet.* **1999,** *22,* 239–247. doi:10.1038/10297
53. Komar, A. A., Ed. *Single Nucleotide Polymorphisms;* Methods in Molecular Biology; Humana Press: New York City, NY, U.S.A., 2009. doi:10.1007/978-1-60327-411-1
54. Sobrino, B.; Brión, M.; Carracedo, A. *Forensic Sci. Int.* **2005,** *154,* 181–194. doi:10.1016/j.forsciint.2004.10.020
55. Kwok, P.-Y. *Annu. Rev. Genomics Hum. Genet.* **2001,** *2,* 235–258. doi:10.1146/annurev.genom.2.1.235
56. Forshew, T.; Murtaza, M.; Parkinson, C.; Gale, D.; Tsui, D. W. Y.; Kaper, F.; Dawson, S.-J.; Piskorz, A. M.; Jimenez-Linan, M.; Bentley, D.; Hadfield, J.; May, A. P.; Caldas, C.; Brenton, J. D.; Rosenfeld, N. *Sci. Transl. Med.* **2012,** *4,* 136ra68. doi:10.1126/scitranslmed.3003726
57. Castells, A.; Puig, P.; Móra, J.; Boadas, J.; Boix, L.; Urgell, E.; Solé, M.; Capellà, G.; Lluís, F.; Fernández-Cruz, L.; Navarro, S.; Farré, A. *J. Clin. Oncol.* **1999,** *17,* 578. doi:10.1200/jco.1999.17.2.578
58. Nygaard, A. D.; Garm Spindler, K.-L.; Pallisgaard, N.; Andersen, R. F.; Jakobsen, A. *Lung Cancer* **2013,** *79,* 312–317. doi:10.1016/j.lungcan.2012.11.016
59. Zhan, C.; Chen, X.-J.; Yi, J.; Li, J.-F.; Wu, D.-Y.; Tian, Z.-Q. *Nat. Rev. Chem.* **2018,** *2,* 216–230. doi:10.1038/s41570-018-0031-9
60. Elghanian, R.; Storhoff, J. J.; Mucic, R. C.; Letsinger, R. L.; Mirkin, C. A. *Science* **1997,** *277,* 1078–1081. doi:10.1126/science.277.5329.1078
61. Storhoff, J. J.; Elghanian, R.; Mucic, R. C.; Mirkin, C. A.; Letsinger, R. L. *J. Am. Chem. Soc.* **1998,** *120,* 1959–1964. doi:10.1021/ja972332i
62. Sato, K.; Hosokawa, K.; Maeda, M. *J. Am. Chem. Soc.* **2003,** *125,* 8102–8103. doi:10.1021/ja034876s
63. Li, H.; Rothberg, L. *Proc. Natl. Acad. Sci. U. S. A.* **2004,** *101,* 14036–14039. doi:10.1073/pnas.0406115101
64. Chen, J.; Tang, L.; Chu, X.; Jiang, J. *Analyst* **2017,** *142,* 3048–3061. doi:10.1039/c7an00967d
65. Zhu, X.; Liu, Y.; Yang, J.; Liang, Z.; Li, G. *Biosens. Bioelectron.* **2010,** *25,* 2135–2139. doi:10.1016/j.bios.2010.02.017
66. Lee, H.; Kang, T.; Yoon, K.-A.; Lee, S. Y.; Joo, S.-W.; Lee, K. *Biosens. Bioelectron.* **2010,** *25,* 1669–1674. doi:10.1016/j.bios.2009.12.002
67. Zhou, W.; Ren, J.; Zhu, J.; Zhou, Z.; Dong, S. *Talanta* **2016,** *161,* 528–534. doi:10.1016/j.talanta.2016.09.007
68. Charrier, A.; Candoni, N.; Liachenko, N.; Thibaudau, F. *Biosens. Bioelectron.* **2007,** *22,* 1881–1886. doi:10.1016/j.bios.2006.07.024
69. Duan, R.; Wang, B.; Hong, F.; Zhang, T.; Jia, Y.; Huang, J.; Hakeem, A.; Liu, N.; Lou, X.; Xia, F. *Nanoscale* **2015,** *7,* 5719–5725. doi:10.1039/c5nr00697j
70. McKenzie, F.; Faulds, K.; Graham, D. *Small* **2007,** *3,* 1866–1868. doi:10.1002/smll.200700225

71. Veigas, B.; Machado, D.; Perdigão, J.; Portugal, I.; Couto, I.; Viveiros, M.; Baptista, P. V. *Nanotechnology* **2010,** *21,* 415101. doi:10.1088/0957-4484/21/41/415101
72. Yun, W.; Jiang, J.; Cai, D.; Zhao, P.; Liao, J.; Sang, G. *Biosens. Bioelectron.* **2016,** *77,* 421–427. doi:10.1016/j.bios.2015.09.065
73. Valentini, P.; Fiammengo, R.; Sabella, S.; Gariboldi, M.; Maiorano, G.; Cingolani, R.; Pompa, P. P. *ACS Nano* **2013,** *7,* 5530–5538. doi:10.1021/nn401757w
74. Su, X.; Kanjanawarut, R. *ACS Nano* **2009,** *3,* 2751–2759. doi:10.1021/nn9005768
75. Murphy, D.; O'Brien, P.; Redmond, G. *Analyst* **2004,** *129,* 970–974. doi:10.1039/b408394f
76. Bao, Y. P.; Huber, M.; Wei, T.-F.; Marla, S. S.; Storhoff, J. J.; Müller, U. R. *Nucleic Acids Res.* **2005,** *33,* e15. doi:10.1093/nar/gni017
77. He, Y.; Zeng, K.; Gurung, A. S.; Baloda, M.; Xu, H.; Zhang, X.; Liu, G. *Anal. Chem. (Washington, DC, U. S.)* **2010,** *82,* 7169–7177. doi:10.1021/ac101275s
78. Quan, K.; Huang, J.; Yang, X.; Yang, Y.; Ying, L.; Wang, H.; Wang, K. *Analyst* **2015,** *140,* 1004–1007. doi:10.1039/c4an02060j
79. Nam, J.-M.; Stoeva, S. I.; Mirkin, C. A. *J. Am. Chem. Soc.* **2004,** *126,* 5932–5933. doi:10.1021/ja049384+
80. Taton, T. A.; Mirkin, C. A.; Letsinger, R. L. *Science* **2000,** *289,* 1757–1760. doi:10.1126/science.289.5485.1757
81. Park, C.; Song, Y.; Jang, K.; Choi, C.-H.; Na, S. *Sens. Actuators, B* **2018,** *261,* 497–504. doi:10.1016/j.snb.2018.01.183
82. Xu, C.; Lan, L.; Yao, Y.; Ping, J.; Li, Y.; Ying, Y. *Sens. Actuators, B* **2018,** *273,* 642–648. doi:10.1016/j.snb.2018.06.035
83. Song, T.; Xiao, S.; Yao, D.; Huang, F.; Hu, M.; Liang, H. *Adv. Mater. (Weinheim, Ger.)* **2014,** *26,* 6181–6185. doi:10.1002/adma.201402314
84. Ma, C.; Wang, W.; Mulchandani, A.; Shi, C. *Anal. Biochem.* **2014,** *457,* 19–23. doi:10.1016/j.ab.2014.04.022
85. Guo, L.; Xu, Y.; Ferhan, A. R.; Chen, G.; Kim, D.-H. *J. Am. Chem. Soc.* **2013,** *135,* 12338–12345. doi:10.1021/ja405371g
86. Fan, A.; Cai, S.; Cao, Z.; Lau, C.; Lu, J. *Analyst* **2010,** *135,* 1400–1405. doi:10.1039/c0an00007h
87. Shawky, S. M.; Bald, D.; Azzazy, H. M. E. *Clin. Biochem.* **2010,** *43,* 1163–1168. doi:10.1016/j.clinbiochem.2010.07.001
88. Hu, Y.; Zhang, L.; Zhang, Y.; Wang, B.; Wang, Y.; Fan, Q.; Huang, W.; Wang, L. *ACS Appl. Mater. Interfaces* **2015,** *7,* 2459–2466. doi:10.1021/am507218g
89. Sedighi, A.; Li, P. C. H. *Anal. Biochem.* **2014,** *448,* 58–64. doi:10.1016/j.ab.2013.11.019
90. Fang, W.-F.; Chen, W.-J.; Yang, J.-T. *Sens. Actuators, B* **2014,** *192,* 77–82. doi:10.1016/j.snb.2013.10.052
91. Kanjanawarut, R.; Su, X. *Anal. Chem. (Washington, DC, U. S.)* **2009,** *81,* 6122–6129. doi:10.1021/ac900525k
92. Lee, H.; Kim, A.; Ahn, I.-S.; Joo, S.-W.; Lee, S. Y.; Yoon, K.-A.; Lee, K. *Chem. Commun.* **2011,** *47,* 11477–11479. doi:10.1039/c1cc15280g
93. Kato, D.; Oishi, M. *ACS Nano* **2014,** *8,* 9988–9997. doi:10.1021/nn503150w
94. Sanromán-Iglesias, M.; Lawrie, C. H.; Schäfer, T.; Grzelczak, M.; Liz-Marzán, L. M. *ACS Sens.* **2016,** *1,* 1110–1116. doi:10.1021/acssensors.6b00393
95. Sanromán-Iglesias, M.; Lawrie, C. H.; Liz-Marzán, L. M.; Grzelczak, M. *Bioconjugate Chem.* **2017,** *28,* 903–906. doi:10.1021/acs.bioconjchem.7b00028
96. Sanromán-Iglesias, M.; Lawrie, C. H.; Liz-Marzán, L. M.; Grzelczak, M. *ACS Appl. Nano Mater.* **2018,** *1,* 3741–3746. doi:10.1021/acsanm.8b00984
97. Piao, J.; Zhao, Q.; Zhou, D.; Peng, W.; Gao, W.; Chen, M.; Shu, G.; Gong, X.; Chang, J. *Anal. Chim. Acta* **2019,** *1052,* 145–152. doi:10.1016/j.aca.2018.11.044
98. Jian, J.-W.; Huang, C.-C. *Chem. – Eur. J.* **2011,** *17,* 2374–2380. doi:10.1002/chem.201002825
99. Jung, Y. L.; Jung, C.; Parab, H.; Cho, D.-Y.; Park, H. G. *ChemBioChem* **2011,** *12,* 1387–1390. doi:10.1002/cbic.201100098
100. Li, J.; Chu, X.; Liu, Y.; Jiang, J.-H.; He, Z.; Zhang, Z.; Shen, G.; Yu, R.-Q. *Nucleic Acids Res.* **2005,** *33,* e168. doi:10.1093/nar/gni163
101. Xu, W.; Xue, X.; Li, T.; Zeng, H.; Liu, X. *Angew. Chem., Int. Ed.* **2009,** *48,* 6849–6852. doi:10.1002/anie.200901772
102. He, Y.; Zeng, K.; Zhang, S.; Gurung, A. S.; Baloda, M.; Zhang, X.; Liu, G. *Biosens. Bioelectron.* **2012,** *31,* 310–315. doi:10.1016/j.bios.2011.10.037
103. Chen, Y.-T.; Hsu, C.-L.; Hou, S.-Y. *Anal. Biochem.* **2008,** *375,* 299–305. doi:10.1016/j.ab.2007.12.036
104. Wang, Q.; Li, R.-D.; Yin, B.-C.; Ye, B.-C. *Analyst* **2015,** *140,* 6306–6312. doi:10.1039/c5an01350j
105. Zou, B.; Cao, X.; Wu, H.; Song, Q.; Wang, J.; Kajiyama, T.; Kambara, H.; Zhou, G. *Biosens. Bioelectron.* **2015,** *66,* 50–54. doi:10.1016/j.bios.2014.10.077
106. Wu, S.; Liang, P.; Yu, H.; Xu, X.; Liu, Y.; Lou, X.; Xiao, Y. *Anal. Chem. (Washington, DC, U. S.)* **2014,** *86,* 3461–3467. doi:10.1021/ac4040373
107. Li, R.-D.; Yin, B.-C.; Ye, B.-C. *Biosens. Bioelectron.* **2016,** *86,* 1011–1016. doi:10.1016/j.bios.2016.07.042
108. Cui, L.; Ke, G.; Zhang, W. Y.; Yang, C. J. *Biosens. Bioelectron.* **2011,** *26,* 2796–2800. doi:10.1016/j.bios.2010.11.005
109. Li, J.; Song, S.; Liu, X.; Wang, L.; Pan, D.; Huang, Q.; Zhao, Y.; Fan, C. *Adv. Mater. (Weinheim, Ger.)* **2008,** *20,* 497–500. doi:10.1002/adma.200701918
110. Xu, W.; Xie, X.; Li, D.; Yang, Z.; Li, T.; Liu, X. *Small* **2012,** *8,* 1846–1850. doi:10.1002/smll.201200263
111. Jung, C.; Chung, J. W.; Kim, U. O.; Kim, M. H.; Park, H. G. *Biosens. Bioelectron.* **2011,** *26,* 1953–1958. doi:10.1016/j.bios.2010.07.088
112. Akiyama, Y.; Shikagawa, H.; Kanayama, N.; Takarada, T.; Maeda, M. *Chem. – Eur. J.* **2014,** *20,* 17420–17425. doi:10.1002/chem.201404801
113. Liu, M.; Yuan, M.; Lou, X.; Mao, H.; Zheng, D.; Zou, R.; Zou, N.; Tang, X.; Zhao, J. *Biosens. Bioelectron.* **2011,** *26,* 4294–4300. doi:10.1016/j.bios.2011.04.014
114. Shen, W.; Deng, H.; Gao, Z. *J. Am. Chem. Soc.* **2012,** *134,* 14678–14681. doi:10.1021/ja306265n
115. Wang, X.; Zou, M.; Huang, H.; Ren, Y.; Li, L.; Yang, X.; Li, N. *Biosens. Bioelectron.* **2013,** *41,* 569–575. doi:10.1016/j.bios.2012.09.023
116. Han, J.; Tan, M.; Sudheendra, L.; Weiss, R. H.; Kennedy, I. M. *Nano Res.* **2014,** *7,* 1302–1310. doi:10.1007/s12274-014-0494-z
117. Kim, H.; Kang, S.; Park, K. S.; Park, H. G. *Sens. Actuators, B* **2018,** *260,* 140–145. doi:10.1016/j.snb.2017.12.137
118. Shan, Y.; Xu, J.-J.; Chen, H.-Y. *Chem. Commun.* **2009,** 905–907. doi:10.1039/b821049g
119. Ren, X.; Xue, Q.; Wen, L.; Li, X.; Wang, H. *Anal. Chim. Acta* **2019,** *1053,* 114–121. doi:10.1016/j.aca.2018.11.060

120. Zhu, D.; Lu, B.; Zhu, Y.; Ma, Z.; Wei, Y.; Su, S.; Wang, L.; Song, S.; Zhu, Y.; Wang, L.; Chao, J. *ACS Appl. Mater. Interfaces* **2019,** *11,* 11220–11226. doi:10.1021/acsami.9b01653
121. Zhou, H.; Liu, J.; Xu, J.-J.; Chen, H.-Y. *Chem. Commun.* **2011,** *47,* 8358–8360. doi:10.1039/c1cc12413g
122. Zeng, Y.-p.; Zhu, G.; Yang, X.-y.; Cao, J.; Jing, Z.-l.; Zhang, C.-y. *Chem. Commun.* **2014,** *50,* 7160. doi:10.1039/c4cc02034k
123. Yang, D.; Guo, Z.; Wang, J.; Jin, Y.; Mei, Q.; Miao, P. *Part. Part. Syst. Charact.* **2019,** *36,* 1900273. doi:10.1002/ppsc.201900273
124. Li, N.; Li, R.; Li, Z.; Yang, Y.; Wang, G.; Gu, Z. *Sens. Actuators, B* **2019,** *283,* 666–676. doi:10.1016/j.snb.2018.12.082
125. Wang, Y.; Howes, P. D.; Kim, E.; Spicer, C. D.; Thomas, M. R.; Lin, Y.; Crowder, S. W.; Pence, I. J.; Stevens, M. M. *ACS Appl. Mater. Interfaces* **2018,** *10,* 28290–28300. doi:10.1021/acsami.8b07250
126. Roy, S.; Soh, J. H.; Ying, J. Y. *Biosens. Bioelectron.* **2016,** *75,* 238–246. doi:10.1016/j.bios.2015.08.039
127. Ihara, T.; Tanaka, S.; Chikaura, Y.; Jyo, A. *Nucleic Acids Res.* **2004,** *32,* e105. doi:10.1093/nar/gnh106
128. Sato, Y.; Sato, K.; Hosokawa, K.; Maeda, M. *Anal. Biochem.* **2006,** *355,* 125–131. doi:10.1016/j.ab.2006.04.035
129. Fong, K. E.; Yung, L.-Y. L. *RSC Adv.* **2013,** *3,* 6076–6084. doi:10.1039/c3ra23162c
130. Ma, X.; Truong, P. L.; Anh, N. H.; Sim, S. J. *Biosens. Bioelectron.* **2015,** *67,* 59–65. doi:10.1016/j.bios.2014.06.038
131. Chakrabarti, R.; Klibanov, A. M. *J. Am. Chem. Soc.* **2003,** *125,* 12531–12540. doi:10.1021/ja035399g
132. Yurke, B.; Turberfield, A. J.; Mills, A. P.; Simmel, F. C.; Neumann, J. L. *Nature* **2000,** *406,* 605–608. doi:10.1038/35020524
133. Dirks, R. M.; Pierce, N. A. *Proc. Natl. Acad. Sci. U. S. A.* **2004,** *101,* 15275–15278. doi:10.1073/pnas.0407024101
134. Bois, J. S.; Venkataraman, S.; Choi, H. M. T.; Spakowitz, A. J.; Wang, Z.-G.; Pierce, N. A. *Nucleic Acids Res.* **2005,** *33,* 4090–4095. doi:10.1093/nar/gki721
135. Dai, W.; Zhang, J.; Meng, X.; He, J.; Zhang, K.; Cao, Y.; Wang, D.; Dong, H.; Zhang, X. *Theranostics* **2018,** *8,* 2646–2656. doi:10.7150/thno.24480
136. Reid, M. S.; Le, X. C.; Zhang, H. *Angew. Chem., Int. Ed.* **2018,** *57,* 11856–11866. doi:10.1002/anie.201712217
137. Zhao, Y.; Chen, F.; Li, Q.; Wang, L.; Fan, C. *Chem. Rev.* **2015,** *115,* 12491–12545. doi:10.1021/acs.chemrev.5b00428
138. Wang, L.; Zhu, Y.; Xu, L.; Chen, W.; Kuang, H.; Liu, L.; Agarwal, A.; Xu, C.; Kotov, N. A. *Angew. Chem., Int. Ed.* **2010,** *49,* 5472–5475. doi:10.1002/anie.200907357
139. Grzelczak, M.; Liz-Marzán, L. M.; Klajn, R. *Chem. Soc. Rev.* **2019,** *48,* 1342–1361. doi:10.1039/c8cs00787j
140. Caracciolo, G.; Safavi-Sohi, R.; Malekzadeh, R.; Poustchi, H.; Vasighi, M.; Zenezini Chiozzi, R.; Capriotti, A. L.; Laganà, A.; Hajipour, M.; Di Domenico, M.; Di Carlo, A.; Caputo, D.; Aghaverdi, H.; Papi, M.; Palmieri, V.; Santoni, A.; Palchetti, S.; Digiacomo, L.; Pozzi, D.; Suslick, K. S.; Mahmoudi, M. *Nanoscale Horiz.* **2019,** *4,* 1063–1076. doi:10.1039/c9nh00097f
141. Cohen, J. D.; Li, L.; Wang, Y.; Thoburn, C.; Afsari, B.; Danilova, L.; Douville, C.; Javed, A. A.; Wong, F.; Mattox, A.; Hruban, R. H.; Wolfgang, C. L.; Goggins, M. G.; Dal Molin, M.; Wang, T.-L.; Roden, R.; Klein, A. P.; Ptak, J.; Dobbyn, L.; Schaefer, J.; Silliman, N.; Popoli, M.; Vogelstein, J. T.; Browne, J. D.; Schoen, R. E.; Brand, R. E.; Tie, J.; Gibbs, P.; Wong, H.-L.; Mansfield, A. S.; Jen, J.; Hanash, S. M.; Falconi, M.; Allen, P. J.; Zhou, S.; Bettegowda, C.; Diaz, L. A., Jr.; Tomasetti, C.; Kinzler, K. W.; Vogelstein, B.; Lennon, A. M.; Papadopoulos, N. *Science* **2018,** *359,* 926–930. doi:10.1126/science.aar3247
142. Banerjee, R.; Jaiswal, A. *Analyst* **2018,** *143,* 1970–1996. doi:10.1039/c8an00307f
143. Huang, X.; Aguilar, Z. P.; Xu, H.; Lai, W.; Xiong, Y. *Biosens. Bioelectron.* **2016,** *75,* 166–180. doi:10.1016/j.bios.2015.08.032
144. Quesada-González, D.; Merkoçi, A. *Biosens. Bioelectron.* **2015,** *73,* 47–63. doi:10.1016/j.bios.2015.05.050
145. Bahadır, E. B.; Sezgintürk, M. K. *TrAC, Trends Anal. Chem.* **2016,** *82,* 286–306. doi:10.1016/j.trac.2016.06.006
146. del Pino, P.; Pelaz, B.; Zhang, Q.; Maffre, P.; Nienhaus, G. U.; Parak, W. J. *Mater. Horiz.* **2014,** *1,* 301–313. doi:10.1039/c3mh00106g

License and Terms

BEILSTEIN JOURNAL OF NANOTECHNOLOGY

Facile biogenic fabrication of hydroxyapatite nanorods using cuttlefish bone and their bactericidal and biocompatibility study

Satheeshkumar Balu[1], Manisha Vidyavathy Sundaradoss[*1], Swetha Andra[2] and Jaison Jeevanandam[3]

Full Research Paper

Open Access

Address:
[1]Department of Ceramic Technology, Alagappa College of Technology, Anna University, Chennai 600025, India, [2]Department of Textile Technology, Alagappa College of Technology, Anna University, Chennai 600025, India and [3]Department of Chemical Engineering, Curtin University, Miri, Sarawak 98009, Malaysia

Email:
Manisha Vidyavathy Sundaradoss[*] - manisha@annauniv.edu

* Corresponding author

Keywords:
antibacterial activity; biocompatibility; bone implant; cuttlefish bone; hard tissue treatment; hydroxyapatite; nanorods

Beilstein J. Nanotechnol. **2020,** *11,* 285–295.
doi:10.3762/bjnano.11.21

Received: 14 September 2019
Accepted: 17 January 2020
Published: 04 February 2020

This article is part of the thematic issue "Engineered nanomedicines for advanced therapies".

Guest Editor: M. K. Danquah

Abstract

Cuttlefish bones are an inexpensive source of calcium carbonate, which are produced in large amounts by the marine food industry, leading to environmental contamination and waste. The nontoxicity, worldwide availability and low production cost of cuttlefish bone products makes them an excellent calcium carbonate precursor for the fabrication of hydroxyapatite. In the present study, a novel oil-bath-mediated precipitation method was introduced for the synthesis of hydroxyapatite (Hap) nanorods using cuttlefish bone powder as a precursor (CB-Hap NRs). The obtained CB-Hap NRs were investigated using transmission electron microscopy (TEM), Fourier transform infrared spectroscopy (FTIR), X-ray diffraction (XRD) and thermogravimetric analysis (TGA) techniques to evaluate their physicochemical properties. The crystallite size (20.86 nm) obtained from XRD data and the elemental analysis (Ca/P molar ratio was estimated to be 1.6) showed that the Hap NRs are similar to that of natural human bone (≈1.67). Moreover, the FTIR data confirmed the presence of phosphate as a functional group and the TGA data revealed the thermal stability of Hap NRs. In addition, the antibacterial study showed a significant inhibitory effect of CB-Hap NRs against *S. aureus* (zone of inhibition – 14.5 ± 0.5 mm) and *E. coli* (13 ± 0.5 mm), whereas the blood compatibility test showed that the CB-Hap NRs exhibited a concentration-mediated hemolytic effect. These biogenic CB-Hap NRs with improved physicochemical properties, blood compatibility and antibacterial efficacy could be highly beneficial for orthopedic applications in the future.

Introduction

Generally, the hard tissue of humans and animals, such as bone and teeth, are composed of natural hydroxyapatite (Hap), which is a bioactive ceramic material with high calcium phosphate concentration whereby the material can encounter damage or loss during an accident, infection, or trauma [1]. Because synthetic Hap exhibits similar chemical and biological properties to that of natural hard tissue, it is widely investigated for various orthopedic and dental treatments to restore damaged hard tissue [2]. It was reported in the literature that synthetic and conventional Hap has been prepared by various chemical procedures such as hydrothermal, sol–gel, mechanochemical, reverse microemulsion and precipitation methods, and the resulting material has been proposed to be highly beneficial in hard tissue treatments [3-5]. However, the hazardous chemicals involved in the synthesis process, which are toxic to healthy cells, is the primary limitation to employ these materials in widespread biomedical and environmental applications. Thus, the nontoxic, ecologically friendly preparation of Hap has received considerable attention in the bone and dental implant field. However, the development of a novel biomaterial for hard tissue treatments is still a major challenge due to the high material cost and lack of biocompatibility. Moreover, a highly biocompatible material, such as calcium phosphate, is required to overcome the increasing demand of biomaterials for hard tissue repair [6,7]. It is noteworthy that marine species, including corals, crabs, and fish bones, possess natural calcium phosphate and are currently being extracted and utilized as drug delivery carriers, tissue engineering scaffolds and dental cements in the biomedical field [8,9]. Hence, natural calcium phosphate from marine organisms plays a major role in recent developments of Hap for use in biomedical applications.

Cuttlefish (*Sepia officinalis*) is an important marine food that is available for human consumption, and tons of cuttlefish bones are produced as waste material every day by the marine food industry across the world, resulting in environmental contamination [10]. In ancient times, cuttlefish bone powder was used as biomedicine in China and India for oral health and is proven to be completely suitable for biomedical applications [11]. Further, the inorganic part of cuttlefish bone contains calcium carbonate ($CaCO_3$) in the form of aragonite, along with other minerals such as sodium, magnesium, and strontium as trace elements, and these minerals play a substantial role in the bone healing process [12,13]. The main advantage of using cuttlefish bone powder to prepare Hap is their cost effectiveness and ecologically friendly nature, high availability, enhanced interconnectivity, and biocompatibility [14].

Recently, it was reported that the bonding ability of the scaffold with surrounding tissues is determined by the porosity of the material and that cuttlefish-bone-derived Hap has a superior porous structure [15]. This porous structure allows the blood vessels, which grow inside the biomaterial, to receive the required minerals and oxygen [16]. Additionally, the porous morphology in nanometer-sized Hap provides unique properties, such as high drug loading capacity and slow drug release in drug delivery systems for progressive advancement in osteoporosis and bone tumor treatments [17]. Various studies have reported the synthesis procedure of Hap nanoparticles from annealed cuttlefish bone using a hydrothermal method, which yields calcium oxide (CaO), and analyzed their physical and biological properties [18-20]. However, the hydrothermal method requires expensive autoclaves to maintain high temperature and pressure and uses toxic chemicals to yield different morphologies of Hap, especially nanorods [21]. These Hap nanorods possess enhanced porosity and high surface-to-volume ratio when compared to spherical nanometer-sized Hap particles, which facilitates interconnectivity and improves targeted cell internalization efficiency [22]. Thus, the aim of the present work is to use a simple, facile, unique, safe and cost-effective precipitation setup via an oil bath approach to synthesize Hap nanorods from cuttlefish bone powders and optimize their synthesis parameters. The systematic characterization using X-ray diffraction (XRD), Fourier transform infrared spectroscopy (FTIR) and transmission electron microscopy (TEM) was performed to confirm the presence of nanorods and to evaluate their physicochemical properties. Furthermore, in vitro antimicrobial studies with gram-positive (*Staphylococcus aureus*) and gram-negative (*Escherichia coli*) bacteria, in addition to hemolysis studies with healthy human blood were performed to evaluate the antibacterial and biocompatible efficacy of the cuttlefish bone powder derived Hap nanorods.

Results and Discussion

Crystallinity and phase formation analysis

The products obtained at various reaction times and the raw cuttlefish bone (CB) powders were characterized using powder XRD, revealing that a prolonged reaction time leads to the formation of highly crystalline Hap nanorods as shown in Figure 1. It is noteworthy that the XRD pattern of CB powder exactly matches with the aragonite crystal structure of calcium carbonate ($CaCO_3$, JCPDS file 75-2230). Interestingly, aragonite $CaCO_3$ was completely transformed into calcite $CaCO_3$ (JCPDS file 71-2396) after 3 h of reaction time. The reflection peaks observed at 23°, 29°, 35°, 39°, 43°, 47°, 48°, 56° and 57° correspond to the (012), (104), (110), (113), (202), (018), (116), (211), and (122) planes, which indicates the rhombohedral structure of calcite [23]. Thus, it is evident that the reaction at basic pH conditions and a temperature of 80 °C supports the relaxation of aragonite calcium carbonate bonds to form calcite

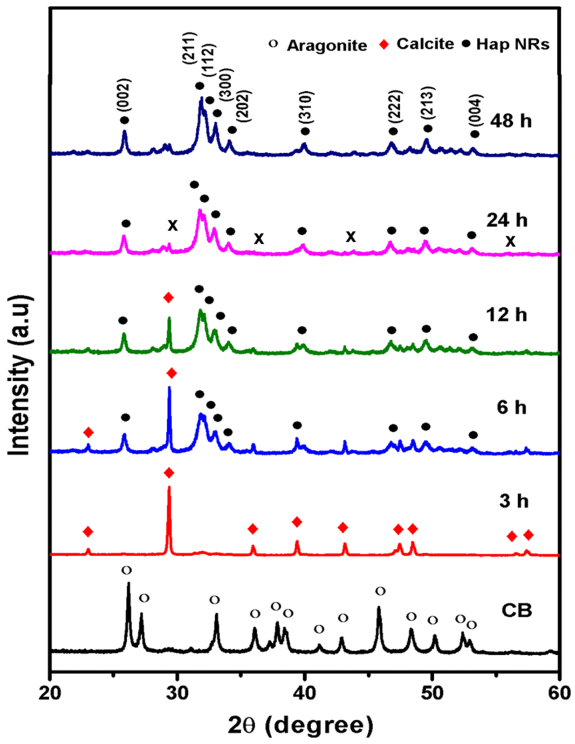

Figure 1: XRD spectrum of aragonite cuttlefish bone (CB), calcite, and hydroxyapatite (Hap) nanorods using cuttlefish bone powder as a precursor (CB-Hap NRs). The impurity peaks are indicated by an "x".

structure in 3 h [24]. It can be noted from the diffraction peaks that the formation of Hap crystal growth was initiated at 6 h of reaction time along with certain traces of calcite. Moreover, the intensity of the calcite at peak positions of 23° and 29° significantly decreased with increasing reaction time. This reveals that prolonged heating of calcite crystal relaxes the lattice of calcite to facilitate the formation of Hap [25]. Then, the calcite peak disappeared due to the complete formation of Hap at 24 h and 48 h of reaction time. The diffraction peaks were recorded at 25°, 31°, 32°, 33°, 34°, 39°, 46°, 49° and 53°, corresponding to the (002), (211), (112), (300), (202), (310), (222), (213), and (004) planes, which suggest that a hexagonal structure of Hap was formed. Even though the XRD peaks of Hap were formed at 24 h of reaction time stable crystallinity was observed. There also exists a certain minor impurity peak at 30°, 35°, 43° and 57°, which affects the purity. Thus, the reaction time was increased further to 48 h, which yields a complete stable crystal of Hap and is confirmed by the XRD peaks in Figure 1. The average crystallite size of the CB Hap is 20.86 nm (measured using full width half maximum of XRD data and the Scherrer equation), which is similar to the crystallite size of natural bone, and the lattice strain was 0.0055 nm.

Evaluation of functional groups

The FTIR spectra of CB and CB-Hap (48 h) with high crystallinity are shown in Figure 2, which is essential to analyze their functional groups. The FTIR spectral bands were recorded

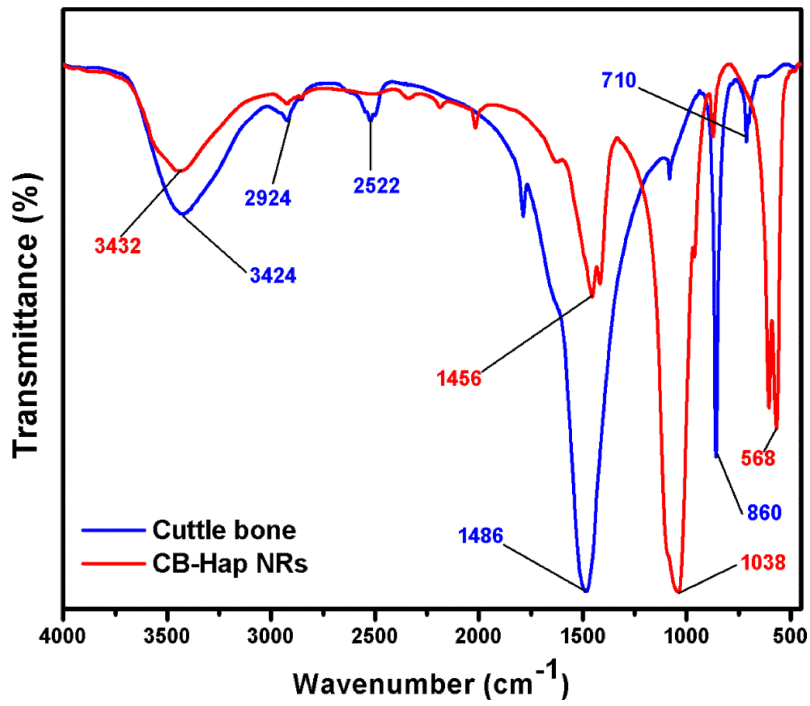

Figure 2: FTIR spectra of cuttlefish bone and hydroxyapatite (Hap) nanorods using cuttlefish bone powder as a precursor (CB-Hap NRs).

at 710, 860, 1486, 2522, and 2924 cm^{-1} for CB which indicates the existence of aragonite carbonates [26]. The presence of a characteristic peak at 3424 cm^{-1} is due to the vibration of O–H stretching, which indicates the presence of alcoholic functional groups [27]. Likewise, the IR bands recorded for the CB-Hap sample at 1038 and 568 cm^{-1} reveals the presence of functional asymmetric and symmetric PO_4^{3-} stretching groups, respectively, which helps in the confirmation of the CB-Hap nanorod formation. Earlier reports suggest that there are two classes of carbonate substitutions on Hap, such as A-type, where the carbonates are substituted at the site of O–H vibrations [28], and B-type, where the substitution takes place at phosphate vibrational sites [29]. Hence, the band at 1456 cm^{-1} indicates the occupancy of B-type carbonates and the carbonated n-Hap are highly beneficial in biomedical applications, especially in hard tissue repair [30,31].

Thermogravimetric analysis

Figure 3 shows the thermogravimetric analysis (TGA) of cuttlefish bone and CB-Hap nanorod powder. Both CB and CB-Hap NRs show a similar gradual weight loss of 6% from 38 to 583 °C due to the evaporation of water and organic substances of cuttlefish [32]. A drastic weight loss of 22% was observed from 583 to 689 °C for CB due to the decomposition of $CaCO_3$, however no weight loss was observed for CB-Hap nanorods due to their thermal stability [33]. Herradi et al. (2017) suggested that a temperature above 750 °C is not suitable for Hap powder fabrication as a phase transformation is observed from 750 °C to 1000 °C [34]. Likewise, Venkatesan and Kim (2010) isolated Hap from *Thunnus obesus* fish and their study revealed that a high temperature facilitates aggregation and increases the crystal size of the nanoparticles [35]. On the other hand, it was proven by Hung et al. (2012) that an increase in the crystallite size will lead to reduction in the mechanical properties of the Hap nanoparticles [36]. Moreover, Ooi et al. (2018) recently reported that a high annealing temperature will affect the porous structure of Hap nanoparticles [37]. In the present study, the TGA (Figure 3) shows 0% weight loss at 600 °C to form CB-Hap NRs due to the complete removal of organic substances and water. Thus, 700 °C is selected as the optimum annealing temperature for the formation of Hap NRs as suggested from previous studies.

Morphology and elemental analysis

TEM micrographs of CB-derived Hap nanorods that are synthesized at a temperature of 80 °C and a reaction time of 48 h are shown in Figure 4a–d, which reveals their morphology and size. It is evident from the TEM micrographs at different magnifications that the morphology of n-Hap is rod-shaped. The average width and length of the nanorods was calculated as 79.05 ± 0.453 nm and 219.66 ± 0.38 nm, respectively, derived from the TEM micrographs using ImageJ software, as shown in Figure 4h,i. Kumar et al. (2015) synthesized Hap nanorods with 40–60 nm width and 500 to 700 nm length using waste shells of snail via a microwave irradiation method [38]. Similarly, Padmanabhan et al. (2009) prepared the Hap NRs using the sol–gel method that had 70–90 nm width and 400–500 nm length [39]. Likewise, Papageorgiou et al. (2014) fabricated

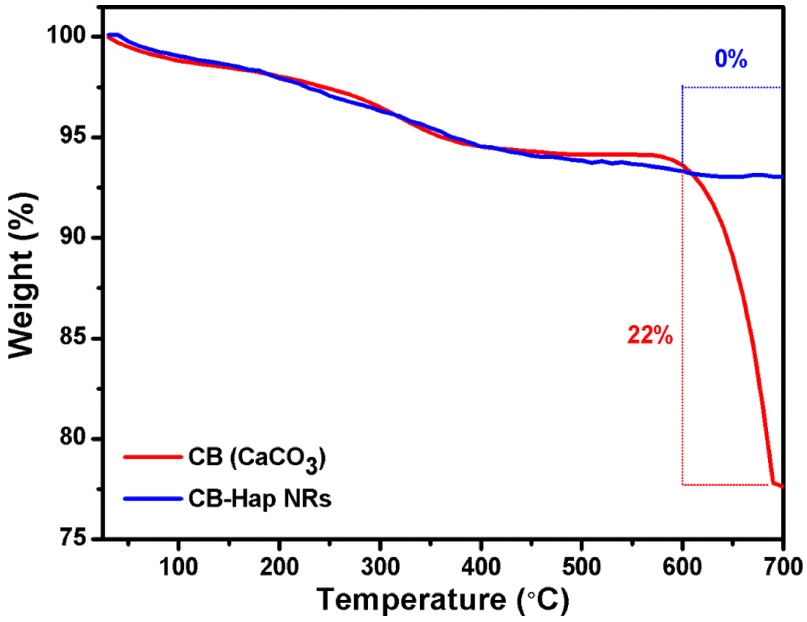

Figure 3: Thermogravimetric analysis (TGA) of cuttlefish bone (CB) powder and hydroxyapatite (Hap) nanorods using cuttlefish bone powder as a precursor (CB-Hap NRs).

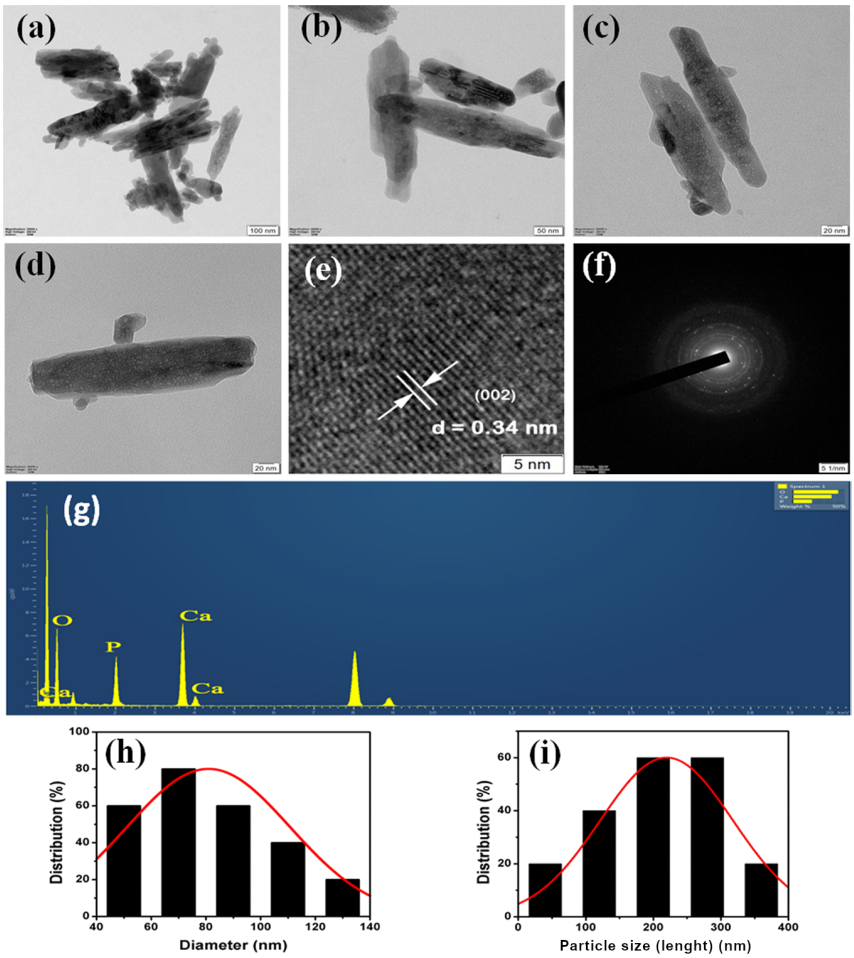

Figure 4: TEM images of hydroxyapatite (Hap) nanorods using cuttlefish bone powder as a precursor (CB-Hap NRs) at (a–d) different magnifications. (e) Calculation of d-spacing of CB-Hap NRs. (f) SAED pattern of CB-Hap NRs. (g) Elemental analysis of CB-Hap NRs and distribution of the (h) width and (i) length of CB-Hap NRs.

Hap NRs with 20 nm width and 400 nm length by the hydrothermal method [40]. Thus, it is evident from the previous studies that the synthesis approach plays a crucial role in altering the size of the Hap NRs, which eventually determines their biological properties [41,42]. In addition, Ivankovic et al. (2009) prepared porous plate and needle-like Hap nanoparticles using cuttlefish bone with a hydrothermal approach [32]. However, the Hap NRs in the present work are nonporous as observed in the TEM images, which may affect the biocompatibility, while utilizing them as scaffolds. Hence, the calcination temperature must be optimized in the future studies to provide porosity in the Hap NRs to improving their biocompatibility with tissue. Further, Jadalannagari et al. (2011) and Zanotto et al. (2012) synthesized Hap NRs with smaller width and length via sol–gel and precipitation approaches, respectively [43,44], as compared to the present study. However, it is noteworthy that the biogenic fabrication of nanometer-sized Hap rods (even though larger in size) as mentioned in this study can help to yield less toxic Hap NRs (refer section "Blood compatibility analysis"), which will be beneficial for biomedical applications, when compared to the non-biogenic synthesized Hap NRs that uses toxic chemicals and lacks ability to control morphology [45-47]. Furthermore, the d-spacing was measured using a Gatan digital micrograph and was found to be around 0.34 nm, which corresponds to the (002) plane as shown in Figure 4e. Additionally, the interplanar distance was determined by the diffraction ring pattern as shown in Figure 4f and was estimated as 0.191, 0.722, and 0.122 nm, which is consistent with the hexagonal structure of Hap nanorods. Figure 4g shows the presence of calcium (Ca), phosphorus (P) and oxygen (O) elements in nanorods and the Ca/P molar ratio was estimated to be 1.6 (1 mole of calcium per 0.6 mole of phosphorus), which is equivalent to that of natural human bone (≈1.67) [48].

Blood compatibility analysis

The hemolytic activity of the CB-Hap nanorods was investigated at various concentrations as shown in Figure 5 and the obtained results were calculated and compared with the American

Society for Testing and Materials standard F756-00. Generally, the addition of hydroxyapatite microcrystals with blood will lead to hemolysis via aggregation of erythrocytes and membrane damage induced by crystals [49]. Moreover, Wiessner et al. (1988) showed that the crystallinity of the Hap plays a crucial role in determining the hemolytic properties [50]. However, the CB-Hap NRs exhibited less than 2% hemolysis up to 75 µg/mL, which indicates that the material is nonhemolytic and nontoxic to blood cells. Additionally, 2% and 3.2% hemolytic activity was recorded when a higher concentration of CB-Hap NRs, such as 100 and 200 µg/mL, respectively, was added to the blood samples. This indicates that the nanorods may exhibit a slight hemolytic behavior at a higher CB-Hap NR concentration. The hemolytic activity at higher concentrations can be attributed to the oxidative stress induced by introducing CB-Hap nanorods along with the blood cells [51]. The lower concentration of CB-Hap NRs may internalize into blood cells and degrade into ions which acts as a nutrient for the blood, whereas a high concentration of NRs may lead to an increase in the internal ions of the cells, elevating the internal pressure of the blood cells and inhibiting them [52]. Further, the length of the nanorods and their aggregation inside the blood vessels also may be the reason for its concentration dependent hemolytic activity [53]. Furthermore, Han et al. (2012) showed that the size and surface charge of Hap nanoparticles are responsible for hemolysis by aggregating red blood cells (RBCs) via bridging force mediated electrostatic interaction [54]. Thus, the hemolytic effect of CB-Hap NRs at high concentration can be reduced by optimizing their surface charge in the future.

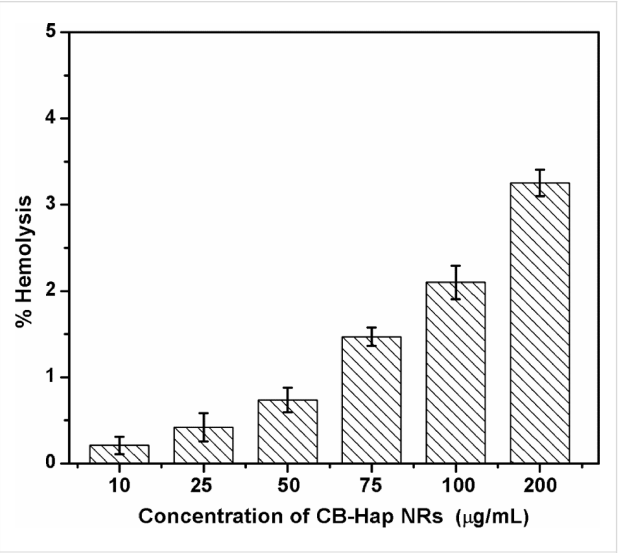

Figure 5: Hemolytic behavior of hydroxyapatite (Hap) nanorods using cuttlefish bone powder as a precursor (CB-Hap NRs) at various concentrations.

Antibacterial activity

Generally, bacterial colonies can grow rapidly on Hap, due to their bioactive property and the presence of calcium and phosphate that act as nutrients for their growth. The formation of a biofilm (bacterial colonies) on Hap is one of the major causes of implant failure, therefore it is essential to study their bactericidal property. It can be noted from the literature that nanometer-sized Hap can effectively inhibit antibacterial activity but only when doped or cationic-substituted [55,56]. In contrast, the CB-derived Hap nanorods in the present study show optimum bactericidal effect on *E. coli* and *S. aureus* due to the size (>50 nm) and morphology of the material. However, no such activity was observed for CB alone. The obtained results are displayed in Figure 6 and the zone of inhibition in Table 1 shows a better bactericidal effect of Hap NRs towards *S. aureus* as compared with *E. coli*. This is due to the variations in cell structure, diffusion rate, metabolism and interaction of the nanoparticles with the microorganisms [57]. A similar study was conducted by Tank et al. (2014) to compare the antibacterial activity of pure and zinc-doped nanometer-sized Hap that are synthesized via a chemical precipitation mediated surfactant approach against gram positive *S. aureus*, *Bacillus cereus*, *Micro-*

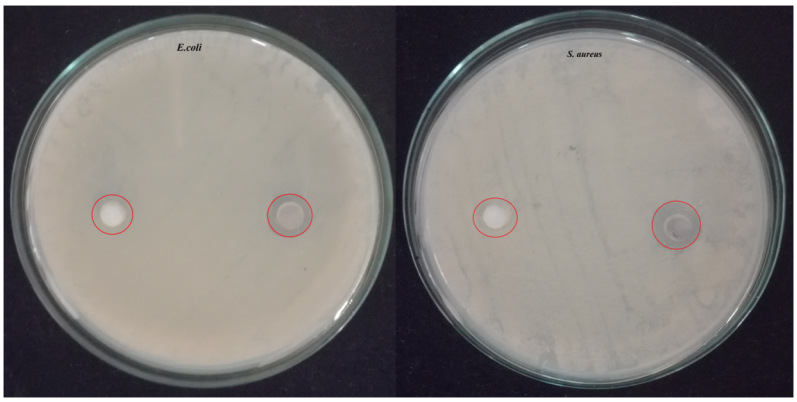

Figure 6: Antibacterial activity of hydroxyapatite (Hap) nanorods using cuttlefish bone powder as a precursor (CB-Hap NRs).

Table 1: Zone of inhibition of cuttlefish bone (CB) and hydroxyapatite (Hap) nanorods using cuttlefish bone powder as a precursor (CB-Hap NRs) towards gram-positive (*S. aureus*) and gram-negative (*E. coli*) bacteria.

Sample	Bacteria	Concentration (μg/mL)	Zone of inhibition (mm)
Hap Nanorods	*E. coli*	50	13 ± 0.5
Hap Nanorods	*S. aureus*	50	14.5 ± 0.5
CB	*E. coli*	50	–
CB	*S. aureus*	50	–

coccus luteus, gram-negative *Pseudomonas aeruginosa* and *Shigella flexnari*. The study revealed that both pure and zinc-doped Hap have a needle-like morphology [58] and exhibited significant antibacterial activity against *M. luteus* and *S. aureus*, whereas moderate antibacterial activity was observed against *B. cereus* and *S. flexnari*. In addition, they also possess non-hemolytic activity with significant activity in simulated body fluid [59]. Hence, it is evident that the antibacterial activity of the present work can be improved via doping and the approach is highly safe to use for biological applications. This is important to emphasize as chemical synthesized nanoparticles may lead to toxic or side effects due to the existence of toxic chemicals [60]. The antibacterial mechanism of CB-Hap NRs may involve (i) the size-mediated penetration of nanorods into the bacterial cell wall to interact with the cellular biomolecules that increases the osmotic potential and its associated irreversible damage and (ii) the generation of free reactive oxygen species (ROS) radicals that are induced by nanorods that interact with the bacterial membrane and result in oxidative stress [61].

Conclusion

This study is a pioneering work in the preparation of hydroxyapatite nanorods using marine waste cuttlefish bones using an oil-bath-mediated precipitation method. The resultant powders from the precipitation process were investigated via systematic characterization methods to confirm the physicochemical properties of the cuttlefish bone-derived nanorods. The XRD data revealed the mechanism behind the transformation of aragonite to calcite and then to Hap NRs of 20.86 nm to be related to crystallite size. The average length and width of the nanorods was determined as 79.05 and 219.66 nm using TEM analysis and the elemental analysis showed the Ca/P molar ratio of 1.6 (1 mole of calcium per 0.6 mole of phosphorus). Both the crystallite size and elemental analysis showed that the Hap NRs are similar to natural human bone and can be used as an implant material in hard tissue treatments. FTIR data further confirms the presence of phosphate groups and TGA data showed that the CB-Hap NRs possess significant thermal stability. Furthermore, the hemolysis study showed better blood compatibility than conventional, chemically synthesized Hap, and the antimicrobial activity showed better activity against gram-positive *S. aureus* bacteria. Moreover, the Hap can be incorporated with metal dopants in future experiments to further elevate their biocompatibility towards blood cells and increase their antibacterial efficacy. These enhanced biological properties of biogenic Hap NRs will be highly useful in the fabrication of novel implants for orthopedic and dental applications.

Materials and Methods

The experiments were performed in a 1000 mL round bottom flask filled with calcium carbonate (CB powder), $(NH_4)_2HPO_4$ and ammonia solution. The oil bath setup was used to maintain the reaction temperature. Silicone oil was used in the oil bath setup from 30 to 250 °C as it possesses high stability towards temperature and oxidation and can provide uniform temperature for long time, as compared to a water bath [62]. The color of the CB-Hap NRs turns light gray from white after annealing which may be due to the removal of organic products such as collagen and protein.

Chemicals and reagents

Marine waste cuttlefish bones were collected as a source of calcium from Kasimedu fish market, which is located in Chennai, Tamil Nadu, India. All chemicals used for this study were of analytical grade such as $(NH_4)_2HPO_4$ (Merck, purity – 99%, molecular weight (MW) – 132.06 g/mol), NH_4OH (Merck, purity – 25%, MW – 35.05 g/mol), C_3H_6O (Sigma-Aldrich, purity – 99.8%, MW – 58.08 g/mol) and $C_4H_8O_2$ (Sigma-Aldrich, purity – 99.9%, MW – 88.11 g/mol), CNa_2O_3 (Sigma-Aldrich, purity – 99.5%, MW – 105.99 g/mol), $Na_3C_6H_5O_7$ (Sigma-Aldrich, purity – 99%, MW – 258.07 g/mol) and phosphate buffer saline (PBS) (pH 7.4).

Preparation of cuttlebone powder

The thick outer layer of the cuttlefish bone part, called the dorsal shield, was removed using a lancet and the inner part (lamellae matrix) was washed with distilled water, followed by acetone and ethanol to remove surface contaminants. The washed bones were dried in a hot air oven (Indfurr model OR-3795) at 60 °C for 24 h and 20 g of cuttlefish bone pieces were taken for top down processing using high-energy ball milling (VB Ceramic Consultants, Chennai) for 5 h. The ground

bone powder was stored in a sterile plastic container at room temperature and placed in a desiccator for future experiments.

Preparation of cuttlebone-Hap nanorods

In the synthesis process, an oil bath was used as a temperature controller for the precipitation process and placed on magnetic stirrer. 1 molar (1.008 g) of cuttlefish bone powder was taken in a round bottom flask and 0.6 molar (0.795 g) of diammonium hydrogen phosphate was added dropwise using a burette. Then, the pH of the reaction was measured with a pH meter (Thermo Scientific, model-eco tester) and was adjusted from 8 to 12 using ammonia solution. This mixture was allowed to stir for various reaction times of 6, 12, 24, and 48 h at 80 °C and then the final precipitate was washed with distilled water and ethanol to remove impurities. Finally, the precipitate was dried at 60 °C in a hot air oven and was crushed into uniform powder using a mortar and pestle. The resultant powder was then annealed at 700 °C for 6 h and further characterized to confirm the presence of CB-Hap NRs as shown in Figure 7. The optimization of parameters such as reaction time, pH, temperature, and concentration plays a key role in the morphology evaluation of the nanomaterials. The parameters were optimized based on the study by Casella et al. (2017), in which Hap nanoparticles were synthesized with various morphologies such as rods, hexagonal prisms, hollow flower structure, and microspheres by adjusting the reaction time [63].

Characterization of cuttlebone-Hap nanorods

X-ray diffraction

The X-ray diffraction (XRD) was carried out using an X-ray powder diffractometer (Bruker, Model D8 Advance) to study the crystallinity and phase formation of Hap nanorods. CB powder samples (ball milled) and CB-Hap NR powder was gently ground using a graphite mortar and pestle and placed on the sample holder. The crystallite size and phase formation of the cuttlefish-bone-derived Hap nanorods were identified and confirmed by comparing the data with standard XRD patterns from JCPDS.

Fourier transform infrared spectroscopy

The presence of functional groups in the cuttlefish bone and cuttlefish-bone-derived Hap nanorods was identified using a Perkin Elmer spectrum model Spectrum one FTIR spectrometer. CB powder (ball milled) and synthesized CB-Hap NR powders were directly placed on the sample holder. The sample was scanned from 4000 to 500 cm^{-1} in attenuated total reflectance (ATR) mode.

Transmission electron microscopy and energy dispersive X-ray analysis (EDX)

TEM micrographs of CB Hap NRs were obtained using TEM (model JEOL, Japan) at an operation voltage of 200 kV. A sufficient quantity of CB-Hap NR powder was placed on the carbon-coated copper grid and allowed to stick. The size and morphology of the synthesized nanohydroxyapatite was observed. The average particle size distribution of CB-Hap NRs was plotted using ImageJ software. The elemental composition analysis via energy dispersive X-ray analysis (EDX) was also performed to confirm the presence of CB-Hap NR conformations.

Thermal behavior analysis

Thermogravimetric analysis (TGA) was performed on raw cuttlebone and CB-Hap nanorods. 5 mg samples were placed on

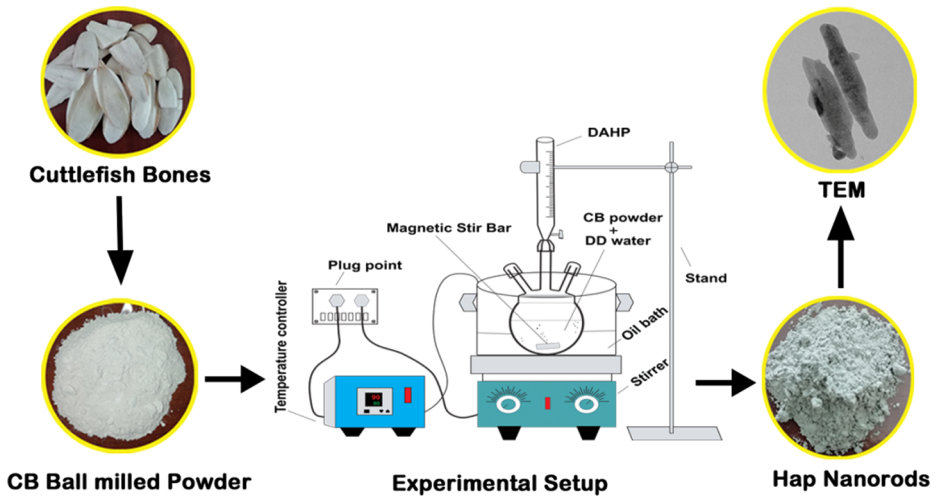

Figure 7: Oil-bath-mediated synthesis of CB-Hap NRs.

the sample holder and the thermal behavior was analyzed from room temperature to 700 °C using TGA model Q50 V20.13 Build 39, at a heating rate of 20 °C/min under 100 mL/min nitrogen flow rate.

Biological studies

Antibacterial study

The bactericidal activity of the CB-Hap NRs was assessed using well diffusion methods against two different gram-positive and gram-negative bacteria, *E. coli*, and *S. aureus*, respectively. The nutrient broth with agar was autoclaved and transferred to a petri dish. Fresh bacterial cultures were spread over using a sterile cotton swab on solidified media. The CB-Hap NR samples were poured into the wells and were punctured in the nutrient agar media using micropipette tips. 50 µg/mL of free CB and CB-Hap NRs were introduced into the wells and the plates were incubated at 37 °C for 24 h, followed by zone of inhibition measurements. The method was repeated three times to check the reproducibility of the results.

Hemolysis assay

The experiments were conducted in accordance with the relevant laws and guidelines of Institutional Animal Ethics Committee (Tamil Nadu Veterinary and Animal Sciences University, Veppery, Chennai, India). The informed consent was obtained from the blood donor for the assay. Human blood was collected from a healthy volunteer with the help of a clinician and the blood was prevented from coagulation by mixing it with 3.2% of trisodium citrate (MW – 258.07 g/mol, purity – 99%) in the ratio 1:10. Various concentrations (200, 100, 75, 50, 25 and 10 µg/mL) of CB-Hap NRs were prepared with phosphate buffer saline (PBS) (purity – 99%, pH 7.4) and anticoagulated blood was used as a test specimen. 0.1% of sodium carbonate (MW – 105.99 g/mol, purity – 99.5%) with anticoagulated blood and anticoagulated blood with PBS were utilized as positive and negative controls, respectively. All of the test samples and controls were incubated at 37 °C for 3 h and then the tubes were centrifuged at 2000 rpm for 5 min. The optical density (OD) of the supernatant was recorded at 540 nm. All the tests were performed in triplicate to ensure reproducibility. The percentage of blood compatibility was calculated using the formula,

$$\text{hemolysis (\%)} = \frac{\left(\begin{array}{c}\text{absorbance}\\ \text{of test sample}\end{array} - \begin{array}{c}\text{absorbance}\\ \text{of negative control}\end{array}\right)}{\left(\begin{array}{c}\text{absorbance}\\ \text{of positive control}\end{array} - \begin{array}{c}\text{absorbance}\\ \text{of negative control}\end{array}\right)} \times 100$$

Ethical approval

All procedures performed in the present study involving human participants are in accordance with the ethical standards of the Institutional Animal Ethics Committee (IAEC), Tamil Nadu Veterinary and Animal Sciences University, Chennai, India. Confidential informed consent was obtained from the participant (blood donor) included in the study.

Acknowledgements

The authors would like to thank the head of the Department of Animal Biotechnology for utilizing biocompatibility assessment facilities at TANUVAS, Veppery, Chennai-07.

ORCID® iDs

Satheeshkumar Balu - https://orcid.org/0000-0003-3639-4243

References

1. Poinern, G. E. J.; Brundavanam, R. K.; Fawcett, D. *Am. J. Biomed. Eng.* **2013,** *3,* 148–168. doi:10.5923/j.ajbe.20130306.04
2. Eliaz, N.; Metoki, N. *Materials* **2017,** *10,* 334. doi:10.3390/ma10040334
3. Earl, J. S.; Wood, D. J.; Milne, S. J. *J. Phys.: Conf. Ser.* **2006,** *26,* 268–271. doi:10.1088/1742-6596/26/1/064
4. Azis, Y.; Adrian, M.; Alfarisi, C. D.; Khairat; Sri, R. M. *IOP Conf. Ser.: Mater. Sci. Eng.* **2018,** *345,* 012040. doi:10.1088/1757-899x/345/1/012040
5. Dorozhkin, S. *Materials* **2009,** *2,* 1975–2045. doi:10.3390/ma2041975
6. Wang, W.; Yeung, K. W. K. *Bioact. Mater.* **2017,** *2,* 224–247. doi:10.1016/j.bioactmat.2017.05.007
7. Jeong, J.; Kim, J. H.; Shim, J. H.; Hwang, N. S.; Heo, C. Y. *Biomater. Res.* **2019,** *23,* 4. doi:10.1186/s40824-018-0149-3
8. Clarke, S. A.; Walsh, P.; Maggs, C. A.; Buchanan, F. *Biotechnol. Adv.* **2011,** *29,* 610–617. doi:10.1016/j.biotechadv.2011.04.003
9. Nandi, S. K.; Kundu, B.; Mukherjee, J.; Mahato, A.; Datta, S.; Balla, V. K. *Mater. Sci. Eng., C* **2015,** *49,* 816–823. doi:10.1016/j.msec.2015.01.078
10. Cadman, J.; Zhou, S.; Chen, Y.; Li, Q. *J. Bionic Eng.* **2012,** *9,* 367–376. doi:10.1016/s1672-6529(11)60132-7
11. Gopal, R.; Vijayakumaran, M.; Venkatesan, R.; Kathiroli, S. *Nat. Prod. Radiance* **2008,** *7,* 139–145.
12. Reinares-Fisac, D.; Veintemillas-Verdaguer, S.; Fernández-Díaz, L. *CrystEngComm* **2017,** *19,* 110–116. doi:10.1039/c6ce01725h
13. Venkatesan, J.; Rekha, P. D.; Anil, S.; Bhatnagar, I.; Sudha, P. N.; Dechsakulwatana, C.; Kim, S.-K.; Shim, M. S. *Biotechnol. Bioprocess Eng.* **2018,** *23,* 383–393. doi:10.1007/s12257-018-0169-9
14. Kim, B.-S.; Kang, H. J.; Yang, S.-S.; Lee, J. *Biomed. Mater.* **2014,** *9,* 025004. doi:10.1088/1748-6041/9/2/025004
15. Dhivya, S.; Selvamurugan, N. Biocomposite Scaffolds Derived from Renewable Resources for Bone Tissue Repair. In *Handbook of Composites from Renewable Materials;* Thakur, V. K.; Thakur, M. K.; Kessler, M. R., Eds.; Scrivener Publishing LLC, 2017; pp 439–485. doi:10.1002/9781119441632.ch99
16. Szcześ, A.; Hołysz, L.; Chibowski, E. *Adv. Colloid Interface Sci.* **2017,** *249,* 321–330. doi:10.1016/j.cis.2017.04.007

17. Milovac, D.; Gallego-Ferrer, G.; Ivankovic, M.; Ivankovic, H. *Mater. Sci. Eng., C* **2014,** *34,* 437–445. doi:10.1016/j.msec.2013.09.036
18. Kim, B.-S.; Kim, J. S.; Sung, H.-M.; You, H.-K.; Lee, J. *J. Biomed. Mater. Res., Part A* **2012,** *100A,* 1673–1679. doi:10.1002/jbm.a.34113
19. Rocha, J. H. G.; Lemos, A. F.; Agathopoulos, S.; Kannan, S.; Valério, P.; Ferreira, J. M. F. *J. Biomed. Mater. Res., Part A* **2006,** *77A,* 160–168. doi:10.1002/jbm.a.30566
20. Palaveniene, A.; Tamburaci, S.; Kimna, C.; Glambaite, K.; Baniukaitiene, O.; Tihminlioğlu, F.; Liesiene, J. *J. Biomater. Appl.* **2019,** *33,* 876–890. doi:10.1177/0885328218811040
21. Jin, X.; Zhuang, J.; Zhang, Z.; Guo, H.; Tan, J. *J. Colloid Interface Sci.* **2015,** *443,* 125–130. doi:10.1016/j.jcis.2014.12.010
22. Yahia, I. S.; Shkir, M.; AlFaify, S.; Ganesh, V.; Zahran, H. Y.; Kilany, M. *Mater. Sci. Eng., C* **2017,** *72,* 472–480. doi:10.1016/j.msec.2016.11.074
23. Rocha, J. H. G.; Lemos, A. F.; Agathopoulos, S.; Valério, P.; Kannan, S.; Oktar, F. N.; Ferreira, J. M. F. *Bone* **2005,** *37,* 850–857. doi:10.1016/j.bone.2005.06.018
24. Kong, J.; Liu, C.; Yang, D.; Yan, Y.; Chen, Y.; Huang, J.; Liu, Y.; Zheng, G.; Xie, L.; Zhang, R. *Cryst. Growth Des.* **2018,** *18,* 3794–3804. doi:10.1021/acs.cgd.8b00025
25. Jensen, A. C. S.; Brif, A.; Pokroy, B.; Hinge, M.; Birkedal, H. *CrystEngComm* **2016,** *18,* 2289–2293. doi:10.1039/c5ce02245b
26. Cozza, N.; Monte, F.; Bonani, W.; Aswath, P.; Motta, A.; Migliaresi, C. *J. Tissue Eng. Regener. Med.* **2018,** *12,* e1131–e1142. doi:10.1002/term.2448
27. Jeevanandam, J.; Chan, Y. S.; Ku, Y. H. *Appl. Biol. Chem.* **2018,** *61,* 197–208. doi:10.1007/s13765-018-0347-7
28. Ślósarczyk, A.; Paszkiewicz, Z.; Paluszkiewicz, C. *J. Mol. Struct.* **2005,** *744-747,* 657–661. doi:10.1016/j.molstruc.2004.11.078
29. Sroka-Bartnicka, A.; Borkowski, L.; Ginalska, G.; Ślósarczyk, A.; Kazarian, S. G. *Spectrochim. Acta, Part A* **2017,** *171,* 155–161. doi:10.1016/j.saa.2016.07.051
30. Hui, P.; Meena, S. L.; Singh, G.; Agarawal, R. D.; Prakash, S. *J. Miner. Mater. Charact. Eng.* **2010,** *09,* 683–692. doi:10.4236/jmmce.2010.98049
31. Naga, S. M.; El-Maghraby, H. F.; Mahmoud, E. M.; Talaat, M. S.; Ibrhim, A. M. *Ceram. Int.* **2015,** *41,* 15010–15016. doi:10.1016/j.ceramint.2015.08.057
32. Ivankovic, H.; Gallego-Ferrer, G.; Tkalcec, E.; Orlic, S.; Ivankovic, M. *J. Mater. Sci.: Mater. Med.* **2009,** *20,* 1039–1046. doi:10.1007/s10856-008-3674-0
33. Aarthy, S.; Thenmuhil, D.; Dharunya, G.; Manohar, P. *J. Mater. Sci.: Mater. Med.* **2019,** *30,* 21. doi:10.1007/s10856-019-6219-9
34. Herradi, S.; El Bali, B.; Khaldi, M.; Lachkar, M. *IOP Conf. Ser.: Mater. Sci. Eng.* **2017,** *186,* 012023. doi:10.1088/1757-899x/186/1/012023
35. Venkatesan, J.; Kim, S. K. *Materials* **2010,** *3,* 4761–4772. doi:10.3390/ma3104761
36. Hung, I.-M.; Shih, W.-J.; Hon, M.-H.; Wang, M.-C. *Int. J. Mol. Sci.* **2012,** *13,* 13569–13586. doi:10.3390/ijms131013569
37. Ooi, C. H.; Pung, S. Y.; Yeoh, F. Y. *Biomed. J. Sci. Tech. Res.* **2018,** *5,* 001239. doi:10.26717/bjstr.2018.05.001239
38. Kumar, G. S.; Sathish, L.; Govindan, R.; Girija, E. K. *RSC Adv.* **2015,** *5,* 39544–39548. doi:10.1039/c5ra04402b
39. Padmanabhan, S. K.; Balakrishnan, A.; Chu, M.-C.; Lee, Y. J.; Kim, T. N.; Cho, S.-J. *Particuology* **2009,** *7,* 466–470. doi:10.1016/j.partic.2009.06.008
40. Papageorgiou, D. G.; Roumeli, E.; Chrissafis, K.; Lioutas, C.; Triantafyllidis, K.; Bikiaris, D.; Boccaccini, A. R. *Phys. Chem. Chem. Phys.* **2014,** *16,* 4830–4842. doi:10.1039/c3cp55103b
41. Shi, Z.; Huang, X.; Cai, Y.; Tang, R.; Yang, D. *Acta Biomater.* **2009,** *5,* 338–345. doi:10.1016/j.actbio.2008.07.023
42. Dasgupta, S.; Tarafder, S.; Bandyopadhyay, A.; Bose, S. *Mater. Sci. Eng., C* **2013,** *33,* 2846–2854. doi:10.1016/j.msec.2013.03.004
43. Jadalannagari, S.; More, S.; Kowshik, M.; Ramanan, S. R. *Mater. Sci. Eng., C* **2011,** *31,* 1534–1538. doi:10.1016/j.msec.2011.07.001
44. Zanotto, A.; Saladino, M. L.; Martino, D. C.; Caponetti, E. *Adv. Nanopart.* **2012,** *1,* 21–28. doi:10.4236/anp.2012.13004
45. Nga, N. K.; Thuy Chau, N. T.; Viet, P. H. *Colloids Surf., B* **2018,** *172,* 769–778. doi:10.1016/j.colsurfb.2018.09.039
46. Kumar, G. S.; Girija, E. K.; Venkatesh, M.; Karunakaran, G.; Kolesnikov, E.; Kuznetsov, D. *Ceram. Int.* **2017,** *43,* 3457–3461. doi:10.1016/j.ceramint.2016.11.163
47. Ji, Y.; Wang, A.; Wu, G.; Yin, H.; Liu, S.; Chen, B.; Liu, F.; Li, X. *Mater. Sci. Eng., C* **2015,** *57,* 14–23. doi:10.1016/j.msec.2015.07.008
48. Pellegrino, E. D.; Biltz, R. M. *Nature* **1968,** *219,* 1261–1262. doi:10.1038/2191261a0
49. Elferink, J. G. R. *Biochem. Med. Metab. Biol.* **1986,** *36,* 25–35. doi:10.1016/0885-4505(86)90103-9
50. Wiessner, J.; Mandel, G.; Halverson, P.; Mandel, N. *Calcif. Tissue Int.* **1988,** *42,* 210–219. doi:10.1007/bf02553746
51. Tee, J. K.; Ong, C. N.; Bay, B. H.; Ho, H. K.; Leong, D. T. *Wiley Interdiscip. Rev.: Nanomed. Nanobiotechnol.* **2016,** *8,* 414–438. doi:10.1002/wnan.1374
52. Jiang, L.; Yu, Y.; Li, Y.; Yu, Y.; Duan, J.; Zou, Y.; Li, Q.; Sun, Z. *Nanoscale Res. Lett.* **2016,** *11,* 57. doi:10.1186/s11671-016-1280-5
53. Chen, L. Q.; Fang, L.; Ling, J.; Ding, C. Z.; Kang, B.; Huang, C. Z. *Chem. Res. Toxicol.* **2015,** *28,* 501–509. doi:10.1021/tx500479m
54. Han, Y.; Wang, X.; Dai, H.; Li, S. *ACS Appl. Mater. Interfaces* **2012,** *4,* 4616–4622. doi:10.1021/am300992x
55. Shi, C.; Gao, J.; Wang, M.; Fu, J.; Wang, D.; Zhu, Y. *Mater. Sci. Eng., C* **2015,** *55,* 497–505. doi:10.1016/j.msec.2015.05.078
56. Furuzono, T.; Azuma, Y.; Niigawa, Y.; Kogai, Y.; Sawa, Y. *ASAIO J.* **2016,** *62,* 197–202. doi:10.1097/mat.0000000000000322
57. Piacenza, E.; Presentato, A.; Zonaro, E.; Lemire, J. A.; Demeter, M.; Vallini, G.; Turner, R. J.; Lampis, S. *Microb. Biotechnol.* **2017,** *10,* 804–818. doi:10.1111/1751-7915.12700
58. Tank, K. P.; Sharma, P.; Kanchan, D. K.; Joshi, M. J. *Cryst. Res. Technol.* **2011,** *46,* 1309–1316. doi:10.1002/crat.201100080
59. Tank, K. P.; Chudasama, K. S.; Thaker, V. S.; Joshi, M. J. *J. Cryst. Growth* **2014,** *401,* 474–479. doi:10.1016/j.jcrysgro.2014.01.062
60. Jeevanandam, J.; Sundaramurthy, A.; Sharma, V.; Murugan, C.; Pal, K.; Abd Elkodous, M. H.; Danquah, M. K. Sustainability of One-Dimensional Nanostructures: Fabrication and Industrial Applications. In *Sustainable nanoscale engineering;* Szekely, G.; Livingston, A., Eds.; Elsevier, 2020; pp 83–113. doi:10.1016/b978-0-12-814681-1.00004-7

61. Khatoon, Z.; McTiernan, C. D.; Suuronen, E. J.; Mah, T.-F.; Alarcon, E. I. *Heliyon* **2018,** *4,* e01067. doi:10.1016/j.heliyon.2018.e01067
62. Mattox, D. M. *Arc Vapor Deposition*. *Handbook of physical vapor deposition (PVD) processing;* William Andrew, 2010; pp 287–300. doi:10.1016/b978-0-8155-2037-5.00008-3
63. Casella, L. A.; Griesshaber, E.; Yin, X.; Ziegler, A.; Mavromatis, V.; Müller, D.; Ritter, A.-C.; Hippler, D.; Harper, E. M.; Dietzel, M.; Immenhauser, A.; Schöne, B. R.; Angiolini, L.; Schmahl, W. W. *Biogeosciences* **2017,** *14,* 1461–1492. doi:10.5194/bg-14-1461-2017

License and Terms

The definitive version of this article is the electronic one which can be found at:
doi:10.3762/bjnano.11.21

BEILSTEIN JOURNAL OF NANOTECHNOLOGY

Understanding nanoparticle flow with a new in vitro experimental and computational approach using hydrogel channels

Armel Boutchuen[1], Dell Zimmerman[1], Abdollah Arabshahi[2], John Melnyczuk[3] and Soubantika Palchoudhury[*1,§]

Full Research Paper

Open Access

Address:
[1]Department of Civil and Chemical Engineering, University of Tennessee at Chattanooga, Chattanooga, Tennessee 37403, United States, [2]SimCenter, University of Tennessee at Chattanooga, Chattanooga, Tennessee 37403, United States and [3]Department of Chemistry, Clark Atlanta University, Georgia 30314, United States

Email:
Soubantika Palchoudhury[*] - soubantika-palchoudhury@utc.edu

* Corresponding author
§ Phone: (423) 425-5455 Fax: (423) 425-5229

Keywords:
computational fluid dynamics; drug delivery; iron oxide nanoparticles; nanoparticle flow; poly(hydroxyethyl methacrylate) (pHEMA) hydrogels

Beilstein J. Nanotechnol. **2020,** *11,* 296–309.
doi:10.3762/bjnano.11.22

Received: 21 September 2019
Accepted: 27 January 2020
Published: 06 February 2020

This article is part of the thematic issue "Engineered nanomedicines for advanced therapies".

Guest Editor: F. Baldelli Bombelli

Abstract

Nanoparticles (NPs) are considered as one of the most promising drug delivery vehicles and a next-generation solution for current medical challenges. In this context, variables related to flow of NPs such as the quantity of NPs lost during transport and flow trajectory greatly affect the clinical efficiency of NP drug delivery systems. Currently, there is little knowledge of the physical mechanisms dominating NP flow inside the human body due to the limitations of available experimental tools for mimicking complex physiological environments at the preclinical stage. Here, we report a coupled experimental and computational fluid dynamics (CFD)-based novel in vitro approach to predict the flow velocity and binding of NP drug delivery systems during transport through vasculature. Poly(hydroxyethyl)methacrylate hydrogels were used to form soft cylindrical constructs mimicking vascular sections as flow channels for synthesized iron oxide NPs in these first-of-its-kind transport experiments. Brownian dynamics and material of the flow channels played key roles in NP flow, based on the measurements of NP flow velocity over seven different mass concentrations. A fully developed laminar flow of the NPs under these conditions was simultaneously predicted using CFD. Results from the mass loss of NPs during flow indicated a diffusion-dominated flow at higher particle concentrations but a flow controlled by the surrounding fluid and Brownian dynamics at the lowest NP concentrations. The CFD model predicted a mass loss of 1.341% and 6.253% for the 4.12 g·mL^{-1} and 2.008 g·mL^{-1} inlet mass concentrations of the NPs, in close confirmation with the experimental results. This further highlights the reliability of our new in vitro technique in providing mechanistic insights of NP flow for potential preclinical stage applications.

Introduction

Current research increasingly highlight the importance of drug delivery systems in engineering new solutions to our medical challenges [1-3]. A drug delivery agent should be biocompatible, easily administered to the patient, and capable of carrying the drug to the disease site before controlled release of the drug [4,5]. NPs, particularly magnetic iron oxide NPs, are highly attractive for drug delivery because they have a higher circulation time compared to the conventional drugs and can be easily delivered to the diseased location through passive, active, or physical targeting [6]. The NPs can essentially transport a large drug payload past the complex physiological microenvironment inside the human body to the target site. In cases of injection of the NPs to the blood stream, the particles must first flow through vascular regimes with high plasma protein concentrations, followed by transvascular transport through vascular networks of varying dimensions within the body, before reaching the action site [7-9]. It is increasingly complex to predict the flow properties of NP-based drug delivery system such as the local velocity and adhesion of the NPs in vivo. If we can predict the flow and interaction, e.g., adhesion or deposition, of the NPs through in vitro techniques, it will significantly enhance the preclinical to clinical translation of NP-based drugs from the current success rate of 8% [10]. Currently, preclinical assessment of NP drug delivery systems relies on animal models to provide a reliable mimic of conditions within the patient's body [11]. Therefore, an in vitro technique that can mimic the transport of NPs through vascular constructs will be a major initial screening tool for a controlled patient-specific environment and will significantly complement existing in vivo methods for a more efficient and reliable evaluation of NP drugs [12]. However, many variables such as the size, surface chemistry, and interaction of the NPs with different biological compounds within the body influence the trajectory of NPs in vivo [13-15]. This makes it challenging to predict the behavior of NP drugs relying on solely experimental approaches [16].

To this end, computational methods have been used in modeling NP-based drug delivery through human vascular networks [17]. Different types of in silico methods have been investigated to date in an effort to cover the vastly different dimension scales of the NPs and the vascular network [18-20]. These simulations can essentially be categorized on the basis of details in the physics used to define and model the system [5]. Ab initio quantum mechanical simulations represent the highest level of detail, but are most applicable for modeling smaller NP systems or optimizing less detailed simulations due to their increased complexity and computational cost [17]. The coarse grained molecular dynamics simulations can characterize larger systems over time scales greater than 1 ms [21]. These slightly coarser models simulate a group of atoms or molecular fragment instead of an individual atom to incorporate a larger system. However, molecular dynamics models in general are more appropriate in understanding the size, surface, interaction, and uptake of a NP rather than their flow over larger dimensions as it models the interactions of molecules and atoms for a specific time scale. Beyond coarse grained models and molecular modeling, dissipative particle dynamics have been used to simulate the hydrodynamic properties of NPs over larger length scales [22,23]. However, even the dissipative particle dynamics models are limited in length scale in terms of simulating NP flow through vascular networks for drug delivery. Therefore, continuum models have been explored for NP transport [24]. For example, advection–diffusion models have been applied for transport of NPs through larger vascular constructs where the blood is represented as a simple Newtonian fluid [25,26]. The convection–diffusion-reaction continuum models were more suitable in terms of modeling the ligand–receptor binding reactions of NPs in transport through microscale vascular channels. Computational fluid dynamics (CFD), traditionally used in modeling fluid flow can be a powerful technique for continuum scale simulations of NP flow. The advantage of CFD in comparison to other computationally expensive techniques is the robustness and simplicity of the underlying physics [27-29]. CFD methods predict NP flow by solving the fundamental Navier–Stokes equation for flow [30,31]. Fullstone et al. have used CFD in couple with flexible large-scale agent based modeling to predict NP distributions in vivo [32]. The size and shape of the NPs greatly influenced the adhesion and path of NPs within the vascular network. This CFD model predicted a higher circulation time for the smaller NPs as these NPs had less chances of adhesion to the walls of the blood vessels, which was observed in some cases of in vitro experiments. The Brownian adhesion dynamics also plays an important role in NP binding compared to microscale structures [33]. Recently, we have developed CFD simulations to reliably model NP flow through plastic channels [34]. One key limitation of these few computational techniques used in understanding NP flow is the lack of suitable experimental data for validation. In order to acquire in vitro experimental results for transport of NPs that can reliably represent the flow and adhesion during drug delivery, it is essential to construct mimics of human vascular network.

Hydrogels are unique three-dimensional (3D) networks of insoluble polymers formed from two or more hydrophilic monomers that can absorb large quantities of water. The hydrogels, being generally soft, elastic, and biocompatible structures with a high water content are highly attractive from a materials perspective for making 3D channels mimicking the human vascular

network [35-37]. Chemically cross-linked hydrogels such as poly(hydroxyethyl)methacrylate (pHEMA) are used as scaffold materials for the 3D bioprinting of biomimetic structures [38,39]. Therefore, we chose pHEMA hydrogels to build straight cylindrical channels mimicking sections of human vasculature for our experimental investigation of NP flow. In addition, we aimed to synthesize the hydrogel flow channels via a new, facile, and cost-effective approach.

Here, we report a combined experimental and computational technique to serve as an in vitro assessment of the flow of NPs using novel pHEMA hydrogel channels as the biomimetic flow path. The flow of NPs was experimentally investigated with different iron oxide NP formulations synthesized via a facile method for monitoring the velocity and mass loss of NPs through the hydrogel channels. The experimental flow of NPs was compared with computational predictions for a reliable assessment of NP flow through soft vascular mimics. An in silico CFD method using the Navier–Stokes-based Tenasi flow solver was applied to investigate the velocity and deposition of the NPs in our study. The results from the complementary experimental and CFD approach provided valuable understanding of the transport mechanisms dominating NP flow at different concentration regimes that has not been reported earlier.

Results and Discussion

NPs such as biocompatible iron oxide NPs have been increasingly explored as carriers of different therapeutic agents to disease locations within the human body. NPs are attractive agents for such drug delivery applications due to their ability for enhanced circulation and controlled delivery to the disease sites compared to conventional drug formulations. In the context of achieving next-generation medical solutions with NPs, an in vitro technique that can mimic or visualize the transport of these NP-based drugs through vascular networks will be a key technological advancement. Such an in vitro method will serve as a complement for existing preclinical animal models and will be able to predict the flow of new NP drugs for increased success in clinical translation. A crucial first step for mimicking NP flow through human vascular network is developing the soft, 3D vascular structures. Hydrogels, soft biocompatible polymers with synthetically tunable physical and chemical properties and a chemical structure capable of retaining high volumes of water similar to the extracellular microenvironments, are considered highly promising materials for 3D vascular constructs. Therefore, we first synthesized a series of chemically cross-linked pHEMA hydrogels and investigated their structural properties and water absorption capability to find the best suitable formulation for fabricating flow channels mimicking a soft vascular platform. In this study, we aimed to design soft flow channels towards a more realistic mimic of biological systems such as vascular constructs for the experimental section of the analysis of NP flow.

Figure 1 shows the images of freshly synthesized pHEMA gels prepared with different quantities of water (1–1.5 mL) using the same cross-linking monomer mixture (2-hydroxyethyl methacrylate (HEMA)/1,2-ethanediol dimethacrylate (EGDMA)) under similar reaction conditions. In general, transparency and softness of the gels decreased with increased use of water during the reaction, consistent with other literature reports [40]. Gels prepared with 1.5 mL of DI water were opaque and tougher compared to the other formulations and considered less suitable for forming flexible flow channels. In addition to mechanical flexibility, surface smoothness of the hydrogels was another key parameter in selecting a suitable material for fabricating the new 3D flow channels. pHEMA hydrogels synthesized with 1, 1.1, and 1.2 mL of DI water showed uneven surface textures owing to the increased softness of these materials. These formulations were not used for the flow channels as their rough surfaces could lead to friction artifacts in the flow of NPs.

The pHEMA hydrogel prepared with 1.3 mL of DI water was considered the most suitable formulation, in terms of mechanical flexibility, mechanical strength, and surface smoothness, for mimicking physiologically relevant microenvironments. This hydrogel also showed the highest capacity to retain water within its structure with a 60% increase in mass from swelling after 1 h of water absorption at pH 11 at ambient temperature (25 °C). The high water content of the pHEMA hydrogels is attractive as it resembles properties of soft tissues and vascular networks.

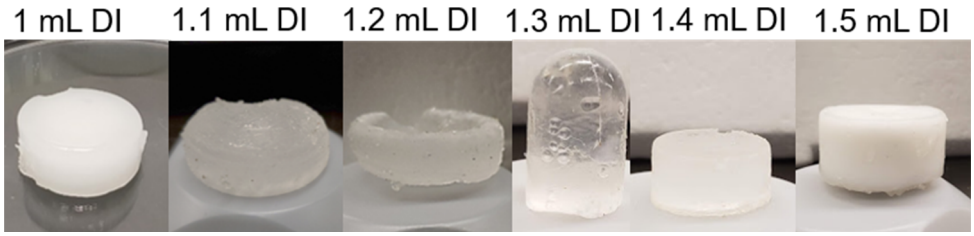

Figure 1: Images of pHEMA gels prepared with different quantities of DI water.

Figure 2 shows the pH- and time-dependent swelling behavior of the pHEMA hydrogels selected for fabrication of the flow channels. In general, the different pHEMA gels showed maximum swelling after 1.5 h and 3.5 h with a 40–50% increase in mass and disintegrated after 7 h of water absorption (Figures S1–S3, Supporting Information File 1). The swelling behavior was highly influenced by the pH value of the solution. The selected gel formulation synthesized with 1.3 mL DI water showed an increased mass of 25% at pH 2, 30% at pH 13, and a maximum of 60% at pH 11.

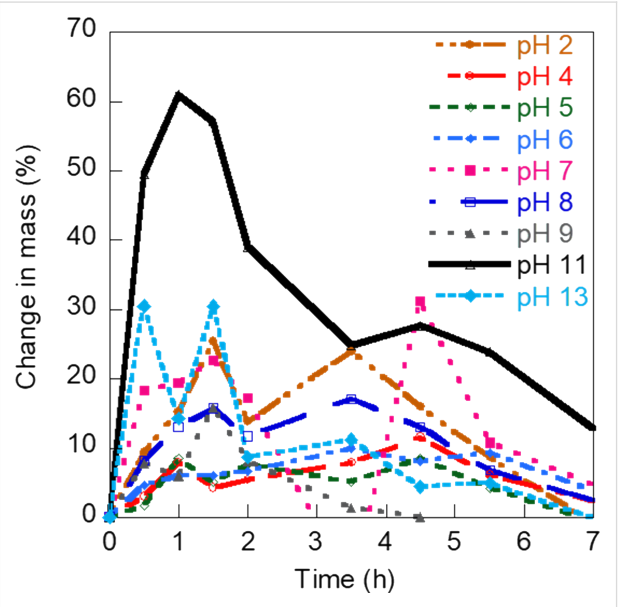

Figure 2: Plot showing pH-dependent swelling behavior of the pHEMA hydrogel prepared with 1.3 mL DI water over a period of 7 h.

Figure 3 shows the scanning electron microscopy (SEM) images of the different pHEMA hydrogels. The SEM characterization provided further insights into the variation of surface texture of the gels with the amount of reactant water used during synthesis. A soft, uneven, and layered texture was seen for the gels prepared with 1 mL DI water. The hydrogel prepared with 1.3 mL DI water showed the smoothest surface of all gel formulations. The gels prepared with 1.5 mL DI water showed a distinctly porous surface structure. Therefore, the 1.3 mL DI water hydrogels were most suitable for making flow channels of negligible friction to resemble the vascular microenvironment.

The hollow 3D hydrogel channels were formed via a facile experimental technique using a newly constructed syringe and plastic tube assembly (Figure 4). The liquid gel was allowed to solidify overnight within the syringe–tube assembly and slowly removed from the assembly after solidification. The resultant final product consisted of soft cylindrical channels with an internal diameter of 4 mm and a length of 47 mm. These dimensions of the conduits are comparable to the optimum vessel diameter reported by Bond et al. for designing a section of single

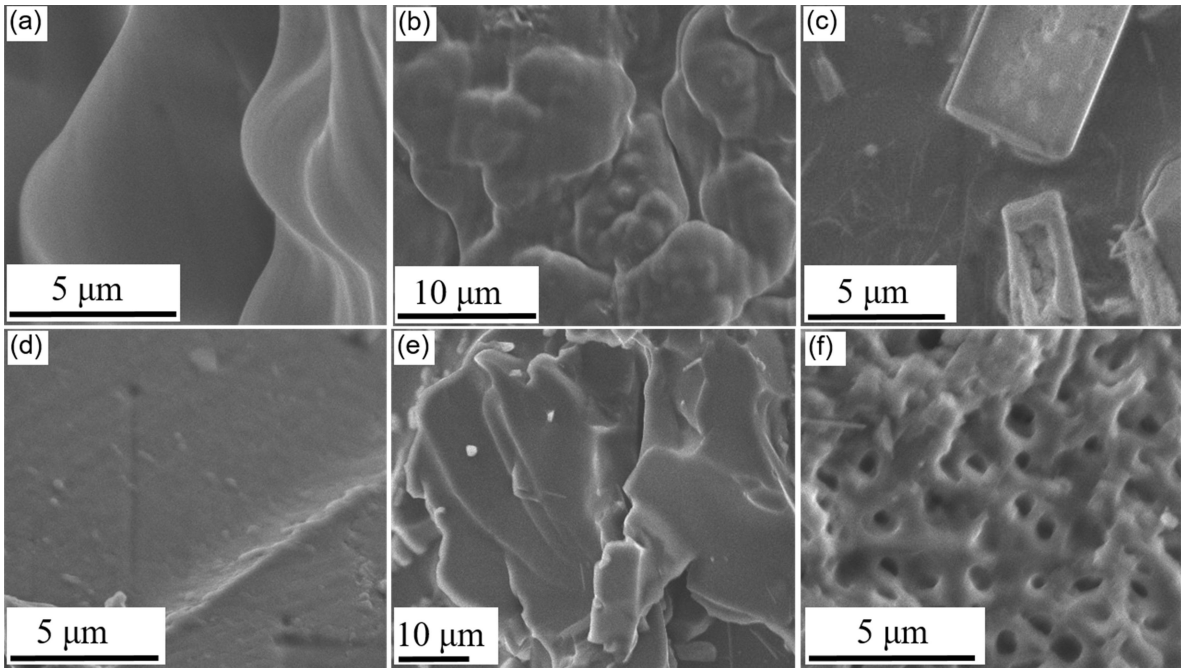

Figure 3: SEM images of pHEMA hydrogel samples synthesized using different quantities of DI water. (a) 1 mL, (b) 1.1 mL, (c) 1.2 mL, (d) 1.3 mL, (e) 1.4 mL, and (f) 1.5 mL.

vascular tube [41]. The hydrogel channels were subsequently used for studying the flow of NPs.

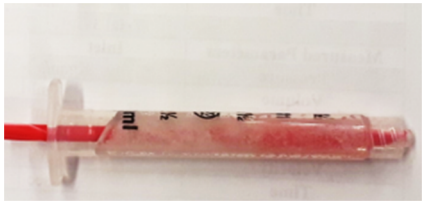

Figure 4: Facile syringe-tube assembly used in fabricating the hydrogel channels.

Iron oxide NPs are extensively investigated in targeted therapy and drug delivery applications owing to their tunable size, surface functionalities, and magnetic properties. In this study, we synthesized four different polyvinylpyrrolidone (PVP)/polyethyleneimine (PEI)-coated iron oxide NPs (i.e., 0.09 mmol PVP/0.0017 mmol PEI, 0.07 mmol PVP/0.005 mmol PEI, 0.06 mmol PVP/0.007 mmol PEI, and 0.05 mmol PVP/0.008 mmol PEI) via a modified polyol method for understanding the flow of nanoscale drugs during drug delivery [34,42]. The different PVP/PEI ligand mixtures were used to obtain varying size and surface charge of the iron oxide NPs and to render the NPs biocompatible. Figure 5a shows a representative schematic of the iron oxide NPs synthesized. The hydrodynamic sizes and zeta potential values of the different iron oxide NPs were investigated in detail using a Litesizer 500 particle analyzer, before applying the aqueous NP solutions for flow experiments. All four types of the iron oxide NPs showed a monodisperse size distribution (Figure 5b). Among these, the iron oxide NPs prepared with 0.06 mmol PVP/0.007 mmol PEI showed the smallest size (69 nm) with a narrow polydispersity index (PDI) of 0.24. The NPs coated with 0.09 mmol PVP/0.0017 mmol PEI ligand mixture were 130 nm in size with a uniform size distribution (PDI: 0.22). In comparison, the 0.07 mmol PVP/0.005 mmol PEI-coated NPs and 0.05 mmol PVP/0.008 mmol PEI-coated NPs were slightly larger with sizes of 144 nm (PDI: 0.17) and 140 nm (PDI: 0.12), respectively. The iron oxide NP formulations showed similar surface charges (Figure 5c). The low absolute values of zeta potential of the NPs suggested positively charged surfaces stabilized via steric hindrances from the polymer coating. The experimental flow velocity and the mass loss during flow under a laminar flow regime were investigated for the four different NP sizes as a first step towards constructing an in vitro technique to complement the existing animal models for predicting flow and interaction of NP-based drugs in vivo.

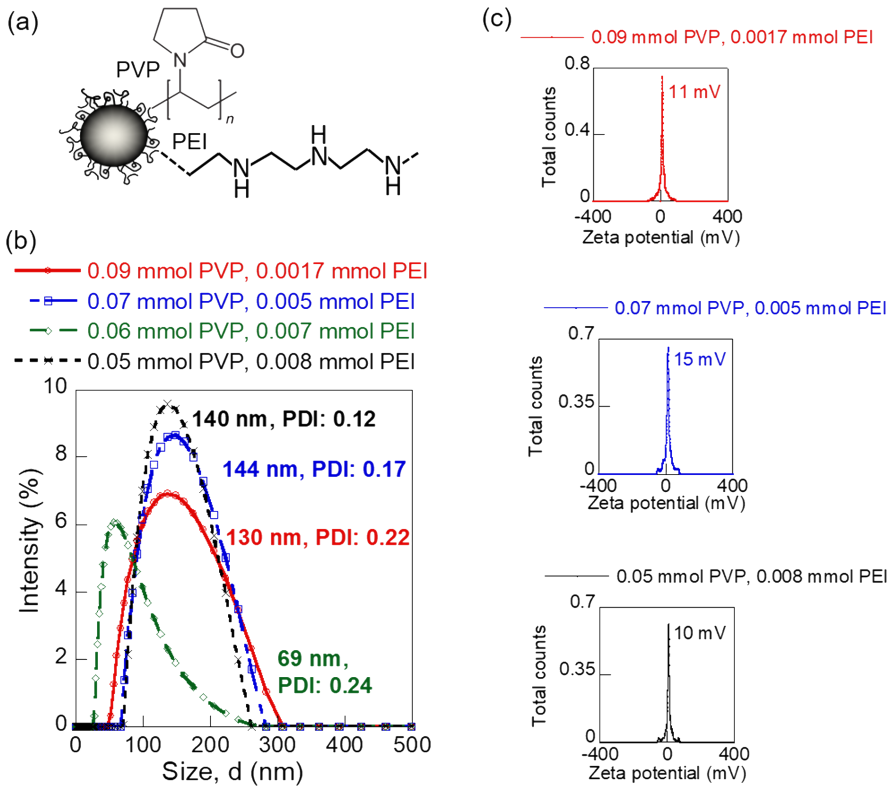

Figure 5: Different iron oxide NPs synthesized for the flow experiments. (a) Schematic overview, (b) hydrodynamic size plots, and (c) zeta potential plots.

A typical flow experiment is shown in Figure 6. The iron oxide NPs were injected through the preformed pHEMA hydrogel channels using a syringe to facilitate a laminar flow. The injection of NPs was conducted manually as shown in Figure 6b in an effort to replicate clinical intravenous delivery conditions, keeping the syringe type and pressure similar for all experiments. Three consecutive experiments have been conducted for each flow condition as described in the experiments to account for variations in inlet pressure due to the manual delivery. Such manual injections have typically been used in drug delivery applications, but the variability in inlet force in this mode of delivery is currently leading to an increasing use of autoinjectors. In our future studies, we will use flow pumps to replicate the case of drug delivery using autoinjectors. The experimental flow profile of each NP was characterized over seven different mass concentrations (2.008–5.240 g) using two primary parameters as markers, the average flow velocity and mass loss of NPs over the flow path measured from the difference in inlet and outlet mass of the NP solutions.

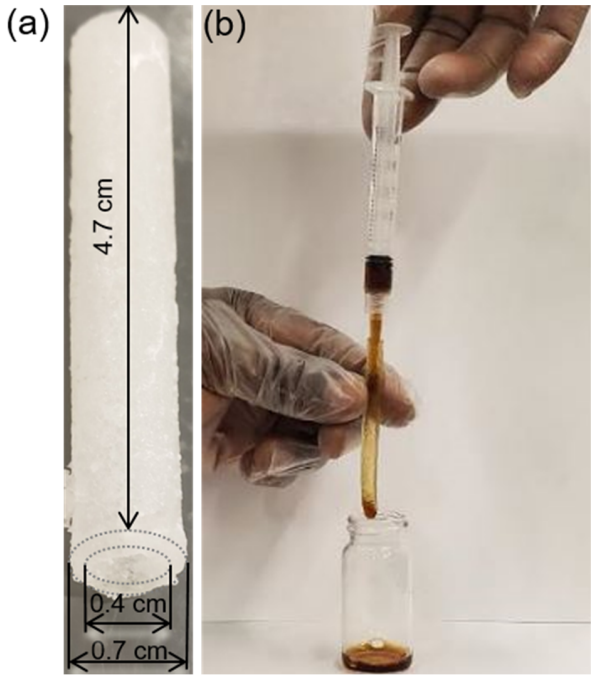

Figure 6: Experimental investigation of NP transport through soft hydrogel flow paths. (a) Representative hydrogel channel and (b) image showing a model flow experiment.

The experimental flow velocity of the four types of iron oxide NPs showed a polynomial variation with respect to NP mass during the transport through soft hydrogel channels (Figure 7a). The average velocity of 0.09 mmol PVP/0.0017 mmol PEI-coated NPs of size 130 nm ranged from 0.47 to 0.58 cm·s^{-1} and was a third-order polynomial function of the NP mass with an R value of 0.87. NPs coated with 0.07 mmol PVP/0.005 mmol PEI of size 144 nm exhibited a flow velocity ranging between 0.51 and 0.61 cm·s^{-1} with a cubic polynomial fit with respect to mass concentration of NPs (R = 0.76). The flow velocity of 0.06 mmol PVP/0.007 mmol PEI-coated iron oxide NPs of size 69 nm varied between 0.55 and 0.64 cm·s^{-1} while the 140 nm sized NPs with 0.05 mmol PVP/0.008 mmol PEI coating showed a velocity range of 0.48–0.6 cm·s^{-1}. General cubic polynomial trends in velocity with respect to NP mass concentration were also observed for these two iron oxide NPs, but with higher deviations compared to the other NP formulations. The detailed experimental data for flow velocity helped us in determining size-dependent variations of the NP flow under physiologically relevant conditions mimicking vascular sections (Figure 7b). The average velocity of the different NPs as measured from seven different mass concentrations decreased with increase in size of the NPs following a power function trend with a reliable fit (R = 0.91). This trend in NP velocity is different from the flow velocity observed through plastic channels, indicating strong influence of the material of the flow channel in the flow trajectory of NPs. In the case of soft hydrogel-based flow channels constructed to mimic vascular networks, the larger sized NPs moved slower than the smaller NPs, similar to trends seen in macroscale objects. This phenomenon could be explained in terms of two factors, a dominance of Brownian forces over diffusion and hydrodynamic forces for the flow of these aqueous NP dispersions and additional frictional forces in the NP flow path due to the soft and uneven surface of the hydrogel channels. This size-dependent flow behavior of aqueous NP solutions within soft biomimetic channels is a key finding in terms of drug delivery applications as it can serve as an in vitro tool to predict the trajectory of NP drugs and their capacity to reach disease sites under clinical conditions. Specifically, the velocity of NPs in these experiments ranged from 0.47 to 0.64 cm·s^{-1}, comparable to blood flowrates in capillaries, liver, or tumor. The blood flowrate vary in the range of 11–66 cm·s^{-1} for aorta, vena cava, and pulmonary arteries [43]. Klarhöfer et al. reported blood flowrates of 4.9–19 cm·s^{-1} in arteries and 1.5–7.1 cm·s^{-1} in veins of the human index finger [44]. Lower blood flowrates (0.08–0.25 cm·s^{-1}) were recorded in capillaries [45]. Blood flow within the tumor and liver are also slower. This induces a fluid flow pattern from the center outwards in these regions and the accumulation of micro- and nanoparticles on the walls of the vasculature [46] leading to a possible loss of NP drugs.

Loss of the NP drug during transport to the disease site plays a major role in clinical efficiency of the drug. It is an important design consideration for engineering drug delivery systems. Therefore, it will be useful to be able to predict the quantity of

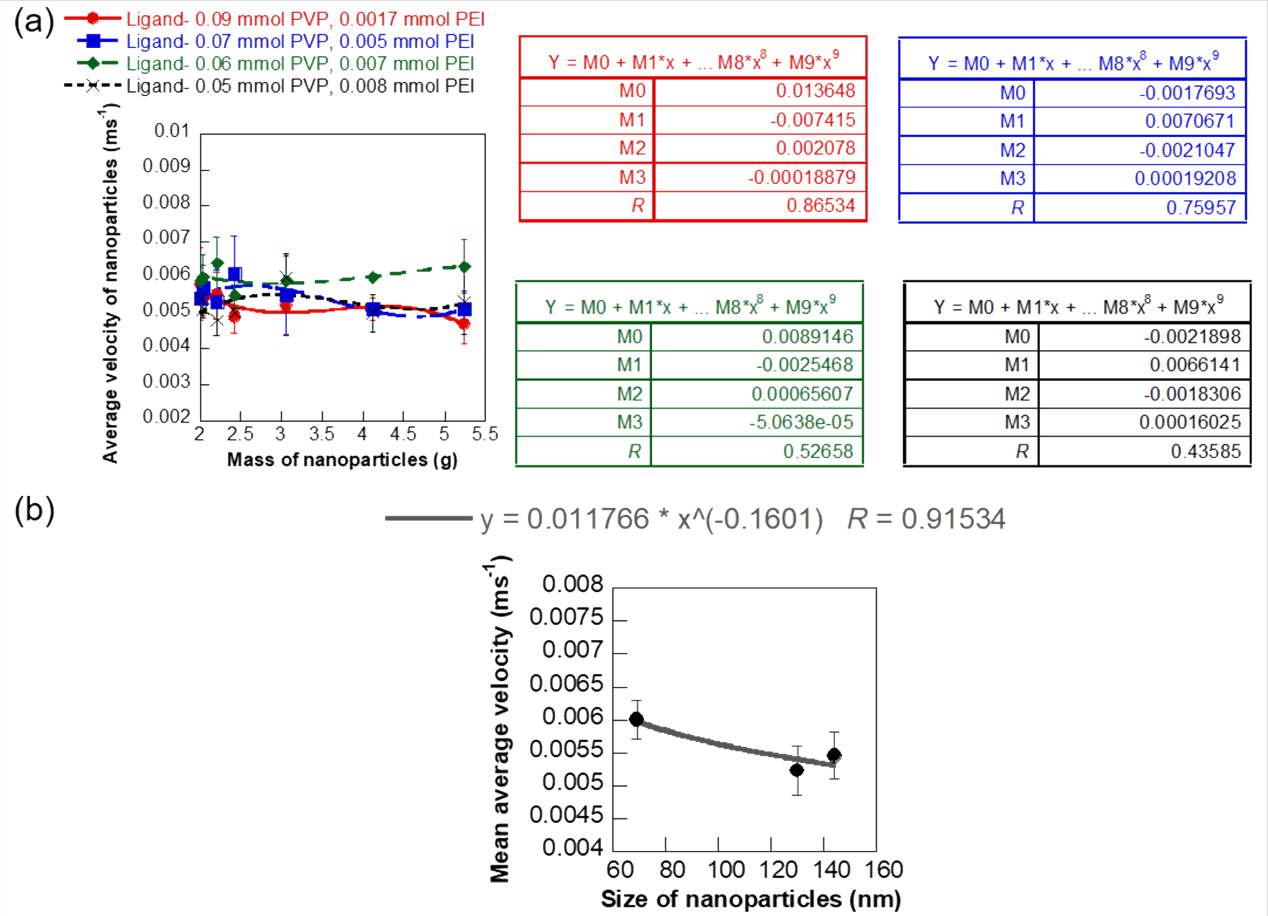

Figure 7: Experimental velocity profile of the iron oxide NPs. (a) Plot showing the average flow velocity of the different iron oxide NPs at different inlet mass concentrations and (b) variation of the average NP velocity with size of the NPs. The error bars represent standard deviation.

NPs lost due to non-specific binding or deposition on the walls of the vascular network. In this study, we investigated the mass loss of the four different types of iron oxide NPs during flow through the soft biomimetic hydrogel channels by monitoring the mass of inlet and outlet solutions (Figure 8a). This experimental mass loss of the NPs in the flow path is also a measure of the NPs bound or deposited on the walls of the hydrogel channels under the specific flow conditions. Mass loss of the NPs was monitored for seven different inlet mass concentrations for each NP type to determine the concentration-dependent trend in NP binding or deposition during the flow. The 130 nm sized NPs coated with 0.09 mmol PVP/0.0017 mmol PEI showed a mass loss ranging between 1.10 and 2.50% with an average of 1.60% and a cubic polynomial trend in mass loss with respect to the inlet NP mass (R = 0.75). The mass loss of the 0.07 mmol PVP/0.005 mmol PEI ligand-coated iron oxide NPs, of size 144 nm, was also a cubic polynomial function of the inlet mass of the NPs, but a wider range of mass loss (0.53–5.96%, R = 0.68) was observed for these NPs with the highest average mass loss (2.45%) among the four types of NPs. In comparison, the smaller 69 nm sized NPs coated with 0.06 mmol PVP/0.007 mmol PEI showed a power function trend in mass loss with respect to the NP inlet mass concentration (R = 0.81). The mass loss varied between 1.09 and 2.45% with an average of 1.77% for these NPs. The 0.05 mmol PVP/0.008 mmol PEI ligand-coated iron oxide NPs, of size 140 nm, had a mass loss ranging from 0.60 to 3.87% with an average of 1.96% and a reliable power function trend with respect to the inlet mass (R = 0.88). Figure 8b shows the influence of NP size on the experimental mass loss from binding or deposition of the NPs during transport. The size-dependent trend in NP adhesion provides key insights into the mechanisms and dominating forces determining the flow trajectory of the NPs. The mass loss percentage of the iron oxide NPs increased with NP size following a reliable quadratic correlation (R = 0.96) in the case of flow through soft channels mimicking vascular constructs. This is similar to the NP mass loss due to binding or deposition observed in plastic flow channels. This general correlation between mass loss percentage and size of the NPs implies that smaller NPs, although having a larger relative surface area for binding show a lower affinity for binding or deposition and are more likely to reach the target diseased site. The lower binding

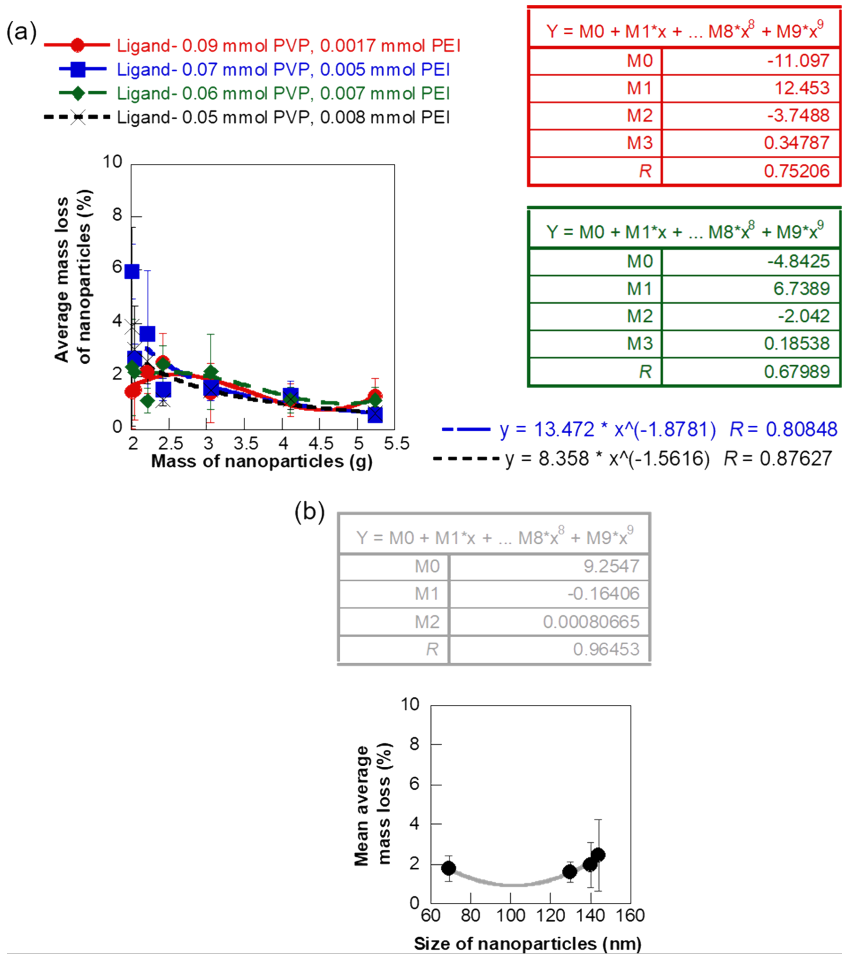

Figure 8: Experimental mass loss of the NPs during flow through hydrogel channels. (a) Plot showing average mass loss at different inlet mass concentrations of NPs and (b) variation in mass loss of NPs during flow with respect to size of the NPs. The error bars represent standard deviation.

affinity of the smaller NPs could be due to the Brownian motion of the particles and the influence of other surrounding particles and fluid. However, it is important to take a closer look at the correlation between mass loss of NPs and size for specific NP mass concentrations to better understand the different forces dominating the flow of NPs.

Figure 9 shows the variation of average mass loss percentage of the NPs as a function of the NP size for three specific inlet mass concentrations of the NPs. The mass loss of NPs during flow through the soft hydrogel channels is primarily caused by the deposition or binding of the NPs to the walls of the channels. Therefore, the mass loss correlations provide experimental insights into the concentration-dependent changes in the binding affinity of NPs that lead us to the mechanisms dominating the NP flow. The mass loss percentage and hence the binding of the NPs increased with NP size following a reliable linear correlation (R = 0.98) for the lowest inlet mass concentration of the NPs (2.008 g Fe). This implied that the smaller NPs, despite having a higher relative surface area had less tendency to deposit or bind at the lower concentrations. Therefore, the NP flow was likely dominated by the velocity of the surrounding fluid and Brownian motion at these concentrations, which prevented the deposition of the lighter, small-sized NPs [18,47,48]. In comparison, the larger NPs had more time for interaction and binding to the walls of the channel as they moved with a slower velocity through the hydrogel flow path. An increase in mass loss with size of NPs was also observed for a higher NP concentration of 4.12 g·mL^{-1} Fe, but the variation was more gradual. This phenomenon suggested a slightly lower influence of the surrounding fluid and Brownian motion on the NP flow in this concentration range. However, the quantity of NPs lost due to binding or deposition showed a decreasing quadratic correlation with NP size at the highest inlet mass concentration (5.24 g Fe). This phenomenon showed a dominance of particle properties and diffusion-dominated binding and

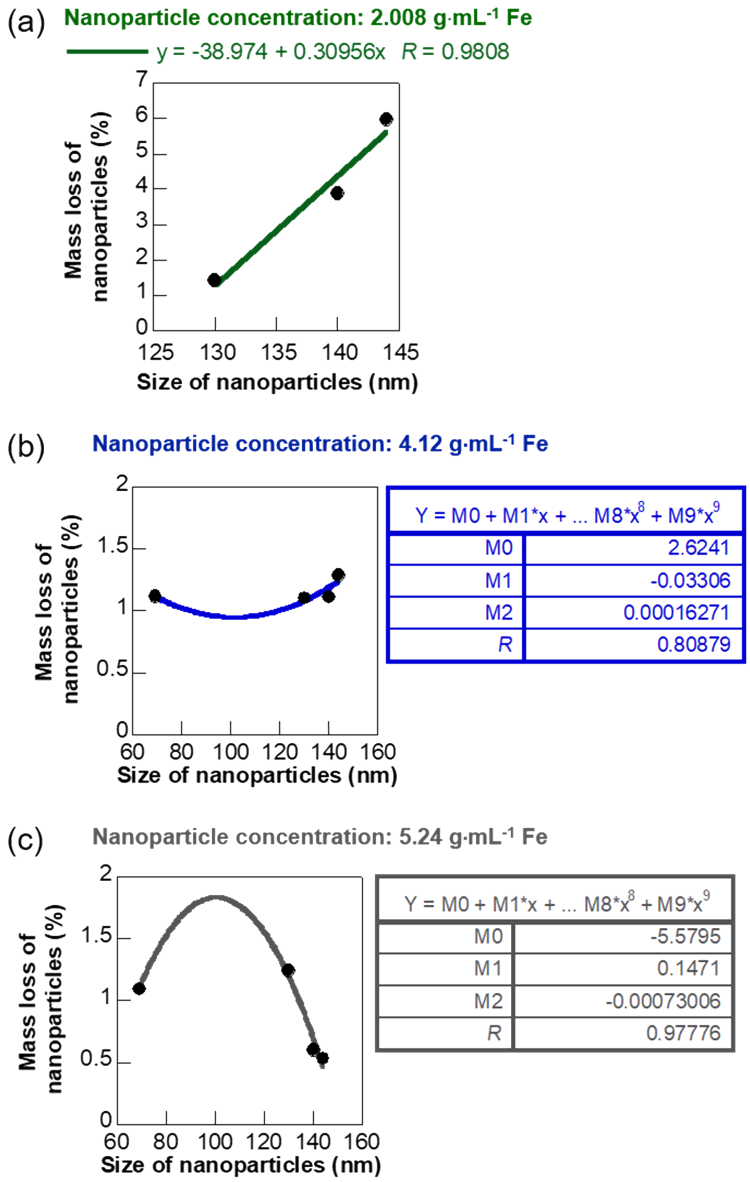

Figure 9: Plot showing the average mass loss percentage of NPs as a function of the size at three different inlet mass concentrations. (a) 2.008 g·mL^{-1} Fe, (b) 4.12 g·mL^{-1} Fe, and (c) 5.24 g·mL^{-1} Fe.

deposition at the highest concentration. Recently, Liu et al. and Decuzzi et al. reported computational models predicting a similar inverse correlation of NP adhesion with size in diffusion-driven flow [18,49]. Thus, the experimental mass loss trend at different concentrations helped us in understanding the different influences on NP flow at these regimes. We further enhanced the reliability of our approach to predict NP flow through physiologically relevant environments by coupling CFD simulation with the experimental results.

A computational analysis was conducted for nanofluid flow through an unbent cylindrical hydrogel channel to further confirm the applicability and accuracy of our experimental results. Two aqueous dispersions of 0.07 mmol PVP/0.005 mmol PEI-coated iron oxide NPs (size: 144 nm) of inlet mass concentrations of 4.12 g and 2.008 g and density of 5.24 g·mL^{-1} were investigated in these CFD simulations. A pointwise mesh generation software was used to generate the geometry and grid for simulating the nanofluid flow. Meshing, typically involves both surface and volume meshing and the generated surface grids greatly affect the quality of volume grids. Therefore, a finer grid scheme was required in the boundary layer to obtain an accurate flow field near the hydrogel channel. The first grid point spacing nearest the wall was

3.0×10^{-4} to achieve a desired value of y+ ≤ 1 value. Since the geometry is an unbent circular tube, the structured mesh is found suitable for the better convergence of simulations. A grid refinement study was made with several different structured meshes in each coordinate direction. The effect of altering the cell size was investigated with grids of 65, 129 and 193 cells in the stream-wise direction and 25, 49 and 97 cells in the radial direction. The computation began with a coarse grid (65 × 25 × 37) and was gradually refined in each coordinate direction until the changes observed in the solutions were insignificant. In this study, grid independency study showed that after the grid quantity reached a certain quantity, a larger number of grids did not affect the accuracy. 462,981 cells (129 × 97 × 37) was found to be the optimum mesh size. This was used as the grid number in our case with inlet, outlet, and no-slip wall of the hydrogel channel as the boundary conditions for the geometry. The nanofluid entered the hydrogel channel with an average velocity of 0.0051 $m \cdot s^{-1}$ and 0.0054 $m \cdot s^{-1}$ for which the Reynolds numbers based on the diameter of the tube were 120.1 and 127.1, respectively. The fluid flow within the hydrogel channel was considered laminar and Newtonian. Particle–particle interactions between erythrocytes and NPs and ligand–receptor binding have not been considered in this model as we first wanted to understand the flow of NPs through soft, biomimetic channels. In addition, particles that came in contact with the wall were assumed to be deposited. Figure 10 shows a representative result of the simulated laminar viscous flow through the hydrogel channel with fully-developed laminar entry flow. The results suggested that the NPs followed the streamlines of the flow field for this laminar flow regime. The computed pathlines, colored by velocity magnitude to visualize the NP flow for the total inlet mass of 4.12 g is presented in Figure 10. The mass losses computed on the refined meshes did not appreciably vary from those computed on the corresponding previous meshes (129 × 49 × 37 and 193 × 97 × 37), and it was safely assumed that the simulation results are grid independent. The computed mass losses of the particles are 1.341% and 6.253% for 4.12 g and 2.008 g inlet concentrations of NP fluid flow in hydrogel channels, respectively. It is observed that the numerical simulation results favorably agree with experimental data (1.286% and 5.96%) collected from the physical model that is reported in the manuscript.

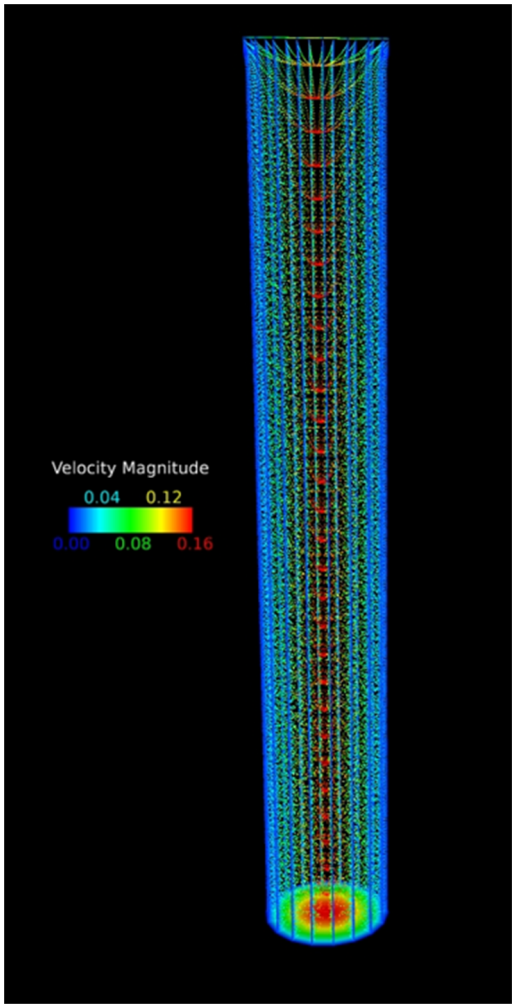

Figure 10: Velocity profile of NPs flowing through the hydrogel channel using CFD.

Conclusion

We developed a new in vitro technique coupling experimental flow studies and CFD analysis for predicting the velocity and binding affinity of the NPs through soft channels mimicking vascular networks. The biomimetic flow channels were synthesized via a new and facile fabrication route using pHEMA hydrogels. We also formed four different size and surface-controlled iron oxide NPs to serve as model nanoscale agents in the experimental analysis of NP flow under physiologically relevant conditions. These engineered experiments for understanding the mechanisms of NP transport in physiological microenvironments with pHEMA hydrogel channels are the first of its kind, to the best of our knowledge. We discovered that the flow trajectory of aqueous NP dispersions was greatly influenced by the Brownian forces, surrounding fluid, and the material of the flow channel at the lower mass concentrations, based on the flow experiments conducted at seven different concentrations for each of the four NP formulations. The NPs showed a diffusion-dominated trend in flow at the highest concentration. These results were in close confirmation with our CFD model for a fully developed laminar flow of NPs through the cylindrical hydrogel constructs. Therefore, this new in vitro method for predicting NP flow is a combination of both experimental and computational techniques targeted at practically relevant flow conditions for drug delivery. The reported in vitro

approach will be highly relevant at the preclinical stages to catalyze higher clinical success rates for drug delivery systems using NPs. Future efforts will be directed at synthesizing hydrogel flow channels with wider ranges of orifice size similar to the human vascular network for further validating the practical applicability of our in vitro NP flow analysis.

Experimental

Chemicals used

Reagents including 2-hydroxyethyl methacrylate (HEMA, Sigma-Aldrich, 97%), 1,2-ethanediol dimethacrylate (EGDMA, Sigma-Aldrich, 98%), ammonium persulfate ($(NH_4)_2S_2O_8$, AmPS, Sigma-Aldrich, 98%), sodium metabisulfite ($Na_2S_2O_5$, NaMBS, Fisher, 99.4%), inhibitor remover (Sigma-Aldrich), iron(III)-2,4-pentanedionate ($Fe(acac)_3$, Alfa Aesar), polyethyleneimine (PEI, Alfa Aesar, 60 kDa – 50 wt % aqueous solution), polyvinylpyrrolidone (PVP, TCI, 10 kDa, 99%), triethylene glycol (TREG, ACROS, 99%), sodium hydroxide (NaOH, Fisher, 99%), hydrochloric acid (HCl, Carolina Biological Supply, 6 M), and deionized water (DI, Fisher) were purchased from Sigma-Aldrich and Fisher and used without further purification.

Synthesis of pHEMA hydrogels

pHEMA hydrogels were formed via chemical cross-linking of two hydrophilic monomers, HEMA and EGDMA in a room temperature synthesis. Six different biocompatible pHEMA hydrogels were synthesized in this study by varying the quantity of DI water used during preparation of the hydrogels, keeping all the other parameters constant. In a typical synthesis, the EGDMA cross-linker was added at an amount of 3 mol % HEMA to six different aqueous solutions of HEMA (38.4 mmol, 5 g) prepared using different quantities of DI water (1–1.5 mL). The HEMA/EGDMA solutions were first mixed well via sonication (Branson 1800, Fisher) at room temperature for one hour. Then, the redox initiators, NaMBS and AmPS were added to the mixtures at a quantity of 1 wt % relative to HEMA. The solutions containing monomers, cross-linkers, and the initiators were stirred at room temperature for 2 h in plastic vials. Finally, the solutions were left to solidify under the chemical hood for 12 h to form the different hydrogels. The hydrogels were subsequently characterized via swelling studies and SEM to find the best suitable soft material for fabrication of flow paths that mimic physiologically relevant properties in terms of flexibility and smoothness.

Synthesis of iron oxide nanoparticles

In a manner closely related to the method in [34], four different iron oxide NP formulations were synthesized as models for NP-based drugs in this study to understand their flow behavior for drug delivery applications. A modified polyol method was used for the synthesis of the NPs. In a typical synthesis, the ligand mixture of PVP and PEI was heated to dissolution in the solvent TREG at 90 °C for 10 min. The iron precursor, $Fe(acac)_3$ was subsequently added to this reactant mixture and thermally decomposed at 290 °C for 1 h to form the iron oxide NPs. The different biocompatible iron oxide NP formulations were synthesized by varying the PVP/PEI ligand mixture (e.g., 0.09 mmol PVP/0.0017 mmol PEI, 0.07 mmol PVP/0.005 mmol PEI, 0.06 mmol PVP/0.007 mmol PEI, and 0.05 mmol PVP/0.008 mmol PEI), keeping all other parameters the same. All syntheses were conducted in a N_2 atmosphere inside a Schlenk line setup. The NP product was directly soluble in water and was further purified via high-speed centrifugation (Fisher Scientific) at 14000 rpm for 30 min to remove the excess organics as supernatants from the NP precipitates. The cleaning via centrifugation was conducted two times and the remaining NP precipitate was re-dissolved in DI water to obtain the final NP product of target concentration. Seven different concentrations ranging from 0.011 to 11.07 $g \cdot mL^{-1}$ were prepared for each type of iron oxide NPs in this study. All NP samples were mixed well via a 30 min sonication (Branson 1800, Fisher) at room temperature for subsequent use in the transport experiments.

Characterization

Characterization of hydrogels

The morphology and texture of the different hydrogels were characterized on a Hitachi S3400 SEM. Hydrogel samples for SEM imaging were prepared by cutting thin cross-sectional slices of 15 mm diameter. The samples were subsequently loaded on to the sample holder for SEM viewing.

The swelling behavior of each pHEMA hydrogel was investigated at 25 °C over a period of two days for pH values ranging from 1 to 13. Aqueous NaOH or HCl was mixed with DI water dropwise to obtain the desired pH values for the swelling characterization of the gels. A section of the respective hydrogel of weight 8 mg was cut and used as the sample for the respective swelling study. The initial weight (W_{dry}) of each gel was measured after drying the gels at room temperature under vacuum for three days. Each gel type was immersed in 13 different solutions (5 mL, pH 1–13) and the weights of the swollen hydrogels ($W_{swollen}$) were recorded at regular intervals after carefully removing the hydrogel from the solution and blotting the surface water with filter paper. The extent of swelling of the hydrogel (W_t) was measured using the following equation:

$$W_t\,(\%) = \left(\frac{W_{swollen} - W_{dry}}{W_{dry}} \right) \times 100.$$

All measurements of weight and degree of swelling of the hydrogels were reported as an average of three swelling studies. Finally, the dynamic swelling behavior of different pHEMA hydrogels synthesized in this study were graphically summarized using 95% student's *t* confidence interval as error bars. A combination of swelling behavior results and surface texture characterization of the gels via SEM imaging was used to select the best suitable hydrogel formulation to fabricate the flow channels mimicking physiological structures for the subsequent transport studies.

Characterization of iron oxide nanoparticles

A Litesizer 500 (Anton Paar) particle analyzer equipped with zeta potential capability was used to measure the hydrodynamic size, stability, and surface charge of aqueous dispersions of iron oxide NPs at pH 7 at room temperature (Figure S4, Supporting Information File 1). The aqueous NP samples were well dispersed via sonication for 15 min (Branson 1800, room temperature) prior to the measurements for representative results. The hydrodynamic sizes of each iron oxide NP sample were obtained as an average of three consecutive measurements for reliability. The zeta potential measurements were conducted at 25 °C using Omega cuvettes. Results for each NP sample were reported based on an average of four consecutive measurements.

Fabrication of hydrogel channels

3D flow channels were engineered using the chemically crosslinked pHEMA hydrogel formulation prepared with 1.3 mL DI water. A plastic syringe and tube assembly was constructed to fabricate the cylindrical hydrogel flowpath. The liquid pHEMA hydrogel mixture was transferred to a 3 mL plastic syringe (Fisher). The thin plastic tube of diameter 4 mm was inserted through the open end of the syringe to form the internal perforation and path for the flow of NPs. The hydrogel was left to solidify for 12 h within the syringe and tube assembly. The soft three-dimensional hydrogel structure was then removed from the syringe to form the channels for subsequent flow studies with iron oxide NPs.

Transport experiments

The flow studies were conducted with four different iron oxide NPs as model drug delivery agents and pHEMA hydrogel channels as model biomimetic vascular structures. Seven different mass concentrations ranging from 2.008 to 5.24 g were used for each NP type to experimentally investigate the velocity and mass loss of NPs during the flow. Tables S1–S4 (Supporting Information File 1) summarize the experimental conditions and results from the flow of NPs through biomimetic hydrogel channels. In a typical transport study, 1 mL aqueous dispersion of NPs was injected via a syringe for vertical flow through the straight hydrogel channel and collected in a vial at the end of the flow path. The mass of NPs was recorded both at the inlet and outlet of the flow path to determine the loss of NPs due to adherence to the walls of the channel. The mass loss of NPs for each flow experiment was measured as a difference of the mass of NPs injected at the inlet of the hydrogel channel and the mass of NPs collected at the outlet. Each experiment for a specific concentration of the NP type was repeated three times, based on which the average mass loss was reported for the specific case. The time taken for the NPs to flow through the length of the channel was recorded for subsequent measurement of velocity of the NPs. All experiments were conducted at room temperature using similar flowpaths constructed with the same formulation of pHEMA hydrogel for consistency.

Computational methods

CFD simulations for nanofluid flow and mass loss of NPs in flow through hydrogel channels were conducted via a previously reported method using our in-house Tenasi flow solver [34,50,51]. Table S5 and Table S6 in Supporting Information File 1 summarize some of the key parameters used for CFD analysis of NP flow through hydrogel channels.

Supporting Information

The supporting information includes the following items: swelling studies of the different pHEMA hydrogel formulations, Tables S1–S4 summarizing the experimental flow velocity and mass loss data for the four different iron oxide NPs, Table S5 and Table S6 describing the important parameters and NP properties used for the CFD simulations, and DLS size plot of representative iron oxide NP after prolonged storage at room temperature.

Supporting Information File 1

Additional experimental and computational data.
[https://www.beilstein-journals.org/bjnano/content/supplementary/2190-4286-11-22-S1.pdf]

Acknowledgements

We acknowledge UTC Chemical Engineering scanning electron facility for the SEM.

Funding

We thank the National Science Foundation (NSF) for the funding and support provided through the NSF REU Award #1852042. We also thank University of Tennessee Chattanooga's (UTC) summer faculty award for funding this project.

ORCID® iDs

Soubantika Palchoudhury - https://orcid.org/0000-0002-0696-0454

References

1. Ruoslahti, E.; Bhatia, S. N.; Sailor, M. J. *J. Cell Biol.* **2010,** *188,* 759–768. doi:10.1083/jcb.200910104
2. Schuerle, S.; Soleimany, A. P.; Yeh, T.; Anand, G. M.; Häberli, M.; Fleming, H. E.; Mirkhani, N.; Qiu, F.; Hauert, S.; Wang, X.; Nelson, B. J.; Bhatia, S. N. *Sci. Adv.* **2019,** *5,* eaav4803. doi:10.1126/sciadv.aav4803
3. Tran, S.; DeGiovanni, P.-J.; Piel, B.; Rai, P. *Clin. Transl. Med.* **2017,** *6,* 44. doi:10.1186/s40169-017-0175-0
4. Moghimi, S. M.; Hunter, A. C.; Murray, J. C. *FASEB J.* **2005,** *19,* 311–330. doi:10.1096/fj.04-2747rev
5. Yu, X.; Trase, I.; Ren, M.; Duval, K.; Guo, X.; Chen, Z. *J. Nanomater.* **2016,** *2016,* 1087250. doi:10.1155/2016/1087250
6. Shi, J.; Kantoff, P. W.; Wooster, R.; Farokhzad, O. C. *Nat. Rev. Cancer* **2017,** *17,* 20–37. doi:10.1038/nrc.2016.108
7. Jain, R. K.; Stylianopoulos, T. *Nat. Rev. Clin. Oncol.* **2010,** *7,* 653–664. doi:10.1038/nrclinonc.2010.139
8. Chauhan, V. P.; Stylianopoulos, T.; Boucher, Y.; Jain, R. K. *Annu. Rev. Chem. Biomol. Eng.* **2011,** *2,* 281–298. doi:10.1146/annurev-chembioeng-061010-114300
9. Nichols, J. W.; Bae, Y. H. *Nano Today* **2012,** *7,* 606–618. doi:10.1016/j.nantod.2012.10.010
10. Mak, I. W. Y.; Evaniew, N.; Ghert, M. *Am. J. Transl. Res.* **2014,** *6,* 114–118.
11. Charbe, N.; McCarron, P. A.; Tambuwala, M. M. *World J. Clin. Oncol.* **2017,** *8,* 21–36. doi:10.5306/wjco.v8.i1.21
12. Bae, H.; Puranik, A. S.; Gauvin, R.; Edalat, F.; Carrillo-Conde, B.; Peppas, N. A.; Khademhosseini, A. *Sci. Transl. Med.* **2012,** *4,* 160ps23. doi:10.1126/scitranslmed.3003688
13. Furlani, E. J.; Furlani, E. P. *J. Magn. Magn. Mater.* **2007,** *312,* 187–193. doi:10.1016/j.jmmm.2006.09.026
14. Furlani, E. P.; Ng, K. C. *Phys. Rev. E* **2006,** *73,* 061919. doi:10.1103/physreve.73.061919
15. Dogra, P.; Adolphi, N. L.; Wang, Z.; Lin, Y.-S.; Butler, K. S.; Durfee, P. N.; Croissant, J. G.; Noureddine, A.; Coker, E. N.; Bearer, E. L.; Cristini, V.; Brinker, C. J. *Nat. Commun.* **2018,** *9,* 4551. doi:10.1038/s41467-018-06730-z
16. Liu, Y.; Shah, S.; Tan, J. *Rev. Nanosci. Nanotechnol.* **2012,** *1,* 66–83. doi:10.1166/rnn.2012.1014
17. Ramezanpour, M.; Leung, S. S. W.; Delgado-Magnero, K. H.; Bashe, B. Y. M.; Thewalt, J.; Tieleman, D. P. *Biochim. Biophys. Acta, Biomembr.* **2016,** *1858,* 1688–1709. doi:10.1016/j.bbamem.2016.02.028
18. Tan, J.; Wang, S.; Yang, J.; Liu, Y. *Comput. Struct.* **2013,** *122,* 128–134. doi:10.1016/j.compstruc.2012.12.019
19. Dogra, P.; Butner, J. D.; Chuang, Y.-l.; Caserta, S.; Goel, S.; Brinker, C. J.; Cristini, V.; Wang, Z. *Biomed. Microdevices* **2019,** *21,* 40. doi:10.1007/s10544-019-0380-2
20. Lee, T.-R.; Choi, M.; Kopacz, A. M.; Yun, S.-H.; Liu, W. K.; Decuzzi, P. *Sci. Rep.* **2013,** *3,* 2079. doi:10.1038/srep02079
21. Angioletti-Uberti, S. *npj Comput. Mater.* **2017,** *3,* 48. doi:10.1038/s41524-017-0050-y
22. Huang, C.; Zhang, Y.; Yuan, H.; Gao, H.; Zhang, S. *Nano Lett.* **2013,** *13,* 4546–4550. doi:10.1021/nl402628n
23. Vácha, R.; Martinez-Veracoechea, F. J.; Frenkel, D. *Nano Lett.* **2011,** *11,* 5391–5395. doi:10.1021/nl2030213
24. Saltzman, W. M.; Radomsky, M. L. *Chem. Eng. Sci.* **1991,** *46,* 2429–2444. doi:10.1016/0009-2509(91)80036-x
25. McDougall, S. R.; Anderson, A. R. A.; Chaplain, M. A. J.; Sherratt, J. A. *Bull. Math. Biol.* **2002,** *64,* 673–702. doi:10.1006/bulm.2002.0293
26. Siepmann, J.; Peppas, N. *Adv. Drug Delivery Rev.* **2001,** *48,* 137–138. doi:10.1016/s0169-409x(01)00111-9
27. Shipley, R. J.; Chapman, S. J. *Bull. Math. Biol.* **2010,** *72,* 1464–1491. doi:10.1007/s11538-010-9504-9
28. Modok, S.; Scott, R.; Alderden, R. A.; Hall, M. D.; Mellor, H. R.; Bohic, S.; Roose, T.; Hambley, T. W.; Callaghan, R. *Br. J. Cancer* **2007,** *97,* 194–200. doi:10.1038/sj.bjc.6603854
29. Li, X. L.; Yao, K. L.; Liu, Z. L. *J. Magn. Magn. Mater.* **2008,** *320,* 1753–1758. doi:10.1016/j.jmmm.2008.01.041
30. Arabshahi, A.; Janus, J. M. *J. Spacecr. Rockets* **2004,** *41,* 469–472. doi:10.2514/1.4528
31. Arabshahi, A.; Taylor, L. K.; Whitfield, D. L. Uncle - Toward a comprehensive time-accurate incompressible Navier-Stokes flow solver. In *AIAA 33rd Aerospace Sciences Meeting,* Reno: NV, 1995. doi:10.2514/6.1995-50
32. Fullstone, G.; Wood, J.; Holcombe, M.; Battaglia, G. *Sci. Rep.* **2015,** *5,* 10649. doi:10.1038/srep10649
33. Furlani, E. P. *Materials* **2010,** *3,* 2412–2446. doi:10.3390/ma3042412
34. Palchoudhury, S.; Arabshahi, A.; Gharge, U.; Albattah, A.; George, O.; Foster, Y. *Phys. Lett. A* **2019,** *383,* 1615–1621. doi:10.1016/j.physleta.2019.02.020
35. Liu, J.; Zheng, H.; Poh, P. S. P.; Machens, H.-G.; Schilling, A. F. *Int. J. Mol. Sci.* **2015,** *16,* 15997–16016. doi:10.3390/ijms160715997
36. Ferreira, L.; Vidal, M. M.; Gil, M. H. *Int. J. Pharm.* **2000,** *194,* 169–180. doi:10.1016/s0378-5173(99)00375-0
37. Slaughter, B. V.; Khurshid, S. S.; Fisher, O. Z.; Khademhosseini, A.; Peppas, N. A. *Adv. Mater. (Weinheim, Ger.)* **2009,** *21,* 3307–3329. doi:10.1002/adma.200802106
38. Sarker, M. D.; Naghieh, S.; Sharma, N. K.; Chen, X. *J. Pharm. Anal.* **2018,** *8,* 277–296. doi:10.1016/j.jpha.2018.08.005
39. Yanagawa, F.; Sugiura, S.; Kanamori, T. *Regener. Ther.* **2016,** *3,* 45–57. doi:10.1016/j.reth.2016.02.007
40. Gulsen, D.; Chauhan, A. *J. Membr. Sci.* **2006,** *269,* 35–48. doi:10.1016/j.memsci.2005.06.024
41. Williams, H. R.; Trask, R. S.; Weaver, P. M.; Bond, I. P. *J. R. Soc., Interface* **2008,** *5,* 55–65. doi:10.1098/rsif.2007.1022
42. Palchoudhury, S.; Lead, J. R. *Environ. Sci. Technol.* **2014,** *48,* 14558–14563. doi:10.1021/es5037755
43. Gabe, I. T.; Gault, J. H.; Ross, J., Jr.; Mason, D. T.; Mills, C. J.; Schillingford, J. P.; Braunwald, E. *Circulation* **1969,** *40,* 603–614. doi:10.1161/01.cir.40.5.603
44. Klarhöfer, M.; Csapo, B.; Balassy, C.; Szeles, J. C.; Moser, E. *Magn. Reson. Med.* **2001,** *45,* 716–719. doi:10.1002/mrm.1096
45. Ivanov, K. P.; Kalinina, M. K.; Levkovich, Y. I. *Microvasc. Res.* **1981,** *22,* 143–155. doi:10.1016/0026-2862(81)90084-4
46. Tsoi, K. M.; MacParland, S. A.; Ma, X.-Z.; Spetzler, V. N.; Echeverri, J.; Ouyang, B.; Fadel, S. M.; Sykes, E. A.; Goldaracena, N.; Kaths, J. M.; Conneely, J. B.; Alman, B. A.; Selzner, M.; Ostrowski, M. A.; Adeyi, O. A.; Zilman, A.; McGilvray, I. D.; Chan, W. C. W. *Nat. Mater.* **2016,** *15,* 1212–1221. doi:10.1038/nmat4718
47. Ermak, D. L.; McCammon, J. A. *J. Chem. Phys.* **1978,** *69,* 1352–1360. doi:10.1063/1.436761
48. Mori, N.; Kumagae, M.; Nakamura, K. *Rheol. Acta* **1998,** *37,* 151–157. doi:10.1007/s003970050101

49. Decuzzi, P.; Godin, B.; Tanaka, T.; Lee, S.-Y.; Chiappini, C.; Liu, X.; Ferrari, M. *J. Controlled Release* **2010,** *141,* 320–327. doi:10.1016/j.jconrel.2009.10.014
50. Gruetzemacher, R., Numerical Simulation of Airflow in a CT-based Human Airway Model With Physiologically Appropriate Boundary Conditions, M.S. Thesis, University of Tennessee at Chattanooga, 2014.
51. Pankajakshan, R.; Mitchell, B. J.; Taylor, L. K. *Comput. Fluids* **2011,** *41,* 20–26. doi:10.1016/j.compfluid.2010.09.020

License and Terms

BEILSTEIN JOURNAL OF NANOTECHNOLOGY

Interactions at the cell membrane and pathways of internalization of nano-sized materials for nanomedicine

Valentina Francia‡, Daphne Montizaan‡ and Anna Salvati*

Review

Open Access

Address:
Groningen Research Institute of Pharmacy, University of Groningen, 9713AV Groningen, Netherlands

Email:
Anna Salvati* - a.salvati@rug.nl

* Corresponding author ‡ Equal contributors

Keywords:
cell receptors; drug targeting; endocytosis; nanoparticle corona; nanoparticle uptake

Beilstein J. Nanotechnol. **2020,** *11,* 338–353.
doi:10.3762/bjnano.11.25

Received: 30 September 2019
Accepted: 27 January 2020
Published: 14 February 2020

This article is part of the thematic issue "Engineered nanomedicines for advanced therapies".

Guest Editor: F. Baldelli Bombelli

Abstract

Nano-sized materials have great potential as drug carriers for nanomedicine applications. Thanks to their size, they can exploit the cellular machinery to enter cells and be trafficked intracellularly, thus they can be used to overcome some of the cellular barriers to drug delivery. Nano-sized drug carriers of very different properties can be prepared, and their surface can be modified by the addition of targeting moieties to recognize specific cells. However, it is still difficult to understand how the material properties affect the subsequent interactions and outcomes at cellular level. As a consequence of this, designing targeted drugs remains a major challenge in drug delivery. Within this context, we discuss the current understanding of the initial steps in the interactions of nano-sized materials with cells in relation to nanomedicine applications. In particular, we focus on the difficult interplay between the initial adhesion of nano-sized materials to the cell surface, the potential recognition by cell receptors, and the subsequent mechanisms cells use to internalize them. The factors affecting these initial events are discussed. Then, we briefly describe the different pathways of endocytosis in cells and illustrate with some examples the challenges in understanding how nanomaterial properties, such as size, charge, and shape, affect the mechanisms cells use for their internalization. Technical difficulties in characterizing these mechanisms are presented. A better understanding of the first interactions of nano-sized materials with cells will help to design nanomedicines with improved targeting.

Introduction

Nano-sized materials are widely studied in nanomedicine for their potential use as drug carriers, in imaging, and for diagnostic purposes [1-3]. Because of their size, they can interact with cells in similar ways as other nano-sized objects, such as proteins, cholesterol particles, and virus particles. These natural nano-sized objects are usually recognized by specific cell receptors at the plasma membrane and they are internalized by cells using the cell endocytic machinery [4]. Similarly, engineered nano-sized materials can exploit the cellular machinery to be internalized by cells. In fact, since the cell mem-

brane blocks diffusion of complexes larger than ca. 1 kDa, nano-sized materials, such as nanomedicines, are transported into cells using energy-dependent mechanisms, unlike many small drugs currently present on the market [5]. This enables nanomedicines to potentially overcome problems associated with the passive diffusion of small molecular drugs through cell membranes, such as their indiscriminate internalization in different cell types and organs, which is often associated with side effects [6]. Additionally, nanomedicines can encapsulate different types of hydrophilic and hydrophobic drugs, and they can be designed to control their release profile [7]. Several other characteristics of nanomaterials such as size, material, shape, surface charge, hydrophobicity, roughness, and elasticity can be tailored in order to meet various needs [3,8]. This high engineering potential can be exploited to control the distribution and behaviour of nanomedicines in biological environments. By tuning nanomedicine design, parameters such as serum–protein interactions, sequestration by the immune system, blood circulation time, biodistribution, and cellular recognition and internalization can be tailored [1-3,7,8]. Moreover, the surface of nanomedicines can be engineered by introducing functional groups to reduce clearance and increase biodistribution, as well as for active targeting purposes [1,2,9,10]. In fact, nanomedicines can be engineered to interact with specific cell receptors, opening up new strategies for targeting specific cell types and organs [9-12]. Despite this high engineering potential, active targeting remains one of the major challenges for nanomedicine success [13,14], and so far only few targeted nanomedicines are currently present in the market, even if several are in clinical trials [6].

Recent advances in the field have shown the complexity of achieving targeted uptake by specific cells. For example, it has been shown that the biomolecules adsorbing on the nanoparticles once they are introduced in biological environments and the resulting corona can screen the targeting moieties [15,16]. At the same time, it has emerged that the corona itself can be recognized by receptors at the cell membrane [17,18] and that this initial recognition can affect the mechanism that cells use for the internalization of the nanoparticles [18]. However, several aspects of the initial recognition of nano-sized materials by cell receptors and of the molecular mechanisms leading to their uptake and intracellular processing are still unclear [19-21]. A better understanding of these processes can help to design smarter nanomedicines and to achieve better targeting [22].

Within this context, in this review we will summarise the current understanding of the very first steps of the interactions of nano-sized materials with cells, with a particular focus on the initial recognition at the cell membrane and the following mechanisms of internalization by cells. We discuss these aspects in relation to the application of nano-sized materials for nanomedicine. Challenges in characterizing these first events will be illustrated, together with a brief description of the known endocytic pathways in cells.

Review

1 Interactions of nano-sized materials at the cell surface and recognition by cell receptors

1.1 Active targeting

The first steps in nanoparticle–cell interactions are those happening at the cell surface, including the adhesion of nanoparticles to the cell membrane and the potential interaction with cell receptors (Figure 1). In order to control and affect these first events, nano-sized carriers can be modified with targeting moieties, such as peptides, proteins, or antibodies to specifically recognize receptors on the cell surface to achieve active

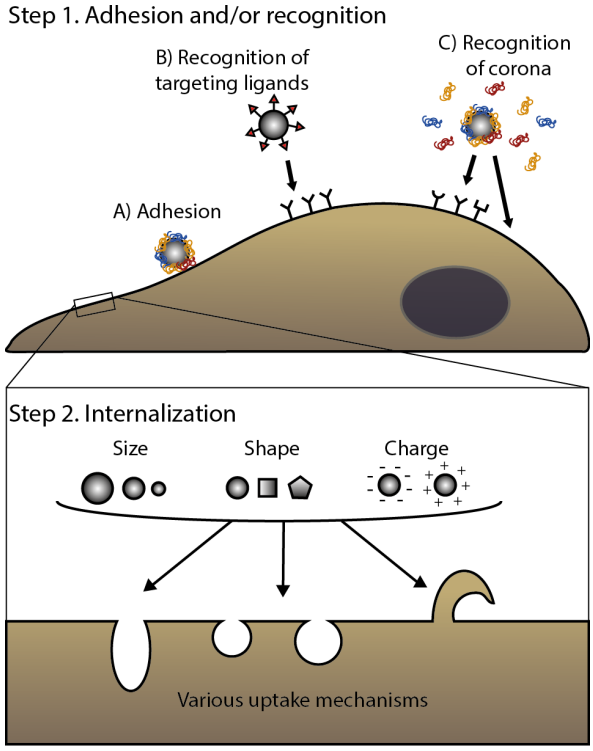

Figure 1: Interaction of nano-sized materials at the cell surface. First, nanoparticles adhere at the plasma membrane (A) and/or are recognized by cell receptors. Recognition can be achieved via targeting moieties, in the case of targeted nanomedicines (B) but also via the biomolecular corona (C) [10,11,17,18]. Secondly, nano-sized objects are internalized via various mechanisms (here illustrated by different shapes in the cell membrane or a membrane protrusion). However, we do not know yet how nanomaterial properties (such as size, shape, charge, as illustrated in the figure) affect or determine the mechanism cells use for the internalization [7,19-22].

targeting [9-12]. These surface-functionalized nanomaterials should be internalized preferentially by cells that overexpress the targeted receptors. Examples of targeting moieties often exploited in nanomedicine are transferrin and folate, which target tumour cells overexpressing the corresponding receptors [23,24], or hyaluronic acid, which directs nanocarriers to CD44-overexpressing tumour cells [25], among many others. While many new targeted nanomedicines are developed, just few of them are currently present on the market [6]. In fact, achieving efficient targeting in vivo remains a crucial challenge for drug delivery and recently the debate on the success of nanomedicine for delivering drugs to their target has been very active [26-28].

Indeed, it is difficult to design nanoparticles that achieve specific targeting [7,9,29]. This is not only because a better understanding of the factors controlling the very first interactions of nano-sized materials with live cells is still needed (as we discuss here), but also because of challenges related to nanoparticle design and presentation of the targeting moiety. For instance, chemical coupling can affect the binding affinity of the targeting ligand to its receptor [30]. Moreover, it is difficult to control the targeting ligand density and its orientation. Both factors are important for the recognition by cell receptors and can affect cellular uptake [31,32]. Several reviews have summarized these and other similar challenges in the surface functionalization of nano-sized drug carriers to achieve targeting [33-35]. Ideally, by better controlling the early interactions with cells, nanomedicines should be recognized by the desired receptors and be trafficked intracellularly to their target.

1.2 Corona formation

Another complication in achieving targeting is the formation of the biomolecular corona. When a nanomedicine (or any nano-sized material) comes in contact with a biological environment (for example, blood, interstitial fluids, or extracellular matrices) after administration, its surface is rapidly covered by various biomolecules leading to the formation of a corona [36-39]. It has been shown that, in some cases, the presence of the corona can mask the targeting moieties grafted on the nanoparticle surface, preventing recognition by cell receptors [15,16,40]. Corona formation can affect not only the targeting ability, but also particle size, stability, and overall surface properties [36]. Recent guidelines have started to highlight the importance of testing nanomedicines in the presence of relevant biological media in order to take corona effects into account [41].

Several strategies have been developed to try to reduce protein adsorption and corona formation. This can be achieved for instance by grafting hydrophilic polymers such as polyethylene glycol (PEG) on the surface of nanomedicines, or by introducing zwitterionic modifications to make nanomaterials almost neutral [42-45]. These modifications reduce the amount of biomolecules bound on the surface of nanomedicines after administration (though it has been shown that PEGylated surfaces can still adsorb proteins [46,47]) and usually also lead to decreased uptake by cells.

At the same time, the corona confers a new biological identity to nanomaterials and can affect the way nanomedicines are recognized and processed by cells [3,7,8,20,21,36,48]. Biomolecules present in the corona can, per se, have targeting capabilities towards particular receptors [17,18,49-52]. For example, apolipoprotein B and immunoglobulin G in the corona of 100 nm silica nanoparticles incubated with human serum were found to interact with their corresponding receptors, low-density lipoprotein receptor and Fc-gamma receptor I, respectively [17]. Similarly, lipid nanoparticles were efficiently targeted to the hepatocytes upon adsorption of apoE on their surface following administration [52,53]. Thus, controlling the corona composition can possibly provide new ways to control the initial interactions of nano-sized materials with cells.

The corona composition depends on nanoparticle physicochemical characteristics, such as size, shape, charge, hydrophobicity, rigidity and surface characteristics [3,7,8,48,54]. By changing these properties, the corona composition might be tuned to contain components that bind to specific cell surface receptors and initiate internalization [17,49,55-57]. Similarly, artificial coronas can be formed to achieve recognition by specific receptors. For instance, Tonigold and colleagues have shown that pre-adsorbed antibodies, which could be seen as a form of pre-formed corona, kept, at least partially, their targeting ability in the presence of serum [40].

From a broader perspective, the effects of the corona on the interactions of nanoparticles with cells are being more and more recognized [41,58,59]. For example, multiple attempts have been made in trying to predict how the presence of the corona affects targeting of nanomedicines [60,61]. Similarly, it is known that the corona composition changes not only with nanoparticle properties [3,7,8,48,54], but also depending on serum origin [62,63], serum preparation [63-65], serum concentration [18,66,67] or health status [68,69]. However, many more facets of corona effects on nanoparticle–cell interactions still need to be understood, and even more so if one aims to exploit the corona for targeting.

Similarly, how receptor interactions affect the subsequent internalisation is also not known. Nano-sized materials and nanomedicines may interact only with one type of receptor (Figure 2A) or with multiple receptors at the same time

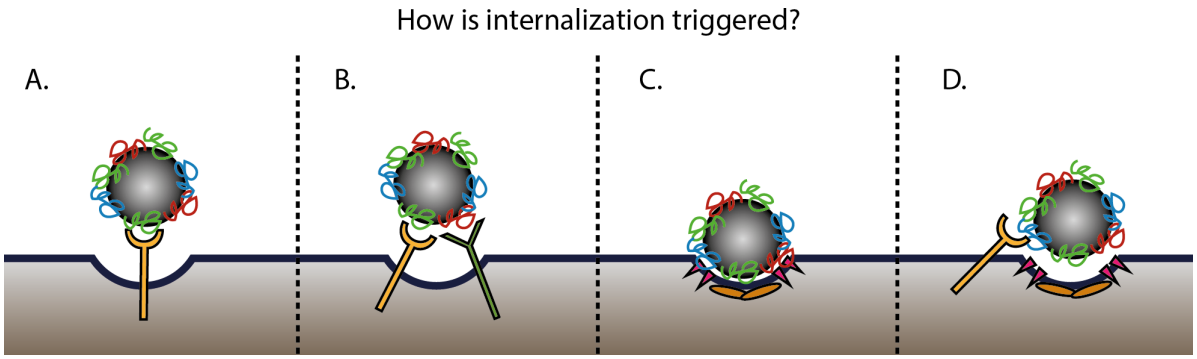

Figure 2: Scheme of possible scenarios that can occur at the cell surface, resulting in nanoparticle uptake. Nanoparticles or their corona can be recognized by one (A) or multiple types of receptors (B), and the recognition by receptors triggers nanoparticle uptake. Alternatively, the adhesion of the nanoparticle to the cell surface may induce internalization without receptor engagement (C) or the receptor is only involved in the initial adhesion of the nanoparticle, then uptake is triggered by different mechanisms, possibly induced by the nanoparticle itself (D).

(Figure 2B), and the recognition by cell receptors triggers uptake. It might be that only high-affinity interactions contribute to the entry, or that internalization occurs after receptor clustering. Alternatively, internalization may happen without recognition by specific receptors (often referred to as unspecific binding and unspecific uptake), possibly triggered by the nano-sized object itself (Figure 2C). Another possibility is that the recognition by cell receptors is involved only in the initial adhesion to the cell membrane, but not in the internalization (Figure 2D). A combination of all these different possibilities may as well be present. In all cases, addressing these open questions relative to the first interactions at the cell surface is required to understand how to achieve a more efficient targeting of nanomedicines.

2 Internalization

After the very first interactions at the plasma membrane, most nano-sized materials are internalized by cells [19-22]. Many questions are still open on how the initial interactions at the cell membrane affect the mechanisms cells use for the subsequent internalization. For instance, does receptor recognition trigger internalization via the same pathway used for its physiological ligands? Or do the receptors mediate just the initial adhesion and is it the nano-sized material itself that triggers its own internalization, perhaps by other ways (as also illustrated in Figure 2D)? How are uptake efficiency and the mechanisms of internalization modulated by the type of receptor engaged and/or by the initial interactions at the cell membrane? These are examples of the many questions that the field needs to address in order to control nanomedicine design to achieve the desired outcomes at cell level.

In the following sections, we will summarize key aspects of the main mechanisms of cellular internalization, i.e., endocytosis. Then, examples of works trying to understand how nanomaterial properties affect the mechanisms of uptake by cells are presented to illustrate the complexity of outcomes observed and the difficulties in drawing conclusions.

2.1 Pathways of endocytosis in cells

Cells developed several mechanisms of endocytosis in order to select and sort different cargoes to their intracellular destination [70,71]. Although these mechanisms differ strongly, they also share a series of common features. As discussed by Johannes and colleagues [72,73], common features required for uptake to occur are (Figure 3):

- a specific lipid composition of the cell membrane at the site of endocytosis (such as the presence of sphingolipids or cholesterol) [70,72,74-76],
- cargo recognition at the cell membrane (receptor-mediated or not) and capture (into coated vesicles or specific carriers) [72,73],
- membrane bending, which occurs through different mechanisms, including the insertion of hydrophobic protein motifs in the membrane, local recruitment of membrane-bending domains, or scaffolding by proteins (the classic example being clathrin) [72,73,77,78], and
- scission of the endocytic vesicle, which can be guided by actin, dynamin and/or other proteins [79-83].

The specific details of each of these steps in the various endocytic mechanisms are extensively discussed in different excellent and specialized reviews [70,71], including some focused on the mechanisms of endocytosis of nanomedicines [19,21,22,85,86]. Here, we briefly summarize some of their key aspects.

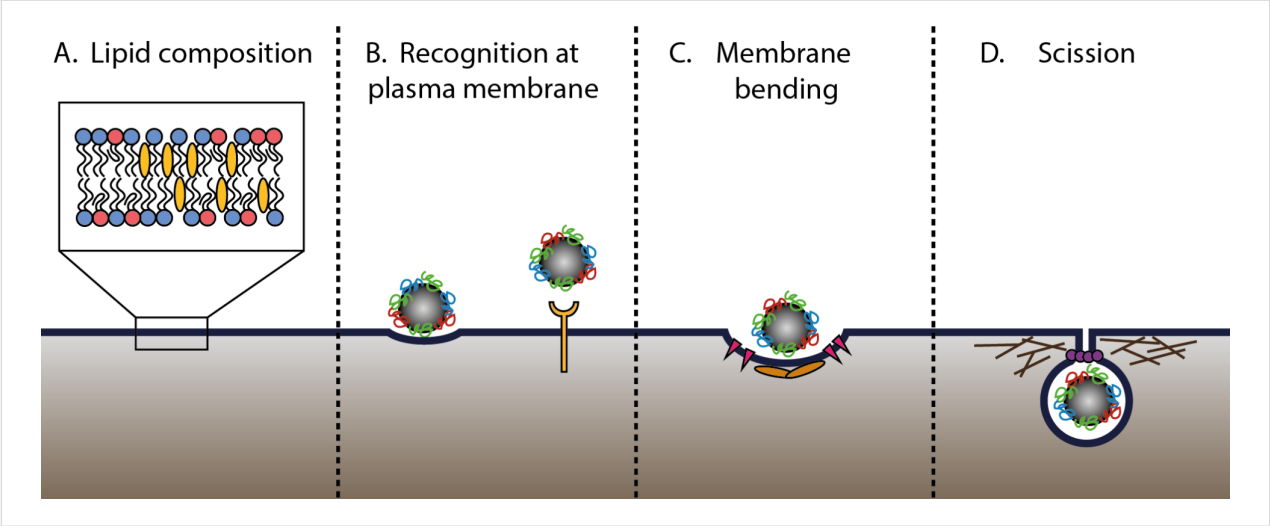

Figure 3: Common features of endocytic pathways [73]. Endocytosis requires a specific cell membrane composition at the site of uptake (A) [72,74-76] and starts with the recognition of the cargo at the cell membrane (B). Subsequently, membrane bending takes place to form a vesicle (C) [72,73,77,78,84]. Lastly, the vesicle is cleaved from the cell membrane via different mechanisms, which can involve various cellular components (e.g., actin and dynamin, here depicted as lines and circles, respectively) (D) [79,80].

One of the most studied endocytic mechanism is clathrin-mediated endocytosis (CME). CME is a form of receptor-mediated endocytosis that is used for the internalization of various biomolecules among which low density lipoprotein for cholesterol uptake and transferrin for iron uptake. After binding of the ligand to its receptor, clathrin, the main actor in CME, is recruited at the cell membrane together with several other proteins and assembles around the forming vesicle to form a clathrin-coated pit. The GTP-binding protein dynamin is then required for the scission of the clathrin-coated pit to form an endocytic vesicle. Although it was thought to be non-essential for CME [87], there are indications suggesting that actin filaments are also involved in the scission [88,89] and especially in the uptake of larger objects [90] via this pathway.

Next to CME, several clathrin-independent endocytic (CIE) pathways have been described [71,91,92]. One of these pathways is macropinocytosis, which cells use to internalize larger volumes of extracellular fluids and solutes. In macropinocytosis, extracellular fluids are engulfed by membrane ruffles and protrusions. Formation of these ruffles requires actin nucleation and in some cells also cholesterol [93,94].

Another frequently studied clathrin-independent pathway is the so-called caveolae-mediated endocytosis. Caveolae are 50–80 nm sized cup-shaped invaginations of the plasma membrane, consisting of lipid rafts enriched in cholesterol and sphingolipids, and coated with caveolins [95-97]. Endocytosis of these invaginations can be both receptor-dependent and -independent and requires actin and dynamin [96,98,99]. Nevertheless, the role of caveolae in endocytosis is currently being debated. Some suggest that caveolae are involved in transcytosis in endothelial cells [100]. According to this hypothesis, caveolae rapidly detach from the apical side of the membrane and fuse with the basal one, or directly form transient pores in thin endothelial cells [101]. Other studies have shown that in many cell types caveolae are normally not involved in endocytosis, but are stable invaginations present at the cell surface [102,103], and only undergo endocytosis upon stimulation [96,104].

Apart from these mechanisms, phagocytosis is a form of receptor-mediated endocytosis of large particles (above 0.5 µm), which requires the involvement of the cytoskeleton for membrane rearrangements. Professional phagocytic cells of the immune system use it to internalize pathogens [105]. However, it has emerged that also non-specialized phagocytic cells can internalize large particles [71,106].

Finally, other clathrin-independent endocytic mechanisms have been described. These include pathways mediated by flotillins, ADP-ribosylation factor 6, endophilins, or tubular structures called clathrin-independent carriers (CLICs). The exact machinery involved in these various clathrin-independent pathways is still investigated and the involvement of components like actin, cholesterol, or dynamin is often debated [71,91,92].

Overall, endocytosis is highly complex and still a very active field of research. This is one of the factors which makes the characterization of the mechanisms by which nano-sized materials enter cells challenging.

2.2 Endocytosis of nanoparticles: effects of material properties

As we described in the Introduction, the capacity of nano-sized objects to interact with the cellular machinery has opened up the possibility of using nano-sized materials to deliver drugs to their target. Nanoparticle design can be tailored to target specific cell types or pathways. Size, charge, shape [107], hydrophobicity [108], rigidity [109,110], roughness [111] and surface functionalization [43,112] of nanomaterials are all parameters that in principle can be tuned in order to affect the pathway of internalization of nano-sized materials and ideally also to direct them towards a specific intracellular location. Still, there is not yet an agreement in the scientific community on the pathways that nano-sized materials, including nanomedicines, use to enter cells [21,22,113,114]. A better characterization of the mechanisms that cells use to internalize nano-sized materials can potentially help us to understand how to tune their design to achieve the desired outcomes at cell level [22] (as we illustrate in Figure 1).

Nanoparticle size: A fundamental parameter that seems to affect the pathway of internalization of nanoparticles is their size. A general observation is that the uptake efficiency of nanomaterials decreases with increasing particle size [115-117], probably because of the extensive membrane rearrangements needed for internalization of larger objects [59,118,119]. Some studies have compared explicitly the uptake efficiency of particles of different sizes trying to define the optimal size for uptake [120-123]. Additionally, it is commonly believed that most nanoparticles with sizes compatible with the size of clathrin-coated pits enter through clathrin-mediated endocytosis [115,124] and, vice versa, that larger ones do not. It was thought that the geometry and 3D structure of clathrin would not allow it. However, results opposing this general idea about size have also been reported [116,125-127]. For example, in one study using HEK293 cells, spherical polystyrene nanoparticles of 100 nm were internalized through actin-dependent but clathrin-independent processes, and vice versa, 200 nm nanoparticles entered by clathrin-mediated endocytosis [127]. Similarly, the uptake of 500 nm PRINT particles was reduced by chlorpromazine (an inhibitor of clathrin-dependent endocytosis) [125] and it has been shown that larger particles could be internalized in pits coated with plaques of clathrin [128-130].

These studies, selected just as examples among many others, already highlight the difficulties in establishing a general rule on how nanoparticle size affects uptake. Similarly, it was believed that particles larger than 200 nm could not be internalized by non-phagocytic cells [7], while opposite observations are often reported. For instance, even cubic nanoparticles of 3 μm could be internalized by HeLa cells [125].

Moreover, the effects of nanoparticle size on the mechanism of uptake may be different in different cell types. For example, it has been shown that murine RAW 264.7 macrophages have a higher uptake efficiency for carboxylated polystyrene nanoparticles compared to human endothelial HCMEC or epithelial HeLa cells [131]. In another study using carboxylated polystyrene nanoparticles of different sizes in different cell types, actin was required for the internalization of nanoparticles of 200 nm, but not for those of 40 nm in 1321N1 astrocytes. Instead, in lung epithelial A549 cells, for both nanoparticle sizes, the uptake was not dependent on actin [132]. Unfortunately, so far, only a few studies have investigated in a systematic way how different cell types internalize nanoparticles of different size, making it difficult to draw conclusions [132-134].

Nanoparticle charge: Apart from size, charge is another easily tunable parameter that can greatly influence the behaviour of nanoparticles in biological media [135] and on cells [136]. In general, positively charged nanoparticles seem to be internalized more efficiently than neutral and negatively charged particles [125,137,138]. However, there are other examples showing exactly the opposite [139]. It has also been reported that uptake increases with charge density (either positive or negative) [140]. Regarding the pathway of internalization, some studies suggested that positively charged nanomaterials are predominantly internalized through clathrin-mediated endocytosis, with a fraction of particles utilizing macropinocytosis, while negatively charged nanoparticles are more likely to use a cholesterol-dependent mechanism for their internalization [21,141]. Contradicting results were reported in which clathrin-mediated endocytosis did not seem to be a relevant pathway for neither positively nor negatively charged nanomaterials, while cholesterol-mediated uptake seems to be equally important for both [142]. Similarly, another study suggested that both negatively and positively charged poly(ethylene glycol)-D,L-polylactic acid particles entered, at least partially, by clathrin-mediated endocytosis and macropinocytosis [143].

It is important to mention that many studies investigating the effect of charge or other nanomaterial properties on cellular interactions were performed in the absence of proteins from biological fluids such as serum. This represents a further issue since the charge of nanomaterials tends towards neutrality upon corona formation, once they are applied in a biological environment. Thus, nanoparticles that in water possess different charges might end up having all a similar charge, close to neutrality upon exposure to biological media [135]. Because of this, it is important to determine whether some of the described charge-related effects disappear once the nanomaterials are applied in a biological environment.

Nanoparticle shape: Another tunable parameter that can influence nanoparticle–cell interactions is shape. Simulations indicated that based on the energy required for membrane bending, the uptake would be the highest for spheres followed by cubes, then rods, and lastly discs [144]. Nevertheless, a recent in vitro study using gold particles, showed that the number of internalized particles was decreasing from rod to cubic, to spherical, to prism-shaped nanoparticles [145]. Often the effect of shape is studied by changing nanoparticle aspect ratio. Most of these studies showed that the uptake is higher when the aspect ratio is smaller [120,146,147]. This could be explained by the higher energy required to wrap a lipid membrane around a nanoparticle with high aspect ratio [148]. However, also in relation to this aspect, conflicting results were found in which cross-linked poly(ethylene glycol) hydrogels or mesoporous silica particles with higher aspect ratio were internalized quicker and more than those with low aspect ratio [125,149]. A few studies have investigated the effect of nanoparticle shape not only on uptake efficiency but also on the endocytic mechanisms involved in uptake [125,134,150]. Cylindric cationic poly(ethylene glycol) hydrogels with two different aspect ratios (1 and 3) were both taken up by HeLa cells by a combination of clathrin-mediated and caveolae-mediated endocytosis (based on cholesterol and tyrosine kinase dependence) [125]. On the other hand, in another study, the entry of cylindric, worm-like, and spherical silica particles in A549 and RAW264.7 cells was independent of cholesterol. Uptake of spherical silica particles was mainly clathrin-dependent, while internalization of worm-like and cylindric silica was primarily microtubule-dependent [134].

Similar studies on the effect of shape on the mechanism of internalization are challenging because of different complicating factors. Firstly, changing the shape also affects the dimensions of the nanomaterial. This means that to compare uptake of differently shaped objects, either the volume, maximum diameter, or a combination of the dimensions should be kept constant. Secondly, non-spherical objects can interact with the cell membrane with different orientation. Thus, depending on the orientation when interacting with the cell membrane, the contact area between the nano-sized object and the cell surface differs. It is thought that in these cases different mechanisms are then triggered based on the orientation of the nanoparticles [134,150]. This might, at least in part, explain why multiple pathways seem to be involved in the uptake of non-spherical nanomaterials.

Nanoparticle rigidity: Recently, there is a high interest in the effect of the rigidity of nanoparticles on the interactions at cellular level [109,110]. Simulations showed a higher energy barrier for the internalization of soft and easily deformable nanoparticles than for that of rigid particles [151,152]. However, nanoparticle–cell interactions cannot be described solely by the energy barrier required to bend the lipid membrane. Other biological factors are also involved, possibly explaining the contrasting results on the effect of rigidity on uptake [110,151-154]. Indeed, while some studies found higher uptake for the more rigid particles [151,153,155], another study suggested that softer particles enter in higher numbers [154]. In this latter study, it was also shown that the more rigid nanomaterial (Young's modulus above 13.8 MPa) was internalized by cells at least in part via clathrin-mediated endocytosis, as opposed to the softer material [154]. Similarly, in another study, lipid covered PGLA particles with different Young's modulus values in the range of gigapascals were also partially internalized by clathrin-mediated endocytosis [151].

Understanding how nanoparticle properties affect the mechanism of uptake by cells: Overall, the examples presented show that the effect of tunable nanoparticle parameters such as size, charge, and shape on the mechanisms of uptake by cells is often ambiguous. To further illustrate this complexity, Table 1 summarizes the few preliminary observations, which we discussed in this section, including references, which support and contrast them. We emphasize that Table 1 is far from complete and the observations included have been selected solely as an example to illustrate the complexity of often contrasting outcomes reported in literature.

A reason of this ambiguity and complexity might be that multiple mechanisms are triggered at the same time, as suggested by several studies [18,115,132,156-159]. It could also be that, besides the generally studied classical routes such as clathrin- and caveolae-mediated endocytosis, other less well-known pathways of internalization are involved in the uptake of nanomedicines, such as those briefly described in Section 2.1. Recently, computer simulations and in vitro studies of nanoparticle–membrane interactions have shown that the surface of nanomaterials can in itself induce several changes at the plasma membrane, by determining sol–gel transitions in the lipid bilayer and impairing lipid lateral diffusion [160,161], or by inducing bending of the plasma membrane [162,163], as already observed with certain viruses [164]. These changes in membrane dynamics might as well be a trigger for the endocytosis of nanoparticles via alternative mechanisms, which are not yet fully characterized.

Extracting conclusions from the available literature is additionally complicated by the fact that most studies have used different conditions with respect to many factors such as, for instance, the presence, source, and concentration of serum, but also the nanomaterial used, the cell type, and the methods applied to characterize the pathways involved. These differ-

Table 1: The table summarizes few selected examples that we discuss in Section 2.2 of observations reported in literature on the effect of nanoparticle properties on the mechanism of uptake by cells. References to literature with supporting as well as opposing observations are included (also discussed in Section 2.2). We emphasize that the table is far from complete and includes only a few examples, selected solely to illustrate the complexity of outcomes. In fact, we consider the observations listed still as preliminary, as also illustrated by apparently contrasting results in the opposing studies included (in most cases performed using different conditions and systems).

reported observation or preliminary statement	supporting studies	opposing studies
nanoparticles uptake efficiency decreases with increasing size	[107-109]	[112]
nanoparticles up to 100 nm in diameter enter through clathrin-dependent endocytosis	[107,113]	[114-116]
non-phagocytic cells can only internalize materials up to 200 nm	[8]	[107,114]
positively charged nanoparticles are internalized more efficiently than negatively charged or neutral nanoparticles	[114,124,125,128,130]	[126,127,129]
positively charged nanoparticles enter (at least partially) through clathrin-dependent endocytosis	[21,128,130]	[129]
nano-sized objects with small aspect ratios are internalized more efficiently	[112,133,134]	[114,136]
more rigid nanoparticles enter more efficiently than softer nanoparticles	[139,141,143]	[142]

ences clearly lead to different outcomes and apparently conflicting results. Only in a few cases, systematic studies using a series of nanomaterials of well-defined properties have been performed in order to try to disentangle the effect of multiple nanomaterial properties on the cellular uptake and on other biological effects [145,165]. Unfortunately, still no clear predictions can be made on how certain nanoparticle properties affect uptake efficiency and the mechanisms involved, and more work along these lines will be required [145,165]. Recent debates in the nanomedicine field pushed the community to address the issue of reproducibility and the development of standardized procedure in nanomedicine testing and application [166,167]. Similar efforts may help to reach a better understanding of how nanomaterial properties affect the mechanism of uptake by cells.

3 Intracellular fate

Another important aspect to consider for nanomedicine applications is the final fate of nano-sized materials following internalization. A recent review has discussed this aspect in more detail [85]. Regardless of the route of entry, many studies report that most nano-sized materials travel via the endosomes until reaching their final localization in the cell, which in most cases has been shown to be the lysosomal compartment [168,169]. In the lysosomes, nano-sized objects, including nanomedicines, may be degraded and release their content, if biodegradable, or may accumulate and persist [122]. While this can be very useful when the target is the lysosomes, it is well known that lysosomal accumulation constitutes an ulterior barrier for the delivery of drugs to any other intracellular target [85,86]. This has led to the development of strategies to induce escape from the endosomal compartment, including – among others – via the so-called “proton sponge effect” [170,171]. Materials capable to induce this proton sponge effect started to find their application in vivo only recently [172]. Several other strategies are being developed, including some inspired by viruses and bacteria capable to travel to other intracellular locations [173-176]. Several reviews fully focused on endo-lysosomal escape have summarised current efforts in this direction [174-177].

Another open question that is debated in the field is whether nano-sized materials, including nanomedicines, can end up in compartments other than the lysosomes. For example, in several reports it appears that nanoparticles can be transcytosed across endothelial cells [178,179]. However, the existence of a dedicated pathway, such as caveolae-mediated endocytosis, for transcytosis of macromolecules is still debated in the endocytosis community [96,102-104].

Understanding how cells recognize and internalize nano-sized materials can help us to address also questions regarding the intracellular fate of nano-sized materials and to define strategies to direct nanomedicines towards different intracellular locations or to promote drug release in cells.

4 Challenges in studying endocytosis of nano-sized materials in vitro

While studying the interactions between nanomaterials and cells is extremely challenging to perform in vivo, in vitro studies can help to unravel the mechanisms involved in their uptake. For such studies, the nanoparticle dispersion, the cell culture conditions, the cell line investigated, and the methods used to characterize the uptake mechanisms are all crucial. Unfortunately, there are often no agreements on how to perform uptake studies in a standardized way. Recently, this problem has gotten much attention in the nanomedicine field [166,167,180]. Within the nanosafety community, dedicated to the study of potential hazards of nanotechnologies, several efforts have been focused

on the establishment of standardized procedures for nanomaterial handling and for cell interaction studies in order to ensure quality in nanosafety testing [181-183]. Some of the knowledge gained there could be helpful also in developing similar standards for studies aimed at characterizing how nano-sized objects, including nanomedicines, enter cells. In the following sections, we will describe some technical challenges concerning in vitro studies of the endocytosis of nano-sized materials.

4.1 Nanoparticle dispersion in biological media: agglomeration and corona formation

One of the most important aspects to consider when studying nanoparticle interactions with cells, as well as when characterizing the mechanism for their internalization, is the stability over time and the potential agglomeration of nanoparticles in biological media. In fact, agglomeration can strongly affect the corona composition, the interaction with cells, as well as the pathways of internalization [59,184,185]. Thus, it is important to characterize the nanoparticle dispersion in the biological media in which the nanomedicine will be applied, and to monitor potential agglomeration and stability over time.

Additionally, studies in which nanoparticles are incubated on cells without serum or other biological fluids may lead to conclusions that are not relevant for biological applications and in vivo studies, because they do not take into account corona-related effects [186-189]. Given the impact of the corona on both recognition and internalization of nano-sized materials, it is important not only to include some biological fluid to allow corona formation, but also to define the appropriate conditions for each application [18,62-65,68,69]. For instance, there are many in vitro studies in which nanoparticles are tested on human cell lines using culture media containing a low percentage of foetal bovine serum [132,133,190-193]. Not only the percentage of serum, but also the species from which the serum originates, as well the use of serum heat inactivation, or the choice of anticoagulant used to prepare plasma are some of the factors affecting corona formation and potentially also the subsequent mechanisms of internalization [18,62-65,68,69]. Similar considerations should be made when characterizing the uptake of nanomedicines administered via other routes. In these cases biological fluids other than serum should be used [185,194].

On a more complex level, it is also known that the corona composition evolves over time [195-197]. Recent studies from Chan and colleagues are trying to explore how the corona composition affects the biological interactions of nanoparticles by performing mass spectrometry screenings and by developing computational models to predict the evolution of their protein corona [60,61,198]. Other studies are trying to understand not only whether certain biomolecules are present on the nanoparticle surface, but also their orientation, which might influence their recognition by cell receptors [17,199]. In order to take into account corona-related effects on nanoparticle interactions with cells, a precise workflow to characterize the corona composition has been proposed, which might help to compare different studies and to find a correlation between corona composition, serum composition and, ultimately, uptake mechanisms [41].

4.2 Cell models

The cell type investigated and its tissue organization are other important factors that can affect the uptake mechanisms of nanoparticles. For example, not all pathways are active in all cell types: HepG2 cells have no endogenous caveolin-1, and therefore they are unable to internalize nanoparticles by caveolae-mediated endocytosis [200]. Similarly, many in vitro studies use immortalized or cancer cell lines, such as HEK293 or HeLa cells, which are easy to transfect and culture. However, these cells can behave quite differently in comparison to primary cells or cells isolated directly from tissues of patients. While, on one hand, the use of primary cells can be recommended, on the other hand, it is also a well-known obstacle for a detailed study of cellular pathways. Most primary cells are difficult to transfect and require interaction with other cell types for their proper differentiation [201-203]. Another important factor known to affect uptake pathways by cells in vitro is the differentiation of cells into barriers and the resulting cell polarization [159]. Uptake by cells grown to a polarized cell barrier is, in fact, different than uptake by the same cells when grown isolated or simply confluent [22,159].

Apart from simpler cell cultures and cell barriers, many advances have been made in the development of cellular models that can better reflect the more complex organization of cells in vivo. Models such as organoids or spheroids, which use one or multiple cell lines organized into 3D structures, have been developed and are likely to become useful also for nanomedicine uptake studies.

4.3 Methods to characterize uptake mechanisms

Further difficulties in the study of the uptake mechanisms of nano-sized materials, such as nanomedicines, arise from the fact that endocytosis represents a complex cellular process with many molecules, feedback loops, and signalling cascades involved. The endocytosis field is still very active and constantly progressing [71,77,204]. Many processes and molecular details of these pathways are still unknown. For instance, in recent years much attention has been paid to non-canonical pathways of endocytosis [71,91,92], which are often more difficult to study, but which might as well constitute possible routes for the internalization of nano-sized materials. In light of this

complexity, the tendency within the nanomedicine field to classify the pathways of internalization of drug carriers as merely macropinocytosis, clathrin-dependent, or caveolae-dependent is for sure an oversimplification. Furthermore, the classification and description of the different mechanisms of uptake by cells are often revised and corrected in the endocytosis field, as research progresses. This is an example of the challenges that interdisciplinary fields such as nanomedicine need to face. In this context, a closer connection with the cell biology and endocytosis communities is desirable [113].

Typical experiments to characterize uptake mechanisms are carried out by altering cellular pathways using different methods in order to determine their involvement in nanoparticle uptake. However, it is well established that perturbation of a cellular mechanism might as well lead to the alteration of other mechanisms. Therefore, when performing such studies, it is important to have appropriate controls to verify the effect of the selected treatment on the pathway of interest and exclude potential artefacts of this kind [22,133,158].

The selection of appropriate controls poses further challenges. For example, fluorescently labelled low-density lipoprotein and transferrin can be used as markers for clathrin-mediated endocytosis [205,206], dextran as a fluid phase marker for phagocytosis and for the CLEE/GEEC pathway [193], and LacCer (C5-lactosylceramide) for cholesterol-dependent uptake [133,207]. However, while cholera toxin and SV40 were previously used as markers of caveolae-mediated endocytosis [95], they have been found to enter cells using preferentially other routes and thus should not be used anymore as markers for this pathway [208-210]. Furthermore, selecting an appropriate control marker can be challenging for several of the more recently described clathrin- and caveolae- independent pathways.

Next to the difficulties related to the choice of control markers, the fact that the endocytic pathways are strongly interconnected and that some components take part in multiple mechanisms also complicates further the interpretation of results. As an example of this, cytochalasin D, an inhibitor of actin polymerization [211], has often been used to test the involvement of macropinocytosis and phagocytosis in the uptake of nanomaterials. However, actin has been shown to be important also for other mechanisms, including clathrin-mediated endocytosis and caveolae-mediated endocytosis. Hence, perturbing the activity of actin affects multiple pathways at the same time [212].

Several techniques can be used for studying the endocytic mechanisms of nano-sized materials, each one with its advantages and drawbacks [22,133]. Among those, RNA interference (RNAi) is often used to shut down the expression of a single protein or even a single isoform. However, the complete depletion of the protein of interest after RNAi requires at least 48–96 h and during this time cells can adapt, for example by upregulating other proteins of the same family or other pathways. Moreover, RNAi does not guarantee the total depletion of a protein from the cell, and in some cases the partial reduction of a protein is not sufficient to fully inhibit its function [22].

Apart from RNAi, so far, many studies on the uptake of nano-sized materials make use of transport inhibitors, whose action on cells is instead very fast. However, some of these inhibitors lack specificity, they might interfere with multiple pathways, and they can cause cellular toxicity [22,133,158,213]. In contrast to these approaches to block uptake pathways, other strategies can be found in which proteins are instead overexpressed, in order to eventually detect an increase in nanoparticle uptake [17]. Nevertheless, also these methods might lead to artefacts, since the overexpression might induce the activation of a pathway that may not be active under physiological conditions [22,214]. Furthermore, some proteins act as heterodimers or in concert with other molecular partners, thus their overexpression might not produce any detectable effect if not combined with the overexpression of those partners as well. Overexpression is often used to allow for the visualization of fluorescently tagged molecules by microscopy. However, also this might lead to additional artefacts. For example, it has been shown that overexpression of GFP-tagged caveolin 1 (CAV1-GFP), the main constituent of caveolae-mediated endocytosis, leads to the creation of artefacts, such as the observation of a specialized endosomal compartment for caveolae, the “caveosome” [214].

Recent advances in cellular imaging and gene editing could overcome some of these issues. For instance, the use of stably transfected cell lines might be a good solution when the total depletion of a protein is required to shut down a pathway (often difficult to achieve with techniques such as RNAi), but also for expressing labelled proteins at physiological levels, thereby avoiding the aforementioned artefacts connected to overexpression. The creation of specific transgenic cell lines to study nanoparticle uptake has been greatly enhanced by gene editing techniques such as CRISPR/CAS9, which allows to cut genes in a much more specific and efficient way than with previously existing methods [215,216]. Similar methodologies can improve our understanding of the involvement of specific proteins in the internalization of nanoparticles.

Other recently developed techniques that are available in cell biology to characterize pathways and that have not yet been used to study the uptake of nano-sized materials

may provide novel insights into this difficult question. For instance, so-called OMICS approaches based on large-scale proteomics and full genome screenings could be of particular use [217-219]. While most of the "classical" methods mentioned so far require previous knowledge on the mechanisms of uptake by cells, a reverse approach could allow for discovering novel targets not yet associated with the endocytosis of nanomaterials.

Overall, it is clear that none of these different methods, alone, can provide a full picture of the mechanisms that nano-sized materials use to interact with cells since they all display different advantages and pitfalls [22,133,158]. The combination of different techniques and the application of proper controls could help us to gain a better knowledge of the endocytic processes involved in the uptake of nano-sized materials.

Conclusion

Nanomedicine aims at delivering drugs more efficiently to their target to treat diseases. Designing the properties of nano-sized materials to be able to control the interactions and the behaviour at cell level is one of the key steps required for successful targeting. Nanomedicines can be functionalized by the addition of targeting moieties to be recognized by specific receptors on the targeted cells. However, achieving this initial recognition for active targeting still holds many challenges.

Additionally, it has emerged that when nano-sized materials are applied in a biological environment, corona formation affects the initial recognition by cells, as well as the following mechanisms of internalization. However, many aspects of the initial recognition of nano-sized materials by cell receptors still need to be understood. Similarly, how the initial recognition affects the following mechanisms of internalization remains to be elucidated and an agreement in the scientific community about the pathways that nano-sized materials, such as nanomedicines, use to enter cells is still missing.

Several factors complicate these studies and make it difficult to draw clear conclusions. The field of endocytosis is still very active and novel pathways are still being described. At the same time there are limits and challenges regarding the many different methods available to characterize uptake mechanisms and the lack of standardized procedures makes it difficult to draw conclusions from available studies. Using a combination of methods and appropriate controls to study the mechanisms by which cells internalize nano-sized materials could potentially help us to understand how these are affected by nanomaterial properties. In this way, nanomedicine design could be tuned to achieve the desired outcomes at cell level and engineer nanomaterials for more efficient drug targeting.

Funding

This work was funded by the European Research Council (ERC) under the European Union's Horizon 2020 Research and Innovation Programme under grant agreement no. 637614 (NanoPaths). A.S. kindly acknowledges the University of Groningen for additional funding (Rosalind Franklin Fellowship).

ORCID® iDs

Valentina Francia - https://orcid.org/0000-0003-4911-6832
Daphne Montizaan - https://orcid.org/0000-0001-8514-0317
Anna Salvati - https://orcid.org/0000-0002-9339-0161

References

1. Wolfram, J.; Ferrari, M. *Nano Today* **2019,** *25,* 85–98. doi:10.1016/j.nantod.2019.02.005
2. Peer, D.; Karp, J. M.; Hong, S.; Farokhzad, O. C.; Margalit, R.; Langer, R. *Nat. Nanotechnol.* **2007,** *2,* 751–760. doi:10.1038/nnano.2007.387
3. Shi, J.; Kantoff, P. W.; Wooster, R.; Farokhzad, O. C. *Nat. Rev. Cancer* **2017,** *17,* 20–37. doi:10.1038/nrc.2016.108
4. Sandvig, K.; van Deurs, B. *Gene Ther.* **2005,** *12,* 865–872. doi:10.1038/sj.gt.3302525
5. Bareford, L. M.; Swaan, P. W. *Adv. Drug Delivery Rev.* **2007,** *59,* 748–758. doi:10.1016/j.addr.2007.06.008
6. Bobo, D.; Robinson, K. J.; Islam, J.; Thurecht, K. J.; Corrie, S. R. *Pharm. Res.* **2016,** *33,* 2373–2387. doi:10.1007/s11095-016-1958-5
7. Petros, R. A.; DeSimone, J. M. *Nat. Rev. Drug Discovery* **2010,** *9,* 615–627. doi:10.1038/nrd2591
8. Duan, X.; Li, Y. *Small* **2013,** *9,* 1521–1532. doi:10.1002/smll.201201390
9. Chauhan, V. P.; Jain, R. K. *Nat. Mater.* **2013,** *12,* 958–962. doi:10.1038/nmat3792
10. Allen, T. M. *Nat. Rev. Cancer* **2002,** *2,* 750–763. doi:10.1038/nrc903
11. Villaverde, G.; Baeza, A. *Beilstein J. Nanotechnol.* **2019,** *10,* 168–181. doi:10.3762/bjnano.10.16
12. Bertrand, N.; Wu, J.; Xu, X.; Kamaly, N.; Farokhzad, O. C. *Adv. Drug Delivery Rev.* **2014,** *66,* 2–25. doi:10.1016/j.addr.2013.11.009
13. Danhier, F.; Feron, O.; Préat, V. *J. Controlled Release* **2010,** *148,* 135–146. doi:10.1016/j.jconrel.2010.08.027
14. Sykes, E. A.; Chen, J.; Zheng, G.; Chan, W. C. W. *ACS Nano* **2014,** *8,* 5696–5706. doi:10.1021/nn500299p
15. Salvati, A.; Pitek, A. S.; Monopoli, M. P.; Prapainop, K.; Bombelli, F. B.; Hristov, D. R.; Kelly, P. M.; Åberg, C.; Mahon, E.; Dawson, K. A. *Nat. Nanotechnol.* **2013,** *8,* 137–143. doi:10.1038/nnano.2012.237
16. Hadjidemetriou, M.; Al-Ahmady, Z.; Mazza, M.; Collins, R. F.; Dawson, K.; Kostarelos, K. *ACS Nano* **2015,** *9,* 8142–8156. doi:10.1021/acsnano.5b03300
17. Lara, S.; Alnasser, F.; Polo, E.; Garry, D.; Lo Giudice, M. C.; Hristov, D. R.; Rocks, L.; Salvati, A.; Yan, Y.; Dawson, K. A. *ACS Nano* **2017,** *11,* 1884–1893. doi:10.1021/acsnano.6b07933
18. Francia, V.; Yang, K.; Deville, S.; Reker-Smit, C.; Nelissen, I.; Salvati, A. *ACS Nano* **2019,** *13,* 11107–11121. doi:10.1021/acsnano.9b03824

19. Duncan, R.; Richardson, S. C. W. *Mol. Pharmaceutics* **2012,** *9,* 2380–2402. doi:10.1021/mp300293n
20. Oh, N.; Park, J. H. *Int. J. Nanomed.* **2014,** *9* (Suppl. 1), 51–63. doi:10.2147/ijn.s26592
21. Sahay, G.; Alakhova, D. Y.; Kabanov, A. V. *J. Controlled Release* **2010,** *145,* 182–195. doi:10.1016/j.jconrel.2010.01.036
22. Iversen, T.-G.; Skotland, T.; Sandvig, K. *Nano Today* **2011,** *6,* 176–185. doi:10.1016/j.nantod.2011.02.003
23. Sudimack, J.; Lee, R. J. *Adv. Drug Delivery Rev.* **2000,** *41,* 147–162. doi:10.1016/s0169-409x(99)00062-9
24. Daniels, T. R.; Bernabeu, E.; Rodríguez, J. A.; Patel, S.; Kozman, M.; Chiappetta, D. A.; Holler, E.; Ljubimova, J. Y.; Helguera, G.; Penichet, M. L. *Biochim. Biophys. Acta, Gen. Subj.* **2012,** *1820,* 291–317. doi:10.1016/j.bbagen.2011.07.016
25. Mattheolabakis, G.; Milane, L.; Singh, A.; Amiji, M. M. *J. Drug Targeting* **2015,** *23,* 605–618. doi:10.3109/1061186x.2015.1052072
26. Wilhelm, S.; Tavares, A. J.; Dai, Q.; Ohta, S.; Audet, J.; Dvorak, H. F.; Chan, W. C. W. *Nat. Rev. Mater.* **2016,** *1,* 16014. doi:10.1038/natrevmats.2016.14
27. McNeil, S. E. *Nat. Rev. Mater.* **2016,** *1,* 16073. doi:10.1038/natrevmats.2016.73
28. Lammers, T.; Kiessling, F.; Ashford, M.; Hennink, W.; Crommelin, D.; Storm, G. *Nat. Rev. Mater.* **2016,** *1,* 16069. doi:10.1038/natrevmats.2016.69
29. Danhier, F. *J. Controlled Release* **2016,** *244,* 108–121. doi:10.1016/j.jconrel.2016.11.015
30. Olivier, V.; Meisen, I.; Meckelein, B.; Hirst, T. R.; Peter-Katalinic, J.; Schmidt, M. A.; Frey, A. *Bioconjugate Chem.* **2003,** *14,* 1203–1208. doi:10.1021/bc034077z
31. Aubin-Tam, M.-E.; Hwang, W.; Hamad-Schifferli, K. *Proc. Natl. Acad. Sci. U. S. A.* **2009,** *106,* 4095–4100. doi:10.1073/pnas.0807299106
32. Kogot, J. M.; Parker, A. M.; Lee, J.; Blaber, M.; Strouse, G. F.; Logan, T. M. *Bioconjugate Chem.* **2009,** *20,* 2106–2113. doi:10.1021/bc900224d
33. Muro, S. *J. Controlled Release* **2012,** *164,* 125–137. doi:10.1016/j.jconrel.2012.05.052
34. Mahon, E.; Salvati, A.; Baldelli Bombelli, F.; Lynch, I.; Dawson, K. A. *J. Controlled Release* **2012,** *161,* 164–174. doi:10.1016/j.jconrel.2012.04.009
35. Ruoslahti, E.; Bhatia, S. N.; Sailor, M. J. *J. Cell Biol.* **2010,** *188,* 759–768. doi:10.1083/jcb.200910104
36. Monopoli, M. P.; Åberg, C.; Salvati, A.; Dawson, K. A. *Nat. Nanotechnol.* **2012,** *7,* 779–786. doi:10.1038/nnano.2012.207
37. Mahmoudi, M.; Lynch, I.; Ejtehadi, M. R.; Monopoli, M. P.; Bombelli, F. B.; Laurent, S. *Chem. Rev.* **2011,** *111,* 5610–5637. doi:10.1021/cr100440g
38. Cedervall, T.; Lynch, I.; Lindman, S.; Berggard, T.; Thulin, E.; Nilsson, H.; Dawson, K. A.; Linse, S. *Proc. Natl. Acad. Sci. U. S. A.* **2007,** *104,* 2050–2055. doi:10.1073/pnas.0608582104
39. Schöttler, S.; Landfester, K.; Mailänder, V. *Angew. Chem., Int. Ed.* **2016,** *55,* 8806–8815. doi:10.1002/anie.201602233
40. Tonigold, M.; Simon, J.; Estupiñán, D.; Kokkinopoulou, M.; Reinholz, J.; Kintzel, U.; Kaltbeitzel, A.; Renz, P.; Domogalla, M. P.; Steinbrink, K.; Lieberwirth, I.; Crespy, D.; Landfester, K.; Mailänder, V. *Nat. Nanotechnol.* **2018,** *13,* 862–869. doi:10.1038/s41565-018-0171-6
41. Chetwynd, A. J.; Wheeler, K. E.; Lynch, I. *Nano Today* **2019,** *28,* 100758. doi:10.1016/j.nantod.2019.06.004
42. Harris, J. M.; Martin, N. E.; Modi, M. *Clin. Pharmacokinet.* **2001,** *40,* 539–551. doi:10.2165/00003088-200140070-00005
43. Howard, M. D.; Jay, M.; Dziubla, T. D.; Lu, X. *J. Biomed. Nanotechnol.* **2008,** *4,* 133–148. doi:10.1166/jbn.2008.021
44. García, K. P.; Zarschler, K.; Barbaro, L.; Barreto, J. A.; O'Malley, W.; Spiccia, L.; Stephan, H.; Graham, B. *Small* **2014,** *10,* 2516–2529. doi:10.1002/smll.201303540
45. Safavi-Sohi, R.; Maghari, S.; Raoufi, M.; Jalali, S. A.; Hajipour, M. J.; Ghassempour, A.; Mahmoudi, M. *ACS Appl. Mater. Interfaces* **2016,** *8,* 22808–22818. doi:10.1021/acsami.6b05099
46. Schöttler, S.; Becker, G.; Winzen, S.; Steinbach, T.; Mohr, K.; Landfester, K.; Mailänder, V.; Wurm, F. R. *Nat. Nanotechnol.* **2016,** *11,* 372–377. doi:10.1038/nnano.2015.330
47. Dai, Q.; Walkey, C.; Chan, W. C. W. *Angew. Chem., Int. Ed.* **2014,** *53,* 5093–5096. doi:10.1002/anie.201309464
48. Lundqvist, M.; Stigler, J.; Elia, G.; Lynch, I.; Cedervall, T.; Dawson, K. A. *Proc. Natl. Acad. Sci. U. S. A.* **2008,** *105,* 14265–14270. doi:10.1073/pnas.0805135105
49. Caracciolo, G.; Cardarelli, F.; Pozzi, D.; Salomone, F.; Maccari, G.; Bardi, G.; Capriotti, A. L.; Cavaliere, C.; Papi, M.; Laganà, A. *ACS Appl. Mater. Interfaces* **2013,** *5,* 13171–13179. doi:10.1021/am404171h
50. Deng, Z. J.; Liang, M.; Monteiro, M.; Toth, I.; Minchin, R. F. *Nat. Nanotechnol.* **2011,** *6,* 39–44. doi:10.1038/nnano.2010.250
51. Gilleron, J.; Querbes, W.; Zeigerer, A.; Borodovsky, A.; Marsico, G.; Schubert, U.; Manygoats, K.; Seifert, S.; Andree, C.; Stöter, M.; Epstein-Barash, H.; Zhang, L.; Koteliansky, V.; Fitzgerald, K.; Fava, E.; Bickle, M.; Kalaidzidis, Y.; Akinc, A.; Maier, M.; Zerial, M. *Nat. Biotechnol.* **2013,** *31,* 638–646. doi:10.1038/nbt.2612
52. Akinc, A.; Querbes, W.; De, S.; Qin, J.; Frank-Kamenetsky, M.; Jayaprakash, K. N.; Jayaraman, M.; Rajeev, K. G.; Cantley, W. L.; Dorkin, J. R.; Butler, J. S.; Qin, L.; Racie, T.; Sprague, A.; Fava, E.; Zeigerer, A.; Hope, M. J.; Zerial, M.; Sah, D. W. Y.; Fitzgerald, K.; Tracy, M. A.; Manoharan, M.; Koteliansky, V.; de Fougerolles, A.; Maier, M. A. *Mol. Ther.* **2010,** *18,* 1357–1364. doi:10.1038/mt.2010.85
53. Akinc, A.; Maier, M. A.; Manoharan, M.; Fitzgerald, K.; Jayaraman, M.; Barros, S.; Ansell, S.; Du, X.; Hope, M. J.; Madden, T. D.; Mui, B. L.; Semple, S. C.; Tam, Y. K.; Ciufolini, M.; Witzigmann, D.; Kulkarni, J. A.; van der Meel, R.; Cullis, P. R. *Nat. Nanotechnol.* **2019,** *14,* 1084–1087. doi:10.1038/s41565-019-0591-y
54. Tenzer, S.; Docter, D.; Rosfa, S.; Wlodarski, A.; Kuharev, J.; Rekik, A.; Knauer, S. K.; Bantz, C.; Nawroth, T.; Bier, C.; Sirirattanapan, J.; Mann, W.; Treuel, L.; Zellner, R.; Maskos, M.; Schild, H.; Stauber, R. H. *ACS Nano* **2011,** *5,* 7155–7167. doi:10.1021/nn201950e
55. Fleischer, C. C.; Payne, C. K. *J. Phys. Chem. B* **2014,** *118,* 14017–14026. doi:10.1021/jp502624n
56. Zhang, Z.; Wang, C.; Zha, Y.; Hu, W.; Gao, Z.; Zang, Y.; Chen, J.; Zhang, J.; Dong, L. *ACS Nano* **2015,** *9,* 2405–2419. doi:10.1021/nn505166x
57. Prapainop, K.; Witter, D. P.; Wentworth, P., Jr. *J. Am. Chem. Soc.* **2012,** *134,* 4100–4103. doi:10.1021/ja300537u
58. Gaspar, R. *Nat. Nanotechnol.* **2013,** *8,* 79–80. doi:10.1038/nnano.2013.11
59. Nel, A. E.; Mädler, L.; Velegol, D.; Xia, T.; Hoek, E. M. V.; Somasundaran, P.; Klaessig, F.; Castranova, V.; Thompson, M. *Nat. Mater.* **2009,** *8,* 543–557. doi:10.1038/nmat2442
60. Lazarovits, J.; Sindhwani, S.; Tavares, A. J.; Zhang, Y.; Song, F.; Audet, J.; Krieger, J. R.; Syed, A. M.; Stordy, B.; Chan, W. C. W. *ACS Nano* **2019,** *13,* 8023–8034. doi:10.1021/acsnano.9b02774

61. Walkey, C. D.; Olsen, J. B.; Song, F.; Liu, R.; Guo, H.; Olsen, D. W. H.; Cohen, Y.; Emili, A.; Chan, W. C. W. *ACS Nano* **2014,** *8,* 2439–2455. doi:10.1021/nn406018q
62. Pisani, C.; Rascol, E.; Dorandeu, C.; Gaillard, J.-C.; Charnay, C.; Guari, Y.; Chopineau, J.; Armengaud, J.; Devoisselle, J.-M.; Prat, O. *PLoS One* **2017,** *12,* e0182906. doi:10.1371/journal.pone.0182906
63. Schöttler, S.; Klein, K.; Landfester, K.; Mailänder, V. *Nanoscale* **2016,** *8,* 5526–5536. doi:10.1039/c5nr08196c
64. Mirshafiee, V.; Kim, R.; Mahmoudi, M.; Kraft, M. L. *Int. J. Biochem. Cell Biol.* **2016,** *75,* 188–195. doi:10.1016/j.biocel.2015.11.019
65. Lesniak, A.; Campbell, A.; Monopoli, M. P.; Lynch, I.; Salvati, A.; Dawson, K. A. *Biomaterials* **2010,** *31,* 9511–9518. doi:10.1016/j.biomaterials.2010.09.049
66. Monopoli, M. P.; Walczyk, D.; Campbell, A.; Elia, G.; Lynch, I.; Baldelli Bombelli, F.; Dawson, K. A. *J. Am. Chem. Soc.* **2011,** *133,* 2525–2534. doi:10.1021/ja107583h
67. Partikel, K.; Korte, R.; Mulac, D.; Humpf, H.-U.; Langer, K. *Beilstein J. Nanotechnol.* **2019,** *10,* 1002–1015. doi:10.3762/bjnano.10.101
68. Hajipour, M. J.; Laurent, S.; Aghaie, A.; Rezaee, F.; Mahmoudi, M. *Biomater. Sci.* **2014,** *2,* 1210. doi:10.1039/c4bm00131a
69. Corbo, C.; Molinaro, R.; Tabatabaei, M.; Farokhzad, O. C.; Mahmoudi, M. *Biomater. Sci.* **2017,** *5,* 378–387. doi:10.1039/c6bm00921b
70. Doherty, G. J.; McMahon, H. T. *Annu. Rev. Biochem.* **2009,** *78,* 857–902. doi:10.1146/annurev.biochem.78.081307.110540
71. Ferreira, A. P. A.; Boucrot, E. *Trends Cell Biol.* **2018,** *28,* 188–200. doi:10.1016/j.tcb.2017.11.004
72. Johannes, L.; Mayor, S. *Cell* **2010,** *142,* 507–510. doi:10.1016/j.cell.2010.08.007
73. Johannes, L.; Parton, R. G.; Bassereau, P.; Mayor, S. *Nat. Rev. Mol. Cell Biol.* **2015,** *16,* 311–321. doi:10.1038/nrm3968
74. Graham, T. R.; Kozlov, M. M. *Curr. Opin. Cell Biol.* **2010,** *22,* 430–436. doi:10.1016/j.ceb.2010.05.002
75. Posor, Y.; Eichhorn-Grünig, M.; Haucke, V. *Biochim. Biophys. Acta, Mol. Cell Biol. Lipids* **2015,** *1851,* 794–804. doi:10.1016/j.bbalip.2014.09.014
76. Johannes, L.; Wunder, C.; Shafaq-Zadah, M. *J. Mol. Biol.* **2016,** *428,* 4792–4818. doi:10.1016/j.jmb.2016.10.027
77. McMahon, H. T.; Boucrot, E. *J. Cell Sci.* **2015,** *128,* 1065–1070. doi:10.1242/jcs.114454
78. McMahon, H. T.; Gallop, J. L. *Nature* **2005,** *438,* 590–596. doi:10.1038/nature04396
79. Boucrot, E.; Pick, A.; Çamdere, G.; Liska, N.; Evergren, E.; McMahon, H. T.; Kozlov, M. M. *Cell* **2012,** *149,* 124–136. doi:10.1016/j.cell.2012.01.047
80. Simunovic, M.; Manneville, J.-B.; Renard, H.-F.; Evergren, E.; Raghunathan, K.; Bhatia, D.; Kenworthy, A. K.; Voth, G. A.; Prost, J.; McMahon, H. T.; Johannes, L.; Bassereau, P.; Callan-Jones, A. *Cell* **2017,** *170,* 172–184.e11. doi:10.1016/j.cell.2017.05.047
81. Römer, W.; Pontani, L.-L.; Sorre, B.; Rentero, C.; Berland, L.; Chambon, V.; Lamaze, C.; Bassereau, P.; Sykes, C.; Gaus, K.; Johannes, L. *Cell* **2010,** *140,* 540–553. doi:10.1016/j.cell.2010.01.010
82. Bashkirov, P. V.; Akimov, S. A.; Evseev, A. I.; Schmid, S. L.; Zimmerberg, J.; Frolov, V. A. *Cell* **2008,** *135,* 1276–1286. doi:10.1016/j.cell.2008.11.028
83. Pucadyil, T. J.; Schmid, S. L. *Cell* **2008,** *135,* 1263–1275. doi:10.1016/j.cell.2008.11.020
84. Johannes, L.; Wunder, C.; Bassereau, P. *Cold Spring Harbor Perspect. Biol.* **2014,** *6,* a016741. doi:10.1101/cshperspect.a016741
85. Patel, S.; Kim, J.; Herrera, M.; Mukherjee, A.; Kabanov, A. V.; Sahay, G. *Adv. Drug Delivery Rev.* **2019,** *144,* 90–111. doi:10.1016/j.addr.2019.08.004
86. Canton, I.; Battaglia, G. *Chem. Soc. Rev.* **2012,** *41,* 2718–2739. doi:10.1039/c2cs15309b
87. Fujimoto, L. M.; Roth, R.; Heuser, J. E.; Schmid, S. L. *Traffic* **2000,** *1,* 161–171. doi:10.1034/j.1600-0854.2000.010208.x
88. Kaksonen, M.; Toret, C. P.; Drubin, D. G. *Nat. Rev. Mol. Cell Biol.* **2006,** *7,* 404–414. doi:10.1038/nrm1940
89. Merrifield, C. J.; Perrais, D.; Zenisek, D. *Cell* **2005,** *121,* 593–606. doi:10.1016/j.cell.2005.03.015
90. Cureton, D. K.; Massol, R. H.; Whelan, S. P. J.; Kirchhausen, T. *PLoS Pathog.* **2010,** *6,* e1001127. doi:10.1371/journal.ppat.1001127
91. Hansen, C. G.; Nichols, B. J. *J. Cell Sci.* **2009,** *122,* 1713–1721. doi:10.1242/jcs.033951
92. Sandvig, K.; Pust, S.; Skotland, T.; van Deurs, B. *Curr. Opin. Cell Biol.* **2011,** *23,* 413–420. doi:10.1016/j.ceb.2011.03.007
93. Gao, Y.-s.; Hubbert, C. C.; Lu, J.; Lee, Y.-S.; Lee, J.-Y.; Yao, T.-P. *Mol. Cell. Biol.* **2007,** *27,* 8637–8647. doi:10.1128/mcb.00393-07
94. Grimmer, S.; van Deurs, B.; Sandvig, K. *J. Cell Sci.* **2002,** *115,* 2953–2962.
95. Pelkmans, L.; Helenius, A. *Traffic* **2002,** *3,* 311–320. doi:10.1034/j.1600-0854.2002.30501.x
96. Kirkham, M.; Parton, R. G. *Biochim. Biophys. Acta, Mol. Cell Res.* **2005,** *1745,* 273–286. doi:10.1016/j.bbamcr.2005.06.002
97. Chaudhary, N.; Gomez, G. A.; Howes, M. T.; Lo, H. P.; McMahon, K.-A.; Rae, J. A.; Schieber, N. L.; Hill, M. M.; Gaus, K.; Yap, A. S.; Parton, R. G. *PLoS Biol.* **2014,** *12,* e1001832. doi:10.1371/journal.pbio.1001832
98. Stoeber, M.; Stoeck, I. K.; Hänni, C.; Bleck, C. K. E.; Balistreri, G.; Helenius, A. *EMBO J.* **2012,** *31,* 2350–2364. doi:10.1038/emboj.2012.98
99. Boucrot, E.; Howes, M. T.; Kirchhausen, T.; Parton, R. G. *J. Cell Sci.* **2011,** *124,* 1965–1972. doi:10.1242/jcs.076570
100. Oh, P.; Borgström, P.; Witkiewicz, H.; Li, Y.; Borgström, B. J.; Chrastina, A.; Iwata, K.; Zinn, K. R.; Baldwin, R.; Testa, J. E.; Schnitzer, J. E. *Nat. Biotechnol.* **2007,** *25,* 327–337. doi:10.1038/nbt1292
101. van Deurs, B.; Roepstorff, K.; Hommelgaard, A. M.; Sandvig, K. *Trends Cell Biol.* **2003,** *13,* 92–100. doi:10.1016/s0962-8924(02)00039-9
102. Shvets, E.; Bitsikas, V.; Howard, G.; Hansen, C. G.; Nichols, B. J. *Nat. Commun.* **2015,** *6,* 6867. doi:10.1038/ncomms7867
103. Thomsen, P.; Roepstorff, K.; Stahlhut, M.; van Deurs, B. *Mol. Biol. Cell* **2002,** *13,* 238–250. doi:10.1091/mbc.01-06-0317
104. Pelkmans, L.; Zerial, M. *Nature* **2005,** *436,* 128–133. doi:10.1038/nature03866
105. Gordon, S. *Immunity* **2016,** *44,* 463–475. doi:10.1016/j.immuni.2016.02.026
106. Lim, J. P.; Gleeson, P. A. *Immunol. Cell Biol.* **2011,** *89,* 836–843. doi:10.1038/icb.2011.20
107. Venkataraman, S.; Hedrick, J. L.; Ong, Z. Y.; Yang, C.; Ee, P. L. R.; Hammond, P. T.; Yang, Y. Y. *Adv. Drug Delivery Rev.* **2011,** *63,* 1228–1246. doi:10.1016/j.addr.2011.06.016
108. Lorenz, S.; Hauser, C. P.; Autenrieth, B.; Weiss, C. K.; Landfester, K.; Mailänder, V. *Macromol. Biosci.* **2010,** *10,* 1034–1042. doi:10.1002/mabi.201000099

109. Yi, X.; Shi, X.; Gao, H. *Phys. Rev. Lett.* **2011,** *107,* 098101. doi:10.1103/physrevlett.107.098101
110. Anselmo, A. C.; Mitragotri, S. *Adv. Drug Delivery Rev.* **2016,** *108,* 51–67. doi:10.1016/j.addr.2016.01.007
111. Niu, Y.; Yu, M.; Meka, A.; Liu, Y.; Zhang, J.; Yang, Y.; Yu, C. *J. Mater. Chem. B* **2016,** *4,* 212–219. doi:10.1039/c5tb01911g
112. Kelf, T. A.; Sreenivasan, V. K. A.; Sun, J.; Kim, E. J.; Goldys, E. M.; Zvyagin, A. V. *Nanotechnology* **2010,** *21,* 285105. doi:10.1088/0957-4484/21/28/285105
113. Editorial 'Time to deliver'. *Nat. Biotechnol.* **2014,** *32,* 961. doi:10.1038/nbt.3045
114. Akinc, A.; Battaglia, G. *Cold Spring Harbor Perspect. Biol.* **2013,** *5,* a016980. doi:10.1101/cshperspect.a016980
115. Rejman, J.; Oberle, V.; Zuhorn, I. S.; Hoekstra, D. *Biochem. J.* **2004,** *377,* 159–169. doi:10.1042/bj20031253
116. Lerch, S.; Dass, M.; Musyanovych, A.; Landfester, K.; Mailänder, V. *Eur. J. Pharm. Biopharm.* **2013,** *84,* 265–274. doi:10.1016/j.ejpb.2013.01.024
117. Foged, C.; Brodin, B.; Frokjaer, S.; Sundblad, A. *Int. J. Pharm.* **2005,** *298,* 315–322. doi:10.1016/j.ijpharm.2005.03.035
118. Decuzzi, P.; Ferrari, M. *Biomaterials* **2007,** *28,* 2915–2922. doi:10.1016/j.biomaterials.2007.02.013
119. Gao, H.; Shi, W.; Freund, L. B. *Proc. Natl. Acad. Sci. U. S. A.* **2005,** *102,* 9469–9474. doi:10.1073/pnas.0503879102
120. Chithrani, B. D.; Ghazani, A. A.; Chan, W. C. W. *Nano Lett.* **2006,** *6,* 662–668. doi:10.1021/nl052396o
121. Zauner, W.; Farrow, N. A.; Haines, A. M. R. *J. Controlled Release* **2001,** *71,* 39–51. doi:10.1016/s0168-3659(00)00358-8
122. Shapero, K.; Fenaroli, F.; Lynch, I.; Cottell, D. C.; Salvati, A.; Dawson, K. A. *Mol. BioSyst.* **2011,** *7,* 371–378. doi:10.1039/c0mb00109k
123. Wang, S.-H.; Lee, C.-W.; Chiou, A.; Wei, P.-K. *J. Nanobiotechnol.* **2010,** *8,* 33. doi:10.1186/1477-3155-8-33
124. Blanco, E.; Shen, H.; Ferrari, M. *Nat. Biotechnol.* **2015,** *33,* 941–951. doi:10.1038/nbt.3330
125. Gratton, S. E. A.; Ropp, P. A.; Pohlhaus, P. D.; Luft, J. C.; Madden, V. J.; Napier, M. E.; DeSimone, J. M. *Proc. Natl. Acad. Sci. U. S. A.* **2008,** *105,* 11613–11618. doi:10.1073/pnas.0801763105
126. Lai, S. K.; Hida, K.; Man, S. T.; Chen, C.; Machamer, C.; Schroer, T. A.; Hanes, J. *Biomaterials* **2007,** *28,* 2876–2884. doi:10.1016/j.biomaterials.2007.02.021
127. Agarwal, R.; Singh, V.; Jurney, P.; Shi, L.; Sreenivasan, S. V.; Roy, K. *Proc. Natl. Acad. Sci. U. S. A.* **2013,** *110,* 17247–17252. doi:10.1073/pnas.1305000110
128. Kirchhausen, T.; Owen, D.; Harrison, S. C. *Cold Spring Harbor Perspect. Biol.* **2014,** *6,* a016725. doi:10.1101/cshperspect.a016725
129. Fotin, A.; Cheng, Y.; Sliz, P.; Grigorieff, N.; Harrison, S. C.; Kirchhausen, T.; Walz, T. *Nature* **2004,** *432,* 573–579. doi:10.1038/nature03079
130. Saffarian, S.; Cocucci, E.; Kirchhausen, T. *PLoS Biol.* **2009,** *7,* e1000191. doi:10.1371/journal.pbio.1000191
131. dos Santos, T.; Varela, J.; Lynch, I.; Salvati, A.; Dawson, K. A. *Small* **2011,** *7,* 3341–3349. doi:10.1002/smll.201101076
132. dos Santos, T.; Varela, J.; Lynch, I.; Salvati, A.; Dawson, K. A. *PLoS One* **2011,** *6,* e24438. doi:10.1371/journal.pone.0024438
133. Vercauteren, D.; Vandenbroucke, R. E.; Jones, A. T.; Rejman, J.; Demeester, J.; De Smedt, S. C.; Sanders, N. N.; Braeckmans, K. *Mol. Ther.* **2010,** *18,* 561–569. doi:10.1038/mt.2009.281
134. Herd, H.; Daum, N.; Jones, A. T.; Huwer, H.; Ghandehari, H.; Lehr, C.-M. *ACS Nano* **2013,** *7,* 1961–1973. doi:10.1021/nn304439f
135. Gessner, A.; Lieske, A.; Paulke, B. R.; Müller, R. H. *Eur. J. Pharm. Biopharm.* **2002,** *54,* 165–170. doi:10.1016/s0939-6411(02)00081-4
136. Fröhlich, E. *Int. J. Nanomed.* **2012,** *2012,* 5577–5591. doi:10.2147/ijn.s36111
137. Hühn, D.; Kantner, K.; Geidel, C.; Brandholt, S.; De Cock, I.; Soenen, S. J. H.; Rivera_Gil, P.; Montenegro, J.-M.; Braeckmans, K.; Müllen, K.; Nienhaus, G. U.; Klapper, M.; Parak, W. J. *ACS Nano* **2013,** *7,* 3253–3263. doi:10.1021/nn3059295
138. Chen, L.; Mccrate, J. M.; Lee, J. C.-M.; Li, H. *Nanotechnology* **2011,** *22,* 105708. doi:10.1088/0957-4484/22/10/105708
139. Schrade, A.; Mailänder, V.; Ritz, S.; Landfester, K.; Ziener, U. *Macromol. Biosci.* **2012,** *12,* 1459–1471. doi:10.1002/mabi.201200166
140. Xiao, K.; Li, Y.; Luo, J.; Lee, J. S.; Xiao, W.; Gonik, A. M.; Agarwal, R. G.; Lam, K. S. *Biomaterials* **2011,** *32,* 3435–3446. doi:10.1016/j.biomaterials.2011.01.021
141. Bannunah, A. M.; Vllasaliu, D.; Lord, J.; Stolnik, S. *Mol. Pharmaceutics* **2014,** *11,* 4363–4373. doi:10.1021/mp500439c
142. Dausend, J.; Musyanovych, A.; Dass, M.; Walther, P.; Schrezenmeier, H.; Landfester, K.; Mailänder, V. *Macromol. Biosci.* **2008,** *8,* 1135–1143. doi:10.1002/mabi.200800123
143. Harush-Frenkel, O.; Rozentur, E.; Benita, S.; Altschuler, Y. *Biomacromolecules* **2008,** *9,* 435–443. doi:10.1021/bm700535p
144. Li, Y.; Kröger, M.; Liu, W. K. *Nanoscale* **2015,** *7,* 16631–16646. doi:10.1039/c5nr02970h
145. Carnovale, C.; Bryant, G.; Shukla, R.; Bansal, V. *ACS Omega* **2019,** *4,* 242–256. doi:10.1021/acsomega.8b03227
146. Qiu, Y.; Liu, Y.; Wang, L.; Xu, L.; Bai, R.; Ji, Y.; Wu, X.; Zhao, Y.; Li, Y.; Chen, C. *Biomaterials* **2010,** *31,* 7606–7619. doi:10.1016/j.biomaterials.2010.06.051
147. Chithrani, B. D.; Chan, W. C. W. *Nano Lett.* **2007,** *7,* 1542–1550. doi:10.1021/nl070363y
148. Dasgupta, S.; Auth, T.; Gompper, G. *Nano Lett.* **2014,** *14,* 687–693. doi:10.1021/nl403949h
149. Huang, X.; Teng, X.; Chen, D.; Tang, F.; He, J. *Biomaterials* **2010,** *31,* 438–448. doi:10.1016/j.biomaterials.2009.09.060
150. Kinnear, C.; Moore, T. L.; Rodriguez-Lorenzo, L.; Rothen-Rutishauser, B.; Petri-Fink, A. *Chem. Rev.* **2017,** *117,* 11476–11521. doi:10.1021/acs.chemrev.7b00194
151. Sun, J.; Zhang, L.; Wang, J.; Feng, Q.; Liu, D.; Yin, Q.; Xu, D.; Wei, Y.; Ding, B.; Shi, X.; Jiang, X. *Adv. Mater. (Weinheim, Ger.)* **2015,** *27,* 1402–1407. doi:10.1002/adma.201404788
152. Shen, Z.; Ye, H.; Yi, X.; Li, Y. *ACS Nano* **2019,** *13,* 215–228. doi:10.1021/acsnano.8b05340
153. Palomba, R.; Palange, A. L.; Rizzuti, I. F.; Ferreira, M.; Cervadoro, A.; Barbato, M. G.; Canale, C.; Decuzzi, P. *ACS Nano* **2018,** *12,* 1433–1444. doi:10.1021/acsnano.7b07797
154. Guo, P.; Liu, D.; Subramanyam, K.; Wang, B.; Yang, J.; Huang, J.; Auguste, D. T.; Moses, M. A. *Nat. Commun.* **2018,** *9,* 130. doi:10.1038/s41467-017-02588-9
155. Anselmo, A. C.; Zhang, M.; Kumar, S.; Vogus, D. R.; Menegatti, S.; Helgeson, M. E.; Mitragotri, S. *ACS Nano* **2015,** *9,* 3169–3177. doi:10.1021/acsnano.5b00147
156. Kuhn, D. A.; Vanhecke, D.; Michen, B.; Blank, F.; Gehr, P.; Petri-Fink, A.; Rothen-Rutishauser, B. *Beilstein J. Nanotechnol.* **2014,** *5,* 1625–1636. doi:10.3762/bjnano.5.174
157. O' Neill, M. J.; Guo, J.; Byrne, C.; Darcy, R.; O' Driscoll, C. M. *Int. J. Pharm.* **2011,** *413,* 174–183. doi:10.1016/j.ijpharm.2011.04.021

158. Francia, V.; Reker-Smit, C.; Boel, G.; Salvati, A. *Nanomedicine (London, U. K.)* **2019,** *14,* 1533–1549. doi:10.2217/nnm-2018-0446
159. Francia, V.; Aliyandi, A.; Salvati, A. *Nanoscale* **2018,** *10,* 16645–16656. doi:10.1039/c8nr03171a
160. Wang, B.; Zhang, L.; Bae, S. C.; Granick, S. *Proc. Natl. Acad. Sci. U. S. A.* **2008,** *105,* 18171–18175. doi:10.1073/pnas.0807296105
161. Rossi, G.; Barnoud, J.; Monticelli, L. *J. Phys. Chem. Lett.* **2014,** *5,* 241–246. doi:10.1021/jz402234c
162. Zhao, W.; Hanson, L.; Lou, H.-Y.; Akamatsu, M.; Chowdary, P. D.; Santoro, F.; Marks, J. R.; Grassart, A.; Drubin, D. G.; Cui, Y.; Cui, B. *Nat. Nanotechnol.* **2017,** 12. doi:10.1038/nnano.2017.98
163. Bahrami, A. H.; Lipowsky, R.; Weikl, T. R. *Soft Matter* **2016,** *12,* 581–587. doi:10.1039/c5sm01793a
164. Ewers, H.; Römer, W.; Smith, A. E.; Bacia, K.; Dmitrieff, S.; Chai, W.; Mancini, R.; Kartenbeck, J.; Chambon, V.; Berland, L.; Oppenheim, A.; Schwarzmann, G.; Feizi, T.; Schwille, P.; Sens, P.; Helenius, A.; Johannes, L. *Nat. Cell Biol.* **2010,** *12,* 11–18. doi:10.1038/ncb1999
165. Xu, M.; Soliman, M. G.; Sun, X.; Pelaz, B.; Feliu, N.; Parak, W. J.; Liu, S. *ACS Nano* **2018,** *12,* 10104–10113. doi:10.1021/acsnano.8b04906
166. Leong, H. S.; Butler, K. S.; Brinker, C. J.; Azzawi, M.; Conlan, S.; Dufés, C.; Owen, A.; Rannard, S.; Scott, C.; Chen, C.; Dobrovolskaia, M. A.; Kozlov, S. V.; Prina-Mello, A.; Schmid, R.; Wick, P.; Caputo, F.; Boisseau, P.; Crist, R. M.; McNeil, S. E.; Fadeel, B.; Tran, L.; Hansen, S. F.; Hartmann, N. B.; Clausen, L. P. W.; Skjolding, L. M.; Baun, A.; Ågerstrand, M.; Gu, Z.; Lamprou, D. A.; Hoskins, C.; Huang, L.; Song, W.; Cao, H.; Liu, X.; Jandt, K. D.; Jiang, W.; Kim, B. Y. S.; Wheeler, K. E.; Chetwynd, A. J.; Lynch, I.; Moghimi, S. M.; Nel, A.; Xia, T.; Weiss, P. S.; Sarmento, B.; das Neves, J.; Santos, H. A.; Santos, L.; Mitragotri, S.; Little, S.; Peer, D.; Amiji, M. M.; Alonso, M. J.; Petri-Fink, A.; Balog, S.; Lee, A.; Drasler, B.; Rothen-Rutishauser, B.; Wilhelm, S.; Acar, H.; Harrison, R. G.; Mao, C.; Mukherjee, P.; Ramesh, R.; McNally, L. R.; Busatto, S.; Wolfram, J.; Bergese, P.; Ferrari, M.; Fang, R. H.; Zhang, L.; Zheng, J.; Peng, C.; Du, B.; Yu, M.; Charron, D. M.; Zheng, G.; Pastore, C. *Nat. Nanotechnol.* **2019,** *14,* 629–635. doi:10.1038/s41565-019-0496-9
167. Lammers, T.; Storm, G. *Nat. Nanotechnol.* **2019,** *14,* 626. doi:10.1038/s41565-019-0497-8
168. Sahay, G.; Querbes, W.; Alabi, C.; Eltoukhy, A.; Sarkar, S.; Zurenko, C.; Karagiannis, E.; Love, K.; Chen, D.; Zoncu, R.; Buganim, Y.; Schroeder, A.; Langer, R.; Anderson, D. G. *Nat. Biotechnol.* **2013,** *31,* 653–658. doi:10.1038/nbt.2614
169. Pangarkar, C.; Dinh, A.-T.; Mitragotri, S. *J. Controlled Release* **2012,** *162,* 76–83. doi:10.1016/j.jconrel.2012.05.022
170. Behr, J. *Chimia* **1997,** *51,* 34–36.
171. Rehman, Z. u.; Hoekstra, D.; Zuhorn, I. S. *ACS Nano* **2013,** *7,* 3767–3777. doi:10.1021/nn3049494
172. El-Sayed, A.; Futaki, S.; Harashima, H. *AAPS J.* **2009,** *11,* 13–22. doi:10.1208/s12248-008-9071-2
173. Krpetić, Ž.; Saleemi, S.; Prior, I. A.; Sée, V.; Qureshi, R.; Brust, M. *ACS Nano* **2011,** *5,* 5195–5201. doi:10.1021/nn201369k
174. Chou, L. Y. T.; Ming, K.; Chan, W. C. W. *Chem. Soc. Rev.* **2011,** *40,* 233–245. doi:10.1039/c0cs00003e
175. Varkouhi, A. K.; Scholte, M.; Storm, G.; Haisma, H. J. *J. Controlled Release* **2011,** *151,* 220–228. doi:10.1016/j.jconrel.2010.11.004
176. Martens, T. F.; Remaut, K.; Demeester, J.; De Smedt, S. C.; Braeckmans, K. *Nano Today* **2014,** *9,* 344–364. doi:10.1016/j.nantod.2014.04.011
177. Smith, S. A.; Selby, L. I.; Johnston, A. P. R.; Such, G. K. *Bioconjugate Chem.* **2019,** *30,* 263–272. doi:10.1021/acs.bioconjchem.8b00732
178. Chai, G.-H.; Hu, F.-Q.; Sun, J.; Du, Y.-Z.; You, J.; Yuan, H. *Mol. Pharmaceutics* **2014,** *11,* 3716–3726. doi:10.1021/mp5004674
179. Ghaffarian, R.; Bhowmick, T.; Muro, S. *J. Controlled Release* **2012,** *163,* 25–33. doi:10.1016/j.jconrel.2012.06.007
180. Rezaei, G.; Daghighi, S. M.; Haririan, I.; Yousefi, I.; Raoufi, M.; Rezaee, F.; Dinarvand, R. *Colloids Surf., B* **2019,** *179,* 505–516. doi:10.1016/j.colsurfb.2019.04.003
181. Krug, H. F. *Angew. Chem., Int. Ed.* **2014,** *53,* 12304–12319. doi:10.1002/anie.201403367
182. Haase, A.; Lynch, I. *NanoImpact* **2018,** *11,* 67–68. doi:10.1016/j.impact.2018.02.005
183. Editorial 'Join the, dialogue'. *Nat. Nanotechnol.* **2012,** *7,* 545. doi:10.1038/nnano.2012.150
184. Malcolm, D. W.; Varghese, J. J.; Sorrells, J. E.; Ovitt, C. E.; Benoit, D. S. W. *ACS Nano* **2018,** *12,* 187–197. doi:10.1021/acsnano.7b05528
185. Lazzari, S.; Moscatelli, D.; Codari, F.; Salmona, M.; Morbidelli, M.; Diomede, L. *J. Nanopart. Res.* **2012,** *14,* 920. doi:10.1007/s11051-012-0920-7
186. Lesniak, A.; Fenaroli, F.; Monopoli, M. P.; Åberg, C.; Dawson, K. A.; Salvati, A. *ACS Nano* **2012,** *6,* 5845–5857. doi:10.1021/nn300223w
187. Kim, J. A.; Salvati, A.; Åberg, C.; Dawson, K. A. *Nanoscale* **2014,** *6,* 14180–14184. doi:10.1039/c4nr04970e
188. Mazzolini, J.; Weber, R. J. M.; Chen, H.-S.; Khan, A.; Guggenheim, E.; Shaw, R. K.; Chipman, J. K.; Viant, M. R.; Rappoport, J. Z. *Biol. Bull. (Woods Hole, MA, U. S.)* **2016,** *231,* 40–60. doi:10.1086/689590
189. Digiacomo, L.; Cardarelli, F.; Pozzi, D.; Palchetti, S.; Digman, M. A.; Gratton, E.; Capriotti, A. L.; Mahmoudi, M.; Caracciolo, G. *Nanoscale* **2017,** *9,* 17254–17262. doi:10.1039/c7nr06437c
190. Voigt, J.; Christensen, J.; Shastri, V. P. *Proc. Natl. Acad. Sci. U. S. A.* **2014,** *111,* 2942–2947. doi:10.1073/pnas.1322356111
191. Hild, W.; Pollinger, K.; Caporale, A.; Cabrele, C.; Keller, M.; Pluym, N.; Buschauer, A.; Rachel, R.; Tessmar, J.; Breunig, M.; Goepferich, A. *Proc. Natl. Acad. Sci. U. S. A.* **2010,** *107,* 10667–10672. doi:10.1073/pnas.0912782107
192. Lunov, O.; Syrovets, T.; Loos, C.; Beil, J.; Delacher, M.; Tron, K.; Nienhaus, G. U.; Musyanovych, A.; Mailänder, V.; Landfester, K.; Simmet, T. *ACS Nano* **2011,** *5,* 1657–1669. doi:10.1021/nn2000756
193. Al Soraj, M.; He, L.; Peynshaert, K.; Cousaert, J.; Vercauteren, D.; Braeckmans, K.; De Smedt, S. C.; Jones, A. T. *J. Controlled Release* **2012,** *161,* 132–141. doi:10.1016/j.jconrel.2012.03.015
194. Choi, H. S.; Ashitate, Y.; Lee, J. H.; Kim, S. H.; Matsui, A.; Insin, N.; Bawendi, M. G.; Semmler-Behnke, M.; Frangioni, J. V.; Tsuda, A. *Nat. Biotechnol.* **2010,** *28,* 1300–1303. doi:10.1038/nbt.1696
195. Barrán-Berdón, A. L.; Pozzi, D.; Caracciolo, G.; Capriotti, A. L.; Caruso, G.; Cavaliere, C.; Riccioli, A.; Palchetti, S.; Laganà, A. *Langmuir* **2013,** *29,* 6485–6494. doi:10.1021/la401192x
196. Casals, E.; Pfaller, T.; Duschl, A.; Oostingh, G. J.; Puntes, V. *ACS Nano* **2010,** *4,* 3623–3632. doi:10.1021/nn901372t
197. Lundqvist, M.; Stigler, J.; Cedervall, T.; Berggård, T.; Flanagan, M. B.; Lynch, I.; Elia, G.; Dawson, K. *ACS Nano* **2011,** *5,* 7503–7509. doi:10.1021/nn202458g

198. Liu, R.; Jiang, W.; Walkey, C. D.; Chan, W. C. W.; Cohen, Y. *Nanoscale* **2015,** *7,* 9664–9675. doi:10.1039/c5nr01537e
199. Kelly, P. M.; Åberg, C.; Polo, E.; O'Connell, A.; Cookman, J.; Fallon, J.; Krpetić, Ž.; Dawson, K. A. *Nat. Nanotechnol.* **2015,** *10,* 1–8. doi:10.1038/nnano.2015.47
200. Fujimoto, T.; Kogo, H.; Nomura, R.; Une, T. *J. Cell Sci.* **2000,** *113,* 3509–3517.
201. Schimpel, C.; Teubl, B.; Absenger, M.; Meindl, C.; Fröhlich, E.; Leitinger, G.; Zimmer, A.; Roblegg, E. *Mol. Pharmaceutics* **2014,** *11,* 808–818. doi:10.1021/mp400507g
202. Gamboa, J. M.; Leong, K. W. *Adv. Drug Delivery Rev.* **2013,** *65,* 800–810. doi:10.1016/j.addr.2013.01.003
203. Costa, E. C.; Gaspar, V. M.; Marques, J. G.; Coutinho, P.; Correia, I. J. *PLoS One* **2013,** *8,* e70072. doi:10.1371/journal.pone.0070072
204. Mayor, S.; Parton, R. G.; Donaldson, J. G. *Cold Spring Harbor Perspect. Biol.* **2014,** *6,* a016758. doi:10.1101/cshperspect.a016758
205. Harding, C.; Heuser, J.; Stahl, P. *J. Cell Biol.* **1983,** *97,* 329–339. doi:10.1083/jcb.97.2.329
206. Vasile, E.; Simionescu, M.; Simionescu, N. *J. Cell Biol.* **1983,** *96,* 1677–1689. doi:10.1083/jcb.96.6.1677
207. Marks, D. L.; Singh, R. D.; Choudhury, A.; Wheatley, C. L.; Pagano, R. E. *Methods* **2005,** *36,* 186–195. doi:10.1016/j.ymeth.2004.12.001
208. Lajoie, P.; Kojic, L. D.; Nim, S.; Li, L.; Dennis, J. W.; Nabi, I. R. *J. Cell. Mol. Med.* **2009,** *13,* 3218–3225. doi:10.1111/j.1582-4934.2009.00732.x
209. Torgersen, M. L.; Skretting, G.; van Deurs, B.; Sandvig, K. *J. Cell Sci.* **2001,** *114,* 3737–3747.
210. Damm, E.-M.; Pelkmans, L.; Kartenbeck, J.; Mezzacasa, A.; Kurzchalia, T.; Helenius, A. *J. Cell Biol.* **2005,** *168,* 477–488. doi:10.1083/jcb.200407113
211. Schliwa, M. *J. Cell Biol.* **1982,** *92,* 79–91. doi:10.1083/jcb.92.1.79
212. Yarar, D.; Waterman-Storer, C. M.; Schmid, S. L. *Mol. Biol. Cell* **2005,** *16,* 964–975. doi:10.1091/mbc.e04-09-0774
213. Ivanov, A. I. Pharmacological Inhibition of Endocytic Pathways: Is It Specific Enough to Be Useful?. In *Exocytosis and Endocytosis;* Ivanov, A. I., Ed.; Methods in Molecular Biolog, Vol. 440; 2008; pp 15–33. doi:10.1007/978-1-59745-178-9_2
214. Hayer, A.; Stoeber, M.; Ritz, D.; Engel, S.; Meyer, H. H.; Helenius, A. *J. Cell Biol.* **2010,** *191,* 615–629. doi:10.1083/jcb.201003086
215. Roberts, B.; Haupt, A.; Tucker, A.; Grancharova, T.; Arakaki, J.; Fuqua, M. A.; Nelson, A.; Hookway, C.; Ludmann, S. A.; Mueller, I. A.; Yang, R.; Horwitz, R.; Rafelski, S. M.; Gunawardane, R. N. *Mol. Biol. Cell* **2017,** *28,* 2854–2874. doi:10.1091/mbc.e17-03-0209
216. Khan, A. O.; Simms, V. A.; Pike, J. A.; Thomas, S. G.; Morgan, N. V. *Sci. Rep.* **2017,** *7,* 8450. doi:10.1038/s41598-017-08493-x
217. Wittrup, A.; Zhang, S.-H.; Svensson, K. J.; Kucharzewska, P.; Johansson, M. C.; Morgelin, M.; Belting, M. *Proc. Natl. Acad. Sci. U. S. A.* **2010,** *107,* 13342–13347. doi:10.1073/pnas.1002622107
218. Yau, E. H.; Rana, T. M. *Methods Mol. Biol. (N. Y., NY, U. S.)* **2018,** *1712,* 203–216. doi:10.1007/978-1-4939-7514-3_13
219. Gosney, J. A.; Wilkey, D. W.; Merchant, M. L.; Ceresa, B. P. *J. Biol. Chem.* **2018,** *293,* 5895–5908. doi:10.1074/jbc.ra117.000632

License and Terms

BEILSTEIN JOURNAL OF NANOTECHNOLOGY

Brome mosaic virus-like particles as siRNA nanocarriers for biomedical purposes

Alfredo Nuñez-Rivera[1,2], Pierrick G. J. Fournier[2], Danna L. Arellano[2], Ana G. Rodriguez-Hernandez[1], Rafael Vazquez-Duhalt[1] and Ruben D. Cadena-Nava[*1,§]

Full Research Paper

Open Access

Address:
[1]Centro de Nanociencias y Nanotecnología - Universidad Nacional Autónoma de México (UNAM) – Ensenada, Baja California, México and [2]Centro de Investigación Científica y de Educación Superior de Ensenada, Baja California, (CICESE), Ensenada, Baja California, México

Email:
Ruben D. Cadena-Nava[*] - rcadena74@gmail.com

* Corresponding author
§ Phone: +52 (646) 175-0650

Keywords:
anti-cancer therapy; brome mosaic virus (BMV); cowpea chlorotic mottle virus (CCMV); nanocarriers; plant virus-like particles (VLPs); siRNA delivery; small interfering RNA (siRNA)

Beilstein J. Nanotechnol. **2020,** *11,* 372–382.
doi:10.3762/bjnano.11.28

Received: 21 November 2019
Accepted: 07 February 2020
Published: 20 February 2020

This article is part of the thematic issue "Engineered nanomedicines for advanced therapies".

Guest Editor: M. K. Danquah

Abstract

There is an increasing interest in the use of plant viruses as vehicles for anti-cancer therapy. In particular, the plant virus brome mosaic virus (BMV) and cowpea chlorotic mottle virus (CCMV) are novel potential nanocarriers for different therapies in nanomedicine. In this work, BMV and CCMV were loaded with a fluorophore and assayed on breast tumor cells. The viruses BMV and CCMV were internalized into breast tumor cells. Both viruses, BMV and CCMV, did not show cytotoxic effects on tumor cells in vitro. However, only BMV did not activate macrophages in vitro. This suggests that BMV is less immunogenic and may be a potential carrier for therapy delivery in tumor cells. Furthermore, BMV virus-like particles (VLPs) were efficiently loaded with small interfering RNA (siRNA) without packaging signal. The gene silencing was demonstrated by VLPs loaded with siGFP and tested on breast tumor cells that constitutively express the green fluorescent protein (GPF). After VLP-siGFP treatment, GFP expression was efficiently inhibited corroborating the cargo release inside tumor cells and the gene silencing. In addition, BMV VLP carring siAkt1 inhibited the tumor growth in mice. These results show the attractive potential of plant virus VLPs to deliver molecular therapy to tumor cells with low immunogenic response.

Introduction

Despite many efforts taken, the efficient and specific delivery of therapeutic molecules to tumor cells is still a unsolved challenge. Cancer therapies are often limited because only a small fraction of the administered dose of the drug arrives into the tumors [1-3]. This can be attributed, in part, to a series of biological barriers that reduce the drug accumulation in tumors [4]

such as sequestration by the mononuclear phagocyte system [5], non-specific distribution [6], limitations in the blood flow of tumor vessels [7], pressure gradients, cellular internalization [8], and the escape of endosomal and lysosomal compartments and drug efflux pumps [9].

The use of nanoparticles as nanovehicles has been proposed to overcome some of these limitations. Nanoparticles offer several advantages such as their size and a surface area that could be functionalized with specific ligands in order to be targeted to specific tissues [10]. Additionally, they can be used to increase the overall solubility of drugs and to modulate their circulation half-life [11-13]. The accumulation of nanoparticles in tumors, either passively or directed, is extensively documented [14]. Thus, there are multiple efforts to design nanoparticles that function as nanovehicles, mainly composed of liposomes, synthetic polymers, dendrimers, and virus-like particles (VLPs) [13,15]. Recently, the use of VLPs with high loading capacity and biocompatibility has reached clinical stages [16,17].

Plant virus VLPs have received less attention, since for most of the viral vector developments bacteriophages and complex mammalian viruses are used. However, due to their easy production, handling, and simple structure, plant viruses are attractive for some biomedical applications. Plant bromoviruses, such as the brome mosaic virus (BMV), are viral bionanoparticles that have been proposed as platforms for drug delivery in different therapies, and as diagnostic imaging agents in cancer [18-20]. The capsids of these viruses result from the assembly of 180 identical proteins with $T = 3$ symmetry that forms the icosahedral shell with a diameter of 28 nm [21]. The N-terminal region of the capsid protein is highly basic and positively charged, which allows for the binding of the viral RNA genome [22]. Also, the casid protein able to encapsidate anionic molecules, such as heterologous RNAs [23], enzymes [24], drugs [25], or gold nanoparticles [26] by charge complementarity with the possibility of directing them to target cells through the functionalization of the external surface of the capsid [25,27]. Similarly, VLPs from the closely related cowpea chlorotic mottle virus (CCMV) have been loaded with different cargos, including gold nanoparticles, negatively charged chromophores, and polymers [22].

Small interfering RNA (siRNA) is a promising therapeutic solution to address gene overexpression or mutations for several pathological conditions such as viral infections, cancer, genetic disorders, and autoimmune disorders such as arthritis [28,29]. Especially, BMV VLPs show potential for delivering siRNA due to easy production and purification, and high stability. Also, they can be readily modified chemically and genetically for potential therapeutic applications [30].

Despite these interesting properties, to our knowledge, the use of BMV VLPs for molecular cancer therapies, especially in delivering siRNA for gene silencing, has been scarcely explored. In this work, important BMV VLPs properties of biomedical interest are demonstrated, such as biocompatibility, tumor cell internalization, and their efficiency as nanocarriers for siRNA delivery. In addition, the capacity of the BMV and CCMV viruses to modulate the immune response in vitro was also analyzed.

Results and Discussion

Cell internalization of VLPs

In order to test the cell internalization of VLPs, BMV and CCMV VLPs were loaded with NanoOrange, a hydrophobic fluorescent dye. Both BMV and CCMV viruses have hydrophobic residues in their capsid protein in which hydrophobic molecules, such as NanoOrange, are bound. Due to the high fluorescence of this fluorophore, the internalization into tumor cells using this labeling technique appears to be better when compared with some previous reports [31-33]. The NanoOrange-loaded BMV and CCMV capsids were then incubated in MCF-7 cell cultures for 4 h to evaluate their internalization into the breast cancer cells. Representative confocal microscopy images showed NanoOrange fluorescence inside the cells (Figure 1A). It is important to point out that the capsids are able to internalize efficiently into tumor cells without any functionalization. The cell internalization has been quantified by flow cytometry (Figure 1B). The differences in the extent of cell internalization could be explained by the surface charge as revealed by zeta potential measurements. The flow cytometry analysis of cell internalization was also performed after trypsin treatment, which promotes detachment of the capsids from the cell surface [31], and thus only internalized capsids are detected.

The results showed a slightly higher efficiency of internalization, but no significant difference, for BMV into the MDA-MB-231 and MCF-7 breast tumor cell lines (Figure 1C). Furthermore, to avoid erroneous results due to possible detachment of NanoOrange from the capsids, FITC fluorophore was covalently conjugated to the capsid surface and analyzed by confocal microscopy (Figure 2 and Figure S1, Supporting Information File 1). The confocal images showed FITC fluorescence inside the cells without colocalization of the plasma membrane stained with FM4-64, evidencing an effective cell internalization of both BMV and CCMV loaded capsids. With the virus loaded with FTIC a similar efficiency of virus internalization in MDA-MB-231 and MCF-7capsids are interacting with the cell plasma membrane, in cells was observed. Flow cytometry analysis showed a 70% virus internalization in the cells treated with both CCMV and BMV capsids (Figure 1B,C).

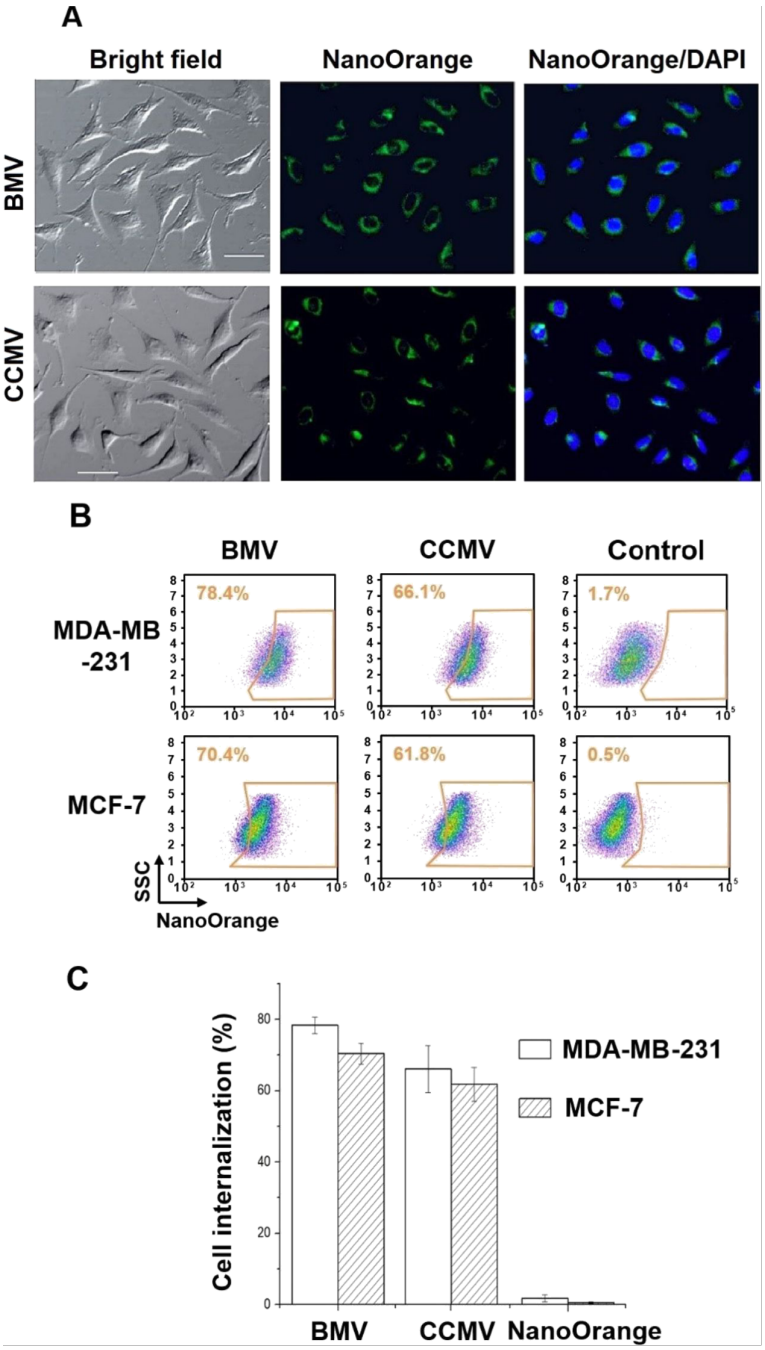

Figure 1: Cellular uptake of CCMV and BMV viruses. (a) Confocal laser scanning microscopy (CLSM) images of MCF-7 cells treated with virus–NanoOrange (green channel). (b) Representative flow cytometry data (c) and the statistical data of virus internalization in MDA-MB-231 and MCF-7 tumor cells. Free NanoOrange (controls) was virtually not internalized. Scale bar = 50 μm. Error bars represent mean ± SD (n = 3).

In addition, confocal microscopy images showed that almost all the cells contained plant viruses with loaded NanoOrange or with covalently conjugated FITC (Figure 1A and Figure 2). The differences in fluorescence intensity detected by confocal microscopy among the treated cells can be attributed to the different amounts of internalized VLPs.

We demonstrate that the BMV and CCMV capsids are efficiently internalized by breast tumor cells, without the need to couple a specific cell ligand. These results differ from those reported for cell internalization of cowpea mosaic virus (CPMV) in the same cell lines, which do not show high levels of vimentin on the cell surface [20,34]. Vimentin is a receptor that

facilitates caveolar endocytosis [35,36], and it has been reported to promote the cellular internalization of CPMV [32,35-37]. Therefore, the cellular internalization of the CPMV virus occurs via endocytosis, which includes multiple routes: clathrin-dependent, caveolar and micropinocytosis [36-38]. Our results showed that the presence of low levels of vimentin on the cell surface is not a limiting factor for the cell internalization of BMV and CCMV. Thus, it seems possible that the capsid internalization could be carried out by macropinocytosis, a process independent of vimentin.

Biocompatibility of CCMV and BMV

A possible virus cytotoxicity was evaluated. BMV and CCMV viruses were incubated for 24 h with MDA-MB-231 cells, using 2.6×10^7 viruses per cell. A similar concentration has been used in cell viability tests with CCMV [25,39] and glycol chitosan nanoparticles [40]. The flow cytometry results showed around 90% cell survival after treatment with both viruses (Figure 3A,B), while almost all cells died after treatment with DMSO (death control). These results agree with previous studies with BMV VLPs in HBE cells [41] and also with other plant viruses, in which even at high virus concentrations, no cytotoxic effect on cells was found [38,42,43]. This high degree of biocompatibility make plant viruses capsids suitable candidates as carriers to deliver therapeutic drugs or siRNA molecules.

Immunogenicity of CCMV and BMV

The RAW 264.7-blue macrophage cell line was used to determine the potential immune response in vitro of both BMV and CCMV viruses. Surprisingly, a remarkable difference was found. CCMV showed a high activation of macrophages, while BMV showed almost no immunogenic response (Figure 3C,D). There is 80% homology in the amino acids sequences of CCMV and BMV [21], however, they differ in their surface charge. The zeta potential at pH 7 was determined. Under these conditions, the zeta potential of CCMV is −9.27 ± 0.47 mV, more negative than that of BMV (−5.16 ± 0.40 mV). The surface charge of the capsid could be the reason why CCMV activates macrophage cells to a greater extent, because it is well known that at a higher anionic charge the particles tend to be phagocytosed by macrophages [44]. Accordingly, the virus uptake by the macrophages can activate intracellular receptors, i.e., toll-like receptors (TLR) 7/8, which can recognize the viral

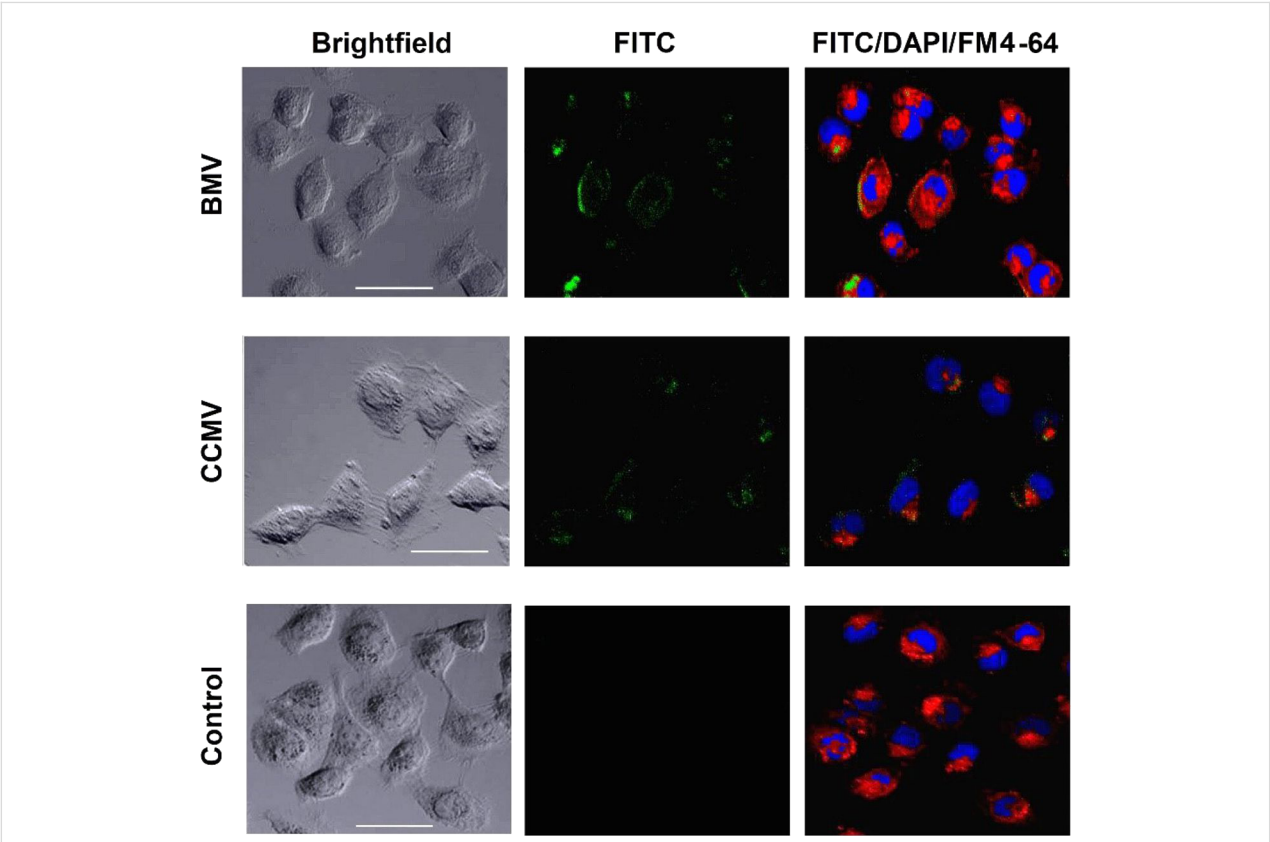

Figure 2: Internalization of CCMV and BMV conjugated with FITC. MDA-MB-231 cells were incubated with BMV-FITC (green channel) and CCMV-FITC (green channel). The cell nucleus was stained with DAPI (blue channel) and the membrane with FM4-64 (red channel). Free FITC did not show internalization. A concentration of 1.3×10^6 viruses/cell was used. Scale bar = 50 µm.

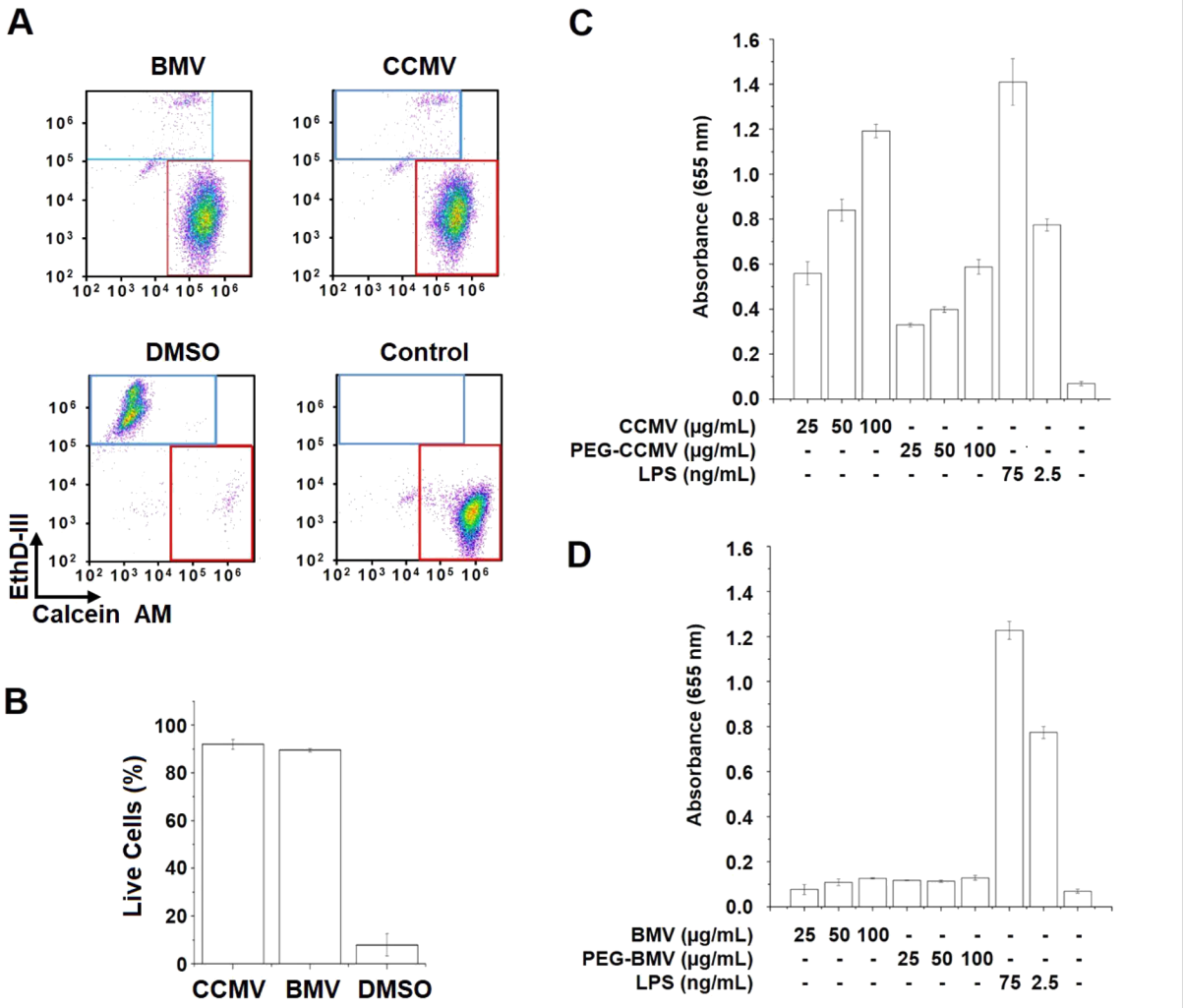

Figure 3: Biocompatibility and immune response of BMV and CCMV. (A) MDA-MB-231 cells were incubated with the virus CCMV and BMV for 24 h with 2.6 × 10^7 viruses/cell. The cytotoxicity was measured by flow cytometry, using calcein AM to quantify live cells and EthD-III for dead cells. (B) Representative statistical data of live cells after virus incubation. Macrophage activation by (C) CCMV, (D) BMV and PEGylated virus nanoparticles (PEG-CCMV/PEG-BMV) at different concentrations were measured using RAW 264.7-Blue cells. Lipopolysaccharide extract (LPS) was used as a control of macrophages activation. Error bars represent mean ± SD (n = 3).

ssRNA genome, promoting the activation of the macrophages. This mechanism of TLR 7/8 activation has been reported using papaya mosaic virus [45].

Both capsids of CCMV and BMV were covered with polyethylene glycol (PEG) to decrease their surface charge and mask the domains of the capsid proteins that could be recognized by the macrophages (Figure 3C,D). PEG is widely used to reduce the immunogenicity of proteins. Also, PEG has been approved by the US Food and Drug Administration, and there are now several PEGylated drugs commercially available. The PEG–drug conjugates show several advantages that include prolonged residence in the body, reduced degradation by metabolic enzymes, and reduced or no protein immunogenicity [46]. Although the PEGylation of CCMV capsids (CCMV-PEG) greatly reduced the immunogenic response, BMV seems to be a better nanocarrier candidate due to its low immunological response. On the other hand, and despite of the immunogenicity of CCMV, which can limit its use for certain therapies, this virus could act as an immunoregulator in immunological therapies to improve some cancer treatments [47,48].

VLP-siRNA synthesis and characterization

Gene silencing through RNA interference (RNAi) is considered to be among the most promising therapies to fight cancer. RNAi pathway influences the translation of mRNA through silencing specific genes in nearly all human cells [49]. The use of siRNA in RNAi has been limited so far by the lack of a vehicle that delivers siRNA to the desired tissue. To solve this problem, we are proposing to use plant viral capsids as nanocar-

riers to deliver siRNA. VLPs nanovehicles containing siRNA were synthesized, taking advantage of the self-assembly of BMV capsid proteins.

As a proof of concept, siRNA to silence the expression of green fluorescent protein (GFP) was encapsidated into BMV capsid proteins. In order to optimize the siRNA encapsidation, different ratios of siGFP and CP were examined, monitoring the uncapsidated GFP. An efficient encapasidation of siRNA to form the VLP-siGFP nanocarriers was obtained using a mass ratio of 1:6 (siGFP/CP). The VLP-siRNA from BMV showed icosahedral VLPs of approximately 27.7 nm in diameter, similar to those of the native virus (T = 3), as corroborated by TEM (Figure 4A and Figure S2a, Supporting Information File 1). Importantly, this is the first report of the encapsidation of nucleic acids in VLPs from BMV without the need for an RNA packaging signal. Previous reports showed that a tRNA-like structure is crucial to assemble BMV-VLPs with nonviral RNA [50,51].

The BMV VLPs containing siGFP were incubated in breast tumor cells MDA-MD-231, which constitutively express GPF. After VLP-siGFP treatment GFP expression was efficiently inhibited, as shown by the reduction in fluorescence after 6 h of treatment (Figure 4C), corroborating the cargo release from BMV VLP inside tumor cells and gene silencing.

BMV VLPs as siAkt1 nanocarriers

The anti-cancer siRNA Akt1 (siAkt1) was also encapsidated in BVM-VLPs (Figure 4B). Akt1 is a kinase involved in the processes of cell proliferation, migration and transformation [52-55]. The siAkt1 encapsidation was performed using a mass ratio of 1:6 (siRNA-Akt1/CP-BMV). VLPs with icosahedral morphology of around 27.8 nm of diameter (T = 3) were obtained,

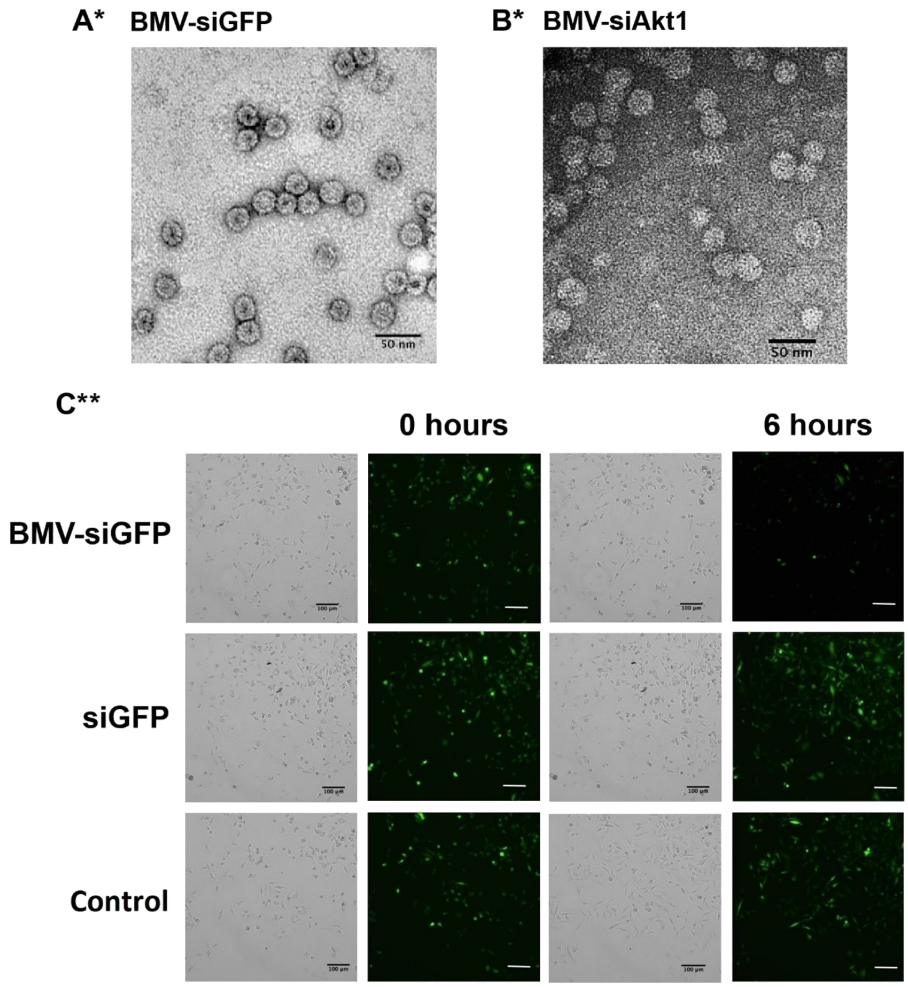

Figure 4: Encapsidation of siRNA in BMV capsid proteins. TEM images of virus-like particles in vitro assembled at a mass ratio of 1:6 (siRNA/CP BMV). (A) BMV VLP-siGFP, (B) BMV VLP-siAkt1. (C) GFP silencing assay using human breast tumor cells MDA-MB-231 that stably express GFP. The cells were incubated with BMV VLP-siGFP and siGFP at a concentration of 50 nM. *Scale bar = 50 µm, **scale bar = 100 µm.

similar to the VLP-siGFP (Figure 4 and Figure S2b, Supporting Information File 1) and the wild-type BMV (29.3 nm). The nanoparticle diameters were in agreement with those from DLS measurements, see Figure S3 (Supporting Information File 1). The amount of BMV capsid protein and siRNA was quantified by fluorescence assays. The correlation between the observed fluorescence and the concentration allows for the estimation of the average concentration of capsid protein and siRNA in the BMV-VLPs suspension (see Figure S4, Supporting Information File 1). With this estimation, together with the data from TEM measurements, an average of 100 µg of CP for 23.8 µg of siRNA was estimated, i.e., an average of 66 siRNA molecules in the T = 3 capsid (180 CP molecules). Thus, the siRNA confinement in BMV-VLPs is 10 times higher than that reported for CCMV VLPs [32]. Considering that siRNA has 42 e^- charges, there are 2,772 negative charges inside of the VLP, which is in agreement with the average of negative charges in the wild-type BMV: 3000 e^- /capsid [21,22].

The synthesized VLP-siAkt with both BMV and CCMV capsids were assayed in vivo. The VLP-siAkt were inoculated into mice with previously induced breast cancer tumors. The tumors were induced in female mice using the mouse cell line 4T1. After ten days of tumor inoculation, doses of 100 µg of the plant virus and VLP-siRNA were administered by injection every three days for two weeks in the periphery of the tumor (Figure 5A). The size of the tumor was evaluated twice a week for 28 days. Significant differences among the treatments were detected (Figure 5B). BMV-siAkt1 showed the highest activity, inhibiting around 50% of tumor size when compared with the control (Figure 5B,C). The efficiency of BMV-VLPs in delivering siRNA is similar to that observed when nanoparticles of multilamellar gold niosomes were used to deliver siRNA-Akt [56]. The mice showed no significant weight differences after the different treatments, suggesting that the VLPs and viral nanoparticles do not alter the mice metabolism, which could influence tumor growth. The slight tumor growth reduction induced by the treatment with the wild type virus could be attributed to their immunogenic capacity. These results are in agreement with the in vitro macrophage activation experiments showed above for CCMV, and also with previous reports on the success of in situ immunoregulation of tumors and the inhibition of metastasis using VLPs of the CPMV virus [57]. It is well known that treatments with CPMV-VLPs show greater inhibition of the tumor than using a highly immunogenic agent such as lipopolysaccharide (LPS), poly (I: C), and DMXAA 47. It seems that CCMV regulates the tumour microenvironment similarly to the CPMV virus [57]. The virus could induce the polarization of macrophages by recognizing intracellular toll-like receptors [45,58,59], or the expression of cytokines and chemokines, which activate infiltrated neutrophils in the tumor producing reactive oxygen species (ROS) [60]. The virus could also modulate and recruit CD8 + T cells, and natural killer cells to generate a cytotoxic effect [60,61]. However, the results obtained with the wild-type BMV are still unclear. Finally, our in vivo results demonstrated that BMV-VLPs nanocarriers containing siRNA are able to be internalized by the tumor cells and deliver the siAkt1 cargo into the tumor.

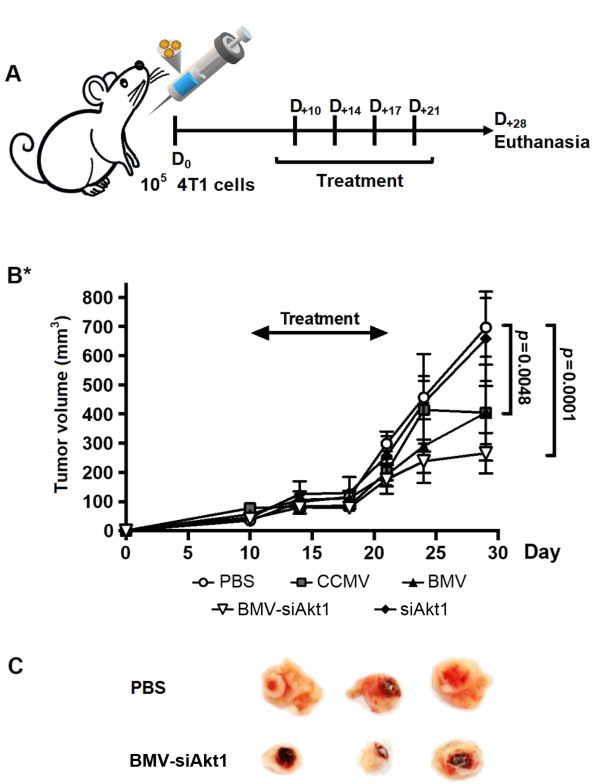

Figure 5: Anti-tumor effect of virus nanoparticles. (A) Schematic illustration of the experimental design. (B) In vivo growth curves of 4T1 tumors on mice after treatments with the virus and VLPs. (C) Ex vivo images of 4T1 breast cancer tumor from BMV VLP-siAkt1 and PBS control treatments on day 28 after tumor challenge. BMV VLP-siAkt1 showed the strongest inhibition effect on the tumor compared to the other nanoparticles. Error bars represent mean ± SD. *P*-values were calculated by 2-way ANOVA with Tukey posttest (*P < 0.01).

Conclusion

The capacity of BMV VLPs to carry and deliver siRNA into tumor cells has been demonstrated. Cell internalization of the plant viruses, BMV and CCMV, showed no cytotoxicity, making the viruses excellent and biocompatible nanocarrier candidates for targeted molecular anti-cancer therapies. BMV-based nanocarriers showed better efficiency in cell transfection without inducing in vitro immunological responses when compared with CCMV. In addition, the efficient synthesis of icosahedral BMV VLP-siRNA and its ability to release the small interference RNA molecules into tumor cells was also demonstrated. Thus, the BMV capsids are a potential candidate to

deliver siRNA. The versatility of these plant virus nanocarriers includes the functionalization of the viral capsid surface with specific ligands, e.g., folic acid, antibodies, or modified mannose, which further increase the recognition of specific targeted tissues or tumor cells. The coupling of drugs and molecular therapies, such as siRNA, in the same nanocarrier seems to be an excellent strategy to increase the efficiency of anticancer therapies.

Experimental

Production and purification of the virus

CCMV and BMV were obtained from infected cowpea and barley plants, respectively. The viruses were purified as described previously [22]. Briefly, one week after germination the plant leaves were slightly damaged mechanically to be able to be infected with the wild-type virus, using the inoculation buffer (0.01 M sodium phosphate buffer, pH 6 and 0.01 M magnesium chloride) containing 0.1 μg/μL of wild-type virus suspension. After the plants showed symptoms of infection the leaves were collected, chopped in a blender with extraction buffer (0.5 M sodium acetate and 0.08 M magnesium acetate, pH 4.5). The mixture was filtered through cheesecloth and then one volume of chloroform was added and the mixture was kept under stirring at 4 °C. To recover the aqueous phase, the mixture was centrifuged at 12,300*g* for 15 min at 4 °C. The aqueous phase was kept under stirring for 2 h and placed on a 10% sucrose cushion to separate the protein fraction. The cushion was ultracentrifuged at 110,000*g* for 120 min using a Beckman SW 32 Ti rotor in a Optima XPN-100 ultracentrifuge. The formed pellet was resuspended with virus suspension buffer and the virus was ultrapurified using a sucrose gradient, which was ultracentrifuged at 110,000*g* at 4 °C for 120 min. The concentration of the virus was calculated by measuring the UV absorbance using a Nanodrop 2000c spectrophotometer (ThermoFisher Scientific). All the procedures were performed at 4 °C. Finally, the purified viruses were stored at −80 °C in 1.5 mL microcentrifuge tubes.

Cell cultures

The breast tumor cell lines MDA-MB-231 and MCF-7 were obtained from the ATCC. The cell line MDA-MB-231/GFPm which constitutively expresses green fluorescent protein (GFP) was obtained from Cell Biolabs. RAW-Blue (InvivoGen) was derived from the mouse macrophage cell line RAW 264.7 after adding the sequence of the secreted embryonic alkaline phosphatase (SEAP) under the control of an NF-κB/AP-1 inducible promoter. RAW-Blue cells can be used as pattern-recognition receptor reporter cells to assess macrophage activation. All these cells were cultured with high-glucose DMEM media (Biowest). The breast-tumor cell line 4T1 (ATCC) was derived from a spontaneously arising mammary tumor from a MMTV+ Balb/C mice and forms tumors when implanted in the mammary fat of Balb/C mice. The 4T1 cells were cultured in RPMI medium (Corning). DMEM and RPMI basal media were supplemented with 10% fetal bovine serum (FBS, Biowest) and antibiotic/antimycotic (ThermoFisher Scientific). The medium for MCF-7 cells was also supplemented with recombinant human insulin (0.01 mg/mL; Sigma-Aldrich) and the medium of the RAW-Blue cells with 100 μg/mL of Normocin and 200 μg/mL of Zeocin antibiotics (InvivoGen). Cells were maintained at 37 °C in a humidified incubator with 5% CO_2.

Virus cell internalization

To visualize the cell internalization, viruses were loaded with NanoOrange. These are hydrophobic molecules that bind to the hydrophobic domains of the capsid proteins of BMV and CCMV. NanoOrange (NanoOrange™ Protein Quantitation Kit; ThermoFisher Scientific) were incubated with 1 μg of BMV or CCMV capsids for 20 min. The virus capsids were also rendered fluorescent by the covalent conjugation of the free amino groups of proteins with fluorescein-5-isothiocyanate (FITC). The FITC conjugation was carried out according to Douglas et al. [27] as follows: 400 μg of viral capsid were labeled in a solution of FITC (10 μg/mL, Molecular Probes) in PBS, under constant agitation, for 2 h at room temperature. The excess of the fluorophore was removed by ultrafiltration using 100 kDa amicon filters (0.5 mL, Millipore). For the controls, free NanoOrange and FITC were utilized at the same concentration to label the viruses.

A suspension containing 10^5 MDA-MB-231 or MCF-7 cells was seeded in 35 mm glass bottom dishes (MatTek Co.) or in 12-well plates. After 12 h, the medium was completely removed and cells were incubated for another 12 h in basal media. BMV or CCMV viral capsids labeled with NanoOrange, or FITC were added to the culture (1.3×10^6 virions per cell) and incubated for 4 h. The amount of virus used is consistent with previous studies with plant viruses [32,35-37,41]. Virus internalization was monitored on live cells or cells fixed with paraformaldehyde, after staining the membrane with FM4-64 (ThermoFisher Scientific) and the nucleus with DAPI (Sigma-Aldrich), using a confocal microscope FV1000 FluoView (Olympus). Additionally, cells were trypsinized, centrifuged (800*g*, 5 min) and resuspended in PBS before analyzing virus internalization using an Attune acoustic focusing cytometer (Thermo Fisher Scientific). Doublets were excluded by plotting the height as a function of the area for the forward scatter and then of the side scatter. Debris were then excluded by plotting the area of the forward scatter as a function of the area of the side scatter. For each sample, a least 7,500 events corresponding to single cells were collected and the Attune Cytometric Software (v2.1) was used to analyze results. For the controls,

the same amount of free NanoOrange was used as the one used to load viruses.

Cell viability assay

MDA-MB-231 cells were seeded in 12-well plates, as described previously. When the cell monolayers reached about 70% confluence, the medium was completely removed and cells were synchronized in basal media for 12 h. The cells were then further incubated in the presence of BMV or CCMV (20 μg/mL, 2.6×10^7 virions per cell) or DMSO (20% v/v) as a control for cell death and PBS as a control medium for 24 h. The Viability/Cytotoxicity Assay Kit (Biotum) was used to assess the amount of live and dead cells. Briefly, cells were trypsinized and labeled with calcein and ethidium homodimer III (EthD-III) to recognize live and dead cells, respectively. Cells were analyzed by flow cytometry. For each sample at least 7,500 events corresponding to single cells were collected as described previously, and the Attune Cytometric Software (v2.1) was used to analyze results.

Surface functionalization of BMV and CCMV with PEG

The external surface of the capsid was PEGylated using polyethylene glycol functionalized with *N*-hydroxylsuccinimide (NHS-PEG, Sigma Aldrich). The use of NHS-PEG enabled the selective conjugation of nanoparticles with PEG via amide bonds. A solution of NHS-PEG (9.12 nmol) was mixed with the capsids suspension (1 mg/mL) in PBS and gently shaken for 2 h at room temperature. The excess of PEG was removed by ultrafiltration using Amicon filters (Millipore) of 100 kDa cutoff.

In vitro immunogenicity of CCMV and BMV viruses

The macrophage cell line RAW-Blue was used to evaluate the in vitro immunogenicity. Experiments were performed according to the manufacturer's guidelines. Cells at 80% confluence were washed twice with sterile PBS, manually detached by scraping and resuspended in fresh medium. Live cells were seeded in 96-well plates (105 per well) and incubated overnight in the presence or absence of CCMV or BMV (20 to 100 μg/mL, 2.6×10^7 to 1.3×10^8 virions per cell), PEGylated or non-functionalized capsids, or as positive control lipopolysaccharides (2.5 or 75 ng/mL). Then, 50 μL of supernatant was transferred into a new 96-well plate and 150 μL of Quantity Blue (InvivoGen) reagent was added and incubated at 37 °C for 1 h. The absorbance at 655 nm was measured using a Multiskan GO plate reader (ThermoFisher Scientific).

Synthesis and characterization of BMV VLP-siRNA

siRNA against GFP and mouse Akt1 were purchased from Dharmacon. The sequences of the siRNA against GFP (siGFP) was 5′-GGCAAGCUGACCCUGAAGUUCAUU-3′ and against Akt1 (siAkt1) was 5′-GACAAGGACGGGCACAUUAUU-3′. BMV VLPs with siRNA were synthetized as described previously [22] using a mass ratio of 1:6 (siRNA/capsid protein). The disassembled BMV capsid protein and siRNA were mixed and dialyzed overnight in an assembly buffer (50 mM NaCl, 10 mM KCl, 5 mM $MgCl_2$, 1 mM DTT, 50 mM Tris-HCl, pH 7.2), followed by dialysis against acidification buffer (50 mM sodium acetate, 8 mM magnesium acetate, pH 4.5) for 8 h and finally the sample was dialyzed in assembly buffer. All dialysis experiments were performed at a temperature of 4 °C using a dialysis membrane with a 14 kDa cut-off (Spectrumlabs).

The morphology of the VLP-siRNA was evaluated by transmission electron microscopy. Copper grids (400 mesh, Ted Pella) were used, in which 6 μL of the sample was placed at a concentration of 0.1 μg/μL and after two minutes the liquid excess was removed by using Whatman No. 2 filter paper. Negative contrast was obtained by the addition of 6 μL of 1% uranyl acetate for 1 min. The size and zeta potential of the viral nanoparticles and VLPs were determined by dynamic light scattering (DLS) using a Malvern NanoSizer.

The siRNA and the capsid protein were quantified from purified BMV VLP-siAkt1 using the Quant-it RiboGreen RNA assay (ThermoFisher Scientific) and NanoOrange protein quantification kit (ThermoFisher Scientific), respectively.

Knockdown of gene expression by VLP-siGFP

MDA-MB-231/GFP cells were seeded in a 12-well plate when the cells reached 70% confluence; they were synchronized in basal media overnight. Cells were then further cultured in complete medium containing 40 μL of BMV VLP-siGFP (50 nM of siGFP) for 6 h. The same concentration of free siGFP (50 nM) was used as a control. The amount of GFP was assessed using a LS720 fluorescence microscope (Etaluma).

Mouse model of mammary fat pad tumor

All animal experiments were performed in compliance with the local ethics committee of the Center for Scientific Research and Higher Education of Ensenada (CICESE). BALB/cAnNHsd female mice were obtained from Envigo. Mice were maintained in an Optimice cage system (Animal Care System), in a controlled environment room (temperature 24 °C and 12 h light/dark cycle) where they received water and food (2018 Teklad Global 18% protein rodent diet, Envigo) ad libitum. Mice were acclimated for at least a week before starting the experiments.

For the development of tumors, a cell suspension of 4T1 mouse breast cancer cells was prepared at a concentration of 2×10^6 cells/mL in PBS. 4T1 cells were then inoculated in the

left, upper (or 2nd) mammary fat pad (10^5 cells in 50 µL) of 8-week old Balb/C female mice. One week after the inoculation, palpable tumors were detected in all the mice that were divided into four groups (n = 4) to receive CCMV, BMV or BMV capsids loaded with siAkt1 (100 µg of coat protein) per mouse, 23.8 µg of free siAkt1 or PBS in the controls. They were inoculated intratumorally three times per week. Tumors were measured with a caliper three times and their size was calculated using the formula $(L{\cdot}w^2)/2$ where L and w stand for tumor length and width, respectively.

Supporting Information

Supporting Information File 1

Internalization of CCMV and BMV in MCF-7 and characterization VLPs (DLS and TEM).
[https://www.beilstein-journals.org/bjnano/content/supplementary/2190-4286-11-28-S1.pdf]

Acknowledgments

We thank Francisco Ruiz-Medina, Olga A. Callejas-Negrete and Dr. Katrin Quester for TEM analysis, fluorescent microscopy and technical assistance respectively.

Funding

This work has been funded by the National Council of Science and Technology of Mexico (CONACYT, Grants CB-239878, PN-247474 and CB-251241).

ORCID® iDs

Pierrick G. J. Fournier - https://orcid.org/0000-0001-7633-8129
Rafael Vazquez-Duhalt - https://orcid.org/0000-0003-1612-2996
Ruben D. Cadena-Nava - https://orcid.org/0000-0001-8428-6701

References

1. Blanco, E.; Shen, H.; Ferrari, M. *Nat. Biotechnol.* **2015,** *33,* 941–951. doi:10.1038/nbt.3330
2. Ferrari, M. *Trends Biotechnol.* **2010,** *28,* 181–188. doi:10.1016/j.tibtech.2009.12.007
3. Michor, F.; Liphardt, J.; Ferrari, M.; Widom, J. *Nat. Rev. Cancer* **2011,** *11,* 657–670. doi:10.1038/nrc3092
4. Moghimi, S. M.; Patel, H. M. *Adv. Drug Delivery Rev.* **1998,** *32,* 45–60. doi:10.1016/s0169-409x(97)00131-2
5. Choi, H. S.; Liu, W.; Liu, F.; Nasr, K.; Misra, P.; Bawendi, M. G.; Frangioni, J. V. *Nat. Nanotechnol.* **2010,** *5,* 42–47. doi:10.1038/nnano.2009.314
6. Lesniak, A.; Salvati, A.; Santos-Martinez, M. J.; Radomski, M. W.; Dawson, K. A.; Åberg, C. *J. Am. Chem. Soc.* **2013,** *135,* 1438–1444. doi:10.1021/ja309812z
7. Decuzzi, P.; Godin, B.; Tanaka, T.; Lee, S.-Y.; Chiappini, C.; Liu, X.; Ferrari, M. *J. Controlled Release* **2010,** *141,* 320–327. doi:10.1016/j.jconrel.2009.10.014
8. Alexis, F.; Pridgen, E.; Molnar, L. K.; Farokhzad, O. C. *Mol. Pharmaceutics* **2008,** *5,* 505–515. doi:10.1021/mp800051m
9. Gottesman, M. M.; Fojo, T.; Bates, S. E. *Nat. Rev. Cancer* **2002,** *2,* 48–58. doi:10.1038/nrc706
10. Longmire, M. R.; Ogawa, M.; Choyke, P. L.; Kobayashi, H. *Bioconjugate Chem.* **2011,** *22,* 993–1000. doi:10.1021/bc200111p
11. Aljabali, A. A. A.; Shukla, S.; Lomonossoff, G. P.; Steinmetz, N. F.; Evans, D. J. *Mol. Pharmaceutics* **2013,** *10,* 3–10. doi:10.1021/mp3002057
12. Xu, R.; Zhang, G.; Mai, J.; Deng, X.; Segura-Ibarra, V.; Wu, S.; Shen, J.; Liu, H.; Hu, Z.; Chen, L.; Huang, Y.; Koay, E.; Huang, Y.; Liu, J.; Ensor, J. E.; Blanco, E.; Liu, X.; Ferrari, M.; Shen, H. *Nat. Biotechnol.* **2016,** *34,* 414–418. doi:10.1038/nbt.3506
13. Chen, Z. G. *Trends Mol. Med.* **2010,** *16,* 594–602. doi:10.1016/j.molmed.2010.08.001
14. Ashley, C. E.; Carnes, E. C.; Phillips, G. K.; Durfee, P. N.; Buley, M. D.; Lino, C. A.; Padilla, D. P.; Phillips, B.; Carter, M. B.; Willman, C. L.; Brinker, C. J.; do Carmo Caldeira, J.; Chackerian, B.; Wharton, W.; Peabody, D. S. *ACS Nano* **2011,** *5,* 5729–5745. doi:10.1021/nn201397z
15. Peer, D.; Karp, J. M.; Hong, S.; Farokhzad, O. C.; Margalit, R.; Langer, R. *Nat. Nanotechnol.* **2007,** *2,* 751–760. doi:10.1038/nnano.2007.387
16. Manchester, M.; Singh, P. *Adv. Drug Delivery Rev.* **2006,** *58,* 1505–1522. doi:10.1016/j.addr.2006.09.014
17. Flenniken, M. L.; Willits, D. A.; Harmsen, A. L.; Liepold, L. O.; Harmsen, A. G.; Young, M. J.; Douglas, T. *Chem. Biol.* **2006,** *13,* 161–170. doi:10.1016/j.chembiol.2005.11.007
18. Lewis, J. D.; Destito, G.; Zijlstra, A.; Gonzalez, M. J.; Quigley, J. P.; Manchester, M.; Stuhlmann, H. *Nat. Med.* **2006,** *12,* 354–360. doi:10.1038/nm1368
19. Muldoon, L. L.; Nilaver, G.; Kroll, R. A.; Pagel, M. A.; Breakefield, X. O.; Chiocca, E. A.; Davidson, B. L.; Weissleder, R.; Neuwelt, E. A. *Am. J. Pathol.* **1995,** *147,* 1840–1851.
20. Räty, J. K.; Liimatainen, T.; Wirth, T.; Airenne, K. J.; Ihalainen, T. O.; Huhtala, T.; Hamerlynck, E.; Vihinen-Ranta, M.; Närvänen, A.; Ylä-Herttuala, S.; Hakumäki, J. M. *Gene Ther.* **2006,** *13,* 1440–1446. doi:10.1038/sj.gt.3302828
21. Speir, J. A.; Munshi, S.; Wang, G.; Baker, T. S.; Johnson, J. E. *Structure* **1995,** *3,* 63–78. doi:10.1016/s0969-2126(01)00135-6
22. Cadena-Nava, R. D.; Comas-Garcia, M.; Garmann, R. F.; Rao, A. L. N.; Knobler, C. M.; Gelbart, W. M. *J. Virol.* **2012,** *86,* 3318–3326. doi:10.1128/jvi.06566-11
23. Azizgolshani, O.; Garmann, R. F.; Cadena-Nava, R.; Knobler, C. M.; Gelbart, W. M. *Virology* **2013,** *441,* 12–17. doi:10.1016/j.virol.2013.03.001
24. Sánchez-Sánchez, L.; Cadena-Nava, R. D.; Palomares, L. A.; Ruiz-Garcia, J.; Koay, M. S. T.; Cornelissen, J. J. M. T.; Vazquez-Duhalt, R. *Enzyme Microb. Technol.* **2014,** *60,* 24–31. doi:10.1016/j.enzmictec.2014.04.003
25. Barwal, I.; Kumar, R.; Kateriya, S.; Dinda, A. K.; Yadav, S. C. *Sci. Rep.* **2016,** *6,* 37096. doi:10.1038/srep37096
26. Sun, J.; DuFort, C.; Daniel, M.-C.; Murali, A.; Chen, C.; Gopinath, K.; Stein, B.; De, M.; Rotello, V. M.; Holzenburg, A.; Kao, C. C.; Dragnea, B. *Proc. Natl. Acad. Sci. U. S. A.* **2007,** *104,* 1354–1359. doi:10.1073/pnas.0610542104
27. Gillitzer, E.; Willits, D.; Young, M.; Douglas, T. *Chem. Commun.* **2002,** 2390–2391. doi:10.1039/b207853h
28. Devi, G. R. *Cancer Gene Ther.* **2006,** *13,* 819–829. doi:10.1038/sj.cgt.7700931

29. Tatiparti, K.; Sau, S.; Kashaw, S. K.; Iyer, A. K. *Nanomaterials* **2017,** *7,* 77. doi:10.3390/nano7040077
30. Yildiz, I.; Tsvetkova, I.; Wen, A. M.; Shukla, S.; Masarapu, M. H.; Dragnea, B.; Steinmetz, N. F. *RSC Adv.* **2012,** *2,* 3670–3677. doi:10.1039/c2ra01376b
31. Black, D. R.; Connell, C. J.; Merigan, T. C. *J. Virol.* **1973,** *12,* 1209–1215. doi:10.1128/jvi.12.6.1209-1215.1973
32. Lam, P.; Steinmetz, N. F. *Biomater. Sci.* **2019,** *7,* 3138–3142. doi:10.1039/c9bm00785g
33. Villagrana-Escareño, M. V.; Reynaga-Hernández, E.; Galicia-Cruz, O. G.; Durán-Meza, A. L.; De la Cruz-González, V.; Hernández-Carballo, C. Y.; Ruíz-García, J. *BioMed Res. Int.* **2019,** *2019,* 1–11. doi:10.1155/2019/4630891
34. Satelli, A.; Li, S. *Cell. Mol. Life Sci.* **2011,** *68,* 3033–3046. doi:10.1007/s00018-011-0735-1
35. Koudelka, K. J.; Destito, G.; Plummer, E. M.; Trauger, S. A.; Siuzdak, G.; Manchester, M. *PLoS Pathog.* **2009,** *5,* e1000417. doi:10.1371/journal.ppat.1000417
36. Plummer, E. M.; Manchester, M. *Mol. Pharmaceutics* **2013,** *10,* 26–32. doi:10.1021/mp300238w
37. Steinmetz, N. F.; Cho, C.-F.; Ablack, A.; Lewis, J. D.; Manchester, M. *Nanomedicine (London, U. K.)* **2011,** *6,* 351–364. doi:10.2217/nnm.10.136
38. Agrawal, A.; Manchester, M. *Biomacromolecules* **2012,** *13,* 3320–3326. doi:10.1021/bm3010885
39. Koudelka, K. J.; Rae, C. S.; Gonzalez, M. J.; Manchester, M. *J. Virol.* **2007,** *81,* 1632–1640. doi:10.1128/jvi.00960-06
40. Nam, H. Y.; Kwon, S. M.; Chung, H.; Lee, S.-Y.; Kwon, S.-H.; Jeon, H.; Kim, Y.; Park, J. H.; Kim, J.; Her, S.; Oh, Y.-K.; Kwon, I. C.; Kim, K.; Jeong, S. Y. *J. Controlled Release* **2009,** *135,* 259–267. doi:10.1016/j.jconrel.2009.01.018
41. Jung, B.; Rao, A. L. N.; Anvari, B. *ACS Nano* **2011,** *5,* 1243–1252. doi:10.1021/nn1028696
42. Singh, P.; Prasuhn, D.; Yeh, R. M.; Destito, G.; Rae, C. S.; Osborn, K.; Finn, M. G.; Manchester, M. *J. Controlled Release* **2007,** *120,* 41–50. doi:10.1016/j.jconrel.2007.04.003
43. Rae, C. S.; Wei Khor, I.; Wang, Q.; Destito, G.; Gonzalez, M. J.; Singh, P.; Thomas, D. M.; Estrada, M. N.; Powell, E.; Finn, M. G.; Manchester, M. *Virology* **2005,** *343,* 224–235. doi:10.1016/j.virol.2005.08.017
44. Lunov, O.; Syrovets, T.; Loos, C.; Beil, J.; Delacher, M.; Tron, K.; Nienhaus, G. U.; Musyanovych, A.; Mailänder, V.; Landfester, K.; Simmet, T. *ACS Nano* **2011,** *5,* 1657–1669. doi:10.1021/nn2000756
45. Carignan, D.; Herblot, S.; Laliberté-Gagné, M.-È.; Bolduc, M.; Duval, M.; Savard, P.; Leclerc, D. *Nanomedicine (N. Y., NY, U. S.)* **2018,** *14,* 2317–2327. doi:10.1016/j.nano.2017.10.015
46. Veronese, F. M.; Pasut, G. *Drug Discovery Today* **2005,** *10,* 1451–1458. doi:10.1016/s1359-6446(05)03575-0
47. Shaw, A. R.; Suzuki, M. *Mol. Ther.–Methods Clin. Dev.* **2019,** *15,* 418–429. doi:10.1016/j.omtm.2019.11.001
48. Xu, W.; Atkinson, V. G.; Menzies, A. M. *Eur. J. Cancer* **2020,** *127,* 1–11. doi:10.1016/j.ejca.2019.12.007
49. Dowdy, S. F. *Nat. Biotechnol.* **2017,** *35,* 222–229. doi:10.1038/nbt.3802
50. Choi, Y. G.; Dreher, T. W.; Rao, A. L. N. *Proc. Natl. Acad. Sci. U. S. A.* **2002,** *99,* 655–660. doi:10.1073/pnas.022618199
51. Choi, Y. G.; Rao, A. L. N. *J. Virol.* **2003,** *77,* 9750–9757. doi:10.1128/jvi.77.18.9750-9757.2003
52. Clark, A. S.; West, K.; Streicher, S.; Dennis, P. A. *Mol. Cancer Ther.* **2002,** *1,* 707–717.
53. Bellacosa, A.; Kumar, C. C.; Di Cristofano, A.; Testa, J. R. *Adv. Cancer Res.* **2005,** *94,* 29–86. doi:10.1016/s0065-230x(05)94002-5
54. Chau, N.-M.; Ashcroft, M. *Breast Cancer Res.* **2003,** *6,* 55. doi:10.1186/bcr739
55. Cheng, J. Q.; Lindsley, C. W.; Cheng, G. Z.; Yang, H.; Nicosia, S. V. *Oncogene* **2005,** *24,* 7482–7492. doi:10.1038/sj.onc.1209088
56. Rajput, S.; Puvvada, N.; Kumar, B. N. P.; Sarkar, S.; Konar, S.; Bharti, R.; Dey, G.; Mazumdar, A.; Pathak, A.; Fisher, P. B.; Mandal, M. *Mol. Pharmaceutics* **2015,** *12,* 4214–4225. doi:10.1021/acs.molpharmaceut.5b00692
57. Lizotte, P. H.; Wen, A. M.; Sheen, M. R.; Fields, J.; Rojanasopondist, P.; Steinmetz, N. F.; Fiering, S. *Nat. Nanotechnol.* **2016,** *11,* 295–303. doi:10.1038/nnano.2015.292
58. Wang, C.; Beiss, V.; Steinmetz, N. F. *J. Virol.* **2019,** *93,* 1–14. doi:10.1128/jvi.00129-19
59. Rodell, C. B.; Arlauckas, S. P.; Cuccarese, M. F.; Garris, C. S.; Li, R.; Ahmed, M. S.; Kohler, R. H.; Pittet, M. J.; Weissleder, R. *Nat. Biomed. Eng.* **2018,** *2,* 578–588. doi:10.1038/s41551-018-0236-8
60. Mantovani, A.; Cassatella, M. A.; Costantini, C.; Jaillon, S. *Nat. Rev. Immunol.* **2011,** *11,* 519–531. doi:10.1038/nri3024
61. Beauvillain, C.; Delneste, Y.; Scotet, M.; Peres, A.; Gascan, H.; Guermonprez, P.; Barnaba, V.; Jeannin, P. *Blood* **2007,** *110,* 2965–2973. doi:10.1182/blood-2006-12-063826

License and Terms

BEILSTEIN JOURNAL OF NANOTECHNOLOGY

Multilayer capsules made of weak polyelectrolytes: a review on the preparation, functionalization and applications in drug delivery

Varsha Sharma[1,2] and Anandhakumar Sundaramurthy[*2,3,§]

Review

Open Access

Address:
[1]Department of Biomedical Engineering, SRM Institute of Science and Technology, Kattankulathur, Tamil Nadu 603203, India, [2]SRM Research Institute, SRM Institute of Science and Technology, Kattankulathur, Tamil Nadu 603203, India and [3]Department of Physics and Nanotechnology, SRM Institute of Science and Technology, Kattankulathur, Tamil Nadu 603203, India

Email:
Anandhakumar Sundaramurthy[*] - anandhas@srmist.edu.in

* Corresponding author
§ Tel: 918838104529

Keywords:
drug delivery; functionalization; multilayer capsules; synthesis; weak polyelectrolytes

Beilstein J. Nanotechnol. **2020,** *11,* 508–532.
doi:10.3762/bjnano.11.41

Received: 11 November 2019
Accepted: 25 February 2020
Published: 27 March 2020

This article is part of the thematic issue "Engineered nanomedicines for advanced therapies".

Guest Editor: M. K. Danquah

Abstract

Multilayer capsules have been of great interest for scientists and medical communities in multidisciplinary fields of research, such as drug delivery, sensing, biomedicine, theranostics and gene therapy. The most essential attributes of a drug delivery system are considered to be multi-functionality and stimuli responsiveness against a range of external and internal stimuli. Apart from the highly explored strong polyelectrolytes, weak polyelectrolytes offer great versatility with a highly controllable architecture, unique stimuli responsiveness and easy tuning of the properties for intracellular delivery of cargo. This review describes the progress in the preparation, functionalization and applications of capsules made of weak polyelectrolytes or their combination with biopolymers. The selection of a sacrificial template for capsule formation, the driving forces involved, the encapsulation of a variety of cargo and release based on different internal and external stimuli have also been addressed. We describe recent perspectives and obstacles of weak polyelectrolyte/biopolymer systems in applications such as therapeutics, biosensing, bioimaging, bioreactors, vaccination, tissue engineering and gene delivery. This review gives an emerging outlook on the advantages and unique responsiveness of weak polyelectrolyte based systems that can enable their widespread use in potential applications.

Review

Introduction

In the last few decades, micrometer and nanometer-sized capsules made of polyelectrolytes (PEs) have been the subject of intensive research because of their significance in biotechnological and nanotechnological frontiers with applications in the fields of chemistry, physics, biology and medicine [1]. The multilayered capsules are fabricated by alternate deposition of

anionic and cationic PEs on a sacrificial colloidal template, followed by the dissolution of the core. The schematic diagram of layer-by-layer (LbL) deposition on colloidal templates, core dissolution and drug encapsulation into LbL-assembled capsules is shown in Figure 1. The method of fabricating core–shell particles and multilayered hollow capsules via LbL assembly was originally proposed and developed by Iller [2] and Decher et al. [3], but it was brought into the limelight by systematic and extensive research by various research groups. The encapsulation of various macromolecules inside the hollow capsules was carried out by adjusting the physiochemical properties of the polymers in order to manipulate the shell permeability [4]. However, most of the work uses strong PEs such as polystyrene sulfonate (PSS) as one of the polymers, and thus, in order to release the payload, a disturbance in the intermolecular forces (e.g., covalent binding, hydrogen bonding and electrostatic interactions) guarding the capsule stability is necessarily required. This led to the observation of various environmental triggers such as pH, ionic strength, polarity and temperature that play a major role in manipulating the capsule permeability by modulating the shell interactive forces [5]. Following this, successful efforts were also made to release the payload under the exposure of external (modern) triggers such as laser light, ultrasound, magnetic field, enzymatic deformation and mechanical deformation. In the latter cases, the capsules were irreversibly ruptured and released the loaded molecules either in a burst or sustained manner. As weak PEs are in ionized form only in a certain range of pH or ionic strength [6], the open and closed state of multilayer capsules could be easily controlled by varying pH or ionic strength, a concept that led to widespread use in in vivo applications [7]. Much progress has also been seen in natural biopolymers such as polypeptides, polynucleotides, lipids and polysaccharides as they are biodegradable under common physiological conditions via enzymatic and pH induced degradation [8].

The advantage of LbL-assembled capsules lies in the versatility of interactions (e.g., covalent and noncovalent) between the PEs used for capsule fabrication and their nature. The multilayers showcase selective permeability by being permeable to low molecular weight compounds while impermeable to larger macromolecules [9]. The size of multilayered hollow capsules can be easily controlled by varying the size of the sacrificial template [10]. The shell thickness can also be altered by the number of layers and the preparation conditions, thus providing control over thickness and morphology. Notably, these capsules have better encapsulation efficiency (EE) and a stable zeta potential mainly due to the chemical nature of the polymers used and the

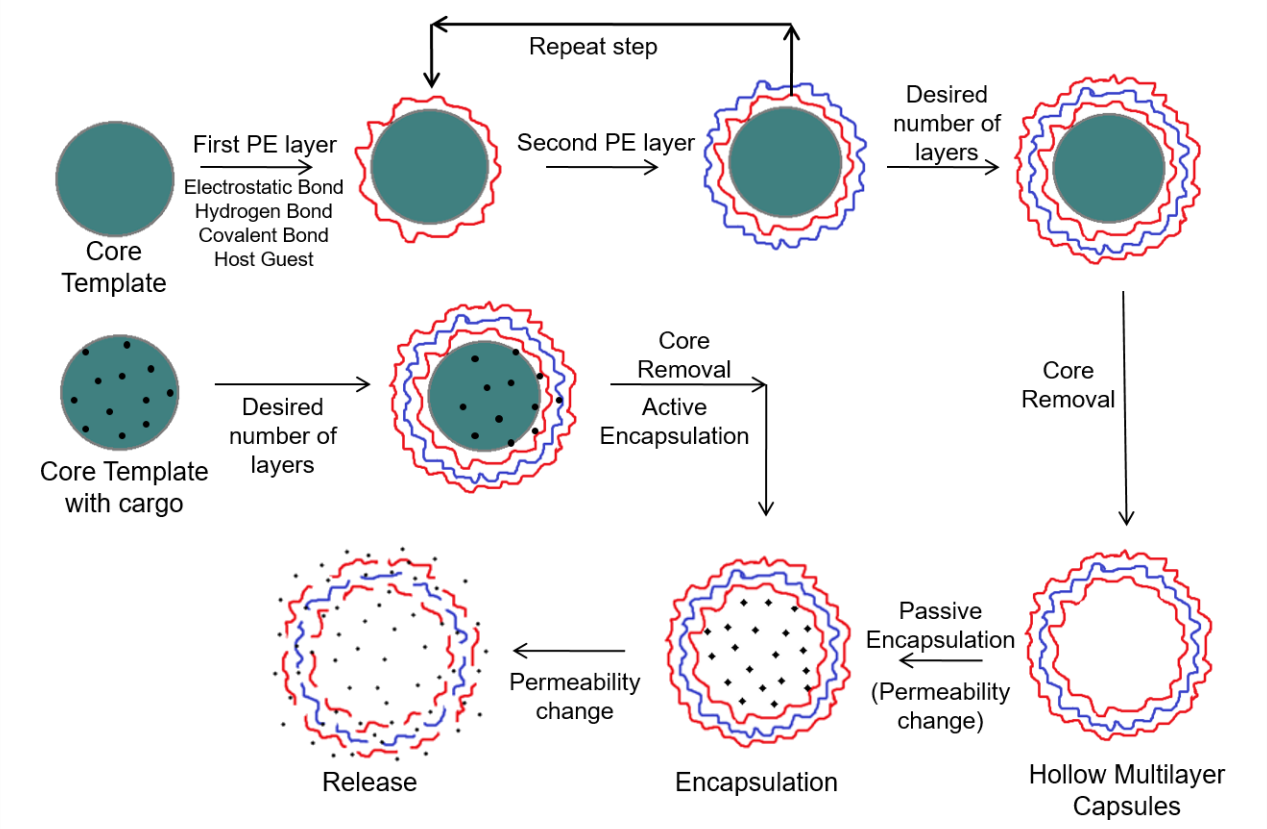

Figure 1: Schematic representation showing the capsule fabrication, drug encapsulation and release of loaded drug molecules.

assembly conditions [11]. Many studies have shown successful permeability changes for encapsulation and release via changes in pH or ionic strength for weak PE systems. The chemical nature of the polymers used along with the type of the core composition defines the mechanical properties such as elastic modulus, toughness, strength and robustness of the hollow capsules [8]. The influence of the above-mentioned properties on capsule morphology and size have been demonstrated by inducing deformations on capsules either by osmotic [12] or physical force [13] using confocal laser scanning microscopy (CLSM), atomic force microscopy (AFM), and reflection interference contrast microscopy (RICM). Fabrication conditions such as the type of polymer (e.g., thicker layers are formed by PEs having lower charge density) [14], concentration of the polymer solution (higher concentration leads to thicker walls) [14], ionic strength [15] and pH [16] also affect the types of interactions, shell thickness and permeability of the capsules.

The easier and successful encapsulation of different molecules/compounds into the capsules demonstrates the potential of multilayer capsules as drug delivery vehicles [17]. They are capable of encapsulating all kinds of substances and/or molecules ranging from enzymes, nucleic acid, peptides, proteins, therapeutic drugs, biomolecules, fluorescent molecules and nanoparticles (NPs) in their hollow cavity [18]. This can be achieved in many ways: by using the material itself as a template, by incorporating the material into core templates, or by encapsulating the drug in preformed capsules by controlling the permeability of the capsules using environmental triggers. These factors along with several introduced functionalities in the shell are also used to carry out the release of the encapsulated payload in a controlled manner. The incorporation of functionalities such as organic molecules, NPs, fluorescent dyes, polymers, nanotubes and other biomolecules into the PE multilayers during the fabrication makes it easy to control the internal structure, mechanical properties and permeability of the shell in order to induce the release of loaded cargo under exposure to external triggers.

Several reports on strong PE capsules to date show their wide use in many practical applications ranging from the loading and controlled release of therapeutic agents upon minor variations in the environmental characteristics, surface modification and suppression of inter-chain interaction to the degradation/rearrangement of LbL films under the action of physical factors [19,20]. In spite of the fact that weak PE systems can also offer many such advantages, only a few works have been reported. For instance, the responsiveness to instantaneous environmental changes (e.g., pH, ionic strength and temperature) come from the physical proximity of weakly charged groups to each other [21]. The effect of PE density can be particularly prominent when there are many charged groups present in the system. The use of different charged groups for LbL assembly can impart unique responsiveness to LbL systems as the residual charges in the multilayer films can play an important role in manipulating the polymer/polymer interactions, thus leading to easy engineering of the properties. Although recent interest has been shown in exploring weak PE system with biopolymers for several applications, their unique responsiveness and advantages are not yet addressed in detail. With the emerging applications of weak PEs, it is imperative to accurately understand their capabilities. In this review, we have summarized the work done on weak PE multilayer capsules. Their fabrication on different types of core templates, driving forces involved between different polymers, and encapsulation strategies used are discussed in detail. We also summarize the different ways of functionalization of the capsules and several internal/external triggers used to release the payload with special focus on their applications. It is believed that weak PE systems can prove to be highly efficient and suitable for several in vivo applications.

Core templates

The most important step for hollow multilayer capsule preparation is the dissolution and complete removal of its core whose size can vary from nanometers to micrometers. The template should be inert and should not affect the chemical and mechanical properties of the polymer shell. A wide range of organic and inorganic particles, NPs, proteins, biological cells, liposomes, DNA, dyes and drugs have served as suitable sacrificial templates [22]. After serving as a support to develop multilayer assembly, the core is dissolved by using suitable solvents.

Organic cores such as melamine formaldehyde (MF) and polystyrene (PS) were the few originally employed as sacrificial templates. Upon dissolution of these templates at pH < 1.6 or by organic solvents such as dimethylformamide (DMF), dimethyl sulfoxide (DMSO), hydrochloric acid (HCl) and tetrahydrofuran, the capsule showed swelling and retraction of the shell in order to diffuse out the dissolved core particles [23]. In the case of the MF template dissolution, the dissolution was incomplete as it interacted with positively charged layer components and resulted in a negatively charged complex inside the hollow capsules [24]. This was also the case with PS template removal, which also affected the shell structure limiting their biological applications [25]. The use of silicon oxide (SiO_2) templates is quite common, however, dissolution using hazardous hydrofluoric acid (HF) limits its application. It is mostly used with strong PE systems but has also been extended to weak PE assemblies [26]. The dissolution of a SiO_2 core in a poly(allylamine hydrochloride) (PAH)/poly(methacrylic acid) (PMA) assembly with ammonium fluoride (NH_4F) at a suitable pH contributed to both multilayer stability and colloidal stability as

shown in the AFM images in Figure 2a–d [24]. It was reported that when an 8- or 16-layer capsule core was dissolved at pH 5 and 4.5, respectively, the structure showed high mean heights suggesting trapped silica gel inside the capsules which may be due to an unsuitable pH or thick shells. However, the dissolution of the core containing 8 layers at pH 4.5 resulted in a thin and smooth capsule [27]. Similarly, biodegradable cores of polylactic acid polymer have also been investigated with several PEs, but limited by poor colloidal stability [28].

In contrast to the above-mentioned studies, inorganic templates such as carbonates are larger in size and dissolve under mild conditions at pH < 3 or by using ethylenediaminetetraacetic acid (EDTA) without affecting the PE multilayer shell. They do not form any complexes with PEs and provided intact hollow capsules after core dissolution [30]. Cores such as calcium, cadmium and manganese carbonate were successfully employed for hollow capsule fabrication [31]. Another important feature was that they can be porous or nonporous. During LbL assembly on porous cores, PE complexes were also formed in the interior and its core dissolution gave rise to a gel matrix, which helped in both protecting the capsules from high osmotic pressure and for encapsulation of macromolecules [32]. Calcium carbonate ($CaCO_3$) cores have been widely used with many combinations of weak PEs to fabricate hollow capsules as in case of PAH/PMA capsules, Figure 2e [29]. More recently, hybrid $CaCO_3$ templates built in with other components such as PSS, poly(styrene)-co-poly(acrylic acid) (PS-PAA) have also been reported as "functional templates" as they endowed the capsules with some special properties and enhanced stability.

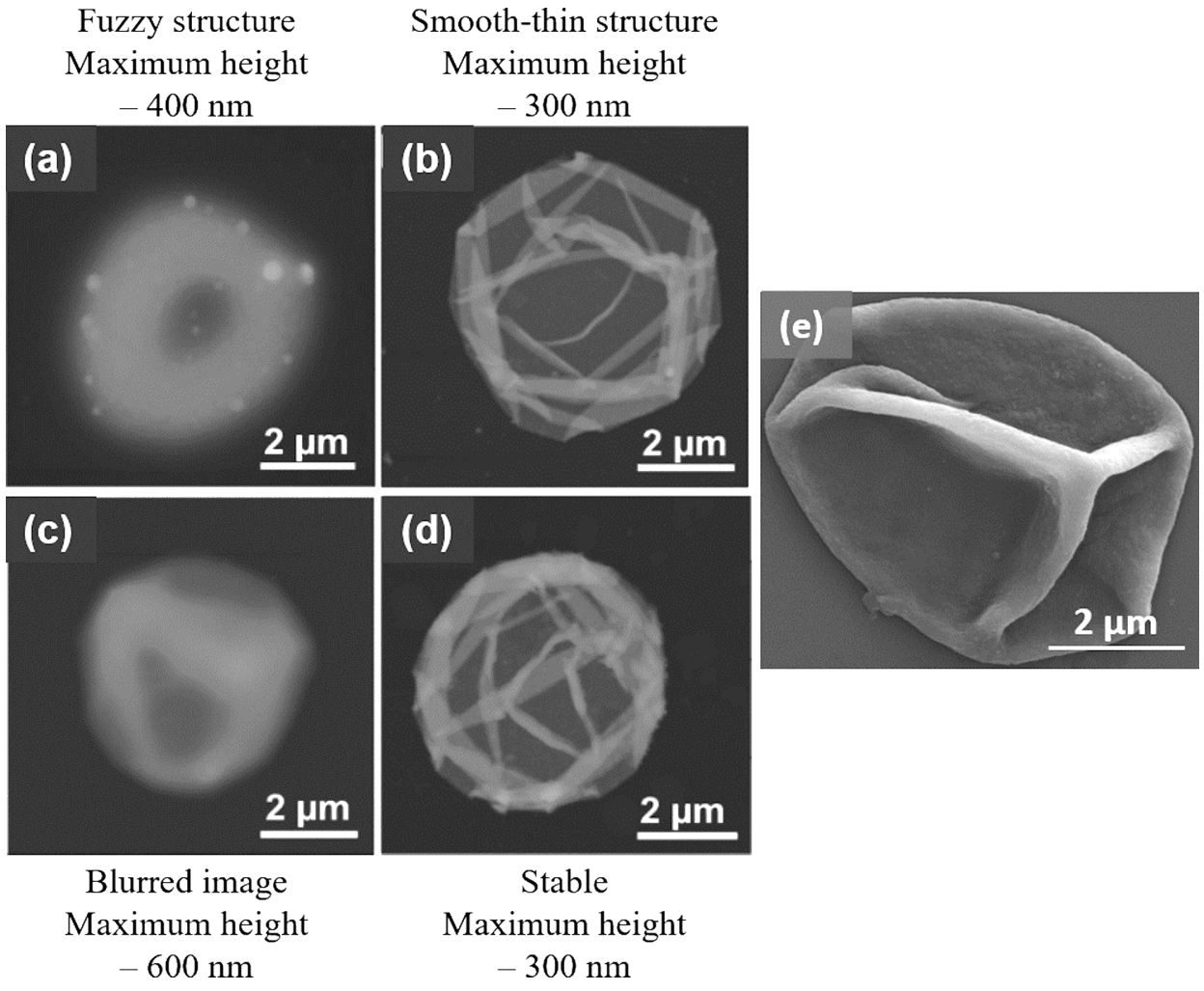

Figure 2: Morphological changes in PAH/PMA capsules templated on a SiO_2 core (a–d). AFM images showing hollow capsules obtained after dissolution of SiO_2 core deposited with (a) 8 PAH/PMA (75 KDa) layers at pH 5, (b) 8 PAH/PMA (75 KDa) layers at pH 4.5, (c) 16 PAH/PMA (75 KDa) layers at pH 4.5, (d) 8 PAH/PMA (790 KDa) layers at pH 4.5 and (e) SEM image of PAH/PMA capsule deposited on $CaCO_3$ core. (Images a–d adapted and reprinted with permission from [24], copyright 2006 American Chemical Society. Image e reprinted from [29], copyright 2010 Elsevier B.V.).

The PAH/PS-PAA multilayer capsules fabricated over PSS-$CaCO_3$ templates retained their 3D shape even after drying and spontaneously entrapped water-soluble positively charged rhodamine B molecules similar to wet capsules [33]. PAH/PMA capsules fabricated using an alginate-doped $CaCO_3$ template displayed an interconnected matrix in the interior of hollow capsules, enhancing encapsulation of cationic molecules [34]. Certain limitations such as low stability and low EE have been reported in organic and inorganic templates, respectively. Interestingly, the deposition of an additional silica layer through a biomimetic mineralization process onto a protamine/PSS microcapsule formed on a $CaCO_3$ template improved the EE, storage stability and resulted in better tolerance for encapsulated enzymes against harsh environment [35]. Although none of the templates can be considered as universal, the $CaCO_3$ cores have been found to be most compatible for encapsulation and release purposes.

Most of the weak PE capsules have been demonstrated with silica or carbonate cores. The crystallization of $CaCO_3$ from supersaturated solutions results in porous gel-like cores which also play an important role for applications in industry and medicine [32]. Such formation depends on the experimental conditions such as pH, salt, concentration, intensity of mixing and agitation. These templates are biocompatible, easy to produce, and dissolvable by EDTA. Although crystallization processes cannot be controlled to provide uniform and homogenous cores, this matrix provides an efficient way for encapsulation. Additionally, hydrogel-based microparticles (10–200 μm) fabricated via stop flow lithography have emerged as useful templates to form custom-shaped and flexible microcapsules of poly-L-lysine (PLL) [36]. The shell was formed by diffusion of PLL into an oppositely charged hydrogel matrix, enabling an easy surface modification that can be applied to a variety of PEs. Multilayer capsules formed on such a variety of cores can reveal specific characteristics and are mostly studied using microscopy techniques such as scanning electron microscopy (SEM) and transmission electron microscopy (TEM) to observe their morphological changes. Moreover, small-angle X-ray scattering (SAXS) of hollow capsules could give a detailed illustration of the inner structure and their size distribution in in situ measurements. SAXS investigations of PAH and poly-L-aspartic acid multilayers deposited on poly(acrylic acid) (PAA) brush modified PS templates indicated that some PAH chains penetrated into the PAA brush [37]. Notably, SAXS proved to be a powerful tool to gain more information about the inner structure of such systems.

Driving forces for capsule formation

The development of capsules with enhanced stimuli responsiveness, controlled loading and release is an important aspect. Different types of driving forces define the physical and chemical properties of the capsules such as permeability, stability, stimuli responsiveness and its application in vitro and in vivo. Self-assembly formed by LbL deposition of alternatively charged PEs is governed by various forces, mostly electrostatic interactions, hydrogen bonding, covalent bonding, host–guest interactions and other interactions (e.g., hydrophobic and biospecific recognition) as shown in Figure 3.

Electrostatic interactions

The LbL assemblies were originally applied to both charged planar substrates and colloidal particles and the main driving force for alternate deposition of oppositely charged PEs was electrostatic interaction (Figure 3a). These interactions occur in assemblies that use polycations and polyanions such as polypeptides (e.g., poly-L-arginine (Parg) and PLL), polysaccharides (e.g., dextran sulfate (DS), heparin and chitosan) and various synthetic polymers (e.g., PAH, PMA and poly(ethyleneimine) (PEI)). When a negatively charged template is dipped in a solution of positively charged PE, or vice versa, a monolayer of excessively adsorbed PEs is formed that leads to the reversal of the surface charge [3]. The coated templates are then rinsed and dipped in a solution of oppositely charged polymer; again, a monolayer deposition takes place but with the restoration of the original surface charge. The rinsing step becomes important, as it would otherwise lead to complex formation and aggregation. This sequential adsorption of layers finally leads to electrostatically bound multilayers in which charge inversion is the main driving force controlling the assembly [40]. The strength and physical principles governing electrostatic interactions was recently explored by Lytle et al. by using a combination of theory, simulation and experiments on the arbitrary sequence of charges [41]. The results indicated that an increase in charge fraction and blockiness generally leads to an increase in the two-phase region of the phase diagram, thereby showing enhanced phase separation by stronger electrostatic interactions. However, the relative position of the blocks also plays a significant role in determining the phase behavior. In another work, the role and binding stoichiometry between cationic and anionic groups of PE and the effect of deposition onto existing layers was studied by using anionic fluorescent probes [42]. The amount of probe bound to an existing layer was linearly dependent on the thickness of multilayers up to 15 nm, and thereafter highly overlapped layers instead of well separated films were observed. Even when the outermost layer was negatively charged, negatively charged probes were permeable into the multilayer films but with a slower diffusion rate. The main advantage of electrostatically bound assemblies is the versatility and high susceptibility towards pH, ionic strength and polarity [43]. As studied under SEM and CLSM, the walls of PAH/PSS microcapsules become disturbed at pH < 6, forming

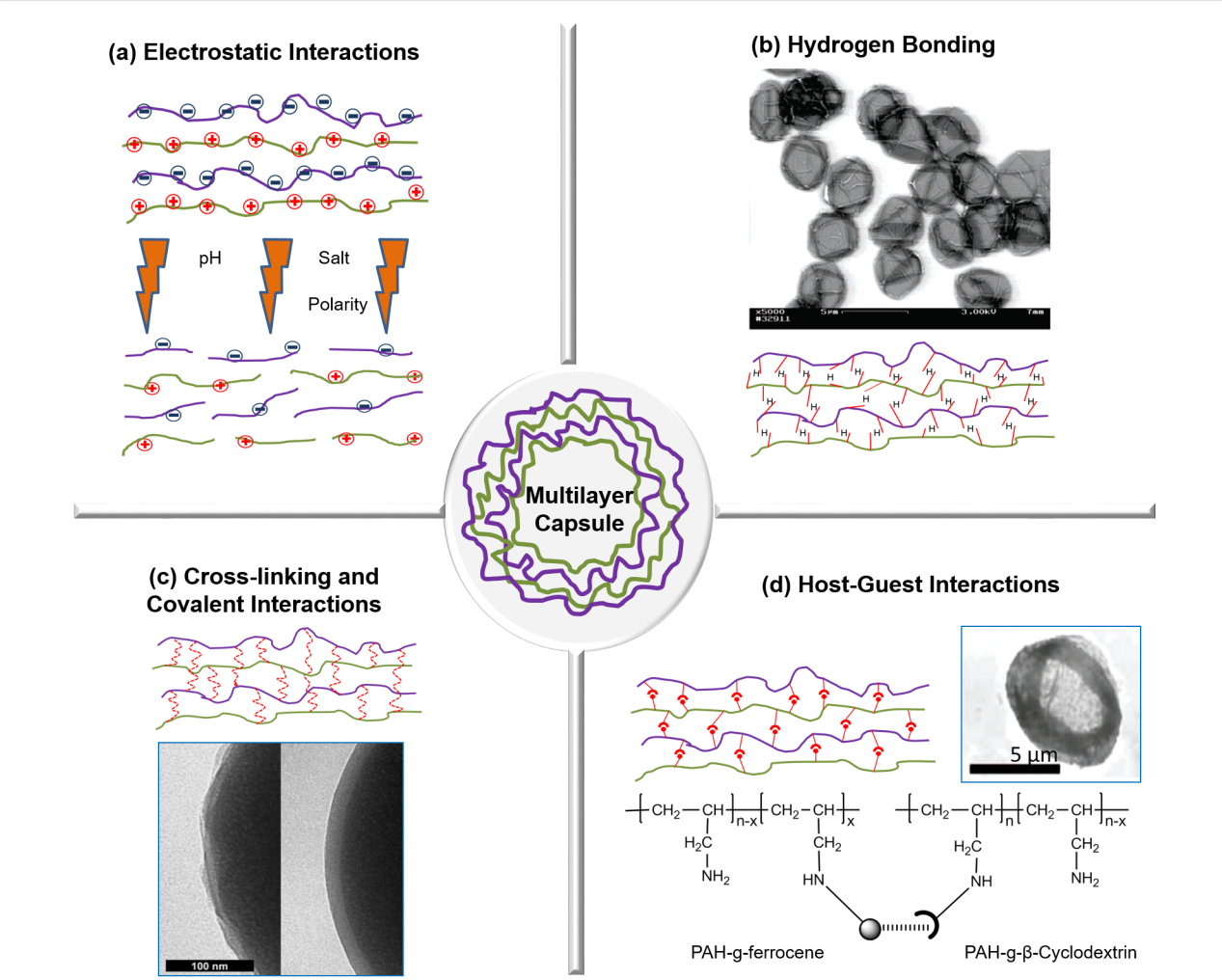

Figure 3: Illustration of driving forces for capsule assembly. (a) Opening of electrostatically bound multilayers upon change in physiological conditions, (b) SEM investigation of hydrogen bonded, temperature sensitive $(PMA/PVCL)_5$ capsules, (c) TEM investigation of 440 nm SiO_2 particles coated with PAH/PAA multilayers before (left) and after (right) covalent crosslinking with EDC and (d) host–guest PAH-cyclodextrin and PAH-ferrocene microcapsule assembly. Image b was adapted and reprinted with permission from [38], copyright 2005 American Chemical Society, image c was adapted and reprinted with permission from [26], copyright 2003 John Wiley and Sons, and image d was adapted and reprinted with permission from [39], copyright 2008 American Chemical Society.

100 nm pores which caused fluorescein isothiocyanate-dextran (FITC-dextran) in the solution to permeate into the hollow capsule. Notably, no structural changes were observed at pH > 8 [44]. Most important was the reversibility of the capsules from open state at pH 3.5 to closed state at pH 10. The pore formation is either due to the weakening of molecular bonds through ionization or osmotic pressure developed during core dissolution. By increasing the NaCl salt concentration from 0.1 to 0.5 M, similar swelling and shrinking was observed due to the charge screening effect on multilayer bonds [44]. Similar morphological changes were observed when the temperature dependence of electrostatically bound capsules was studied with various PEs that are thermo-responsive [45]. Additionally, the effect of the dissolution of the core on the permeability of capsules was observed. At basic pH, the flow of FITC-dextran into the MF-templated capsules was immediate as compared to carbonate cores, wherein it occurred after 10 min [44]. This was explained by the fact that MF core dissolution leaves some remains inside the capsule. Upon pH change, these remains contribute to charging of wall components and affect the wall structure, thereby affecting the capsule wall integrity. In spite of the versatility, in addition to the inexpensive and easy fabrication of electrostatic assemblies, the response over a wide pH range becomes a limitation as it is biologically irrelevant. Several crosslinking methods were researched to improve the mechanical strength, lower the permeability of the walls and enhance the stability of electrostatically bound hollow capsules made of weak PEs. The electrostatic assemblies are limited to

the use of charged and water soluble polymers that could lead to the problem of fouling in biological systems and decreased efficiency.

Hydrogen bonding

Hydrogen bonding can be used with uncharged polymers for the capsule assembly to make it responsive towards stimuli relevant to physiological conditions. The working pH range of the capsule is based on the strength of the hydrogen bond between the pair, making it suitable for specific drug delivery applications. Hydrogen bonded PAA/polyvinylpyrrolidone (PVP) multilayer films on planar surfaces were first reported by Wang et al. in 1997 [46]. It was later extended to 3D systems in 2003 wherein PVP/methyl phenol formaldehyde resin (MPR) multilayered hollow nanocapsules were obtained using SiO_2 as a sacrificial template [47]. Notably, the excess charges induced into the multilayer films by the deprotonation of carboxylic acid groups at pH > 5 played a key role in destabilizing the hydrogen bonded films [48]. As the critical pH is closer to physiological pH, no additional changes are required to release the loaded cargo.

The fabrication of a multilayer assembly as well as its post formation manipulation is affected by molecular weight, pH, ionic strength and temperature [49]. When the critical pH is approached, the morphological changes in PVP/PMA capsules were seen with the decrease in multilayer thickness due to disruption of hydrogen bonds [50]. When the same was crosslinked by carbodiimide chemistry, the swelling was observed at higher pH, leading to the formation of highly swollen hydrogels. To induce temperature responsiveness for multilayer capsules, the hydrogen bonded assembly is more convenient in the form of polymers with lower critical solution temperature (LCST) behavior such as poly(*N*-isopropylacrylamide) (PNIPAM), poly(*N*-vinylcaprolactam) (PVCL) and poly(vinyl methyl ether) (PVME) for use as layer components [38]. The morphological changes along with the collapse of structure can be seen close to the LCST. Stable $(PMA/PVCL)_5$ capsules prepared at ambient temperature and pH 2 are shown in Figure 3b. While the increase in molecular weight of the layer components led to the decrease of the film erosion rate, the effect of ionic strength was largely dependent on the type and valence state of the salts [51]. Although the hydrogen bond is much weaker than the electrostatic interactions, and could be easily damaged by the dissolution processes, their stimuli responsiveness and the ability to disintegrate at physiological pH makes them more versatile for biomedical applications.

Crosslinking and covalent interactions

Unlike electrostatic and hydrogen bonding interactions, the covalently linked multilayers provide a more robust way to manipulate permeability, stability and mechanical strength. Various reactions have been reported to improve the binding strength in order to increase the mechanical resistance and long term stability of the capsules. Several post fabrication treatments have also been used to strengthen the weak intermolecular interactions to fabricate stable cross-linked capsules. The PAA/poly(acrylamide) (PAAm) capsules were chemically cross-linked by water soluble 1-ethyl-3-(3-dimethylaminopropyl) carbodiimide (EDC), rendering them high stability in vitro [52]. In another work, copper ions were used to form a complex with carboxylic groups of PAA, facilitating the formation of PAA/PAH capsules via EDC crosslinking (Figure 3c) [26]. Similarly, the post crosslinking of PEI/PAA microcapsules via glutaraldehyde (GA) chemistry also resulted in better stability over a wide pH range [53]. These capsules successfully encapsulated dextran (2000 KDa) molecules without any compromise in pH responsiveness. The multilayers such as PVA/PAA and PEI/PAA could be cross-linked thermally or chemically to obtain stable hollow capsules for use in separation processes of various ionic compounds [54]. It is noteworthy that the parameters such as the nature of polycation, deposition conditions, number of polycation layers, cross-linker concentration and the nature of the dyes could significantly influence the encapsulation of anionic dyes or molecules [54].

Another method uses direct covalent chemical reactions as the driving force between comprising polymers yielding simultaneous crosslinking without the need of post treatment [55]. Stable multilayered hollow capsules of *N*-methyl-2-nitrodiphenylamine-4-diazoresin/m-methylphenol-formaldehyde resin (NDR/MPR) on a PS core based on in situ coupling were found to withstand solvent etching without further processing [55]. The reaction between epoxides and amines resulted in ultrathin, smooth and highly cross-linked structures for poly(glycidyl methylacrylate) (PGMA)/PAH hollow capsules fabricated over SiO_2 templates [56]. These capsules were stable at extreme pH conditions (1.2–12.8) and elevated temperatures showing an elastic modulus as high as 910 MPa. By making use of the reaction between amine and aldehyde via GA chemistry, a single polymer PAH capsule can be fabricated [57]. The deposition of one PAH layer was followed by suspending the particles in GA solution to induce free aldehyde groups for deposition of the next PAH layer. A similar assembly of PEI was also reported to show the effect of the polymer molecular weight over the capsule structure [58]. When the molecular weight of the PEI was increased, the shell permeability was decreased. Notably, the covalent bonding helps in constructing single PE networks so that one polymeric component does not hinder the specific functionality of other polymeric components (e.g., biocompatibility and biodegradability). Moreover, no charge

reversal process occurs, which improves the stability of multilayer capsules.

Host–guest interactions

Host–guest types of interactions are found within the supramolecular assemblies. Supramolecular polymers such as cyclodextrins, calixarenes, resorcinarenes and crown ethers play as host monomer units. The cup-like shape of calixerene, resorcinarenes units represents the host for their homoditopic or heterodipotic structures, i.e., two calixarene units covalently bound in various ways. Although there are many reports on calixerene [59], cyclodextrins offer a wide scope for such interactions in biological applications. They could act as a host for many biomolecules or drugs via hydrogen bonding, hydrophobic interaction or van der Waals interactions [60-63]. For instance, positively charged ferrocene-modified PAA thin films over β-cyclodextrin dimer were first fabricated in 2002, showing that LbL assemblies can be formed by overcoming electrostatic repulsion [60]. Similar attempts were made to construct LbL films by interaction between β-cyclodextrin monolayers as host and polymers modified with adamantyl groups as guests, which also resulted in stable multilayers [61]. The first stimuli-responsive supramolecular hydrogels films based on these reactions were built in 2006 using β-cyclodextrin and adamantyl modified chitosan derivatives [62]. Photo-responsive and redox-responsive hydrogels of cyclodextrin with guest molecules of azobenzene and ferrocene have also been constructed [63]. Very few attempts have been made for fabrication of weak PE capsules under this category, as shown in Figure 3d [39]. Notably, the host and guest interactions are based on their matching degree and concentration. Thus, the difficulty lies in the availability of these host and guest molecules coupled to charge repulsion between polymers.

Encapsulation

The formulation of nanocarrier systems is effective only if sufficient encapsulation of molecules can be easily carried out. Various types of cargo such as proteins, enzymes, dyes, biomolecules, drugs and fluorescent molecules have been successfully encapsulated in hollow PE capsules by different encapsulation methods [64]. One way of encapsulation is active encapsulation, i.e., using the encapsulation material itself as a core or co-precipitation of encapsulation material within the core. Very few such studies are reported using a weak PE capsule. An anti-inflammatory drug, ibuprofen crystals of 5–40 μm in size, were encapsulated by chitosan/DS and chitosan/carboxymethyl cellulose multilayers [65]. The drug release time could be extended by increasing the crystal size and thickness of the multilayer films. Alternatively, the protein aggregates or DNA could also be used as templates to encapsulate them in PLL-succinylated PLL layers for model viral assembly or gene transfer [66].

Another way of encapsulation of cargo is passive encapsulation, wherein the substances of interest are loaded into the capsules by altering the permeability of the shell using physical or chemical factors. The pH-induced encapsulation is mostly used for weak PE capsules as the changes in pH results in the generation of excessive charges. The loading of ciprofloxacin hydrochloride with an EE of 32% [29], doxorubicin (Dox) with an EE of 89% [67], enzyme-like catalase [68], horseradish peroxidase with 2.2×10^8 molecules/capsule [69], and proteins like BSA with an EE of up to 65% [70] have been successfully reported in weak PE capsules by changing the open and closed state of the capsules. PAH/PMA microcapsules were successfully loaded with fluorescein isothiocyanate-bovine serum albumin (FITC-BSA) at pH < 4 [70]. Confocal microscopy was used to visualize the open and closed state of the capsules at pH 3 and 7, respectively (Figure 4a,b). Figure 4c,d shows the capsule images after encapsulation at pH 3 and after release at pH 7.4. In a similar work, the encapsulation of FITC-BSA was observed in carboxymethyl cellulose/PAH microcapsules at pH 3, which was then released at pH > 7 by manipulating the shell permeability [71]. Similar to the capsule made of strong PE, the permeability of the shell could be easily controlled by varying the ionic strength. The microcapsules underwent swelling at high salt concentrations due to the weakening of the electrostatic interactions between the PE layers by the charge screening effect [39]. The open and closed states at high and low salt concentrations were successfully demonstrated for encapsulation and release of macromolecules. The temperature-induced shrinking of the capsules was also demonstrated for the encapsulation of fluorescent model molecules [72]. The shell thickening at elevated temperatures was responsible for trapping the macromolecules inside the capsules. The hydrophobic molecules could be loaded into multilayer capsules by changing the state of the capsules from open to closed via a polarity change [73]. Alternatively, water soluble, positively charged substances were encapsulated into hollow capsules of weak PE by spontaneous as well as charge-controlled mechanisms [70,74]. The net negative charge caused by either complex formation or preloaded PE molecules in the interior of the capsule is the driving force for the encapsulation processes [75]. Another most commonly used method is the movement of cargo from lower to higher concentration via a concentration gradient based diffusion process such as in case of Dox loading in GA cross-linked $(\text{chitosan-alginate})_5$ microcapsules [76]. At low feeding concentrations (e.g., 750 μg/mL), the drug loading was attributed to the accumulation effect, whereas the overall loading was influenced by both the accumulation effect and normal diffusion processes at high feeding concentrations.

The gel-like matrix cores of inorganic $CaCO_3$ and SiO_2 provide a larger surface area for encapsulation than normal cores due to

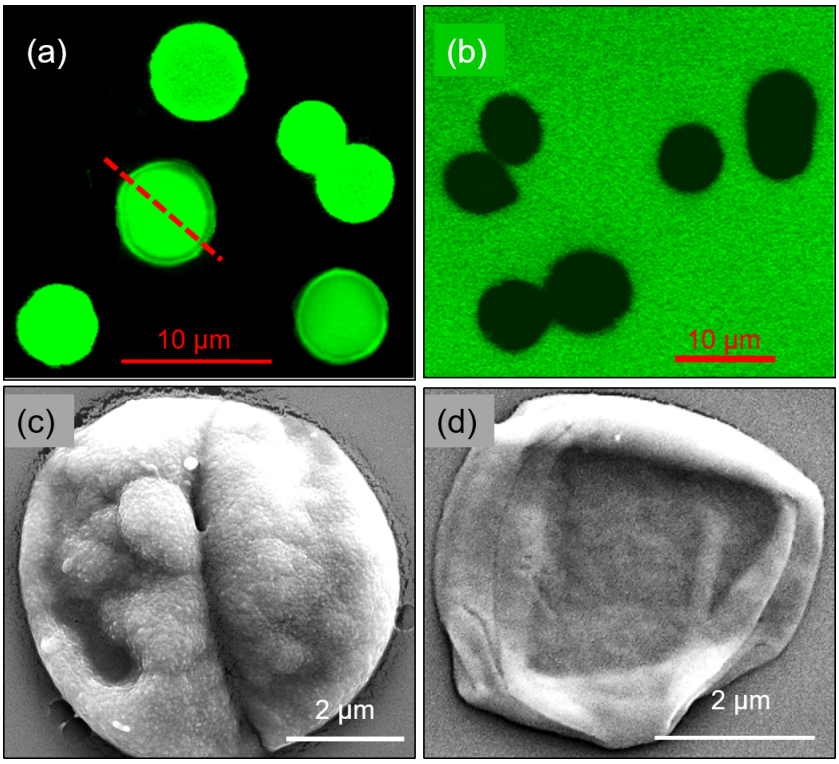

Figure 4: CLSM images of PAH/PMA microcapsules incubated with FITC-BSA at (a) pH 3 and (b) pH 7. SEM investigation of (c) a BSA-loaded capsule at pH 3 and (d) a capsule after the release of BSA at pH 7.4. The images in a–d were reprinted with permission from [70], copyright 2010 Elsevier B.V.

their porous nature. They can encapsulate both hydrophilic as well as hydrophobic compounds. The encapsulation of proteins in such porous structures can be done by either adsorbing model protein into core particles before PE multilayer deposition [77] or co-precipitation of protein molecules during the formation of cores [78]. The encapsulation was five times more for the latter one. After core dissolution, the capsules were encapsulated with proteins. Mostly, these studies have been demonstrated for strong PE systems. This method is not used convincingly for weak PE systems, mostly due to poor stability of the capsules and contamination issues during the core dissolution processes. Thus, despite the lower EE and drug absorption in the capsule wall rather than in the interior, pH and salt based approaches are the most widely used in weak PE systems.

Functionalization

The surface properties of the capsule determine its permeability, which in turn influences the release profile. In order to alter the surface properties, the PE multilayer capsules can be functionalized with various organic and inorganic materials that would lead to a new way for different biological applications. These include metal NPs, magnetic NPs, click moieties, smart polymers and biomolecules such as proteins, peptides, nucleic acids, and enzymes.

Nanoparticle incorporation

When NPs are embedded into the multilayer shell, the translocation, guiding and release of encapsulated cargo from the capsule is enabled by selectively changing the integrity or permeability. Magnetic NPs have shown greater cytotoxicity in comparison with microcapsules containing an equivalent amount of magnetite [79]. The first and foremost way of incorporating NPs into the shell is either by the adsorption of NPs over the sacrificial template or using the NP assembly itself as a template. When the sacrificial template dissolves, it truly encapsulates the NPs within the multilayers, however, the core dissolution may affect the properties of the NPs. To circumvent this limitation, preformed NPs were used as a layer component to fabricate hollow capsules incorporated with NPs. Although it resulted in stable capsules, the amount of adsorbed NPs is substantially less [80]. The third method involves the incorporation of preformed NPs into preformed hollow capsules by changing the wall permeability through several triggers [81]. Lastly, in situ synthesis of NPs in the shell itself via the polyol reduction method has proved to be effective as it results in a dense and homogenous distribution of the NPs within the capsules [74]. Figure 5a,b shows TEM and AFM images of the successful incorporation and distribution of in situ synthesized silver NPs within the PAH/DS capsule. The

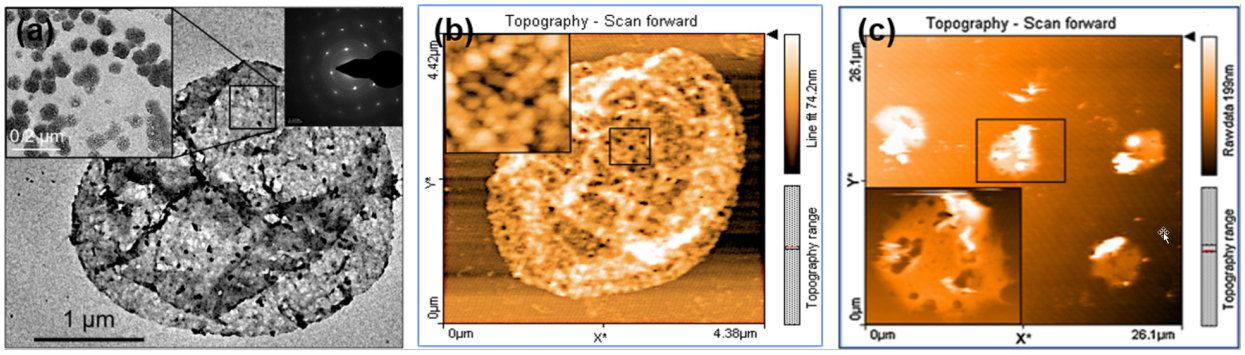

Figure 5: The morphological investigation of PAH/DS capsules incorporating silver NPs by (a) TEM, (b) AFM and (c) its rupture after laser irradiation. The images in a–c are reprinted with permission from [74], copyright 2011 Elsevier.

rupture and deformation of the capsules occurred via the formation of pores on the surface after laser irradiation at 530 nm (Figure 5c).

The encapsulation of silver, gold and iron oxide NPs has been the most common in most of the studies [80,82-84]. The incorporation of magnetic NPs (e.g., iron oxide and cobalt oxide NPs) into capsules allows them to respond to magnetic stimuli and produce heat due to magnetic energy dissipation, mechanical vibrations and motion induced in the film, thus releasing the cargo [80]. The Fe_2O_4-PAH capsules studied with A549 cancer cell line showed a rapid uptake, demonstrating the potential for cancer therapy. Silica and gold NPs were assembled in a one pot assembly of specifically tailored diblock polymers of PLL and poly-L-cysteine [82]. The electrostatic binding between the positively charged lysine blocks and negatively charged silica NPs as well as the disulfide linkages between cysteine blocks and gold NPs resulted in two types of functionalities in the capsule. In a similar way, the capsules incorporated with noble metal NPs (e.g., gold and silver) respond to external light illumination by increased surface plasmon resonance of the outer shell electrons present in noble metals. The absorbed light is converted to heat energy, which causes layer damage, thereby opening the capsules and releasing the encapsulated material [83]. The parameters such as the preparation condition of capsules, the distribution and aggregation of NPs within the capsules, the laser power and exposure time decide the sensitivity of the capsule towards laser light induced release. For example, the presence of aggregated NPs led to the generation of more heat and thus required relatively less intense laser irradiation [84]. While the moderate intensity of radiation successfully breaks the shell and releases the loaded cargo, high intensity leads to the generation of high heat, which helps in destroying the surrounding cancer cells. Even though the advantages of NP incorporation in capsules have been immense, similar work in weak PE assemblies is still at initial stages.

Supramolecular functionalization

Supramolecular chemistry is the chemistry of structure, function and intermolecular bonds of supramolecular structures formed by various methods of copolymerization or binding of a substrate to molecular receptors. This can be used for specific applications such as molecular recognition, selective transport processes and the design of supramolecular devices with functional (e.g., electroactive and photoactive) components [85]. “Smart polymers” emerged from supramolecular chemistry provide reversibility of noncovalent interactions that make them responsive to external stimuli such as temperature, light and chemical environment. They might also have the capability to self-assemble into functional materials via hydrogen bonding, hydrophobic interaction, metal–ligand interaction and van der Waals forces. Among them, the major driving force of such capsules is host–guest interactions as in the case of polymers such as cyclodextrins, calixarenes, resorcinarenes and crown ethers, wherein they play as host monomer units [59,86]. Such capsules made from strong PE assemblies showed pH switchable on–off capability of the polymers without breaking their polymeric structure [87]. The pH control helped the self-assembled capsules in precipitation and dissolution by trapping of guest molecules inside. Furthermore, it led to a new strategy involving hydrogen bonding and carbamate chemistry (between carbon dioxide and amines) which resulted in supramolecular capsules that are switchable by two parameters, namely, solvent polarity and temperature [47]. Multilayer β-cyclodextrin films with ferrocene-modified PAA, adamantyl-modified dedrimer and adamantyl-modified poly(isobutene-alt-maleic acid) have been successfully reported with weak PE systems [60,61,88]. First stimuli responsive supramolecular hydrogel films based on β-cyclodextrin and adamantyl-modified chitosan derivatives have demonstrated a reversible swelling and shrinking upon changing the ionic strength [62]. At high ionic strength, the decrease in the electrostatic repulsive effect between the layers causes the compression of the assembly owing

to the mass decrease and release of trapped water. The viscosity of the multilayers increased with increase in salinity. Although many hydrogels have been reported with β-cyclodextrins, only few attempts have been made in capsule formation [63]. In one successful attempt, the multiresponsive hollow capsules of PAH were fabricated by β-cyclodextrin-ferrocene reaction on sacrificial carbonate particles [39]. The swelling was progressive when the microcapsules were kept in β-cyclodextrin solution due to the gradual decrease in the degree of crosslinking. At low pH or ionic strength, the shrinking of the capsules was observed due to the alteration of charge repulsion in the PAH backbone. Moreover, this effect was reversible, rendering several applications for the controllable loading and release of cargo as demonstrated by fluorescent dextran in this study. Block copolymers such as PMA and PAAm-dimethyldiallylammonium chloride (PAAm-DMDAAC) were used to combine the electrostatic and hydrogen bonding interactions, making them stable over a broader pH range by switching the interactions between the electrostatic and hydrogen binding state [89]. While the PAAm-PMA assembly was found to be unstable at pH > 5.5 due to disruptions in hydrogen bonding, the block PAAm-DMDAAC copolymer assembly was stable even until pH 8 due to the transition from hydrogen bonding to electrostatic interactions.

Click chemistry

Click chemistry is the tagging of macromolecules with click moieties in order to form covalently stabilized multilayer films. This technique offers many advantages as it can be formed in aqueous as well as organic solvents. It is also applicable to a wide range of polymers, proteins, NPs and other biological molecules. The LbL click linkages have excellent physicochemical properties and are highly stable towards hydrolysis, oxidation and reduction. The different types of click reactions are as follows. First, a copper-catalyzed alkyne-azide cycloaddition (CuAAC) reaction of an azide with an alkyne catalyzed by copper is reported to form a stable triazole ring between the successive layers of the LbL assembly. Second, a strain-promoted Cu-free alkyne-azide cycloaddition (SPAAC) uses strained alkynes for reaction with azide, thereby ruling out the issues with toxic copper. A third type of click reaction, the Diels–Alder cycloaddition (DAC), is a reversible reaction between different types of diene and dienophile resulting in thermo-responsive products. A fourth type, the thiol-ene reaction, is a reaction between thiol and alkene groups in the presence of a radical source as catalyst. The radicals can be generated through light, thermal or a redox initiated approach. The most studied is the azide-alkyne cycloaddition reaction due to the high regioselectivity and quantitative transformation with no side reactions. The detailed description of these methods can be found in a recent review by Such et al. [90].

The first application in 2006 utilized CuAAc for LbL assembly of PAA functionalized by alkyne (PAA-Alk) and azide (PAA-Az) in the presence of copper to form covalent PAA films which were stable over a broad pH range [91]. This method was later extended to various other polymer films such as combinations of PAA-PAH-poly(*N*-hydroxypropylmethacrylamide) (PHPMA) [92]. The first hollow capsules based on CuAAc method was formed by azide and alkyne modified PAA along with rhodamine dye over a silica template. The hollow capsules exhibited a pH responsive behavior with reversible swelling and shrinking at acidic and basic pH [93]. In a separate study, the poly(ethylene glycol) (PEG)-based post-functionalization of pH-responsive click capsules of biodegradable PLL and poly(L-glutamic acid) (PGA) rendered their low fouling capability against specific protein binding [94]. Hydrogen bonded films and hollow capsules of alkyne-modified PVP and PMA were stabilized with a bifunctional azide crosslinker containing disulfide bonds [95]. The exposure of these capsules to pH 7.2 led to the breaking of hydrogen bonds and complete removal of PMA, resulting in stable PVP capsules with intracellularly degradable disulfide linkages. These multilayers were also found to be low-fouling to various proteins and negligibly cytotoxic. In a related work, the PEG-based films and capsules fabricated with redox responsive moieties via disulfide linkage showed high stability in biological buffers, low toxicity to human cells and low fouling characteristics [96]. Similar low-fouling hybrid capsules with a controlled degradation profile were prepared by combining two different systems of PVP_{Alk}-PMA and PGA_{Alk}-PVP to form stratified PGA_{Alk}-PVP_{Alk} capsules [97]. The degradation could be controlled by the number as well as position of the non-degradable PVP_{Alk} layer. The drug-loaded PVP_{Alk} capsules were even shown to overcome multidrug resistance with Dox and paclitaxel against LIM1899 colorectal cancer cells [98]. A new kind of dual (pH and redox) responsive, charge shifting click capsules based on poly(2-diisopropylaminoethyl methacrylate) (PDPA) were also fabricated by a similar method [99]. These capsules were stable and showed 50% size reduction at physiological pH (7.4), however, under stimulated intracellular pH they swelled up to 120% by degradation of disulfide bonds. A rapid and efficient release could be obtained by the synergistic effect of dual stimuli.

Other click chemistries like thiol-ene have also been reported because of their light-initiated and metal-catalyst-free approach. PVP along with PMA functionalized by thiol (PMA_{Thiol}) and ene (PMA_{Ene}) groups were used to fabricate hydrogen bonded hollow capsules via UV crosslinking [100]. It was further demonstrated that these capsules can be incorporated with functionalized PEG_{Ene} to induce reactive and low fouling properties. Notably, the SPAAC and DAC approaches have not been widely used for synthesis of capsules. The use of the click ap-

proach highly depends on the type of application. For instance, the use of UV light in the thiol-ene approach limits its application in drug delivery as it can damage DNA and cross-react with cysteine residues in proteins. The DAC approach may also affect cysteine residues in proteins that might undergo Michael addition to result in malemides [90]. Similarly, the use of copper in CuAAC may be undesirable in certain biological applications as it is toxic to cells. This copper content can also cause aggregation of proteins and degradation of some biomolecules, which can be avoided by using chelating agents [101].

Incorporation of biomolecules

Biomolecular ligands such as proteins (e.g., antibodies, peptides, receptor molecules, etc.), lipids and carbohydrates have long been used for targeted delivery. The attachment of these ligands to the external multilayers can be achieved by covalent as well as noncovalent interactions. For example, the HuA33 antibody specific to A33 antigens expressed on colorectal cancer cells were adsorbed on capsules from a buffer at pH 7.4 [102]. Both electrostatic and hydrogen bonding contributed to the binding of antibodies to the capsule external layer and to retaining their immunological activity. As mentioned in the previous section, the antibodies were used to functionalize PVP_{Alk} low fouling capsules using covalent click chemistry to target cancer cells [101]. They were very effective against LIM2405 colorectal cancer cells even at a low concentration of 0.1% cancer cells in the total cell population. Protein A (obtained from Staphylococcus aureus) was adsorbed on PGA/PLL film via electrostatic attraction and the in vitro cell contact with this protein mainly occurred via local film degradation [103]. The antitumoral, antitoxic, anticarcenogenic, antifungal and antiparasitic properties of protein A could be a good application in implants or tissue engineering. Another strategy for biomolecular functionalization is covalently linking the receptor specific ligands to one of the layer components that are known to interact with cancer cell receptors. For instance, the improved cell adhesion and proliferation was observed in multilayer films such as PGA/PLL, PAH/PAAm and hyaluronic acid (HA)/chitosan when one of the polymeric pair is grafted with an arginine–glycine–aspartic acid (RGD) peptide sequence [104-106]. Similarly, the PLL/PGA film showed better cell attachment when plain PGA was replaced with a laminin 5 peptide grafted PGA [107].

The homogeneous adsorption of charged lipids such as dipalmitoyldiphosphatidic acid (DPPA), dipalmitoyldiphosphatidylcholine (DPPC) and sphingosine over a capsule surface has been achieved in two ways: 1) the adsorption of lipid vesicles via electrostatic interactions and 2) the solvent exchange mechanism wherein lipid molecules dissolved in organic solvents were slowly exchanged with water [108]. The addition of the lipid layer not only provided long term stability but also slowed down the rate of permeation of small molecules through the capsule wall, making them efficient carriers for controlled release. The later work on capsule/lipid systems incorporated with neoglycolipid or folate-linked lipid showed high affinity to lectin (concanavalin A) and breast cancer cells (MCF-7) [109]. The efficient delivery of the daunorubicin hydrochloride (DNR) anticancer drug to cancer cells was achieved through folate-targeted sodium alginate/chitosan capsules. The lipid coating on the PAH/PSS microcapsule surface significantly reduced the permeability of the capsule walls [110]. Alternatively, carbohydrate functionalization has been widely used in hepatic drug delivery systems. For instance, the capsules incorporating a galactose branched polymer (PGEDMC) as one of the PE have shown specific recognition abilities with peanut agglutinin (PNA) lectin rather than nonspecific concanavalin A [111]. Although carbohydrate-related functionalization has been mostly explored for strong PE systems, DNA functionalization was also reported for thiol-functionalized PMA-PVP multilayer capsules [112]. Thus, the capsules functionalized with biomolecules have shown better performance for both sustained and targeted drug delivery applications [113].

Carbon compounds

Several other components have been utilized to functionalize capsules in many ways. Hollow capsules of approximately 400 nm in size with negligible toxicity to cells were reported by the oxidative self-polymerization of dopamine solution onto silica particles [114]. The thickness of multilayer films is comparable to the LbL multistep technique and can be easily controlled by varying the polymerization time. This single-step technique resulted in a wall thickness similar to the LbL multistep technique and was applicable to other particles of different size and porosity. Because of the broad absorption and interesting mechanical properties, carbon-based materials were also reported for the functionalization of hollow capsules. When the microcapsules were embedded with carbon nanotubes (CNTs) in the shell, the rigidity of the shell was improved upon drying and resulted in freestanding structures. The capsules modified with CNTs ruptured upon laser light irradiation [115]. The introduction of graphene oxide (GO) nanosheets with PDDA as multilayers caused the migration and rearrangement of chains compared to PDDA/PAA multilayers [116]. The PDDA/GO multilayers showed improved resistance to damage and maintained a defect-free surface even after several post treatments with NaClO/NaOH/HCl solutions. It is worth noting that GO/PAH multilayer microcapsules showed a unique permeability when compared to conventional capsules and provide the option to encapsulate multiple drugs by simple incubation (Figure 6a) [117]. Notably, FITC-BSA and Dox were adsorbed onto the GO layer through multiple interactions (e.g., electrostatic interac-

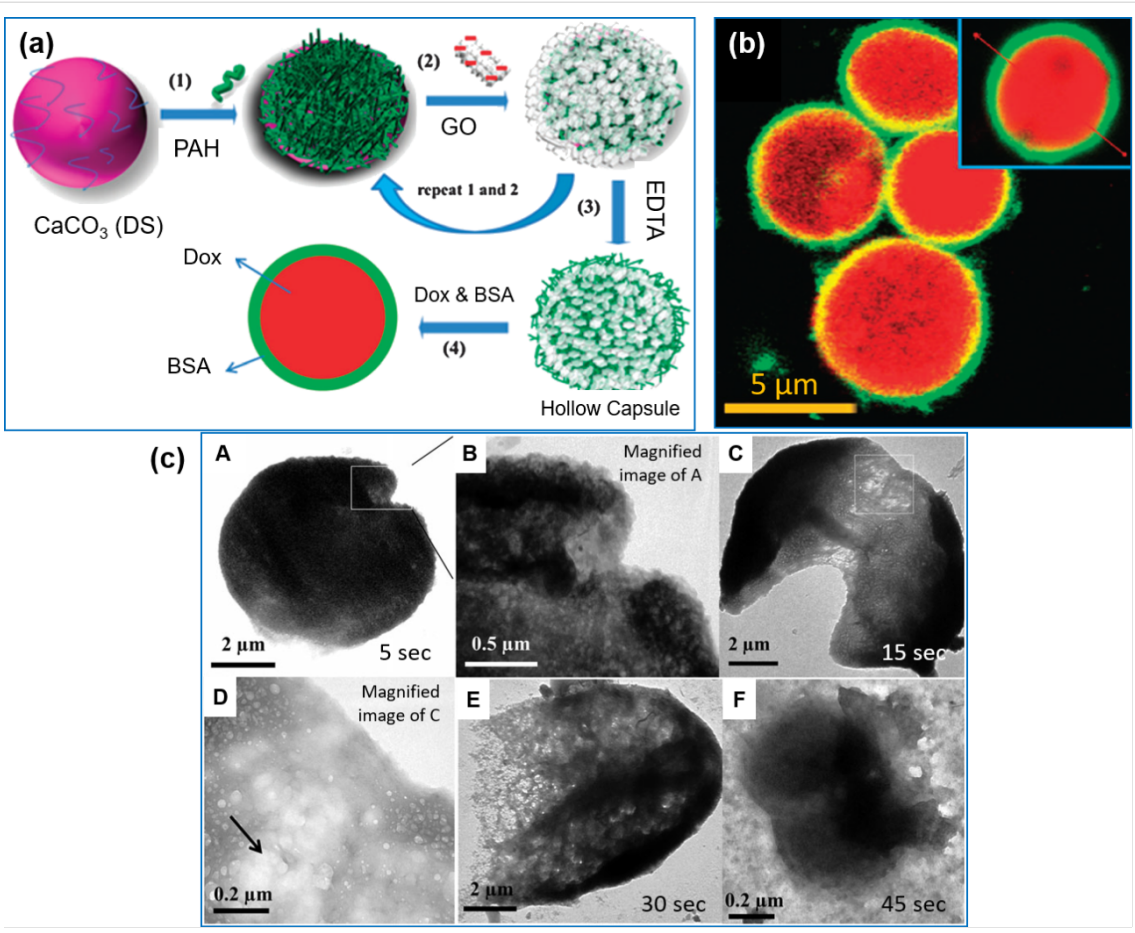

Figure 6: (a) Illustration of the fabrication of PAH/GO microcapsules, (b) CLSM investigation showing the encapsulation of Dox and FITC-BSA in PAH/GO capsules and (c) the response of the GO/PAH capsules to laser light at 1064 nm over an exposure time of 5 to 45 s. The images in a,b were republished with permission from [117], copyright 2012 Royal Society of Chemistry and the image in c was republished with permission from [118], copyright 2013 Royal Society of Chemistry.

tions, π–π stacking forces, hydrophobic and hydrogen bonding) between oxygen functional groups of GO and nitrogen/oxygen groups of BSA (Figure 6b). The near-infrared (NIR) responsiveness of the system as a function of time was also later explored for externally controlled drug delivery as shown in Figure 6c [118]. As the irradiation time was increased from 5 to 45 s, the pore formation and expansion of the capsules was seen followed by complete rupture at 45 s.

Triggers for drug release

Key requirements for drug delivery vehicles is the successful release of the encapsulated drug at the diseased site for effective action in a controlled manner. The chemical and physical properties of the capsule can be easily altered by the shell constituents and its thickness. The PE membranes are mostly permeable to low molecular weight dyes and ions but are impermeable to high molecular weight molecules. In addition, the functionalization of the membrane provides a means to alter the permeability and imparts stimuli responsiveness. Internal stimuli include chemical or biological stimulus encountered internally such as pH, ionic strength, polarity, temperature, enzyme function and receptor recognition. The external stimulus, on the other hand, is the interaction with externally applied fields such as a magnetic field, ultrasound, laser light, or mechanical stress.

Internal triggers

pH-responsive systems: The human body and other tissues exhibit variations in pH (e.g., stomach pH 1–2, intestine pH 8.4, endosomal pH 6–6.5, normal tissues pH > 7.4 and cancerous tissues pH < 6.8) which makes pH sensitive systems interesting for drug delivery. As the change in external pH affects the interaction of the PE complex, the release could be triggered by targeting different parts of the body. When the pH is altered close to the pK_a value, the protonation/deprotonation of the PE occurs and leads to the swelling of the capsules by generation/reduction of residual charges in the multilayer films [119]. Notably, the charge density of weak PEs decreases at the pK_a

value, making it less charged and leading to decreased multilayer stability due to weaker interactions between the layer components. The most studied pair in multilayer capsules is PAH/PSS wherein PAH provides the pH responsiveness to the system. As discussed in encapsulation studies, the PAH/PSS capsules displayed an open state at pH < 6 leading to the release of encapsulated FITC-dextran [120] and FITC-albumin [44]. It is important to note that the nature of the core and its dissolution process also significantly affects the pH response of the capsule. Notably, the oligomers left after the dissolution of MF templates affect the capsule permeability, especially for low molecular weight cargo, by increasing the osmotic pressure inside [44]. The molecular weight of the polymer and the number of layers also has a significant effect on the pH response [25]. The pH-responsive PAH/PMA capsules fabricated via crosslinking were found to be stable over a wide pH range of 2.5–11.5 and showed reversible swelling between pH 2.7–2.6 [121]. At low pH, the hydrophobic forces of PMA counteracted the weaker electrostatic attractions between the layer components and stabilized the capsules. Using the same balance of electrostatic and counteracting hydrophobic interactions, the PVP/PMA capsules exhibited pH sensitivity in both acidic and basic solutions [122]. Biodegradable capsules of chitosan/PGA with unique acidic pH responsiveness were reported by Imoto et al. [123]. While the encapsulated FITC-dextran was completely released at pH 1, the release was lower at neutral and alkaline pH. In a different work, the biocompatible and biodegradable alginate/chitosan capsules templated on liposomes showed pH responsiveness based on the end layer, i.e., the end layer effect [124]. Notably, the capsules with chitosan as the outer layer were stable at acidic pH while the capsules with alginate as the outer layer were stable at all pH values between 4.6 and 8. The methods such as GA-mediated covalent LbL crosslinking [53,58] and click chemistry [93] have also resulted in pH-tunable capsules showing impermeability over a specific pH range while being permeable at other pH values. Furthermore, these methods can be applied to a range of polymers, enzymes and proteins. The cyclodextrins-modified dextran supramolecular capsules encapsulated with Dox via host–guest interactions have demonstrated the tumor-specific release of Dox [125]. While the capsules were found to be stable at physiological pH, they burst released the loaded drug and inhibited growth of HeLa cells at acidic pH of cancerous tissues.

Ionic strength: The swelling and shrinking of microcapsules has been established upon exposure to different salt concentrations. Unlike the pH-based approach, the permeability change is not restricted to weak PEs but can be effectively used for strong PE systems as well. The salt ions screen the electrostatic interactions between charged polymers, leading either to the softening of the layer structure due to weakened electrostatic attractions or to the formation the pores in the multilayer network [126]. The permeability coefficient exhibits a non-linear dependence on the salt concentration. It is worth noting that the high concentration of NaCl could be used to prevent the dissolution of the poly(ethylene oxide) (PEO)/PMA film at high pH by reducing the electrostatic repulsions among the ionized groups of hydrogen bonded layers [48]. With the same phenomenon, the hydroxypropylcellulose (HPC)-PAA capsule size is decreased as a function of increasing salt concentration [127]. The effect of a wide range of NaCl concentrations from 5 to 500 mM has been studied to show that the ionic strength influences the range as well as the amplitude of electrostatic forces [128]. The capsule shrinking is largely dependent on the absolute concentration of the salt at equilibrium state and the nature of the salt. Notably, the strongest effect is observed for weakly hydrated anions [129]. The PMA hydrogel capsules also showed a gradual decrease in diameter by 1.6 times with increasing salt concentration [130]. The successful release of encapsulated FITC-dextran was achieved at a high salt concentration of 600 mM.

Polarity: Organic solvents have been used to alter the permeability of polymer capsules to encapsulate molecules of interest inside the hollow capsules. By changing the polarity of the solvent, the urease enzyme was easily encapsulated in PSS/PAH microcapsules [131]. The capsules demonstrated a closed state in water and an open state in ethanol. Such opening and closing of capsules is reversible and can be used for the release of the encapsulated drug. The environmental triggers are advantageous for their reversible properties and can be experimented with weak PE systems as well.

External triggers

Magnetic field: As human tissues are transparent to magnetic fields, the functionalization of capsules with magnetic NPs allows targeted delivery under an externally applied magnetic field. The first ever magnetic multilayer shell was formed by integration of iron oxide in poly(diallyldimethylammonium chloride) (PDADMAC)-PAH multilayers adsorbed on PS latex beads [132]. The same technique was extended to form the first hollow magnetically responsive capsules by removal of the core and incorporating magnetic NPs in the shell [44,133]. The uptake of capsules by cells can be drastically increased by exposure to magnetic fields. When PAH/PSS capsules functionalized with magnetic NPs and fluorescent NPs were injected into a flow channel system cultured with breast cancer cells, the accumulation of capsules was observed at the edge of the applied magnetic field [44]. It resulted in an increased local concentration and drastic internalization of capsules into cells at the edge as compared to places where the magnetic field was absent. Along with the targeting of capsules at a specific loca-

tion, the magnetic field can also lead to shell rupture by inducing magnetic energy dissipation and mechanical vibration of NPs in the capsules. The high frequency magnetic field (HFMF) of 50–100 kHz directly caused heat generation and conformational changes in iron-oxide-coated PAH/PSS microcapsules due to the motion of the NPs [80]. The enhanced release of entrapped Dox was observed through the formation of nanocavities in the PAH capsule shell. This heat generation might even result in complete rupture of capsules depending on the external magnetic field and duration of the applied stimulus. These capsules also showed high intake by A5495 cancerous cell lines. Both the heating and stress on the PE shell due to magnetic NP alignment was responsible for the increased permeability in the capsules. Similar magnetoresponsive microcapsules were prepared with an additional lipid bilayer coating, in which the magnetic stimuli resulted in a phase transition of the lipid membrane due to heating of the NPs and release of fluorescent calcein without rupturing the capsules [134]. Another way is to combine both magnetic and metal NPs, wherein the magnetic NPs take care of targeting and the vibrations caused in the metal NPs work to distort the layer, making it extremely permeable to macromolecules like FITC-dextran [135]. Ferromagnetic gold-coated cobalt (Co@Au) NPs embedded inside PAH/PSS walls were observed to rotate when an external alternating magnetic field of 100–300 Hz was applied, which subsequently disturbed and distorted the capsule wall and drastically increased its permeability to FITC-labeled dextran [136]. The release rate of entrapped drug could be controlled by the strength of the magnetic field, duration of exposure, and the amount of NPs deposited onto the capsule wall [137]. These characteristics make them a suitable carrier for in vivo drug delivery.

Laser light irradiation: Once the capsules have reached the targeted site, the heat generation by various light stimuli can be used for destruction of the shell and releasing the encapsulated molecules. When capsules incorporated with metal NPs, light-sensitive polymers or photodynamic therapy (PDT) molecules are exposed to an external light stimulus, the heat generation at the interphase of the NP/polymer causes the rupture and change in permeability. The use of anisotropic gold/silver NPs as light absorbing moieties within the capsule provides an advantage of absorption in the NIR region (700–1400 nm), a spectral region that has high transmission and low absorption by biological tissues [137]. When exposed to NIR light of 1064 nm and 10 ns pulse, the PSS/PAH capsules incorporated with gold NPs showed 850% increase in the release of encapsulated FITC-dextran [138]. Notably, there was no significant release from the control capsules. While a lipid (dilauroylphosphatidylethanolamine) layer coating on the capsule shell helps in preventing drug leakage before release, the capsules functionalized with monoclonal IgG antibodies could facilitate the delivery to a target site. It is to be noted that in situ synthesis of metal NPs is much more efficient for such applications as they spread homogenously [139]. This was carried out by a polyol reduction method in PAH/DS capsules. The capsules showed a significant increase in the permeability under laser light exposure at 530 nm due to creation of nanometer sized pores and finally resulting in complete rupture of the capsules. The rupture of capsules is largely dependent on parameters such as NP size, their distribution, laser energy and time of exposure. It is worth noting that the moderate exposure of light can also help in the cellular uptake of the capsules and release cargo into the cytosol of cells, however, high exposures may also lead to cell death [140]. While IR laser light at high intensity can destroy capsules, the capsules could be used for bioimaging by exposing them to lower intensity light [83]. The microwave illumination of polymer capsules containing NPs showed that the molecular vibrations occurred by electromagnetic polarization with minimal heat generation. The parameters such as the frequency, power of radiation and presence of NPs controlled the extent of the deformation of the capsules [83]. Upon exposure to microwaves (2.5 GHz, 100 mW), the gold NP incorporated capsules showed burst release in about 4 min, whereas, the capsules without NPs took about 10 min to break the capsule wall, which can be useful in sustained drug release.

The release of cargo by ultraviolet (UV) radiation has also been studied in many systems [141]. UV radiation causes chemical changes in the PEs showing pronounced shrinkage in PE containing aromatic groups and negligible shrinkage in PE without aromatic groups [142]. In 2010, Koo et al. fabricated capsules with walls containing photoacid generators (PAGs). These PAGs decreased the pH of the solution by releasing protons upon UV radiation, which in turn caused swelling of the capsules [143]. The opening and closing of the capsules was thus obtained by alternate UV exposure and washing with neutral water. Azobenzene-modified polymers have also shown conformational changes in the entire chain upon UV exposure [144]. In a recent study, hematite NPs of gadolium oxide (doped with europium and terbium) were used as templates for PAH/PSS multilayers and radioluminescence-based Dox release was demonstrated [145]. Here, radioluminescence offers the advantage of greater tissue penetration and thus helps to image thick tissues. These capsules showed enhanced release at pH 5, and are thus more effective for cancer treatment. Their paramagnetic properties also make them potential MRI contrast agents. However, such light-triggered systems may also be harmful to human cells as in the case of UV-based approaches. UV-based methods have limited penetration in living tissues and also might damage the normal cells. Compared to this, NIR-triggered systems are more suitable as they have deeper

penetration into living cells, can be easily focused and have no harmful effects on normal cells. Radio waves have deeper penetration but they are difficult to focus and hence cannot be used for deep tissue.

Ultrasound: The use of ultrasound waves in various hospital equipment prove their efficiency to be used for release purposes both in vitro and in vivo without affecting healthy tissues. The release is activated due to the occurrence of cavitations in fluids when ultrasonic waves with a frequency more than 20 kHz are used. As the waves pass through the sonic probe, microbubbles of air are formed that start to oscillate in the surrounding fluid and finally collapse causing cavitation and formation of enormous energy in the fluid. This induces shear forces in the capsule layer leading to its disruption [146]. On applying ultrasonic waves, the capsule shell is torn into pieces leading to the release of the drug. The presence of NPs make the capsules mechanically more stable during shorter treatment times [147]. On increasing the ultrasonic power (100 to 500 W) on PAH/PSS capsules embedded with iron oxide NPs, the capsules break into small pieces of about 2–16 μM in size due to the increase in the size of the cavitation bubbles [148]. Notably, the capsules without NPs were only deformed after sonication. For a homogenous distribution of NPs, in situ synthesis of silver NPs in PAH/DS capsules has also been reported [149]. The burst release of FITC-dextran within 5 s was observed upon exposure to ultrasonic irradiation of 170 W and 50 Hz. Kolesnikova and co-workers explained that the varying concentration of zinc oxide NPs in the capsule shell can increase the sensitivity of the capsules to ultrasound [150]. They presented a theory according to which the change in volume fraction of zinc oxide NPs can control the mechanical properties by decreasing the Young's modulus and shell elasticity while increasing the fragility and sensitivity to ultrasound.

The core material also influences the deformation upon ultrasonic treatment. The capsules formed over inorganic $CaCO_3$ templates became fully ruptured [147] while the capsules formed over organic templates (e.g., PS and MF) were only deformed [148,150] after 10 s of ultrasound treatment at 20–100 W. The insoluble complexes observed in the interior of the capsules played an important role in the rupturing process. Mostly, an ultrasound frequency of >1 MHz has been used in medicine as it has deeper penetration with minimal side effects. The rupture of capsules at low power causes the capsules to disintegrate to an extent enough to cause drug release. However, the use of high power results in the unnecessary destruction of the entire capsules. Further, the shell properties can be tuned to achieve better sensitivity to ultrasonic waves. Owing to its vast use in present applications, the use of ultrasound as an external trigger has great potential to be explored.

Temperature: The most developed approach for thermally induced release from capsules is by introducing temperature responsive polymer derivatives of poly(*N*-isopropylacrylamide) (PNIPAM). Above its LCST, PNIPAM chains undergo a phase transition from a coiled to a globule state, making hydrophobic connections with surrounding polymer chains. The PNIPAM-based systems are extensively investigated for temperature-induced release processes as the LCST temperature is closer to physiological temperature. The PNIPAM-PAH microgel thin films fabricated over a glass substrate exhibited temperature-induced release of insulin and Dox [151]. When multilayer capsules of PNIPAM/PAA were subjected to a temperature higher than its LCST, the permeability of PNIPAM was suppressed which was otherwise reversible in nature [152]. Also, the hydrogen bonded thermoresponsive PNIPAM/PAA multilayer films showed reversible encapsulation and release behavior when the temperature is changed [153]. The most adapted way to fabricate temperature-responsive microcapsules is to use PNIPAM block copolymers, including short anionic or cationic chains. Notably, the capsules fabricated by cationic and anionic PNIPAM block copolymers showed considerable decrease in size and permeability at elevated temperatures due to structural rearrangements in the shell [154]. However, the thermoresponsive behavior of the capsules was limited as this process was only partially reversible. Recently, poly(2-oxazoline)/tannic acid (TA) based multilayer capsules have shown stability over a wide range of pH and demonstrated the ability to release loaded bioactive molecules at a physiological temperature of 37 °C [155-157]. The tuning of the temperature responsiveness by addition of salts has also been reported [158]. The LCST temperature decreased upon addition of salts causing precipitation of PNIPAM chains inside the capsules. The configurational transition of PNIPAM from a globule to a coiled state occurred upon cooling the capsules below LCST. As this phenomenon is reversible, the temperature responsiveness becomes repeatable and reversible with retained thermosensitivity. By using poly(*N*,*N*-dimethylaminoethyl methacrylate) (PDMAEMA) as one of the layer components, the temperature and pH (i.e., dual) responsive microcapsules were fabricated via LbL assembly [159]. When the pH was increased, the capsules shrunk, showing the transition from open to closed state at a narrow pH range of 7–8. Similarly, at an elevated temperature of 60 °C, capsule shrinkage of about 54% was observed, thus allowing easy loading with high efficiency. Notably, the increased ionic strength resulted in increased permeability due to salt-induced PE rearrangements.

Applications

Easy fabrication, efficient encapsulation and the ability to alter the properties of LbL-assembled PE capsules, make them useful in various areas ranging from drug delivery, imaging,

sensing, tissue engineering and medicine [160,161]. Additionally, the possibility to introduce different functionalities on the capsule surface provides external control over the capsule's release properties. Biocompatible polymers and crosslinking of weak PEs have been used to improve the stability in various biological applications.

Therapeutics

Multifunctional carrier systems have been reported to effectively deliver drugs into the target cells or tissues [8]. Along with hydrophilic drugs, even hydrophobic drugs have been efficiently encapsulated by different methods. The cellular uptake of capsules loaded with hydrophobic drugs for PDT demonstrated their use as anticancer agents [76]. The coating of capsules with low fouling polymers such as PEG provides protection from various degrading proteins and the body's phagocytic system [94]. Chitosan-DS nanocapsules loaded with ciprofloxacin or ceftriaxone were proposed as effective therapeutics against the intraphagosomal pathogen *Salmonella* [162]. In vitro and in vivo experiments showed effective clearance of the infection at a dosage significantly lower than free antibiotics due to the increased retention time of ciprofloxacin in blood and organs when it was delivered by capsules. Theranostic applications were recently observed by ultrasonically irradiating the capsules made of PVP and TA in order to deliver Dox as shown in the schematics in Figure 7a,b [163]. AFM and SEM images of the fabricated capsules are also shown in Figure 7c,d. The release of loaded molecules could be easily changed from sustained to burst profile by increasing the power of ultrasonic irradiation.

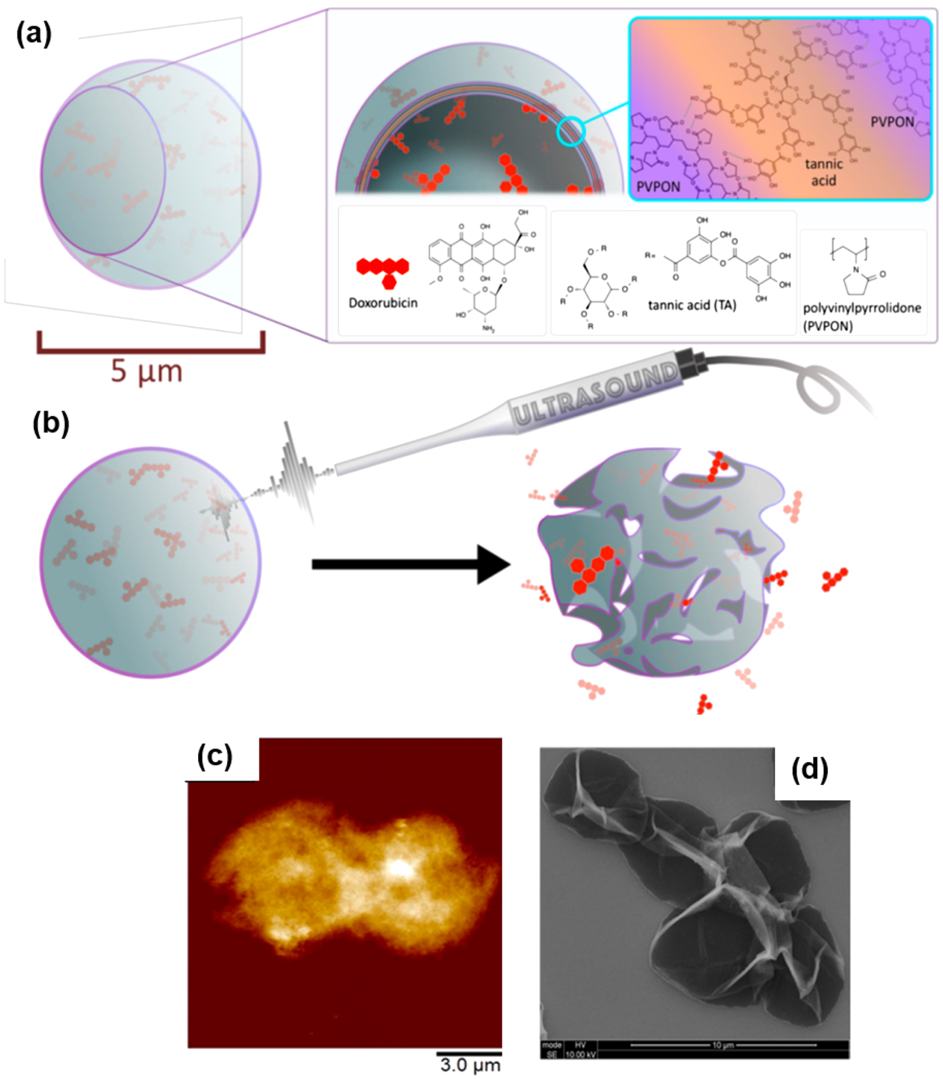

Figure 7: Schematic illustration of (a) the formation of PVP/TA capsules loaded with Dox, (b) the ultrasound triggered release of Dox, along with images from a morphological investigation of the capsules by (c) AFM and (d) SEM. The images in a–d were adapted and reprinted with permission from [163], copyright 2017 American Chemical Society.

Anticancer therapy

The successful release of chemotherapeutic drugs from click capsules made of weak PEs has been demonstrated for intracellular environmental triggers such as pH [164]. Notably, microcapsules functionalized with monoclonal antibodies showed better specificity and cellular uptake during the in vitro experiments to target colorectal cancer cells [101,102]. In vivo experiments of chitosan/alginate multilayered capsules in mice models demonstrated the successful release of loaded Dox into acidic cancer cells [76]. The direct injection of drug-loaded capsules into the xenograft tumor of a mouse showed a sustained release of anticancer drug that led to reduced tumor growth. It is worth noting that the drug-loaded microcapsules showed better tumor regression than free drug [165].

Cancer cells are heterogeneous in many aspects, such as, some may have an elevated glutathione (GSH) level (leading to their acidic nature) or some may produce extra reactive oxygen species (ROS). A tumor may be at any stage or even these stages may coexist in different regions of one tumor. Capsules responding to one particular stimulus may release the drug only in one region of the tumor, thereby proving to be less effective. Thus Wang et al. reported capsules using a self-assembled amphiphilic chemotherapeutic pro-drug of thioester linked SN38 that responded to both GSH and ROS by releasing the parent drug SN38 via thiolysis [166]. The nanocapsules (≈100 nm in diameter) were successfully able to target tumor cells by enhanced permeability and retention (EPR) effect. Recently, it has been demonstrated that a microcapsule system fabricated over calcium chalcogenide NIPAM nanocrystals released the loaded Dox under NIR light irradiation [167]. The local temperature increase of laser light irradiation made the thermoresponsive capsule shrink and release the loaded Dox molecules. In vitro and in vivo chemotherapeutic results indicated their potential in chemotherapy and photothermal therapy.

Vaccination

Self-exploding capsules with a semipermeable multilayer shell made over a microgel core offer excellent carriers in viscous environments such as mucus. The encapsulated cargo is given strong propulsion into the environment and can travel longer distances in a shorter time unlike other capsules from which release occur at a slower rate by Brownian diffusion [168]. Such microcapsules were designed to be vaccine delivery systems and a single injection may include different microcapsules, exploding at different time intervals. PMA hydrogel capsules have been used for DNA encapsulation and oligopeptide delivery to white blood cells in vitro and in vivo. Ovalbumin encapsulated in PMA hydrogen bonded capsules were shown to enhance antigen presentation to CD4 T-cells [169], whereas the same encapsulated in DS/Parg electrostatic capsules enhanced antigen presentation to CD8 T-cells [170]. These systems provided fast and efficient induction of immune response in mice experiments. Immunocompatibility studies with peripheral blood mononuclear cells stated no occurrence of apoptotic activity when incubated with different multilayer capsules having either a positively or negatively charged outer surface [171].

Medical imaging

LbL capsules have proved to be promising candidates as imaging probes for magnetic resonance imaging (MRI) by incorporating either paramagnetic metal–ligand complexes (mostly gadolinium ligands) conjugated with polymer or superparamagnetic iron oxide NPs [172]. Magnetically responsive nanocapsules with the option for both pH-triggered drug release and MRI imaging were prepared recently by PLL/alginate multilayer deposition over silica-coated iron cores, delivering Dox and diethylenetriaminepentaacetic acid gadolinium(III) dihydrogen (Gd-DTPA) to MCF-7 breast cancer cells [173]. The release rate of Gd-DTPA, an MRI contrast agent, was much slower as compared to Dox showing its enhanced stability and advantage in multimodal MRI tracking of the magnetic capsules and the drug. Multifunctional, water soluble and biocompatible MRI contrast agents were fabricated by assembling a PLL/PGA cross-linked shell (via EDC coupling) with superparamagnetic iron oxide NPs followed by assembly with G5.NH_2-FI-FA dendrimers [174]. By using folic acid (FA) as a targeting ligand for cancer cells and fluorescein isothiocyanate (FI) dye as an imaging probe, a multilayer capsule could be effectively used for MRI imaging of cancer cells. Reported by Shi et al., this was the first example of a successful in vivo MRI study in mice which showed a significant decrease in tumor signal intensity within 24 h [174]. Biodegradable trifunctional cross-linked PMA capsules with size of 300 nm were fabricated for co-encapsulation of Dox and perfluorohexance (PHF) for use in ultrasound imaging and ultrasound-induced drug delivery [175]. The in vitro cell assay showed the ability of these capsules to enter the cytoplasm of tumor cells via the EPR effect and the intracellular delivery of Dox. Notably, the use of PHF enhanced the imaging signal through acoustic droplet vaporization. More recently, multifunctional microcapsules incorporated with either single-walled carbon nanotubes or gold NPs on the surface have been reported for both NIR-induced release and photoacoustic imaging [176]. They served as a very good absorber in the NIR region and provided strong enhancement of photoacoustic imaging modality in both water and blood. Parg/DS microcapsules functionalized with Fe_3O_4 NPs have proved to be effective magnetic resonance contrast agents [177]. Low frequency alternating magnetic fields have also proven effective in inducing subtle changes in doxycycline release from PAH/PSS/Fe_3O_4 microcapsules without inflicting

damage to the cells after 30 min of exposure [178]. Furthermore, doxycycline delivered by magnetic microcapsules enabled site specific delivery and local function using a static magnetic field, while non-targeted sites remained unaffected.

Biosensors

Capsules containing one or more weak PEs can be directly used as pH sensors because intracellular pH plays an important role in most of the cellular events. By linking pH sensitive seminaphtho-rhodafluor-1-dye (SNARF) with layer components (e.g., dextran), the multilayer capsules can be used as a pH sensor [179]. Notably, the functionalized capsules emitted red fluorescence in alkaline conditions while emitting green fluorescence after entering into the cells due to the acidic environment in cell compartments. By monitoring the color changes, the location of ingested capsules in the lysosomal/endosomal compartments of the cell could be visualized. Polymer capsules with ratiometric ion sensitivity towards ions such as protons, sodium, potassium and chloride have also been described at the single capsule level by conjugating different probes and indicators to dextran molecules [180]. The fluorescence response was measured by titration fluorimetry and fluorescence microscopy. It is worth noting that the detection of several ions in parallel can be tricky due to emission overlap, cross talk of indicators to non-target analytes and interference with sample pH. To overcome these problems, bar-coded capsules were proposed wherein each capsule was externally tagged by a unique luminescent code [181]. This was done by functionalizing the outermost layer with quantum dot codes of different sizes in appropriate ratios while encapsulating the enzyme and indicators in the inner core. Proton sensitive multilayer capsules with encapsulated ion fluorophores were taken up by cells and resided in lysosomes for days [182]. Upon cellular stimulation with pH-active agents, the real time measurements revealed the kinetics and mechanisms involved for intracellular pH changes with respect to different agents.

The successful encapsulation of enzymes in capsules provides protection against the degradation on the one hand while providing the option to tune the permeability of loaded enzymes at the required rate for enzymatic reactions in sensor applications on the other hand. As substrates and reaction products can easily diffuse through the membrane, it can be used for continuous reactions. Microcapsules incorporated with a fluorescence resonance energy transfer (FRET) couple could be used as a continuous glucose sensor. The competitive replacement of one of the partners in a FRET couple led to a decrease in the fluorescence that could be correlated to the amount of analyte [183]. Chinnayelka and McShane [183] used dextran and apo-glucose oxidase (high affinity to β-D-glucose) as the FRET couple to detect glucose. Glucose easily permeated through the capsule membrane, replaced apo-glucose oxidase and decreased the fluorescence intensity. The decrease in the intensity of fluorescence is a function of the glucose concentration present in the sample. This type of optical biosensor, termed as "smart tattoo", has been reported for the encapsulation and release of anti-inflammatory drugs over a long period of 4 weeks [184]. The anti-inflammatory drug was observed to reduce the inflammation at the implant site in vivo. Various capsule-based metabolite sensors for urea, cholesterol and glucose, and even a single capsule sensing system for lactate and oxygen have also been fabricated recently [185].

Bioreactors

Capsules having the ability to accommodate active biomolecules in the large cavity have found application in the biomedical field as microreactors, cell mimics and artificial organelles [186,187]. A wide variety of enzymatic reactions have been performed in the polymer capsules. The PAH/DS/TA microcapsules exhibited an excellent scavenging capacity for hydrogen peroxide and hydroxyl radical, suggesting better antioxidant properties [188]. Catalase enzyme encapsulated in the capsules was used to prevent oxidative stress in an in vitro inflammation model depicting that the PE shell can make encapsulated enzymes more stable compared to free enzymes. The capsules made of PVP copolymer containing a manganoporphyrin modality (MnP-PVP) and TA can mimic enzymatic antioxidant superoxide dismutase-like and catalase-like activity for efficient free radical scavenging [189]. The schematic illustration of the formation of the capsules is depicted in Figure 8a. The inclusion of a MnP-PVP layer as an outer layer enhanced radical scavenging as compared to localization of a MnP-PVP layer either in the middle or inner part of the capsule shell. Another system of PAH/DS incorporating gold anisotropic nanorods was investigated for continuous reduction reaction of *p*-nitrophenol to *p*-aminophenol [190]. TEM images of gold nanorods and gold bipyramids incorporated in PAH/DS microcapsules are shown in Figure 8b,c. Thus, these capsules have high potential as microreactors in the field of catalysis as well.

Tissue engineering and artificial cells

Tissue engineering requires production of the extracellular matrix (ECM) from stem cells which is difficult to achieve in vitro. The encapsulation of stem cells into PLL/HA multilayers provides a suitable environment for better interaction of stem cells and growth and instructional molecules to achieve desired matrices [191]. The subcompartmentalization or fusion of capsules represent a major step towards the fabrication of artificial cells [192]. The multilayers have also proved to be efficient in vascular therapies for the development of suitable grafts for repairing damaged vessels or arteries [193].

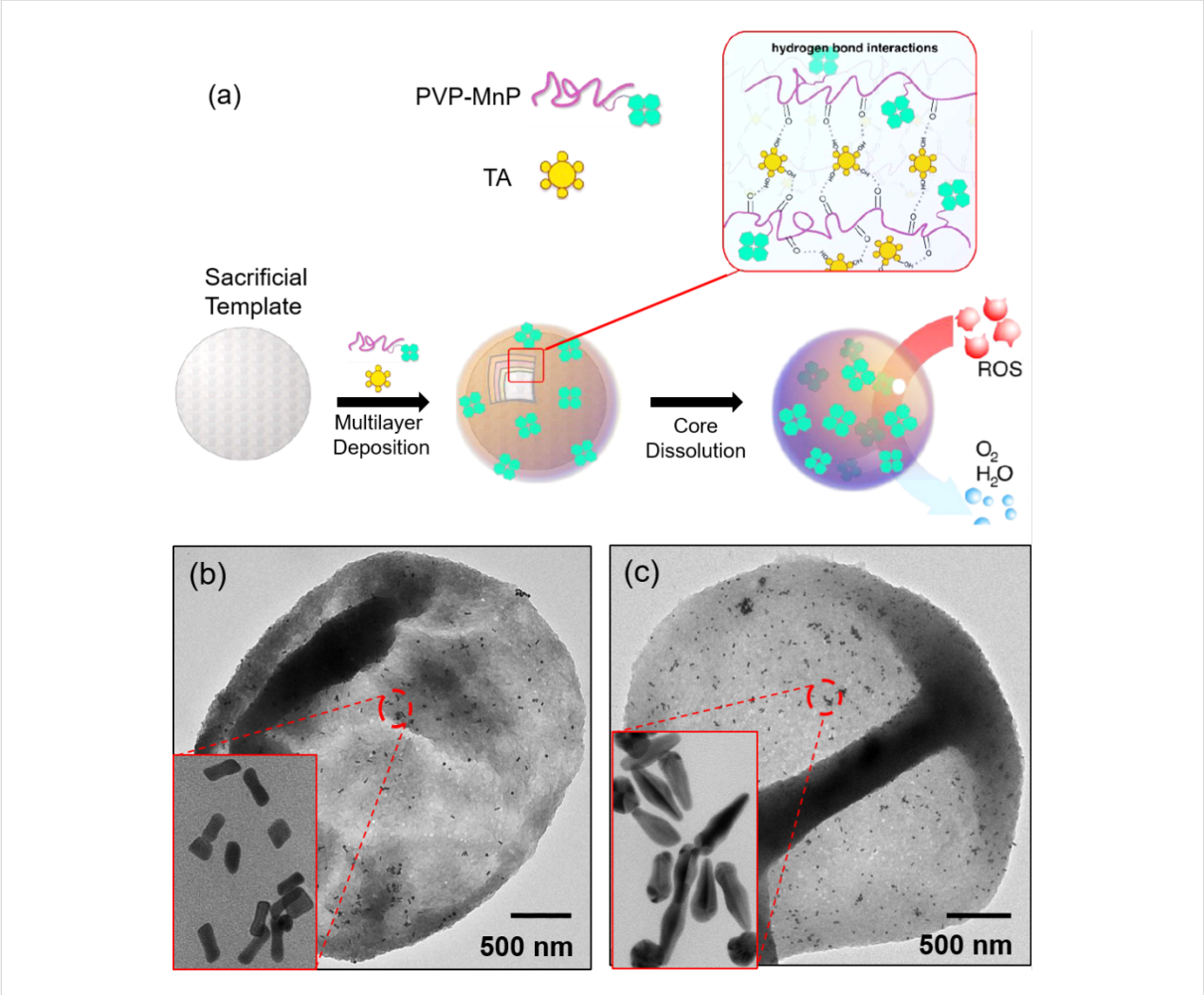

Figure 8: (a) Schematic representation showing the assembly of MnP-PVP/TA multilayers on silica template to obtain a hollow capsule for ROS scavenging. TEM investigation of PAH/DS microcapsules incorporating (b) gold nanorods and (c) gold bipyramids for catalysis application. The image in a was adapted and reprinted with permission from [189], copyright 2017 American Chemical Society and the images in b,c were adapted and reprinted with permission from [190], copyright 2019 American Chemical Society. Further permissions related to the material excerpted should be directed to the American Chemical Society.

Delivery of nucleic acids

Polymer capsules for the delivery of genes and siRNA to the cell nucleus or cytoplasm have been proven to be efficient in protecting them from denaturation in endo-lysosome, oxidizing bloodstream, and extracellular environments [194]. Cross-linked PMA hydrogel and PMA/PLL capsules were used for successful encapsulation and release of siRNA in a reduced environment to target the cancer-related anti-apoptotic factor survinin [195]. DS/Parg microcapsules have also been reported as safe, efficient and non-viral delivery systems for the delivery of CRISPR-Cas9, a gene editing tool for the treatment of various genetic diseases [196]. The internalization of capsules labeled with cyanine-7 into HEK293T-d tomato cells was studied by CLSM and 3D reconstruction images. In addition to low toxicity and high internalization, the capsules could also be degraded to release the cargo into the cell microenvironment, indicating high potential for gene delivery.

Conclusion

Over the past few decades, multilayer capsules have proved their ability in the fields of therapy, medicine, sensing and genetics. In this review, we have summarized the recent progress in the use of weak PEs for the fabrication of multilayer capsules. Their unique responsiveness to internal/external stimuli and easy manipulation of properties makes them efficient candidates for various applications. The advantages and disadvantages of driving forces involved in the formation of multilayers and encapsulation of cargo is also described. Notably, the crosslinking between the polymer layers have resulted in stable systems, however at the expense of stimuli

responsiveness. The capsules modified with metal/magnetic NPs or biomolecules could be easily targeted with external stimuli for the release of encapsulated cargo. Recent progress in the use of multilayer capsules for therapy, biosensing, bioreactors, and gene therapy applications paves the way for their widespread use. Thus, exploring the use of such weak PE systems can prove to have high potential in in vivo applications.

Funding

We would like to acknowledge the financial support from the Council of Scientific and Industrial Research (CSIR) and the Department of Science and Technology (DST) - Science and Engineering Research Board (SERB), Government of India.

ORCID® iDs

Anandhakumar Sundaramurthy - https://orcid.org/0000-0001-6870-7318

References

1. Kurapati, R.; Groth, T. W.; Raichur, A. M. *ACS Appl. Bio Mater.* **2019,** *2,* 5512–5527. doi:10.1021/acsabm.9b00703
2. Iler, R. K. *J. Colloid Interface Sci.* **1966,** *21,* 569–594. doi:10.1016/0095-8522(66)90018-3
3. Decher, G.; Hong, J. D. *Ber. Bunsen-Ges.* **1991,** *95,* 1430–1434. doi:10.1002/bbpc.19910951122
4. Skirtach, A. G.; Yashchenok, A. M.; Möhwald, H. *Chem. Commun.* **2011,** *47,* 12736–12746. doi:10.1039/c1cc13453a
5. Esser-Kahn, A. P.; Odom, S. A.; Sottos, N. R.; White, S. R.; Moore, J. S. *Macromolecules* **2011,** *44,* 5539–5553. doi:10.1021/ma201014n
6. Kharlampieva, E.; Sukhishvili, S. A. *Langmuir* **2003,** *19,* 1235–1243. doi:10.1021/la026546b
7. Sukhishvili, S. A. *Curr. Opin. Colloid Interface Sci.* **2005,** *10,* 37–44. doi:10.1016/j.cocis.2005.05.001
8. Gil, P. R.; del Mercato, L. L.; del Pino, P.; Muñoz-Javier, A.; Parak, W. J. *Nano Today* **2008,** *3,* 12–21. doi:10.1016/s1748-0132(08)70040-9
9. Sukhorukov, G. B.; Brumen, M.; Donath, E.; Möhwald, H. *J. Phys. Chem. B* **1999,** *103,* 6434–6440. doi:10.1021/jp990095v
10. Sukhorukov, G. B.; Rogach, A. L.; Zebli, B.; Liedl, T.; Skirtach, A. G.; Köhler, K.; Antipov, A. A.; Gaponik, N.; Susha, A. S.; Winterhalter, M.; Parak, W. J. *Small* **2005,** *1,* 194–200. doi:10.1002/smll.200400075
11. Mora-Huertas, C. E.; Fessi, H.; Elaissari, A. *Int. J. Pharm.* **2010,** *385,* 113–142. doi:10.1016/j.ijpharm.2009.10.018
12. Gao, C.; Donath, E.; Moya, S.; Dudnik, V.; Möhwald, H. *Eur. Phys. J. E: Soft Matter Biol. Phys.* **2001,** *5,* 21–27. doi:10.1007/s101890170083
13. Dubreuil, F.; Elsner, N.; Fery, A. *Eur. Phys. J. E: Soft Matter Biol. Phys.* **2003,** *12,* 215–221. doi:10.1140/epje/i2003-10056-0
14. Dubas, S. T.; Schlenoff, J. B. *Macromolecules* **1999,** *32,* 8153–8160. doi:10.1021/ma981927a
15. Izumrudov, V.; Kharlampieva, E.; Sukhishvili, S. A. *Macromolecules* **2004,** *37,* 8400–8406. doi:10.1021/ma048907v
16. Shiratori, S. S.; Rubner, M. F. *Macromolecules* **2000,** *33,* 4213–4219. doi:10.1021/ma991645q
17. Sundaramurthy, A. Responsive polyelectrolyte multilayer nanofilms for drug delivery applications. In *Stimuli Responsive Polymeric Nanocarriers for Drug Delivery Applications;* Makhlouf, A. S. H.; Abu-Thabit, N. Y., Eds.; Elsevier, 2018; Vol. 1. doi:10.1016/b978-0-08-101997-9.00013-8
18. Zyuzin, M. V.; Timin, A. S.; Sukhorukov, G. B. *Langmuir* **2019,** *35,* 4747–4762. doi:10.1021/acs.langmuir.8b04280
19. Izumrudov, V. A.; Mussabayeva, B. K.; Murzagulova, K. B. *Russ. Chem. Rev.* **2018,** *87,* 192–200. doi:10.1070/rcr4767
20. Ghiorghita, C.-A.; Bucatariu, F.; Dragan, E. S. *Mater. Sci. Eng., C* **2019,** *105,* 110050. doi:10.1016/j.msec.2019.110050
21. Rathee, V. S.; Sidky, H.; Sikora, B. J.; Whitmer, J. K. *Polymers (Basel, Switz.)* **2019,** *11,* 183. doi:10.3390/polym11010183
22. De Koker, S.; Hoogenboom, R.; De Geest, B. G. *Chem. Soc. Rev.* **2012,** *41,* 2867–2884. doi:10.1039/c2cs15296g
23. Gao, C.; Moya, S.; Lichtenfeld, H.; Casoli, A.; Fiedler, H.; Donath, E.; Möhwald, H. *Macromol. Mater. Eng.* **2001,** *286,* 355–361. doi:10.1002/1439-2054(20010601)286:6<355::aid-mame355>3.0.co;2-9
24. Mauser, T.; Déjugnat, C.; Möhwald, H.; Sukhorukov, G. B. *Langmuir* **2006,** *22,* 5888–5893. doi:10.1021/la060088f
25. Déjugnat, C.; Sukhorukov, G. B. *Langmuir* **2004,** *20,* 7265–7269. doi:10.1021/la049706n
26. Schuetz, P.; Caruso, F. *Adv. Funct. Mater.* **2003,** *13,* 929–937. doi:10.1002/adfm.200304483
27. Caruso, F.; Trau, D.; Möhwald, H.; Renneberg, R. *Langmuir* **2000,** *16,* 1485–1488. doi:10.1021/la991161n
28. Shenoy, D. B.; Antipov, A. A.; Sukhorukov, G. B.; Möhwald, H. *Biomacromolecules* **2003,** *4,* 265–272. doi:10.1021/bm025661y
29. Anandhakumar, S.; Debapriya, M.; Nagaraja, V.; Raichur, A. M. *Mater. Sci. Eng., C* **2010,** *31,* 342–349. doi:10.1016/j.msec.2010.10.005
30. Volodkin, D.; Skirtach, A.; Möhwald, H. LbL Films as Reservoirs for Bioactive Molecules. In *Bioactive Surfaces;* Börner, H. G.; Lutz, J.-F., Eds.; Advances in Polymer Science, Vol. 240; Springer Berlin: Berlin, Germany, 2010; pp 135–161. doi:10.1007/12_2010_79
31. Antipov, A. A.; Shchukin, D.; Fedutik, Y.; Petrov, A. I.; Sukhorukov, G. B.; Möhwald, H. *Colloids Surf., A* **2003,** *224,* 175–183. doi:10.1016/s0927-7757(03)00195-x
32. Volodkin, D. V.; Petrov, A. I.; Prevot, M.; Sukhorukov, G. B. *Langmuir* **2004,** *20,* 3398–3406. doi:10.1021/la036177z
33. Chen, Y. D.; Xu, J. J.; Wang, Y.; Chen, H.; Luo, Q. J.; Li, X. D.; Zhu, W. P. *RSC Adv.* **2017,** *7,* 1260–1265. doi:10.1039/c6ra25613a
34. Sundaramurthy, A.; Sundramoorthy, A. K. *Int. J. Biol. Macromol.* **2018,** *107,* 2251–2261. doi:10.1016/j.ijbiomac.2017.10.096
35. Li, J.; Jiang, Z.; Wu, H.; Zhang, L.; Long, L.; Jiang, Y. *Soft Matter* **2010,** *6,* 542–550. doi:10.1039/b918218g
36. Chen, L.; An, H. Z.; Doyle, P. S. *Langmuir* **2015,** *31,* 9228–9235. doi:10.1021/acs.langmuir.5b02200
37. Tian, Y.; Li, L.; Han, H.; Wang, W.; Wang, Y.; Ye, Z.; Guo, X. *Polymers (Basel, Switz.)* **2016,** *8,* 145. doi:10.3390/polym8040145
38. Kharlampieva, E.; Kozlovskaya, V.; Tyutina, J.; Sukhishvili, S. A. *Macromolecules* **2005,** *38,* 10523–10531. doi:10.1021/ma0516891
39. Wang, Z.; Feng, Z.; Gao, C. *Chem. Mater.* **2008,** *20,* 4194–4199. doi:10.1021/cm8003358
40. Joanny, J. F. *Eur. Phys. J. B* **1999,** *9,* 117–122. doi:10.1007/s100510050747
41. Lytle, T. K.; Chang, L.-W.; Markiewicz, N.; Perry, S. L.; Sing, C. E. *ACS Cent. Sci.* **2019,** *5,* 709–718. doi:10.1021/acscentsci.9b00087

42. Caruso, F.; Lichtenfeld, H.; Donath, E.; Möhwald, H. *Macromolecules* **1999,** *32,* 2317–2328. doi:10.1021/ma980674i
43. Philipp, B.; Dautzenberg, H.; Linow, K.-J.; Kötz, J.; Dawydoff, W. *Prog. Polym. Sci.* **1989,** *14,* 91–172. doi:10.1016/0079-6700(89)90018-x
44. Antipov, A. A.; Sukhorukov, G. B.; Leporatti, S.; Radtchenko, I. L.; Donath, E.; Möhwald, H. *Colloids Surf., A* **2002,** *198–200,* 535–541. doi:10.1016/s0927-7757(01)00956-6
45. Steitz, R.; Leiner, V.; Tauer, K.; Khrenov, V.; von Klitzing, R. *Appl. Phys. A: Mater. Sci. Process.* **2002,** *74,* s519–s521. doi:10.1007/s003390201782
46. Wang, L.; Wang, Z.; Zhang, X.; Shen, J.; Chi, L.; Fuchs, H. *Macromol. Rapid Commun.* **1997,** *18,* 509–514. doi:10.1002/marc.1997.030180609
47. Zhang, Y.; Guan, Y.; Yang, S.; Xu, J.; Han, C. C. *Adv. Mater. (Weinheim, Ger.)* **2003,** *15,* 832–835. doi:10.1002/adma.200304315
48. Sukhishvili, S. A.; Granick, S. *Macromolecules* **2002,** *35,* 301–310. doi:10.1021/ma011346c
49. Kharlampieva, E.; Sukhishvili, S. A. *Polym. Rev. (Philadelphia, PA, U. S.)* **2006,** *46,* 377–395. doi:10.1080/15583720600945386
50. Kozlovskaya, V.; Sukhishvili, S. A. *Macromolecules* **2006,** *39,* 5569–5572. doi:10.1021/ma0607923
51. Kharlampieva, E.; Kozlovskaya, V.; Sukhishvili, S. A. *Adv. Mater. (Weinheim, Ger.)* **2009,** *21,* 3053–3065. doi:10.1002/adma.200803653
52. Yang, S. Y.; Lee, D.; Cohen, R. E.; Rubner, M. F. *Langmuir* **2004,** *20,* 5978–5981. doi:10.1021/la0490442
53. Tong, W.; Gao, C.; Möhwald, H. *Macromolecules* **2006,** *39,* 335–340. doi:10.1021/ma0517648
54. Bucatariu, F.; Ghiorghita, C.-A.; Dragan, E. S. *Colloids Surf., A* **2018,** *537,* 53–60. doi:10.1016/j.colsurfa.2017.10.021
55. Zhang, Y.; Yang, S.; Guan, Y.; Cao, W.; Xu, J. *Macromolecules* **2003,** *36,* 4238–4240. doi:10.1021/ma0342729
56. Feng, Z.; Wang, Z.; Gao, C.; Shen, J. *Adv. Mater. (Weinheim, Ger.)* **2007,** *19,* 3687–3691. doi:10.1002/adma.200700541
57. Tong, W.; Gao, C.; Möhwald, H. *Macromol. Rapid Commun.* **2006,** *27,* 2078–2083. doi:10.1002/marc.200600533
58. Tong, W.; Gao, C.; Möhwald, H. *Polym. Adv. Technol.* **2008,** *19,* 817–823. doi:10.1002/pat.1040
59. Guo, D.-S.; Liu, Y. *Chem. Soc. Rev.* **2012,** *41,* 5907–5921. doi:10.1039/c2cs35075k
60. Suzuki, I.; Egawa, Y.; Mizukawa, Y.; Hoshi, T.; Anzai, J.-i. *Chem. Commun.* **2002,** 164–165. doi:10.1039/b108771c
61. Crespo-Biel, O.; Dordi, B.; Reinhoudt, D. N.; Huskens, J. *J. Am. Chem. Soc.* **2005,** *127,* 7594–7600. doi:10.1021/ja051093t
62. Van der Heyden, A.; Wilczewski, M.; Labbé, P.; Auzély, R. *Chem. Commun.* **2006,** 3220–3222. doi:10.1039/b604672j
63. Tomatsu, I.; Hashidzume, A.; Harada, A. *Macromol. Rapid Commun.* **2006,** *27,* 238–241. doi:10.1002/marc.200500793
64. Guzmán, E.; Mateos-Maroto, A.; Ruano, M.; Ortega, F.; Rubio, R. G. *Adv. Colloid Interface Sci.* **2017,** *249,* 290–307. doi:10.1016/j.cis.2017.04.009
65. Qiu, X.; Leporatti, S.; Donath, E.; Möhwald, H. *Langmuir* **2001,** *17,* 5375–5380. doi:10.1021/la010201w
66. Trubetskoy, V. S.; Loomis, A.; Hagstrom, J. E.; Budker, V. G.; Wolff, J. A. *Nucleic Acids Res.* **1999,** *27,* 3090–3095. doi:10.1093/nar/27.15.3090
67. Thomas, M. B.; Radhakrishnan, K.; Gnanadhas, D. P.; Chakravortty, D.; Raichur, A. M. *Int. J. Nanomed.* **2013,** *8,* 267–273. doi:10.2147/ijn.s37737
68. Wang, Y.; Caruso, F. *Chem. Mater.* **2005,** *17,* 953–961. doi:10.1021/cm0483137
69. Balabushevich, N. G.; Tiourina, O. P.; Volodkin, D. V.; Larionova, N. I.; Sukhorukov, G. B. *Biomacromolecules* **2003,** *4,* 1191–1197. doi:10.1021/bm0340321
70. Anandhakumar, S.; Nagaraja, V.; Raichur, A. M. *Colloids Surf., B* **2010,** *78,* 266–274. doi:10.1016/j.colsurfb.2010.03.016
71. Tripathy, J.; Raichur, A. M. *Colloids Surf., B* **2013,** *101,* 487–492. doi:10.1016/j.colsurfb.2012.07.025
72. Köhler, K.; Shchukin, D. G.; Möhwald, H.; Sukhorukov, G. B. *J. Phys. Chem. B* **2005,** *109,* 18250–18259. doi:10.1021/jp052208i
73. Radtchenko, I. L.; Sukhorukov, G. B.; Möhwald, H. *Int. J. Pharm.* **2002,** *242,* 219–223. doi:10.1016/s0378-5173(02)00161-8
74. Anandhakumar, S.; Raichur, A. M. *Colloids Surf., B* **2011,** *84,* 379–383. doi:10.1016/j.colsurfb.2011.01.029
75. Gao, C.; Donath, E.; Möhwald, H.; Shen, J. *Angew. Chem., Int. Ed.* **2002,** *41,* 3789–3793. doi:10.1002/1521-3773(20021018)41:20<3789::aid-anie3789>3.0.co;2-d
76. Zhao, Q.; Han, B.; Wang, Z.; Gao, C.; Peng, C.; Shen, J. *Nanomedicine (N. Y., NY, U. S.)* **2007,** *3,* 63–74. doi:10.1016/j.nano.2006.11.007
77. Kurapati, R.; Raichur, A. M. *J. Mater. Chem. B* **2013,** *1,* 3175–3184. doi:10.1039/c3tb20192a
78. Petrov, A. I.; Volodkin, D. V.; Sukhorukov, G. B. *Biotechnol. Prog.* **2005,** *21,* 918–925. doi:10.1021/bp0495825
79. Minaeva, O. V.; Brodovskaya, E. P.; Pyataev, M. A.; Gerasimov, M. V.; Zharkov, M. N.; Yurlov, I. A.; Kulikov, O. A.; Kotlyarov, A. A.; Balykova, L. A.; Kokorev, A. V.; Zaborovskiy, A. V.; Pyataev, N. A.; Sukhorukov, G. B. *J. Phys.: Conf. Ser.* **2017,** *784,* 012038. doi:10.1088/1742-6596/784/1/012038
80. Hu, S.-H.; Tsai, C.-H.; Liao, C.-F.; Liu, D.-M.; Chen, S.-Y. *Langmuir* **2008,** *24,* 11811–11818. doi:10.1021/la801138e
81. Lee, D.; Rubner, M. F.; Cohen, R. E. *Chem. Mater.* **2005,** *17,* 1099–1105. doi:10.1021/cm048441v
82. Wong, M. S.; Cha, J. N.; Choi, K.-S.; Deming, T. J.; Stucky, G. D. *Nano Lett.* **2002,** *2,* 583–587. doi:10.1021/nl020244c
83. De Geest, B. G.; Skirtach, A. G.; De Beer, T. R.; Sukhorukov, G. B.; Bracke, L.; Baeyens, W. R.; Demeester, J.; De Smedt, S. C. *Macromol. Rapid Commun.* **2007,** *28,* 88–95. doi:10.1002/marc.200600631
84. Bédard, M. F.; Braun, D.; Sukhorukov, G. B.; Skirtach, A. G. *ACS Nano* **2008,** *2,* 1807–1816. doi:10.1021/nn8002168
85. Lehn, J.-M. *Angew. Chem., Int. Ed. Engl.* **1990,** *29,* 1304–1319. doi:10.1002/anie.199013041
86. Zheng, B.; Wang, F.; Dong, S.; Huang, F. *Chem. Soc. Rev.* **2012,** *41,* 1621–1636. doi:10.1039/c1cs15220c
87. Xu, H.; Stampp, S. P.; Rudkevich, D. M. *Org. Lett.* **2003,** *5,* 4583–4586. doi:10.1021/ol0357301
88. Crespo-Biel, O.; Péter, M.; Bruinink, C. M.; Ravoo, B. J.; Reinhoudt, D. N.; Huskens, J. *Chem. – Eur. J.* **2005,** *11,* 2426–2432. doi:10.1002/chem.200400393
89. Kharlampieva, E.; Sukhishvili, S. A. *Macromolecules* **2003,** *36,* 9950–9956. doi:10.1021/ma0350821
90. Such, G. K.; Johnston, A. P. R.; Liang, K.; Caruso, F. *Prog. Polym. Sci.* **2012,** *37,* 985–1003. doi:10.1016/j.progpolymsci.2011.12.002

91. Such, G. K.; Quinn, J. F.; Quinn, A.; Tjipto, E.; Caruso, F. *J. Am. Chem. Soc.* **2006,** *128,* 9318–9319. doi:10.1021/ja063043+
92. Jierry, L.; Ben Ameur, N.; Thomann, J.-S.; Frisch, B.; Gonthier, E.; Voegel, J.-C.; Senger, B.; Decher, G.; Felix, O.; Schaaf, P.; Mesini, P.; Boulmedais, F. *Macromolecules* **2010,** *43,* 3994–3997. doi:10.1021/ma100402v
93. Such, G. K.; Tjipto, E.; Postma, A.; Johnston, A. P. R.; Caruso, F. *Nano Lett.* **2007,** *7,* 1706–1710. doi:10.1021/nl070698f
94. Ochs, C. J.; Such, G. K.; Städler, B.; Caruso, F. *Biomacromolecules* **2008,** *9,* 3389–3396. doi:10.1021/bm800794w
95. Kinnane, C. R.; Such, G. K.; Antequera-Garcia, G.; Yan, Y.; Dodds, S. J.; Liz-Marzan, L. M.; Caruso, F. *Biomacromolecules* **2009,** *10,* 2839–2846. doi:10.1021/bm900673m
96. Leung, M. K. M.; Such, G. K.; Johnston, A. P. R.; Biswas, D. P.; Zhu, Z.; Yan, Y.; Lutz, J.-F.; Caruso, F. *Small* **2011,** *7,* 1075–1085. doi:10.1002/smll.201002258
97. Ochs, C. J.; Such, G. K.; Caruso, F. *Langmuir* **2011,** *27,* 1275–1280. doi:10.1021/la104232r
98. Yan, Y.; Ochs, C. J.; Such, G. K.; Heath, J. K.; Nice, E. C.; Caruso, F. *Adv. Mater. (Weinheim, Ger.)* **2010,** *22,* 5398–5403. doi:10.1002/adma.201003162
99. Liang, K.; Such, G. K.; Zhu, Z.; Yan, Y.; Lomas, H.; Caruso, F. *Adv. Mater. (Weinheim, Ger.)* **2011,** *23,* H273–H277. doi:10.1002/adma.201101690
100. Connal, L. A.; Kinnane, C. R.; Zelikin, A. N.; Caruso, F. *Chem. Mater.* **2009,** *21,* 576–578. doi:10.1021/cm803011w
101. Kamphuis, M. M. J.; Johnston, A. P. R.; Such, G. K.; Dam, H. H.; Evans, R. A.; Scott, A. M.; Nice, E. C.; Heath, J. K.; Caruso, F. *J. Am. Chem. Soc.* **2010,** *132,* 15881–15883. doi:10.1021/ja106405c
102. Cortez, C.; Tomaskovic-Crook, E.; Johnston, A. P. R.; Radt, B.; Cody, S. H.; Scott, A. M.; Nice, E. C.; Heath, J. K.; Caruso, F. *Adv. Mater. (Weinheim, Ger.)* **2006,** *18,* 1998–2003. doi:10.1002/adma.200600564
103. Leguen, E.; Chassepot, A.; Decher, G.; Schaaf, P.; Voegel, J.-C.; Jessel, N. *Biomol. Eng.* **2007,** *24,* 33–41. doi:10.1016/j.bioeng.2006.05.023
104. Berg, M. C.; Yang, S. Y.; Hammond, P. T.; Rubner, M. F. *Langmuir* **2004,** *20,* 1362–1368. doi:10.1021/la0355489
105. Picart, C.; Elkaim, R.; Richert, L.; Audoin, F.; Arntz, Y.; Da Silva Cardoso, M.; Schaaf, P.; Voegel, J.-C.; Frisch, B. *Adv. Funct. Mater.* **2005,** *15,* 83–94. doi:10.1002/adfm.200400106
106. Chua, P.-H.; Neoh, K.-G.; Kang, E.-T.; Wang, W. *Biomaterials* **2008,** *29,* 1412–1421. doi:10.1016/j.biomaterials.2007.12.019
107. Werner, S.; Huck, O.; Frisch, B.; Vautier, D.; Elkaim, R.; Voegel, J.-C.; Brunel, G.; Tenenbaum, H. *Biomaterials* **2009,** *30,* 2291–2301. doi:10.1016/j.biomaterials.2009.01.004
108. Moya, S.; Donath, E.; Sukhorukov, G. B.; Auch, M.; Bäumler, H.; Lichtenfeld, H.; Möhwald, H. *Macromolecules* **2000,** *33,* 4538–4544. doi:10.1021/ma9914974
109. Qi, W.; Wang, A.; Yang, Y.; Du, M.; Bouchu, M. N.; Boullanger, P.; Li, J. *J. Mater. Chem.* **2010,** *20,* 2121–2127. doi:10.1039/b920469p
110. Krishna, G.; Shutava, T.; Lvov, Y. *Chem. Commun.* **2005,** *22,* 2796–2798. doi:10.1039/b415774e
111. Zhang, F.; Wu, Q.; Chen, Z.-C.; Li, X.; Jiang, X.-M.; Lin, X.-F. *Langmuir* **2006,** *22,* 8458–8464. doi:10.1021/la060847u
112. Zelikin, A. N.; Li, Q.; Caruso, F. *Angew. Chem., Int. Ed.* **2006,** *45,* 7743–7745. doi:10.1002/anie.200602779
113. Thompson, M. T.; Berg, M. C.; Tobias, I. S.; Lichter, J. A.; Rubner, M. F.; Van Vliet, K. J. *Biomacromolecules* **2006,** *7,* 1990–1995. doi:10.1021/bm060146b
114. Postma, A.; Yan, Y.; Wang, Y.; Zelikin, A. N.; Tjipto, E.; Caruso, F. *Chem. Mater.* **2009,** *21,* 3042–3044. doi:10.1021/cm901293e
115. Yashchenok, A. M.; Bratashov, D. N.; Gorin, D. A.; Lomova, M. V.; Pavlov, A. M.; Sapelkin, A. V.; Shim, B. S.; Khomutov, G. B.; Kotov, N. A.; Sukhorukov, G. B.; Möhwald, H.; Skirtach, A. G. *Adv. Funct. Mater.* **2010,** *20,* 3136–3142. doi:10.1002/adfm.201000846
116. Wang, L.; Wang, N.; Yang, H.; An, Q.; Zeng, T.; Ji, S. *Sep. Purif. Technol.* **2018,** *193,* 274–282. doi:10.1016/j.seppur.2017.10.061
117. Kurapati, R.; Raichur, A. M. *Chem. Commun.* **2012,** *48,* 6013–6015. doi:10.1039/c2cc32248j
118. Kurapati, R.; Raichur, A. M. *Chem. Commun.* **2013,** *49,* 734–736. doi:10.1039/c2cc38417e
119. Sui, Z.; Schlenoff, J. B. *Langmuir* **2004,** *20,* 6026–6031. doi:10.1021/la0495985
120. Sukhorukov, G. B.; Antipov, A. A.; Voigt, A.; Donath, E.; Möhwald, H. *Macromol. Rapid Commun.* **2001,** *22,* 44–46. doi:10.1002/1521-3927(20010101)22:1<44::aid-marc44>3.0.co;2-u
121. Mauser, T.; Déjugnat, C.; Sukhorukov, G. B. *Macromol. Rapid Commun.* **2004,** *25,* 1781–1785. doi:10.1002/marc.200400331
122. Mauser, T.; Déjugnat, C.; Sukhorukov, G. B. *J. Phys. Chem. B* **2006,** *110,* 20246–20253. doi:10.1021/jp063502t
123. Imoto, T.; Kida, T.; Matsusaki, M.; Akashi, M. *Macromol. Biosci.* **2010,** *10,* 271–277. doi:10.1002/mabi.200900272
124. Cuomo, F.; Lopez, F.; Ceglie, A.; Maiuro, L.; Miguel, M. G.; Lindman, B. *Soft Matter* **2012,** *8,* 4415–4420. doi:10.1039/c2sm07388a
125. Luo, G.-F.; Xu, X.-D.; Zhang, J.; Yang, J.; Gong, Y.-H.; Lei, Q.; Jia, H.-Z.; Li, C.; Zhuo, R.-X.; Zhang, X.-Z. *ACS Appl. Mater. Interfaces* **2012,** *4,* 5317–5324. doi:10.1021/am301258a
126. Antipov, A. A.; Sukhorukov, G. B.; Möhwald, H. *Langmuir* **2003,** *19,* 2444–2448. doi:10.1021/la026101n
127. Guan, Y.; Zhang, Y.; Zhou, T.; Zhou, S. *Soft Matter* **2009,** *5,* 842–849. doi:10.1039/b815913k
128. Gao, C.; Leporatti, S.; Moya, S.; Donath, E.; Möhwald, H. *Chem. – Eur. J.* **2003,** *9,* 915–920. doi:10.1002/chem.200390113
129. Heuvingh, J.; Zappa, M.; Fery, A. *Langmuir* **2005,** *21,* 3165–3171. doi:10.1021/la047388m
130. Kozlovskaya, V.; Kharlampieva, E.; Mansfield, M. L.; Sukhishvili, S. A. *Chem. Mater.* **2006,** *18,* 328–336. doi:10.1021/cm0517364
131. Lvov, Y.; Antipov, A. A.; Mamedov, A.; Möhwald, H.; Sukhorukov, G. B. *Nano Lett.* **2001,** *1,* 125–128. doi:10.1021/nl0100015
132. Caruso, F.; Susha, A. S.; Giersig, M.; Möhwald, H. *Adv. Mater. (Weinheim, Ger.)* **1999,** *11,* 950–953. doi:10.1002/(sici)1521-4095(199908)11:11<950::aid-adma950>3.0.co;2-t
133. Pastoriza-Santos, I.; Schöler, B.; Caruso, F. *Adv. Funct. Mater.* **2001,** *11,* 122–128. doi:10.1002/1616-3028(200104)11:2<122::aid-adfm122>3.0.co;2-n
134. Katagiri, K.; Nakamura, M.; Koumoto, K. *ACS Appl. Mater. Interfaces* **2010,** *2,* 768–773. doi:10.1021/am900784a
135. Gorin, D. A.; Portnov, S. A.; Inozemtseva, O. A.; Luklinska, Z.; Yashchenok, A. M.; Pavlov, A. M.; Skirtach, A. G.; Möhwald, H.; Sukhorukov, G. B. *Phys. Chem. Chem. Phys.* **2008,** *10,* 6899–6905. doi:10.1039/b809696a

136. Lu, Z.; Prouty, M. D.; Guo, Z.; Golub, V. O.; Kumar, C. S. S. R.; Lvov, Y. M. *Langmuir* **2005,** *21,* 2042–2050. doi:10.1021/la047629q
137. Katagiri, K.; Imai, Y.; Koumoto, K. *J. Colloid Interface Sci.* **2011,** *361,* 109–114. doi:10.1016/j.jcis.2011.05.035
138. Angelatos, A. S.; Radt, B.; Caruso, F. *J. Phys. Chem. B* **2005,** *109,* 3071–3076. doi:10.1021/jp045070x
139. Anandhakumar, S.; Vijayalakshmi, S. P.; Jagadeesh, G.; Raichur, A. M. *ACS Appl. Mater. Interfaces* **2011,** *3,* 3419–3424. doi:10.1021/am200651t
140. Muñoz Javier, A.; del Pino, P.; Bedard, M. F.; Ho, D.; Skirtach, A. G.; Sukhorukov, G. B.; Plank, C.; Parak, W. J. *Langmuir* **2008,** *24,* 12517–12520. doi:10.1021/la802448z
141. Yi, Q.; Sukhorukov, G. B. *Adv. Colloid Interface Sci.* **2014,** *207,* 280–289. doi:10.1016/j.cis.2013.11.009
142. Katagiri, K.; Matsuda, A.; Caruso, F. *Macromolecules* **2006,** *39,* 8067–8074. doi:10.1021/ma0615598
143. Koo, H. Y.; Lee, H.-J.; Kim, J. K.; San Choi, W. *J. Mater. Chem.* **2010,** *20,* 3932–3937. doi:10.1039/b924282a
144. Grama, S.; Moleavin, I.-A.; Hodorog-Rusu, A.; Hurduc, N.; Prisacaru, I.; Ibanescu, C. *Mater. Plast. (Bucharest, Rom.)* **2013,** *50,* 60–64.
145. Chen, H.; Moore, T.; Qi, B.; Colvin, D. C.; Jelen, E. K.; Hitchcock, D. A.; He, J.; Mefford, O. T.; Gore, J. C.; Alexis, F.; Anker, J. N. *ACS Nano* **2013,** *7,* 1178–1187. doi:10.1021/nn304369m
146. Antipina, M. N.; Sukhorukov, G. B. *Adv. Drug Delivery Rev.* **2011,** *63,* 716–729. doi:10.1016/j.addr.2011.03.012
147. De Geest, B. G.; Skirtach, A. G.; Mamedov, A. A.; Antipov, A. A.; Kotov, N. A.; De Smedt, S. C.; Sukhorukov, G. B. *Small* **2007,** *3,* 804–808. doi:10.1002/smll.200600441
148. Shchukin, D. G.; Gorin, D. A.; Möhwald, H. *Langmuir* **2006,** *22,* 7400–7404. doi:10.1021/la061047m
149. Anandhakumar, S.; Mahalakshmi, V.; Raichur, A. M. *Mater. Sci. Eng., C* **2012,** *32,* 2349–2355. doi:10.1016/j.msec.2012.07.006
150. Kolesnikova, T. A.; Gorin, D. A.; Fernandes, P.; Kessel, S.; Khomutov, G. B.; Fery, A.; Shchukin, D. G.; Möhwald, H. *Adv. Funct. Mater.* **2010,** *20,* 1189–1195. doi:10.1002/adfm.200902233
151. Serpe, M. J.; Yarmey, K. A.; Nolan, C. M.; Lyon, L. A. *Biomacromolecules* **2005,** *6,* 408–413. doi:10.1021/bm049455x
152. Serizawa, T.; Matsukuma, D.; Nanameki, K.; Uemura, M.; Kurusu, F.; Akashi, M. *Macromolecules* **2004,** *37,* 6531–6536. doi:10.1021/ma049154f
153. Quinn, J. F.; Caruso, F. *Langmuir* **2004,** *20,* 20–22. doi:10.1021/la0360310
154. Glinel, K.; Sukhorukov, G. B.; Möhwald, H.; Khrenov, V.; Tauer, K. *Macromol. Chem. Phys.* **2003,** *204,* 1784–1790. doi:10.1002/macp.200350033
155. Mathivanan, N.; Paramasivam, G.; Vergaelen, M.; Rajendran, J.; Hoogenboom, R.; Sundaramurthy, A. *Langmuir* **2019,** *35,* 14712–14724. doi:10.1021/acs.langmuir.9b02938
156. Paramasivam, G.; Vergaelen, M.; Ganesh, M. R.; Hoogenboom, R.; Sundaramurthy, A. *J. Mater. Chem. B* **2017,** *5,* 8967–8974. doi:10.1039/c7tb02284k
157. Sundaramurthy, A.; Vergaelen, M.; Maji, S.; AuzélyVelty, R.; Zhang, Z.; De Geest, B. G.; Hoogenboom, R. *Adv. Healthcare Mater.* **2014,** *3,* 2040–2047. doi:10.1002/adhm.201400377
158. Prevot, M.; Déjugnat, C.; Möhwald, H.; Sukhorukov, G. B. *ChemPhysChem* **2006,** *7,* 2497–2502. doi:10.1002/cphc.200600167
159. Xu, W.; Ledin, P. A.; Plamper, F. A.; Synatschke, C. V.; Müller, A. H. E.; Tsukruk, V. V. *Macromolecules* **2014,** *47,* 7858–7868. doi:10.1021/ma501853c
160. Timin, A. S.; Gould, D. J.; Sukhorukov, G. B. *Expert Opin. Drug Delivery* **2017,** *14,* 583–587. doi:10.1080/17425247.2017.1285279
161. De Geest, B. G.; De Koker, S.; Sukhorukov, G. B.; Kreft, O.; Parak, W. J.; Skirtach, A. G.; Demeester, J.; De Smedt, S. C.; Hennink, W. E. *Soft Matter* **2009,** *5,* 282–291. doi:10.1039/b808262f
162. Gnanadhas, D. P.; Ben Thomas, M.; Elango, M.; Raichur, A. M.; Chakravortty, D. *J. Antimicrob. Chemother.* **2013,** *68,* 2576–2586. doi:10.1093/jac/dkt252
163. Chen, J.; Ratnayaka, S.; Alford, A.; Kozlovskaya, V.; Liu, F.; Xue, B.; Hoyt, K.; Kharlampieva, E. *ACS Nano* **2017,** *11,* 3135–3146. doi:10.1021/acsnano.7b00151
164. Ochs, C. J.; Such, G. K.; Yan, Y.; van Koeverden, M. P.; Caruso, F. *ACS Nano* **2010,** *4,* 1653–1663. doi:10.1021/nn9014278
165. Han, B.; Shen, B.; Wang, Z.; Shi, M.; Li, H.; Peng, C.; Zhao, Q.; Gao, C. *Polym. Adv. Technol.* **2008,** *19,* 36–46. doi:10.1002/pat.966
166. Wang, J.; Sun, X.; Mao, W.; Sun, W.; Tang, J.; Sui, M.; Shen, Y.; Gu, Z. *Adv. Mater. (Weinheim, Ger.)* **2013,** *25,* 3670–3676. doi:10.1002/adma.201300929
167. Huang, S.; Liu, J.; He, Q.; Chen, H.; Cui, J.; Xu, S.; Zhao, Y.; Chen, C.; Wang, L. *Nano Res.* **2015,** *8,* 4038–4047. doi:10.1007/s12274-015-0905-9
168. De Geest, B. G.; Van Camp, W.; Du Prez, F. E.; De Smedt, S. C.; Demeester, J.; Hennink, W. E. *Macromol. Rapid Commun.* **2008,** *29,* 1111–1118. doi:10.1002/marc.200800093
169. Sexton, A.; Whitney, P. G.; Chong, S.-F.; Zelikin, A. N.; Johnston, A. P. R.; De Rose, R.; Brooks, A. G.; Caruso, F.; Kent, S. J. *ACS Nano* **2009,** *3,* 3391–3400. doi:10.1021/nn900715g
170. De Cock, L. J.; Lenoir, J.; De Koker, S.; Vermeersch, V.; Skirtach, A. G.; Dubruel, P.; Adriaens, E.; Vervaet, C.; Remon, J. P.; De Geest, B. G. *Biomaterials* **2011,** *32,* 1967–1977. doi:10.1016/j.biomaterials.2010.11.012
171. Zyuzin, M. V.; Díez, P.; Goldsmith, M.; Carregal-Romero, S.; Teodosio, C.; Rejman, J.; Feliu, N.; Escudero, A.; Almendral, M. J.; Linne, U.; Peer, D.; Fuentes, M.; Parak, W. J. *Bioconjugate Chem.* **2017,** *28,* 556–564. doi:10.1021/acs.bioconjchem.6b00657
172. Ai, H. *Adv. Drug Delivery Rev.* **2011,** *63,* 772–788. doi:10.1016/j.addr.2011.03.013
173. Chen, H.; Sulejmanovic, D.; Moore, T.; Colvin, D. C.; Qi, B.; Mefford, O. T.; Gore, J. C.; Alexis, F.; Hwu, S.-J.; Anker, J. N. *Chem. Mater.* **2014,** *26,* 2105–2112. doi:10.1021/cm404168a
174. Shi, X.; Wang, S. H.; Swanson, S. D.; Ge, S.; Cao, Z.; Van Antwerp, M. E.; Landmark, K. J.; Baker, J. R., Jr. *Adv. Mater. (Weinheim, Ger.)* **2008,** *20,* 1671–1678. doi:10.1002/adma.200702770
175. Yang, P.; Li, D.; Jin, S.; Ding, J.; Guo, J.; Shi, W.; Wang, C. *Biomaterials* **2014,** *35,* 2079–2088. doi:10.1016/j.biomaterials.2013.11.057
176. Yashchenok, A. M.; Jose, J.; Trochet, P.; Sukhorukov, G. B.; Gorin, D. A. *J. Biophotonics* **2016,** *9,* 792–799. doi:10.1002/jbio.201500293
177. Kozlova, A. A.; German, S. V.; Novoselova, M. V.; Demina, P. A.; Atkin, V. S.; Zuev, V. V.; Gorin, D. A. *J. Phys.: Conf. Ser.* **2018,** *1092,* 012067. doi:10.1088/1742-6596/1092/1/012067
178. Luo, D.; Poston, R. N.; Gould, D. J.; Sukhorukov, G. B. *Mater. Sci. Eng., C* **2019,** *94,* 647–655. doi:10.1016/j.msec.2018.10.031

179. Kreft, O.; Javier, A. M.; Sukhorukov, G. B.; Parak, W. J. *J. Mater. Chem.* **2007,** *17,* 4471–4476. doi:10.1039/b705419j
180. del Mercato, L. L.; Abbasi, A. Z.; Parak, W. J. *Small* **2011,** *7,* 351–363. doi:10.1002/smll.201001144
181. del Mercato, L. L.; Abbasi, A. Z.; Ochs, M.; Parak, W. J. *ACS Nano* **2011,** *5,* 9668–9674. doi:10.1021/nn203344w
182. RiveraGil, P.; Nazarenus, M.; Ashraf, S.; Parak, W. J. *Small* **2012,** *8,* 943–948. doi:10.1002/smll.201101780
183. Chinnayelka, S.; McShane, M. J. *Anal. Chem. (Washington, DC, U. S.)* **2005,** *77,* 5501–5511. doi:10.1021/ac050755u
184. Srivastava, R.; Jayant, R. D.; Chaudhary, A.; McShane, M. J. *J. Diabetes Sci. Technol.* **2011,** *5,* 76–85. doi:10.1177/193229681100500111
185. Kazakova, L. I.; Shabarchina, L. I.; Anastasova, S.; Pavlov, A. M.; Vadgama, P.; Skirtach, A. G.; Sukhorukov, G. B. *Anal. Bioanal. Chem.* **2013,** *405,* 1559–1568. doi:10.1007/s00216-012-6381-0
186. Palivan, C. G.; Goers, R.; Najer, A.; Zhang, X.; Car, A.; Meier, W. *Chem. Soc. Rev.* **2016,** *45,* 377–411. doi:10.1039/c5cs00569h
187. Larrañaga, A.; Lomora, M.; Sarasua, J.-R.; Palivan, C. G.; Pandit, A. *Prog. Mater. Sci.* **2017,** *90,* 325–357. doi:10.1016/j.pmatsci.2017.08.002
188. Larrañaga, A.; Isa, I. L. M.; Patil, V.; Thamboo, S.; Lomora, M.; Fernández-Yague, M. A.; Sarasua, J.-R.; Palivan, C. G.; Pandit, A. *Acta Biomater.* **2018,** *67,* 21–31. doi:10.1016/j.actbio.2017.12.014
189. Alford, A.; Kozlovskaya, V.; Xue, B.; Gupta, N.; Higgins, W.; Pham-Hua, D.; He, L.; Urban, V. S.; Tse, H. M.; Kharlampieva, E. *Chem. Mater.* **2018,** *30,* 344–357. doi:10.1021/acs.chemmater.7b03502
190. Sharma, V.; Sundaramurthy, A. *ACS Omega* **2019,** *4,* 628–636. doi:10.1021/acsomega.8b02820
191. Veerabadran, N. G.; Goli, P. L.; StewartClark, S. S.; Lvov, Y. M.; Mills, D. K. *Macromol. Biosci.* **2007,** *7,* 877–882. doi:10.1002/mabi.200700061
192. Städler, B.; Price, A. D.; Chandrawati, R.; Hosta-Rigau, L.; Zelikin, A. N.; Caruso, F. *Nanoscale* **2009,** *1,* 68–73. doi:10.1039/b9nr00143c
193. Kerdjoudj, H.; Berthelemy, N.; Boulmedais, F.; Stoltz, J.-F.; Menu, P.; Voegel, J. C. *Soft Matter* **2010,** *6,* 3722–3734. doi:10.1039/b920729e
194. Zhang, X.; Oulad-Abdelghani, M.; Zelkin, A. N.; Wang, Y.; Haîkel, Y.; Mainard, D.; Voegel, J.-C.; Caruso, F.; Benkirane-Jessel, N. *Biomaterials* **2010,** *31,* 1699–1706. doi:10.1016/j.biomaterials.2009.11.032
195. Becker, A. L.; Orlotti, N. I.; Folini, M.; Cavalieri, F.; Zelikin, A. N.; Johnston, A. P. R.; Zaffaroni, N.; Caruso, F. *ACS Nano* **2011,** *5,* 1335–1344. doi:10.1021/nn103044z
196. Timin, A. S.; Muslimov, A. R.; Lepik, K. V.; Epifanovskaya, O. S.; Shakirova, A. I.; Mock, U.; Riecken, K.; Okilova, M. V.; Sergeev, V. S.; Afanasyev, B. V.; Fehse, B.; Sukhorukov, G. B. *Nanomedicine (N. Y., NY, U. S.)* **2018,** *14,* 97–108. doi:10.1016/j.nano.2017.09.001

License and Terms

The definitive version of this article is the electronic one which can be found at:
doi:10.3762/bjnano.11.41

BEILSTEIN JOURNAL OF NANOTECHNOLOGY

Luminescent gold nanoclusters for bioimaging applications

Nonappa[1,2]

Review

Open Access

Address:
[1]Department of Applied Physics, Aalto University School of Science, Puumiehenkuja 2, FI-02150, Espoo, Finland, and [2]Bioproducts and Biosystems, Aalto University School of Chemical Engineering, Kemistintie 1, FI-02150, Espoo, Finland

Email:
Nonappa - nonappa@aalto.fi

Keywords:
bioimaging; biosensing; gold nanoclusters; immunoassay; luminescence; self-assembly; theranostics

Beilstein J. Nanotechnol. **2020,** *11,* 533–546.
doi:10.3762/bjnano.11.42

Received: 08 January 2020
Accepted: 18 March 2020
Published: 30 March 2020

This article is part of the thematic issue "Engineered nanomedicines for advanced therapies".

Guest Editor: F. Baldelli Bombelli

Abstract

Luminescent nanomaterials have emerged as attractive candidates for sensing, catalysis and bioimaging applications in recent years. For practical use in bioimaging, nanomaterials with high photoluminescence, quantum yield, photostability and large Stokes shifts are needed. While offering high photoluminescence and quantum yield, semiconductor quantum dots suffer from toxicity and are susceptible to oxidation. In this context, atomically precise gold nanoclusters protected by thiol monolayers have emerged as a new class of luminescent nanomaterials. Low toxicity, bioavailability, photostability as well as tunable size, composition, and opto-electronic properties make them suitable for bioimaging and biosensing applications. In this review, an overview of the sensing of pathogens, and of in vitro and in vivo bioimaging using luminescent gold nanoclusters along with the limitations with selected examples are discussed.

Introduction

Imaging methods play a central role in understanding the structural and functional biological processes of biomolecules, cells, tissues, organs, and even entire living organisms [1,2]. The importance of bioimaging in preclinical, clinical evaluation and patient treatment has encouraged extensive investigation to develop new imaging methods [3,4]. Among several imaging techniques, fluorescence microscopy has evolved as a widely used non-invasive method to visualize real-time biological processes with high spatial resolution [5,6]. The image quality of biological structures under fluorescence microscopy also depends on the performance of the fluorophores. Furthermore, bioimaging of cells and tissues faces additional challenges due to background autofluorescence generated from the intrinsic emission of biomolecules [7]. Antibodies conjugated to low molecular weight fluorescent dyes have been used for various bioimaging applications [8]. Despite their cost-effectiveness, and water solubility, organic dyes display a small Stokes shift, low photochemical stability and they undergo photobleaching [9,10]. Luminescence can also be achieved via intramolecular energy transfer between an organic ligand and lanthanide metal

ions through chelation [11]. Large Stokes shift, high quantum yield and long fluorescence lifetime make lanthanide complexes excellent candidates in imaging applications [12,13]. The lanthanide complexes primarily rely on chelation of metal ions with carboxylic groups, therefore the diversity of ligand design is limited. The discovery of green fluorescent protein (GFP) led to remarkable progress in bioimaging including protein quantification, tracking, sensing as well as imaging various biochemical processes [14-17]. The large molecular mass of GFP might affect the folding process of tagged proteins, or a possible aggregation may lead to cytotoxicity. Beyond molecular and biomolecular luminescent materials, colloidal luminescent nanomaterials have gained attention in recent years [18,19]. Luminescent nanomaterials including semiconductor quantum dots, carbon dots, metal-doped nanoparticles, noble-metal nanoparticles, and organic–inorganic hybrid nanoparticles, have been studied for their ultrabright photoluminescence (PL) [20-23]. Semiconductor quantum dots (SCQDs) such as CdSe, CdTe, CdS, ZnS, ZnSe, PbS and PbSe have widely been studied as luminescent nanomaterials [24,25]. This is attributed to the possibilities to tune their size, surface functionalities, quantum confinement and high quantum yield (60–90%) [26,27]. Importantly, SCQDs display a broad spectrum of colors covering ultraviolet to near-infrared (NIR). Furthermore, SCQDs offer better sensitivity, stability against photobleaching, and a narrow spectral bandwidth compared to conventional organic dyes. However, due to their cytotoxicity, the tendency to undergo aggregation inside the cells, and easy oxidation, the extensive use in bioimaging remained a challenge. Therefore, efforts have been made to prepare silicon quantum dots (SQDs) [28]. SQDs exhibit relatively low cytotoxicity and better biocompatibility compared to SCQDs. Moreover, SQDs show broad absorption spectra, higher photostability, and the PL can be tuned from the visible to the NIR region [29]. Similar to SCQDs, SQDs undergo oxidation at room temperature and have limited water solubility.

Recently, gold nanoparticles (AuNPs) with tunable size and shape-specific physicochemical properties have emerged as attractive luminescent nanomaterials [30]. Despite the early discovery of the luminescence phenomenon in bulk gold and gold films, the PL of gold remained unexplored for several decades [31,32]. This is attributed to the low quantum yield (10^{-10}), which limited the practical application and the understanding of the luminescence phenomenon in detail. The realization by Wilcoxon et al. that AuNPs with sizes of less than 5 nm show luminescence has provided the foundation for extensive investigation on various nanostructures [33]. Since the 1990s, several groups have reported AuNPs, including gold nanorods showing luminescence that is million-fold higher than that of the bulk metal [34-37].

The ability to control the properties by tuning the particle shape and surface functionalities further advanced the applications of AuNPs in a wide range of research fields. However, fundamental challenges remained related to their aggregation tendencies, polydispersity and difficulties in controlling the directionalities. In this context, atomically precise gold nanoclusters (AuNCs) opened a new opportunity for the field of colloidal science [38-40]. Atomically precise NCs with a core diameter below 3 nm contain an exact number of metal atoms and surface ligands (Figure 1A,B). Therefore, NCs are considered as colloidal molecules. Similar to plasmonic nanoparticles, the stability of NCs can be controlled by ligand passivation using small molecules, synthetic polymers or biomacromolecules. A significant difference between plasmonic AuNPs and AuNCs can be stated regarding the sensitivity. For observable changes to occur in physicochemical properties of plasmonic NPs, at least a layer of atoms needs to be removed (ca. 0.5 nm), whereas NCs already display remarkable changes after addition or removal of a single atom. Additionally, due to covalently bound ligands, the NCs show extraordinary stability under ambient conditions. While plasmonic AuNPs display size-dependent surface plasmon resonance (SPR), NCs display characteristic molecule-like electronic spectra. This is attributed to the small size and quantum confinement, and the evolution of continuous or quasicontinuous bands (of bulk gold) into discrete electronic states [40]. Another attractive property of AuNCs is photoluminescence (PL), a phenomenon that is much less understood than the surface plasmon resonance of plasmonic gold nanoparticles.

Review

Luminescent gold nanoclusters

Luminescent AuNCs show high photostability and biocompatibility and are nontoxic [41]. Their size is highly precise and small compared to QDs, offering a better internalization in cells and tissues [42-47]. The presence of surface ligands allows for a selective modification and biomolecular tagging. Therefore, AuNCs find potential applications in sensing, photodynamic therapy, labeling and bioimaging. However, there are challenges because the number of luminescent gold NCs is limited and the PL quantum yield is low compared to organic dyes, lanthanide complexes and SCQD-based nanomaterials. To improve the quantum yield and PL, various approaches have been developed including ligand engineering, selective doping to create alloy clusters, aggregation-induced emission, selective etching and self-assembly [48-58].

Ligands play an important role in the luminesce properties of NCs [48,55]. For example, a phenylethane thiol (PET)-capped organically soluble Au_{25} nanocluster ($Au_{25}PET_{18}$) showed similar behavior as Au_{25}NCs capped with long-chain alkanes [59]. However, it was shown that by choosing the appropriate sur-

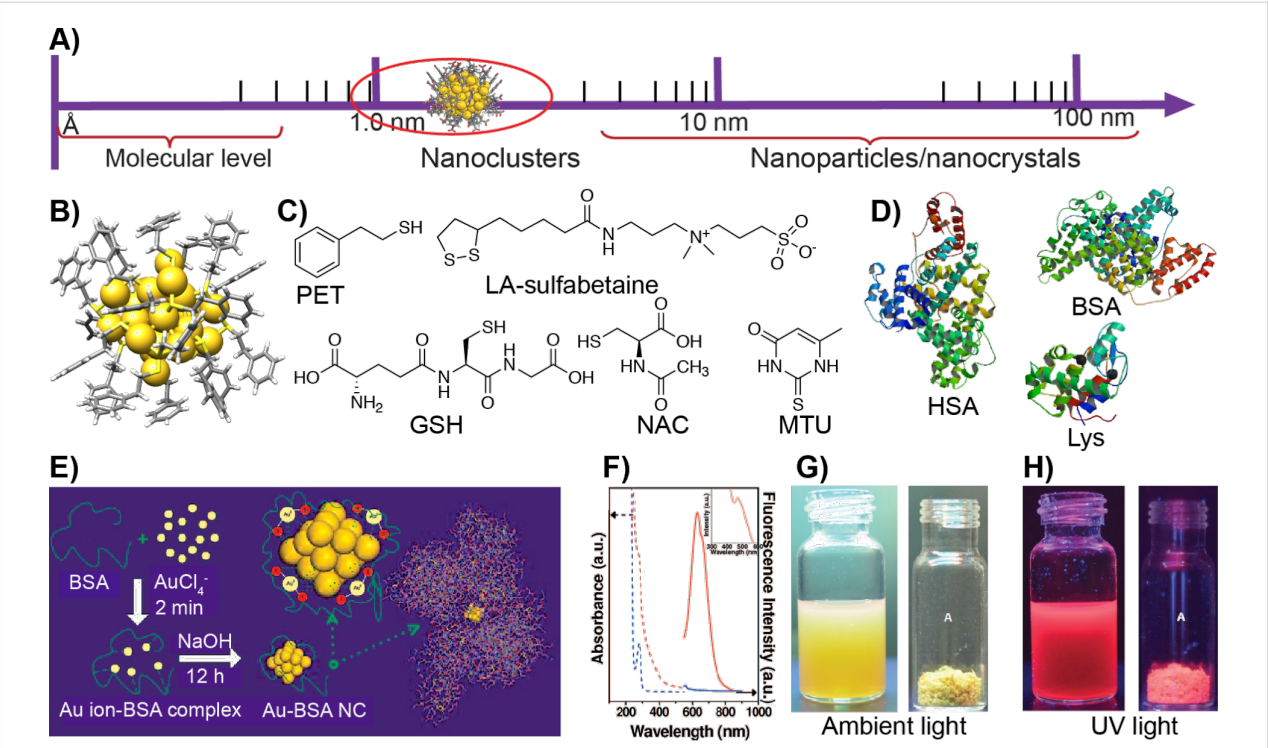

Figure 1: Structure, synthesis and properties of gold nanoclusters. A) Nanoclusters provide a link between molecular complexes and plasmonic nanoparticles. B) X-ray structure of [$Au_{25}(PET)_{18}$], from CSD entry JACVOB. C) Chemical structure of some of the organic thiols discussed in this review (PET: phenylethane thiol; LA: lipoic acid; GSH: glutathione; NAC: *N*-acetylcysteine; MTU: 5-methyl-2-thiouracil). D) Structures of biomolecular ligands (HSA: human serum albumin, PDB ID IE78; BSA: bovine serum albumin, PDB ID 3VO3, and Lys: lysozyme, PDB ID 3WUN). E) Schematic representation showing Au-BSA NC synthesis. F) Absorbance and fluorescence spectra of Au-BSA NCs. G, H) Photographs of Au-BSA NCs in solution and in the solid state under ambient light and UV light, respectively. Figure panel 1E is adapted and panel 1F is reused with permission from [63], copyright 2009 American Chemical Society. Figure panels 1G,H are adapted with permission from [64], copyright 2016 American Chemical Society.

face ligands and introducing a proper steric nature, the metal-to-ligand charge transfer can be tuned [60]. As a consequence, the PL of Au_{25} NCs has been enhanced. The electron-donor ability of ligands and the direct donation of the delocalized electron from electron-rich atoms of the ligands to the metallic kernel affect the PL of the NCs [61]. For example, for Au_{25} NCs, the PL intensity increased with increasing the charge-donor capacity of the ligands in the order of $HSC_2H_4Ph > HSC_{12}H_{25} > HSC_6H_{13}$. Furthermore, it was demonstrated that the PL was enhanced by 6.5 times for 2-naphthalen-2-yl ethanethiolate-capped Au_{25} NCs compared to that of PET-capped Au_{25} NCs [43]. Water-soluble glutathione-capped [$Au_{25}(SG)_{18}$] NCs have been shown to display higher PL than the [$Au_{25}(PET)_{18}$] counterpart. Partial ligand exchange can also lead to enhanced PL in certain AuNCs. Shibu et al. partially exchanged the glutathione ligands in $Au_{25}(SG)_{18}$ NCs with three different ligands [62]. It has been shown that in the case of 3-mercapto-2-butanol (MB)-substituted products [$Au_{25}(MB)_x(SG)_{18-x}$] the PL spectra exhibit a blueshift in excitation and emission compared the initial [$Au_{25}(SG)_{18}$] nanocluster. However, no significant changes were observed in *N*-acetylglutathione (NAGSH) and *N*-formylglutathione (NFGSH) ligands. Xie and co-workers reported the synthesis of a bovine serum albumin (BSA)-protected water-soluble Au_{25} nanocluster (Au-BSA) having a red emission at ca. 640 nm with a PL quantum yield of 6% (Figure 1E,F) [63]. More importantly, the Au-BSA NCs are stable under ambient conditions and retain their PL even after drying (Figure 1G,H) allowing for long-term storage [64]. Several other proteins including lysozyme, human serum albumin (HSA) and insulin have been used to prepare inherently luminescent AuNCs [65-70]. Aggregation-induced emission (AIE) is another approach where non-emissive or weakly luminescent molecules or particles emit intensely upon aggregation, boosting quantum yields by two orders of magnitude. A majority of the chromophores show high luminescence in their dilute solutions. However, in the solid state, due to aggregation-caused quenching, they turn less emissive. Luo et al. in 2001 have shown that when water was added to a solution of 1-methyl-1,2,3,4,5-pentaphenylsilole in ethanol, it turned intensely emissive [71]. The quantum yield of silole increased by 333 times in a water/ethanol (90/10 v/v) mixture compared to that of in pure ethanol solution. In solution, the dynamic intramolecular rotation serves as a route for nonradiative relaxation process. Upon aggregation, the intramolecular rotations are restricted, which blocks the non-

radiative pathways and opens the radiative decay channel resulting in highly emissive aggregates [72]. The AIE phenomenon has been observed in several organic compounds of low molecular weight and in polymers [73]. The aggregation-induced luminescence of NCs has been achieved either using solvent-induced aggregation or addition of additives such as ionic polymers, proteins or peptides [74-76]. Recently, Dichiarante et al. reported NIR-luminescent AuNCs bearing superfluorinated (SF) ligands with strong emission at 1050 nm with a quantum yield of 12% [77]. An extensive account of the PL of NCs is beyond the scope of this review and has been previously summarized in several reports [54,78-82]. This review discusses an overview of the application of gold NCs in biosensing and bioimaging. Importantly, the sensing of pathogenic bacteria and viruses, in vitro imaging of cell lines and in vivo bioimaging using animal models are presented. In each section representative early examples along with the recent examples are discussed.

Biosensing and imaging of pathogens

Chan et al. reported human serum albumin (HSA)-stabilized gold NCs (Au-HSA) for sensing *Staphylococcus aureus* (SA) and methicillin-resistant *Staphylococcus aureus* (MRSA) bacterial strains [83]. The resulting Au-HSA NCs showed reddish PL. The ability of HSA to bind and chelate various ions as well as small molecules was exploited to design a NC-based assay. The directly synthesized Au-HAS NCs showed binding affinities for SA and MRSA strains (Figure 2). A systematic study used several other pathogenic bacteria, including *Streptococcus pyogenes*, vancomycin-resistant *Enterococcus faecalis* (VRE), *E. Coli* J96, *Pseudomonas aeruginosa*, pandrug-resistant *Acinetobacter baumannii* and *Enterobacter cloacae* in phosphate-buffered saline (PBS) at pH 6 (Figure 2A). Importantly, a reddish precipitate was formed when the Au-HSA NCs interacted with SA and MRSA. Whereas for all other pathogens a pale blue precipitate was obtained at the bottom of the Eppendorf tubes after slow centrifugation. The detection limit using Au-HSA NCs was 4.2×10^8 cells/mL, which is two orders of magnitude lower than that without sensing probes in the bacterial samples. Further, Au-HSA NCs can interact with a target analyte in complex biological samples as demonstrated using urine samples containing SA strains. However, this sensing approach was not able to distinguish SA and MRSA. Therefore, sensing combined with MALDI–MS was utilized to distinguish SA and MRSA based on MALDI–MS fingerprinting. Finally, using the principal component analysis (PCA) method two different strains were qualitatively distinguished.

The possible explanation of a selective binding purely based on electrostatic interaction was ruled out. Instead, the authors assumed that it might be a specific peptide motif of HSA that interacts with the bacterial cell wall. The trypsin digestion of Au-HSA NCs was studied and various fragments were identified using MALDI–MS. To confirm further whether the peptides can interact with *S. aureus*, DVFLGRGGGC (Pep10) and RHPDYSVVLLLRGGGC (Pep16), containing the sequences no. 348 to 352 and no. 361 to 372, were synthesized and used for the synthesis of Au-Pep10 and Au-pep16 NCs. Interestingly, both Au-pep10 and Au-pep16 NCs yielded similar results suggesting that these peptides are responsible for binding. However, there was no significant binding with only one of the peptides or only HSA. Similarly, sufficient binding was not observed when a control experiment was performed with Au-BSA NCs. The above experiments suggest that in Au-HSA NCs, HSA might adopt a conformation that assists better binding.

Zhu et al. reported a rigid host–guest assembly to improve the PL of AuNCs, their antibacterial activity and bioimaging [84]. In their work, 5-methyl-2-thiouracil (MTU)-capped AuNCs (Au-MTU) were prepared. The Au-MTU NCs were then treated with protamine (Prot), a cationic peptide capable of penetrating bacterial biofilms with abundant arginine residue. The hydrogen bonding between the MTU ligands on the surface of Au-MTU NCs and the arginine residues in protamine form a supramolecular host–guest complex, i.e., Au-MTU/Prot. The supramolecular host–guest interactions rigidify the surface resulting in a 28-fold increase in the PL of Au-MTU/Prot NCs compared to that of Au-MTU NCs. The resulting Au-MTU/Prot NCs displayed antibacterial properties with abilities to kill both Gram-positive and Gram-negative bacteria, which was shown using *E. coli* and SA strains. The addition of protamine also lowered the minimum inhibitory concentration by two orders of magnitude. This is attributed to the enhanced catalytic activity upon binding with protamine, which resulted in altered oxidative stress and a higher generation of reactive oxygen species (ROS).

Kurdekar et al. developed a fluorescent gold nanocluster immunoassay (AuNCIA) for early and sensitive detection of human immune deficiency virus (HIV) infection in vitro and HIV-infected patient samples [85]. For this study, glutathione-capped AuNCs were coupled with streptavidin (Au-SA) using EDS/NHS coupling. The strong noncovalent interaction between streptavidin and biotin was exploited. To achieve the immunoassay, an antibody–antigen–antibody sandwich approach was utilized (Figure 3). The substrates were first coated with capture antibodies that will interact strongly with HIV-1 p24 antigen, a target viral protein expressed in abundance in the early stages of HIV infection. Then, a biotinylated detection antibody was added, which resulted in a sandwich complex leaving the biotin accessible for streptavidin binding. Finally,

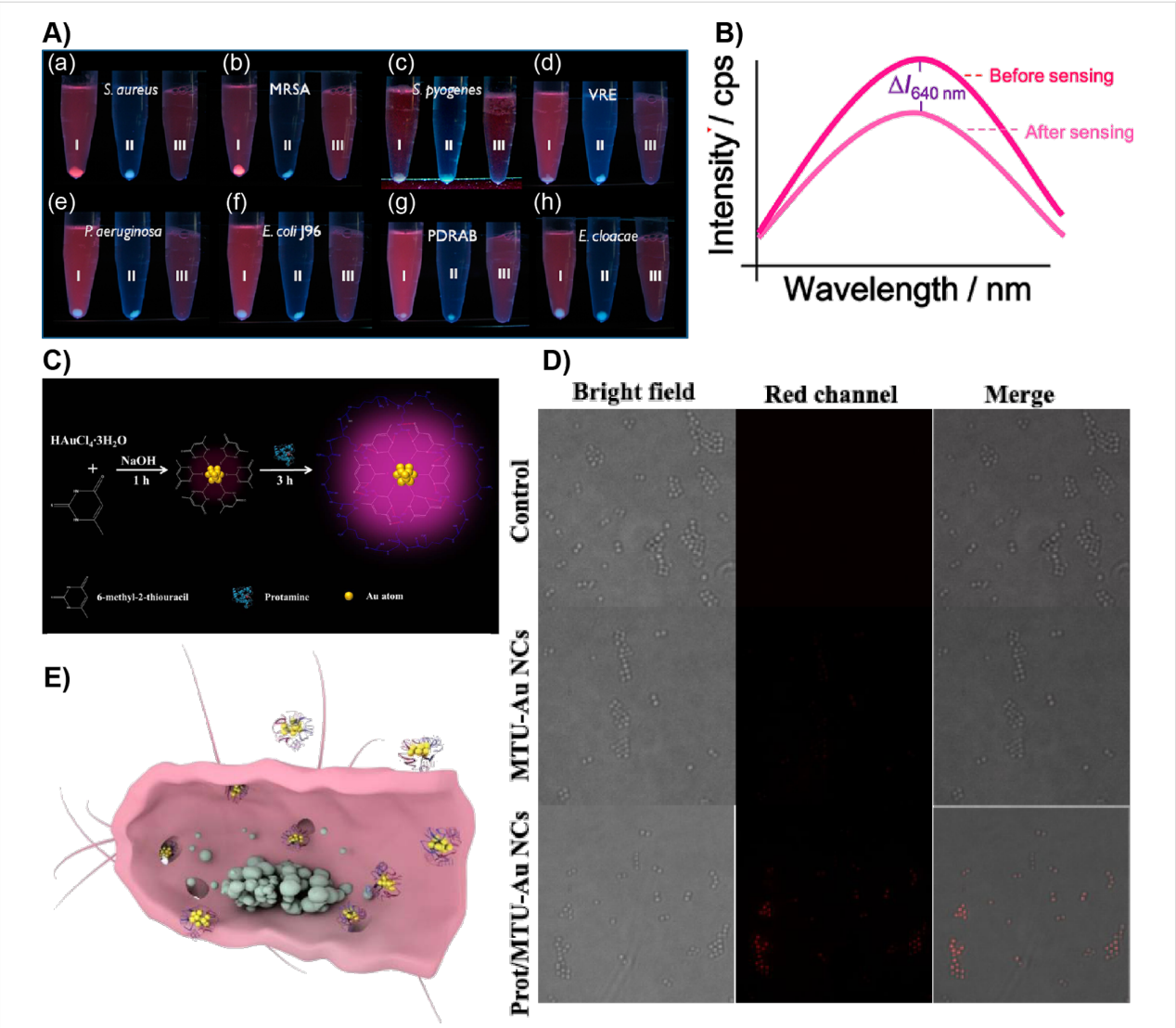

Figure 2: AuNC-based pathogen sensing and imaging. A) (a–h) Photographs showing the sensing of various pathogenic bacterial strains after incubating them with 0.12 mg/mL of Au-HSA NCs followed by centrifugation at 3500 rpm (tubes labeled as "I") in PBS buffer at pH 6.0. Tubes labeled as "II" in each panel contained only bacteria. Tubes labeled as "III" in each panel show the solution containing only Au-HSA NCs. B) Fluorescence spectra showing a change in the fluorescence intensity at 640 nm of Au-HSA NCs after bacterial sensing. C) Schematic representation of Au-MTU/Prot NC synthesis. D) Microscopy images of *S. aureus* after treatment with Au-MTU/Prot NCs, Au-MTU/Prot NCs, and control. The red channel was excited at 405 nm. The images were 40 µm × 40 µm. E) A cross-sectional schematic view of a bacterium treated with Au-MTU/Prot. Figure panel 2A is adapted and panel 2B is reused with permission from [83], copyright 2012 American Chemical Society. Figure panels 2C–E are reused with permission from [84], copyright 2019 Americal Chemical Society.

the interaction between the biotin in the detector antibody and the streptavidin in Au-SA NCs allowed for rapid detection. It was shown that AuNCIA has an analytical sensitivity at the picogram level and the sensitivity is equivalent or even better than that of other colorimetric assays such as enzyme-linked immunosorbent assay (ELISA). The AuNCIA is specific for HIV, which was shown by spiking Hepatitis C viruses with HIV-1 p24 antigen. The clinical validation using samples from HIV-positive tested patients also demonstrated the efficacy of AuNCIA detection and no false negatives were observed. This suggests that AuNCs with appropriate labeling and surface functionalization offer new avenues for rapid detection and the development of new immunoassays.

Imaging and labeling mammalian cell lines

Beyond their antibacterial effect and pathogen sensing, the surface functionalities of NCs allow for selective labeling for the detection of biomolecules, intracellular metal ion sensing, live-cell imaging as well as cellular apoptosis studies. Lin et al. reported 11-mercaptoundecanoic acid (MUDA)-capped AuNCs (Au-MUDA) as luminescent probes for nuclear targeting and intracellular imaging [86]. The Au-MUDA NCs were conju-

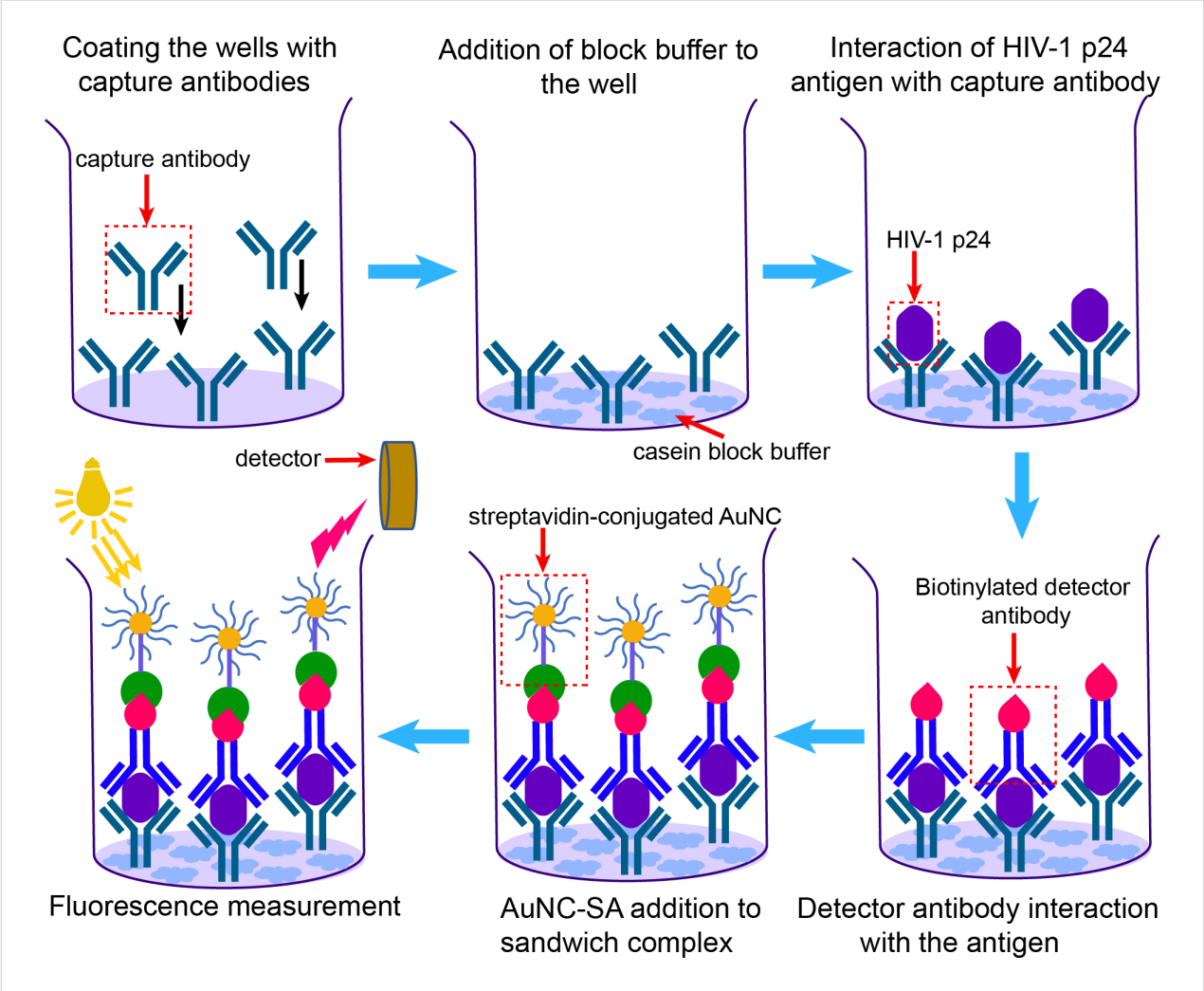

Figure 3: Schematic representation of AuNCIA in the detection of HIV-1 p24 antigen inspired by [85].

gated with SV40 (PKKKRKV), a specific peptide for nuclear-localization signal (NLS). The Au-MUDA-NLS NCs were easily internalized and distributed in the nucleus when studied using HeLa cell lines (Figure 4A). The intracellular and nuclear distribution was studied using a membrane dye WGA-Alexa 594 and a nuclear dye, SYTO59. This suggested that Au-MUDA-NLS NCs were well distributed in the cytoplasm as well as in the nucleus. Muhammed et al. reported brightly NIR-emitting Au_{23} and Au_{25} NCs using single-phase and biphasic etching of $[Au_{25}(SG)_{18}]$ (Figure 4B) [87]. The Au_{23} clusters were selectively conjugated with streptavidin for a specific labeling of cells. Here the strong binding of streptavidin with biotin was exploited for imaging human hepatoma cells (HepG2, Figure 4C). HepG2 are cancerous cells that contain excess biotin.

Retnakumari et al. studied the surface functionalization of Au-BSA NCs with folic acid (FA) for selective binding, internalization and imaging of folate receptor-positive (FR^+) oral squamous cell carcinoma (KB) and breast cancer adenocarcinoma MCF-7 cell lines [88]. Since then, there have been numerous other reports that have shown various surface modifications to image a wide variety of cell lines.

Pan et al. reported composite core–shell nanoparticle–nanocluster agglomerates as luminescent nanocarriers for imaging and combination therapy [89,90]. Core–shell nanoparticles consisting of oleic acid-capped superparamagnetic iron oxide nanoparticles (IONPs, $d = 6.7 \pm 1.2$ nm) were used (Figure 5A). The IONPs were subsequently coated with a gold shell using the citrate reduction of Au(III) salts resulting in core–shell (IO@Au) nanoparticles of 9.3 ± 2.6 nm. The core–shell particles underwent lysozyme-mediated aggregation (IO@Au-Lys). The aggregated structures were further treated with Au-BSA NCs (IO@Au-Lys-Au-BSA) to form a composite structure. The combination allowed for plasmonic and magnetic resonance,

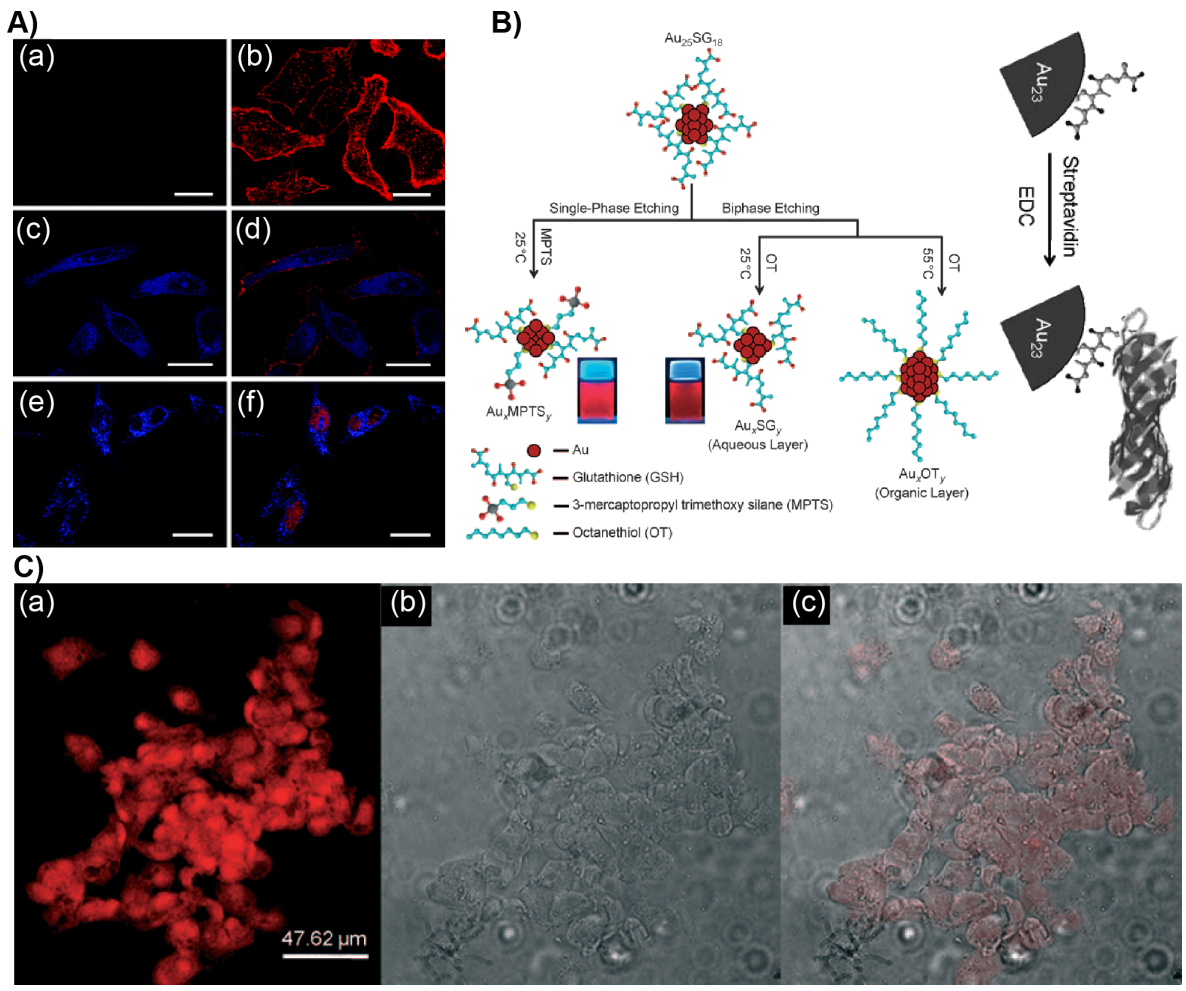

Figure 4: Cellular labeling and imaging using AuNCs. A) HeLa cells were treated with (a, b) Au-MUDA NCs and (e, f) Au-MUDA-NLS NCs for 1.5 h. The left panel shows the one-color image. The right panel shows the two-color colocalization image of HeLa cells incubated with Au-MUDA-NLS NCs and counterstained with membrane dye WGA–Alexa 594 and nuclear dye SYTO 59; scale bar: 25 µm. B) Schematics showing the etching method to prepare luminescent AuNCs and their conjugation with streptavidin. C) (a) Fluorescence, (b) bright-field, (c) and overlay of fluorescent and bright-field images of human hepatoma (HepG2) cells stained with streptavidin-conjugated Au_{23} NCs. Figure panel 4A is adapted with permission from [86], copyright 2008 The Royal Society of Chemistry. Figure panel 4B is reused and panel 4C is adapted with permission [87], copyright 2009 Wiley-VCH Verlag GmbH & Co. KGaA, Weinheim.

and luminescence in a single composite system for plasmonic photothermal therapy (PPTT). The bioimaging capability of the plasmonic magneto-luminescent multifunctional nanocarrier (PML-MF) systems were studied in vitro using three types of cancer cells, namely, HeLa, HepG2 and A375, as well as a normal HEK cell line (Figure 5B). Confocal imaging confirmed the internalization of the nanocarriers. After incubating the cell lines with sodium azide, there was a decrease by 82% of uptake of the nanocarriers, suggesting that the internalization is through endocytosis. The superparamagnetic nature of the PML-MF allowed for the magnetic targeting of the nanocarriers. Further, the ability of BSA to encapsulate drug molecules was explored to load doxorubicin (DPML-MF) in the nanocarriers.

The release kinetics of doxorubicin studied at pH 7.4 and 4.4 were found to be identical with a fast release up to 6 h and a slow release up to 20 h in PBS buffer, possibly due to diffusion-driven drug release. DPML-MF remained stable in human blood serum up to 24 h. DPML-MF showed a significant effect on HeLa, HepG2 and A375 cell lines with IC_{50} values 200-fold higher compared to that of free doxorubicin, presumably due to slow release from the nanocarriers. Alternatively, a significant killing efficiency of HeLa cells was achieved using just 0.46 µg/mL of free doxorubicin in combination with 200 µg/mL of PML-MF and laser irradiation for 10 min, further showing the potential for photothermal therapy. While PML-MF alone was not toxic to healthy HEK cell lines, the treatment with DPML-MF showed a similar antiproliferative effect on healthy

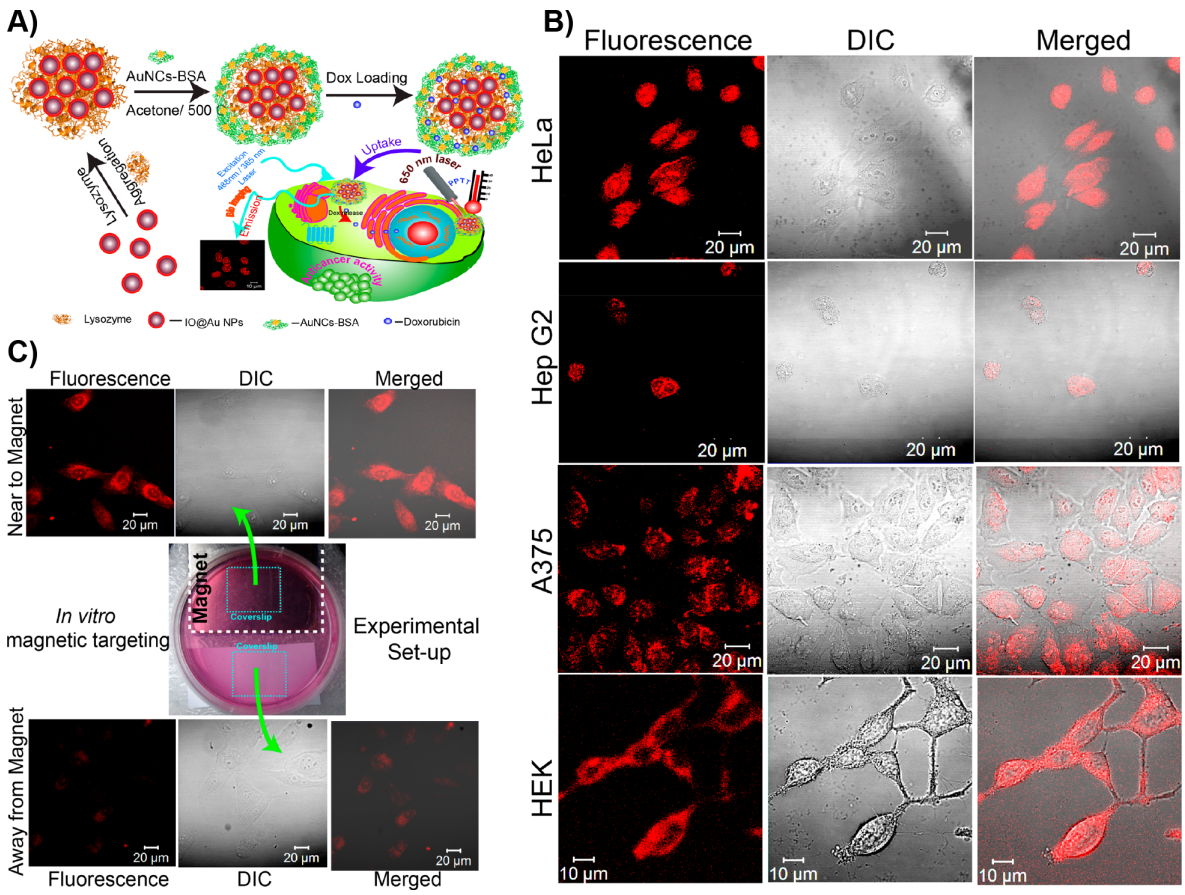

Figure 5: Plasmonic magnetoluminescent agglomerates. A) Schematic representation of the fabrication of the PML-MF nanocarriers and their application in photothermal therapy. B) CLSM images of HeLa, HepG2, A375, and HEK cells treated with the PML-MF nanocarrier for 2 h; images were recorded with a 488 nm excitation laser. C) In vitro magnetic targeting of HeLa cells treated with the PML-MF nanocarriers. Figure panels 5A–C are reused with permission from [90], copyright 2019 Americal Chemical Society.

cell lines as that of cancerous cells. Therefore, the selective killing of cancer cells was not achieved. The superparamagnetic property of the nanocarriers also allowed for magnetic targeting (Figure 5C). In another recent study, Pan et al. using glutathione-capped AuNCs showed that the aggregation-induced emission could be sensitive to the viscosity of the medium and that can potentially be used for intracellular viscosity imaging [91].

Recently Duan et al. reported the synthesis of NIR-luminescent AuNCs capped with *N*-acetyl-L-cysteine (NAC-CS) for long-time imaging [92]. The Au-NAC-CS NCs were insensitive to hydrogen peroxide and trypsin in contrast to Au NCs coated with BSA or other proteins, allowing for extended imaging times in HeLa cells (Figure 6A). When incubated with HeLa cell lines up to 4 h, strong fluorescence was observed. Unlike Au-BSA NCs, even after 8 h, weak fluorescence was still observed. Biodistribution studies of Au-NAC-CS NCs in different organs of mice, including heart, liver, spleen, lung and kidney, were analyzed (Figure 6B). A strong fluorescence signal appeared in the liver and kidney of normal mice after 6 h of NC injection. An apparent decrease in fluorescence after more than 6 h suggested the efficient clearance of NCs and there is no accumulation leading to cytotoxicity.

A proper functionalization of AuNCs also offers opportunities to develop NC-based radiosensitizers for cancer radiotherapy. Jia et al. reported atomically precise Au_8 NCs capped with levonorgestrel $[Au_8(C_{21}H_{27}O_2)_8]$ NCs with yellow-green luminescence and a quantum yield of 58.7% as a radiosensitizer for enhanced cancer therapy [93]. The toxicity studies using human oesophageal squamous cancer cells (EC1) showed that when $[Au_8(C_{21}H_{27}O_2)_8]$ was used at a concentration near its IC_{10} value, the luminescence of the incubated samples increased from 0 to 8 h. The luminescence, however, disappeared after 24 h indicating endocytosis of NCs. The generation of ROS

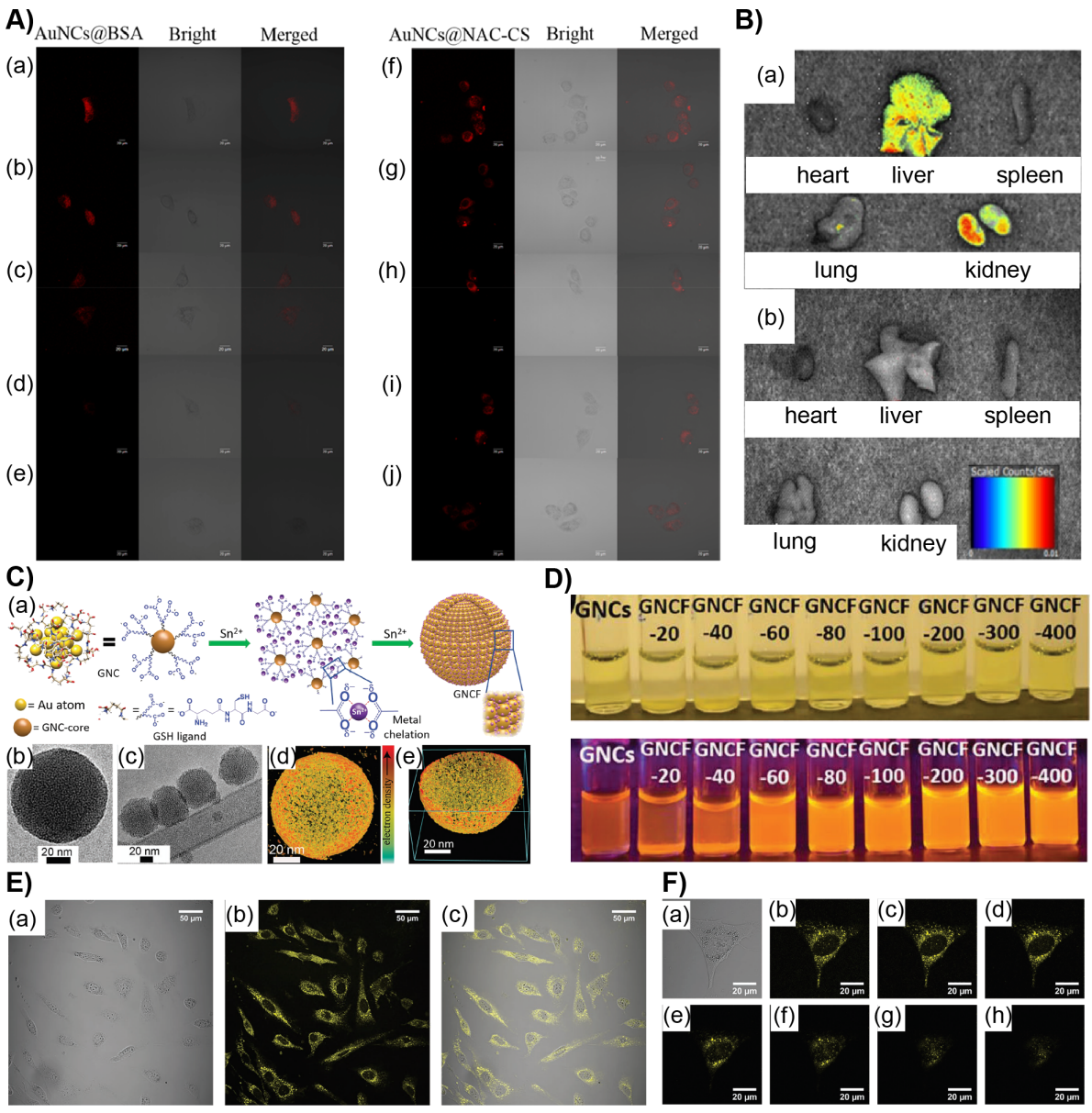

Figure 6: A) Confocal fluorescent microscopy images showing the metabolism of Au-BSA NCs and Au-NAC-CS NCs in living Hela cells beginning 1 h after incubation and imaged at (a, f) 0 h, (b, g) 1 h, (c, h) 2 h, (d, i) 4 h and (e, j) 8 h. B) Ex vivo fluorescence images of isolated organs (heart, liver, spleen, lung, kidney) from (a) mice 6 h after injection and (b) isolated organs from the untreated mice. C) (a) Schematics of AuNCF synthesis, (b, c) cryo-TEM images and (d, e) electron tomography of the AuNCF superstructure. D) Photographs under ambient light (top) and UV light (bottom) with varying concentrations of $SnCl_2$ added to Au-GSH NCs. E) Confocal microscopy images of NIH3T3 cell lines incubated with AuNCFs for 1 day (a) bright-field image, (b) confocal fluorescence image and (c) merged image of a cell. F) Image of a single NIH3T3 cell and its *Z*-stacks (a–h) with 1.0 μm intervals of the same cell. Figure panels 6A,B are adapted with permission from [92], copyright 2018 American Chemical Society. Figure panels 6C,D are reused and panels 6E,F are adapted with permission from [53], copyright 2019 Wiley-VCH Verlag GmbH & Co. KGaA, Weinheim.

upon X-ray irradiation in the presence of $[Au_8(C_{21}H_{27}O_2)_8]$ significantly suppressed the tumorigenicity in vivo after one radiotherapy treatment in mouse models.

Because of their well-defined surface functionalities and small size, the dispersion behavior of NCs is similar to that of supramolecular complexes. Therefore, they are excellent building blocks to achieve the formation of hierarchical supracolloidal structures. However, there are substantial challenges as the interactions between the nanoclusters are close to the thermal fluctuation energy of the surrounding media [94]. Nevertheless, hydrogen bonding has been utilized to achieve two-dimensional (2D) and three-dimensional (3D) nanocluster superstructures [95,96]. The NC assemblies have been used to encapsu-

late poorly water-soluble fluorinated drugs through nanoconfinement [97]. Chandra et al. recently reported highly luminescent gold nanocluster frameworks (AuNCFs) using self-assembly through metal chelation [53]. Glutathione-capped AuNCs [$Au_{25}(SG)_{18}$] spontaneously self-assembled into spherical AuNCFs upon controlled addition of $SnCl_2$ (Figure 6C). The size of the AuNCFs was tunable from 30 to 200 nm in diameter, and the luminescence increased dramatically upon framework formation. Interestingly, the quantum yield was increased from 2.5% for [$Au_{25}(SG)_{18}$] to 25% for AuNCFs. Cell counting kit 8 (CCK-8) assay and trypan blue tests with NIH3T3 and A549 cells showed no significant cytotoxicity in vitro (Figure 6D–F). Interestingly, the NC frameworks led to a higher cell viability compared to [$Au_{25}(SG)_{18}$]. This is attributed to the fact that smaller nanoparticles produce reactive oxygen species and possibly aggregate in the cellular medium. The superstructures were also found to show excellent bioavailability and luminescence and were non-toxic. The AuNCFs frameworks, because of their highly luminescent nature, also allowed for better imaging compared to [$Au_{25}(SG)_{18}$]-treated cells.

In vivo bioimaging

Conpared to cell-line and isolated in vitro studies, in vivo imaging using animal models faces additional challenges. This is attributed to an increased complexity, a decreased transmission of visible light through biological tissues, the interaction with various biomolecules and a possible degradation of the luminescent materials. However, NIR emission, biocompatibility, and photothermal stability make luminescent AuNCs potential candidates for in vivo imaging. Using NIR-emitting Au-BSA NCs, Wu et al. successfully demonstrated in vivo imaging in a mouse model [98]. The Au-BSA NCs were subcutaneously injected to test the efficiency of a localized signal under a few millimeters of tissue (Figure 7A,B). It was shown that a strong emission at 710 nm was easily separated from autofluorescence. The detection limit was found to be 0.235 mg/mL of AuNCs. Intravenous injection of Au-BSA NC solution to BALB/c nude mice allowed for real-time imaging of the whole body. The fluorescence emission of NCs was visualized in the superficial vasculature of the whole body immediately upon tail vein injection of NC solution. However, as the blood circulation continued, the emission intensity decreased gradually and

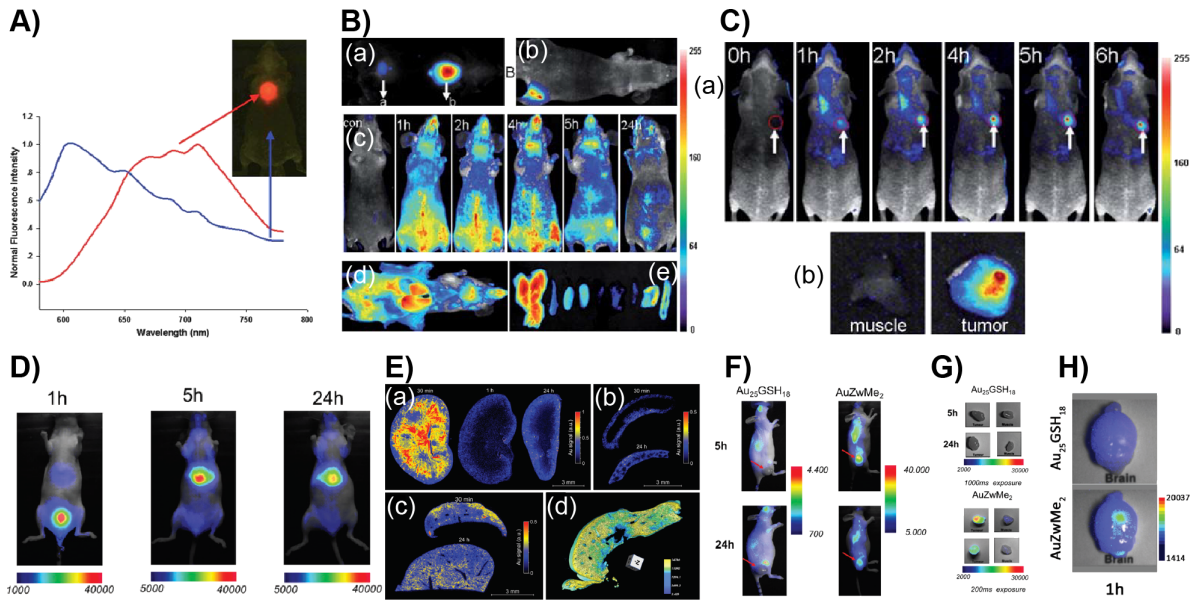

Figure 7: In vivo bioimaging using luminescent AuNCs. A) NIR fluorescence imaging of BALB/c mouse treated with the Au-BSA NCs. The blue line shows the autofluorescence and Au-BSA NCs signal in red in the fluorescence spectra. B) In vivo fluorescence image of Au-BSA NCs injected (a) subcutaneously and (b) intramuscularly into the mice, (c) post-injection real-time in vivo abdomen imaging of intravenously injected with AuNCs as a function of time, (d) ex vivo imaging of anatomized mice after injection of 200 mL of AuNCs and (e) some dissected organs (liver, spleen, left kidney, right kidney, heart, lung, muscle, skin, and intestine from left to right). C) (a) Fluorescence images of mice bearing an MDA-MB-45 tumor and (b) ex vivo fluorescence image of the tumor tissue and the muscle tissue around the tumor from the mice. D) In vivo whole-body fluorescence imaging at time intervals of 1, 5 and 24 h after intravenous injection of $AuZwMe_2$. (E) (a) LIBS measurement of kidney slices 30 min, 1 h, and 24 h post-injection of $AuZwMe_2$ NCs. LIBS measurement of (b) spleen and (c) liver slices 30 min and 24 h post-injection of $AuZwMe_2$. (d) False-color 3D reconstruction of 600 µm thickness of a mouse liver 5 h post-injection of $AuZwMe_2$ by means of X-ray phase-contrast tomography imaging. F) In vivo whole-body fluorescence imaging 5 and 24 h after intravenous injection of $AuZwMe_2$ or $Au_{25}GSH_{18}$. G) Ex vivo fluorescence imaging of the tumor (top) and muscle (bottom) 5 and 24 h after $AuZwMe_2$ and $Au_{25}GSH_{18}$ intravenous injection. H) Ex vivo fluorescence imaging of $Au_{25}GSH_{18}$ (top) and $AuZwMe_2$ (bottom) in isolated orthotopic U87MG glioblastoma-bearing brains, 1 h post-injection. Figure panel 7A is reused and panels 7B,C are adapted with permission from [98], copyright 2010 The Royal Society of Chemistry. Figure panels 7D and 7F–H are reused, and panel 7E is adapted with permission from [99], copyright 2018 The Royal Society of Chemistry.

remained visible up to 5 h post-injection. A notable decrease in luminescence was observed after 24 h in the whole body except liver and bladder, suggesting the clearance of the Au-BSA NCs through the urinary clearance system. Under ex vivo imaging conditions, the harvested organs, including liver, spleen, kidney, heart, lung muscle, skin, and intestine, showed a fluorescence comparable to that of the in vivo imaging at 5 h post-injection.

Guevel et al. reported AuNCs stabilized by zwitterionic molecules for subcutaneous and orthotropic glioblastoma mice models [99]. Two types of Au_{25} NCs were used, namely, glutathione-capped [$Au_{25}(SG)_{18}$] and lipoic acid-sulfobetaine zwitterion-capped [$Au_{25}(ZWMe_2)_{18}$] NCs. Intravenous injection of [$Au_{25}(ZWMe_2)_{18}$] and in vivo fluorescence imaging after 1 h showed a strong signal in the bladder indicating a high and fast renal clearance. Further, a strong fluorescence in the NIR region (that of NCs) was observed in urine generated during the first hour after injection (Figure 7D). This is an indication that the NCs are not metabolized in vivo and retain their structure upon excretion. Similar to many other studies, the fluorescence signal was still observed in the liver after 5 h and to a lesser extent after 24 h, presumably due to NC aggregation. The ex vivo imaging of organs harvested at 1, 5 and 24 h exhibited a low level of fluorescence in the kidney further showing renal clearance (Figure 7E). A decrease of 66% in the NC signal between 1 and 5 h was observed. Using multi-elemental laser-induced breakdown spectroscopy (LIBS) particle clearance and Au content in tissues were studied. A strong signal of Au was observed in the kidney within 30 min mostly in the medulla and decreased after 1 h with a weak residual cortical uptake. However, in the liver, a weak Au signal remained intact up to 24 h possibly due to the accumulation and internalization of NCs in Kupffer cells. Histological studies of the organs revealed that there are no necrotic cells or atrophic tubes or specific immunogenic infiltration between 5 and 24 h post-injection. This indicates that there is no acute toxicity. X-ray tomography confirmed the uniform distribution of Au in the liver. The tumor uptake studies were performed for [$Au_{25}(SG)_{18}$] and [$Au_{25}(ZWMe_2)_{18}$] intravenously injected in mice bearing a subcutaneous U87MG tumor by tracking the NCs using fluorescence imaging. No signal was detected after 5 or 24 h for [$Au_{25}(SG)_{18}$]. However, strong fluorescence was observed for [$Au_{25}(ZWMe_2)_{18}$] in the tumor after 5 h and a slight decrease after 24 h. The tumor-to-skin ratio was determined after 1 and 24 h. It was found to be higher for [$Au_{25}(ZWMe_2)_{18}$] and remained constant. To further validate the uptake in orthotropic brain tumors, NCs were injected into mice bearing U87MG tumors engrafted in the brain (Figure 7F). Again, [$Au_{25}(ZWMe_2)_{18}$] was found to yield a three times stronger signal than [$Au_{25}(SG)_{18}$] at 1 h post-injection. Chen et al. have shown that zwitterionic LA-sulfobetaine-capped AuNCs can be used for in vivo shortwave infrared imaging using a mouse model [100]. Li et al. reported nanoparticle assemblies of pea protein isolate (PPI)-capped AuNCs with red fluorescence for in vitro and in vivo imaging. The nanoparticles were coated with red blood cell membranes to improve their blood circulation and enhance their enrichment in tumors [101].

Lai et al. reported the in vivo formation of fluorescent gold nanoclusters for imaging the brain affected by Alzheimer's disease (AD) [102]. The redox microenvironment in the AD brain is characterized by relatively low oxygen metabolism and more free radicals compared to that of a healthy brain. When AD occurs, a large amount of ascorbate and an elevated level of hydrogen peroxide, other free radicals and redox ligands appear at the lesions in the brain. Thus, $HAuCl_4$ ions accumulated in the hippocampus can be can be potentially reduced. After tail-vein injection into four-month-old APP/PS1 male mice, imaging was performed in vivo. For ex vivo imaging, the harvested organs of mice at 30 h post-injection were used. The maximum fluorescence appeared 18 h after injection. Afterward, the fluorescence signal and imaging area decreased. However, the control group did not show any fluorescence further allowing for selective formation and imaging (Figure 8).

Conclusion

The unique chemical, optical and catalytic properties of gold nanoclusters have led to rapid progress in their application. This can be attributed to tunable photoluminescence, low toxicity, high bioavailability and renal clearance. The studies on bioimaging based on gold nanoclusters started only a decade ago. However, progress has already been made regarding potential applications in the rapid sensing of biomolecules and pathogens, in vitro imaging of various cell lines, and in vivo imaging. Appropriate modifications also offer an opportunity for the rational design of nanocarriers encapsulating poorly soluble drugs for targeted delivery. Cell line-based studies have provided enough evidence that the internalization of AuNCs occurs through endocytosis. However, there are several challenges to utilize AuNCs in bacterial sensing due to their inability to distinguish different strains. Similarly, AuNC-based radiotherapeutic applications are not able to distinguish healthy mammalian cells from infected cells. Further, in vivo imaging has provided crucial insights on uptake and excretion, which are comparably fast. In a majority of the cases, Au_{25}NCs have been utilized. Furthermore, mostly protein-coated or glutathione-capped NCs have been studied. It is important to note that currently only a limited number of AuNCs with an acceptable level of PL and quantum yield are reported. Like many other nanomaterials, AuNCs have shown not to undergo metabolism inside the body. Hence, the accumulation in the liver is still one

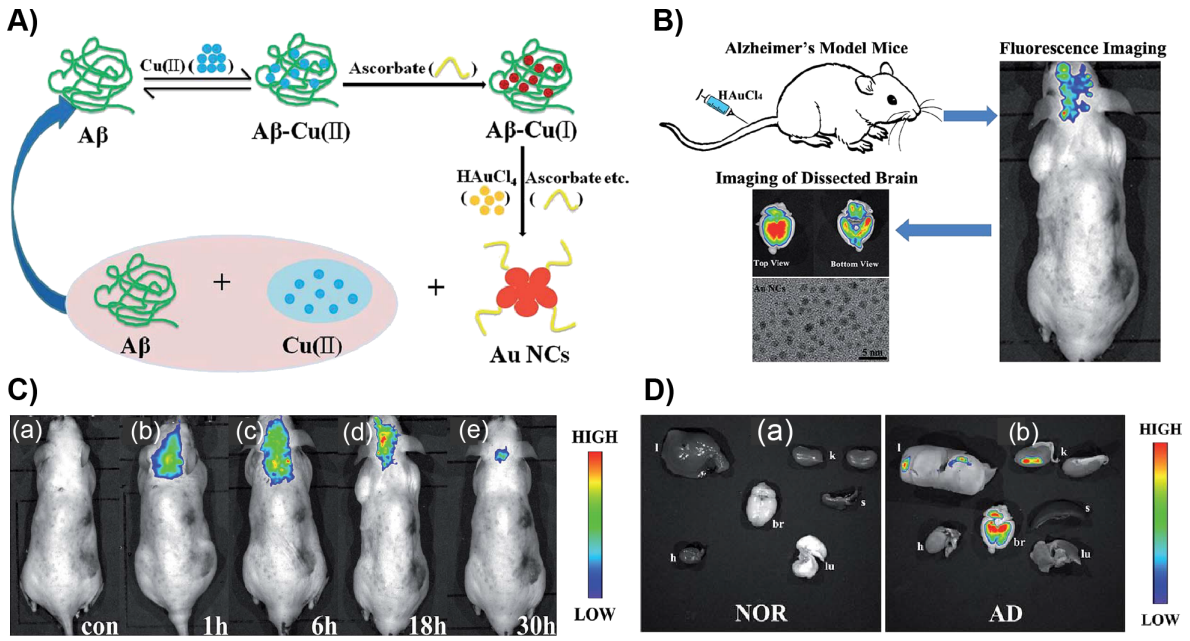

Figure 8: A) Principle of Aβ/copper and ascorbate- or Fe(II)-catalyzed formation of AuNCs. B) Illustration of fluorescence biomarking of mice brain with Alzheimer's disease. C) Fluorescence imaging of (a) the control group of AD mice (without given $HAuCl_4$). (b–e) Fluorescence imaging of the same AD model mice after tail-vein injection of $HAuCl_4$ solution after different periods of time (1, 6, 18 and 30 h). D) Fluorescence imaging of harvested organs (l: liver, h: heart, br: brain, k: kidney, s: spleen, and lu: lung) of the control group and of AD model mice after tail-vein injection of $HAuCl_4$ solution at 30 h post-injection. Figure panels 8A and 8B are reused and panels 8C and 8D are adapted with permission from [102], copyright 2016 The Royal Society of Chemistry.

of the concerns. The fate of accumulated AuNCs in the liver is unknown. Corresponding studies will be useful to realize the development of new bioimaging methods and their practical applications.

ORCID® iDs

Nonappa - https://orcid.org/0000-0002-6804-4128

References

1. Meijering, E.; Carpenter, A. E.; Peng, H.; Hamprecht, F. A.; Olivo-Marin, J.-C. *Nat. Biotechnol.* **2016,** *34,* 1250–1255. doi:10.1038/nbt.3722
2. Giepmans, B. N. G.; Adams, S. R.; Ellisman, M. H.; Tsien, R. Y. *Science* **2006,** *312,* 217–224. doi:10.1126/science.1124618
3. Cho, U.; Riordan, D. P.; Ciepla, P.; Kocherlakota, K. S.; Chen, J. K.; Harbury, P. B. *Nat. Chem. Biol.* **2018,** *14,* 15–21. doi:10.1038/nchembio.2513
4. Lichtman, J. W.; Conchello, J.-A. *Nat. Methods* **2005,** *2,* 910–919. doi:10.1038/nmeth817
5. Rusk, N. *Nat. Cell Biol.* **2009,** *11,* S8–S9. doi:10.1038/ncb1941
6. Fernández-Suárez, M.; Ting, A. Y. *Nat. Rev. Mol. Cell Biol.* **2008,** *9,* 929–943. doi:10.1038/nrm2531
7. Bartolomé, F.; Abramov, A. Y. *Methods Mol. Biol. (N. Y., NY, U. S.)* **2015,** *1264,* 263–270. doi:10.1007/978-1-4939-2257-4_23
8. Grimm, J. B.; Heckman, L. M.; Lavis, L. D. *Prog. Mol. Biol. Transl. Sci.* **2013,** *113,* 1–34. doi:10.1016/b978-0-12-386932-6.00001-6
9. Li, J.-B.; Liu, H.-W.; Fu, T.; Wang, R.; Zhang, X.-B.; Tan, W. *Trends Chem.* **2019,** *1,* 224–234. doi:10.1016/j.trechm.2019.03.002
10. Gorka, A. P.; Nani, R. R.; Schnermann, M. J. *Org. Biomol. Chem.* **2015,** *13,* 7584–7598. doi:10.1039/c5ob00788g
11. Moore, E. G.; Jocher, C. J.; Xu, J.; Werner, E. J.; Raymond, K. N. *Inorg. Chem.* **2007,** *46,* 5468–5470. doi:10.1021/ic700364t
12. Montgomery, C. P.; Murray, B. S.; New, E. J.; Pal, R.; Parker, D. *Acc. Chem. Res.* **2009,** *42,* 925–937. doi:10.1021/ar800174z
13. Bünzli, J.-C. G. *Chem. Rev.* **2010,** *110,* 2729–2755. doi:10.1021/cr900362e
14. Lippincott-Schwartz, J.; Patterson, G. H. *Science* **2003,** *300,* 87–91. doi:10.1126/science.1082520
15. Hoffman, R. M. *Nat. Rev. Cancer* **2005,** *5,* 796–806. doi:10.1038/nrc1717
16. Nienhaus, G. U. *Angew. Chem., Int. Ed.* **2008,** *47,* 8992–8994. doi:10.1002/anie.200804998
17. Hedde, P. N.; Nienhaus, G. U. *Biophys. Rev.* **2010,** *2,* 147–158. doi:10.1007/s12551-010-0037-0
18. Stark, W. J. *Angew. Chem., Int. Ed.* **2011,** *50,* 1242–1258. doi:10.1002/anie.200906684
19. Goesmann, H.; Feldmann, C. *Angew. Chem., Int. Ed.* **2010,** *49,* 1362–1395. doi:10.1002/anie.200903053
20. McHugh, K. J.; Jing, L.; Behrens, A. M.; Jayawardena, S.; Tan, W.; Gao, M.; Langer, R.; Jaklenec, A. *Adv. Mater. (Weinheim, Ger.)* **2018,** *30,* 1706356. doi:10.1002/adma.201706356
21. Li, H.; Kang, Z.; Liu, Y.; Lee, S.-T. *J. Mater. Chem.* **2012,** *22,* 24230–24253. doi:10.1039/c2jm34690g
22. Zhang, W.-H.; Hu, X.-X.; Zhang, X.-B. *Nanomaterials* **2016,** *6,* 81. doi:10.3390/nano6050081

23. Bouzigues, C.; Gacoin, T.; Alexandrou, A. *ACS Nano* **2011,** *5,* 8488–8505. doi:10.1021/nn202378b
24. Kairdolf, B. A.; Smith, A. M.; Stokes, T. H.; Wang, M. D.; Young, A. N.; Nie, S. *Annu. Rev. Anal. Chem.* **2013,** *6,* 143–162. doi:10.1146/annurev-anchem-060908-155136
25. Zhou, J.; Yang, Y.; Zhang, C.-y. *Chem. Rev.* **2015,** *115,* 11669–11717. doi:10.1021/acs.chemrev.5b00049
26. Resch-Genger, U.; Grabolle, M.; Cavaliere-Jaricot, S.; Nitschke, R.; Nann, T. *Nat. Methods* **2008,** *5,* 763–775. doi:10.1038/nmeth.1248
27. Alivisatos, A. P. *Science* **1996,** *271,* 933–937. doi:10.1126/science.271.5251.933
28. Montalti, M.; Cantellia, A.; Battistelli, G. *Chem. Soc. Rev.* **2015,** *44,* 4853–4921. doi:10.1039/c4cs00486h
29. Chinnathambi, S.; Chen, S.; Ganesan, S.; Hanagata, N. *Adv. Healthcare Mater.* **2014,** *3,* 10–29. doi:10.1002/adhm.201300157
30. Zheng, J.; Zhou, C.; Yu, M.; Liu, J. *Nanoscale* **2012,** *4,* 4073–4083. doi:10.1039/c2nr31192e
31. Mooradian, A. *Phys. Rev. Lett.* **1969,** *22,* 185–187. doi:10.1103/physrevlett.22.185
32. Boyd, G. T.; Yu, Z. H.; Shen, Y. R. *Phys. Rev. B* **1986,** *33,* 7923–7936. doi:10.1103/physrevb.33.7923
33. Wilcoxon, J. P.; Martin, J. E.; Parsapour, F.; Wiedenman, B.; Kelley, D. F. *J. Chem. Phys.* **1998,** *108,* 9137–9143. doi:10.1063/1.476360
34. Mohamed, M. B.; Volkov, V.; Link, S.; El-Sayed, M. A. *Chem. Phys. Lett.* **2000,** *317,* 517–523. doi:10.1016/s0009-2614(99)01414-1
35. Bigioni, T. P.; Whetten, R. L.; Dag, Ö. *J. Phys. Chem. B* **2000,** *104,* 6983–6986. doi:10.1021/jp993867w
36. Huang, T.; Murray, R. W. *J. Phys. Chem. B* **2001,** *105,* 12498–12502. doi:10.1021/jp0041151
37. Link, S.; Beeby, A.; FitzGerald, S.; El-Sayed, M. A.; Schaaff, T. G.; Whetten, R. L. *J. Phys. Chem. B* **2002,** *106,* 3410–3415. doi:10.1021/jp014259v
38. Chakraborty, I.; Pradeep, T. *Chem. Rev.* **2017,** *117,* 8208–8271. doi:10.1021/acs.chemrev.6b00769
39. Jin, R.; Zeng, C.; Zhou, M.; Chen, Y. *Chem. Rev.* **2016,** *116,* 10346–10413. doi:10.1021/acs.chemrev.5b00703
40. Tsukuda, T.; Häkkinen, H. *Protected Metal Clusters: From Fundamentals to Applications,* 1st ed.; Elsevier, 2015. doi:10.1016/b978-0-08-100086-1.00001-4
41. Peng, C.; Yu, M.; Zheng, J. *Nano Lett.* **2020,** *20,* 1378–1382. doi:10.1021/acs.nanolett.9b04911
42. Luo, Z.; Zheng, K.; Xie, J. *Chem. Commun.* **2014,** *50,* 5143–5155. doi:10.1039/c3cc47512c
43. Wu, Z.; Jin, R. *Nano Lett.* **2010,** *10,* 2568–2573. doi:10.1021/nl101225f
44. Zheng, J.; Zhang, C.; Dickson, R. M. *Phys. Rev. Lett.* **2004,** *93,* 077402. doi:10.1103/physrevlett.93.077402
45. Zheng, J.; Petty, J. T.; Dickson, R. M. *J. Am. Chem. Soc.* **2003,** *125,* 7780–7781. doi:10.1021/ja035473v
46. Luo, Z.; Yuan, X.; Yu, Y.; Zhang, Q.; Leong, D. T.; Lee, J. Y.; Xie, J. *J. Am. Chem. Soc.* **2012,** *134,* 16662–16670. doi:10.1021/ja306199p
47. Yu, Y.; Luo, Z.; Chevrier, D. M.; Leong, D. T.; Zhang, P.; Jiang, D.; Xie, J. *J. Am. Chem. Soc.* **2014,** *136,* 1246–1249. doi:10.1021/ja411643u
48. Pyo, K.; Thanthirige, V. D.; Kwak, K.; Pandurangan, P.; Ramakrishna, G.; Lee, D. *J. Am. Chem. Soc.* **2015,** *137,* 8244–8250. doi:10.1021/jacs.5b04210
49. Dou, X.; Yuan, X.; Yu, Y.; Luo, Z.; Yao, Q.; Leong, D. T.; Xie, J. *Nanoscale* **2014,** *6,* 157–161. doi:10.1039/c3nr04490d
50. Zhang, L.; He, N.; Lu, C. *Anal. Chem. (Washington, DC, U. S.)* **2015,** *87,* 1351–1357. doi:10.1021/ac5041605
51. Ghosh, A.; Mohammed, O. F.; Bakr, O. M. *Acc. Chem. Res.* **2018,** *51,* 3094–3103. doi:10.1021/acs.accounts.8b00412
52. You, J.-G.; Tseng, W.-L. *Anal. Chim. Acta* **2019,** *1078,* 101–111. doi:10.1016/j.aca.2019.05.069
53. Chandra, S.; Nonappa; Beaune, G.; Som, A.; Zhou, S.; Lahtinen, J.; Jiang, H.; Timonen, J. V. I.; Ikkala, O.; Ras, R. H. A. *Adv. Opt. Mater.* **2019,** *7,* 1900620. doi:10.1002/adom.201900620
54. Kang, X.; Zhu, M. *Chem. Soc. Rev.* **2019,** *48,* 2422–2457. doi:10.1039/c8cs00800k
55. Duan, H.; Nie, S. *J. Am. Chem. Soc.* **2007,** *129,* 2412–2413. doi:10.1021/ja067727t
56. Habeeb Muhammed, M. A.; Ramesh, S.; Sinha, S. S.; Pal, S. K.; Pradeep, T. *Nano Res.* **2008,** *1,* 333–340. doi:10.1007/s12274-008-8035-2
57. Habeeb Muhammed, M. A.; Verma, P. K.; Pal, S. K.; Retnakumari, A.; Koyakutty, M.; Nair, S.; Pradeep, T. *Chem. – Eur. J.* **2010,** *16,* 10103–10112. doi:10.1002/chem.201000841
58. Shang, L.; Dörlich, R. M.; Brandholt, S.; Schneider, R.; Trouillet, V.; Bruns, M.; Gerthsen, D.; Nienhaus, G. U. *Nanoscale* **2011,** *3,* 2009–2014. doi:10.1039/c0nr00947d
59. Kang, X.; Chong, H.; Zhu, M. *Nanoscale* **2018,** *10,* 10758–10834. doi:10.1039/c8nr02973c
60. Pramanik, G.; Humpolickova, J.; Valenta, J.; Kundu, P.; Bals, S.; Bour, P.; Dracinsky, M.; Cigler, P. *Nanoscale* **2018,** *10,* 3792–3798. doi:10.1039/c7nr06050e
61. AbdulHalim, L. G.; Kothalawala, N.; Sinatra, L.; Dass, A.; Bakr, O. M. *J. Am. Chem. Soc.* **2014,** *136,* 15865–15868. doi:10.1021/ja508860b
62. Shibu, E. S.; Muhammed, M. A. H.; Tsukuda, T.; Pradeep, T. *J. Phys. Chem. C* **2008,** *112,* 12168–12176. doi:10.1021/jp800508d
63. Xie, J.; Zheng, Y.; Ying, J. Y. *J. Am. Chem. Soc.* **2009,** *131,* 888–889. doi:10.1021/ja806804u
64. Mohammed, N.; Baidya, A.; Murugesan, V.; Kumar, A. A.; Ganayee, M. A.; Mohanty, J. S.; Tam, K. C.; Pradeep, T. *ACS Sustainable Chem. Eng.* **2016,** *4,* 6167–6176. doi:10.1021/acssuschemeng.6b01674
65. Goswami, N.; Yao, Q.; Luo, Z.; Li, J.; Chen, T.; Xie, J. *J. Phys. Chem. Lett.* **2016,** *7,* 962–975. doi:10.1021/acs.jpclett.5b02765
66. Zheng, K.; Yuan, X.; Kuah, K.; Luo, Z.; Yao, Q.; Zhang, Q.; Xie, J. *Chem. Commun.* **2015,** *51,* 15165–15168. doi:10.1039/c5cc04858c
67. Wu, X.; Li, L.; Zhang, L.; Wang, T.; Wang, C.; Su, Z. *J. Mater. Chem. B* **2015,** *3,* 2421–2425. doi:10.1039/c4tb02009j
68. Yahia-Ammar, A.; Sierra, D.; Mérola, F.; Hildebrandt, N.; Le Guével, X. *ACS Nano* **2016,** *10,* 2591–2599. doi:10.1021/acsnano.5b07596
69. Goswami, N.; Lin, F.; Liu, Y.; Leong, D. T.; Xie, J. *Chem. Mater.* **2016,** *28,* 4009–4016. doi:10.1021/acs.chemmater.6b01431
70. Liu, C.-L.; Wu, H.-T.; Hsiao, Y.-H.; Lai, C.-W.; Shih, C.-W.; Peng, Y.-K.; Tang, K.-C.; Chang, H.-W.; Chien, Y.-C.; Hsiao, J.-K.; Cheng, J.-T.; Chou, P.-T. *Angew. Chem., Int. Ed.* **2011,** *50,* 7056–7060. doi:10.1002/anie.201100299
71. Luo, J.; Xie, Z.; Lam, J. W. Y.; Cheng, L.; Chen, H.; Qiu, C.; Kwok, H. S.; Zhan, X.; Liu, Y.; Zhu, D.; Tang, B. Z. *Chem. Commun.* **2001,** 1740–1741. doi:10.1039/b105159h
72. Ding, D.; Li, K.; Liu, B.; Tang, B. Z. *Acc. Chem. Res.* **2013,** *46,* 2441–2453. doi:10.1021/ar3003464

73. Qin, A.; Lam, J. W. Y.; Tang, B. Z. *Prog. Polym. Sci.* **2012,** *37,* 182–209. doi:10.1016/j.progpolymsci.2011.08.002
74. Wang, Z.; Xiong, Y.; Kershaw, S. V.; Chen, B.; Yang, X.; Goswami, N.; Lai, W.-F.; Xie, J.; Rogach, A. L. *Chem. Mater.* **2017,** *29,* 10206–10211. doi:10.1021/acs.chemmater.7b04239
75. Hembury, M.; Beztsinna, N.; Asadi, H.; van den Dikkenberg, J. B.; Meeldijk, J. D.; Hennink, W. E.; Vermonden, T. *Biomacromolecules* **2018,** *19,* 2841–2848. doi:10.1021/acs.biomac.8b00414
76. Wen, F.; Dong, Y.; Feng, L.; Wang, S.; Zhang, S.; Zhang, X. *Anal. Chem. (Washington, DC, U. S.)* **2011,** *83,* 1193–1196. doi:10.1021/ac1031447
77. Dichiarante, V.; Tirotta, I.; Catalano, L.; Terraneo, G.; Raffaini, G.; Chierotti, M. R.; Gobetto, R.; Baldelli Bombelli, F.; Metrangolo, P. *Chem. Commun.* **2017,** *53,* 621–624. doi:10.1039/c6cc09324h
78. Chen, L.-Y.; Wang, C.-W.; Yuan, Z.; Chang, H.-T. *Anal. Chem. (Washington, DC, U. S.)* **2015,** *87,* 216–229. doi:10.1021/ac503636j
79. Yang, J.; Wang, F.; Yuan, H.; Zhang, L.; Jiang, Y.; Zhang, X.; Liu, C.; Chai, L.; Li, H.; Stenzel, M. *Nanoscale* **2019,** *11,* 17967–17980. doi:10.1039/c9nr04301b
80. Cantelli, A.; Guidetti, G.; Manzi, J.; Caponetti, V.; Montalti, M. *Eur. J. Inorg. Chem.* **2017,** 5068–5084. doi:10.1002/ejic.201700735
81. Olesiak-Banska, J.; Waszkielewicz, M.; Obstarczyk, P.; Samoc, M. *Chem. Soc. Rev.* **2019,** *48,* 4087–4117. doi:10.1039/c8cs00849c
82. He, Z.; Shu, T.; Su, L.; Zhang, X. *Molecules* **2019,** *24,* 3045. doi:10.3390/molecules24173045
83. Chan, P.-H.; Chen, Y.-C. *Anal. Chem. (Washington, DC, U. S.)* **2012,** *84,* 8952–8956. doi:10.1021/ac302417k
84. Zhu, H.; Li, J.; Wang, J.; Wang, E. *ACS Appl. Mater. Interfaces* **2019,** *11,* 36831–36838. doi:10.1021/acsami.9b11026
85. Kurdekar, A. D.; Avinash Chunduri, L. A.; Manohar, C. S.; Haleyurgirisetty, M. K.; Hewlett, I. K.; Venkataramaniah, K. *Sci. Adv.* **2018,** *4,* eaar6280. doi:10.1126/sciadv.aar6280
86. Lin, S.-Y.; Chen, N.-T.; Sum, S.-P.; Lo, L.-W.; Yang, C.-S. *Chem. Commun.* **2008,** 4762–4764. doi:10.1039/b808207c
87. Muhammed, M. A. H.; Verma, P. K.; Pal, S. K.; Kumar, R. C. A.; Paul, S.; Omkumar, R. V.; Pradeep, T. *Chem. – Eur. J.* **2009,** *15,* 10110–10120. doi:10.1002/chem.200901425
88. Retnakumari, A.; Setua, S.; Menon, D.; Ravindran, P.; Muhammed, H.; Pradeep, T.; Nair, S.; Koyakutty, M. *Nanotechnology* **2010,** *21,* 055103. doi:10.1088/0957-4484/21/5/055103
89. Pan, U. N.; Khandelia, R.; Sanpui, P.; Das, S.; Paul, A.; Chattopadhyay, A. *ACS Appl. Mater. Interfaces* **2017,** *9,* 19495–19501. doi:10.1021/acsami.6b06099
90. Pan, U. N.; Sanpui, P.; Paul, A.; Chattopadhyay, A. *ACS Appl. Bio Mater.* **2019,** *2,* 3144–3152. doi:10.1021/acsabm.9b00210
91. Pan, S.; Zhou, J.; Liu, W.; Ye, Y.; Chen, G.; Xu, J.; Qian, Z.; Chen, J.; Feng, H. *Analyst* **2019,** *144,* 4483–4487. doi:10.1039/c9an01035a
92. Duan, Y.; Duan, R.; Liu, R.; Guan, M.; Chen, W.; Ma, J.; Chen, M.; Du, B.; Zhang, Q. *ACS Biomater. Sci. Eng.* **2018,** *4,* 1055–1063. doi:10.1021/acsbiomaterials.7b00975
93. Jia, T.-T.; Yang, G.; Mo, S.-J.; Wang, Z.-Y.; Li, B.-J.; Ma, W.; Guo, Y.-X.; Chen, X.; Zhao, X.; Liu, J.-Q.; Zang, S.-Q. *ACS Nano* **2019,** *13,* 8320–8328. doi:10.1021/acsnano.9b03767
94. Nonappa; Ikkala, O. *Adv. Funct. Mater.* **2018,** *28,* 1704328. doi:10.1002/adfm.201704328
95. Nonappa; Lahtinen, T.; Haataja, J. S.; Tero, T.-R.; Häkkinen, H.; Ikkala, O. *Angew. Chem., Int. Ed.* **2016,** *55,* 16035–16038. doi:10.1002/anie.201609036
96. Chakraborty, A.; Fernandez, A. C.; Som, A.; Mondal, B.; Natarajan, G.; Paramasivam, G.; Lahtinen, T.; Häkkinen, H.; Nonappa; Pradeep, T. *Angew. Chem., Int. Ed.* **2018,** *57,* 6522–6526. doi:10.1002/anie.201802420
97. Pigliacelli, C.; Maiolo, D.; Nonappa; Haataja, J. S.; Amenitsch, H.; Michelet, C.; Sánchez Moreno, P.; Tirotta, I.; Metrangolo, P.; Baldelli Bombelli, F. *Angew. Chem., Int. Ed.* **2017,** *56,* 16186–16190. doi:10.1002/anie.201710230
98. Wu, X.; He, X.; Wang, K.; Xie, C.; Zhou, B.; Qing, Z. *Nanoscale* **2010,** *2,* 2244–2249. doi:10.1039/c0nr00359j
99. Le Guével, X.; Henry, M.; Motto-Ros, V.; Longo, E.; Montañez, M. I.; Pelascini, F.; de La Rochefoucauld, O.; Zeitoun, P.; Coll, J.-L.; Josserand, V.; Sancey, L. *Nanoscale* **2018,** *10,* 18657–18664. doi:10.1039/c8nr05299a
100. Chen, Y.; Montana, D. M.; Wei, H.; Cordero, J. M.; Schneider, M.; Le Guével, X.; Chen, O.; Bruns, O. T.; Bawendi, M. G. *Nano Lett.* **2017,** *17,* 6330–6334. doi:10.1021/acs.nanolett.7b03070
101. Li, Z.; Peng, H.; Liu, J.; Tian, Y.; Yang, W.; Yao, J.; Shao, Z.; Chen, X. *ACS Appl. Mater. Interfaces* **2018,** *10,* 83–90. doi:10.1021/acsami.7b13088
102. Lai, L.; Zhao, C.; Li, X.; Liu, X.; Jiang, H.; Selke, M.; Wang, X. *RSC Adv.* **2016,** *6,* 30081–30088. doi:10.1039/c6ra01027j

License and Terms

BEILSTEIN JOURNAL OF NANOTECHNOLOGY

Identification of physicochemical properties that modulate nanoparticle aggregation in blood

Ludovica Soddu[1,2], Duong N. Trinh[3], Eimear Dunne[2], Dermot Kenny[2], Giorgia Bernardini[1,3], Ida Kokalari[1], Arianna Marucco[1], Marco P. Monopoli[*3] and Ivana Fenoglio[*1]

Full Research Paper

Open Access

Address:
[1]Department of Chemistry, University of Torino, 10125 Torino, Italy, [2]Molecular and Cellular Therapeutics, Royal College of Surgeons in Ireland (RCSI), 123 St Stephen Green, Dublin 2, Ireland and [3]Department of Chemistry, Royal College of Surgeons in Ireland (RCSI), 123 St Stephen Green, Dublin 2, Ireland

Email:
Marco P. Monopoli[*] - marcomonopoli@rcsi.ie;
Ivana Fenoglio[*] - ivana.fenoglio@unito.it

* Corresponding author

Keywords:
aggregation; nanoparticles; platelet aggregation; size; surface chemistry

Beilstein J. Nanotechnol. **2020,** *11,* 550–567.
doi:10.3762/bjnano.11.44

Received: 28 September 2019
Accepted: 28 February 2020
Published: 03 April 2020

This article is part of the thematic issue "Engineered nanomedicines for advanced therapies".

Guest Editor: F. Baldelli Bombelli

Abstract

Inorganic materials are receiving significant interest in medicine given their usefulness for therapeutic applications such as targeted drug delivery, active pharmaceutical carriers and medical imaging. However, poor knowledge of the side effects related to their use is an obstacle to clinical translation. For the development of molecular drugs, the concept of safe-by-design has become an efficient pharmaceutical strategy with the aim of reducing costs, which can also accelerate the translation into the market. In the case of materials, the application these approaches is hampered by poor knowledge of how the physical and chemical properties of the material trigger the biological response. Hemocompatibility is a crucial aspect to take into consideration for those materials that are intended for medical applications. The formation of nanoparticle agglomerates can cause severe side effects that may induce occlusion of blood vessels and thrombotic events. Additionally, nanoparticles can interfere with the coagulation cascade causing both pro- and anti-coagulant properties. There is contrasting evidence on how the physicochemical properties of the material modulate these effects. In this work, we developed two sets of tailored carbon and silica nanoparticles with three different diameters in the 100–500 nm range with the purpose of investigating the role of surface curvature and chemistry on platelet aggregation, activation and adhesion. Substantial differences were found in the composition of the protein corona depending on the chemical nature of the nanoparticles, while the surface curvature was found to play a minor role. On the other hand, large carbon nanoparticles (but not small carbon nanoparticles or silica nanoparticles) have a clear tendency to form aggregates both in plasma and blood. This effect was observed both in the presence or absence of platelets and was independent of platelet activation. Overall, the results presented

herein suggest the existence of independent modes of action that are differently affected by the physicochemical properties of the materials, potentially leading to vessel occlusion and/or formation of thrombi in vivo.

Introduction

Nanomedicine is one of the most exciting fields of research in the branch of nanotechnology as it has the potential to generate practical and effective solutions to tackle chronic diseases and to solve unmet clinical challenges. However, a tremendous gap exists between the number of numerous formulation types synthesised in research laboratories and those approved for clinics [1], mainly due to the lack of understanding on the nanoparticles (NPs) behaviour in complex media that can affect their efficacy and their biocompatibility [2].

Safe-by-design (SbD) approaches have great potential in accelerating the entry of medicines into the market [3] with the aim of reducing the preclinical research time and the associated costs for production. A deep knowledge of the processes leading to the adverse effects and of the physicochemical properties governing such processes are required to build structure–activity relationships (SARs) that in turn enable the SbD approaches. To the latter aspect, knowledge can only be derived by substantial screening of libraries of nanomaterials with well defined synthetic properties.

The understanding of the processes occurring in the bloodstream is particularly relevant not only for nanoformulations administered by intravenous injection, but also for any material that is introduced into the body by other routes as they have the potential to cross biological barriers and subsequently enter into the bloodstream. Previous studies have shown that specific NPs have been able to bind to biomolecules from the coagulation system and induce haemorrhage or thrombosis [4]. The depletion of soluble coagulation factors (e.g., fibrinogen, XII factor) may occur following adsorption of the factors at the NP surface. On the other hand, the activation of some factors by surface-driven exposure of cryptic domains following adsorption was reported in some studies [5,6]. Other studies have reported the NPs ability to damage or activate platelets, endothelial cells or monocytes [4].

Some physicochemical properties, including the surface charge and the particle size, were found to be critical in influencing the nanomaterial's ability to induce adverse effects [7]. However, although such properties were shown to clearly affect the pro-/anticoagulant activity of NPs, the direction of the effect varies depending on the tested material, and it is currently not clear which properties lead to the activation of the coagulation. For example, positive charged dendritic NPs were found to be more thrombogenic than negatively charged ones while positive and negative charged polystyrene NPs both induce platelet activation [7,8].

Carbon and silica nanomaterials are among the most studied inorganic materials for medical applications due to their promising properties. However, some studies have shown that they are both capable of inducing the formation of thrombi, and the relevant mechanisms of action are still under debate [9]. In fact, single-walled (SWCNTs) and multiwalled carbon nanotubes (MWCNTs) can induce platelet activation by inducing depletion of intracellular Ca^{2+} [10,11], an effect that was hypothesised to be caused by the interaction of CNTs with plasma and dense tubular system membranes likely related to the fibrous shape [12]. On the other hand, contrasting data have been reported on the potential of isometric carbon nanoparticles (CNPs) like carbon black, fullerenes and diesel exhaust particles to induce platelet activation and NP aggregation [10,11,13]. Systemic administration of carbon black in mice resulted in fibrinogen and platelet deposition in post-capillary venules in the liver and heart, suggesting the role of this protein in nanoparticle-mediated platelet aggregation [14,15].

Silica nanoparticles (SNPs) of different sizes were found to activate glycoprotein IIb/IIIa and to induce the expression of P-selectin in platelets [16]. Additionally, SNPs were found to induce pre-thrombotic states through surface-driven activation of the coagulation factor XII [17,18]. Finally, SNPs are known to induce oxidative stress in several cell lines including endothelial cells [19] and leucocytes [20,21], a process that in vivo may indirectly induce platelet aggregation.

The interference with the coagulation system is not the only possible mechanism that may induce vascular occlusion, as the NP have a strong tendency to agglomerate also in water. The degree of the agglomeration is controlled by the size, shape and surface chemistry of the particles. Strong repulsive electrostatic charges and steric hindrance may stabilize the NPs and prevent agglomeration. In the bloodstream, agglomeration is related to the formation of a biocorona that modifies the electrostatic and steric repulsion among particles [22]. Finally, protein–protein interaction may lead to bridging among particles, thus promoting agglomeration [23].

In the present study, a set of six silica and carbon NPs of known size and morphology was used to evaluate the effect of the size and surface properties on the protein corona composition, platelet activation and aggregation.

Materials and Methods

Reagents

Sodium polyacrylate, D-(+)-glucose, thionine acetate salt, phosphate buffered saline powder, EDTA, glutathione reduced and 5,5′-dithiobis(2-nitrobenzoic acid), tetraethyl orthosilicate (TEOS), phosphate buffered saline (PBS) tablets were obtained from Sigma-Aldrich (Germany). 5,5-dimethyl-1-pyrroline *N*-oxide (DMPO) was obtained from Cayman Chemicals (USA). Ultrapure water was obtained from a Milli-Q Plus system (Millipore, Bedford, MA, USA). All other chemicals and solvents used were at least of analytical grade.

Synthesis of carbon nanoparticles

Carbon nanoparticles (CNPs) were produced starting from glucose using a one-step hydrothermal process as previously described by Kokalari et al. 2019 [24]. Briefly, glucose was dissolved in 50 mL of ultrapure water followed by the addition of 15 mg of sodium polyacrilate. The solution was introduced in a pressure reactor system (Büchi AG) and heated at 190 °C for 3 or 8 h. The parameters used during the synthesis are described in detail in Table 1. The CNPs were then purified with ultrapure water either by centrifugation for large carbon nanoparticles (CNP-L) or by tangential flow ultrafiltration (Vivaflow 50R, MW 30 kDa) for the medium and small carbon nanoparticles (CNP-M and CNP-S, respectively).

Synthesis of silica nanoparticles

Silica nanoparticles (SNPs) were prepared by hydrolysis and condensation of TEOS in the presence of ammonia as a catalyst following the Stöber process [25]. Briefly, a defined amount of TEOS was added to a solution containing ethanol, ammonia (33%) and ultrapure water under magnetic stirring and at room temperature for 30–40 min. The ratio of the reagents was modified in order to control the NPs size (Table 2). The NP suspension was centrifuged at 11,000 rcf for 15 min and the particles re-suspended in ethanol once, centrifuged, and re-suspended in ultrapure water. The procedure was repeated three times. The purified NPs were suspended in ultrapure water and stored at 4 °C until use.

Scanning electron microscopy (SEM)

The NPs morphology was characterised using scanning electron microscopy (SEM), using a Zeiss Evo 50XVP (Assing) instrument. CNPs and SNPs suspensions were diluted up to 0.05 mg/mL in ultrapure water. A volume of 20 µL of the diluted suspensions was mounted on aluminium stubs using double-sided adhesive carbon tape and silicon wafers. The samples were dried overnight at room temperature. In the case of SNPs, the samples were sputter-coated with a thick gold film (≈17 nm) under argon atmosphere to improve secondary electron emission during SEM imaging. The NPs morphology was observed at an acceleration voltage of 20 kV.

Dynamic light scattering (DLS)

The mean diameter and polydispersity index (PDI) of the NPs were obtained using a Zetasizer (Nano ZS Malvern Instruments, UK) instrument based on the dynamic light scattering (DLS)

Table 1: Synthesis parameters used for the CNPs.

	Glucose (g)	Surfactant (mg)	Time (h)	Temperature (°C)
CNP-S	2	15	3	190
CNP-M	2	15	8	190
CNP-L	5	15	8	190

Table 2: Synthesis parameters for SNPs.

	TEOS (mL)	Ethanol (mL)	NH_3 (mL)	H_2O (mL)	Time (min)
SNP-S	0.76	20	0.85	0.83	40
SNP-M	0.76	20	1.70	1.07	40
SNP-L	0.33	44	18	–	30

technique. The measurements were performed on purified NPs by analysing 0.5 mL of the suspension in ultrapure water, placed in a square polystyrene cuvette, at 25 °C. PBS 0.01 M, pH 7.4, Sigma-Aldrich, was used as the diluent in the case of the evaluation of the size after the protein corona formation.

Nanoparticle tracking analysis (NTA)

An analysis of the size distribution and concentration of CNPs and SNPs were performed by NTA using a Nanosight NS300 (Malvern, UK) instrument equipped with a blue laser (488 nm) and a quartz chamber for sample injection, equipped with an O-ring top plate. For the NP/hard protein corona complexes, the samples were diluted in PBS (0.01 M, pH 7.4). The dilution factor was chosen in order to obtain 30 particles per frame, as suggested by the manufacturer's recommendations. The measurement duration was set at 60 s.

Zeta potential

Zeta-potential measurements were performed based on the electrophoretic light scattering (ELS) technique, using a Zetasizer (Nano ZS Malvern Instruments, UK) instrument, as a function of the pH in the range from 2–9. The NP suspensions were diluted in ultrapure water at a final concentration of 0.5 mg/mL. The pH of the suspensions was adjusted by adding diluted NaOH or HCl solutions and the samples were introduced into disposable folded capillary cuvettes (Malvern Panalytical).

Protein corona characterization

Access to blood plasma for the corona study

The blood plasma used for the corona studies was obtained from the Irish Blood Transfusion service (IBTS) St Vincent's Hospital, Dublin. The plasma, derived from eight different donors, was polled, aliquoted and stored −80 °C until use. The use of this biological fluid for corona studies is covered by the RCSI REC 1246b.

Methods

On the day of the experiment, an aliquot of blood plasma was thawed and allowed to reach room temperature. Once thawed, the sample was centrifuged for 3 min at 16,000 rcf in order to pellet any aggregated proteins. The supernatant was then used for the incubation step while the pellet was discarded.

Blood plasma was diluted in PBS in order to obtain solutions with increasing protein. CNPs and SNPs were then added to the solution and were incubated for 1 h at 37 °C under agitation (150 rpm). Sample normalisation was carrred out throughout the experiments to ensure total surface area of 1.0×10^{-2} m^2 per incubation step.

After the NPs incubation with human plasma, the nanoparticle–protein corona complexes were pelleted by centrifugation and re-suspended in PBS three times in order to remove the loosely binding coronas as previously described [26]. After the last washing step, the pelleted samples were suspended in 20 µL PBS and 10 µL of 3X Blue Loading Buffer Reagents (New England biolabs) that contained DTT in a ratio of 1:10 following the manufacturer instructions. The samples were sonicated for 5 min in an ultrasonic bath and then heated for 5 min at 95 °C to complete the protein denaturation.

The protein corona was resolved in a 4% stacking gel / 12% acrylamide and the electrophoretic analysis was conducted at 130 V as previously described [26]. After the electrophoretic separation, the gels were stained in Imperial Protein stain (Thermo Scientific) for 1 h and distained overnight (in ultrapure water). The densitometry analysis was performed using the software ImageJ (NIH).

Mass spectrometry analysis

The samples were run on a sodium dodecyl sulfate–polyacrylamide gel electrophoresis (SDS-PAGE) instrument for 10 min before the protein bands were excised from the gel in order to allow the whole corona proteins to migrate into a single gel band. The proteins in the gel pieces were reduced with dithiothreitol, alkylated with iodoacetamide and digested with trypsin (Promega Corporation) overnight at 37 °C. The peptides were then extracted from the gel matrix and prepared for MS analysis by using Pierce C18 Tips (Thermo Fisher) following the manufacturer's procedure.

The peptide samples were analysed on a quadrupole Orbitrap (Q-Exactive, Thermo Scientific) mass spectrometer equipped with a reversed-phase NanoLC UltiMate 3000 HPLC system (Thermo Scientific). The samples were loaded onto C18 reversed phase columns (10 cm length, 75 µm inner diameter) and eluted with a linear gradient from 2 to 27% acetonitrile containing 0.5% acetic acid in 58 min at a flow rate of 250 nL/min. The injection volume was 5 µL. The mass spectrometer was operated in data dependent mode, automatically switching between MS and MS2 acquisition. Survey full scan MS spectra (m/z 300–1600) were acquired in the Orbitrap with a resolution of 70,000. MS2 spectra had a resolution of 17,500. The twelve most intense ions were sequentially isolated and fragmented by higher-energy C-trap dissociation.

MS raw files were processed with MaxQuant software (version 1.6.2). The peak lists were searched against the human FASTA database. The search included the modifications of cysteine carbamidomethylation, methionine oxidation and protein N-terminal acetylation. A maximum of two missed trypsin

cleavages were allowed in the database search. The false discovery rate for both peptides and proteins was set at 1%. After that, the ProteinGroup file from Maxquant was processed, filtered and analysed with Perseus software to generate the top abundance table, hierarchical clustering graph and numeric Venn diagrams.

Preparation of blood and platelet-rich plasma (PRP)

Access to human blood for the platelet aggregation study

Blood collection for this study was approved by the Royal College of Surgeons in Ireland and Beaumont Hospital ethics committees REC1415. Written informed consent was obtained from all donors prior to phlebotomy. All blood samples were taken in accordance with the declaration of Helsinki.

Study participants

25 healthy donors were recruited for this study. All donors had no previous history of any major disease and were free from any medication such as statins, antihypertensive medication, antiplatelet agents such as aspirin, or anti-inflammatory medications such ibuprofen, for at least 12 days prior to blood draw.

Preparation of blood and platelet-rich plasma (PRP)

Venous blood was drawn from the antecubital vein using a 19-gauge butterfly needle connected to a sterile polypropylene syringe. Blood was drawn into 3.2% (w/v) trisodium citrate anticoagulant (1:9 volume of citrate to blood, final citrate concentration of 0.32%). Blood samples were kept at room temperature with gentle rocking and used within 1 h of phlebotomy. Whole blood cell counts were recorded for each donor, using a Sysmex-KX21N haematology analyser (Kobe, Japan). Blood samples were centrifuged at 170*g* for 10 min to obtain platelet-rich plasma (PRP) (Centrifuge 5417R, BIOTOOLS, CA).

Light transmission aggregometry (LTA)

Platelet aggregation was monitored by light transmission aggregometry (LTA) in a Chronolog-490D aggregometer (CHRONO-LOG® Corporation, Havertown, PA). Adenosine diphosphate (ADP) and collagen were used as activators of platelet aggregation.

The NPs were first suspended in phosphate buffered saline (PBS) and then they were added to 250 µL PRP and incubated for 1 min. The concentration of NPs to use during the incubation step was calculated on the base of mean diameter (DLS) and nanoparticle concentration number (NTA) to have a total of 8.6×10^{-4} m^2/mL of exposed surface area, equal to 1 mg/mL for CNP-S. In the case of CNP-L the concentration was lower to avoid interference (7.25×10^{-5} m^2/mL). 2.5 µL of 10 µM ADP or 12.5 µL of 10 µM collagen was then added and aggregation was monitored for 5 min with the suspension continuously stirred. The optical density was also measured for NPs suspended in PRP in the absence of agonists for up to 40 min of incubation. PRP without NPs was used as the control. The data are expressed as the mean of three independent experiments.

Flow cytometry fluorescence-activated cell sorting (FACS)

Flow cytometry fluorescence-activated cell sorting (FACS) was used to evaluate platelet activation. The NPs were suspended in PRP at the same concentration used for LTA. 2.5 µL of the fluorophore-conjugated antibody (CD62P) (1.5 µg/mL) (Becton Dickinson, Oxford, UK), which binds P-selectin, and 87.5 µL of PBS were added to 10 µL of the suspension and incubated for 10 min. The reactions were stopped by the addition of PBS to a final volume of 1 mL. The mean fluorescence intensity (MFI) was read on a Beckman Coulter Cytomics FC500 flow cytometer. The experiments were repeated by adding 5 µL of ADP (10 µM). The data are expressed as the mean of three independent experiments.

Dynamic platelet function assay (DPFA)

The DPFA is a well-characterised real-time assay of platelet interaction with von Willebrand factor (VWF) under conditions of arterial shear [27-29].

The initial phases of platelet aggregation were assayed using the DPFA as previously described [25,26]. Briefly, custom parallel plate perfusion chambers were coated overnight with 100 µg/mL VWF, washed with phosphate-buffered saline and blocked with 1% bovine serum albumin for 1 h prior to use. Whole blood was labelled with 1 µM $DiOC_6$ (Sigma-Aldrich, Ireland) for 5 min at 37 °C prior to perfusion through the chamber at an arterial rate of shear (1500 s^{-1}). Platelet translocation behaviour was recorded using real-time video microscopy at a rate of 19 frames per second. Image stacks were analysed by a custom-designed and validated software package [27]. The assay measurements obtained from this analysis include the number of platelets that interacted with the VWF surface (platelet tracks), the number of platelets that translocate over VWF (translocating platelets), the average speed at which platelet translocation occurred (platelet translocation speed), the distance a platelet translocated along the VWF surface (platelet translocation distance), the number of platelets that stably adhered to the VWF-coated surface (static platelets), and the percent surface coverage on the final frame (percentage of platelet surface coverage). For this study we only considered the platelet adhesion parameters.

Results

Synthesis and characterisation of the libraries of silica and carbon nanoparticles

In this study, we synthesised two matching sets of SNPs and CNPs that had a similar hydrodynamic diameter. The mean hydrodynamic diameter based on DLS and NTA confirmed a similar size distribution between the two materials (Table 3). The low polydispersity index (PDI) indicates high colloidal stability and narrow size range distribution.

The hydrodynamic diameter of the samples measured by DLS was similar to that measured by NTA, with the exception of the large samples, where the detected diameter with the latter technique was lower than the ones detected with the DLS. In fact, NTA detected four populations of particles of different size (Supporting Information File 1, Figure S1), while in DLS they appeared as a unique polydisperse population. This data explains also the higher PDI values obtained for the large nanoparticle samples comparing to the small ones.

SEM analysis confirmed that all particles appear spherical with a uniform size, confirming the DLS analysis (Figure 1).

The zeta potential of the samples was measured by electrophoretic light scattering (ELS) in the pH range from 2 to 9 (Figure 2a). As expected, both SNPs and CNPs exhibited a negative zeta potential across the whole pH range. It gradually increased with the increase of the pH of the suspension although it never reached positive values, indicating the presence of weakly acidic groups at the surface. In the case of CNPs, acidic carboxylic or phenolic groups formed during the synthesis are expected, while the presence of surface hydroxyl groups are expected for SNPs. At physiological pH (7.4), all particles exhibit a zeta potential in the range of −40 to −70 mV. CNPs exhibit a zeta potential more negative than the corresponding SNPs of the same size range. Note that the zeta potential curve of CNP-L is not reported since this sample rapidly agglomerates by lowering the pH value, making the measurement unfeasible.

Table 3: Mean hydrodynamic diameter, PDI and standard deviation of each sample measured after purification obtained with DLS compared with the mean of hydrodynamic diameter and standard deviation obtained using NTA.

	DLS			NTA	
	Hydrodynamic diameter (nm)	Standard dev.	PDI	Hydrodynamic diameter (nm)	Standard dev.
SNP-S	114.1	±0.351	0.081	115.0	±1.52
SNP-M	235.1	±4.754	0.012	217.3	±4.16
SNP-L	488.1	±5.387	0.031	333.3	±14.5
CNP-S	179.5	±3.482	0.074	128.3	±2.52
CNP-M	259.7	±2.193	0.010	232.0	±6.08
CNP-L	485.2	±2.452	0.123	349.0	±4.36

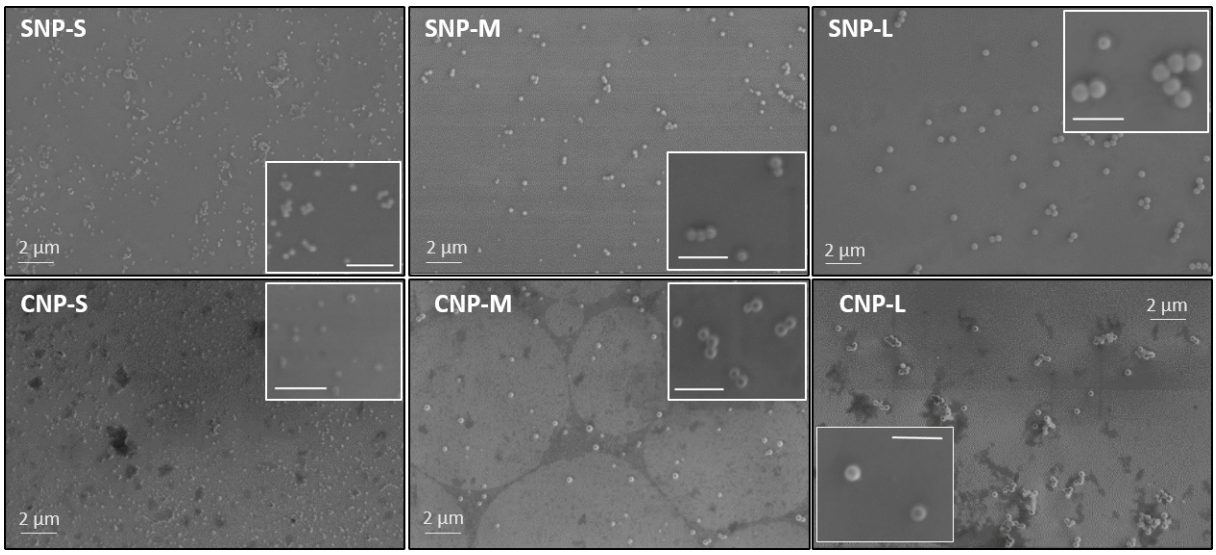

Figure 1: Representative SEM micrographs of silica and carbon nanoparticles. The scale bar in each inset is 1 µm.

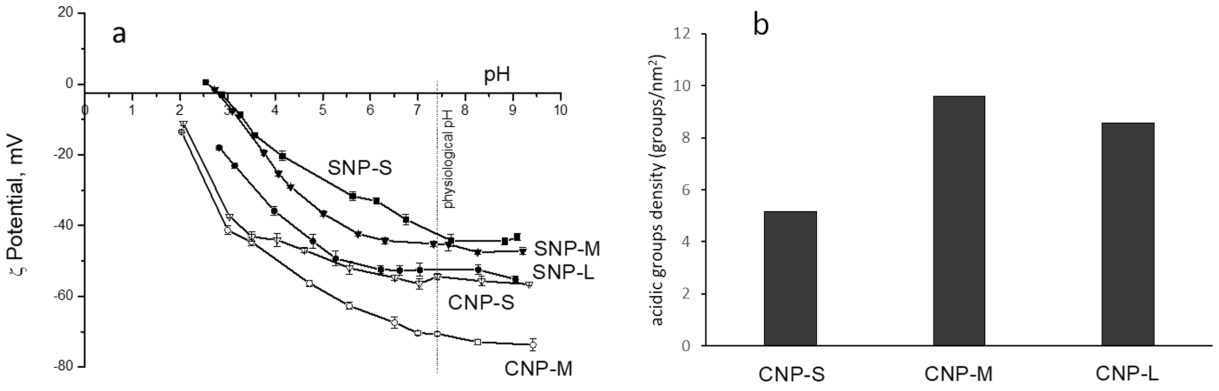

Figure 2: a) Zeta potential versus pH curves for carbon nanoparticles (CNP-M and CNP-S) and silica nanoparticles (SNP-L, SNP-M and SNP-S) suspended in water. b) Density of acid groups exposed at the surface of carbon nanoparticles.

The presence of acidic groups at the surface of CNPs was quantified by titration using the dye thionine acetate [30]. The density values of acidic groups for the CNPs are shown in Figure 2b. The three samples slightly differ in terms of the density of acidic surface groups, with the small NPs having the lowest density in agreement with the observed less negative zeta potential value. The density of the acidic hydroxyl groups for SNPs was not determined here since the value is available in literature [31-33].

Physicochemical and proteomics characterisation of the nanoparticle/hard corona

We then evaluated how the NP physicochemical properties would affect the biomolecular corona formation. For this purpose, we exposed the same surface area of silica and carbon NPs of three different sizes to an increasing concentration of human plasma, from 10% to 80%, to mimic the in vitro and in vivo conditions, respectively. In Figure 3 the we show the SDS-PAGE gels for the small silica and carbon nanoparticles. The corona composition between the two materials has some similarities when incubated at 10% plasma; however, it becomes highly specific to the NP surface properties at higher concentrations as confirmed by the significant difference in the corona composition.

In particular, at 10% of plasma, both NPs preferentially adsorb three gel bands of 72, 60 and 50 kDa, later identified as fibrinogen alpha, beta and gamma chain, respectively. Significant differences were also observed at a lower molecular weight where a gel band of 25 kDa was detected in the silica corona only, while in the carbon NP corona, 3 gel bands formed in the

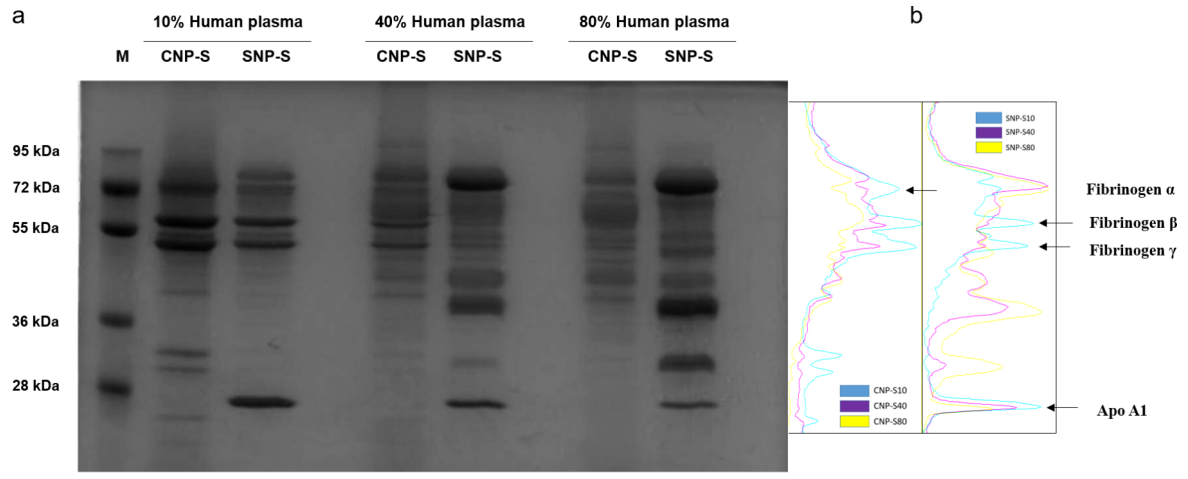

Figure 3: a) SDS-PAGE gel of hard protein corona formed after 1 h of incubation in human plasma. b) Densitometry of the gel bands corresponding to fibrinogen and apolipoprotein A1.

region of 36–30 kDa in addition to a less pronounced band of MW lower than 28 kDa. At higher plasma concentration, the corona composition of the SNP changed significantly where the fibrinogen gel bands were displaced by three predominant bands of 90 kDa and a duplet of 50 kDa, later identified as histidine-rich glycoprotein. These findings are in agreement with a previous study where a similar effect was detected for 200 nm SNPs [26].

Small differences in the protein corona composition of NPs of different sizes were found (Supporting Information File 1, Figure S2), suggesting that the surface curvature plays a minor role. This is only apparently in contrast with a previous study showing more significant differences in the protein corona for NPs of different size [34]. In fact, the size range considered here is even larger than in the referenced study.

Label-free mass spectrometry analysis was used to obtain the semiquantitative protein abundance of the corona across three different plasma concentrations. Notably, the percent of fibrinogen varies greatly across all conditions while remaining an abundant corona binder protein (Figure 4).

A total of 118 proteins were found in the biomolecular corona of small carbon and silica NPs after incubation with human plasma at 10, 40 and 80%. Table 4 contains the top 20 proteins detected in each condition by MS.

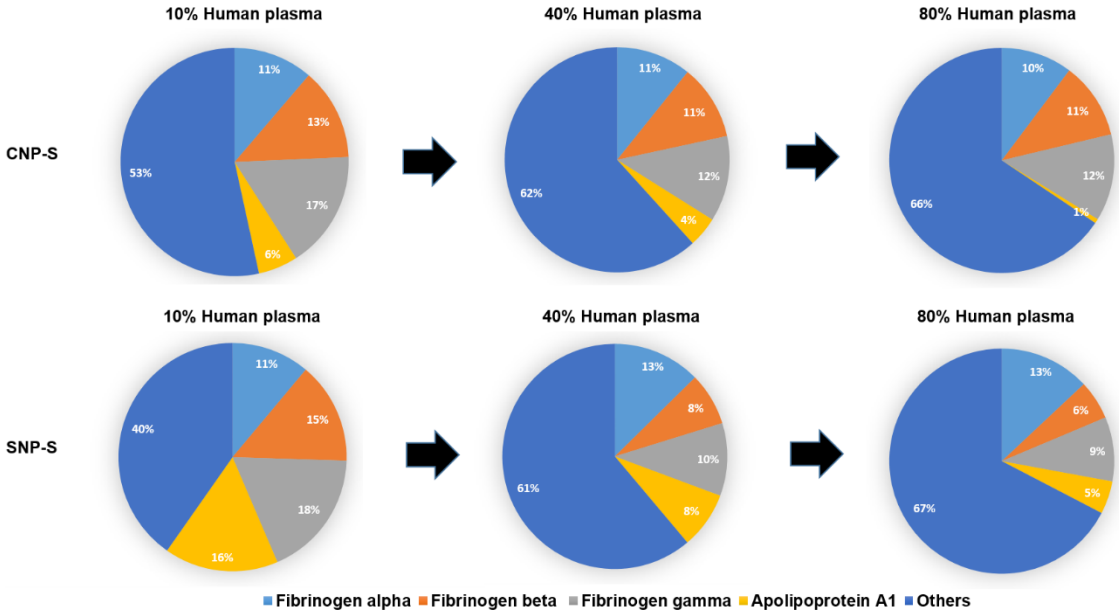

Figure 4: Abundance of fibrinogen and apolipoprotein A1 in silica and carbon nanoparticle corona at different plasma concentrations.

Table 4: Top 20 most abundant proteins in small silica (SNP-S) and carbon (CNP-S) nanoparticle hard corona samples at three different plasma concentrations (10, 40, 80%) based on the LFQ intensity.

Order of abundance	SNP-S			CNP-S		
	10% human plasma	40% human plasma	80% human plasma	10% human plasma	40% human plasma	80% human plasma
1	fibrinogen gamma chain	kininogen-1	kininogen-1	fibrinogen beta chain	fibrinogen beta chain	kininogen-1
2	fibrinogen alpha chain	fibrinogen alpha chain	histidine-rich glycoprotein	fibrinogen alpha chain	fibrinogen gamma chain	fibrinogen alpha chain
3	fibrinogen beta chain	fibrinogen beta chain	kallikrein B	fibrinogen gamma chain	fibrinogen alpha chain	ITIH4 protein
4	apolipoprotein A-I	fibrinogen gamma chain	coagulation factor XI	apolipoprotein B-100	kininogen-1	fibrinogen beta chain

Table 4: Top 20 most abundant proteins in small silica (SNP-S) and carbon (CNP-S) nanoparticle hard corona samples at three different plasma concentrations (10, 40, 80%) based on the LFQ intensity. (continued)

5	kininogen-1	apolipoprotein A-I	plasminogen	histidine-rich glycoprotein	ITIH4 protein	fibrinogen gamma chain
6	apolipoprotein E	histidine-rich glycoprotein	apolipoprotein A-I	kininogen-1	vitronectin	coagulation factor XI
7	histidine-rich glycoprotein	kallikrein B	plasma protease C1 inhibitor	vitronectin	apolipoprotein B-100	vitronectin
8	apolipoprotein B-100	coagulation factor XI	fibrinogen alpha chain	complement C1q	plasma kallikrein	kallikrein B
9	kallikrein B	apolipoprotein E	apolipoprotein B-100	complement component 4B	apolipoprotein E	histidine-rich glycoprotein
10	plasma protease C1 inhibitor	coagulation factor XII	fibrinogen beta chain	complement factor H	complement component 4B	apolipoprotein B-100
11	selenoprotein P	selenoprotein P	fibrinogen gamma chain	apolipoprotein E	coagulation factor XI	apolipoprotein E
12	coagulation factor XII	plasminogen	serum albumin	ITIH4 protein	serum albumin	serum albumin
13	ITIH4 protein	plasma protease C1 inhibitor	ITIH4 protein	serum albumin	complement factor H	complement C3
14	serum albumin	serum albumin	selenoprotein P	complement component 1	complement component 1	Ig gamma-3 chain C region
15	complement C3	ITIH4 protein	apolipoprotein E	complement C3	complement C3	isoform C of Proteoglycan 4
16	plasminogen	Ig gamma-3 chain C region	serine protease inhibitor	kallikrein B	serine protease inhibitor	Ig mu chain C region
17	coagulation factor XI	complement C3	Ig kappa chain C region	apolipoprotein A-I	complement factor H-related protein 1	selenoprotein P
18	isoform C of Fibulin-1	Ig alpha-1 chain C region	Ig gamma-3 chain C region	Ig gamma-3 chain C region	protease C1 inhibitor	serine protease inhibitor
19	apolipoprotein A-II	apolipoprotein A-II	Ig alpha-1 chain C region	Ig mu chain C region	complement C1q	Ig kappa chain C region
20	apolipoprotein C-I	vitronectin	complement C3	coagulation factor XI	Ig gamma-3 chain C region	complement factor H-related protein 1

Venn diagrams (Figure 5) highlight that the majority of the proteins were detected both in the SNP-S and CNP-S at higher plasma concentrations, while a minor overlap occurred at 10%. However, a pronounced difference was observed when we compared the protein abundance by means of the label-free quantification (LFQ) across all conditions (Table 4 and Figure 6).

Protein grouping (Figure 7) confirmed that the coagulation factors are highly enriched in the corona across all conditions although with different percentage (55–75%).

The presence of fibrinogen decreased significantly with increasing plasma concentration (80%) in silica corona, where it was displaced by less abundant proteins that had higher affinity pro-

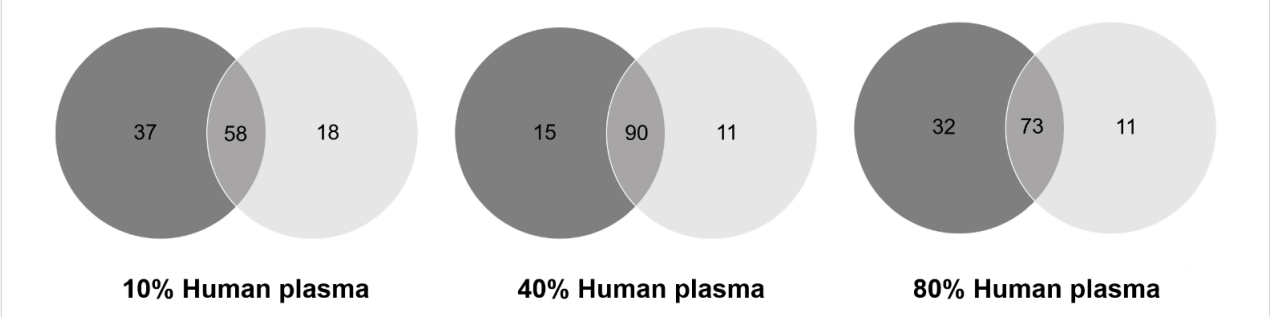

Figure 5: Venn diagrams showing the number of proteins shared by small silica (black) and carbon nanoparticle (grey) protein corona formed at different plasma concentrations.

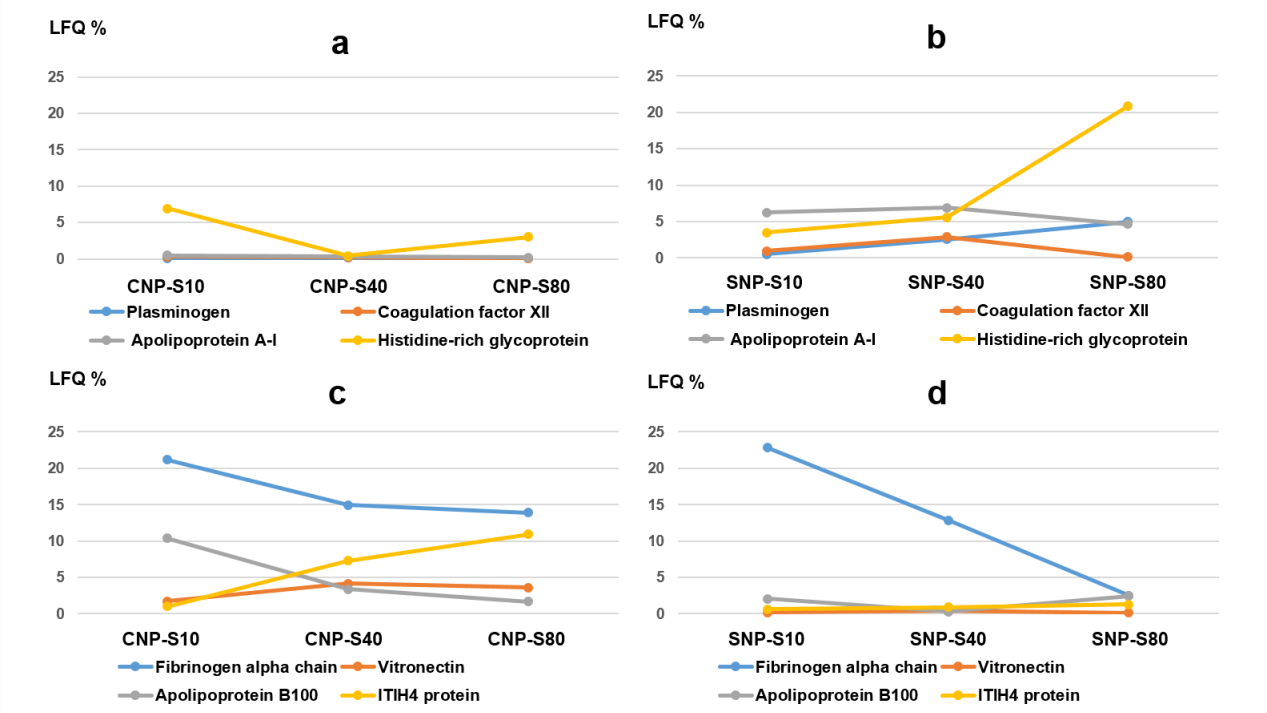

Figure 6: Relative concentration of proteins on small silica (SNP-S) and carbon (CNP-S) nanoparticle coronas at plasma concentrations of 10, 40 and 80%. a–d): semiquantitative protein abundance – comparison between CNP-S and SNP-S coronas. The percentages were calculated based on the total LFQ intensity in each sample.

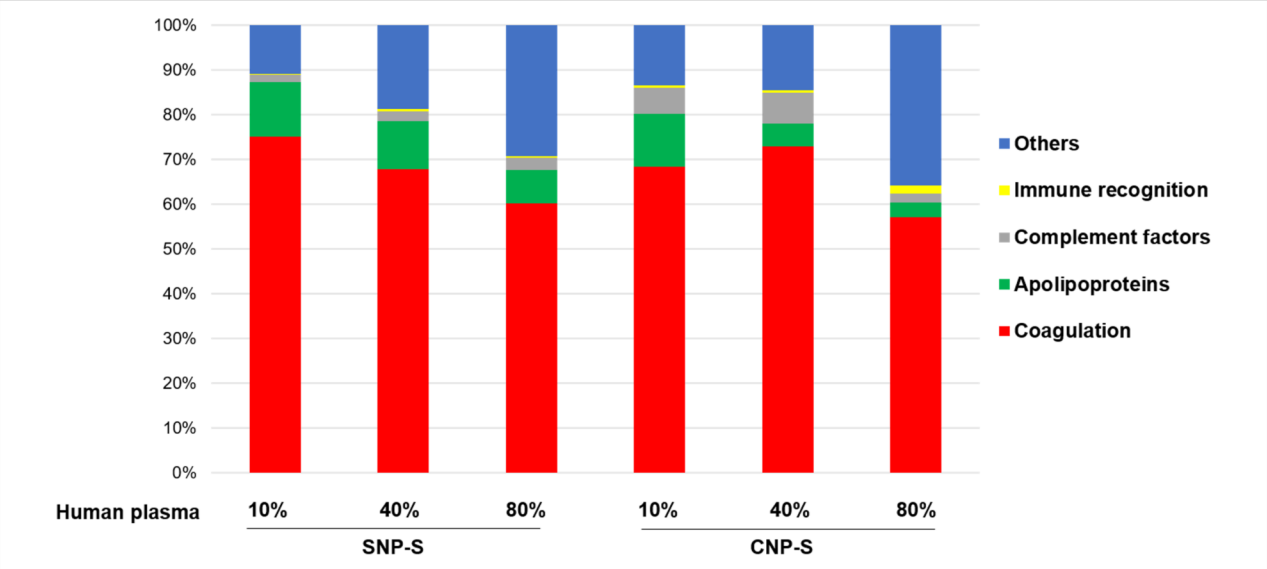

Figure 7: Classification of the human plasma corona proteins identified on small silica (SNP-S) and carbon (CNP-S) nanoparticles according to their biological functions. The LFQ intensity is used to calculate the percentages of protein groups.

teins towards the NP surface, such as histidine-rich glycoprotein, kallikrein B and plasminogen as already shown in the literature [26].

Apolipoprotein A1, a major protein that forms the high-density lipoprotein (HDL), has shown to have a preferential affinity towards silica NPs since it was detected across all conditions. The findings were also in agreement with the SDS-PAGE results where a gel band of 28 kDa was detected only for silica NPs. Other HDL apolipopoproteins including apoA2 and A4 were also more abundant in the silica nanoparticle corona than the carbon one.

In contrast to what was observed for silica, fibrinogen was found to strongly bind to the CNPs also at higher concentrations of plasma. Similarly, ApoB100 and histidine-rich glycoprotein were enriched at 10% plasma, but they were displaced by other proteins such as vitronectin and ITIH4 at higher concentrations of plasma. Interestingly, albumin (66 kDa), the most abundant protein in human plasma, is outside the top 10 proteins identified with MS in all samples, confirming that the composition of the protein corona is independent of the protein original abundance.

In terms of molecular weights, most proteins found in the corona of both nanomaterials are between 20–60 kDa in weight, which accounts for about 70% of proteins (Supporting Information File 1, Figure S3). Around 8% of the total corona proteins have high molecular weights (>150 kDa).

Effect of hard corona on agglomeration

The effect of the protein corona on the tendency of NPs to agglomerate was evaluated. The NP-hard corona complexes were diluted in PBS immediately after the sample preparation and the size distribution was measured by NTA. The mean hydrodynamic diameter of the particles with the protein corona generated at three different plasma concentrations (10, 40 and 80%) is compared in Figure 8 to the mean hydrodynamic diameter of the pristine NPs.

The presence of the hard protein corona induced substantial agglomeration in all CNPs and this effect was particularly enhanced for the protein corona formed in plasma at 10% concentration. By increasing the plasma concentration, the mean hydrodynamic size of the small carbon nanoparticles becomes similar to the NPs without the protein corona. Conversely, large and average size carbon nanoparticles remain highly agglomerated with a mean diameter greater than 1 µm. In the case of silica nanoparticles, no agglomeration was observed for all concentrations of plasma tested.

Platelet aggregation

The effect of the NPs on platelet aggregation was measured using LTA. The NPs were added to platelet-rich plasma (PRP) in the absence or presence of two platelet activators, collagen and ADP.

In Figure 9a,b, we show the percent of platelet aggregation induced by silica and carbon NP samples after 5 min from the ad-

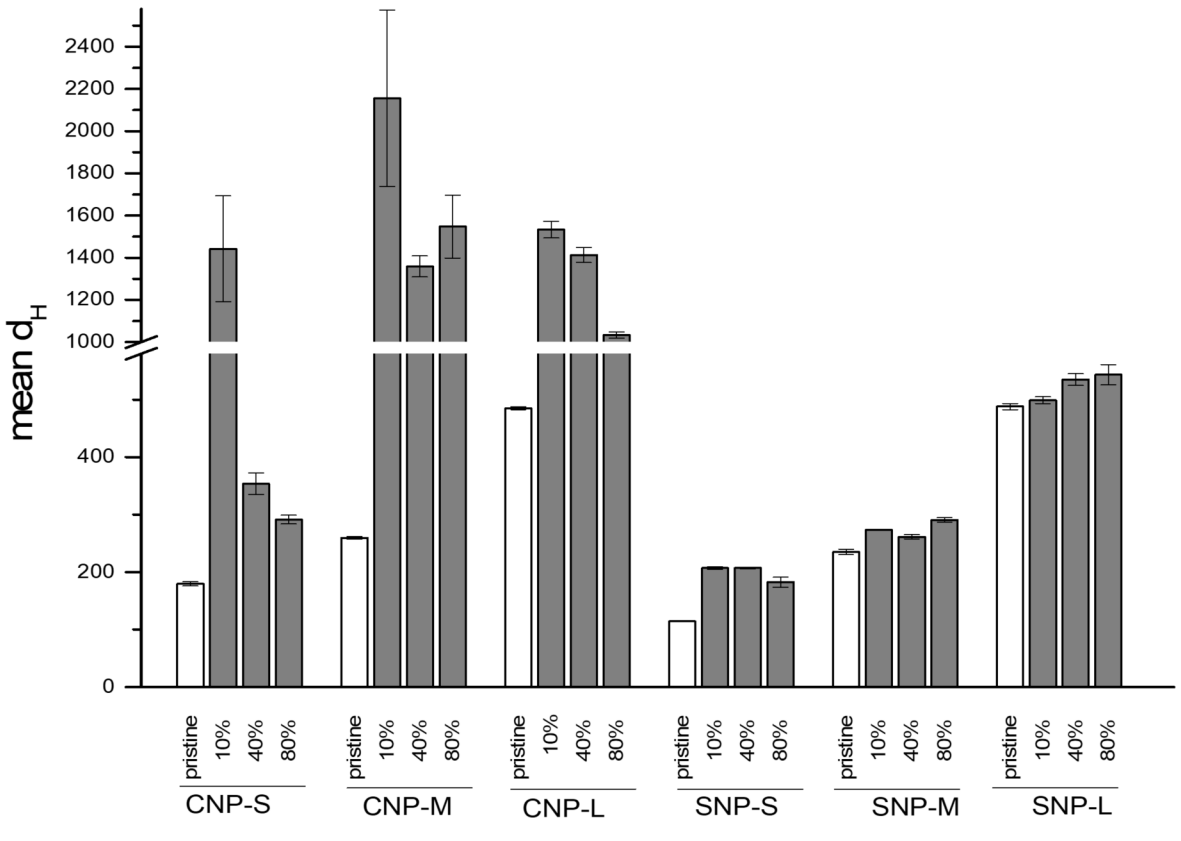

Figure 8: Effect of hard corona formed at different plasma concentrations on nanoparticles agglomeration in water.

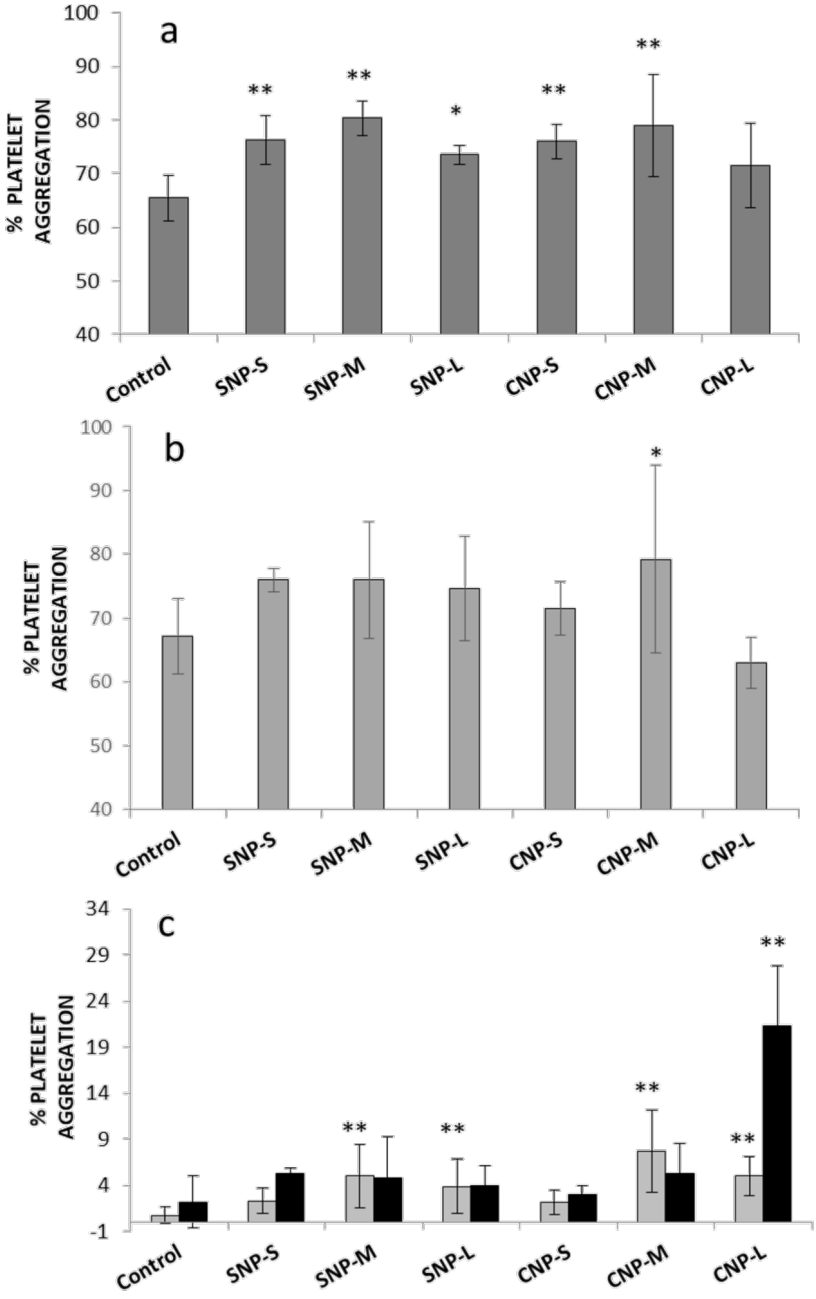

Figure 9: Effect of nanoparticles on platelet aggregation. a) Platelets activated by collagen; b) platelets activated by ADP; c) nonactivated platelets; after 5 (grey bars) and 40 (dark bars) minutes of incubation. ** $p < 0.01$, * $p < 0.05$.

dition of ADP or collagen, which are known agonists for platelet aggregation. When the platelets were activated by collagen, a slight but significant increase in aggregation was observed for all samples. A similar trend was also observed in the presence of ADP as activator, albeit the values did not significantly differ from the control. In the case of medium and large CNPs (CNP-M and CNP-L), a progressive decrease in optical density was observed upon the addition of the NPs (Supporting Information File 1, Figure S4). To monitor this process, the optical density was measured up to 40 min after addition of the NPs in the absence of the activators (Figure 9c, Supporting Information File 1, Figure S5).

Significant aggregation was detected for both silica and carbon medium and large nanoparticles, with a major effect observed for CNP-L. This effect was previously reported by Bihiari and

co-workers for SWCNTs [11] and was attributed to the formation of nanoparticle–platelet aggregates. Note that for large and medium size carbon nanoparticles, black aggregates were clearly visible at the end of the experiments (Supporting Information File 1, Figure S6).

Platelet activation

The activation of platelets by the silica and carbon nanoparticles was evaluated by flow cytometry. Activation was evaluated by using a specific antibody, which binds the antigen CD62P (P-selectin) that is expressed on the surface of activated platelets (Figure 10). No significant activation was detected in the absence of activators. When platelets were activated with ADP, an increase of activation was observed for both silica and carbon nanoparticles of mean size only. This increase was evident, but not statistically significant due to the high variability of the response from one donor to the other.

The intensity of forward scattered (FS) and side scattered (SS) light was also measured to evaluate the size of platelets and the granularity, respectively (Supporting Information File 1, Figure S7). A slight increase of platelet size was observed in the presence of the silica and carbon NPs of medium size. The analysis of the platelet activation by flow cytometry is particularly critical in the presence of particles due to the possible interference in the intensity of scattered light. However, here this is not the case, since particles are clearly visible in the forward scattered (FS) and side scattered (SS) light plot (Supporting Information File 1, Figure S8) as separate populations having a size smaller than platelets, and therefore excluded by the measurement. However, possible interference may derive from aggregates of particles.

Platelet adhesion

Activated platelets are physiologically programmed to adhere to the endothelial wall of damaged blood vessels. The VWF anchored to damaged endothelial cells plays a major role in this process, encouraging platelets to tether, roll and finally adhere at the site of damage. Dynamic platelet function assay (DPFA) was then used to investigate possible interference of the NPs on this process. This well-characterised assay monitors shear-mediated dynamic platelet interactions with surface-immobilised VWF. Adhesion was measured as the total number of platelets adhering to the substrate (Figure 11) in the presence or absence of the NPs.

A size dependent decrease in the number of platelets adhering to the substrate was detected (Figure 11a). Figure 11b shows two representative images of the VWF-coated microfluidic channel captured during the flow run. For CNP-L, large aggregates were observed at the surface of the substrate (circles). These aggregates were not visible for the other samples.

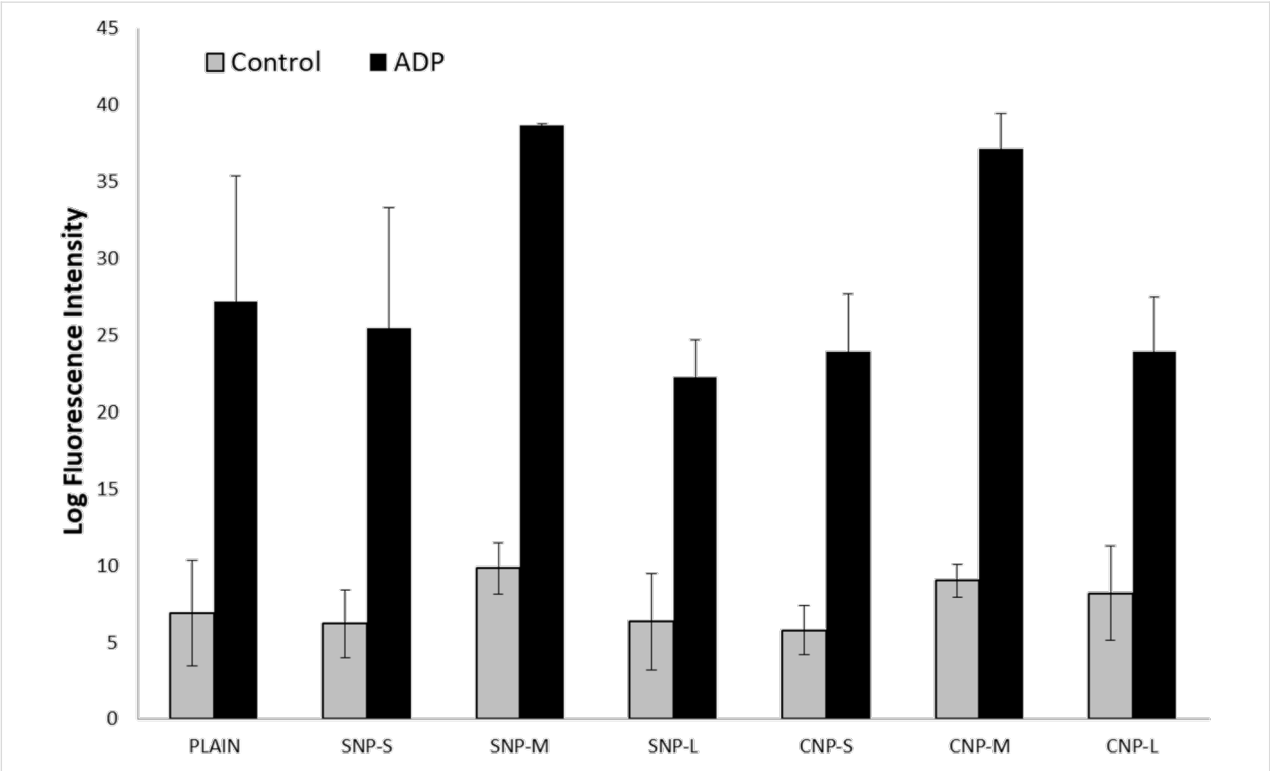

Figure 10: Effect of the nanoparticles on platelet activation measured as secretion of P-selectin.

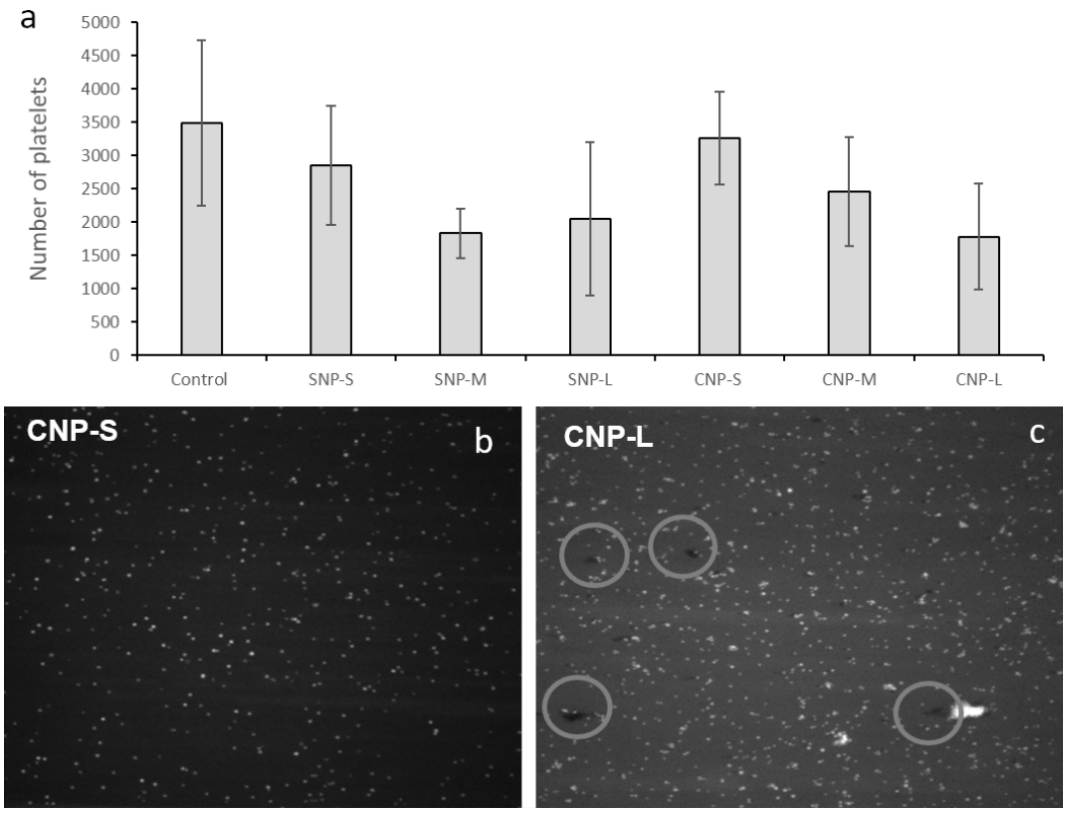

Figure 11: Effect of the nanoparticles on platelet adhesion. a) Total number of platelets adhering to the substrate; b) and c) representative images of the substrate during the measurements for CNP-S and CNP-L, respectively.

Discussion

The identification of the correlations existing among the physical and chemical properties of a substance and the biological effects is a laborious but necessary process, allowing the design of more efficacious and safer medicines. In the case of (nano)biomaterials, this process is more challenging than for molecular substances, due to the higher number of parameters to be controlled. A library of nanomaterials that differs by one single property at time and accurate testing strategies are necessary. This is not always straightforward due to the interdependence between the various chemical and physical properties.

In the present study, two sets of nanoparticles were prepared with the aim to specifically investigate the effect of the surface curvature and surface chemistry on platelet-dependent and independent aggregation, platelet activation and adhesion. Silica and carbon nanoparticles were chosen since both are highly studied for medical applications. Furthermore, being produced by wet methods, the selected nanoparticles have both hydrophilic surfaces and are negatively charged. Their comparison, therefore, excludes surface charge and hydrophilicity as variables to be investigated. In Figure 12 we summarise the strategy used to unravel possible SARs.

This strategy allowed us to identify the surface chemistry as the key factor in the protein corona composition while both surface chemistry and size modulate a platelet-independent aggregation potential of particles in blood.

Platelet aggregation is a complex process modulated by several chemical and physical parameters. Ordinarily platelets circulate in blood in a quiescent state near the endothelial cells lining the blood vessels without forming stable adhesions. After infringement of the vasculature proteins like VWF, collagen and fibronectin are exposed on the sub-endothelial matrix and act as ligands for the platelet surface receptors, such as glycoproteins like GPVI and GPIbα, that lead the platelet adhesion to the affected area [35-37]. These receptor–ligand interactions initiate a cascade of intracellular responses resulting in amplification of platelet activation through the secretion of soluble agonists including thromboxane A2 (TXA2) and ADP. TXA2 and ADP act jointly with the engaged platelet receptors to mobilize intracellular Ca^{2+}, which instigates platelet shape change, degranulation, and up-regulation of the adhesive function of another platelet surface receptor, integrin αIIbβ3 [35]. The active conformation of αIIbβ3 integrin can then bind fibrinogen, VWF and fibronectin with high affinity, allowing haemostatic

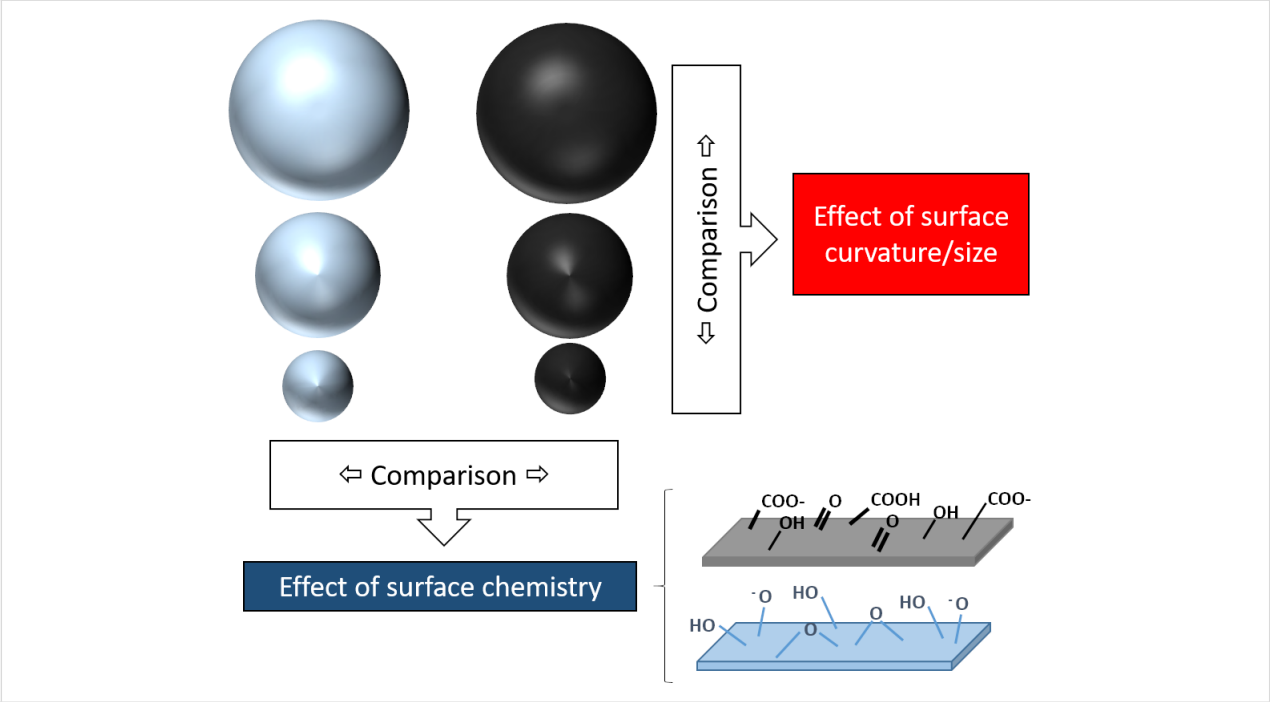

Figure 12: The strategy used to unravel possible structure–activity relationships in the present study.

platelets to aggregate and thrombus formation [38]. Fibrinogen plays a key role in platelet aggregation, forming bridges between platelets and acting as an aggregation glue. On the other hand, fibrinogen also has a key role in NP aggregation. Fibrinogen has a high affinity for surfaces [39], and it is commonly present in the protein layer/corona of several materials [26,40]. On hydrophilic surfaces, this protein tends to be displaced by other proteins by a mechanism known as Vroman's effect [39]. However, in some cases fibrinogen remains bound to the surface and undergoes conformational changes, thus exposing cryptic domains. Platelets may adhere to fibrinogen immobilised onto biomaterials through integrins, a mechanism that may lead to thrombotic events. Furthermore, in the case of NPs, this protein may act as glue in a similar way to that observed with platelets [21], inducing NP aggregation. However, in this case the effect is not due to the interaction with integrin, but it is a non-specific process due to the tendency of fibrinogen to form fibrils similar to fibrin. This tendency is a consequence of the specific fibrinogen arrangement onto surfaces, modulated by the surface properties [23].

Fibrinogen is not the only plasma protein that may be activated by the surface-inducing pro-thrombotic effects. Several studies report the activation by anionic NPs of the coagulation factor XII [17,18], an effect that is modulated by the NP size [41].

Fibrinogen was found in in both SNP-S and CNP-S protein corona, regardless of the NP size, but its presence was particularly enhanced in CNP-S when incubated with highly concentrated plasma. A similar behaviour was already reported for SNPs indicating that the surface area / protein abundance in the biological milieu strongly affects the protein binding to these surfaces [26].

Both SNPs and CNPs interact with plasma proteins forming a protein corona. The presence of the protein corona clearly induced platelet-independent agglomeration of carbon nanoparticles but not for silica (Figure 8). Notably, aggregation was observed for medium size CNPs and large CNP at all plasma concentrations tested, while in the case of small CNPs, aggregation was observed only with 10% of plasma, corresponding to the condition used in in vitro tests, but not in vivo. The latter is in agreement with that recently found on Au nanoparticles by Ho and co-workers [42].

The differences in platelet-independent aggregation behaviour observed among the SNP and CNP might be a consequence of the different composition of the protein corona, or to a different arrangement of protein molecules at the surface, as a consequence of a different ability of the surfaces to interact with the proteins [22]. The affinity of a protein for a certain surface and the mode of interaction rise from the interplay of electrostatic interactions, hydrogen bondings, and hydrophobic forces [32]. Both nanomaterials are negatively charged at physiological pH. However, SNPs exhibit a less negative zeta potential when compared to CNPs of a similar size, likely due to a lower mean

Brönsted acidity of the CNPs surface, being the density of acidic carboxyl/phenolic groups at the carbon surface similar to the expected density of silanols (Si–OH) at a fully hydroxylated surface, i.e., of 4–5 groups/nm^2 [31,32]. Both surfaces exhibit surface sites able to form hydrogen bonds or hydrophobic interaction with proteins. However, such tendency may be different since hydrogen bond formation obeys geometrical constraints due to the directional character of this bond. On the other hand, both silica and carbon surfaces exhibit hydrophobic patches, i.e., siloxane bridges and carbon–carbon bonds, respectively. These moieties have a different nature, exhibiting a higher dipolar character.

Previous studies reported fibrinogen-induced aggregation for silica nanoparticles [23,40]. However, in these studies, pyrogenic silica was used. This material is very different to silica produced by sol–gel methods, being formed by large aggregates and having a surface with a lower degree of hydrophilicity [20]. A different arrangement of the fibrinogen molecule at the surface of silica is therefore likely to occur. In fact, we previously reported that the tendency of fibrinogen to self-assemble to form fibrin-like fibrils increased by decreasing the hydrophilic character of silica [23].

When incubated in the presence of platelets, SNPs induced only mild aggregation (Figure 9). This is in agreement with that previously found on SNPs of similar size [16]. Similarly, CNPs induce mild aggregation only, regardless of the presence of several proteins involved in the coagulation cascade in the hard corona of the NPs. On the other hand, with large carbon nanoparticles, aggregation was observed for a prolonged incubation time. This process does not involve platelet activation and appears related to the ability of particles to act as bridges among platelets, similar to that observed by other authors with other carbon nanomaterials [11,13]. This was confirmed for large nanoparticles (Figure 10), while for medium size particles, platelet activation cannot be excluded.

In light of this evidence, the observed reduction of VWF-mediated adhesion of platelets to the endothelial wall induced by all NPs should be regarded as a consequence of the sequestration of platelets by particles. In fact, this effect is more evident for large particles.

The different aggregation potential of CNPs depending on their size may explain the contrasting data found in the literature on isometric carbon nanoparticles. In fact, secretion of P-selectin in vitro was observed for carbon black [13] but not diesel exhaust particles [11], while platelet aggregation was observed for amorphous CNPs but not for the small-sized fullerenes [10]. Note however that limited information relating to the physicochemical properties of the materials was given in these studies, making a critical analysis of the results difficult. Moreover, while CNTs were reported to induce platelet aggregation [10,11] CNPs did not. This supports the hypothesis by De Paoli Lacerda and co-workers that an elongated shape is necessary for this process [12].

Conclusion

In conclusion, the present study suggests that highly stable and monodispersed NPs may generate aggregates in specific exposing conditions by platelet-independent pathways and stresses the importance of the need to characterise nanomaterials in relevant biological fluids (in this case blood plasma or blood). This result should be regarded with concern, since aggregates might induce vessel occlusion in vivo. However, the reduction of the diameter to less than 100 nm appears to improve the stability of CNPs and possibly their biocompatibility. Further in vivo investigations will be necessary to confirm this hypothesis.

Supporting Information

Supporting Information File 1

Additional figures.
[https://www.beilstein-journals.org/bjnano/content/supplementary/2190-4286-11-44-S1.pdf]

Funding

This project was founded by the European Union's Horizon 2020 Research and Innovation Program "BIORIMA" under grant agreement No. 760928 and Irish Research Council (Enterprise Partnership Scheme project EPSPG/2019/511).

ORCID® iDs

Ludovica Soddu - https://orcid.org/0000-0001-6675-2318
Dermot Kenny - https://orcid.org/0000-0001-5548-3263
Giorgia Bernardini - https://orcid.org/0000-0002-2752-8230
Ida Kokalari - https://orcid.org/0000-0003-0859-1354
Marco P. Monopoli - https://orcid.org/0000-0002-2035-6894
Ivana Fenoglio - https://orcid.org/0000-0002-6946-3105

Preprint

A non-peer-reviewed version of this article has been previously published as a preprint doi:10.3762/bxiv.2019.112.v1

References

1. Coty, J.-B.; Vauthier, C. *J. Controlled Release* **2018,** *275,* 254–268. doi:10.1016/j.jconrel.2018.02.013
2. Khorasani, A. A.; Weaver, J. L.; Salvador-Morales, C. *Int. J. Nanomed.* **2014,** *9,* 5729–5751. doi:10.2147/ijn.s72479

3. Fadeel, B. *J. Intern. Med.* **2013,** *274,* 578–580. doi:10.1111/joim.12137
4. Ilinskaya, A. N.; Dobrovolskaia, M. A. *Nanomedicine (London, U. K.)* **2013,** *8,* 773–784. doi:10.2217/nnm.13.48
5. Deng, Z. J.; Liang, M. T.; Monteiro, M.; Toth, I.; Minchin, R. F. *Nat. Nanotechnol.* **2011,** *6,* 39–44. doi:10.1038/nnano.2010.250
6. Kushida, T.; Saha, K.; Subramani, C.; Nandwana, V.; Rotello, V. M. *Nanoscale* **2014,** *6,* 14484–14487. doi:10.1039/c4nr04128c
7. Dobrovolskaia, M. A.; Patri, A. K.; Simak, J.; Hall, J. B.; Semberova, J.; De Paoli Lacerda, S. H.; McNeil, S. E. *Mol. Pharmaceutics* **2012,** *9,* 382–393. doi:10.1021/mp200463e
8. Jones, C. F.; Campbell, R. A.; Franks, Z.; Gibson, C. C.; Thiagarajan, G.; Vieira-de-Abreu, A.; Sukavaneshvar, S.; Mohammad, S. F.; Li, D. Y.; Ghandehari, H.; Weyrich, A. S.; Brooks, B. D.; Grainger, D. W. *Mol. Pharmaceutics* **2012,** *9,* 1599–1611. doi:10.1021/mp2006054
9. Gubala, V.; Giovannini, G.; Kunc, F.; Monopoli, M. P.; Moore, C. J. *Cancer Nanotechnol.* **2020,** *11,* 1. doi:10.1186/s12645-019-0056-x
10. Semberova, J.; De Paoli Lacerda, S. H.; Simakova, O.; Holada, K.; Gelderman, M. P.; Simak, J. *Nano Lett.* **2009,** *9,* 3312–3317. doi:10.1021/nl901603k
11. Bihari, P.; Holzer, M.; Praetner, M.; Fent, J.; Lerchenberger, M.; Reichel, C. A.; Rehberg, M.; Lakatos, S.; Krombach, F. *Toxicology* **2010,** *269,* 148–154. doi:10.1016/j.tox.2009.08.011
12. De Paoli Lacerda, S. H.; Semberova, J.; Holada, K.; Simakova, O.; Hudson, S. D.; Simak, J. *ACS Nano* **2011,** *5,* 5808–5813. doi:10.1021/nn2015369
13. Holzer, M.; Bihari, P.; Praetner, M.; Uhl, B.; Reichel, C.; Fent, J.; Vippola, M.; Lakatos, S.; Krombach, F. *J. Appl. Toxicol.* **2014,** *34,* 1167–1176. doi:10.1002/jat.2996
14. Khandoga, A.; Stoeger, T.; Khandoga, A. G.; Bihari, P.; Karg, E.; Ettehadieh, D.; Lakatos, S.; Fent, J.; Schulz, H.; Krombach, F. *J. Thromb. Haemostasis* **2010,** *8,* 1632–1640. doi:10.1111/j.1538-7836.2010.03904.x
15. Khandoga, A.; Stampfl, A.; Takenaka, S.; Schulz, H.; Radykewicz, R.; Kreyling, W.; Krombach, F. *Circulation* **2004,** *109,* 1320–1325. doi:10.1161/01.cir.0000118524.62298.e8
16. Corbalan, J. J.; Medina, C.; Jacoby, A.; Malinski, T.; Radomski, M. W. *Int. J. Nanomed.* **2012,** *7,* 631–639. doi:10.2147/ijn.s28293
17. Jiang, L.; Li, Y.; Li, Y.; Guo, C.; Yu, Y.; Zou, Y.; Yang, Y.; Yu, Y.; Duan, J.; Geng, W.; Li, Q.; Sun, Z. *Toxicol. Res. (Cambridge, U. K.)* **2015,** *4,* 1453–1464. doi:10.1039/c5tx00118h
18. Yoshida, T.; Yoshioka, Y.; Morishita, Y.; Aoyama, M.; Tochigi, S.; Hirai, T.; Tanaka, K.; Nagano, K.; Kamada, H.; Tsunoda, S.; Nabeshi, H.; Yoshikawa, T.; Higashisaka, K.; Tsutsumi, Y. *Nanotechnology* **2015,** *26,* 245101. doi:10.1088/0957-4484/26/24/245101
19. Napierska, D.; Thomassen, L. C. J.; Rabolli, V.; Lison, D.; Gonzalez, L.; Kirsch-Volders, M.; Martens, J. A.; Hoet, P. H. *Small* **2009,** *5,* 846–853. doi:10.1002/smll.200800461
20. Gazzano, E.; Ghiazza, M.; Polimeni, M.; Bolis, V.; Fenoglio, I.; Attanasio, A.; Mazzucco, G.; Fubini, B.; Ghigo, G. *Toxicol. Sci.* **2012,** *128,* 158–170. doi:10.1093/toxsci/kfs128
21. Marucco, A.; Gazzano, E.; Ghigo, D.; Enrico, E.; Fenoglio, I. *Nanotoxicology* **2014,** *10,* 1–9. doi:10.3109/17435390.2014.978405
22. Fenoglio, I.; Fubini, B.; Ghibaudi, E. M.; Turci, F. *Adv. Drug Delivery Rev.* **2011,** *63,* 1186–1209. doi:10.1016/j.addr.2011.08.001
23. Marucco, A.; Turci, F.; O'Neill, L.; Byrne, H. J.; Fubini, B.; Fenoglio, I. *J. Colloid Interface Sci.* **2014,** *419,* 86–94. doi:10.1016/j.jcis.2013.12.025
24. Kokalari, I.; Gassino, R.; Giovannozzi, A. M.; Croin, L.; Gazzano, E.; Bergamaschi, E.; Rossi, A. M.; Perrone, G.; Riganti, C.; Ponti, J.; Fenoglio, I. *Free Radical Biol. Med.* **2019,** *134,* 165–176. doi:10.1016/j.freeradbiomed.2019.01.013
25. Stöber, W.; Fink, A.; Bohn, E. *J. Colloid Interface Sci.* **1968,** *26,* 62–69. doi:10.1016/0021-9797(68)90272-5
26. Monopoli, M. P.; Walczyk, D.; Campbell, A.; Elia, G.; Lynch, I.; Baldelli Bombelli, F.; Dawson, K. A. *J. Am. Chem. Soc.* **2011,** *133,* 2525–2534. doi:10.1021/ja107583h
27. Ralph, A.; Somers, M.; Cowman, J.; Voisin, B.; Hogan, E.; Dunne, H.; Dunne, E.; Byrne, B.; Kent, N.; Ricco, A. J.; Kenny, D.; Wong, S. *Cardiovasc. Eng. Tech.* **2016,** *7,* 389–405. doi:10.1007/s13239-016-0282-x
28. Cowman, J.; Richter, L.; Walsh, R.; Keegan, N.; Tinago, W.; Ricco, A. J.; Hennessy, B. T.; Kenny, D.; Dunne, E. *Platelets* **2019,** *30,* 737–742. doi:10.1080/09537104.2018.1513475
29. Dunne, E.; Qi, Q. M.; Shaqfeh, E. S.; O'Sullivan, J. M.; Schoen, I.; Ricco, A. J.; O'Donnell, J. S.; Kenny, D. *Blood* **2019,** *133,* 1371–1377. doi:10.1182/blood-2018-06-855528
30. Pietroiusti, A.; Massimiani, M.; Fenoglio, I.; Colonna, M.; Valentini, F.; Palleschi, G.; Camaioni, A.; Magrini, A.; Siracusa, G.; Bergamaschi, A.; Sgambato, A.; Campagnolo, L. *ACS Nano* **2011,** *5,* 4624–4633. doi:10.1021/nn200372g
31. Iler, R. K. *The Chemistry of Silica;* Wiley and Sons: New York, 1979.
32. Rimola, A.; Costa, D.; Sodupe, M.; Lambert, J.-F.; Ugliengo, P. *Chem. Rev.* **2013,** *113,* 4216–4313. doi:10.1021/cr3003054
33. Ek, S.; Root, A.; Peussa, M.; Niinisto, L. *Thermochim. Acta* **2001,** *379,* 201–212. doi:10.1016/s0040-6031(01)00618-9
34. Lundqvist, M.; Augustsson, C.; Lilja, M.; Lundkvist, K.; Dahlbäck, B.; Linse, S.; Cedervall, T. *PLoS One* **2017,** *12,* e0175871. doi:10.1371/journal.pone.0175871
35. McFadyen, J. D.; Kaplan, Z. S. *Transfus. Med. Rev.* **2015,** *29,* 110–119. doi:10.1016/j.tmrv.2014.11.006
36. Ruggeri, Z. M. *Microcirculation* **2009,** *16,* 58–83. doi:10.1080/10739680802651477
37. Jackson, S. P. *Blood* **2007,** *109,* 5087–5095. doi:10.1182/blood-2006-12-027698
38. McFadyen, J. D.; Jackson, S. P. *Thromb. Haemostasis* **2013,** *110,* 859–867. doi:10.1160/th13-05-0379
39. Vroman, L.; Adams, A. L.; Fischer, G. C.; Munoz, P. C. *Blood* **1980,** *55,* 156–159. doi:10.1182/blood.v55.1.156.156
40. Kendall, M.; Ding, P.; Kendall, K. *Nanotoxicology* **2011,** *5,* 55–65. doi:10.3109/17435390.2010.489724
41. Hao, F.; Liu, Q. S.; Chen, X.; Zhao, X.; Zhou, Q.; Liao, C.; Jiang, G. *ACS Nano* **2019,** *13,* 1990–2003. doi:10.1021/acsnano.8b08471
42. Ho, Y. T.; Azman, N.'A.; Loh, F. W. Y.; Ong, G. K. T.; Engudar, G.; Kriz, S. A.; Kah, J. C. Y. *Bioconjugate Chem.* **2018,** *29,* 3923–3934. doi:10.1021/acs.bioconjchem.8b00743